10 April 2009 | $10

Science

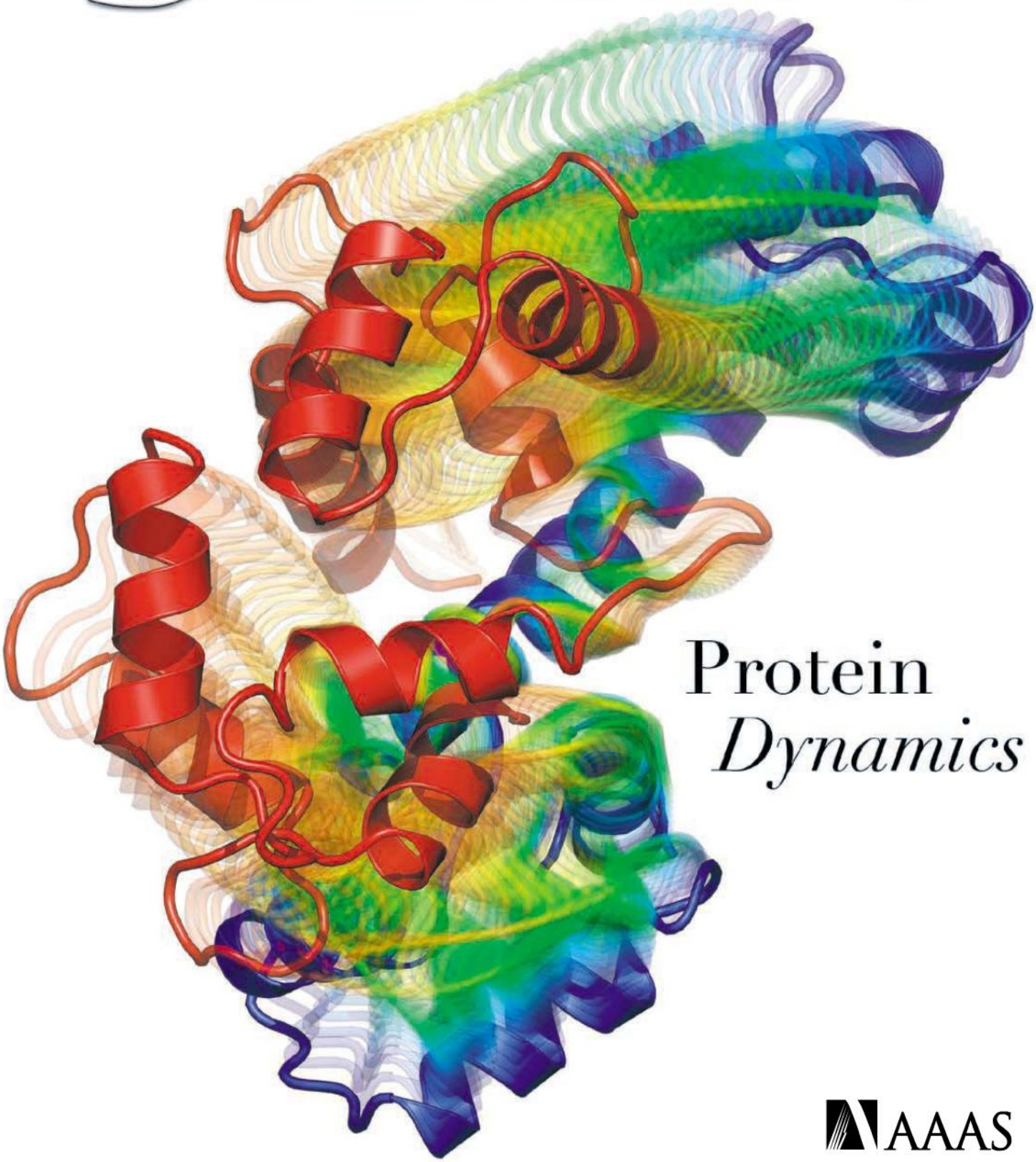

Protein *Dynamics*

AAAS

Affymetrix

Revolutionize life

With a limited view, you're simply left guessing.

With GeneChip® Exon and Gene Arrays, you don't have to guess. Whole-transcript expression arrays allow you to measure the entire transcript, enabling you to detect gene-level expression, exon-level expression, and alternative splicing in a single experiment. Why settle for incomplete results when you can look beyond the 3' end of a gene? Extrapolation can only take you so far—Affymetrix will take you the rest of the way.

See the real biology at www.affymetrix.com/genechip/wtexpression

cell sciences®

www.CytokineCenter.com

www.cellsciences.com

Cytokine Center

Browse our web site with over 1300 proteins, including recombinant cytokines, growth factors, chemokines and neurotrophins. Daily shipping and competitive pricing are offered. Bulk quantities of many proteins available.

PROTEINS

4-1BBL
4-1BB Receptor
6 Ckine
ACAD8
ACAT2
gAcrp30/Adipolean
Activin A
Activin B
ACY1
ADAT1
Adiponectin
ADRP
AITRL
Akt1
Alpha-Feto Protein (AFP)
Alpha-Galactosidase A
Angiopoietin-1 (Ang-1)
Angiopoietin-2 (Ang-2)
Angiostatin K1-3
Annexin-V
apo-SAA
Apoliprotein A-1
Apoliprotein E2
Apoliprotein E3
Apoliprotein E4
APRIL
Artemin
ATF2
Aurora A
Aurora B
BAFF
BAFF Receptor
BCA-1 / BLC / CXCL13
BCMA
BD-1
BD-2
BD-3
BDNF
Betacellulin
Bivalirudin
BMP-2
BMP-4
BMP-6
BMP-7
BMP-13
sBMPR-1A
Brain Natriuretic Protein
BRAK
Breast Tumor Antigen
C5a
C5L2 Peptide
C-10
C-Reactive Protein
C-Src
Calbindin D-9K
Calbindin D-28K
Calbindin D-29K
Calmodulin
Calcitonin Acetate
Carbonic Anhydrase III
Carcino-embryonic Antigen
Cardiotrophin-1
Caspase-3
Caspase-6
CD4
CD14
CD22
CD40 Ligand / TRAP
CD95 / sFas Ligand
CD105 / Endoglin
CHIPS
CNTF
Collagen
CREB
CTACK / CCL27
CTGF
CTGFL / WISP-2
CTLA-4 / Fc
CXCL16
CYR61
Cytokeratin 8
DEP-1
Desmopressin
Disulfide Oxidoreductase
E-selectin
ECGF
EGF
Elafin / SKALP
EMAP-II
ENA-78 / CXCL5
Endostatin
Enteropeptidase
Eotaxin / CCL11
Eotaxin-2
Eotaxin-3 (TSC)
EPHB2
EPHB4
Epigen
Epiregulin
Eptifbatide
Erk-2
Erythropoietin (EPO)
Exodus-2
Fas Ligand
Fas Receptor
FGF-1 (acidic)
FGF-2 (basic)
FGF-4
FGF-5
FGF-6
FGF-7 / KGF
FGF-8
FGF-9
FGF-10
FGF-16
FGF-17
FGF-18
FGF-19
FGF-20
sFGFR-1 (IIIc) / Fc Chimera
sFGFR-2 (IIIc) / Fc Chimera
sFGFR-3 / Fc Chimera
sFGFR-4 / Fc Chimera
sFlt-1 (native)
sFlt-1 (D3)
sFlt-1 (D4)
sFlt-1 (D5)
sFlt-1 (D7)
Flt3-Ligand
sFlt-4
sFlt-4 / Fc Chimera
Follistatin
FSH
Fractalkine / CX3C
G-CSF
α-Galactosidase A
Galectin-1
Galectin-3
Gastrointestinal CA
GCP-2
GDF-3
GDF-9
GDF-11
GDNF
GLP-1
Glucagon
GM-CSF
Goserelin
GPBB
Granzyme B
GROα
GROβ
GROγ
GRO/MGSA
Growth Hormone
Growth Hormone BP
GST-p21/WAF-1
HB-EGF
HCC-1
HGF
Histdyl-tRNA synthetase
Histrelin
HRG1-β1
I-309
I-TAC
IFN-α
IFN-α A
IFN-α 2a
IFN-α 2b
IFN-β
IFN-γ
IFN-Omega
IGF-I
IGF-II
proIGF-II
IGFBP-1
IGFBP-2
IGFBP-3
IGFBP-4
IGFBP-5
IGFBP-6
IGFBP-7
IL-1α
IL-1β
IL-2
IL-3
IL-4
sIL-4 Receptor
IL-5
IL-6
sIL-6 Receptor
IL-7
IL-8 (72 a.a.)
IL-8 (77 a.a.)
IL-9
IL-10
IL-11
IL-12
IL-13
IL-13 analog
IL-15
IL-16 (121 a.a.)
IL-16 (130 a.a.)
IL-17
IL-17B
IL-17D
IL-17E
IL-17F
IL-19
IL-20
IL-21
IL-22
IL-31
Insulin
IP-10
JE
JNK2a1
JNK2a2
KC / CXCL1
KGF
L-asparaginase
LAG-1
LALF Peptide
LAR-PTP
LBP
LC-1
LD-78β
LDH
LEC / NCC-4
Leptin
LIGHT
LIX
LKM
LL-37
Lungkine / CXCL15
Lymphotactin
sLYVE-1
M-CSF
MCP-1 (MCAF)
MCP-2
MCP-3
MCP-4
MCP-5
MDC (67 a.a.)
MDC (69 a.a.)
MDH
MEC
Mek-1
MIA
Midkine
MIG / CXCL9
MIP-1α / CCL3
MIP-1β / CCL4
MIP-3 / CCL23
MIP-3α / CCL20
MIP-3β / CCL19
MIP-4 (PARC) / CCL18
MIP-5 / CCL15
MMP-3
MMP-7
MMP-13
Myostatin
Nanog
NAP-2
Neurturin
NFAT-1
β-NGF
NOGGIN
NOV
NP-1
NT-1/BCSF-3
NT-3
NT-4
Ocreotide
Oncostatin M
Osteoprotegerin (OPG)
OTOR
Oxytocin
p38-α
PAI-1
Parathyroid Hormone
PDGF-AA
PDGF-AB
PDGF-BB
PDGF-CC
Persephin
PF-4
PIGF-1
PIGF-2
PKA α-subunit
PKC-α
PKC-γ
Pleiotrophin
PLGF-1
Polymyxin B (PMB)
PRAS40
PRL-1
PRL-2
PRL-3
Prokineticin-2
Prolactin
Protirelin
PTHrP
PTP1B
PTP-IA2
PTP-MEG2
PTP-PEST
sRANK
sRANKL
RANTES
RELM-α
RELM-β
Resistin
RPTPβ
RPTPγ
RPTPμ
SCF
SCGF-α
SCGF-β
SDF-1α
SDF-1β
Secretin
SF20
SHP-2
STAT1
c-Src
TACI
TARC
TC-PTP
TECK
TFF2
TGF-α
TGF-β1
TGF-β2
TGF-β3
Thymosin α1
sTIE-1/Fc Chimera
sTIE-2/Fc Chimera
TL-1A
TNF-α
TNF-β
sTNF-receptor Type I
sTNF-receptor Type II
TPO
sTRAIL R-1 (DR4)
sTRAIL R-2 (DR5)
TRAIL/Apo2L
TSG
TSH
TSLP
TWEAK
TWEAK Receptor
Urokinase
EG-VEGF
VEGF121
VEGF145
VEGF165
VEGF-C
VEGF-C I125
VEGF-E
HB-VEGF-E
sVEGFR-1
sVEGFR-2
sVEGFR-3
Visfatin
WISP-1
WISP-2
WISP-3
WNT-1

480 Neponset Street, Building 12A, Canton, MA 02021 • TEL (781) 828-0610 • EMAIL info@cellsciences.com

CALL TOLL FREE (888) 769-1246 • FAX (781) 828-0542 • VISIT www.cellsciences.com

Whole Transcriptome Profiling Using the SOLiD™ 3 System

Sequence-based approaches to the study of gene expression have the advantage of querying known as well as previously unknown RNAs in a sample, also termed 'hypothesis-neutral' discovery. The only requirement is being able to make cDNA copies of all of the RNA present in the sample, sequencing them, mapping the sequences back to a reference genome, and deducing the structure using bioinformatic tools. Here, we describe the Whole Transcriptome Library Protocol recently released by Applied Biosystems, which allows the rapid construction of strand-specific libraries from a wide range of RNA species. The easy-to-use, sensitive method uses existing commercial products to clone RNA fragments and sequence the resulting cDNAs using the SOLiD™ 3 System. Applied Biosystems open source and freely available analysis tools also facilitate mapping sequences to a reference, counting each short read mapped to a given site, and identifying exon/exon junctions.

Experimental Considerations in Transcriptome Analysis

Successful whole transcriptome analysis depends on RNA quality and efficient, accurate RNA size fractionation, as this will dictate what sequences are generated. There are currently two approaches available for whole transcriptome libraries. One approach is to start with RNA that has been enriched for polyA RNA or RNAs that have polyA tails. Another approach is to start with total RNA. Total RNA contains all the different species of RNA molecules found in the cell (polyA RNA, ncRNA, rRNA, tRNA, etc.). Because of the abundance of the structural RNAs like rRNA and tRNA, these require depletion prior to deep sequencing. These non-target RNAs represent over 90% of total cellular RNA, depleting them from the pool of RNAs enriches the pool for target RNAs of interest. Using rRNA-depleted RNA for whole transcriptome research allows the study of all non-coding RNAs (ncRNA) in addition to coding RNAs (polyA RNA). Recent studies have shown an abundance of ncRNAs in the cell, which suggests the role they may have in the control of gene expression [1].

MATERIALS AND METHODS

RNA Isolation

Five micrograms of total RNA from the Human Brain Reference RNA (Ambion, P/N AM6050) is used as starting material for whole transcriptome library construction. If the library is to be made from polyA RNA, Poly(A)Purist™ Kits (Ambion, P/N AM1916 or AM1922) have been shown to give high-quality polyA RNA. Ribosomal RNA removal can be accomplished using the RiboMinus™ Eukaryote Kit for RNA-Seq (Invitrogen, P/N A10837-08, or A10838-08 for plants). Approximately 0.5 µg of polyA RNA or rRNA-depleted RNA is needed for making libraries.

Whole Transcriptome RNA Library Preparation

The RNA is randomly fragmented using RNase III (Ambion, P/N AM2290), and 100–200 bp fragments are isolated after gel electrophoresis. The RNA fragments are then converted to cDNA libraries in a strand-specific manner using the **Whole Transcriptome Library Protocol (solid.appliedbiosystems.com).** DNA 'barcodes' can be incorporated into the libraries to allow pooling of multiple samples on a single sequencing run if desired.

SOLiD Sequencing

The cDNA libraries are clonally amplified onto beads by emulsion PCR using standard protocols from the SOLiD System User Manual (solid.appliedbiosystems.com). These beads are enriched and deposited onto the surface of a glass slide for sequencing. Current scientific publications estimate that 40–50 million mappable RNA sequences are needed to detect the maximum number of known transcripts from a library constructed from polyA RNA. This number should be considered as the minimum number of sequences needed for a whole transcriptome experiment. The SOLiD 3 System is capable of sequencing more than 400 million individual reads in a single run.

Analysis

The sequences generated by the SOLiD 3 System can be analyzed using a number of analytical tools. Applied Biosystems has developed the **Applied Biosystems Whole Transcriptome Analysis Pipeline (solidsoftwaretools.com/gf/project/transcriptome/)**, which will allow basic analysis such as mapping sequences to a reference, counting the number of sequences mapped to known RNAs, and identifying both known as well as novel exon/exon junctions. The data output from this pipeline is readily imported to the UC Santa Cruz genome browser for visualization of the results.This tool has been designed to allow additional downstream analysis scripts to be developed for further investigation.

RESULTS

Reproducibility and Dynamic Range

The technical reproducibility of the system was measured by comparing the sequencing results from two independent runs of HBR RNA (Figure 1). As can be seen, a Spearman Rank correlation of >0.98 is obtained and more than 22,000 transcripts are detected. Additionally, the levels of 95% of the transcripts do not vary in the two samples by more than 2.3-fold. Figure 1 shows that the entire system, from library generation to sequencing to data analysis, is highly reproducible. This high reproducibility is critical for comparing different samples and will allow fewer technical replicates to be run. A wide dynamic range is very desirable for any gene expression system. Figure 1 also displays the dynamic range of known transcripts detected in these samples, and in this case it is measured to be between 10^5 and 10^6.

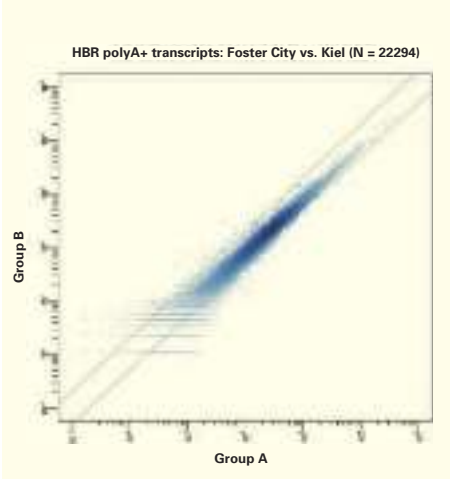

Figure 1. PolyA+ Transcript Level Count Reproducibility Scatterplot. The number of known transcripts identified from HBR RNA was obtained from a library that was sequenced completely independently by two different groups. Transcripts were counted as present calls if 1 or more reads mapped in both data sets. The dynamic range of known transcripts detected in these samples is between 10^5 and 10^6. Green lines indicate 2-fold change, and the blue markers darken with higher density.

Reliable Mapping of Sequences to the Genome and to Known RefSeqs

To assess the ability of the SOLiD System to detect known transcripts, a large number of clones were sequenced and mapped back to the RefSeq database. The number of known transcripts detected was calculated as a function of the number of sequence reads required and plotted in Figure 2. The number of sequence tags per kilobase of transcript length (TPKB) required to map to a RefSeq transcript before the RefSeq is called as 'present' [2] dictates the fraction of RefSeqs that will be detected at any given number of sequences mapped (Figure 2). The more sequences that are required to map to a transcript per unit length, the higher the confidence of accurately measuring the amount of that transcript present in the sample.

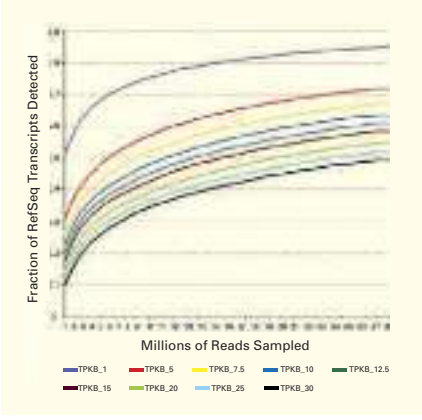

Figure 2. Fraction of known RefSeqs detected in a library prepared from the MAQC UHR RNA sample. The fraction of known RefSeqs begins to plateau as 30 million mappable tags are detected, when 40–45 million mappable sequences are used for analysis. The length of transcript mapped number of sequence tags per kilobase of transcript length (TPKB) is required to map to a RefSeq transcript. It is observed in the graph that as the number of sequence tags mapped per kilobase of RefSeq increases, a smaller fraction of total RefSeqs are detected.

Detection of Known and Novel Exons

Another important feature for whole transcriptome analysis is the ability to analyze all currently annotated exons, as well as novel exons arising from previously unrecognized splice sequences. To achieve this, it is necessary to have uniform coverage across all transcripts, and sufficient coverage to have confidence that the exon has been correctly identified. The large number of unique tags generated by the SOLiD 3 System—greater than 400 million per run—assures high confidence of uniform coverage across the transcriptome.

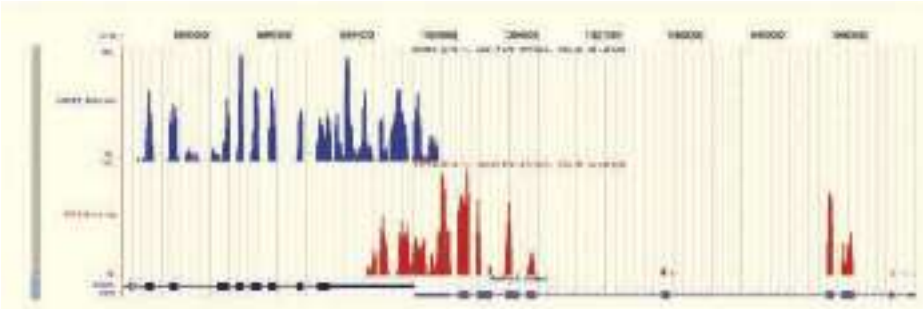

Figure 3. Strand-specific Read Distribution. UCSC genome browser showing a region of the human genome where the 3' ends of two genes overlap. If individual RNA molecules are mapped uniquely to the strand of the DNA from which it was synthesized, the strandedness of the RNA is said to be preserved. It is clear that this is the case with the sequences generated from the two genes. The data also suggest that the current annotation for these genes is not complete, as there are sequences mapping beyond the current exons.

The 50 base reads generated by the SOLiD 3 System allow the Whole Transcriptome Analysis Pipeline tool to unambiguously identify novel exons.

Genomic DNA Strand Specificity

Recent publications using high-throughput sequencing have shown that as many as 6000 known transcripts are also synthesized from the 'antisense' strand of the same DNA region [3]. This work suggests antisense transcription is not the exception, but is common in humans and most likely other higher organisms. Additionally, other types of ncRNAs have been shown to represent a significant fraction of the genome. These transcripts are synthesized from both strands of DNA. Because of the large number of antisense transcripts present, and the need to accurately map ncRNAs, it is important to know which strand of the DNA each RNA transcript maps to [4]. The whole transcriptome system used with the SOLiD System preserves the "strandedness" of the RNA by specific ligation of adapters to either the 5' or 3' ends of the RNA molecules before conversion to double-stranded cDNA (Figure 3). This differs from other methods in which the adapters are ligated to the double-stranded cDNA molecules, or methods that utilize random cDNA priming; with such methods it is not possible to know which strand of the DNA the sequences are mapping to, and therefore it is not possible to know which transcript the sequences were derived from [2].

CONCLUSION

High-throughput sequencing allows scientists to study the complexity of the RNA synthesized in complex genomes. The massively parallel short-read sequencing technology achieved by the SOLiD 3 System is ideally suited for whole transcriptome analysis. The addition of the Applied Biosystems Whole Transcriptome Analysis Kit enables the detection of known and novel RNA molecules as well as the resolution of strand specificity. The Whole Transcriptome Analysis Pipeline allows the data generated to be mapped and viewed easily. This complete system provides a powerful solution for the study of complex transcriptomes.

REFERENCES

1. Huang A (2008) 'Noncoding' RNA Shown to Silence Cancer Suppressor Gene. *The Gazette, Johns Hopkins University,* Vol. ***37*** No. 19.
2. Mortazavi A, Williams BA, McCue K, Schaeffer L, Wold B (2008) Mapping and quantifying mammalian transcriptomes by RNA-Seq. *Nature Methods,* **5(7)**:621–628.
3. He Y, Vogelstein B, Velculescu VE, Papadopoulos N, Kinzler KW (2008) The antisense transcriptomes of human cells. *Science,* 19; **322**(5909):1855–1857.
4. Cloonan N, Grimmond SM (2008) Transcriptome content and dynamics at single-nucleotide resolution. *Genome Biology,* **9**(9):234.
5. Pan Q, Shai O, Lee LJ, Frey BJ, Blencowe BJ (2008) Deep surveying of alternative splicing complexity in the human transcriptome by high-throughput sequencing. *Nature Genetics,* **40**:1413–1415.

Biacore systems

from inspiration ...to publication

Highest quality, information-rich interaction data from Biacore™ systems deepen your understanding of molecular mechanisms and interaction pathways and enable you to add function to structure.

Select the perfect solution for your application and draw conclusions with confidence – from the company that continues to set the standard for label-free protein interaction analysis.

For further information or register to have one of our scientific experts contact you, please visit **www.gelifesciences.com/biacore-science**

Biacore T100
unmatched performance

Biacore X100
ready to run research system

Biacore Flexchip
array-based comparative profiling

imagination at work

SPECIAL SECTION

Protein Dynamics

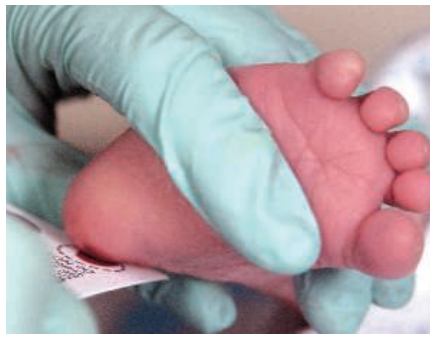

page 166

CONTENTS continued **>>**

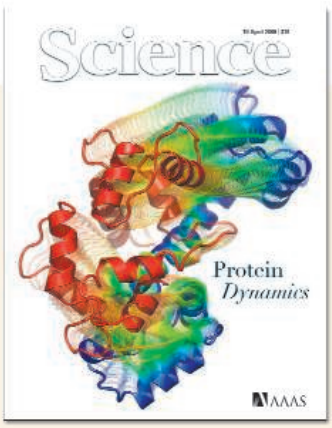

COVER

The dynamic nature of the master calcium signaling protein, calmodulin, schematically illustrated by snapshots from an interpolation between its calcium-bound state (blue) and its structure bound to both calcium and a peptide derived from one of its downstream cellular targets, myosin light chain kinase (red), generated using the Yale Morph Server and PyMol software. See the special section beginning on page 197.

Image: Robert Smock and Lila Gierasch

DEPARTMENTS

Published by AAAS

Team Spirit
What do conductors and beekeepers have in common? Leica Microsystems has mapped its corporate values. For more information, visit our website.

Mr. Hedinger, how do you integrate the user in the team?

According to Andreas Hedinger, engineer and Head of the Industry Division at Leica Microsystems, team spirit needs the strengths of the individual, open doors and ambitious joint goals. These goals can only be attained through the planned integration of users, with direct access to their ideas and needs. They therefore form part of the team and take part in developments: for day-to-day cooperation in a spirit of trust and responsibility.

www.leica-microsystems.com

Living up to Life

Leica
MICROSYSTEMS

BREVIA

RESEARCH ARTICLE

REPORTS

CONTENTS continued **>>**

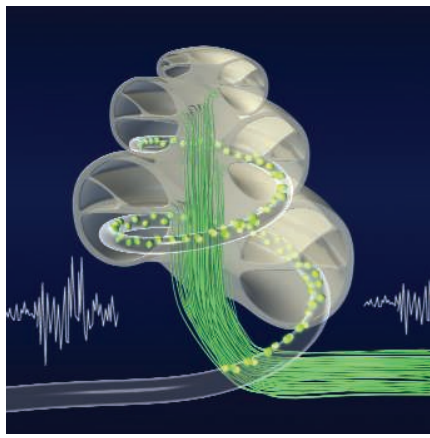

page 185

page 232

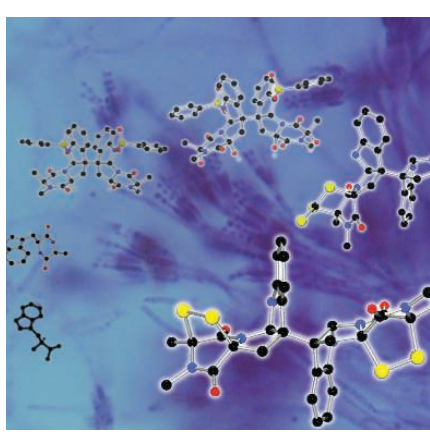

page 238

economicalm.

RESEARCH. TOGETHER.

Panic is unproductive.

Let's get rational. Tough decisions lie ahead as budgets tighten. But discovery will endure. One name has been here for more than 50 years, providing stability, reliability, and quality to researchers like you: Bio-Rad.

From the beginning we have been a stable presence, offering you products that spark your imagination without burning your budget. Because great results should be within your means.

Proceed with caution. But proceed, nonetheless.

You don't have to lose your shirt outfitting your lab.
Quite the opposite, in fact.
Visit www.bio-rad.com/economicalm/
for more information.

To find your local sales office, visit **www.bio-rad.com/contact/**
In the U.S., call toll free at 1-800-4BIORAD (1-800-424-6723)

Visit us at www.bio-rad.com

BIO-RAD

SCIENCEONLINE

SCIENCEXPRESS
www.sciencexpress.org

Two-Color Single-Photon Photoinitiation and Photoinhibition for Subdiffraction Photolithography
T. F. Scott et al.

Polymerization activated by a beam of light was halted by inhibitors generated by a surrounding halo of a different color.
10.1126/science.1167610

Confining Light to Deep Subwavelength Dimensions to Enable Optical Nanopatterning
T. L. Andrew et al.

Molecules that photoisomerize and change in transparency are used to define narrow features on photoresists.
10.1126/science.1167704

Achieving λ/20 Resolution by One-Color Initiation and Deactivation of Polymerization
L. Li et al.

Polymerization activated by a pulsed light beam was halted by a continuous beam of the same color in a surrounding halo.
10.1126/science.1168996

Development of a Second-Generation Antiandrogen for Treatment of Advanced Prostate Cancer
C. Tran et al.

A drug that binds to the androgen receptor acts by disrupting its activity in the cell nucleus.
10.1126/science.1168175
>> News story p. 165

Cell Movements at Hensen's Node Establish Left/Right Asymmetric Gene Expression in the Chick
J. Gros et al.

Asymmetric gene expression is passively set up in the early chick embryo by cell rearrangements.
10.1126/science.1172478

SCIENCENOW
www.sciencenow.org
Highlights From Our Daily News Coverage

Double Amputees Shed Light on Brain's Flexibility
Brain reorganizes itself to accommodate new left and right hands.

Oldest Stone Blades Uncovered
Sophisticated cutting tools predate *Homo sapiens*.

Tropical Parents More Likely to Hear, 'It's a Girl!'
First global study on human sex ratios finds more girls born at warmer latitudes.

SCIENCESIGNALING
www.sciencesignaling.org
The Signal Transduction Knowledge Environment

RESEARCH ARTICLE: Spatiotemporal Patterning During T Cell Activation Is Highly Diverse
K. L. Singleton et al.

The timing and the distribution of signaling intermediates reflects the efficiency and nature of T cell receptor activation.

PERSPECTIVE: Partitioning the Synaptic Landscape—Distinct Microdomains for Spontaneous and Spike-Triggered Neurotransmission
M. A. Sutton and E. M. Schuman

Spontaneous and evoked release of glutamate activates distinct NMDA receptor pools.

PERSPECTIVE: Brx Shines a Light on the Route from Hyperosmolarity to NFAT5
J. Aramburu and C. López-Rodríguez

The guanine nucleotide exchange factor Brx mediates an early event in lymphocytes exposed to osmotic stress.

PERSPECTIVE: Parkinson's Disease—To Live or Die by Autophagy
I. Irrcher and D. S. Park

The autophagic degradation of a neuronal survival factor is inhibited by a protein encoded by a Parkinson's disease–linked gene.

PODCAST
B. D. Manning and A. M. VanHook

The sets of kinases required by different cancer cell lines are highly divergent.

SCIENCECAREERS
www.sciencecareers.org/career_magazine
Free Career Resources for Scientists

Making Room for Research During Residency
K. Hede

Research residencies give physician-scientists time for research during their clinical training.

Financial Crisis Reshaping the Life Sciences Industry
C. Mintz

Layoffs and mergers in life sciences companies make for a challenging job market.

Science Careers Blog
Science *Careers Staff*

Find advice, opinions, news, and funding opportunities at http://blogs.sciencemag.org/sciencecareers/.

SCIENCEPODCAST
www.sciencemag.org/multimedia/podcast
Free Weekly Show

Download the 10 April *Science* Podcast to hear about animal flight dynamics, rebuilding America's ocean ecosystems, genetic screening in newborns, and more.

ORIGINSBLOG
blogs.sciencemag.org/origins
A History of Beginnings

SCIENCEINSIDER
blogs.sciencemag.org/scienceinsider
Science Policy News and Analysis

QUARTERLY AUTHOR INDEX
www.sciencemag.org/feature/data/aindex.dtl

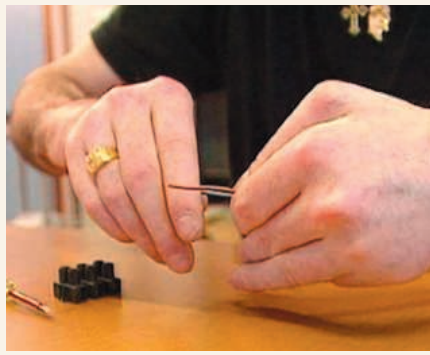

SCIENCENOW
Delicate work after double hand transplant.

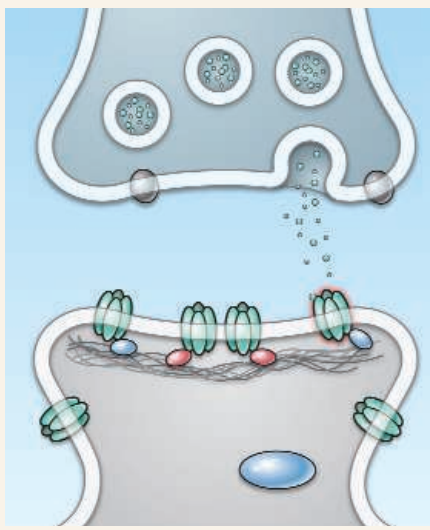

SCIENCESIGNALING
Activating a synaptic microdomain.

SCIENCE (ISSN 0036-8075) is published weekly on Friday, except the last week in December, by the American Association for the Advancement of Science, 1200 New York Avenue, NW, Washington, DC 20005. Periodicals Mail postage (publication No. 484460) paid at Washington, DC, and additional mailing offices. The title SCIENCE is a registered trademark of the AAAS. Domestic individual membership and subscription (51 issues): $146 ($74 allocated to subscription). Domestic institutional subscription (51 issues): $835; Foreign postage extra: Mexico, Caribbean (surface mail) $55; other countries (air assist delivery) $85. First class, airmail, student, and emeritus rates on request. Canadian rates with GST available upon request, GST #1254 88122. Publications Mail Agreement Number 1069624. **Printed in the U.S.A.**

Change of address: Allow 4 weeks, giving old and new addresses and 8-digit account number. **Postmaster:** Send change of address to AAAS, P.O. Box 96178, Washington, DC 20090–6178. **Single-copy sales:** $10.00 current issue, $15.00 back issue prepaid includes surface postage; bulk rates on request. **Authorization to photocopy** material for internal or personal use under circumstances not falling within the fair use provisions of the Copyright Act is granted by AAAS to libraries and other users registered with the Copyright Clearance Center (CCC) Transactional Reporting Service, provided that $20.00 per article is paid directly to CCC, 222 Rosewood Drive, Danvers, MA 01923. The identification code for *Science* is 0036-8075. *Science* is indexed in the *Reader's Guide to Periodical Literature* and in several specialized indexes.

AAAS
ADVANCING SCIENCE, SERVING SOCIETY

CREDITS: (*SCIENCE NOW*) *PNAS*; (*SCIENCE SIGNALING*) CHRIS BICKEL

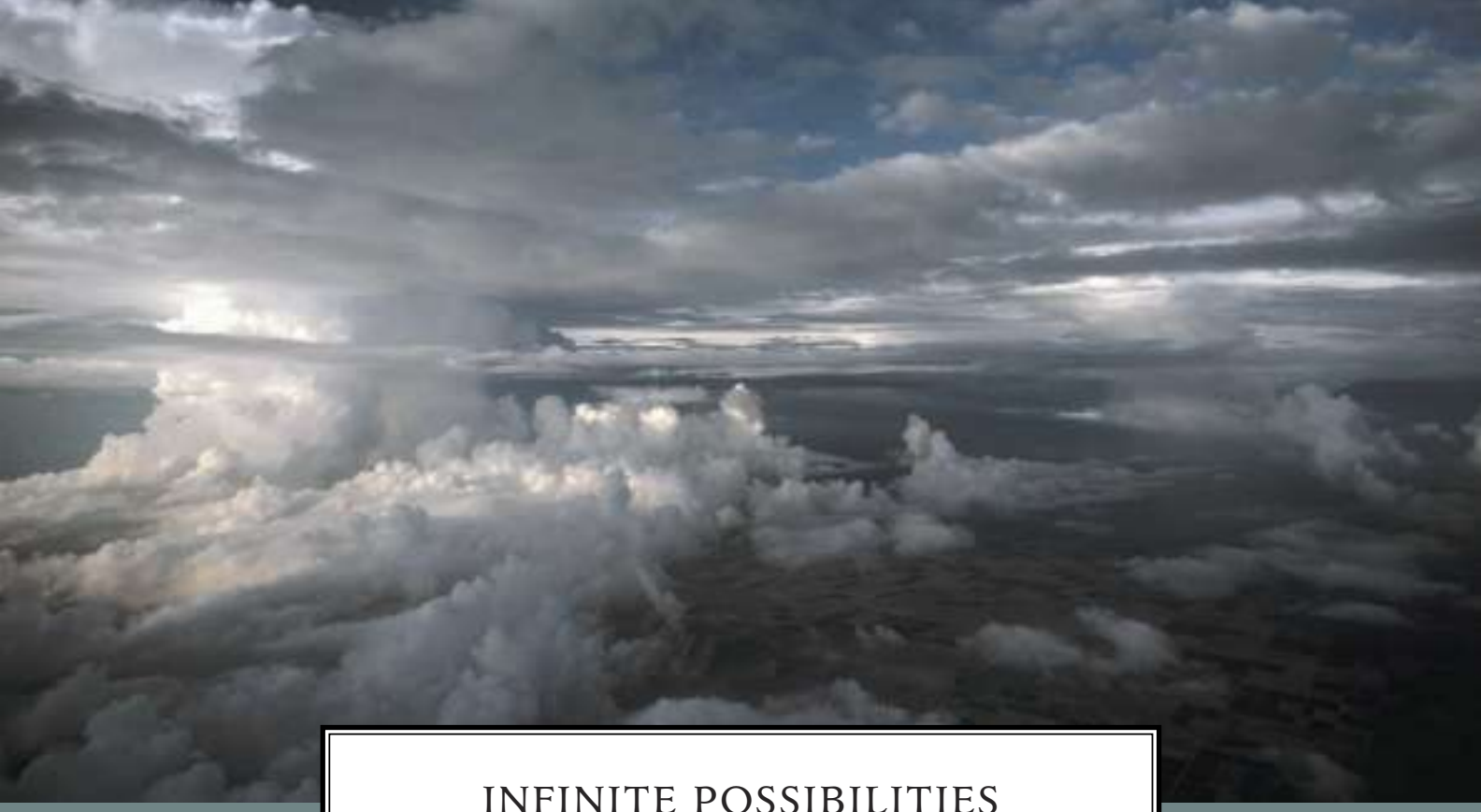

INFINITE POSSIBILITIES

Cellular Imaging & Analysis

NEB introduces SNAP-tag™ and CLIP-tag™ protein labeling systems. These innovative technologies provide simplicity and extraordinary versatility to the imaging of mammalian proteins *in vivo*, and to protein capture experiments *in vitro*. The creation of a single genetic construct generates a fusion protein which, when covalently attached to a variety of fluorophores, biotin, or beads provides a powerful tool for studying the role of proteins in living and fixed cells.

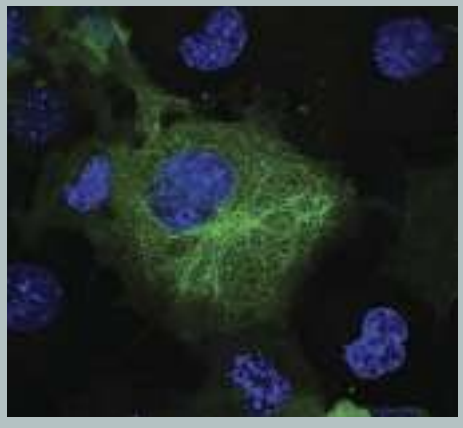

Live COS-7 cells transiently transfected with pSNAPm-Tubulinβ. Cells were labeled with SNAP-Cell TMR-Star (green pseudocolor) for 30 minutes and counterstained with Hoechst 33342 (blue) for nuclei.

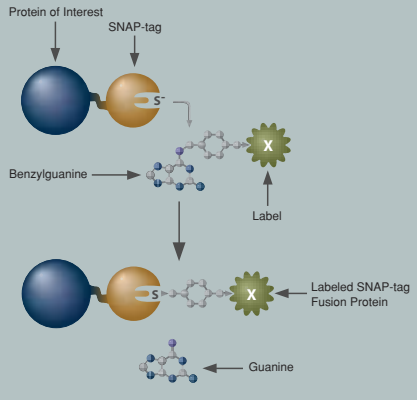

SNAP-tag Technology: *SNAP-tag (gold) fused to the protein of interest (blue) self labels releasing guanine.*

Advantages:

Versatile - Compatible systems enable dual labeling

Flexible - Multiple fluorophores allow for choice & flexibility

Innovative - A range of applications is possible with a single construct

NEW ENGLAND BioLabs® Inc.

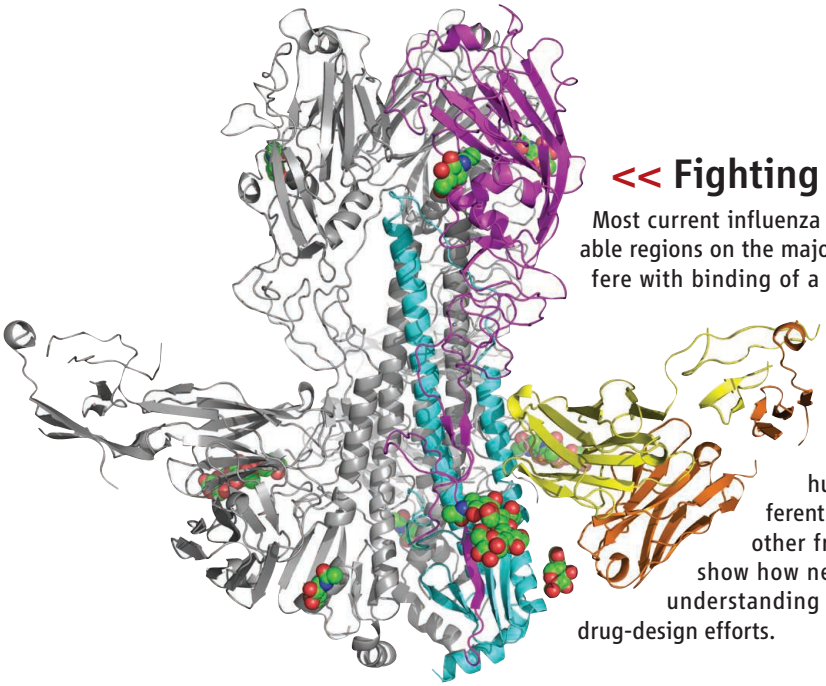

<< Fighting Flu

Most current influenza vaccines elicit antibodies that target hypervariable regions on the major surface antigen hemagglutinin (HA) and interfere with binding of a specific flu strain to host cells. Recently, more broadly neutralizing antibodies have been described that raise the hope of designing more general therapies. Now **Ekiert *et al.*** (p. 246, published online 26 February) have determined crystal structures of the antigen-binding region of the broadly neutralizing human antibody CR6261 in complex with two different HAs, one from the 1918 influenza virus and the other from H5N1 avian influenza virus. The structures show how neutralization is achieved. This molecular-level understanding of the binding epitope will guide vaccine and drug-design efforts.

Tallying Translation

Messenger RNA (mRNA) abundance measurements by microarrays and, more recently, by deep sequencing have had dramatic impact on diverse areas of biology. By far the most common use of such mRNA abundance measurements is to provide an estimate of which proteins a cell is making. However, because cells use many translational control mechanisms, mRNA measurements are an imperfect proxy for protein synthesis. **Ingolia *et al.*** (p. 218, published online 12 February; see 13 February news story by **Service**) now present a technique for measuring translation by deep sequencing of the mRNA fragments occupied by ribosomes in living cells. This approach, ribosome profiling, allows the quantification of translation with high precision. The ribosome profiling strategy is simple, comprehensive, and can be adapted easily to other organisms.

Bending Light in Air

When ultra-intense laser pulses are shot into a dielectric, a plasma can be created with the light ionizing a channel as it travels. Under the right conditions, the light pulses can be self-focused, creating a "light bullet." Propagating in air, this effect has been used to control lightning. So far, the trigger pulses used have resulted in the generation of plasma channels and filaments that propagate in a straight line as, perhaps, you would expect from light. Using structured light (or Airy) beams, **Polynkin *et al.*** (p. 229; see the Perspective by **Kasparian and Wolf**) show that the nonlinear optical effects at such high intensities can generate filaments that split from the main plasma channel, effectively sending the light bullets around bends. Possible applications of this technology include remote sensing or in the study of intense laser beams.

Solomon Island Quake

On 1 April 2007, a large magnitude 8 earthquake ruptured across a complex plate boundary in the South Pacific, revealing the dynamics of the boundary and more broadly, how strain is accommodated in the colliding plates. **Furlong *et al.*** (p. 226) describe how the earthquake ruptured where two plates containing very young oceanic crust are subducting beneath the overriding Pacific plates in two directions. Thus subduction of young crust can produce great earthquakes. Furthermore the dynamics of uplift associated with the quake implies that most of the strain before the quake was accommodated in the overriding plates.

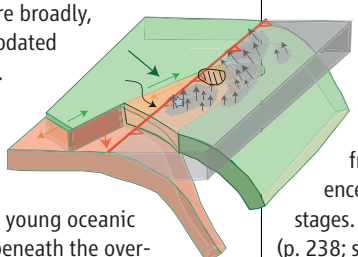

Gallium Droplet Micro-Movers

The spontaneous motion of particles, such as Robert Brown's observation of dancing pollen particles, has long been a topic of fascination and interest. In the evaporation of arsenic from a gallium arsenide surface, gallium droplets can form and migrate. **Tersoff *et al.*** (p. 236) monitored the motion of the Ga droplets as they moved back and forth during the evaporation of hundreds of surface layers. While one might expect the droplet velocity to increase with increasing temperature, instead the authors observed a temperature at which the motion of the droplets would cease, with an increase in velocity both above and below this temperature. The motion results from the interplay between surface evaporation effects and the motion of the droplets, which prevent the evaporation of the regions they are covering.

Fourfold Oxidation

Biosynthetic pathways often rely on enzymes to append hydroxyl and thiol groups in specific locations on an already-assembled complex molecular framework, thereby preventing interference from these reactive groups at earlier stages. Inspired by this propensity, **Kim *et al.*** (p. 238; see the Perspective by **Miller**) adopted an analogous strategy in chemical synthesis of the fungal metabolite (+)-11,11′-dideoxyverticillin A, a dimer of alanine-tryptophan dipeptide derivatives with a sensitive bridging disulfide motif. The authors prepared the dimer framework first, and then relied on its stereochemistry to direct the simultaneous introduction of four OH groups using an experimentally optimized oxidant. The next step stereoselectively replaced all four hydroxyls with sulfur, yielding an intermediate that was easily oxidized to the final product. The efficient 10-step synthesis yielded sufficient product for crystallographic characterization.

Regulated Responses to Irregular Signals

Experiments on the effects of hormones or cytokines often compare responses of cells

Continued on page 145

CREDITS (TOP TO BOTTOM): EKIERT *ET AL.*; FURLONG *ET AL.*

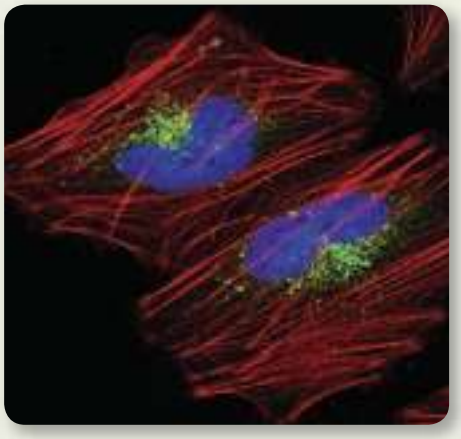

*Confocal immunofluorescent analysis of HeLa cells using **RagC Antibody #3360** (green). Actin filaments have been labeled with DY-554 phalloidin (red). Blue pseudocolor = DRAQ5™ (fluorescent DNA dye).*

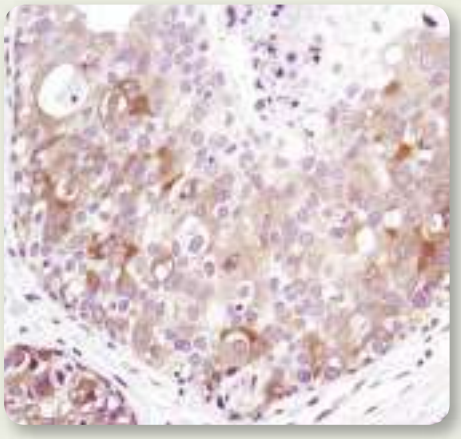

*Immunohistochemical analysis of paraffin-embedded human breast carcinoma using **Phospho-PRAS40 (Thr246) (C77D7) Rabbit mAb #2997.***

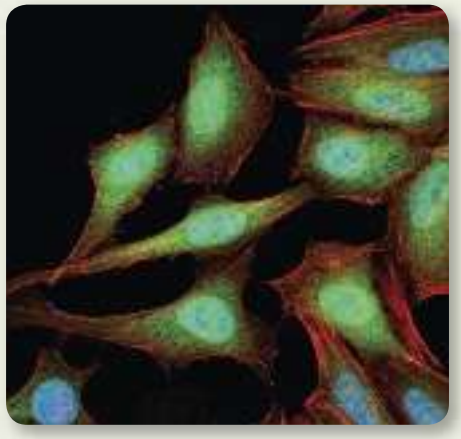

*Confocal immunofluorescent analysis of HeLa cells using **4E-BP1 (53H11) Rabbit mAb #9644** (green). Actin filaments have been labeled with Alexa Fluor® 555 phalloidin (red). Blue pseudocolor = DRAQ5™ (fluorescent DNA dye).*

Cutting-edge

mTOR Signaling Antibodies

...from Cell Signaling Technology®

Unparalleled product quality, validation and technical support.

:: Innovative products from Cell Signaling Technology offer unsurpassed sensitivity, specificity and performance.

:: Extensive in-house validation means that optimization is not left up to you, the user.

:: Technical support provided by the same scientists who produce and validate the antibodies — this translates into a thorough, fast and accurate response.

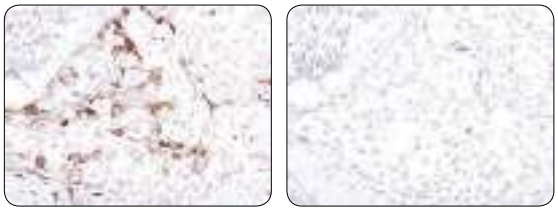

*Immunohistochemical analysis of paraffin-embedded human breast carcinoma using **Phospho-S6 Ribosomal Protein (Ser235/236) (D57.2.2E) Rabbit mAb #4858** in the presence of control peptide (left) or Phospho-S6 Ribosomal Protein (Ser235/236) Blocking Peptide #1220 (right).*

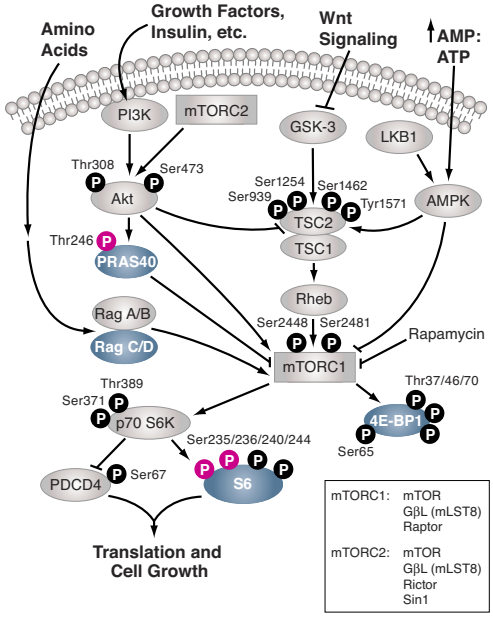

Antibodies against all of the targets in this pathway are available from Cell Signaling Technology.

for the most up-to-date product listing visit:

www.cellsignal.com

Cell Signaling TECHNOLOGY®

Orders (toll-free) 1-877-616-2355 | **Technical support** (toll-free) 1-877-678-8324 support@cellsignal.com | **Inquiries** info@cellsignal.com | **Environmental Commitment** eco.cellsignal.com

Continued from page 143

incubated in the presence or absence of the activating compound. But in vivo, cells experience variations in the amount of stimulus that may be irregular or pulsatile. **Ashall *et al.*** (p. 242) explored the response of the transcription factor NF-κB (a major mediator of transcriptional responses in immune function) to short pulses of exposure to the cytokine tumor necrosis factor–α (TNFα). Oscillations in the movement of the transcription factor into and out of the nucleus could be synchronized by exposure of cells to pulses of TNFα. Furthermore, whether transcription of particular genes was activated or not, depended on the frequency of stimulation and consequent timing of NFκB translocation. Cells in inflammatory tissues may experience similar changes in stimulation by TNFα, and thus respond in distinct ways, depending on the timing of the signals received in the cells.

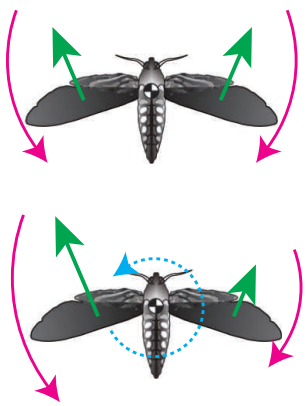

Flight Plan

To fly with precision, flying animals need to be able to maneuver and stabilize their course and orientation immediately following a change of direction. However, the dynamics of turning are poorly understood. **Hedrick *et al.*** (p. 252; see the Perspective by **Tobalske**) develop a framework for predicting maneuverability and stability in flying animals, then use it to predict turning dynamics of seven very different flying animals (including insects, bats, and birds). Geometrically similar animals have turning dynamics in ''wingbeat time'' regardless of size; fruit flies and hummingbirds both require the same number of wingbeats to finish a turn. An increase in wingbeat frequency allows animals to enhance both maneuverability and stability, two properties previously thought to be in opposition.

Synonymous, Not the Same

The genetic code is redundant—many of the 20 common amino acids can be coded for by more than one codon, known as synonymous codons—which means that different DNA sequences can code for the same protein sequence. Synonymous codon usage has been thought to be determined by the abundances of iso-accepting transfer RNAs, which can play an important role in either increasing the efficiency or the accuracy of protein synthesis by the ribosome. To test this idea, **Kudla *et al.*** (p. 255) created 154 synonymous variants of the green fluorescent protein gene. Rather than synonymous codon usage playing a dominant role in overall translational efficiency, instead, the secondary structure of the messenger RNA, especially at its 5′-end, was most critical. Thus, with regard to protein synthesis, initiation of translation rather than elongation, is limiting for gene expression.

Mosquito Immune Mediation

Mosquitoes are vectors of numerous human and animal diseases, including malaria. Approaches that enhance or otherwise alter the natural defense mechanisms of mosquitoes could help to reduce or eliminate their competence as vectors of disease. Proteins containing leucine-rich repeats (LRIM1 and APL1C) are known to mediate immune responses in the mosquito, *Anopheles gambiae,* against the malaria parasite, *Plasmodium berghei*. **Povelones *et al.*** (p. 258, published online 5 March) used gene silencing to show that these proteins produce an immune cascade together with a complement-like protein, binding to the surface of the parasite targeting it for destruction. LRIM1 and APL1C are members of an extensive family of secreted leucine-rich repeat containing proteins that are unique to mosquitoes.

The Enzymology of Brain Cancer

Many human gliomas (a type of brain tumor) harbor somatic mutations in two genes encoding isocitrate dehydrogenases (IDHs). By structural modeling and biochemical analyses, **Zhao *et al.*** (p. 261; see the Perspective by **Pollard and Ratcliffe**) show that tumor-associated mutations in IDH1 lead to a loss of enzyme activity in a dominant manner through the formation of catalytically inactive heterodimers. Expression of mutant IDH1 reduces formation of the enzyme product, α-ketoglutarate, and enhances the expression of hypoxia-inducible factor–1α (HIF-1α), a subunit of a transcription factor that helps cells to survive and grow when oxygen levels are low. Thus, the *IDH1* gene is likely to function as a tumor suppressor that, when inactivated by mutation, facilitates tumor growth through effects on the HIF-1 pathway.

CREDIT: HEDRICK *ET AL.*

Published by AAAS

www.roche-applied-science.com

Genome Sequencer FLX System

Introducing the GS FLX Titanium Reagents

Length Really Matters

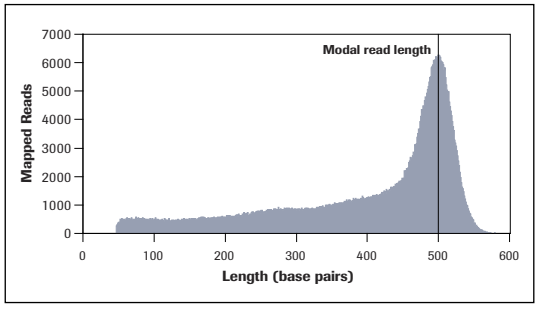

Example Read Length Distribution of 629,643 reads from *E. coli* K-12 (Genome size ~4.5 Mb) with a modal read length of 504 bases.

- Obtain sequencing read lengths of 400 to 500 bases.
- Generate more than 1 million sequencing reads per 10-hour instrument run.
- Improve performance by using GS FLX Titanium series reagents – without instrument upgrades.
- Accelerate the pace of discovery with easy-to-use analysis tools for straightforward interpretation of data and biologically meaningful results.

Performance, Results, Impact

Learn more at ***www.genome-sequencing.com***

454 LIFE SCIENCES

Roche Diagnostics GmbH
Roche Applied Science
68298 Mannheim, Germany

Roche

Neal Lane is the Malcolm Gillis University Professor and Senior Fellow of the James A. Baker III Institute for Public Policy at Rice University in Houston, TX.

Helping the President

PRESIDENT OBAMA'S EARLY STRONG STATEMENTS ABOUT SCIENCE, UNDERSCORED BY THE outstanding team of scientific experts he has assembled and big bucks in the stimulus package, have been a breath of fresh air. Understandably, there is some temptation to rest easy and not worry about happenings in Washington, comforted by the thought that U.S. science and science policy are in good hands. This would be a huge mistake.

Let me offer a few brief comments from the perspective of a former science adviser to President Clinton, who also understood the importance of science. I don't presume to tell the new science adviser, John Holdren, how to do his job. Rather, I want to share a few lessons I learned that might shed some light on the environment in which the science adviser operates, and suggest how the scientific community can be helpful in forging a strong science agenda for the nation.

First, the matters that consume most of the president's time include immediate crises (the economy), security threats, foreign policy, health care, education, energy, climate change, and the environment. Science is important to these but rarely urgent. Second, all of the president's senior advisers have the president's ear, so providing advice to the president means reaching these senior aides—including the Chief of Staff, director of the Office of Management and Budget (OMB), National Economic Advisor, Domestic Policy Advisor, National Security Advisor, and White House czars, among others—and building consensus among them on science and technology issues. Third, the science adviser cannot be seen as a representative of the science community. Rather, the adviser must focus on providing the president with the best confidential advice on scientific and technical matters and evidence-based policy options.

One of the greatest challenges a science adviser faces is motivating federal agencies to open their silo doors and work together on behalf of the president's priorities, which are usually larger than a single agency. Interagency cooperation is difficult in large part because of Congress, where appropriations subcommittees wield enormous influence over how agencies spend money. Here, the science adviser can make use of the National Science and Technology Council (NSTC), which is chaired by the president and includes the vice president, director of the Office of Science Technology and Policy, and heads of OMB and most of the federal agencies. The NSTC deals with issues that cut across many federal agencies, such as high-performance computing and information technology, emerging technologies, energy, and climate change. If the president wishes to consider a new initiative, an assessment of the nation's current situation and future opportunities is carried out by a working group that includes experts from all the relevant agencies, who are in touch with the research community. Once the report is approved by the NSTC principals, the president can decide whether to support the recommendations in the next budget request. This is how the National Nanotechnology Initiative was developed in the Clinton administration. Congress recognizes the importance of the NSTC.

For President Obama's science agenda to succeed, he and Holdren will need the scientific community's best ideas, active participation, and widened involvement with the public—most specifically with Congress. Congress needs to hear from the various disciplines and sectors of our diverse research community. And this community must speak with one voice on fundamental issues of policy such as education, underrepresentation and the workforce, research funding and accountability, the challenges to early-career researchers, government regulation, and scientific integrity.

One way of accomplishing such a goal is for the leading science, mathematics, engineering, and biomedical research societies to work together to make this effort a top priority. Perhaps the American Association for the Advancement of Science could get this started, inasmuch as it includes all of these disciplines. It would take considerable leadership to pull this off, but the politicians would be speechless and the positive impact could be enormous. The world's economic crisis makes it difficult for nations to focus on long-term investments. It is up to the scientific community in each nation to keep these issues front and center. **– Neal Lane**

10.1126/science.1174364

Published by AAAS

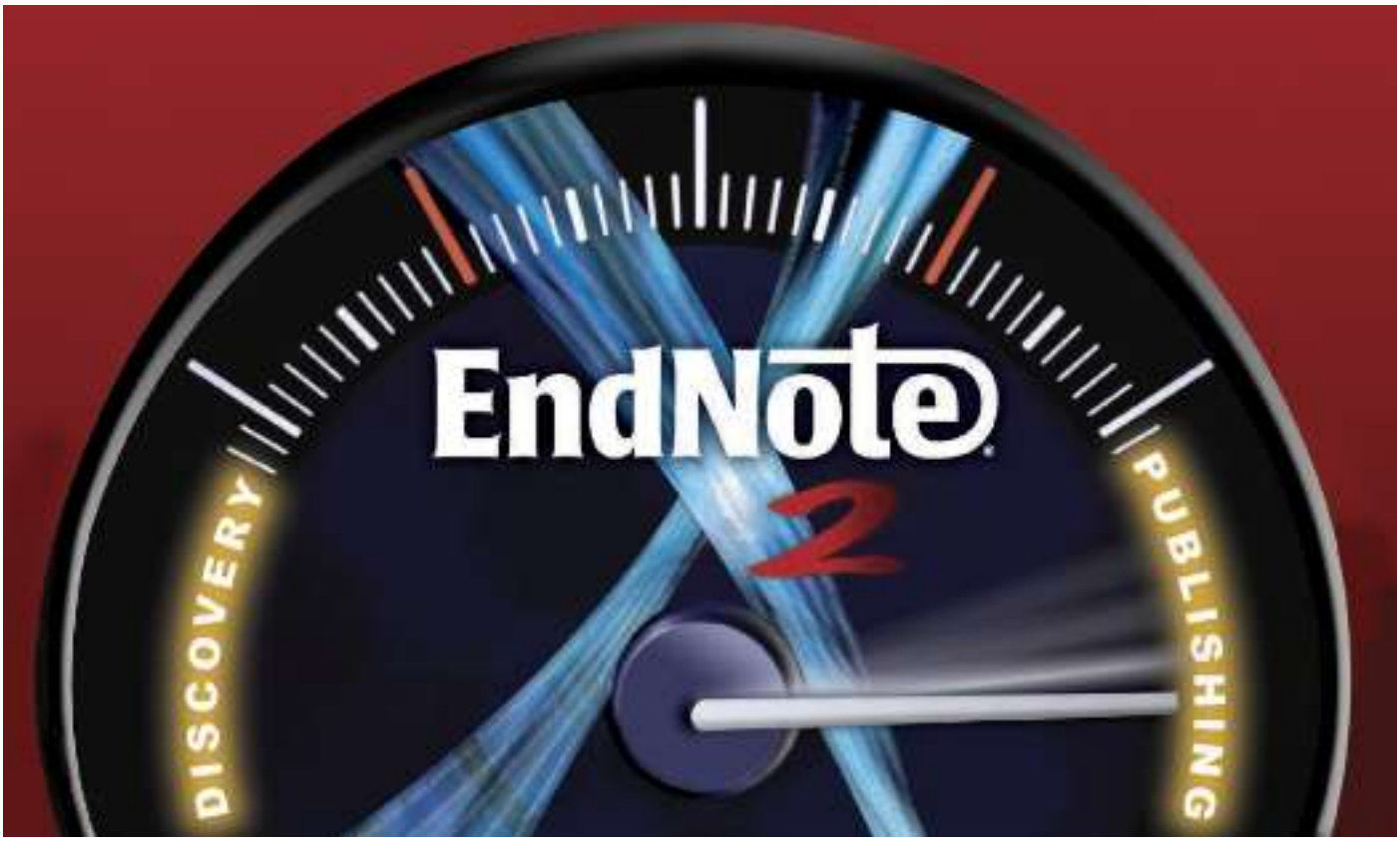

FROM DISCOVERY TO PUBLISHING
ENDNOTE X2 GETS YOU THERE FASTER.

Don't waste time in the slow to publish lane. Let EndNote X2 take you there, faster. Revered by millions for its blazing online search speeds, instantaneous Cite While You Write™ technology and organizing references in a snap, EndNote X2 has all the high performance features you could possibly want in an easy-to-use bibliography software, and more.

Now, EndNote X2 can locate full text and connect it with references while you move on down the research road. Within a single window you can group references automatically, search your favorite online databases and transfer to and from your EndNote Web account, all in record time.

CELEBRATING 20 YEARS OF INNOVATION

So now that you're up to speed on what EndNote X2 has to offer, it's easy to see how EndNote makes you the leader of the pack.

Download your free demo or buy online today
www.endnote.com

800-722-1227 • 760-438-5526 • rs.info@thomson.com

THOMSON REUTERS

OCEAN SCIENCE

Toxic Assets

Atmospheric aerosols can be important sources of nutrients and trace metals, such as phosphorus and iron, to marine organisms, and have been shown to stimulate productivity under favorable conditions, but they also have the potential to be toxic. Predicting what the effects of aerosol deposition might be on biological activity in the surface ocean depends on a complex array of parameters, such as the specific composition of the aerosols, the chemistry of the ocean, and the types of organisms present. Paytan *et al.* begin to investigate some of the effects of aerosols on marine phytoplankton with a combination of laboratory experiments and field work, concluding that copper may be a source of the toxic effects that they observe in the northern Red Sea. They show that different plankton respond in different ways to chemically different aerosols, and that aerosol deposition is not always an asset to marine ecosystems. Because dust deposition is likely to increase over the coming century, and anthropogenic pollutants such as copper have increased greatly over the past 150 years (and likely will continue to increase as growing populations continue to use more resources) aerosols could have substantial effects on marine ecosystems. — HJS

Proc. Natl. Acad. Sci. U.S.A. **106**, 4601 (2009).

CREDITS (TOP TO BOTTOM): NASA; CHUNG *ET AL.*, *ADV. MATER.* **21**, 1358 (2009)

CHEMISTRY

All in the Family

The nitrogen column in the periodic table is perhaps the most diverse, ranging from the light, tightly bound N_2 gas, through cluster-prone phosphorus and arsenic (As), on down to the semi-metals antimony (Sb) and bismuth (Bi). Molecular phosphoramides that combine the two lighter elements are well known, and recently a simple compound of phosphorus (P) and As emerged stably from solution (see Cossairt *et al.*, Brevia, 30 January 2009, p. 602). Alloys of the heavier elements, in keeping with their semimetallic character, are also known. However, coordination complexes of As with its heavier congeners are comparatively rare. Conrad *et al.* present a straightforward synthetic route to this class of compounds, mixing trialkyl or triaryl arsines with chlorinated Sb and Bi substrates in dichloromethane solution. In addition to a neutral As-Sb adduct, the authors isolated cationic As-Sb and As_2-Bi adducts after chloride abstraction by trimethylsilyltriflate, as well as a fourth cationic As-Sb adduct using aluminum trichloride as the abstracting agent. All three structures were crystallographically characterized and exhibited geometries consistent with electron donation from As to the heavier acceptor. — JSY

J. Am. Chem. Soc. **131**, 10.1021/ja900968j (2009).

CELL BIOLOGY

Tagging Troublesome Trash

Huntington's disease is caused by the accumulation of a mutant form of the protein huntingtin, which folds improperly, leading to neurodegeneration and death. Autophagy provides a means by which cells can degrade aberrant cytosolic proteins within lysosomes. Jeong *et al.* wondered if the damage caused by mutant huntingtin could be prevented by promoting the clearance of the misfolded protein from affected neurons. In animal and cellular models of Huntington's disease, they found that increasing acetylation of the pathological form of huntingtin enhanced its trafficking via autophagy into lysosomes and its subsequent degradation. Blocking acetylation promoted neurodegeneration in cultured neurons and in mutant mice. Thus, this posttranslational modification might be exploited therapeutically if some means can be devised for the specific acetylation of pathological aggregates of huntingtin. — SMH

Cell **137**, 10.1016/j.cell.2009.03.018 (2009).

MATERIALS SCIENCE

A Wrinkle in Time and Space

If you squeeze together a supported piece of paper, or place a weight on a constrained plastic film, a wrinkled pattern will appear. The wrinkles tend to form perpendicular to the axis of the principal stress, so that it is possible to obtain concentric ring patterns (like an archery target) or spoke-like patterns (like a bicycle wheel) or combinations thereof. The correlation between film properties, applied stress, and the static wrinkle patterns that form are now well understood. Chung *et al.* examined the dynamics of the wrinkling process—specifically, by monitoring patterns that formed during toluene swelling of polystyrene that

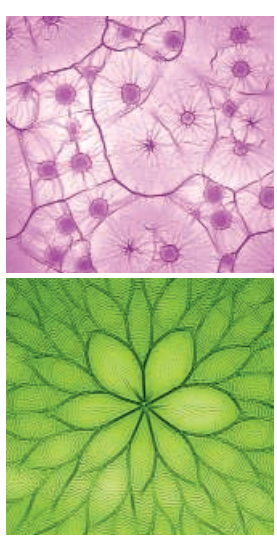

Continued on page 151

Published by AAAS

Work in tandem for absolute total protein quantitation.

Accurately identify and quantify thousands of proteins in a given sample – in a single experiment. Use the Thermo Scientific Tandem Mass Tag (TMT®) Kits with your mass spectrometry instrument for high-throughput protein biomarker discovery.

- ID and quantitate multiple samples from cells, tissues or biological fluids; efficiently label samples, including membrane and post-translationally modified proteins
- Efficient transition from method development to multiplex quantitation
- Identify disease biomarkers
- Quantitatively analyze proteins for which no antibodies are available

To learn more, visit www.thermo.com/TMT or call 815-968-0747 or 800-874-3723

A total solution for quantitative protein expression analysis. Thermo Scientific TMT Protein Labeling Chemistry complements our industry-leading mass spectrometry instruments and software.

Moving science forward

Thermo SCIENTIFIC

Part of Thermo Fisher Scientific

Continued from page 149

had been partially surface–cross-linked through exposure to ultraviolet light and ozone (UVO). For low UVO exposure times, spoke patterns emerged, which the authors attribute to Fickian diffusion of the toluene with a radial growth rate that scaled with the square root of time. Longer UVO exposure generated a thicker cross-linked layer, with the toluene diffusion limited by this barrier. For these films, an induction time was required before wrinkling occurred, and a linear concentration could develop within the rubbery parts of the film, causing a concentric ring pattern to form. In all cases, the initiation and focal points of the patterns appeared to be at surface defects. The authors tested this observation either by masking a portion of the film with glass beads before UVO exposure, to create an elevated area that was not cross-linked, or by indenting the film after UVO exposure to make a gap in the cross-linked surface: These sites proved to be the focal points for the wrinkling on toluene exposure. Because the wrinkling patterns reflect the solvent front and the diffusion kinetics, the authors envision that this technique could be used to easily extract diffusion coefficients for a range of solvent/polymer pairs. — MSL

Adv. Mater. **21**, 1358 (2009).

BIOCHEMISTRY

Nonlethal Drugs

The repeated appearance of bacteria that have developed resistance to the latest generation of antibiotics has fueled the search for other kinds of anti-infective drugs. Gutierrez *et al.* have targeted quorum sensing, the process by which bacteria signal to each other through molecules called autoinducers. These signals coordinate gene expression across individuals in a community, can enhance survival, and in the case of pathogenic bacteria, regulate virulence. The bacterial enzyme 5′-methylthioadenosine/*S*-adenosylhomocysteine nucleosidase (MTAN) is involved in the production of autoinducers. Transition-state analogs that inhibited MTAN activity in vitro also inhibited the production of autoinducers in vivo but did not affect the growth of *Vibrio cholerae* or *Escherichia coli.* This sensitivity persisted during growth for 26 generations in the presence of the inhibitor; furthermore, a reduction in the formation of biofilms—a protective lifestyle for bacteria—was also observed. MTAN is expressed by other bacterial pathogens, so attacking virulence in this nonlethal manner may delay the development of drug resistance. — LC

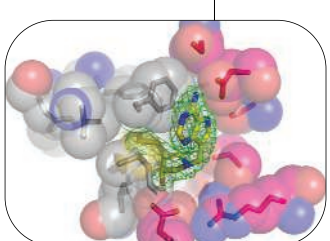

Complex of MTAN (red + gray) and inhibitor (yellow + blue).

CREDIT: GUTIERREZ *ET AL.*, *NAT. CHEM. BIOL.* **5**, 251 (2009)

Nat. Chem. Biol. **5**, 251 (2009).

EVOLUTION

Enforced Separation

Speciation resulting from divergence within a population (sympatry) generally assumes that gene flow is a constraint; however, evidence for this has come from correlations that sidestep the possibility that multiple causal pathways could be important. In order to determine whether gene flow can indeed hold back divergence, Nosil investigated this effect in polymorphic populations of the stick insect *Timema cristinae* in two different habitats. Each population was tracked over several years, and about halfway through this period, the gene flow between one pair was interrupted. In contrast to the control groups, the perturbed populations showed a divergence in morph frequencies in following generations that were attributed to a lack of dispersal and reduced population size. This study provides experimental evidence showing that gene flow does constrain adaptive divergence in the wild. — LMZ

Evolution **63**, 10.1111/j.1558-5646.2009.00671.x (2009).

SYSTEMS BIOLOGY

Intrinsically Responsive

Members of the mitogen-activated protein kinase family regulate a wide range of biological processes. Macia *et al.* have found that although the activity of the yeast mitogen-activated protein kinase (MAPK) Hog1, which helps yeast to survive osmotic stress, increases when yeast is exposed to high salt concentrations, the kinase appeared to be active under basal conditions. In fact, signaling activity in the absence of stress was held in check by a negative feedback loop that required the kinase activity of Hog1. A model of this circuit recapitulated the experimental data and suggested that intrinsic basal signaling poises the system to respond rapidly to even small changes in osmolarity. A similar basal activity was detected for two additional yeast MAPKs, which are involved in the pheromone response, suggesting that high basal signaling may be a common property of MAPK pathways. — NRG*

Sci. Signal. **2**, ra13 (2009).

*Nancy Gough is Editor of *Science Signaling.*

Published by AAAS

www.sciencemag.org

Science

1200 New York Avenue, NW
Washington, DC 20005
Editorial: 202-326-6550, FAX 202-289-7562
News: 202-326-6581, FAX 202-371-9227
Bateman House, 82-88 Hills Road
Cambridge, UK CB2 1LQ
+44 (0) 1223 326500, FAX +44 (0) 1223 326501

Subscription Services For change of address, missing issues, new orders and renewals, and payment questions: 866-434-AAAS (2227) or 202-326-6417, FAX 202-842-1065. Mailing addresses: AAAS, P.O. Box 96178, Washington, DC 20090-6178 or AAAS Member Services, 1200 New York Avenue, NW, Washington, DC 20005

Institutional Site Licenses please call 202-326-6755 for any questions or information

Reprints: Author Inquiries 800-635-7181
Commercial Inquiries 803-359-4578

Permissions 202-326-7074, FAX 202-682-0816

Member Benefits AAAS/Barnes&Noble.com bookstore www.aaas.org/bn; AAAS Online Store www.apisource.com/aaas/ code MKB6; AAAS Travels: Betchart Expeditions 800-252-4910; Apple Store www.apple/eppstore/aaas; Bank of America MasterCard 1-800-833-6262 priority code FAA3YU; Cold Spring Harbor Laboratory Press Publications www.cshlpress.com/affiliates/aaas.htm; GEICO Auto Insurance www.geico.com/landingpage/go51.htm?logo=17624; Hertz 800-654-2200 CDP#343457; Office Depot https://bsd.officedepot.com/portalLogin.do; Seabury & Smith Life Insurance 800-424-9883; Subaru VIP Program 202-326-6417; VIP Moving Services www.vipmayflower.com/domestic/index.html; Other Benefits: AAAS Member Services 202-326-6417 or www.aaasmember.org.

science_editors@aaas.org	(for general editorial queries)
science_letters@aaas.org	(for queries about letters)
science_reviews@aaas.org	(for returning manuscript reviews)
science_bookrevs@aaas.org	(for book review queries)

Published by the American Association for the Advancement of Science (AAAS), *Science* serves its readers as a forum for the presentation and discussion of important issues related to the advancement of science, including the presentation of minority or conflicting points of view, rather than by publishing only material on which a consensus has been reached. Accordingly, all articles published in *Science*—including editorials, news and comment, and book reviews—are signed and reflect the individual views of the authors and not official points of view adopted by AAAS or the institutions with which the authors are affiliated.

AAAS was founded in 1848 and incorporated in 1874. Its mission is to advance science, engineering, and innovation throughout the world for the benefit of all people. The goals of the association are to: enhance communication among scientists, engineers, and the public; promote and defend the integrity of science and its use; strengthen support for the science and technology enterprise; provide a voice for science on societal issues; promote the responsible use of science in public policy; strengthen and diversify the science and technology workforce; foster education in science and technology for everyone; increase public engagement with science and technology; and advance international cooperation in science.

Information for Authors
See pages 807 and 808 of the 6 February 2009 issue or access www.sciencemag.org/about/authors

EDITOR-IN-CHIEF **Bruce Alberts**
EXECUTIVE EDITOR **Monica M. Bradford**
NEWS EDITOR **Colin Norman**
MANAGING EDITOR, RESEARCH JOURNALS **Katrina L. Kelner**
DEPUTY EDITORS **R. Brooks Hanson, Barbara R. Jasny, Andrew M. Sugden**

Editorial senior editor/perspectives Lisa D. Chong; **senior editors** Gilbert J. Chin, Pamela J. Hines, Paula A. Kiberstis (Boston), Marc S. Lavine (Toronto), Beverly A. Purnell, L. Bryan Ray, Guy Riddihough, H. Jesse Smith, Phillip D. Szuromi (Tennessee), Valda Vinson; **associate editors** Kristen L. Mueller, Jake S. Yeston, Laura M. Zahn; **online editor** Stewart Wills; **associate online editors** Robert Frederick, Tara S. Marathe; **web content developer** Martyn Green; **book review editor** Sherman J. Suter; **associate letters editor** Jennifer Sills; **editorial manager** Cara Tate; **senior copy editors** Jeffrey E. Cook, Cynthia Howe, Harry Jach, Barbara P. Ordway, Trista Wagoner; **copy editors** Chris Filiatreau, Lauren Kmec; **editorial coordinators** Carolyn Kyle, Beverly Shields; **publications assistants** Ramatoulaye Diop, Joi S. Granger, Jeffrey Hearn, Lisa Johnson, Scott Miller, Jerry Richardson, Jennifer A. Seibert, Brian White, Anita Wynn; **editorial assistants** Carlos L. Durham, Emily Guise, Michael Hicks, Patricia M. Moore; **executive assistant** Sylvia S. Kihara; **administrative support** Maryrose Madrid

News deputy news editors Robert Coontz, Eliot Marshall, Jeffrey Mervis, Leslie Roberts; **contributing editors** Elizabeth Culotta, Polly Shulman; **news writers** Yudhijit Bhattacharjee, Adrian Cho, Jennifer Couzin, David Grimm, Constance Holden, Jocelyn Kaiser, Richard A. Kerr, Eli Kintisch, Andrew Lawler (New England), Greg Miller, Elizabeth Pennisi, Robert F. Service (Pacific NW), Erik Stokstad; **intern** Jackie D. Grom; **contributing correspondents** Dan Charles, Jon Cohen (San Diego, CA), Daniel Ferber, Ann Gibbons, Robert Koenig, Mitch Leslie, Charles C. Mann, Virginia Morell, Evelyn Strauss, Gary Taubes; **copy editors** Linda B. Felaco, Melvin Gatling, Melissa Raimondi; **administrative support** Scherraine Mack, Fannie Groom; **bureaus** New England: 207-549-7755, San Diego, CA: 760-942-3252, FAX 760-942-4979, Pacific Northwest: 503-963-1940

Production director James Landry; **senior manager** Wendy K. Shank; **assistant manager** Rebecca Doshi; **senior specialists** Steve Forrester, Chris Redwood; **specialist** Anthony Rosen; **Preflight director** David M. Tompkins; **manager** Marcus Spiegler

Art director Yael Kats; **associate art director** Laura Creveling; **illustrators** Chris Bickel, Katharine Sutliff; **senior art associates** Holly Bishop, Preston Huey, Nayomi Kevitiyagala; **art associate** Jessica Newfield; **photo editor** Leslie Blizard

***Science* International**

Europe (science@science-int.co.uk) **editorial: international managing editor** Andrew M. Sugden; **senior editor/perspectives** Julia Fahrenkamp-Uppenbrink; **senior editors** Caroline Ash, Stella M. Hurtley, Ian S. Osborne, Peter Stern; **associate editor** Maria Cruz; **locum editor** Helen Pickersgill; **editorial support** Deborah Dennison, Rachel Roberts, Alice Whaley; **administrative support** John Cannell, Janet Clements; **news: europe news editor** John Travis; **deputy news editor** Daniel Clery; **contributing correspondents** Michael Balter (Paris), John Bohannon (Vienna), Martin Enserink (Amsterdam and Paris), Gretchen Vogel (Berlin); **intern** Sara Coelho

Asia Japan Office: Asca Corporation, Eiko Ishioka, Fusako Tamura, 1-8-13, Hirano-cho, Chuo-ku, Osaka-shi, Osaka, 541-0046 Japan; +81 (0) 6 6202 6272, FAX +81 (0) 6 6202 6271; asca@os.gulf.or.jp; **asia news editor** Richard Stone (Beijing: rstone@aaas.org); **contributing correspondents** Dennis Normile (Japan: +81 (0) 3 3391 0630, FAX +81 (0) 3 5936 3531; dnormile@gol.com); Hao Xin (China: +86 (0) 10 6307 4439 or 6307 3676, FAX +86 (0) 10 6307 4358; cindyhao@gmail.com); Pallava Bagla (South Asia: +91 (0) 11 2271 2896; pbagla@vsnl.com)

EXECUTIVE PUBLISHER **Alan I. Leshner**
PUBLISHER **Beth Rosner**

Fulfillment Systems and Operations (membership@aaas.org); **director** Waylon Butler; **senior systems analyst** Jonny Blaker; **customer service supervisor** Pat Butler; **specialists** Latoya Casteel, LaVonda Crawford, Vicki Linton, April Marshall; **data entry supervisor** Cynthia Johnson; **specialists** Eintou Bowden, Tarrika Hill, William Jones

Business Operations and Administration director Deborah Rivera-Wienhold; **assistant director, business operations** Randy Yi; **manager, business analysis** Michael LoBue; **manager, business operations** Jessica Tierney; **financial analysts** Priti Pamnani, Celeste Troxler; **rights and permissions: administrator** Emilie David; **associate** Elizabeth Sandler; **marketing director** Ian King; **marketing manager** Allison Pritchard; **marketing associates** Aimee Aponte, Alison Chandler, Mary Ellen Crowley, Julianne Wielga, Wendy Wise; **marketing executive** Jennifer Reeves; **marketing/member services executive** Linda Rusk; **director, site licensing** Tom Ryan; **director, corporate relations** Eileen Bernadette Moran; **publisher relations, eresources specialist** Kiki Forsythe; **senior publisher relations specialist** Catherine Holland; **publisher relations, east coast** Phillip Smith; **publisher relations, west coast** Philip Tsolakidis; **fulfillment supervisor** Iquo Edim; **fulfillment coordinator** Laura Clemens; **electronic media: manager** Lizabeth Harman; **project manager** Trista Snyder; **assistant manager** Lisa Stanford; **senior production specialists** Christopher Coleman, Walter Jones; **production specialists** Nichele Johnston, Kimberly Oster

Advertising director, worldwide ad sales Bill Moran

Product (science_advertising@aaas.org); **midwest/west coast/w. canada** Rick Bongiovanni: 330-405-7080, FAX 330-405-7081; **east coast/e. canada** Laurie Faraday: 508-747-9395, FAX 617-507-8189; **uk/europe/asia** Roger Goncalves: TEL/FAX +41 43 243 1358; **japan** Mashy Yoshikawa: +81 (0) 3 3235 5961, FAX +81 (0) 3 3235 5852; **senior traffic associate** Deiandra Simms

Commercial Editor Sean Sanders: 202-326-6430

Project Director, Outreach Brianna Blaser

Classified (advertise@sciencecareers.org); **inside sales manager: midwest/canada** Daryl Anderson: 202-326-6543; **inside sales representative** Karen Foote: 202-326-6740; **key account manager** Joribah Able; **northeast** Alexis Fleming: 202-326-6578; **southeast** Tina Burks: 202-326-6577; **west** Nicholas Hintibidze: 202-326-6533; **sales coordinators** Rohan Edmonson, Shirley Young; **international: sales manager** Tracy Holmes: +44 (0) 1223 326525, FAX +44 (0) 1223 326532; **sales** Susanne Kharraz, Dan Pennington, Alex Palmer; **sales assistant** Louise Moore; **japan** Mashy Yoshikawa: +81 (0) 3 3235 5961, FAX +81 (0) 3 3235 5852; **advertising production operations manager** Deborah Tompkins; **senior production specialist/graphic designer** Amy Hardcastle; **senior production specialist** Robert Buck; **senior traffic associate** Christine Hall; **publications assistant** Mary Lagnaoui

AAAS Board of Directors retiring president, chair James J. McCarthy; **president** Peter C. Agre; **president-elect** Alice Huang; **treasurer** David E. Shaw; **chief executive officer** Alan I. Leshner; **board** Alice Gast, Linda P. B. Katehi, Nancy Knowlton, Cherry A. Murray, Julia M. Phillips, Thomas D. Pollard, David S. Sabatini, Thomas A. Woolsey

AAAS
ADVANCING SCIENCE, SERVING SOCIETY

SOLiD 3

YOUR TRANSCRIPTOME ANALYSIS

&MPOWERED

The SOLiD™ 3 System empowers you to discover new insights into gene regulation. With a hypothesis-generating, highly-sensitive assay that preserves the strand information of the original RNA molecule, the SOLiD 3 System enables you to detect novel transcripts, including non-coding RNA and distinguish strand-specific expression patterns. The combination of 400 million sequence tags and sample multiplexing capabilities allows for cost effective analysis of multiple samples in a single run while maintaining the sensitivity to detect low abundance transcripts. Combined with the SOLiD Small RNA Expression Kits, Whole Transcriptome Analysis Kits and application specific data analysis tools, the SOLiD 3 System provides a comprehensive solution that takes you from RNA to results.

For more SOLID PROOF, visit solid.appliedbiosystems.com

Applied Biosystems

Sigma Antibodies

Multiplying Like Bunnies!

SIGMA Life Science

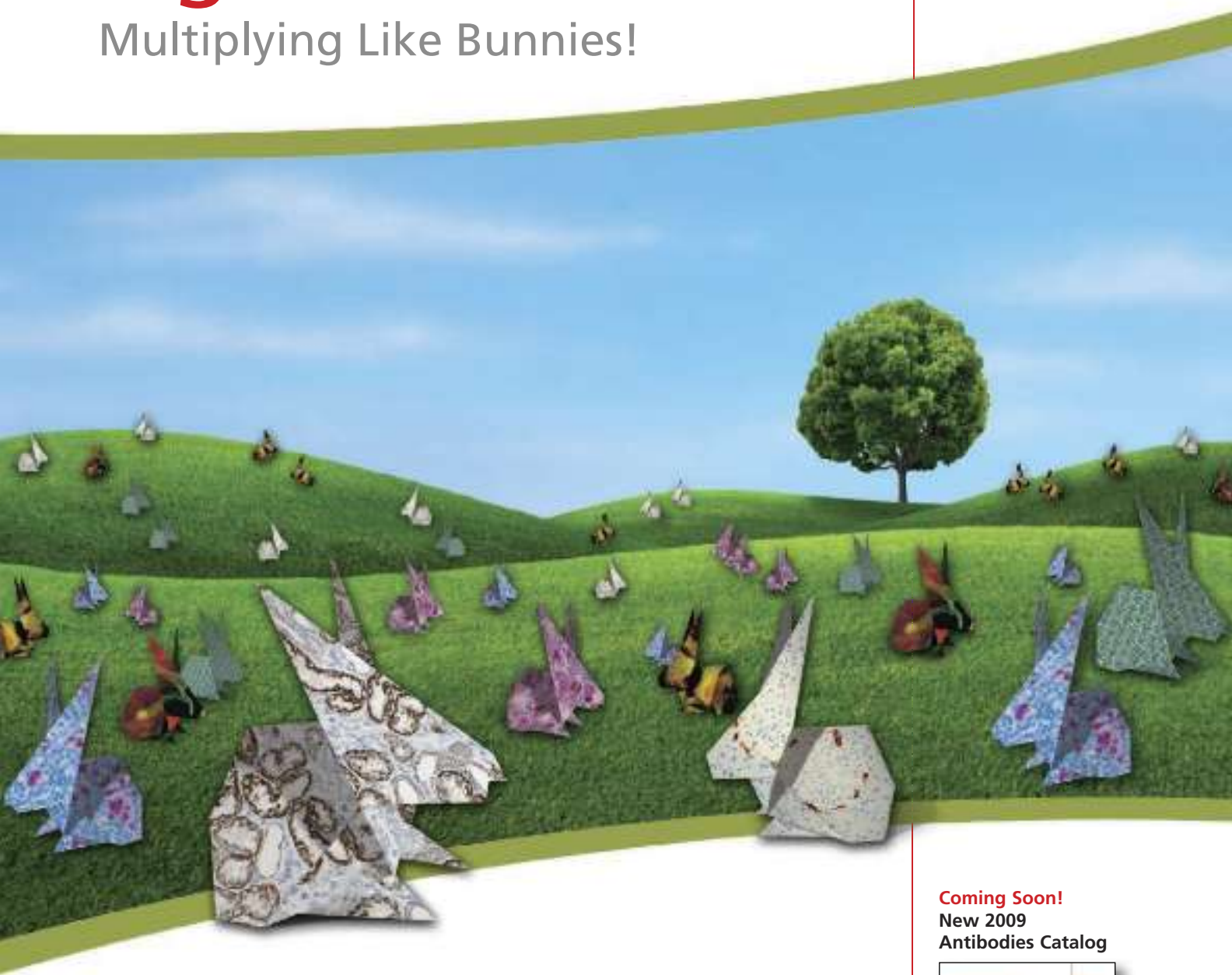

Over 8,000 new monoclonal and polyclonal antibodies with more added every day.

- Validation using a variety of applications -- WB, IHC, IF, ELISA
- Broad coverage of both primary and secondary antibodies
- Convenient target searches with advanced web tools
- World-renowned technical service

Go to *sigma.com/antibody* for more information.

Coming Soon!
New 2009
Antibodies Catalog

Reserve your copy at
sigma.com/reserve

Our Innovation, Your Research — Shaping the Future of Life Science

sigma-aldrich.com

SIGMA-ALDRICH®

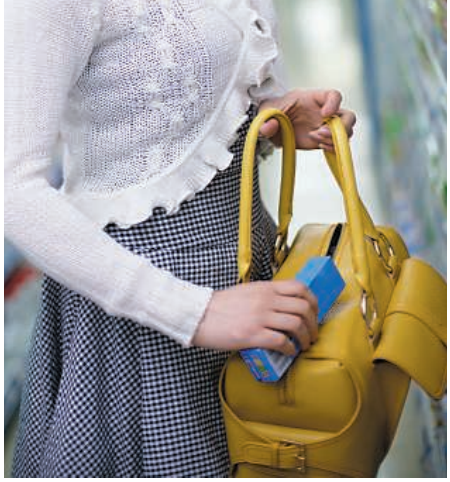

The Urge to Lift

For compulsive shoplifters, covertly pinching a lipstick or a blouse brings a rush "similar to a cocaine or heroin high," says Jon Grant, a psychiatrist at the University of Minnesota School of Medicine in Minneapolis. That's why some psychiatrists prescribe naltrexone, a drug used to treat addicts, for the problem.

Naltrexone blocks the same brain receptors used by opioids, but there's little published evidence about its effectiveness in treating kleptomania. Now, in the April issue of *Biological Psychiatry*, Grant and colleagues report the first placebo-controlled trial of any drug against the disorder.

Subjects were 25 kleptomaniacs aged 17 to 65, 18 of them women. Almost all had been arrested for shoplifting at least once. For 8 weeks, half were given naltrexone daily and the rest a placebo. "Two-thirds of those on naltrexone had complete remission of their symptoms," says Grant. Psychiatrist Samuel Chamberlain of the University of Cambridge in the U.K. says the results "suggest that the brain circuits involved in compulsive stealing overlap with those involved in addictions more broadly." Grant hopes to get funding for a larger study.

Grad Student Sentenced

As a graduate student in anthropology at Stony Brook University in New York since 2006, Ian Wallace has done fieldwork in Kenya with Meave Leakey and published at least five papers. But he also has a past that's come back to haunt him.

In 2001, Wallace and an accomplice in the radical environmental group Earth Liberation Front (ELF) tried—unsuccessfully—to firebomb two buildings at Michigan Technological University where scientists were doing research on genetically modified plants.

On 23 March, a federal judge sentenced Wallace, 27, to 3 years in prison after he pleaded guilty and admitted to participating in several other acts of ecoterrorism that caused more than $1.6 million in property damage.

Wallace faced a maximum sentence of 10 years but apparently received consideration for helping authorities solve a 2000 ELF attack that damaged 500 research trees in Rhinelander, Wisconsin. In a brief e-mail to *Science*, Wallace said, "My future plans are still taking shape, but this experience has not altered my dreams of receiving a Ph.D. and pursuing a career in science." His graduate adviser, Brigitte Demes, is standing by him. "He is an extremely talented young man and has great promise," she says. "He has turned his life around."

Old Age Not for Pessimists

Having negative ideas about old people may harm your own health later in life, a longitudinal study suggests.

Yale University social psychologist Becca Levy and colleagues at the National Institute on Aging analyzed data from 386 subjects in the long-running Baltimore Longitudinal Study of Aging. On joining the study, the participants—healthy adults under 50—filled out a questionnaire that asked about "stereotypes" such as whether old people are "absent-minded" or "less intelligent."

The researchers found that people with worse-than-average age stereotypes were likely to have heart attacks or strokes at younger ages. For example, 30 years after filling out the form, 25% of those with negative attitudes had had a cardiovascular event, compared with 13% of those with positive attitudes (see graph), the researchers reported last month online in the journal *Psychological Science*. Levy believes, on the basis of earlier research, that people with negative age stereotypes are also more susceptible to stress.

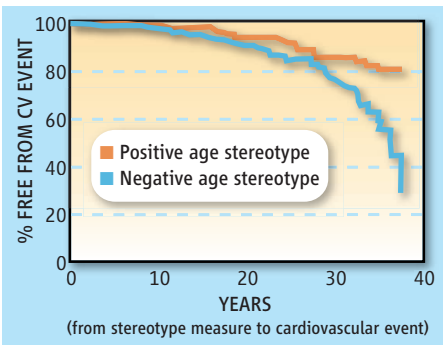

"What's unique about [this study] is that they show the effects of attitudes at relatively young ages on health many years later," says David Weir, director of the Health and Retirement Study at the University of Michigan, Ann Arbor. Because the analysis controls for the effects of depression, "in theory, their finding is of something more specific than just 'general negativity,' " Weir says. It remains to be seen, he adds, whether the finding will hold up in a larger sample.

Big Teeth, Tiny Brain

Rebecca Meah of the American Museum of Natural History in New York City works on a reconstruction of the *Coryphodon*, a bog wader that lived above the Arctic Circle 50 million years ago. It will form part of a diorama recreating the warm, humid environment of Ellesmere Island, Canada's northernmost tip, to be featured in an exhibit on "Extreme Mammals" opening 23 May. The meter-tall creature had short tusks that helped it uproot swamp plants. One of the extreme things about *Coryphodon* was that it had one of the smallest brains for its size of any mammal.

CREDITS (TOP TO BOTTOM): SIMON MARCUS/CORBIS; B. LEVY *ET AL.*, *PSYCHOLOGICAL SCIENCE* 20, 3 (2009); RODERICK MICKENS/AMERICAN MUSEUM OF NATURAL HISTORY

Your Power for Health

greiner bio-one

Challenging Experiments?

Advanced TC™ cell culture vessels from Greiner Bio-One

- Innovative polymer modification improves cellular adhesion
- Positive effects on cell functionality and performance
- Enhanced propagation of fastidious cells
- Improved cell expansion under limited growth conditions
- Better assay consistency
- Long-term stability and storage at room temperature

Germany (Main office): Greiner Bio-One GmbH, info@de.gbo.com I **Austria:** Greiner Bio-One GmbH, office@at.gbo.com
Belgium: Greiner Bio-One BVBA/SPRL, info@be.gbo.com I **Brazil:** Greiner Bio-One Brasil, office@br.gbo.com I **China:** Greiner Bio-One GmbH, info@cn.gbo.com
France: Greiner Bio-One SAS, infos@fr.gbo.com I **Japan:** Greiner Bio-One Co. Ltd., info@jp.gbo.com I **Netherlands:** Greiner Bio-One B.V., info@nl.gbo.com
UK: Greiner Bio-One Ltd., info@uk.gbo.com I **USA:** Greiner Bio-One North America Inc., info@us.gbo.com

www.gbo.com/bioscience

Q&A with U.S. education secretary
159

Promise and pitfalls of newborn blood collections
166

RECESSION FALLOUT

Harvard's Financial Crunch Raises Tensions Among Biology Programs

CAMBRIDGE, MASSACHUSETTS—The richest school in the world reached into its pockets early this year to pay some bills and discovered that it didn't have enough cash. In January, Harvard University felt the simultaneous pinch of a 22% decline in its endowment and a loss of "liquidity." The financial crisis had arrived here with a bang. Budget cuts since then have raised tensions with city politicians and exposed some fault lines within the faculty over an emphasis on stem cell medicine and a push for more collaborative, interdisciplinary work.

This week, Harvard began the painful task of deciding how many and which of 1600 workers offered a severance deal will be let go. City politicians weighed in, telling Harvard it should not lay off janitors but should cut the pay of top academics. The college's daily paper, *The Harvard Crimson*, responded in a pragmatic editorial that workers need help, but Harvard cannot provide all of it—certainly not if it risks putting the university at a disadvantage—and politicians should "lay off our budget."

For scientists, the budget crunch hit home in February when Harvard President Drew Gilpin Faust announced that construction of a massive science facility in Allston, Massachusetts, about a 20-minute walk from Harvard Square, would proceed at a "slower pace" (*Science*, 27 February p. 1157). The reality is an indefinite delay. That announcement has had a domino effect, raising tensions between two departments in biology.

The older one, called the Department of Molecular and Cellular Biology (MCB), includes well-known senior investigators and science leaders, such as molecular biologist Tom Maniatis, biochemist Matthew Meselson, and epigenetics researcher Catherine Dulac (the chair). The second department, initiated 2 years ago partly as an example of a scientific rebirth planned by Provost Steven Hyman and Harvard's then-president Lawrence Summers, is known as the Department of Stem Cell and Regenerative Biology (SCRB). "Scrub," Hyman calls it.

Co-chaired by stem cell biologist Douglas Melton and Harvard Medical School hematologist David Scadden, Scrub is collaborative, hands-on, and interdisciplinary. It is the first department to bridge two schools (reporting to two deans) in Harvard's 373-year history. It's also the first to enlist basic scientists and physicians to run joint research projects and teach undergraduate courses.

This upstart department also anchors a new Harvard Stem Cell Institute, headed by Melton and Scadden, which has raised more than $100 million in promised support, including $25 million over 5 years from the drugmaker GlaxoSmithKline. Its aim is to invent treatments for disease—Melton's dream is to create implantable beta cells that can supply insulin to diabetics—and put them into people. Melton says this will require "some version of the word 'commercialization,' " which raises hackles. But Melton is proud of the practical focus and says he likes working with business people. He regrets that the institute will not soon be nestling up alongside the Harvard Business School, in a promised building on the Allston campus.

"Among my defects, impatience is high on the list," says Melton. "There is no way I'm going to just sit and bide my time and say we're going to do all these things 5 years from now." In fact, the stem cell institute and its celebrated scientists—featured in a 9 February *Time* cover story—have not been asked to bide their time. Almost in the same breath that officials disclosed the Allston delay, they announced that by reconfiguring existing facilities, Harvard could assemble the elite cadre of stem cell scientists—some now located on the Boston medical campus—on Harvard's main campus in Cambridge. Doing this requires that all other MCB department members move out of the building in which they've been located for years, to make space available. It also requires a very expensive renovation.

According to *The Crimson*, Dulac contacted MCB faculty members individually to deliver the news that they would have to move. Maniatis, Meselson, and biochemist Guido Guidotti reportedly were displeased. *The Crimson* also reported that Meselson expressed doubts about giving high priority to a specialized field such as stem cell research. Maniatis, according to two Harvard scientists who asked to remain anonymous, has told colleagues that he will leave the university. Maniatis did not respond to phone messages left for him. Guidotti confirmed that he had spoken to *The Crimson* but declined further ▶

CREDIT: JUSTIN IDE/HARVARD UNIVERSITY NEWS OFFICE

Researcher in motion. Stem cell scientist Douglas Melton co-chairs a department that's changing the rules.

comment. Meselson and Dulac did not respond to phone messages. One MCB scientist, who requested anonymity, told *Science* that Dulac had asked strictly that these events not be discussed with reporters.

In recent weeks, the administration has reached out to the senior MCB scientists and offered them new labs, Hyman says, in "a brand-new building" where they will have "an opportunity to configure [space] to their liking." The university also plans to give special consideration in tenure review to junior MCB faculty members to compensate for the disruption of their research. Regarding his abrupt handling of this business, Hyman adds, "I will admit that in the acute emergency I had to make some decisions" without the full consultation "that I normally engage in."

As the dust settles, Harvard is going ahead full steam with plans for a new layer of universitywide science, led by Scrub. Melton recently gave a formal presentation to the faculty of a new concentration (or major) for undergraduates based on stem cell and regenerative medicine. The first students will enroll in September. It will focus on diseases that might be treated with stem cells or advanced biological engineering, and some courses will be taught by some of Harvard's superstar physicians, including, in addition to Scadden, hematologists George Daley and Leonard Zon of Children's Hospital in Boston, both funded by the selective Howard Hughes Medical Institute.

Melton dismisses gibes about running a premed course. "Really, as strongly as we can say it, No!" he insists. Melton argues that the availability of human stem cells and induced pluripotent cells—and a growing digital archive of data on human disease—now make it possible to teach basic biology using the human as a model organism. He already has undergraduates experimenting with stem cells. When students see cardiomyocytes in a dish begin to pulse with an incipient heartbeat, they ask deep questions, he says. Diseases will be examined as a portal into basic science. This is at least as good, he argues, as Harvard's traditional "eat-your-spinach" approach that required math, physics, or organic chemistry "before you can do what you want to do."

Endowment losses will affect everyone, Hyman says, but they won't reset the priority to forge novel collaborations or cross-disciplinary projects in science: "It would be a terrible error" to give every program "the same haircut."

Melton says he's still waiting to hear where he and his people will go temporarily while labs are being renovated. Meanwhile, he's busy on something new: "I'm going to do my own reprogramming and become an immunologist," he says. After a lot of reading, he has decided to make a broad attack on autoimmunity—"the whole thing." One specific goal is to reconstruct a model of human diabetes in a mouse and examine how the disease begins.

–ELIOT MARSHALL

COSMOLOGY

Unlucky CLOVER: U.K. Halts Unfinished Telescope Project

The United Kingdom has canceled a cosmology experiment that would have been Europe's prime contender in the race to trace the gravitational waves that rippled through the infant universe. U.K. physicists complain that, to save less than £3 million, the nation's cash-strapped Science and Technology Facilities Council (STFC) is abandoning a most promising field of inquiry. But the project—a suite of microwave telescopes called CLOVER—was 50% over budget and 3 years behind schedule, and scientists not associated with the project say they are not entirely surprised that STFC axed it.

Too late. Still being assembled (*above*), the CLOVER telescopes may not get a chance to see the sky's microwaves.

"I'm really disappointed," says Radek Stompor, a cosmologist at the University of Paris 7 in France. "The fact that CLOVER is getting canceled really puts Europe at a disadvantage." Nevertheless, the delays and cost overruns made the project vulnerable, Stompor says.

The CLOVER telescopes would have studied the faint afterglow of the big bang, the so-called cosmic microwave background. That radiation is polarized, and the gravitational waves thought to have zipped through the primordial soup of subatomic particles just after the big bang should have created swirling patterns in the polarization that would linger in the sky 13.7 billion years later. More than half a dozen ground-based, balloon-borne, and satellite experiments—most from the United States—will search for those swirls in coming years.

CLOVER should have gotten a jump on the rest of the field. Approved in 2004 for £4.78 million, the project originally consisted of three microwave telescopes of identical design but different sizes that would measure microwaves at three different frequencies. The array was supposed to be deployed starting in 2006 at a French-Italian base in Antarctica, with the French and Italian governments picking up the tab for maintaining the equipment at the site.

Then things went awry. The telescopes would not fit at the Antarctic site, says CLOVER team member Michael Jones, an astrophysicist at the University of Oxford. So researchers switched to a site in Chile's Atacama Desert. But that meant the United Kingdom had to bear the costs of getting the equipment in place and maintaining it. The project was also over its design budget, and after a February 2007 review, CLOVER was "descoped" to two telescopes, one of which would work at both of the two higher frequencies.

Researchers were also behind their goal of fully deploying the array this year, as neither telescope is complete. And STFC has been struggling to address ongoing budget problems (*Science*, 21 December 2007, p. 1851). In December, after another review, it decided to cancel CLOVER, says STFC spokesperson Julia Maddock.

The CLOVER team contends that the chance to discover primordial gravitational waves is worth the extra £2.55 million needed to complete the project. "I would still argue that in terms of the science impact it might make, this is a very cheap experiment," Jones says. But, says Maddock, "They spent their contingency, they had one cost increase, and now they were asking for another. To fund additional costs to CLOVER, we would have to make cuts to some other project."

CLOVER team members have one last shot. If they're lucky, a private donor could rescue the project.

–ADRIAN CHO

CREDITS: CLOVER/UNIVERSITY OF OXFORD PHYSICS DEPARTMENT

Published by AAAS

Listen up. Duncan joins President Obama at a Washington, D.C. elementary school.

NEWSMAKER INTERVIEW

Arne Duncan Hopes a Team Approach Will Improve U.S. Schools

After graduating from Harvard University in 1987, Arne Duncan followed his dream and joined Australia's top basketball league. Although the Melbourne Eastside Spectres dropped him after 2 years, the high-scoring forward signed on with a Tasmanian team and was ready to settle down Down Under. "I had accomplished my goal to be a pro player," he says. "I was making lots of money, doing something I loved. … Had I stayed another year or two, I would still be there."

Instead, Duncan returned in 1991 to his hometown of Chicago, Illinois, to work with underprivileged children. "I know it sounds corny, … but I had been given extraordinary opportunities growing up in Chicago, educationally, socially, and athletically, and I felt I owed something to the community." A decade later, he was running the third largest school district in the country. And in December, President-elect Barack Obama, a fellow Chicagoan, chose Duncan to be the next U.S. secretary of education.

The 44-year-old Duncan has displayed impressive offensive skills in his first few months at the $50-billion-a-year federal agency. He's barnstormed with the president to highlight the $100 billion in education spending that's part of the $787 billion stimulus package. On his own, he's touted the Administration's education initiatives—in particular, expanding preschool programs, shifting the emphasis from testing students to raising standards and improving teacher quality, and making college more affordable. At every turn, Duncan has hammered on the same themes: School districts need to find fresh ways to improve student achievement, from alternative teacher certification to differential pay to Saturday classes, and the federal government is eager to scale up what works.

Duncan expanded on those points during a recent interview with *Science* in his Washington, D.C., office. **–JEFFREY MERVIS**

Online
sciencemag.org
A more complete interview with Secretary Arne Duncan.

Q: What is it about effective teachers that makes a difference?
A.D.: It sounds like common sense, but still, having teachers that truly know the content is critically important. You can't teach what you don't know. Beyond that, great teachers are passionate, they have high expectations, they go way beyond the call of duty. And they are really able to differentiate instruction, to work with kids who are struggling and those on track to becoming the next generation of chemists and physicists.

Q: What can the federal government do?
A.D.: A lot. We have very significant resources that can go to professional development, that can go to sending folks back to universities to get endorsements in math and science. I'm pushing hard to pay math and science teachers more. I think we also have to think about compartmentalization in the middle school level, getting folks that really know the content.

Q: What evidence do you have that higher pay will attract better STEM (science, technology, engineering, and mathematics) teachers?
A.D.: I don't think money alone is the answer. We've had shortages for decades. So let's do something different. When you have an imbalance between supply and demand, let's do something to create larger demand. I think that one of the few benefits of the current economic recession is that more folks may start to think about alternative certification. It's a chance for us to get some really smart folks to come in from industry.

Q: The 2010 budget contains a $2.5 billion fund for college completion. Leaving aside the cost of tuition, why is there so much attrition?
A.D.: It's interesting to me that in recent years we have become very aware of high school graduation rates. But nobody really knows what college graduation and dropout rates are. And there are very few incentives for universities to graduate students. They get money based on kids coming in the door. There's no back-end incentive.

Q: What should they be doing?
A.D.: It's the same thing that works in high school. It's a strategy, it's a culture, it's a set of supports. It's a commitment to working with those students. It's looking at kids, one by one, and figuring out who's at risk, and who's not, and what adults are available, and what type of supports [they need] to make sure they come out the back end.

Q: Do you think we have clear definitions and agreement on what students should know about science before they leave high school?
A.D.: I would say that, across the board, we need to get clearer, higher, fewer standards. We talk a lot about internationally benchmarked standards. And I would argue that in many places around the country, our standards are far too low.

Q: You've said we're lying to kids by having these different, low standards. And you've also said you want to do what works. If we know what works, why don't we just mandate it?
A.D.: You could, although I think that would ultimately fail … because there would be such a backlash. The goal here is to get it done and not create a lot of drama. … And having it come from the states, and from the community, rather than top-down, is much more powerful.

CREDIT: JEFF HAYNES/REUTERS/LANDOV

Published by AAAS

MILLIPORE™

FLOW CYTOMETRY

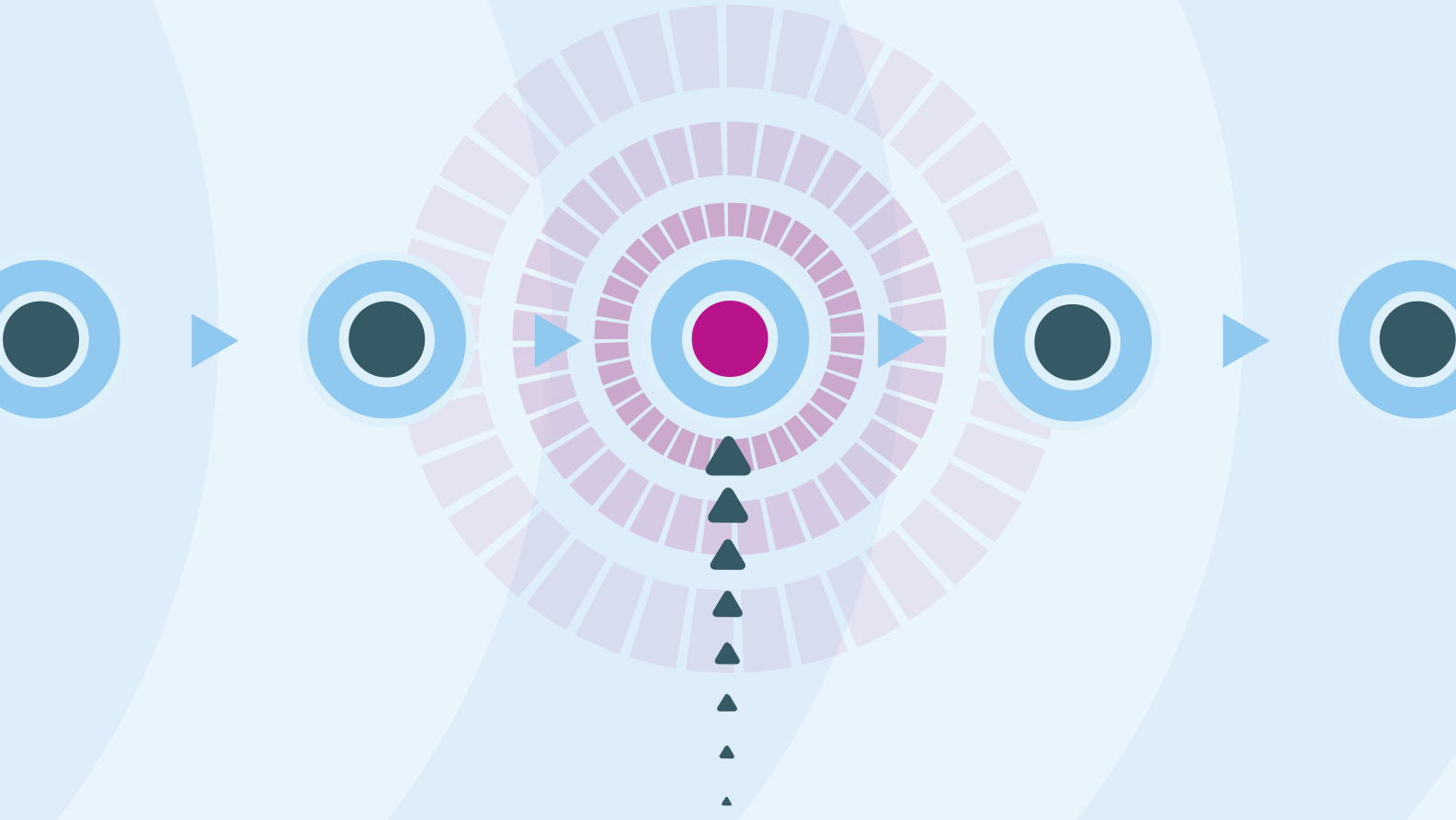

Why go with the flow when you can leap ahead?

Make a quantum leap with Millipore's breakthrough portfolio of FlowCellect™ cytometry kits optimized to monitor stem cell differentiation, GPCR expression and signaling pathways. Visit **www.millipore.com/flowcytometry** to learn how these assays combine with the Guava® system to provide turnkey solutions.

ADVANCING LIFE SCIENCE TOGETHER™
Research. Development. Production.

THE EXPERTISE OF
CHEMICON® AND UPSTATE®
IS NOW PART OF MILLIPORE

MEETINGBRIEFS>>

LUNAR AND PLANETARY SCIENCE CONFERENCE | 23–27 MARCH 2009 | THE WOODLANDS, TEXAS

A Primal Crust Found on the Moon, While Mercury's Proves Elusive

Our moon's bright highlands—set against dark "seas" of frozen lava to form the man in the moon—have undergone centuries of ever-closer scrutiny. But it was not until scientists could put moon soil under the microscope that they had any idea where the highlands came from. The highlands, some decided, were the remains of rocky scum that floated to the top of a churning ocean of moon-girdling magma soon after the moon formed.

The "lunar magma ocean" hypothesis gained support from later Apollo, ground-based, and orbital observations to become the paradigm for how planetary bodies get their first, or primary, crust. But nearly 40 years after Apollo, no one had directly and unequivocally confirmed the true nature of the lunar highlands.

At the meeting, researchers from two ongoing missions to the moon reported that they now have the final, direct proof. The latest spectroscopy from lunar orbit shows that the key diagnostic rock "is everywhere," said planetary spectroscopist Carlé Pieters of Brown University. Orbiting spectrometers can finally see the lunar surface in fine enough detail and split the spectral colors of the surface into small enough bits to reveal the composition of the highlands unambiguously, speakers said.

Mineralogists expected the whitish mineral plagioclase to crystallize from any lunar magma ocean and float to the top. There it would form a primary crust tens of kilometers thick made of anorthosite, rock consisting of nearly 100% plagioclase. Although cruder spectroscopic searches showed strong hints of anorthosite, a thin surface layer—perhaps impact debris—seemed to be at least partially masking the long-sought primary crust.

Pieters, principal investigator of NASA's Moon Mineralogy Mapper instrument flying onboard India's Chandrayaan-1 spacecraft, reported that "the entire Inner Rook Mountains is anorthosite. That validates the magma ocean." The huge impact that formed the great Mare Orientale basin threw up those mountains to expose the anorthosite. And Makiko Ohtake of the Japan Aerospace Exploration Agency in Sagamihara, Kanagawa, and her colleagues operating the Multiband Imager on JAXA's Kaguya spacecraft reported finding anorthosite exposed in 70 impact craters around the moon. Case closed.

Meanwhile, scientists trying to tell a similar story about another once-magma-covered body—the planet Mercury—continue to draw blanks. "We're not even sure what [its primary crust] would look like," says planetary geologist James Head III of Brown, summing up meeting presentations. The MESSENGER spacecraft has now imaged 90% of Mercury's surface during two flybys, MESSENGER team members including Head reported, and there's no sign of anorthosite but plenty of younger lavas. But Mercury's rock is lower in iron than the moon's is, so entirely different minerals may have floated to form a crust. MESSENGER scientists may be seeing such an alternative primary crust where impacts have punched through the lavas, but they have yet to recognize it. Perhaps after MESSENGER goes into orbit around Mercury in 2011, all will become plain there as well. **–RICHARD A. KERR**

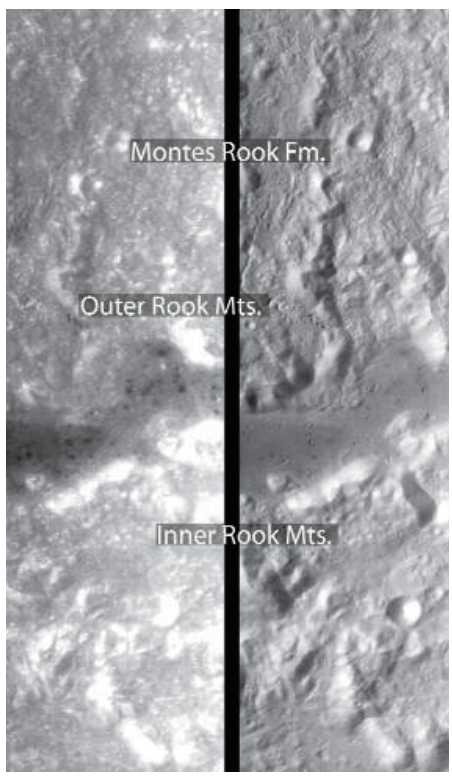

Bright pay dirt. Regions bright at visible wavelengths (*left*, 40-kilometer-wide swath) mark the moon's first crust of nearly pure plagioclase.

CREDIT: CARLÉ PIETERS/M³/INDIAN SPACE RESEARCH ORGANIZATION

Water Everywhere on Mars, But Is Any of It Ever Liquid?

Water on Mars is nothing new. It's been "discovered" many times, but it's always frozen. The liquid form would be so much more exciting in an astrobiological way. At the meeting, meteorologist Nilton Renno of the University of Michigan, Ann Arbor, and 21 of his teammates on the Phoenix mission to Mars reported Phoenix observations buttressed with thermodynamic arguments that suggest to Renno, at least, that briny liquid water exists at the Phoenix site. Not everyone agrees.

Renno starts with the discovery of both ice and salts in the soil of the Phoenix landing site. As he sees it, temperature swings from day to day or millennium to millennium should drive water from the ice into the salts, which become wet and dissolve. Even when it gets much colder, the briny water will stay liquid longer.

Renno points to blobs adhering to a leg of the Phoenix lander as evidence that local salts will keep water liquid even under current Mars conditions. In still images of the leg, he sees the blobs—apparently blown there by the Phoenix landing rockets—growing, moving, and dripping. And where the Phoenix arm dug through icy soil, he sees signs of soft frozen brine rather than hard, clean ice. "Not everyone [on the team] agrees with everything," he says, "but I think they're moving toward agreement."

Not yet. Some team members, such as physicist Michael Hecht of NASA's Jet Propulsion Laboratory in Pasadena, California, who is not a co-author, contest Renno on almost every point. But Renno co-author and chemist Samuel Kounaves of Tufts University in Medford, Massachusetts, says, "Nilton may be right about what we have under Phoenix, but the environment there during landing was extreme and very different. It doesn't mean [liquid water] is possible on Mars. We need some lab experiments, but even then we may never know." **–R.A.K.**

Published by AAAS

EVOLUTIONARY MEDICINE

Darwin Applies to Medical School

When George Williams and Randolph Nesse made their first pitches for Darwinian medicine in the early 1990s, they turned some heads, but not the right ones. Reviving and building on European traditions that melded medicine and evolutionary biology, the duo argued that diseases could be best understood from an evolutionary perspective. Their first meeting on the subject in 1996 attracted 60 enthusiasts but few practicing clinicians, probably because physicians couldn't envision practical applications. "The folks who were excited about it weren't in a position to do anything about it," recalls anthropologist Peter Ellison of Harvard University. Although a better understanding of the evolution of drug resistance has helped shape the use of antibiotics, when it comes to evolution, "medical schools are mostly oblivious," says Nesse, a psychiatrist at the University of Michigan, Ann Arbor.

But times may be changing. Last week, a similar meeting* in Washington, D.C., attracted dozens of physicians, including the dean of Harvard Medical School and the president of the Institute of Medicine (IOM). Several participants described new medical school programs at the University of Auckland, New Zealand, and at Johns Hopkins University in Baltimore, Maryland, involving evolutionary medicine, as well as a pending textbook. "A thoughtful strategy for the future education for health professionals would incorporate a strong evolutionary perspective," says IOM President Harvey Feinberg.

At the meeting, researchers reported headway in understanding drug resistance through the lens of evolution. Others described progress linking past evolutionary adaptations with current health problems. For instance, anthropologist Kathleen Barnes of Johns Hopkins University has evidence that for some asthmatics, this overly energetic inflammatory response may be a holdover from the body's successes in coping with parasitic disease.

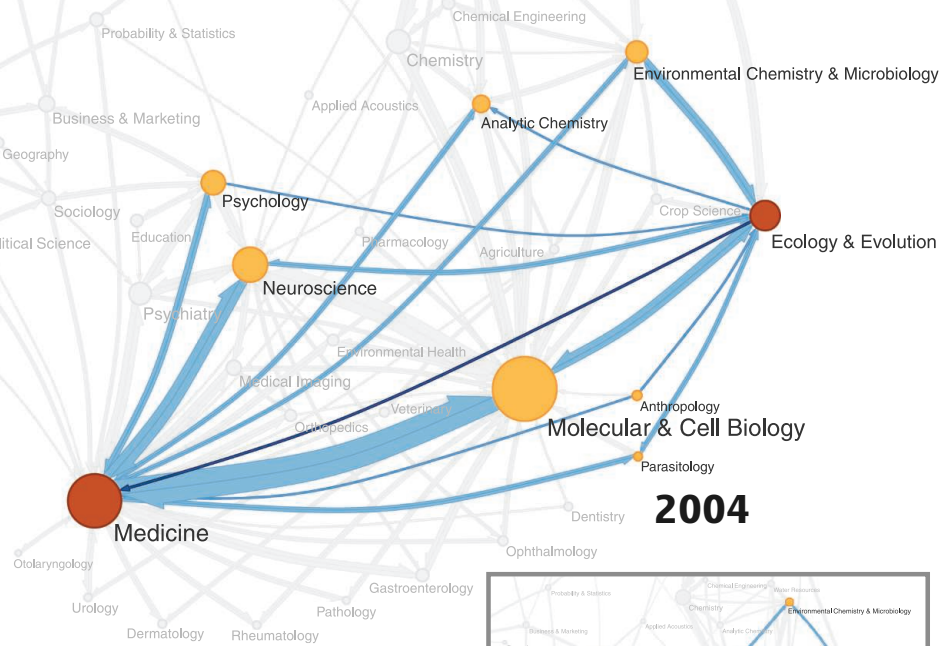

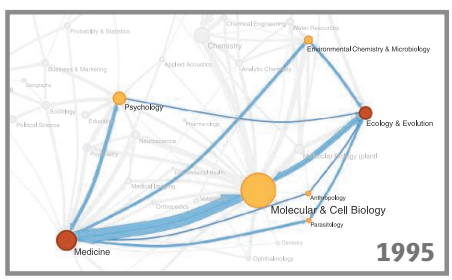

Connections. Citation maps from 1995 and 2004 (*above*) reveal a sevenfold increase in direct interactions between evolutionary biology and medicine.

Despite the intellectual appeal of adding evolution to the medical school curriculum, medical schools are already straining from an explosion in information and technology, and clamors for change come from many directions. "Medical schools have a lot on their plate," says James Lupski of Baylor College of Medicine in Houston, Texas. And, notes Harvard evolutionary biologist David Haig, "Evolutionary thinking is not going to give cheap medical solutions."

Proponents counter that evolutionary thinking can provide a fresh way of looking at the human body and a framework for organiz-

*Evolution in Health and Medicine was held at the National Academy of Sciences in Washington, D.C., 2–3 April 2009.

Two Sides of the Same Coin?

Scientists have long puzzled over the persistence of schizophrenia—a deleterious condition that by rights should have been pretty much bred out of the human gene pool.

At the Sackler Colloquium on Evolution in Health and Medicine held last week at the National Academy of Sciences (NAS) in Washington, D.C., evolutionary geneticist Bernard Crespi of Simon Fraser University in Burnaby, Canada, threw some evolutionary firepower at the question. He proposes that both schizophrenia and autism are disorders of the "social brain"—but at opposite ends of the same spectrum. Psychiatrist Ezra Susser of Columbia University calls it an "imaginative proposal, … although I don't think it's supported yet by the data."

Last year Crespi, with Christopher Badcock of the London School of Economics, presented the hypothesis in a lengthy article in *Behavioral and Brain Sciences*. At the NAS meeting, Crespi claimed that recent research on copy number variations (CNV), segments of DNA containing duplications or deletions, further bolster his case. These new studies suggest that schizophrenia may be the result of multiple rare mutations that occur spontaneously. A number of studies have shown some overlap in genomic "hot spots" for CNVs in schizophrenia and autism, with, in some cases, deletions in one condition just where there are duplications for the other. Some scientists suspect some overlap between the two conditions. Crespi and Badcock think, rather, that they are diametric opposites, occupying the same continuum and thus affecting the same pathways.

That would fit with their theory that psychotic disorders—including not only schizophrenia but also bipolar disorder and some major depression—result from "overdevelopment" of the social brain, and autism spectrum disorders reflect underdevelopment of that brain. Many scientists believe socialization is the main force behind the rapid expansion of human brains, said Crespi, pointing out that in primates the size of the cortex increases with size of social groups. The components of the social brain, according to Crespi, include language, self-awareness, "social emotions" such as pride and guilt, logical thinking, pursuit of goals, and awareness of the mental states of others.

In autism, he pointed out, these functions are deficient. In schizophrenia, on the other hand, they are out of control—the language function leads to auditory hallucinations; awareness of

CREDIT: M. ROSVALL AND C. T. BERGSTROM, *PNAS* **105**, 1118-1123 (2008); EIGENFACTOR PROJECT; (DATA SOURCE) THOMSON-REUTERS' JOURNAL CITATION REPORTS

Published by AAAS

ing a deluge of new genomic information. Those new data are driving home how tightly disease is linked to evolution, says David Valle, a geneticist at Johns Hopkins University School of Medicine. He and others want to move away from viewing the human body as a generic, one-size-fits-all machine. Individuals vary not just in their genetic makeup but in their connections to the microbes in their gut and their environmental exposures. "All this must somehow be understood" to manage disease, says Diddahally R. Govindaraju, a Boston University geneticist who co-organized the meeting. With genomic data in hand, "medical students are much more equipped to understand the connections between all organisms," he adds.

During her talk, Barnes presented several examples that suggest that how humans evolved to cope with past parasitic diseases has predisposed some of us to contemporary health problems. The malaria parasite *Plasmodium vivax*, for instance, depends on a surface protein called Duffy to gain entry into human red blood cells. In certain malaria-endemic areas, a mutation in the gene for Duffy, called *DARC*, leads to the loss of this surface protein, and malaria can't gain a foothold. But Duffy also acts as a sponge to keep immune system messengers in check; otherwise excess immunoglobulin E (IgE), which underlies allergic asthma and other allergic reactions, may be produced. Barnes and her colleagues have found that asthma is associated with the defective Duffy gene in populations in Brazil, Columbia, and the Caribbean whose recent African ancestors lived where malaria was endemic.

Similarly, others have found asthma associated with high IgE in areas such as Egypt where schistosomiasis is common. Today, cockroach and dust mite allergens are well-established triggers for asthma, and those proteins are quite similar to the schistosomiasis worm protein tropomyosin, which sets off the IgE response. People with high IgE are most able to curb parasite infection, but there can be a downside. "Individuals who are most resistant in these [worm-ridden] environments are the ones who produce the most IgE, and they are primed to respond to the common household allergens," says Barnes. She has traced this sensitivity to some variants of the gene for the immune system messenger interleukin 13.

"She has sophisticated evolutionary thinking that she's applied to two different medical problems, and she has not just clinical and epidemiological data, she has the genetic underpinnings. She has the complete story," says Nesse.

Knowing these evolutionary connections could help physicians recognize who might be at increased risk for asthma and who should take precautions to limit exposure to allergens, says Barnes.

At the beginning of the meeting, Harvard Medical School Dean Jeffrey Flier called himself agnostic about the need to incorporate evolution into medical education. But now, "I want to start to influence the medical curriculum toward that," he announced as the meeting wrapped up. "Evolutionary biology needs to get in the queue."

At last, says meeting co-organizer Stephen Stearns of Yale University, "we've gotten the attention of the medical community."

–ELIZABETH PENNISI

others' mental states becomes paranoia; and logic is distorted by uninhibited associations.

Although the data are admittedly preliminary, Crespi maintains they support the notion that autism and schizophrenia are "cognitive, neurodevelopmental, and genomic opposites." He pointed out that some existing theories about the disorders complement this view—for example, some have proposed that glutamate, the brain's main neurotransmitter, is deficient in schizophrenia and overactive in autism.

To evolutionary biologist Randolph Nesse of the University of Michigan, Ann Arbor, who organized the talks on evolution and mental health, the hypothesis shows "the heuristic value of an evolutionary approach in medicine." If correct, "it will fundamentally change our understanding of schizophrenia and autism, … [and] even if it is not, the research is deepening our understanding."

–CONSTANCE HOLDEN

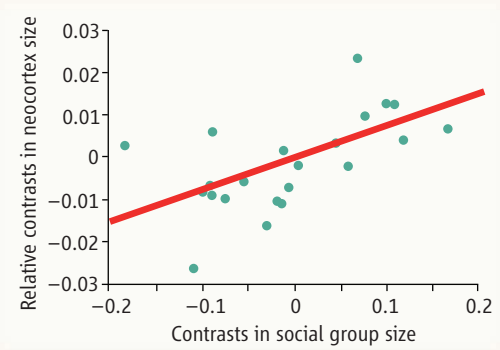

Social brain. In existing primate species, the size of the neocortex in relation to total brain increases with group size.

CREDITS (TOP TO BOTTOM): C. R. JOHNSON AND S. MCBREARTY/UNIVERSITY OF CONNECTICUT; ADAPTED FROM R. A. BARTON, *PROC. BIOL. SCI.* **263**, 1367 (22 FEBRUARY 1996) THE ROYAL SOCIETY

ScienceNOW.org

From *Science*'s Online Daily News Site

Bugs build batteries. Green technology just went viral. Researchers have used viruses to create rechargeable batteries similar to those found in hybrid cars and laptops. Until now, batteries like these were made in chemically intensive, high-heat processes. The results could herald a low-energy, environmentally friendly alternative. http://tinyurl.com/csuebz

Oldest stone blades uncovered. Paleoanthropologists working in Africa have discovered stone blades more than a half-million years old. That pushes the date of the earliest known blades back a remarkable 150,000 years and raises a question: Which human ancestor made them? http://tinyurl.com/dajyf7

Tropical parents more likely to hear, "It's a girl!" Wondering about the gender of your future offspring? Check your GPS. Girls are more likely to be born at tropical latitudes than in temperate or subarctic climes, according to new research. The study provides the first global look at human sex ratios and could shed light on how temperature and day length influence human reproduction. http://tinyurl.com/dfbxag

Heat and acidity ganging up on coral. Human-caused emissions of carbon dioxide are starting to harm marine life with a one-two punch of rising temperatures and stronger ocean acidity. Now a study of a reef in the Red Sea confirms the impact of rising acidity and suggests that it could eventually make reefs across the globe dissolve. "This is a very significant and important result," says Ben McNeil of the University of New South Wales in Sydney, Australia. "We are finally moving towards a more complete picture of how coral reefs will respond to a high CO_2 and warmer ocean." http://tinyurl.com/chn9ej

Read the full postings, comments, and more at **sciencenow.sciencemag.org**.

Published by AAAS

Eppendorf Consumables – it's your sample

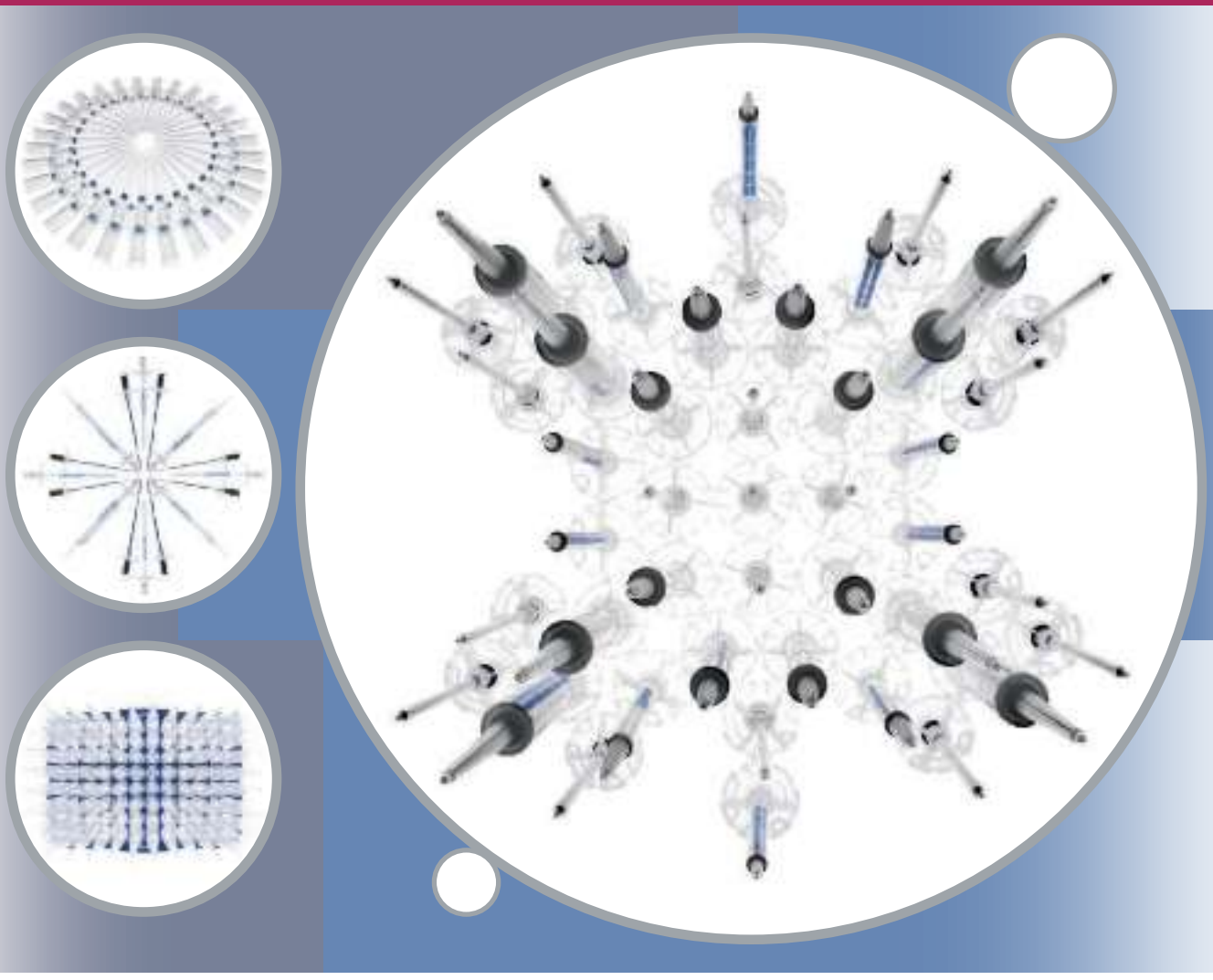

Make the best of it!

Top quality for your sample

Each of your valuable samples deserves the best treatment. See for yourself how the Eppendorf tips will save time and reduce costs.

With respect to material, fit, design and operating forces our tips set new standards. The close environment of each sample should be adapted to its specific quality and purity needs. This can involve a specific purity level or the absence of certain substances, but also stability, reliability, or geometry. The Eppendorf tips are designed to cover all of the specific needs of your samples!

Dispensing at its best! Eppendorf Combitips® plus

- Precise dispensing of liquids with high vapor pressure or higher viscosity
- Contamination-free dispensing due to positive-displacement principle
- Dispensing from 1 µl to 50 ml through 9 different sizes
- Automatic Combitip recognition with Multipette®* plus and Multipette* stream/Xstream®

Learn more about Eppendorf Combitips plus:
www.eppendorf.com/CBT

*Repeater in the U.S.

eppendorf

In touch with life

Your local distributor www.eppendorf.com/worldwide · **Application Support** E-Mail: support@eppendorf.com
Eppendorf AG · Hamburg · Germany · Tel: +49 40 538 01-0 · Eppendorf North America, Inc. · USA · Tel.: +1 800 645 3050

DRUG DEVELOPMENT

New Way to Target Hormone Receptor Thwarts Prostate Cancer

For the unlucky 10% of men diagnosed with prostate cancer who have the most aggressive form, the prognosis is grim. The available prostate cancer drugs may initially shrink their tumors, but the remaining cancer cells usually grow out of control again after a couple of years. These drug-resistant cases account for nearly 29,000 annual deaths in the United States from prostate cancer.

Researchers led by Charles Sawyers at Memorial Sloan-Kettering Cancer Center in New York City have now developed a compound that could prevent some of the deaths. They report online in *Science* (www.sciencemag.org/cgi/content/abstract/1168175) this week that in mice the compound shrank implanted human prostate tumors untreatable with current drugs and that it showed signs of arresting tumor growth in men with similarly drug-resistant cancer. Although more clinical studies are needed, cancer researchers are excited about the potential drug, which tackles prostate cancer by a mechanism different from that of current drugs. "It's possibly a new and better way of treating prostate cancer," says oncologist Philip Kantoff of the Dana-Farber Cancer Institute in Boston.

In prostate cancer, genetic changes within cells allow testosterone and similar hormones, known as androgens, to fuel unrestrained cell growth. Most patients receive drugs to limit the body's production of androgens. If the tumor continues to grow, physicians prescribe other drugs that bind to the androgen receptor in the prostate cell's cytoplasm so that the hormone cannot land on the receptor and turn it on. But these drugs usually fail after a time.

This problem intrigued Sawyers, who had earlier worked on resistance to Gleevec, a potent leukemia drug he helped develop. In 2003, Sawyers's team showed why cells from advanced prostate tumors eventually thwart standard drugs: The cells produce high levels of the androgen receptor, and this makes them so sensitive to androgens that even the receptor-blocking drugs can stimulate the cells to grow. Sawyers next joined forces with chemist Michael Jung, whose group at the University of California, Los Angeles, synthesized nearly 200 androgen-like compounds. The researchers screened the molecules, selecting ones that bound tightly to the androgen receptor but didn't activate it. Jung's group then tweaked promising candidates to make two potential drugs.

In addition to binding to the androgen receptor, the new compounds seem to hinder it from getting into the cell's nucleus, binding to DNA, and triggering the expression of genes, the team reports. "It's a beautiful story," says cancer pharmacologist Donald McDonnell of Duke University in Durham, North Carolina.

In a clinical study with one of the compounds, dubbed MDV3100, levels of prostate-specific antigen—a marker for prostate tumor growth—dropped by at least 50% in 13 of 30 patients with advanced disease for whom other treatments had failed. "For this group of patients, this is a very impressive result," says Sawyers. Medivation Inc. in San Francisco, California, which collaborated on this work, is now testing the drug at higher doses on more patients. (Sawyers is a consultant for the company and is a co-inventor on a patent for MDV3100.)

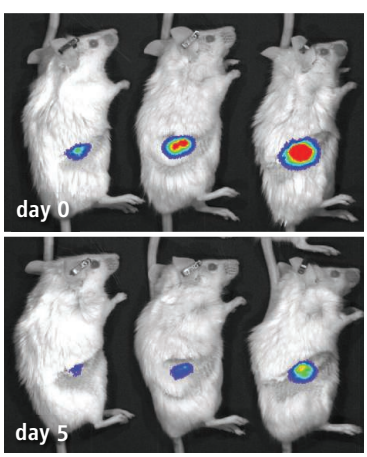

Smart weapon. A new compound that gums up the androgen receptor shrank drug-resistant prostate cancer tumors in mice (*lower row*, tumors after 5 days).

Even if MDV3100 extends the lives of men with advanced prostate cancer, their tumors will likely become resistant to it, too. But researchers hope the compound can be combined with another drug candidate, developed by a different team but also in trials, that stops cancer cells from making their own supply of androgens. "A very exciting possibility" is that a cocktail of these drugs will prevent men with early prostate cancer from ever reaching the drug-resistant stage, says Kantoff, who heads one of several centers that are testing MDV3100.

–JOCELYN KAISER

CREDIT: C. TRAN *ET AL.*, *SCIENCE*

ScienceInsider

From the *Science* Policy Blog

A federal appeals court in Washington, D.C., last week ruled that the sequence of DNA obtained from a known protein is obvious and therefore unpatentable. The court was ruling on a case, *In re Kubin*, involving a **patented gene sequence** for the human immune protein NAIL, owned by Amgen Inc. in Thousand Oaks, California. The judges ruled that it took no original insight to work out the gene's code. The decision is the latest blow to **gene patents**, which are facing increased scrutiny.

A scientist targeted by animal-rights extremists is taking to the streets to **rally support for research using animals.** In March, animal-rights terrorists burned the car of University of California, Los Angeles, neuroscientist J. David Jentsch, the latest in a string of such attacks on UCLA faculty. Now Jentsch has founded a chapter of Pro-Test, a British group supportive of animal research. A rally at UCLA on 22 April coincides with a planned animal-rights rally elsewhere on campus, but Jentsch says he is not looking for a confrontation.

News that the Howard Hughes Medical Institute's new batch of 50 **early-career awards** includes only nine women is causing a stir among those working to broaden participation in science. The institute says its decisions were based strictly on scientific merit and notes that only a quarter of the applicants were women.

Elsewhere … Oceanographers took issue with recent reports that a German-Indian experiment to **fertilize the ocean with iron** shows the technique can't work. The nomination of a new Census director drew applause from scientists and criticism from some legislators. The blog also noted Japanese plans to send a **walking robot** to study the moon, a new **tornado hunting** program, plans by Stanford University to publicize **payments to faculty members** from drug or device firms, and police protection for the head of **India's space program** against a possible terrorist attack.

For the full postings and more, go to **blogs.sciencemag.org/scienceinsider**.

Published by AAAS

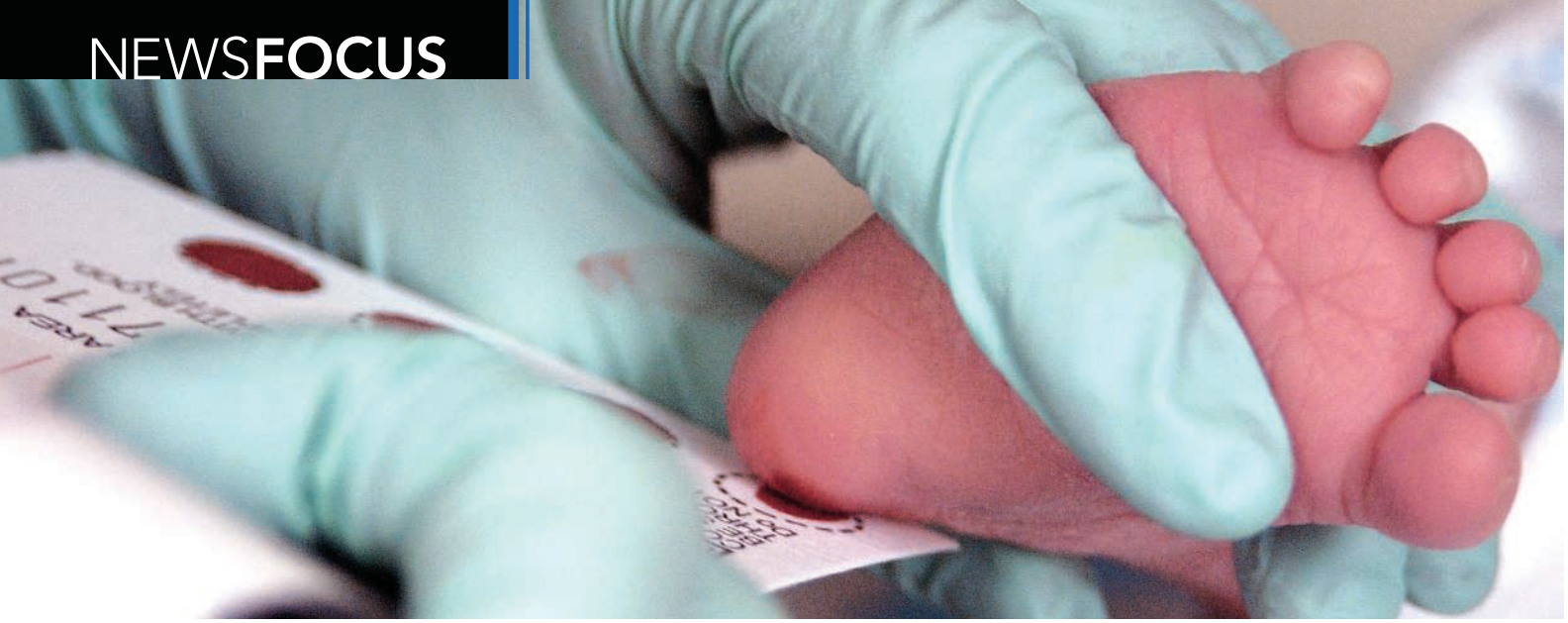

Science Gold Mine, Ethical Minefield

Health agencies launched a system 40 years ago to identify babies at risk. Now there are millions of blood samples in files that researchers want to access, raising public concern

FROM MINNEAPOLIS TO PARIS TO AUCKLAND, nearly every new baby experiences the same procedure hours after birth: a prick of the heel to draw a few drops of blood, which are applied onto filter paper. The paper is shipped off and tested for rare metabolic diseases, which can be devastating if they're not treated early.

Most parents have only the faintest idea that this testing occurs; they are even less likely to know that health agencies are storing their child's blood for years, in some cases indefinitely, in dusty file boxes or deep-frozen in giant warehouses. This growing treasure trove of samples is catching the attention of researchers, who are turning to them to study everything from the origins of childhood leukemia to toxin exposures in utero. The blood spots have been "vastly underexploited in the past," says Mel Greaves, a pediatric cancer biologist at the Institute of Cancer Research in London.

But the same feature that makes blood-spot repositories so potent—mandatory screening means that they capture entire populations—also makes them ethically and legally tenuous. Parents of newborns are rarely informed that samples will be stored and made available for research. And if studies do take place, they're likely to be done anonymously; most families will never know the findings on their child's blood.

The newborn-screening system has skirted some questions about consent in the past. But as more locales shift to long-term storage and more researchers seek access to the blood spots, it now faces direct challenges. In Minnesota, a group promoting confidentiality in health care has been engaged in a 6-year battle with the state legislature and the courts over whether its newborn-screening program violates privacy by storing and disseminating samples. Last month, a civil rights group sued the state of Texas, charging that its screening program is unconstitutional because it stores samples long-term without obtaining informed consent.

Such objections reflect a discomfort with government agencies gathering and filing away everyone's DNA without explicit notification. "It's one thing to justify the testing at the time of birth for disease," says James Harrington, director of the Texas Civil Rights Project in Austin, whose organization filed the lawsuit against the Texas screening program. "It's quite another just to keep it for something as nebulous as scientific use at a later date." Parents, he says, are "not led to think" that anything more than testing of their baby is taking place, and "that deception is troublesome."

A federal committee that advises the secretary of the U.S. Department of Health and Human Services on newborn screening is now considering the use of blood spots. Among other issues, the panel is reviewing how long samples should be stored and under what conditions they should be available to researchers. It hopes to make recommendations later this year.

Some states, such as Michigan, are trying to stay ahead of the critics, consulting bioethicists and residents as they transform their repository of 4 million blood spots into one that's friendlier to researchers. "It's become a real social and, I think, political hot potato," says Aaron Goldenberg, a bioethicist at Case Western Reserve University in Cleveland, Ohio, who has studied Michigan's efforts. "Is the use of these samples … a big enough shift to make us rethink issues of informed consent? A lot of screeners are afraid to go there because they don't want to damage the system."

More than a PKU test

Newborn screening began in the 1960s, when physicians recognized that babies with certain rare diseases, such as phenylketonuria (PKU), could be saved from a lifetime of mental retardation if they were identified immediately. Many countries initiated mass-screening programs, which have expanded dramatically as new technologies made it easier to test for many gene mutations at once. In 2005, the American College of Medical Genetics recommended that all U.S. states screen for 29 conditions. Most states quickly adopted this as a minimum, and today some test for as many as 50.

At the same time, "everyone began to see the value of these specimens in terms of future research," and many locales shifted from quickly discarding the samples to storing

Online
sciencemag.org
Podcast interview with author Jennifer Couzin-Frankel.

CREDIT: ERIC T. SHELER/WIKIPEDIA

Published by AAAS

them long-term, says Brad Therrell, director of the federally funded National Newborn Screening and Genetics Resource Center, which is based at the University of Texas Health Science Center at San Antonio and provides information on newborn screening to the public and health care workers. In North Carolina, epidemiologist Andrew Olshan of the University of North Carolina, Chapel Hill, and other researchers lobbied the state health department not to throw away samples after just 1 year. Today, North Carolina stores blood spots in perpetuity. In the United Kingdom, storage varies by region from 2 months to indefinitely; at Great Ormond Street Hospital for Children in London, the blood-spot card of every child with leukemia in the area is yanked from the repository at the time of diagnosis to ensure that it will be available for studies. Normally, London-based samples are stored for 10 years.

Greaves pushed for this change, after pioneering a blood-spot technique in the mid-1990s called "backtracking." When children were diagnosed with leukemia, he and others turned to their blood spots to determine whether the signature abnormalities in their cancer cells were also present at birth. "By the time you see the patient and you characterize the mutation, it's too late" to understand when and how cancer began, says Greaves. Hunting for preleukemic DNA in the sea of 30,000 white blood cells that make up each blood spot, he found that in 50% to 100% of cases, depending on the form of leukemia, genetic mutations were present—suggesting that the cancer was seeded in utero.

Epidemiologist Gary Shaw of Stanford University in Palo Alto, California, meanwhile, has used blood spots to examine interactions between genes and the environment. For example, he's focused on the intricate dance between cigarettes, folate in the maternal diet, and birth defects such as cleft lip. By studying genes that metabolize cigarette smoke and those that code for folate, he's found that maternal smoking compromises folic acid's role in healthy fetal development and raises the risk of cleft lip—a discovery, he says, that required an enormous number of DNA samples.

Shaw is keen on another hot area as well: examining not DNA but contaminants, such as pesticides, that may be present in blood spots. By combing through hundreds or thousands of samples, epidemiologists can assess exposure levels across a population or compare different regions. Or they can match exposure with certain health problems. Henry Spliethoff, an environmental health scientist at the New York State Department of Health Center for Environmental Health in Troy, wondered whether phasing out products that contained perfluorinated compounds around the year 2000 had reduced exposure levels in utero. By comparing blood spots collected before 2000 with those collected after, he found that exposure had gone down by as much as 70% between 1999 and 2004 and had dropped further after that. Such studies are still in their infancy.

Just gaining access to the spots can be a logistical challenge because many U.S. state health departments are strapped for cash and don't have the staff to handle a growing number of requests. At Maryland's health department, Christopher Loffredo, an epidemiologist at Georgetown University Medical Center in Washington, D.C., says, "I spent 6 months of my life going through boxes and boxes and boxes of blood spots looking for the ones I needed" for a study on congenital heart disease. California, which has stored samples since 1983 and now has 14 million, gets about one research request every 2 weeks. But because it is short of staff, it hasn't been filling them for more than a year.

Safeguards and gaps

In most countries, researchers must seek approval from an ethics board before getting their hands on the blood spots they want to study. They generally obtain informed consent in cases in which a blood spot could be identified—for example, when detailed health information is needed. Greaves, for example, seeks consent from families of the children with cancer he studies. In cases without consent, the health department might provide researchers with an anonymous sampling of blood spots, offering them, say, geographic information but nothing more; or it might provide control samples for a study of a particular disease.

Many people consider such protections insufficient. In the Netherlands, where samples are kept for 5 years and sometimes used in research studies, the newborn-screening program was thrust into turmoil in 2000. A fireworks depot exploded in the Dutch city of Enschede, killing 22 people and injuring almost 1000; officials discussed using blood spots to help identify the dead. An outcry ensued, because the Dutch public hadn't realized the samples were being banked. "People were very angry. … It was never kept secret, but it wasn't clear," says J. Gerard Loeber, a member of the steering committee for the Dutch screening program and president of the International Society for Neonatal Screening. Since then, the country has incorporated informed consent for the program into its prenatal care. Midwives offer the chance to opt out of sample storage, something about 100 to 150 families do each year, says Loeber.

Consent standards vary wildly between and even within countries. In Australia, screening programs do not seek consent for sample storage; in New Zealand, practices differ from region to region. In France, where samples are stored for at least 1 year, researchers generally must have families sign their children's blood-spot card if they wish to perform a specific study, says Jean-Louis Dhondt of the Catholic University in Lille, who heads up the screening lab of one French region, Nord-Pas de Calais. "We have no right to look at other genes" beyond those

NEWBORN BLOOD'S VARIED USES

Scientific question	Researcher and Institution
Origins of childhood leukemia	Mel Greaves, Institute of Cancer Research, U.K.
Birth defects and folate	Gary Shaw, Stanford University, California
Gene-environment origins of congenital heart disease	Christopher Loffredo, Georgetown University, Washington, D.C.
Contaminant exposure in utero	Henry Spliethoff, New York State Department of Health
Genetics of preterm birth	Mads Melbye, Statens Serum Institut, Denmark

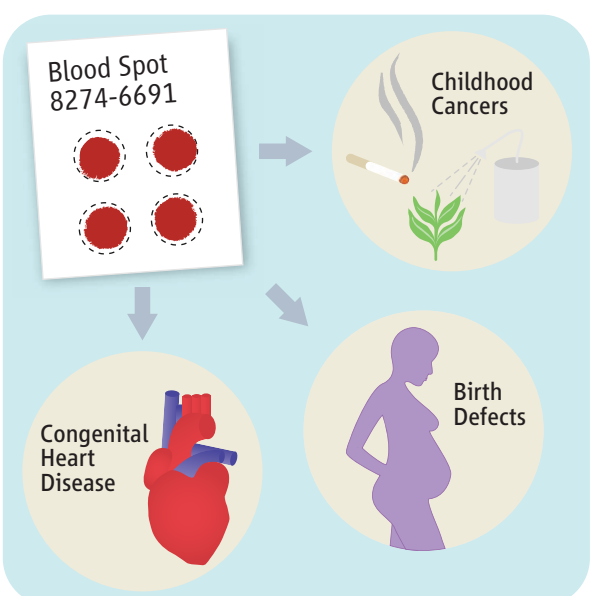

CREDIT: NEWBORN GRAPHIC: J. NEWFIELD/*SCIENCE*

Published by AAAS

already being tested for, Dhondt says.

In Denmark, where the public enthusiastically participates in national biobanks, sample storage is discussed in newspapers and elsewhere, and residents "certainly know" that research is performed on the blood spots, says Mads Melbye, head of epidemiology at the Statens Serum Institut in Copenhagen. Individuals can opt out of having their samples used in research if they wish.

The patchwork U.S. system changes from state to state: Blood-spot cards are kept indefinitely in some places and discarded immediately after initial testing in others. A handful of states, including California and Michigan, have statutes that provide legal authority to store the blood spots.

But nearly everywhere in the United States, there is no informed consent for any element of the screening program. Families can decline to participate on religious or other grounds, or accept screening but refuse to have the sample stored. But they must know to do so in advance, and most do not. Even though some states distribute information sheets at a child's birth, "many people aren't aware of the infant-screening program," says Tom Tomlinson, a bioethicist at Michigan State University in East Lansing. And "you can't do research on people without their consent."

Tomlinson was recruited to advise the Michigan Department of Community Health, which plans to make its repository more accessible to researchers and is considering the ethical minefields around doing so. Samples there are stored in perpetuity. The Michigan Neonatal BioTrust, as the effort is called, is trying to shift storage from room temperature to freezing to better preserve the samples, improve tracking of what's been distributed to researchers, and encourage community input into how samples are studied.

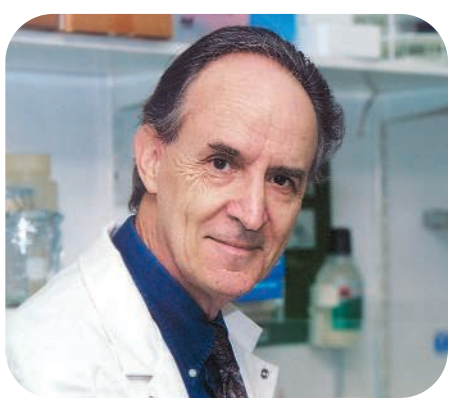

Research treasure. Cancer biologist Mel Greaves uses blood spots to track the trajectory of childhood leukemia.

"There's an ethical gap" in how federal rules govern protection of human subjects, says Tomlinson. "They are all about protecting individuals against risk" and guarding privacy. But "people have other [concerns about] the way in which their materials are used," for example, to study medical conditions that could stigmatize an ethnic group to which they belong.

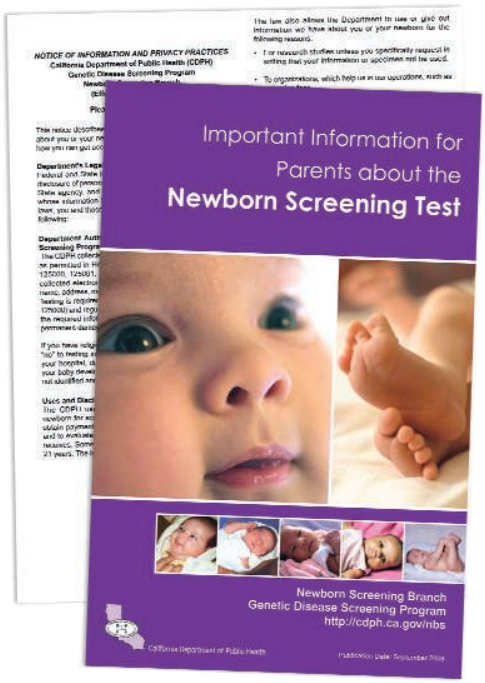

In brief. California tells families that they must opt out if they don't want a child's blood used in research studies.

Delayed impact

Information from a baby's blood spot may pose other difficult questions. For example, should parents be told if researchers discover that their child carries a gene that increases the risk of disease? In New Zealand, one group inquired about using samples to examine the prevalence of gene mutations for long QT syndrome, a condition that can cause sudden cardiac death. "We went to an ethics committee and they said, 'It's not ethical to do this [anonymously] because you might find information that's useful to families,' " says Dianne Webster, director of the New Zealand Newborn Metabolic Screening Programme in Auckland. But gathering permission from families was deemed "too logistically difficult," and the project was abandoned.

In Denmark, Melbye and his colleagues have funding from the U.S. National Institutes of Health (NIH) to examine gene sequences that might contribute to preterm birth in 4000 mothers and their babies. (Samples were collected by the country's biobanks and a study on pregnant women.) The Danish ethics committee chose not to mandate seeking permission from the mothers, concluding that the project was unlikely to come up with genetic risk factors that would make preterm birth extremely likely in a future pregnancy. If that happens, however, says Melbye, "we will write to the scientific ethics committee and say, 'This is a very strong marker, it's important for the mothers to know—they will decide what needs to be done.' "

Obtaining consent years or decades after a blood spot was collected may not be possible, some say. Furthermore, seeking consent at any time could potentially be alarming to families. Imagine, for example, a study that finds a mutation in blood spots whose medical significance is fuzzy, says Jeffrey Botkin, a pediatrician and bioethicist at the University of Utah. "No way can you call those families up and say, 'We've found something about your child,' " because there's no guidance anyone can offer. "You're not going to do anything with that information." Botkin received NIH funding last year to examine the ethical issues and public attitudes involved in retention and research use of blood spots.

Tomlinson, however, notes that in his experience in Michigan, a "significant minority" of the people he speaks with would prefer that researchers obtain consent from individuals whose blood spots are used in a given study. That desire may be important to heed, in part to maintain good community relations.

Leaders of newborn-screening programs are sensitive to public perceptions: A misstep, they fear, could taint the entire program, leading families to decline screening altogether. "These are extremely valuable samples for public health research," says Logan Spector, a childhood cancer epidemiologist at the University of Minnesota. "That's why I would support strengthening the law to protect them from any perceived misuse"—for example, invoking a "firewall" that allows for research but not nonresearch uses, like those involving law enforcement. Botkin favors obtaining consent from a couple before a child's birth for storage and potential research. After the lawsuit in Texas was filed in March, members of the Texas House of Representatives introduced legislation to require consent.

Opening up the inner workings of the screening program is crucial to keeping samples in the world of science, says Loeber, citing his own experience after the explosion at the Dutch fireworks depot. "If you don't do that, some parents will always feel that something secret is going on. … The general population has always the sense of, 'Hmmmm, what are they doing with the blood of my baby?' "

–JENNIFER COUZIN-FRANKEL

CREDITS (TOP TO BOTTOM): CALIFORNIA DEPARTMENT OF PUBLIC HEALTH; COURTESY OF MEL GREAVES

Pay dirt. A sauropod is emerging from this riverside dig. (*Inset*: Bones in orange recovered in 2007, blue in 2008.)

PALEONTOLOGY

The 'Tamba Dragon' Has Japanese Dinosaur Hunters All Fired Up

A serendipitous sauropod specimen could shed light on the evolution of our planet's largest land animals

TAMBA, JAPAN—Haruo Saegusa's 17 years of encounters with amateur fossil hunters didn't prepare him for the surprise he was in for on 9 August 2006. Ordinarily, he says, people who bring specimens to the Museum of Nature and Human Activities in Sanda, in central Japan's Hyogo Prefecture, suffer from "fossil mania," imagining that oddly shaped rocks or round stones they've found are dinosaur bones or eggs. So when a pair of elderly men showed up with two objects pulled from the bank of the Sasayama River, Saegusa, a paleontologist at the Sanda museum, had low expectations. But the fossils were bona fide. "I was astonished," he says.

After Saegusa visited the site in nearby Tamba with museum colleagues the next day, he says, "I thought we might get one or two bones and that would be it." Instead, they hit the jackpot. So far, Saegusa's team has unearthed 50 large bones—about one-third of a skeleton of a sauropod from the early Cretaceous, dating to 120 million to 140 million years ago.

"It could be a really great skeleton," says Jeffrey Wilson, a paleontologist at the University of Michigan, Ann Arbor. The find, a work in progress, could be a new species, filling an evolutionary gap in this diverse group of colossal plant eaters. The specimen, along with other fossils recovered recently in Japan, raises questions about when sauropods spread across Asia. But the challenges of prizing the rest of *Tamba-ryu*—the Tamba dragon, as it has been dubbed—from the riverbank may prove insurmountable.

The fossil haul includes the dinosaur's sacrum (the bone at the base of the spine), parts of the pelvis, numerous vertebrae, several ribs, some teeth, and the braincase, a rare find. Saegusa and colleagues estimate that the dinosaur was 18 to 20 meters long—average among sauropods, which diversified during the Jurassic and became common in the Cretaceous. Its chevrons—bones along the tail's underside—have a mix of primitive features and advanced ones previously thought to be restricted to the titanosaurs, a group that arose later in the Cretaceous. "The derivation of titanosaurs from [earlier dinosaurs] is more complicated than previously assumed," Saegusa says.

The find could shed light on the evolution of characteristics such as body size and neck length, says Wilson. He is particularly excited about the braincase because it preserves anatomical information useful for comparing sauropod specimens. "The pattern of genealogy is really important because it tells us about the timing and sequence of the appearance of certain characteristics," he says. The ability to clarify lineages and relationships would make the Tamba dragon "a very important specimen," adds Yoichi Azuma, a paleontologist at Fukui Prefectural Dinosaur Museum in Katsuyama.

Stay tuned. More remains may be entombed behind Haruo Saegusa.

The Tamba dragon also has a tale to tell based on when and where it lived. During the Jurassic, sauropod species such as *Brachiosaurus* and *Diplodocus* were "running all over" North America, Africa, and Europe, Wilson says, but "they don't appear in Asia," suggesting a geographic barrier. Then during the Cretaceous, sauropods boomed in Asia. "There is a real change in the fauna in Asia right around the Jurassic-Cretaceous boundary, and we don't know why that is," Wilson says. The Tamba dinosaur "will allow us to see in a clearer way what the Asian sauropod fauna looked like," he says.

A sharper view may hinge on recovering more of the Tamba dinosaur. The 5-meter-deep excavation is submerged much of the year: during spring runoff, the summer rainy season, and when typhoons hit in the fall. This limits digging to 2 months in late winter when the river is at its lowest. The team recovered fewer bones this year than in the previous two seasons, and Saegusa worries that more of the skeleton might be scattered in a rock layer that dives under the riverbed. Following it much deeper would require a costly and difficult diversion of the Sasayama, which Saegusa says would be hard to justify unless they could guarantee a payoff. Digging will resume next winter, he says, but "money could be a problem going beyond that."

Tracking the formation to other exposures in search of additional specimens is also problematic. Earthquakes and volcanic activity have warped Japan's geologic layers, resulting in few complete dinosaur skeletons, says Makoto Manabe, a paleontologist at the National Museum of Nature and Science in Tokyo. And because much of the country is covered with lush vegetation or concrete, Manabe says, "it's very difficult to prospect for fossils in Japan." Meanwhile, a legal loophole in Japan impedes serendipitous discoveries: Although builders must inform authorities if they find archeological artifacts at construction sites, the law does not apply to fossils.

Such circumstances make the Tamba dragon all the more remarkable. "It was like hitting the lottery," says Saegusa.

–DENNIS NORMILE

CREDITS: D. NORMILE/*SCIENCE*; MUSEUM OF NATURE AND HUMAN ACTIVITIES, HYOGO

GLOBAL FISHERIES

Détente in the Fisheries War

After a controversial projection that wild-caught fish will disappear, top researchers buried the Dhatchet to examine the status of fisheries—and what to do about it

All gone? A controversial projection of exhausted fisheries led to a new look at the oceans.

Doomsday will come to fishes across the world's oceans by 2048. That was the startling implication of findings published in 2006 by marine ecologist Boris Worm of Dalhousie University in Halifax, Canada, and several colleagues. The projection was merely a side note in a paper in *Science* about the relationship between biodiversity and ecosystem services in the oceans, which concluded that the world's oceans were in bad shape, in part because of overfishing. Then, in the next-to-last paragraph, the authors extrapolated from the percentage of fisheries that have already collapsed and predicted that in 32 years no more fish would be caught in the ocean. That point, not their larger conclusions on the role of biodiversity in ecosystem functions, was highlighted in press releases and then garnered headlines around the world.

Many fisheries scientists were appalled. Trained in quantitative techniques for determining the abundance of fish stocks, they questioned the methods used in Worm's global assessment, such as a reliance on the mass of fish reported caught. They also blasted the paper for ignoring fisheries that are doing well, like those in the northeastern Pacific and New Zealand, and those that are now recovering from decades of overfishing.

One particularly prominent critic was Ray Hilborn of the University of Washington, Seattle. In media interviews, he called the analysis "incredibly sloppy" and the projection "mind-boggling[ly] stupid." Worm and his colleagues defended their analyses in responses in *Science* and elsewhere. The conflict continued a charged and long-simmering debate between marine ecologists and fisheries scientists about the status of the world's ocean ecosystems.

Yet less than a year later, Hilborn and Worm began meeting on neutral ground to hammer out their differences—to the amazement of some observers. "There were such extreme attacks on the [Worm *et al*. paper] that it was a little hard to imagine that they would have a constructive dialog," says ecologist Larry Crowder of Duke University in Durham, North Carolina. Working under the auspices of the National Center for Ecological Analysis and Synthesis (NCEAS) in Santa Barbara, California, a grant-funded center run by the University of California to facilitate collaboration among ecologists, Hilborn and Worm have brought together some 20 scientists from their respective disciplines as well as dozens of graduate students who they hope will also learn to think more broadly. "This is the most interesting thing I've been involved in in a long time," Hilborn says.

The goal was to figure out why their different data or methods yield such divergent impressions of ocean ecosystems—and in the process create better databases that both camps deem reliable and informative. Perhaps more importantly, they have used the new databases to develop a common vision of how to balance fishing and conservation most effectively. Joint publications are expected to start appearing later this year. "I have high expectations that they'll come back with useful outcomes," says Steven Murawski, chief scientist of the National Oceanic and Atmospheric Administration (NOAA) Fisheries Service in Silver Spring, Maryland, who participated in the first meeting.

Head to head

In large part, the Worm-Hilborn clash reflects the different worldviews of the two disciplines. Fisheries scientists see marine ecosystems as a resource to be used, whereas marine ecologists usually envision pristine, unfished habitats as the ideal.

> *"There are a lot of problems, but things may not be as bad as ecologists have thought."*
>
> —RAY HILBORN, UNIVERSITY OF WASHINGTON, SEATTLE

The two fields also tend to rely on different types of data. In their 2006 *Science* paper, Worm and his co-authors were trying to look at the global impacts of marine biodiversity loss. For that, they had to rely on the most comprehensive kind of data available: the tonnages that countries report are caught. Fisheries scientists, by contrast, tend to look at individual stocks of fish and typically use sparser data gathered

CREDIT: ARNULF HUSMO/GETTY IMAGES

Published by AAAS

by scientific means; they consider catch reports unreliable.

High-profile journals have been publishing dire warnings about the impact of fishing on ocean ecosystems for years. One of the first was a 1998 *Science* paper by Daniel Pauly of the University of British Columbia in Vancouver, Canada, one of the few fisheries biologists who takes a global perspective (*Science*, 6 February 1998, p. 860). He and his colleagues speculated provocatively that with continued overfishing, only jellyfish and plankton would remain to be harvested.

In 2003, a paper in *Nature* continued that tradition. Written by Worm and the late Ransom Myers of Dalhousie, the paper concluded that industrial fishing had reduced global populations of sharks, tuna, and other large open-water predators by 90%. Again, the conclusion attracted international media attention. It was also the first big paper for Worm, then a postdoc. Now 39, he is a rising star among marine ecologists; soft-spoken and media-savvy, Worm is a passionate conservationist.

Fisheries scientists fought back. Leading the charge was Hilborn, who received the Volvo Environment Prize in 2006 in part for his work on mathematical models and fisheries management. In a scathing opinion piece titled "Faith-based Fisheries," which was published in *Fisheries* in November 2006, Hilborn accused Worm, Myers, and others of cherry-picking data to support "sensational but unsubstantiated headlines" and asserted a "lack of the basic skepticism needed in science." Swinging widely, he also took *Science* and *Nature* to task for seeking publicity at the expense of rigorous peer review.

A crack in the ice emerged when the two scientists were invited to talk on a National Public Radio call-in show about the future of fish not long after publication of the 2006 paper. When they started to discuss the issue on air, Worm recalls, they didn't seem to be that far apart. The two continued to converse by phone and agreed to collaborate at NCEAS. "Ray and I realized independently this [public disagreement] was not going to make the science any better, because you have the danger of being blind in one eye," Worm recalls.

Splitting the difference

In large part, it was the prospect of looking at new data sets that brought Worm and Hilborn to the table. The two decided to assemble a resource they both could agree on. "It's being data-driven that's led us to common ground," says Hilborn, who is now a member of *Science*'s Board of Reviewing Editors. The results are much more comprehensive and rigorous databases to examine the status of the world's fisheries, NOAA's Murawski says.

The first target was an updated collection of stock assessments, the gold standard of analysis in fisheries science. These consist of surveys and statistical models of fish populations. Second, they compiled a similar database of trawl surveys, a broader sampling of fish populations usually conducted by research vessels. They also collected about two dozen ecosystem models, which show the interactions of various species in a particular fishery. Finally, they also examined the catch data that Worm and his colleagues had relied on in their 2006 paper.

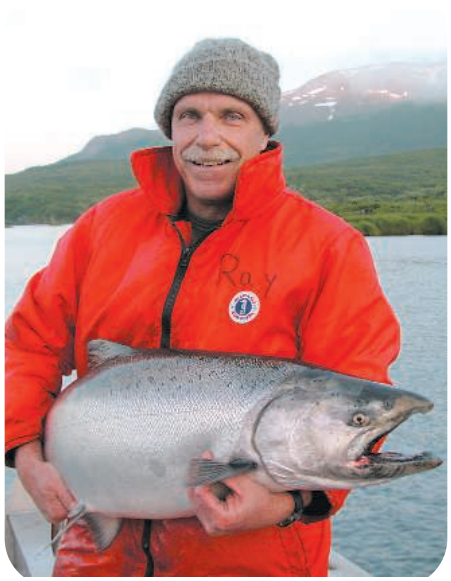

Hooked. Boris Worm (*top*) and Ray Hilborn set aside past disagreements to launch a joint study on the state of the world's fisheries.

The databases had to be a joint effort, they say, because that showed that the group was not trying to attack fisheries management—and that helped persuade fisheries scientists elsewhere to contribute data. "There's trust because there are checks and balances in the group, there are people from each field," Worm says.

With these new tools, the group is now taking a fresh stab at assessing the status and trends in world fisheries and ecosystems. They plan to publish an overview this summer. Although Worm and Hilborn don't agree on everything—such as the projection that first triggered the project, the disappearance of wild-caught fish by 2048—they have found middle ground about the present. "There are a lot of problems, but things may not be as bad as ecologists have thought," Hilborn says. For his part, Worm says he's surprised by the number of places where managers have gradually reduced fishing over the past 10 years.

Both agree that more needs to be done. They are outlining a balance between extraction and conservation, a way to most effectively manage the world's oceans for human use while maintaining biodiversity and the structure of natural ecosystems. The key conclusion—coming from comparisons of management in both successful and failing sites—is that a little change in fishing practices could go a long way. The current practice is for fisheries scientists to set a target called maximum sustainable yield (although in practice, many stocks are overfished). Hilborn and others had already noted that it is more economical to fish less than this (*Science*, 7 December 2007, p. 1601). The new findings show that somewhat reducing fishing offers biological benefits as well, including more preservation of biodiversity. "There is this new area of consensus, that fishing below maximum sustainable yield would be beneficial in all these realms," Worm says.

In their final meeting next month, the researchers and graduate students will summarize what they've learned and finalize results of the main papers. "You can already see how things will trickle down and be taken up and processed by the next generation of scientists, who hopefully will not be part of that polarized debate anymore," Worm says. Although it can sometimes be useful to have contrasting views, he says, "there is only one world, and we need to work on it together."

–ERIK STOKSTAD

CREDITS (TOP TO BOTTOM): D. ABRIEL/DALHOUSIE UNIVERSITY; PETER WESTLEY

Cash crop. The fields of west Texas are producing a harvest of electricity, along with cotton.

ENERGY

Renewables Test IQ of the Grid

Everybody agrees that tomorrow's electrical grid must incorporate wind and solar power seamlessly. But solving the reliability issue won't be easy

In the afternoon of 26 February 2008, the winds died down in a stretch of west Texas that's home to thousands of tall wind turbines. Over a span of 3 hours, the turbines' contribution to the state's electricity grid fell by 75%. That 1500-megawatt (MW) drop—equivalent to the output of three midsized coal-burning power plants—coincided with a spike in demand. At 6:30 p.m., the alternating current in the state's transmission lines started to alternate more sluggishly, an ominous signal that the system was approaching collapse.

Fortunately, managers of the state's power network had struck a set of agreements with large industrial customers allowing them to cut off power temporarily in exchange for lower rates. Within 10 minutes, about 1200 MW of load was sliced from the sagging electrical grid, and the system stabilized. Texans were blissfully unaware that the state's grid had just dodged a bullet. But the episode was an unsettling reminder that not all electricity is created equal, and that clean energy harvested from nature can complicate the job of keeping the lights on.

Such episodes could become more common—and disrupt service—if plans for a massive expansion of wind and solar power are realized. Both sources of energy are variable and relatively unpredictable. Those traits will require the electrical grid to become smarter and more agile, so that it doesn't stumble and collapse when the wind stops blowing or clouds obscure the sun.

Calls for a "smart grid" have become routine in Washington, D.C., and President Barack Obama's stimulus package includes $4.5 billion for "smart grid demonstration projects." Utilities, national laboratories, and universities are all gearing up to compete for those funds. One focus is installing "smart meters" in homes that show consumers how much energy they are using. Another involves planning high-capacity transmission lines to bring wind and solar power from the nation's high plains and deserts to its cities, creating an interstate highway for green power.

But the most important piece of the renewable-energy puzzle may be finding a solution to its erratic spikes and dips. "Everyone understands the need for transmission," says Arshad Mansoor, vice president for power delivery and utilization at the Electric Power Research Institute (EPRI) in Palo Alto, California. "Not everyone understands the reliability issue."

Dance partners

The electrical grid demands exquisite balance. At every instant, the supply of electricity throughout the system—thousands of power plants, substations, and transmission lines—must equal demand. If not, wires overheat, voltage drops, and circuit breakers snap open to protect parts of the grid where supply still matches demand.

To keep the system running smoothly, grid managers line up generating capacity ahead of time. Then, as actual demand swells and falls, minute by minute, gas turbines automatically throttle up and down and coal-fired plants deliver more steam to generators. "Utilities have become accustomed to variations in the time frame of minutes to hours," says Loren Toole, an electrical engineer at Los Alamos National Laboratory in New Mexico. But Toole says the current system isn't nimble enough for wind and solar generators, which can produce surges and drops in electricity within a few seconds or minutes.

That variability hasn't caused problems yet for the overall U.S. grid because solar and wind power supply just over 1% of the country's electricity. But many states, including California, New York, and Illinois, have passed laws requiring that at least 20% of their electricity come from renew-

CREDIT: JOSIAH DAVIDSON/GETTY IMAGES

Published by AAAS

able sources within a decade or two (see map, below). Congress is drafting a similar requirement for the entire country.

A study that General Electric prepared for the Electricity Reliability Council of Texas shows the impact on the Texas grid of incorporating 15,000 MW of wind power—four times the amount it now receives. About twice a year, the study predicts, grid managers would see the supply of wind-derived electricity fall by 2400 MW—the equivalent of four or five midsized coal plants—in less than 30 minutes. Power from photovoltaic panels, meanwhile, can drop when clouds come over, only to spike back up a few minutes later.

What utilities desperately need, according to industry insiders, is an array of "dance partners"—sources of additional power that can mirror every tricky move from the forces of nature, stepping forward without missing a beat as the winds die down and retreating when the wind picks up. Potential dance partners include equipment for storing large amounts of electricity, bigger transmission networks that allow utilities to draw power from a larger area, and the ability to control demand by turning off appliances in their customers' homes.

Several technologies in a future "smart grid" could help manage this dance. They include sensors that monitor the state of high-voltage transmission lines and react instantly when conditions deteriorate. Such technologies already exist, but deploying them on a large scale will cost billions of dollars.

Bringing more renewables online may also require more sophisticated analysis of the grid's behavior when power comes from thousands of independently controlled solar panels and wind turbines. Marija Ilic, a specialist on electrical power systems at Carnegie Mellon University in Pittsburgh, Pennsylvania, says researchers at universities and national laboratories are leading the way. "Some utilities are just waking up" to the problem, she says.

Utilities also need more accurate predictions of the weather. "If I can't forecast the wind accurately, I have no choice but to start a bunch of [coal- or gas-burning] units" to serve as a reserve in case the wind dies, says David Hawkins of the California Independent System Operator (CAISO), which manages that state's electrical system. "If I have to do that, I've lost all the advantages of the green energy."

CAISO buys forecasts of its wind power from AWS Truewind LLC, one of a handful of companies selling such a service. "They're getting good," says Hawkins. The day-ahead forecasts—which provide hour-by-hour predictions of a wind farm's power production—used to be off by 40% or more, but "now we're getting errors in the low 20s, heading toward 15 to 17%." The forecasts are continually updated, and "within the hour, we can usually nail it," says Hawkins. The National Center for Atmospheric Research in Boulder, Colorado, recently got funding from Xcel Energy to develop an "advanced wind-prediction system."

Storing power underground

The ideal dance partner is hydroelectric power. Dams are giant energy-storage devices, and they can react quickly, releasing exactly enough electricity to balance what the fickle winds deliver. Denmark is able to meet 20% of its electrical demands with wind power, for example, by drawing upon imported hydropower from Norway.

Unfortunately, there isn't nearly enough hydropower to go around. EPRI is promoting what it considers the next best thing, storing power in the form of air pumped into underground caverns under high pressure. "Compressed air is one of the few options we have for real bulk power storage," says EPRI's Dan Rastler. Two such facilities already exist in the United States and Germany. EPRI and a consortium of utilities are planning a more efficient and larger one that would drive a standard gas turbine and generate 400 MW of electricity for up to 10 hours.

Smaller storage projects are also in the works. The Bonneville Power Administration, a federal agency based in Portland, Oregon, already generates enough wind power to satisfy 20% of its peak demand (see graph), and it's working with CAISO to build a facility that stores energy in spinning flywheels. The flywheels are meant to smooth out small fluctuations in wind power, storing excess electricity from brief gusts of wind and releasing it when the wind turbines slow down.

Utilities also have their eye on the batteries of plug-in hybrid vehicles. Those vehicles could become a nightmare for utilities if their owners insist on charging them up after arriving home from work, when power use is at a peak. "My view is, that's no time to charge customers 6 cents per kilowatt-hour; that's a time to charge 6 bucks!" says David Mohler, who's in charge of "smart grid" efforts for Duke Energy, headquartered in Charlotte, North Carolina.

But under some circumstances, those batteries could be a boon to the electric grid. Managers of the grid could pay vehicle owners for the right to control when the charging occurs and eventually the discharging, too. They could fill up the batteries of plug-in hybrids when electricity is

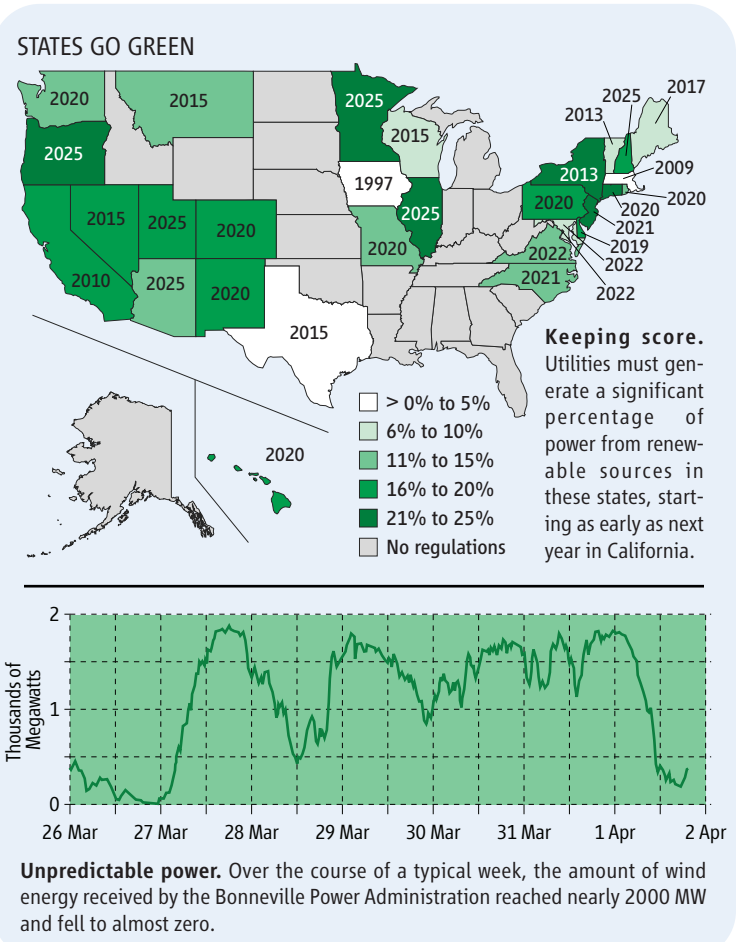

Unpredictable power. Over the course of a typical week, the amount of wind energy received by the Bonneville Power Administration reached nearly 2000 MW and fell to almost zero.

SOURCES (TOP TO BOTTOM): DEPARTMENT OF ENERGY; SOURCE: BONNEVILLE POWER ADMINISTRATION

Meet your new lab partner.

The new Thermo Scientific NanoDrop 2000 and 2000c Spectrophotometers offer true micro-sample analysis, with sample size capability as low as 0.5 µl and a measurement time of less than five seconds. Either of these is the perfect instrument for all your quantitation needs—DNA, RNA, proteins and more. Providing full spectrum UV-Vis results, both instruments can analyze samples with concentrations greater than 15,000 ng/µl (dsDNA) without dilutions. Innovative software makes it easy to build your own methods, design reports and export data. And with both pedestal and cuvette capability, the NanoDrop™ 2000c is the one spectrophotometer that does it all.

Test-drive the NanoDrop 2000 or 2000c in your own lab!*

Visit **www.nanodrop.com** to schedule your test-drive. Try out an instrument and run your own samples. It's completely free.

* Available only in US and Canada

Thermo Scientific NanoDrop 2000c

The only spectrophotometer that combines micro-volume pedestal technology and cuvette capability

Moving science forward

Thermo SCIENTIFIC

Part of Thermo Fisher Scientific

Students Energized by Power Engineering

The study of electrical power generation and transmission has long occupied the dusty back corners of U.S. academia. The field was neglected by funders and students alike. When power engineers retired from university faculty positions, they often weren't replaced.

Students avoided the field, in part because deregulated utilities, anxious to cut costs, weren't hiring, says Anjan Bose, a professor of power engineering at Washington State University, Pullman. A National Science Foundation–sponsored workshop in 2007 on the future power-engineering work force called the situation "a national crisis."

With energy back in the headlines, the tide appears to have turned. The evidence is mostly anecdotal because there is no national census of power-engineering students. But engineers at many U.S. universities tell the same story: Students are back, and faculty members are expecting a big increase in funding opportunities as demand grows for a "smart grid."

"Classrooms are full, and we have this very alive group now," says Marija Ilic of Carnegie Mellon University in Pittsburgh, Pennsylvania. At the University of Wisconsin, Madison, says Christopher DeMarco, "we're definitely seeing a greater influx of students at the graduate level." For many years, these programs relied heavily on students from abroad. DeMarco was grateful for those students, but he admits to being "frustrated" by the scarcity of U.S. students. "That's changed dramatically in the last 2 or 3 years," he says.

Empowered. Marija Ilic says students like the idea of improving the grid.

Ilic herself was born in Yugoslavia (in the part that is now Serbia) and studied electrical engineering in Belgrade before receiving a D.Sc. degree from Washington University in St. Louis, Missouri, in 1980. The field itself has changed, she says. Instead of focusing strictly on technical skills, faculty members now encourage students to explore the political and economic context and environmental impacts of power systems. Students also arrive with different expectations. "People are not just thinking about this as doing engineering but as something that's good for mankind," Ilic says.

One clear sign of renewed interest is at the University of Michigan, which abandoned power engineering in the 1970s because of a general lack of interest. "There was not much of a market for it," says Khalil Najafi, chair of the electrical and computer engineering department. Last fall, the department hired Ian Hiskins, an authority on power grid control, and it is about to add another specialist in energy systems. A third faculty position may open up next year, Najafi adds. **–D.E.C.**

abundant in the wee hours of the morning, then draw on that stored-up power in available vehicles to respond to power shortages in the middle of the day.

The two-way communications needed for such a system are part of what is now being called the "smart grid." Such links, allowing utilities to directly control appliances in people's homes, could become one of the most important tools for adapting to variable power from the sun and wind.

Florida Power & Light (FPL) Co. has been doing this for years to handle peak demand. Almost a million customers have signed up for FPL's "On Call" program, which allows the utility to turn off their water heaters, pool pumps, and sometimes air conditioners for short periods of time. FPL communicates with control boxes on those appliances with signals sent directly over power lines. In an emergency, On Call can quickly cut FPL's peak energy load by 4%.

Many utilities are now experimenting with more ambitious versions of this technology. Duke Energy has outfitted the homes of 32 customers in Ohio with an "energy optimization engine" that allows the utility to manage the most energy-hungry home appliances in the home in exchange for cheaper electricity bills. So far, the utility has only used its power to prevent ovens or water heaters in the same neighborhood from turning on at exactly the same time.

The utilities are treading carefully to avoid a backlash from customers who cherish their ability to dry clothes at their convenience. Mohler says utilities could probably use this tool to cut their load by 10% or 20%. "But could we do it without customers noticing? Probably not."

Green freeloaders?

Christopher DeMarco, an electrical engineer at the University of Wisconsin, Madison, is examining a more subtle feature of green power, namely, its reluctance to perform certain unglamorous but essential functions that keep the grid on solid footing. Old-style power plants, for instance, provide some extra "reactive power" that helps keep voltage stable on the grid. Without it, voltage in an AC system tends to sag.

Early versions of wind farms and solar panels did not help to support the voltage. "It costs them money," says EPRI's Stephen Lee. "So independent power producers, including renewable generators, just pump power onto the grid and depend on the transmission company to provide voltage support." That approach may have been okay when renewables were a boutique source of energy. But as their presence grows, grid managers are requiring many of them to provide voltage support.

DeMarco says solar and wind power also do little to cushion the grid from shocks such as a power plant shutting down unexpectedly. Traditional power plants do this naturally, he says, through the sheer physical mass of machinery that is rotating exactly in time with the oscillation of the grid's alternating current. This system "has a very nice stabilizing dynamic effect," says DeMarco. If a factory operator somewhere flips a switch and pulls more power from the grid, DeMarco says, the generator responds instantly. "It will slow down slightly, and what was kinetic energy gets converted into electrical energy going out the wire."

Solar and wind generators could mimic this response, says DeMarco, but it would require them to reduce their output by a few percentage points and have that power poised to respond instantly to shocks on the grid. Without their cooperation, he predicts, "we are going to run into hard limits on how much renewable generation we can live with, without destabilizing the operation of the grid." DeMarco and his fellow researchers are trying to determine just where those "hard limits" lie.

"There is a tendency in some circles to paint renewables as a threat to the grid," says DeMarco, but he thinks the two can work in harmony. "You need to spend a little money to make them compatible with the grid," he explains, "but there's no insurmountable hurdle." **–DAN CHARLES**

CREDIT: KEN ANDREYO

Published by AAAS

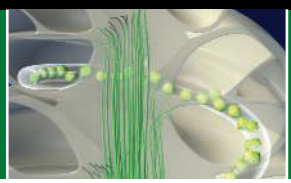

LETTERS

edited by Jennifer Sills

Advancing Human Rights Through Science

THE LAUNCH OF THE AAAS SCIENCE AND HUMAN RIGHTS COALITION, held in Washington, DC, on 14 to 16 January, offered an opportunity for AAAS-affiliated scientific organizations to participate in bridging communities of scientists and human rights organizations. A shared goal of this coalition is to articulate the right to "share in scientific advancement and its benefits" (*1*). I believe that this launch offers a rare opportunity in higher education to enhance partnerships between academicians in the sciences and the arts and humanities to engage student learning at all levels. Mary Robinson, a human rights advocate and former president of Ireland, pointed out an example: Physicians for Human Rights investigated an outbreak of cholera in Zimbabwe and found that it was due to the centralization of the water system by the Zimbabwean government and the subsequent degradation due to lack of proper maintenance (*2*).

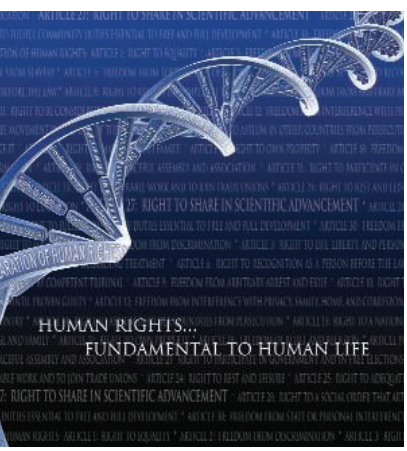

The AAAS Science and Human Rights Program.

AAAS has established a "scientists on call" program (*3*) to contribute to humanitarian efforts such as this. Imagine the engagement of an undergraduate student in a science teaching laboratory analyzing data from sub-Saharan Africa that could provide critical insight for a human rights effort, ranging from analysis of contaminated water to biological samples from a suspected incident of genocide. With appropriate regulatory compliance and faculty supervision, a grassroots "students on call" effort could ensue. Techniques such as polymerase chain reaction or water analysis that are commonplace in the developed world may not be feasible or attainable in regions in crisis in the developing world. Incorporation of human rights into both science and general education curricula could have a profound effect on higher education and, importantly, on K–12 education by engagement of future teachers.

JEFFREY H. TONEY

College of Natural, Applied and Health Sciences, Kean University, Union, NJ 07083, USA. E-mail: jetoney@kean.edu

References

1. United Nations Universal Declaration of Human Rights, Article 27.
2. C. Beyrer, F. Donaghue, *The Washington Post*, 8 January 2009, p. A15.
3. AAAS Science and Human Rights Program, "On-Call" Scientists (http://oncallscientists.aaas.org/default.aspx).

Tracing Fossil History

IN THEIR PERSPECTIVE "NEW AND ANCIENT trace makers" (16 January, p. 346), S. Bengtson and B. Rasmussen implied that trace fossil workers (in general) assume that all trace fossils are the result of animal activities. According to the operational definition that I have used since student days, trace fossils are the result of organismal behavior irrespective of the identity of maker (*1*). The skepticism about Precambrian trace fossils, as I perceive it, concerns not whether they were produced by animals, but a more fundamental question: Are these sedimentary structures, in fact, trace fossils?

I would be interested in the authors' assessment of the structures produced by these giant shelled amoebas (*Gromia*). Are these structures the result of directed activity (a true trace fossil) or are they merely incidental, perhaps produced by current- or gravity-induced movement of *Gromia* (a sedimentary structure but not a trace fossil)?

RONALD MCDOWELL

West Virginia Geological and Economic Survey, Morgantown, WV 26508, USA. E-mail: mcdowell@geosrv.wvnet.edu

Reference

1. R. Frey, in *The Study of Trace Fossils*, R. Frey, Ed. (Springer, New York, 1975), pp. 13–38.

Response

TRACE FOSSILS ARE INDEED DEFINED INDEpendently of the identity of the trace maker. A definition, however, is not the same as interpretational practice. Although most trace fossil workers are aware that organisms other than animals may leave traces, one doesn't have to dig deep into the literature to find statements indicating that trace fossils only exist since the time of animals (*1*). We believe that trace fossils greatly precede animals in the fossil record.

McDowell has heard skepticism voiced about whether Precambrian trace fossils are sedimentary structures rather than trace fossils. So have we. There are of course plenty of instances where alleged trace fossils, whatever their age, have been convincingly explained as products of sedimentary or tectonic processes [e.g., (*2*)]. We are little impressed, however, by blanket dismissals of Precambrian trace fossils.

Is it possible that the grooves and ridges associated with modern *Gromia* are not traces at all, but sedimentary structures, which were produced by "current- or gravity-induced movement," and that *Gromia* served merely as a passive tool? It's certainly an option we have

Published by AAAS

Mapping hybrids
187

Flight maneuvers
190

considered. At 720- to 780-m depth, the sea floor is below hurricane wave base, but hurricanes may generate strong currents affecting deeper continental shelf and slope (*3*). However, current- or gravity-induced forces would not be likely to push adjacent *Gromia* in opposite directions or up steep slope gradients. Indeed, Matz *et al*. (*4*) list a number of persuasive arguments against just such an interpretation of passive movement. We have made similar arguments for the Paleoproterozoic *Myxomitodes* traces (*5*). There is clearly more we need to know about how *Gromia* moves, but available data strongly indicate that it was an active mover and thereby a producer of genuine trace fossils.

STEFAN BENGTSON[1]* AND BIRGER RASMUSSEN[2]

[1]Nordic Center for Earth Evolution and Department of Palaeozoology, Swedish Museum of Natural History, Box 50007, SE-10405 Stockholm, Sweden. [2]Department of Applied Geology, Curtin University of Technology, GPO Box U1987, Perth, WA 6845, Australia.

*To whom correspondence should be addressed. E-mail: stefan.bengtson@nrm.se

References

1. R. R. McDowell, *Geol. Soc. Am. Abstr. Prog*. **39**, 74 (2007).
2. A. Seilacher, M. Meschede, E. W. Bolton, H. Luginsland, *Geology* **28**, 235 (1999).
3. W. J. Teague, E. Jarosz, D. W. Wang, D. A. Mitchell, *J. Phys. Oceanogr*. **37**, 2181 (2007).
4. M. V. Matz, T. M. Frank, N. J. Marshall, E. A. Widder, J. Sönke, *Curr. Biol*. **18**, 1849 (2008).
5. S. Bengtson, B. Rasmussen, B. Krapež, *Paleobiology* **33**, 351 (2007).

Risks of Extreme Heat and Unpredictability

IN THEIR REPORT "HISTORICAL WARNINGS OF future food insecurity with unprecedented seasonal heat" (9 January, p. 240), D. S. Battisti and R. L. Naylor argue that because agricultural yields are severely reduced in anomalously hot years, a general rise in average growing season temperature over this century will threaten food security. The authors identify a crucial issue but, by focusing on historic extremes, they frame it incorrectly. Extreme events are rare and result in lower yields primarily because farmers do not plan for them and crop breeders do not breed for them. If the currently extreme temperatures become the norm, then we would expect farmers to adapt, maintaining yields by selecting alternative crop varieties, species, and cultivation techniques. Examining the performance of agriculture under unprecedented conditions tells us little about how it will adapt to future climates.

We are more concerned about the expected increase (*1*, *2*) in interannual variability of growing season temperatures. Generally, it is uncertainty in biophysical conditions that causes agricultural losses, and higher uncertainty reduces the chance of selecting appropriate crop varieties and species that yield adequately in a particular year. However, improved long-range forecasting may offset this. The future productivity of world agriculture will therefore depend on whether the development and adoption of new varieties and techniques can keep pace with the changing climate and whether improvements in long-range forecasting can keep pace with increases in interseasonal variation. Commercial interests will probably ensure this happens for major crops and richer countries, but substantial public service breeding will be needed for minor crops that are currently prevalent in many tropical areas.

NEAL HOCKLEY,* JAMES M. GIBBONS, GARETH EDWARDS-JONES

School of the Environment and Natural Resources, Bangor University, LL57 2UW, UK.

*To whom correspondence should be addressed. E-mail: neal.hockley@univ.bangor.ac.uk

References

1. F. Giorgi, X. Bi, J. Pal, *Clim. Dyn.* **23**, 839 (2004).
2. P. L. Vidale D. Lüthi, R. Wegmann, C. Schär, *Clim. Change* **81**, 209 (2007).

CREDIT: PETER HOEY/WWW.PETERHOEY.COM

LIFE IN SCIENCE

Seeds of Doubt

My students and I were returning from some weeks in the field, where we had been examining the selectivity in food choices made by some tropical birds. Our procedure was to compare stomach contents of seed-eating birds with the abundance of different seeds available, most of which were of various species of grasses. We planned to do the actual analyses in our lab at home, so we arrived at the Miami International Airport with several boxes of bird stomachs and vials of seeds. All were properly presented to the agriculture authorities, and, armed with the necessary papers and seals, we proceeded to the customs bench. We were an unkempt group, as might be expected after days of fieldwork and spartan living conditions, so we were not surprised to be asked to open our cases and backpacks and to account for their contents. "What is this?" asked the officer, picking up several of our vials. I explained that the vials contained seeds. "What kind of seeds?" he persisted. I replied that they were merely grass seeds.

An instant later the red light on the officer's desk began flashing, and I found myself surrounded by a phalanx of uniforms. A senior officer quickly joined the group, looked at the vials, scrutinized me and my perplexed expression—after all, I did have Agriculture Department clearance—and then solemnly intoned, "Anyone so square as to tell you they are transporting grass seeds is bound to be okay." To this day, the students that accompanied me still giggle at the recollection, although whether they're laughing because I was accused of transporting marijuana, or because I was "too square" to pull off the role, I'll never know. **PETER H. KLOPFER**

Department of Biology, Duke University, Durham, NC 27708, USA. E-mail: phk@duke.edu

EDITOR'S NOTE

This is an occasional feature highlighting some of the day-to-day humorous realities that face our readers. Can you top this? Submit your best stories at www.submit2science.org.

See us at AACR Booth #641

Live Cell LCM

MDS Analytical Technologies introduces the Arcturus® Live Cell Module for its Arcturus$^{XT™}$ Laser Capture Microdissection (LCM) instrument. The Arcturus^{XT} instrument, the industry leader for tissue-based microdissection, is now capable of imaging and microdissecting living cells from a Petri dish format.

- Live Cell Microdissection from Petri Dish
  - Isolate cells for subsequent reculture
  - Process collected cells for downstream molecular analysis
- Live Cell Imaging from Petri Dish
  - Nikon Eclipse T*i*-E research microscope base
  - Optional high resolution camera with MetaMorph® imaging software
- Modular Petri Dish Stage Insert
  - User-installable
  - Easy exchange for standard tissue microdissection
    - Standard slides (25 mm)
    - Large format slides (38 mm and 50 mm)

For more information, visit **http://www.moleculardevices.com/pages/instruments/arcturusXT.html.**

MDS Analytical Technologies

tel. +1-800-635-5577 | www.moleculardevices.com

See us at Experimental Biology, Booth #1102

More Resolution

The Axon GenePix® 4300A and GenePix® 4400A microarray scanning and analysis systems from MDS Analytical Technologies combine increased imaging resolution with a host of enhancements to offer the highest performance of any slide-based microarray scanners. Our open platforms will enable image acquisition of any fluorescent microarray, even the newest ultra-high density formats.

Axon GenePix 4300A and GenePix 4400A Scanners

- Increased resolution: 2.5 µm per-pixel imaging in the GenePix 4400A system for the highest-density arrays; 5 µm resolution in the GenePix 4300A system can be upgraded after purchase
- Controlled uniformity: obtain more consistently reproducible results
- Improved sensitivity: revised optics give unmatched limit of detection
- Superior configurability: choose from four lasers and employ up to 16 different emission filters
- Enhanced automation: minimize your interaction and your time with a fully automated system

Axon GenePix Pro 7 Software

- Powerful multiplexing: independent image acquisition and analysis of multiple arrays per slide
- Complete hardware compatibility: control any Axon GenePix scanner, new or old
- Operating system flexibility: use 32- or 64-bit versions of Microsoft Windows Vista or Microsoft Windows XP

For more information, visit **http://www.moleculardevices.com/pages/instruments/microarray_main.html.**

MDS Analytical Technologies

tel. +1-800-635-5577 | www.moleculardevices.com

Response

EMPIRICAL AND PROCESS-BASED MODELS show that yields decrease with increasing temperature, across many regions of the globe and for numerous important crops such as maize, wheat, and rice. Typical yield declines are 10% per 1°C increase (ranging from 2.5 to 17%), regardless of whether the temperature anomaly is typical (e.g., 1σ) or extreme (as referenced, for example, in our Report and Supporting Online Material). Our Report shows that in the tropics and subtropics, the average growing season temperature will increase by 3° to 5°C, even under the middle-of-the-road emission scenario, regardless of whether there is an increase in the variability in summer temperature. History reveals that, without major forms of planned adaptation such as large-scale breeding programs or new crop rotations, substantial yield losses should be expected throughout large portions of these regions. As Hockley *et al*. note, much of the planned adaptation in developing countries will need to be funded through public sources (*1*).

Some models have projected that the variability in summer average temperature may increase somewhat in a world with increased greenhouse gas concentrations because of changes in the land-atmosphere feedback (*2*, *3*). Unfortunately, most of the climate models used in the most recent Intergovernmental Panel on Climate Change (IPCC) assessment display much greater variability in summer temperature in their control (modern day) simulations than is observed (*4*). The source of these biases appears to be physical processes that are not well represented in the regional and global models (in particular, the treatment of clouds, the soil layer, and the planetary boundary layer). They are also the same processes that are thought to be responsible for the projected amplification of summer temperature variance (*4*). For these reasons, we took a conservative approach and assumed that the natural variability will not change. Should the variability in growing season average temperature (or precipitation) also increase at the end of this century, farmers and agricultural institutions will face even greater challenges than we have shown.

DAVID S. BATTISTI[1]* AND ROSAMOND L. NAYLOR[2]

[1]Department of Atmospheric Sciences, University of Washington, Seattle, WA 98195, USA. [2]Woods Institute for the Environment, Stanford University, Stanford, CA 94305, USA.

*To whom correspondence should be addressed. E-mail: battisti@washington.edu

References and Notes

1. In recent decades, the trend in public funding for agricultural research and development in the poorest countries has been negative [P. G. Pardey, N. M. Bientema, S. Dehmer, S. Wood, "Agricultural research: A growing global divide?" (International Food Policy Research Institute, August 2006), pp. 1–24].
2. A. Weisheimer, T. N. Palmer, *Geophys. Res. Lett.* **32**, L20721 (2005).
3. S. I. Senevirante, D. Luthi, M. Litschi, C. Schar, *Nature* **443**, 205 (2006).
4. P. L. Vidale, D. Luthi, R. Wegmann, C. Schar, *Clim. Change* **81**, 209 (2007).

Letters to the Editor

Letters (~300 words) discuss material published in *Science* in the previous 3 months or issues of general interest. They can be submitted through the Web (www.submit2science.org) or by regular mail (1200 New York Ave., NW, Washington, DC 20005, USA). Letters are not acknowledged upon receipt, nor are authors generally consulted before publication. Whether published in full or in part, letters are subject to editing for clarity and space.

ADVANCES IN CANCER GENOMICS

WEBINAR

Thursday, April 30, 2009

12 noon ET, 9 a.m. PT, 4 p.m. GMT

Cancer is a complex family of diseases, characterized by the deregulation or dysregulation of the normal control pathways for cellular growth and/or apoptosis. Traditional research programs have focused on identifying and quantifying environmental and inherited factors associated with cancers found in particular tissues. Despite many advances, these approaches have historically been limited in scope due to technological limitations or excessive cost. With next-generation genomic platforms, scientists are now able to cost-effectively assay individual cancer genomes and characterize them in terms of the global genetic, epigenetic, and transcriptional changes. In-depth characterization of these events—and the relationships between them—will lead to better understanding of the mechanisms of tumorigenesis, metastasis, and therapeutic response. In this timely webinar, a panel of distinguished scientists will share their latest advances in cancer genomics and offer their views on the road ahead for this important area of research.

During the webinar, you will:

- Obtain a general overview of current technologies applied in cancer genomics research
- Learn about new technologies being used to advance the study of cancer
- See recent data provided by experts in the field
- Have your questions answered live!

Participating Experts:

Sean Grimmond, Ph.D.
Institute for Molecular Bioscience
The University of Queensland, Australia

David Wheeler, Ph.D.
Baylor College of Medicine
Houston, Texas

John McPherson, Ph.D.
Ontario Institute for Cancer Research
Toronto, Canada

Join our panel of experts in a live discussion. Register to participate.

Questions can be submitted live to the panel during the webinar or in advance via e-mail provided with registration. To register, visit

www.sciencemag.org/webinar

Science
AAAS

Brought to you by the
AAAS/*Science* Business Office

Webinar sponsored by Applied Biosystems

DEVELOPMENT

Learning from Errors

Manfred D. Laubichler

> A pathological condition is created at will, the intensity of which can be regulated by the duration of the experiment. And, master of all variables, one can dispose of the problem in such a way as to provide the greatest opportunity for a rigorous solution.
>
> –Isidore Geoffroy Saint-Hilaire (*1*)

Scientists and lay people alike have been drawn to monsters, because they do not fit into existing paradigms, violate common held assumptions (as well as social norms), and thus have the allure of the illicit, the impossible, and the forbidden. Monsters have, for instance, played important parts in undermining arguments in favor of the fixity of species, a performationist view of development, and a strictly gradualist conception of evolutionary change. Mark S. Blumberg (a developmental psychobiologist at the University of Iowa) has capitalized on this fascination with the forbidden to communicate his views on development and evolution to a wider audience. The result, *Freaks of Nature*, is a highly readable, entertaining, and informative introduction to the science and culture connected with freaks and monsters.

Blumberg presents the reader with a Wunderkammer of animal curiosities that includes conjoined twins, cyclops, two-headed snakes, two-legged dogs, and goats walking upright as well as the whole menagerie of P. T. Barnum from the Bearded Lady and the Elephant Man to armless wonders and the man "from whose belly another man issued." For each of these "freaks," Blumberg offers a highly informative account of the developmental basis of their condition, thus highlighting the central role of development in explaining phenotypic variation. In this sense, his book is a passionate argument for a renewed interest in teratology and teratogeny as a way to understand phenotypic evolution.

But, like most previous students of monsters, Blumberg has an additional agenda. He wants to draw attention to what he considers a continuing neglect of a developmental systems perspective by the current establishment in evolutionary and developmental biology.

The reviewer is at the School of Life Sciences, Arizona State University, Tempe, AZ 85287–4501, USA. E-mail: manfred.laubichler@asu.edu

Freaks of Nature
What Anomalies Tell Us About Development and Evolution / And What They Tell Us About Development and Evolution

by Mark S. Blumberg

Oxford University Press, New York, 2009. 340 pp. $22.95. ISBN 9780195322828. Oxford. 352 pp. £12.99. ISBN 9780199213054.

This central claim of the book places Blumberg in the middle of ongoing debates about the genetics underlying evolutionary change and the role of development in explaining phenotypic evolution. *Science*'s readers are familiar with what is at stake in these debates (*2*): Is phenotypic evolution primarily the result of gradual genetic change of protein coding genes (*3*)? Or is it rather a consequence of changes in the cis-regulatory regions of the genome that control gene expression (*4*, *5*)? A subsequent question, and one closer to Blumberg's examples, deals with the role of developmental processes in enabling and constraining phenotypic evolution. This problem was the main focus of attention of the late Pere Alberch, whose work has inspired most of Blumberg's substantive arguments about such processes' importance (*6*).

Research into the developmental basis of these freaks holds the promise of making substantial contributions to these debates. Simple logic dictates that all phenotypic variation (the foundation of natural selection) is the product of development. Thus all explanations of phenotypic evolution must include an understanding of the mechanisms of development and differentiation and of the roles that inherited factors (e.g., genomes and maternal effects) play in these mechanisms. Mechanistic and comparative studies have already revealed much about the complex regulatory networks that govern the development of phenotypes, so we are in a position to productively apply these insights to study the kinds of examples Blumberg discusses. Monsters, which demonstrate the kinds of phenotypic changes that are possible due to small changes in the regulatory logic of development, represent ideal natural experiments for exploring the complexities of the genotype-phenotype map and developmental regulation.

Besides raising and contributing examples to these substantive questions about a mechanistic theory of phenotypic evolution, Blumberg has a third agenda. Both his choice of examples (monsters and freaks as outcasts in nature and culture) and his constant evocation of "heretic" or "renegade" scientists reflect his desire to transform biology into "an evolutionary framework that is as exquisitely integrated as the animals that we seek to explain." As his frequent references to the philosophical perspective of "developmental systems theory" make clear, Blumberg wants to overcome the reductionism he thinks is at the center of gene-based and population-based evolutionary biology. By reducing phenotypic evolution to the abstract dynamics of genes in populations, he argues, we miss what Alberch attempted to accomplish, a "*theory of form* … where 'the properties of interactions …' take precedence over any 'specific genetic constitution.'"

However, current work toward a mechanistic theory of phenotypic evolution has moved far away from simple genetic reductionism. There are many detailed comparative and experimental studies on gene regulatory networks and their role in explaining the mechanisms of differentiation in development and the logic of phenotypic transformations (*5*). Studies on phenotypic plasticity demonstrate how environmental cues interact with the developmental system by provid-

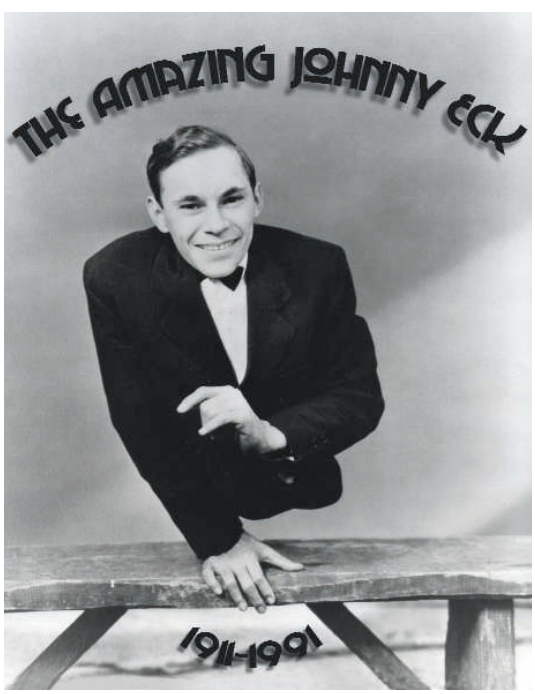

Adapting during development. Born without functioning legs, Johnny Eck "grew naturally into a hand-walker, exhibiting graceful movements with no sign of handicap or exertion."

CREDIT: COURTESY OF THE JOHNNY ECK MUSEUM, BALTIMORE/WWW.JOHNNYECKMUSEUM.COM

Published by AAAS

ing crucial input into the developmental cascades (including underlying gene regulatory networks) and thereby cause dramatic phenotypic transformations—for example, between queen and worker in social insects (*7*). Such work amply demonstrates that current studies in developmental evolution have moved far beyond the ideological posturing of some early versions of evo-devo.

As a consequence, Blumberg's account is itself a hybrid. By insisting that we take full advantage of these famed experiments of nature (which he describes so well), he provides an illustrative set of examples and research challenges. But by framing his natural history of freaks within an outdated and strangely ideological "holistic" outline of evo-devo, he places himself outside the kind of science that can actually explain these phenomena in a mechanistic fashion.

References

1. I. Geoffroy Saint-Hilaire, *La Vie, Travaux et Doctrine Scientifique d'Étienne Geoffroy Saint-Hilaire* (P. Bertrand, Paris, 1847).
2. E. Pennisi, *Science* **321**, 760 (2008).
3. J. A. Coyne, H. Hoeckstra, *Evolution* **61**, 995 (2007).
4. S. B. Carroll, *Cell* **134**, 25 (2008).
5. E. H. Davidson, *The Regulatory Genome: Gene Regulatory Networks in Development and Evolution* (Academic Press, Burlingame, MA, 2006); reviewed by D. Arendt, *Science* **314**, 1085 (2006).
6. P. Alberch, *Geobios* **19**, 21 (1989).
7. R. E. Page, G. V. Amdam, *Bioessays* **29**, 334 (2007).

10.1126/science.1168303

ENTOMOLOGY

Social Selection

Nigel R. Franks

The Lives of Ants has an unusual ontogeny. The first author, Laurent Keller, is an exceptionally talented evolutionary biologist (at the University of Lausanne); the second, Élisabeth Gordon, is a French journalist, and the product of their union has been translated from français to anglais by a third party. Unfortunately, this ménage à trois has produced a book uncertain of its target. That is a pity, as it seems such a sound idea: to team a pioneering scientist with a professional wordsmith to the benefit of all. Indeed, writing has been described as the painful physiological process of "turning blood into ink." So, employ a surrogate to take the strain. But beware: This book, arguably as a result, does not work perfectly either as popular science or as a biology text.

Food sharing. Trophallaxis between two *Oecophylla smaragdina* workers (Queensland, Australia).

Several aspects of the book limit its value to hands-on biologists. Many of the examples are not attributed to the scientists who made the discoveries or had the insights. The recommended reading list does not compensate for the absence of a full bibliography and formal citations. The inclusion of a glossary and a comprehensive index would have made the book more useful for all its readers.

Sadly, the book also falls a little short in serving the general reader. The authors aim for a popular audience by, for example, occasionally referring to larvae as "baby ants." This is cloyingly, nay nauseatingly, cute and seems to deny metamorphosis. The text sometimes seems to ignore the difference between scent and smell. Given that much of ant society is regulated by chemical signals, it is worth distinguishing between scents and sensibility. Producing a scent and sensing it are two separate processes. As the great lexicographer Samuel Johnson once put it to a lady who had complained that he smelled, "No, madam. I stink! You smell." There are also inconsistencies: At the beginning of the book, the authors proclaim that "unlike bees, [ants] never go in for dancing." Later, we find a section headed "Dancing and squeaking" in which we are told that ants may even gesture to one another in "little dances." But readers who wish to explore the matter further will find no specific references.

Quirkily, the humor found in the book appears to be accidental. For example, the text notes that wood ant mounds get wonderfully warm and then describes them as only "the tip of the iceberg." It refers to Pierre-André Latreille being imprisoned during the French revolution despite his description of the societies of ants as a "republic" and follows up with his friends referring to him as a "prince of entomologists." Dangerous talk: Off with his head? Perhaps this book had Mrs. Malaprop as a ghost editor?

Despite its eccentricities, the book offers readers a fascinating account of the biology of ants. The authors, for example, describe Keller's discovery, with others, of the extraordinary reproductive biology of the native fire ant *Wasmannia auropunctata* in French Guiana. Colonies have many queens and such societies bud-off from one another. (These are ants as fungi.) Remarkably, all the queens were genetically identical, and all the workers had inherited the same paternal genes. Surely, one male could not have mated with every queen? No, males clone themselves: "At fertilization, their spermatozoa, which are kept in the queen's spermatheca, penetrate the eggs and reach their nuclei. … some of them apparently eliminate the maternal genome and take its place." The authors note, "This mode of reproduction is absolutely without parallel anywhere in the animal kingdom." This represents Keller at his best—direct, enthusiastic, and modestly declaring that the discovery of this bizarre biology was one of his "greatest … flukes."

On balance, the book will reward its readers. Its strengths greatly exceed its shortcomings—but it could have been so much better.

The writer Clive James simultaneously stated and demonstrated his talent to "turn a phrase until it catches the light." But James's writing is also vivid because he captures his own experiences. More broadly, consider a telling story (possibly apocryphal) about Roosevelt and Churchill. After the two met for important discussions, Churchill had flown home and FDR was deciding how to report their progress to the American people. Someone switched on the wireless, and Churchill's unmistakable voice filled the room. Churchill had got the scoop by writing his own bulletin. A White House aide commented: "He rolls his own, Mr. President." There is more to this than simply being swift by cutting out the intermediary. Writing directly from personal experience is surely a better way to show leadership and for scientists to capture the delights of discovery and their passion for progress. Inadvertently, *The Lives of Ants* offers a very strong argument for scientists to find their own voices. There is a need for a popular book based on Keller's wonderful discoveries (especially in social genetics), and there must be a way to cite the literature for specialists that does not dilute the narrative. So, my hope is that next time Laurent Keller will roll his own.

10.1126/science.1172822

The Lives of Ants

by Laurent Keller and Élisabeth Gordon

Oxford University Press, Oxford, 2009. 272 pp. $27.95, £14.99. ISBN 9780199541867.

The reviewer is at the School of Biological Sciences, Woodland Road, University of Bristol, Bristol BS8 1UG, UK. E-mail: NigelFranks@bristol.ac.uk

OCEANS

Legal Bedrock for Rebuilding America's Ocean Ecosystems

The public trust doctrine would provide a powerful framework for restructuring the way we manage U.S. oceans.

Mary Turnipseed,[1]* Larry B. Crowder,[2] Raphael D. Sagarin,[3] Stephen E. Roady[1,4]

Recent discussions about ocean policy reform have focused on ecosystem-based management, which fully incorporates humans and considers the cumulative impacts of their activities on ecosystems and the services they provide (*1*). This approach is logical given the highly interconnected social-ecological systems of the ocean (*2*) and may be best realized through comprehensive marine spatial planning and ocean zoning (*3*). But U.S. ocean governance as currently configured cannot easily accommodate ecosystem-based management (*4*).

Federal waters, which include the territorial sea and the Exclusive Economic Zone (EEZ), reach from the 3- or 9-nm (nautical mile) borders of state waters out to the 200-nm outer boundary of the EEZ, an ocean area in which the United States has rights to explore, exploit, and manage living and nonliving resources (*5*–*7*). Because of the United States' extensive coastlines and territorial holdings, these waters cover 3.6 million nautical square miles (11.4 km^2), an area that is larger than the combined land area of the 50 states. Over 20 federal agencies operating under dozens of laws regulate activities, support ocean-based commerce, and protect marine species and habitats in the territorial sea and EEZ (*8*) (see figure, right). These agencies separately manage parts of marine ecosystems, without any systematic effort to coordinate their actions for the public good (*9*).

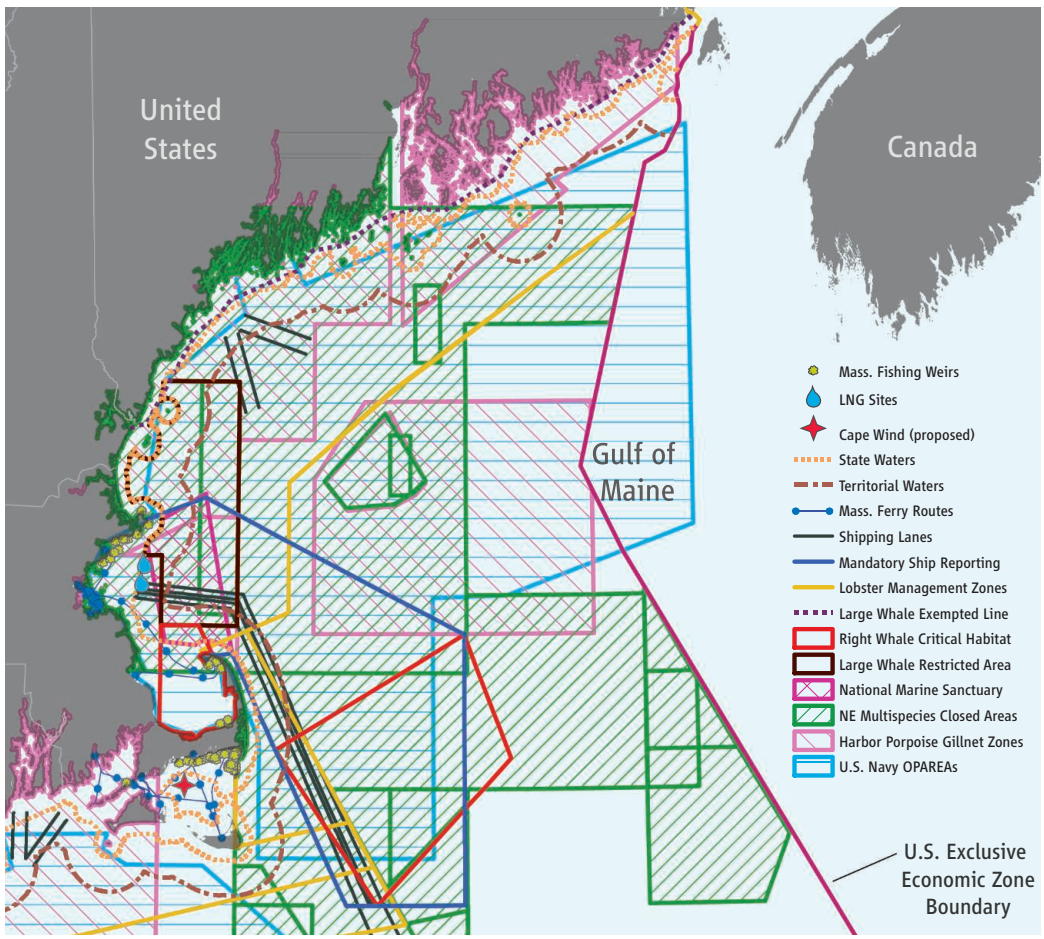

Uncoordinated sectoral ocean governance. A cacophony of activities, most regulated by separate federal agencies, crowd ocean waters in the Gulf of Maine. A federal public trust doctrine extended to all U.S. ocean waters would identify these agencies as trustees of the U.S. ocean public trust, unifying them for the first time under a common mandate to manage marine resources sustainably. LNG, liquified natural gas; OPAREAs, Operating areas.

With new leadership in place in Washington, U.S. ocean policy is poised for a long-overdue transformation. Since two national ocean commissions highlighted the need for dramatic reform 5 years ago (*8*, *10*), progress has been made toward understanding how to rebuild ocean ecosystems [e.g. (*11*, *12*)]. But implementing a new, ecosystem-based policy regime for federal ocean waters will require a solid legal foundation that provides the authority for, and imposes responsibility upon, disparate federal agencies to collaborate in their management of ocean resources. The public trust doctrine would provide this critical foundation.

The doctrine is a simple but powerful legal concept that obliges state governments to manage certain natural resources in the best interests of their citizens (*13*). More generally, a "trust" is a legal relationship in which a person or entity (the "trustee") manages a property or resource for the benefit of another person or group. The trustee is legally bound to preserve the assets of the trust, allowing only judicious use of the assets and repairing the trust should it be harmed. The trustee must also manage the trust exclusively in the interests of the beneficiaries (*14*). The beneficiaries of states' public

[1]Nicholas School of the Environment, Duke University, Durham, NC 27708, USA. [2]Center for Marine Conservation, Nicholas School of the Environment, Duke University, Beaufort, NC 28516, USA. [3]Nicholas Institute for Environmental Policy Solutions, Duke University, Durham, NC 27708, USA. [4]Duke University Law School, Duke University, Durham, NC 27708, USA, and Earthjustice, Washington, DC 20036, USA.

*Author for correspondence. E-mail: mary.turnipseed@duke.edu

CREDIT: CAROLINE GOOD

Published by AAAS

trusts include living and future citizens (*15*). Thus, inherent to the doctrine is the idea of intergenerational equity; trustees must manage trust assets so that needs of current beneficiaries are met without sacrificing needs of future beneficiaries. A federal public trust doctrine, if formally extended from state waters to the outer edges of the EEZ, would identify federal agencies as having responsibility for marine resources as trustees of the U.S. ocean public trust and U.S. citizens as the sole beneficiaries.

Many analysts, including the presidentially appointed U.S. Commission on Ocean Policy, have assumed that the doctrine already encompasses the vast space of the territorial sea and EEZ (*8*) [supporting online material (SOM) text]. But our recent review (*16*) reveals that the legal authority and responsibility of the federal government to manage marine resources in the best interests of U.S. citizens as a trustee under a federal public trust doctrine have not been formally articulated by the courts or established in statutory law. Instead, the doctrine is well established in the United States only at the state level (*15*), where courts have consistently held that the public trust doctrine requires state agencies and attorneys general to seek legal action against private parties infringing on the public trust. Furthermore, state trustees cannot abdicate their responsibility to manage the trust; if they do, the doctrine enables citizens to seek judicial review of their actions [or inaction (SOM text)]. In some states, courts have used the public trust doctrine to protect coastal ecosystem services (*17*, *18*), and Massachusetts recently passed the first state law mandating a comprehensive ocean management plan "to ensure its effective stewardship of the ocean waters held in trust for the benefit of the public" (*19*). Although states do work cooperatively with federal agencies on issues such as coastal zone and fisheries management, they alone cannot protect U.S. ocean resources and the services they provide. Ocean ecosystems are interconnected across state and federal political lines, and states have limited authority in federal waters (SOM text).

In addition to providing a consistent framework for federal ocean agencies implementing ecosystem-based management, a public trust doctrine for U.S. federal waters would be a policy backstop for these agencies to enforce the public trust against infringing parties. The doctrine would also extend greater standing to U.S. citizens to protect their interests in the management of ocean trust resources in the instance of abuse or neglect of the trust (SOM text). And, with the current scientific understanding of the necessity of coordinated, comprehensive action to stem the widespread decline of U.S. marine ecosystems (*9*), it would be difficult for a federal agency operating under a public trust mandate to avoid working cooperatively with agencies that manage other components of the ocean ecosystem. Therefore, explicitly mandating the common responsibility of these agencies to protect the ocean public trust could catalyze interagency ecosystem-based management in U.S. oceans.

A federal public trust doctrine for U.S. ocean waters could be established in a number of ways:

Executive order: The president could make expanding the doctrine a signature of his administration through an executive order that directs all federal ocean agencies to apply their resources toward cooperatively and sustainably managing the ocean public trust (SOM text).

Judicial interpretation: Federal judges could extend the doctrine into the territorial sea and EEZ by invoking the same instruments relied upon by state courts to enlarge the reach of the doctrine—judicial precedents, language in existing statutes, and the common law (SOM text).

Congressional mandate: The Congress could unambiguously write the doctrine into federal oceans law. As one example, the National Oceanic and Atmospheric Administration (NOAA) could be given the following directive: "NOAA's mission is to manage and protect public trust resources within the waters and atmosphere of the U.S. with the cooperation of other federal and state agencies." Once mandated, the doctrine could be put into practice via agency memoranda—a top-down approach to implementing broad changes in agency practice for which there is ample precedent [e.g. (*20*)]—directing all workers to carry out the legislated work of their agencies under their newly articulated duties as trustees of the ocean public trust.

Just as assets in our economy are inextricably linked, assets in our ocean trust portfolio are linked with one another. To move past the failing status quo in U.S. ocean management and to build a vigorous mandate that provides both the authority and the responsibility for federal agencies to jointly work to manage U.S. oceans as whole ecosystems will require that we answer, as soon as possible, two critical questions: For whom should our country's oceans be managed, and for what purpose? The public trust doctrine answers both of these questions. By insisting that federal agencies manage the U.S. ocean public trust for the long-term benefit of all American citizens, citizens and the governments they elect can begin to harmonize the concepts of representative democracy and sustainable resource use and stewardship.

References and Notes

1. K. L. McLeod *et al.*, *Scientific Consensus Statement on Marine Ecosystem-Based Management* (Communication Partnership for Science and the Sea, 2005).
2. J. S. Shackeroff, E. L. Hazen, L. B. Crowder, in *Ecosystem-Based Management for the Oceans*, K. L. McLeod and H. Leslie, Eds. (Island Press, Washington, DC, in press).
3. F. Douvere, *Mar. Policy* **32**, 762 (2008).
4. P. A. Parenteau, D. C. Baur, J. L. Schorr, in *Ocean and Coastal Law and Policy*, D. C. Baur, T. Eichenberg, M. Sutton, Eds. (American Bar Association, Chicago, IL, 2008), chap. 19.
5. State waters of Texas and off Florida's western coast extend to 9 nm offshore. The territorial sea lies seaward of state waters out to 12 nm.
6. Presidential Proclamation 5030, "Exclusive Economic Zone of the United States of America," 48 *Fed. Reg.* 10605 (1983).
7. Global Maritime Boundaries Database, August 2007 version; www.gd-ais.com/index.cfm?acronym=gmbd.
8. U.S. Commission on Ocean Policy, *An Ocean Blueprint for the 21st Century: Final Report* (U.S. Commission on Ocean Policy, Washington, DC, 2004).
9. L. B. Crowder *et al.*, *Science* **313**, 617 (2006).
10. Pew Oceans Commission, *America's Living Oceans: Charting a Course for Sea Change: A Report to the Nation* (Pew Oceans Commission, Arlington, VA, 2003).
11. A. A. Rosenberg, J. H. Swasey, M. Bowman, *Front. Ecol. Environ.* **4**, 303 (2006).
12. National Research Council, *Dynamic Changes in Marine Ecosystems: Fishing, Food Webs, and Future Options* (National Academies of Science, Washington, DC, 2006).
13. Though these resources initially only included the lands and living and nonliving resources submerged under navigable and tidal waters, states' doctrines today typically cover wetlands and terrestrial wildlife, among other natural resources.
14. Restatement (Third) of Trusts §2 (2003).
15. J. H. Archer *et al.*, *The Public Trust Doctrine and the Management of America's Coasts* (Univ. of Massachusetts Press, Amherst, MA, 1994).
16. M. Turnipseed, S. E. Roady, R. Sagarin, L. B. Crowder, *Ecology L. Q.* **36**, 1 (2009).
17. J. B. Ruhl, J. Salzman, *Southeast. Environ. Law J.* **15**, 223 (2006).
18. "[O]ne of the most important public uses of the tidelands … is the preservation of those lands in their natural state, so that they may serve as … environments which provide food and habitat for birds and marine life?…." *Marks v. Whitney*, 491 P.2d 374, 380 (Cal. 1971).
19. Massachusetts Oceans Act, § 4C(a) (2008).
20. Director of the National Marine Fisheries Service, Memorandum to the Regional Administrators, *Guidance for Developing Environmental Impact Statements for Essential Fish Habitat per the American Oceans Campaign v. Daley Court Order* (NMFS, Silver Spring, MD, 22 January 2001).

21. We are grateful to N. Baron, M. Barrett, A. Dave, S. Gary, M. Gopnik, L. Joppa, A. Schick Kenney, D. Klinger, B. Simler, M. Wright, S. Lozier, K. Rumble, and three anonymous referees for their comments on earlier versions of this article. We especially thank C. Good for contributing the figure. The Nicholas Institute and the Nicholas School provided support. L.B.C. thanks the Gordon and Betty Moore Foundation for support during this research. R.D.S. acknowledges support from the David and Lucile Packard Foundation.

Supporting Online Material

www.sciencemag.org/cgi/content/full/324/5923/183/DC1

10.1126/science.1170889

APPLIED PHYSICS

Electrode-Cellular Interface

Electrode materials that facilitate interaction with living cells are crucial for the development of next-generation bionic devices.

G. G. Wallace, S. E. Moulton, G. M. Clark

Pacemakers and bionic ears (cochlear implants) (*1*) were the first medical bionic devices to be used successfully in humans. On the horizon there is the prospect of a neural prosthesis capable of operating prosthetic limbs (*2*), a bionic eye (*3*), as well as other devices for the restoration of body function. These developments are crucially dependent on successfully connecting the device to cellular tissue. The development of organic polymer conductors is contributing to achieving that success.

In a bionic ear, sound is coded as electrical pulses via a speech processor (see the figure) This temporal pulse pattern stimulates nerve cells in specific areas of the cochlea (the auditory portion of the inner ear) that correspond to different frequencies. The transmission of the pulses is critically dependent on the efficacy of the electrode-cellular interface. The electrode structure must be biologically compatible, not be prone to infection, and be stable for a time appropriate to the application. Control over the electrode's composition and its physical and mechanical properties—including surface roughness, porosity, and modulus—is therefore required. Because the electrode must be integrated into a package suitable for implantation, processability and fabrication methods are also important considerations.

For effective transmission of charge from electrodes to cells, the interface created by implantation must have low electrical impedance. However, the impedance inevitably increases after implantation because of tissue scarring—the process that attempts to separate the implant from the body. An in vitro model has been developed to investigate the factors, such as cell type, that influence the impedance changes (*4*). The model mirrors results obtained in vivo in that electrical stimulation of a cell-covered electrode initially reduced the impedance, followed by recovery to prestimulation levels during inactive periods (*4*).

Since the pioneering frog's leg experiments conducted by Luigi Galvani in 1783, the electrodes of choice for bionic applications have been based on inert metals. These include platinum and iridium oxide (*5*). Platinum and iridium alloys have been used in deep brain stimulator electrodes (*6*). Nanostructuring of such electrodes improves performance by reducing impedance and influencing cell compatibility. Organic conducting polymers have also been used for electrode-cellular interfaces. These electrodes are compatible with biological molecules such as enzymes and antibodies (*7*), and may also act as reservoirs for biologically active molecules and drugs that could then be released in response to electrical stimuli (*8*, *9*). In vitro studies with living cells indicate that polypyrroles are not toxic to cells (*10*). Polythiophene-based structures have also been used successfully (*11*).

Studies with living cells also indicate that using organic polymer electrodes to interface to cells would be diverse and multifunctional. For example, Schmidt *et al.* (*12*) have electrically stimulated cells either by applying a constant potential across two electrodes or by directly passing a current through the conducting film. As the field has progressed, materials with improved mechanical, electrical, and biological properties have emerged. In parallel, material processing and fabrication approaches that enable organic conductors to be produced in useful forms have also been developed. Organic conducting polymer electrodes can now be produced with numerous approaches including electroplating, electrospinning to produce nanofibers, wet spinning of long length microfibers, and even inkjet printing of tracks or patterns with micrometer dimensions.

These advances have led to a flurry of activity addressing more specifically targeted applications and have helped define the electrical stimulation that can be acceptably applied. For example, when using such materials to communicate with spiral ganglion cells in a cochlear implant, the stimulation must be charge balanced and restricted to charge densities below 75 $\mu C/cm^2$. Despite these limitations on the stimulation parameters, beneficial effects (in terms of neurite outgrowth) are obtained by direct electrical stimulation; furthermore, that same stimulation can be used to release nerve growth factors (*13*) just where they are needed.

Another exciting feature of organic conducting polymers is the ability to create the electrode under physiological conditions, which permits fabrication in the presence of living cells. Campbell *et al.* (*14*) used facile polymerization conditions to incorporate red blood cells into a polypyrrole matrix, and another protocol allowed formation of a conducting polymer in the presence of living cells in vitro (*15*). These approaches enable the integration of an electrode with living cells, and should facilitate improvements in the performance of electrode-based biomedical devices.

Other organic electrode structures to emerge are those based on nanostructured carbons: carbon nanotubes and graphene. Both provide an inherently electrochemically stable organic interface. Carbon nanotube–based interfaces produce electrodes with high capacitance and low impedance. These materials have been used to accelerate the growth of osteoblasts (cells important in bone regrowth) (*16*). Providing electrical stimulation to neurons via a carbon nanotube–based platform (*17*) has led to the formation of a functional neural network of neural stem cells (*18*). The ability to separate and assemble sheets of graphene into electrode substrates has created new bionic electrode possibilities. Graphene sheets are not toxic to cells (*19*), and electrical stimulation facilitates osteoblast proliferation (*20*).

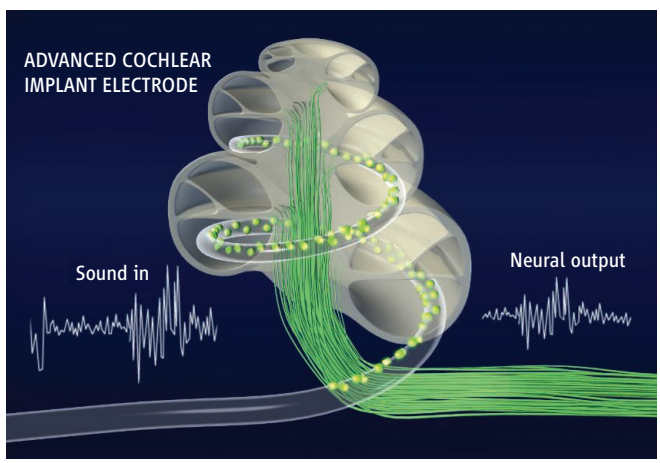

Wiring up cells. The fabrication of organic conducting polymers that can deliver neurotrophic factors and promote the survival of auditory spiral ganglion neurons is being developed in conjunction with the advanced cochlear electrode fabrication.

CREDIT: MATS BJORKLUND/MAGIPICS

Australian Research Council Centre of Excellence for Electromaterials Science, Intelligent Polymer Research Institute, University of Wollongong, New South Wales 2522, Australia. E-mail: gwallace@uow.edu.au

Published by AAAS

The inherent strength of carbon nanotubes and graphene (or nanocomposites containing them) make them well suited to use in bone regrowth, where matching the mechanical properties of an implant with that of the bone to be regrown is critical. Another attractive feature is that they can be processed at high temperature, enabling composites to be formed with melt-extrudable materials that are known to be biocompatible.

The bionic materials store is well and truly stacked, and many tools are available to characterize and use the contents. The challenge lies in determining the most appropriate electrode materials for a particular application. For medical bionic applications involving tissue engineering—such as implants for peripheral nerve, spinal cord repair, or muscle regeneration—the ability to produce biodegradable and bioabsorbable materials with appropriate function and lifetime profiles will be critical. For bionic prosthetics, challenges include reducing power requirements, finding natural (biological) power supplies, and extending device lifetime. In the case of bionic repair systems, devices should be biodegradable. Our increasing understanding of the properties of new electrodes and of how to design and control the electrode-cellular interface promises exciting advances in medical bionics.

References

1. G. M. Clark, *Philos. Trans. R. Soc.* **B361**, 791 (2006).
2. G. S. Dhillon, S. M. Lawrence, D. T. Hutchinson, K. W. Horch, *J. Hand Surg.* **29A**, 605 (2004).
3. Y. T. Wong *et al.*, *IEEE Trans. Neur. Syst. Rehab. Eng*. **15**, 425 (2007).
4. C. Newbold *et al.*, *J. Neural. Eng.* **1**, 218 (2004).
5. S. F. Cogan, *Annu. Rev. Biomed. Eng*. **10**, 275 (2008).
6. J. A. Boockvar *et al.*, *J. Neurosurg*. **93**, 140 (2000).
7. M. Gerard, A. Chaubey, B. D. Malhotra, *Biosens. Bioelectron.* **17**, 345 (2002).
8. Y. Lin, G. G. Wallace, *J. Controlled Release* **30**, 137 (1994).
9. A. J. Hodgson *et al.*, *Supramol. Sci.* **1**, 77 (1994).
10. X. Wang *et al.*, *J. Biomed. Mater. Res.* **68A**, 411 (2004).
11. A. S. Widge, M. Jeffries-El, X. Cui, C. F. Lagenaur, Y. Matsuoka, *Biosens. Bioelectron.* **22**, 1723 (2007).
12. C. E. Schmidt, V. R. Shastri, J. P. Vacanti, R. Langer, *Proc. Natl. Acad. Sci. U.S.A.* **94**, 8948 (1997).
13. B. C. Thompson *et al.*, *J. Controlled Release* **116**, 285 (2006).
14. T. E. Campbell, A. J. Hodgson, G. G. Wallace, *Electroanalysis* **11**, 215 (1999).
15. S. M. Richardson-Burns *et al.*, *Biomaterials* **28**, 1539 (2007).
16. P. R. Supronowicz *et al.*, *J. Biomed. Mater. Res*. **59**, 499 (2002).
17. K. Wang, H. A. Fishman, H. J. Dai, J. S. Harris, *Nano Lett*. **6**, 2043 (2006).
18. N. W. S. Kam, E. Jan, N. A. Kotov, *Nano Lett*. **9**, 273 (2009).
19. H. Chen, M. B. Muller, K. J. Gilmore, G. G. Wallace, D. Li, *Adv. Mater*. **20**, 3557 (2008).
20. J. S. Czarnecki, K. Lafdi, P. A. Tsonis, *Tissue Eng.* **14**, 255 (2008).

10.1126/science.1168346

CHEMISTRY

Total Chemical Synthesis Peers into the Biosynthetic Black Box

Key steps in a natural product synthesis route may relate to nature's strategies and catalysts.

Scott J. Miller

The structures, endemic roles, biosynthetic origins, and chemical reactivities of complex natural products contribute to their allure as enduring subjects of scientific inquiry (*1*). Embedded in each molecular framework is an evolutionary history, a functional role to be unveiled in a complex biological milieu, and deep mystery with respect to the reaction sequences that might lead to the assembly of the structure, either in nature or in the laboratory (*2*). Such is the narrative in the study by Kim *et al.* on page 238 of this issue (*3*). The authors have achieved a chemical synthesis of the highly complex molecule (+)-11,11′-dideoxyverticillin A (see the figure), a natural product isolated from the fungus *Shiraia bambusicola* (*4*) that possesses anticancer activity (*5*). Their laboratory synthesis, inspired by an analysis of the possible biosynthetic route, reveals much about chemical reactivity in a highly complex molecular environment.

The key reactions used by the authors lead to barely stable structures that might otherwise only be seen under the auspices of biosynthetic enzymes. The synthetic achievement thus raises provocative questions about the biosynthetic enzymes involved in the natural production of (+)-11,11′-dideoxyverticillin A. Such questions may now fuel further inquiry, and the insights gained by the authors may assist in the annotation of the biosynthetic gene cluster connected to (+)-11,11′-dideoxyverticillin A, which contains several proteins of unassigned function (*6*).

The structure of (+)-11,11′-dideoxyverticillin A is extremely complex, with many sterically congested, contiguous stereogenic centers as well as acid- and base-labile and redox-sensitive functionality. Any synthetic strategy must take into account that advanced synthetic intermediates may be unstable. The strategy must therefore include plausible intermediates that are sufficiently stable to survive a range of reaction conditions. Consideration of this type of structure also compels the chemist to turn to the biosynthetic pathway for clues as to how it might be synthesized in the laboratory.

Molecules such as (+)-11,11′-dideoxyverticillin A have some analogy in other natural products, including dithiodiketopiperazines (*7*–*13*). However, (+)-11,11′-dideoxyverticillin A is dimeric, increasing the magnitude of the synthetic challenge. Issues of diastereomerism, steric congestion, and the union of the two complex domains heighten the sensitivity of intermediates toward decomposition and greatly restrict options for assembly. It is even more difficult to execute a tetraoxidation reaction, followed by tetrathiolation/disulfide bond formation. Selective oxidations of the type found in the synthesis of Kim *et al.* would be challenging to achieve with selectivity and efficiency individually; to achieve them all at the same time is another matter altogether. Multisite reactions (*12*) set the stage for devastating losses of material due to the multiplicative amplification of fractional yields in such polyfunctionalization reactions.

Essentially every step in this synthesis is of interest. The authors use few protecting-group manipulations to mask undesired reactivity, and little extraneous oxidation state adjustment. The cobalt-based chemistry underlying the key dimerization step stands on the pioneering work of the authors' laboratory (*13*). The tetraoxidation chemistry, one of the key aspects of the synthesis, is conducted under carefully optimized conditions with a unique manganese-based reagent. In one approach to the final step to form (+)-11,11′-dideoxyverticillin A, the authors use a hafnium-mediated tetrathiolation/oxidation sequence. The reduction of these difficult steps to practice reveals not only the viability of a daring biosynthetically inspired strategy, but also the power of

Department of Chemistry, Yale University, New Haven, CT 06520, USA. E-mail: scott.miller@yale.edu

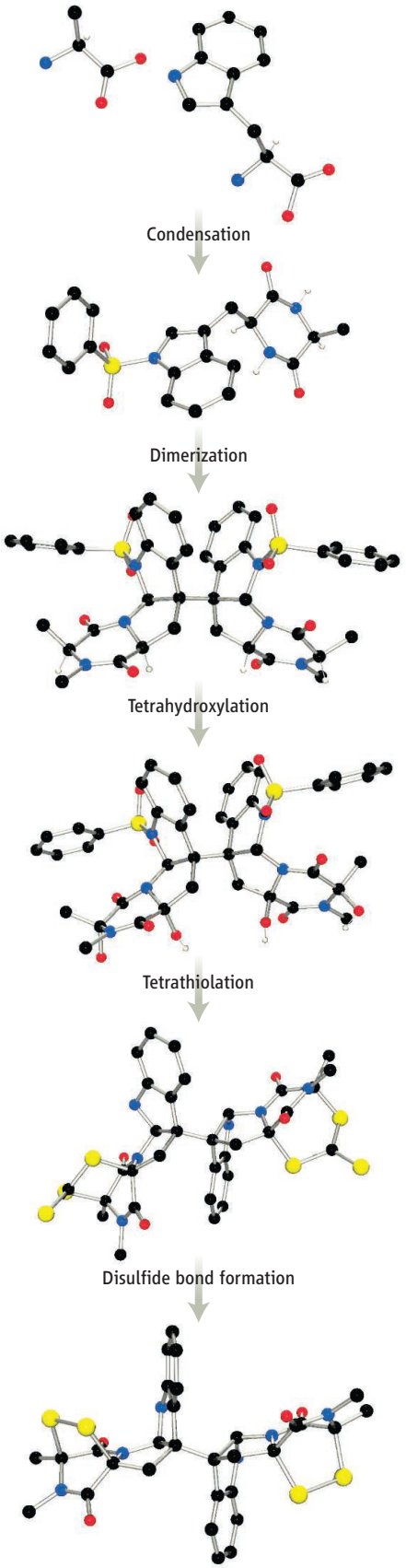

Rising to the challenge. Kim *et al.* report a striking total synthesis of the highly complex natural product (+)-11,11′-dideoxyverticillin A.

remote reaches of the periodical table for diverse bond-forming processes.

Kim *et al.*'s successful strategy for assembly of (+)-11,11′-dideoxyverticillin A suggests that the biosynthetic route may also rely on sophisticated, near-simultaneous multisite oxidation reactions (*3*). But how might such reactions be achieved biosynthetically? The authors point to work by Kirby *et al.* (*14*) and by Fox and Howlett (*6*), who have studied the biosynthesis and the gene cluster responsible for the production of related natural products. Proteins of unassigned function in this cluster bear homologous analogy to p450 oxidase enzymes; the unassigned proteins may be oxidases that mediate multisite oxidations of the type postulated and demonstrated by the current authors.

Kim *et al.* have achieved a remarkable chemical synthesis of a truly complex molecule. Although the final strategy makes the whole endeavor look straightforward, the chemical sophistication of the work is very high. Furthermore, the chemistry has stimulated detailed thinking about the biosynthetic pathway and the biosynthetic genes. In this way, complex molecule synthesis and complex chemical reactivity serve as central intellectual constructs in driving the fields of chemistry and biology forward.

References

1. J. Clardy, C. T. Walsh, *Nature* **432**, 829 (2004).
2. K. C. Nicolaou, D. Vourloumis, N. Winssinger, P. S. Baran, *Angew. Chem. Int. Ed.* **39**, 45 (2000).
3. J. Kim, J. A. Ashenhurst, M. Movassaghi, *Science* **324**, 238 (2009).
4. B. W. Son, P. R. Jensen, C. A, Kauffman, W. Fenical, *Nat. Prod. Res*. **13**, 213 (1999).
5. Y. Chen *et al.*, *Biochem. Biophys. Res. Commun*. **39**, 1334 (2005).
6. E. M. Fox, B. J. Howlett, *Mycol. Res.* **112**, 162 (2008).
7. D. M. Gardiner, P. Waring, B. J. Howlett, *Microbiology* **151**, 1021 (2005).
8. Y. Kishi, T. Fukuyama, S. Nakatsuka, *J. Am. Chem. Soc.* **95**, 6490 (1973).
9. R. M. Williams, W. H. Rastetter, *J. Org. Chem.* **45**, 2625 (1980).
10. T. Fukuyama, S. Nakatsuka, Y. Kishi, *Tetrahedron* **37**, 2045 (1981).
11. L. E. Overman, T. Sato, *Org. Lett.* **9**, 5267 (2007).
12. G. A. Crispino, P. T. Ho, K. B. Sharpless, *Science* **259**, 64 (1993).
13. M. Movassaghi, M. A. Schmidt, *Angew. Chem. Int. Ed.* **46**, 3725 (2007).
14. G. W. Kirby, D. J. Robins, in *The Biosynthesis of Mycotoxins: A Study in Secondary Metabolism*, P. S. Steyn, Ed. (Academic Press, New York, 1980), pp. 301–326.

10.1126/science.1172081

GENETICS

Leishmania Exploit Sex

Michael A. Miles, Matthew Yeo, Isabel L. Mauricio

Leishmania are the last of the three major groups of trypanosomatid parasites to give up their secret—a healthy capacity for genetic exchange.

Protozoan parasites of the genus *Leishmania* (*Kinetoplastida: Trypanosomatidae*) cause widespread and devastating human diseases. Visceral leishmaniasis is responsible for overwhelming fatal epidemics, and cutaneous leishmaniasis can lead to destructive and life-threatening mucocutaneous lesions (*1*). Since the discovery of these disease agents more than a century ago, there has been debate as to whether they reproduce entirely clonally or undergo genetic exchange, although naturally occurring putative hybrids have been described (*2*). That debate is now over. On page 265 of this issue, Akopyants *et al.* (*3*) provide evidence for genetic exchange in *Leishmania*. This represents the latest in a series of discoveries of sexual cycles operating in eukaryotic pathogens previously thought to be asexual (*4*).

Leishmania infect phagocytic cells of their mammalian hosts, where they are visible as tiny, ovoid cells (amastigotes) with a nucleus and a kinetoplast. The kinetoplast contains a network of minicircle and maxicircle mitochondrial DNA and is a distinctive feature of both *Leishmania* and *Trypanosoma* (a related genus of trypanosomatid parasites). In the sand fly vectors of *Leishmania*, morphology is somewhat more diverse than in the mammal, with various flagellated forms (promastigotes). Yet no distinct male and female gametes or sexual cycle have been described.

Despite the apparent morphological simplicity of *Leishmania*, their taxonomy is complex. They have been divided into two subgenera, *Leishmania* and *Viannia*, and numerous species, partly based on the clinical presentation of infection. Molecular markers have

Pathogen Molecular Biology Unit, Department of Infectious and Tropical Diseases, London School of Hygiene and Tropical Medicine, Keppel Street, London WC1E 7HT, UK. E-mail: michael.miles@lshtm.ac.uk

robust & reliable

Now it's easier to go green.

GoTaq® Hot Start with Green Buffer:

- High-performance PCR buffer
- Built-in gel loading buffer and tracking dyes
- Master mix and standalone formats

www.gotaqgreen.com

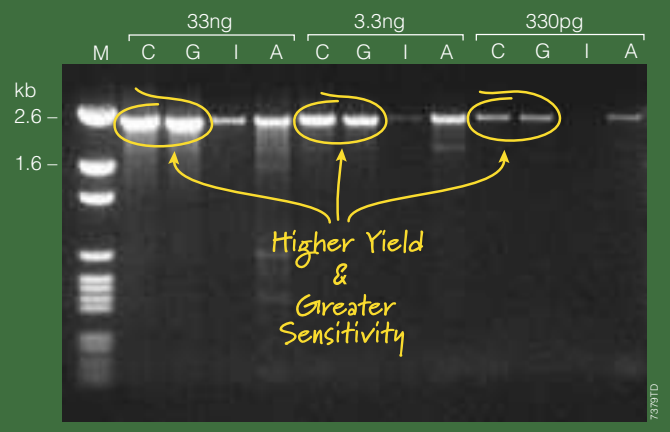

More convenient. More Productive. More Flexible.

GoTaq® Hot Start Polymerase with Colorless Flexi Buffer (C) and with Green Flexi Buffer (G) outperforms antibody (I) or chemically modified (A) competitor hot-start DNA polymerases for amplification of a 2.4kb fragment of the human APC gene.

Purchase GoTaq Hot Start, and Promega will plant a tree*

*offer valid from March 1 to May 31, 2009. See Web site for details.

amplify trees

Promega

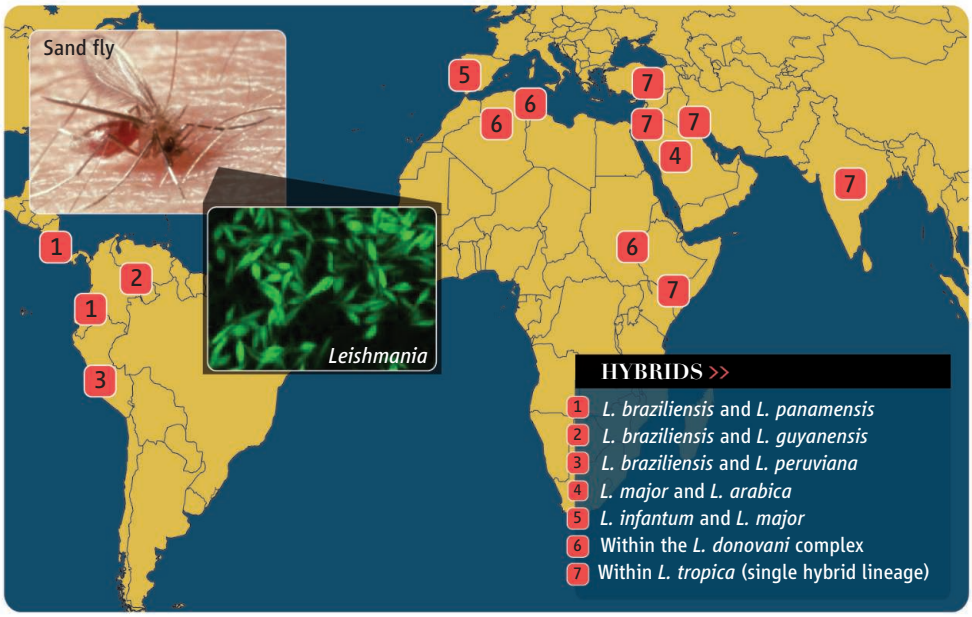

Mapping hybrids. The geographical distribution of interspecific and intraspecific *Leishmania* hybrids is shown. **(Inset)** A green fluorescent transgenic strain of *L. donovani* and a sand fly vector of *Leishmania*.

provided a more objective means to analyze genetic diversity and structure of natural *Leishmania* populations, and the results have been striking: Several recognized species clearly are not valid, and the taxonomy should be reassessed (*2*). More fundamentally, evidence for genetic exchange in natural populations of *Leishmania* repeatedly emerges, in the form of interspecific or intraspecific hybrids and recombinant genotypes (*2*) (see the figure).

Akopyants *et al.* infected the natural sand fly vector with pairs of transgenic *Leishmania* strains resistant to different selective drugs and reisolated parasites that were resistant to both drugs. Nine double–drug-resistant populations were recovered from cultures of infected sand flies and two from mice bitten by such flies; these yielded a total of 18 progeny clones. Single-nucleotide polymorphism analysis of homozygous parental markers (assigned to several chromosomes) showed that all progeny clones carried both parental alleles. However, mitochondrial maxicircle genotypes were inherited from a single parent—12 of the 18 genotypes derived from one parent and six from the other; both of these genotypes were recovered from two of the sand flies.

The *Leishmania* genotypes obtained by Akopyants *et al.* are consistent with cell division that generates haploid gametes (meiosis) and thus heterozygous first-generation progeny. Intriguingly, for 7 of the 18 clones, analysis of DNA content implied three sets of chromosomes (triploidy), and therefore alternative genetic mechanisms should be considered. All the hybrid clones showed two traits (recognition by monoclonal antibody and "clumpy" cultures) that were unique to one of the parents, and were thus presumed to be dominant phenotypic characteristics. Surprisingly, not one, but two distinct virulence traits emerged among progeny clones in infected mice, implying that at least one of the parental *Leishmania* strains must have been heterozygous for virulence genotype; five triploid clones all had slow lesion development ("slow virulence").

Genetic exchange in the related agent of African trypanosomiasis, *Trypanosoma brucei*, was demonstrated as long ago as 1986 (*5*). Nevertheless, in the 1990s, a prominent theory to explain population structures of trypanosomatid protozoa was that of clonality, with genetic exchange considered to be absent or rare and of little consequence (*6*). However, many crosses have since been performed between the subspecies of *T. brucei*. Gibson *et al.* (*7*) used transgenic fluorescent red and green trypanosomes to detect yellow hybrids, demonstrating that genetic exchange takes place in salivary glands of the tsetse fly vector and involves meiosis, although the precise mechanism has yet to be resolved.

Trypanosoma cruzi, the agent of American trypanosomiasis or Chagas disease, was also considered to be clonal. Yet natural hybrid groups exist, and genetic exchange was demonstrated by infection with pairs of transgenic strains and selection of double–drug-resistant progeny (*8*). The mechanism in *T. cruzi* appears different from that in *T. brucei*, with hybridization by fusion of parents followed by genome erosion, reminiscent of parasexual processes in fungi (*4*).

The fact that *Leishmania* can undergo genetic exchange is of epidemiological importance. Nolder *et al.* (*9*) found evidence of the emergence and spread of multiple *L. braziliensis–L. peruviana* hybrids in Peru. Volf *et al.* (*10*) demonstrated that *L. infantum–L. major* hybrids could be transmitted efficiently by the otherwise *L. major*–specific vector, implying heterosis (hybrid vigor). Further, a widespread lineage of *L. tropica* appears to be disseminated from a recent hybridization event (*11*). By analogy, hybrid lineages of *T. cruzi* (TcIId and IIe) predominate in domestic transmission cycles in the vast Gran Chaco region of South America, where severe human Chagas disease occurs (*12*). Genetic exchange has led to the emergence and spread of virulent *Toxoplasma gondii* (*13*), and meiotic recombination has recently been discovered in *Giardia*, in line with its extensive genetic diversity (*14*).

Sex may be of little consequence to a clonal parasite with exponential growth in an ideal environment. However, once conditions become stressful, genetic exchange may be crucial to survival and expansion (*4*). Hybridization may allow adaptation to new ecological niches, vectors, and hosts, including humans and domestic animals, and the efficient spread of new traits. In future, fluorescent transgenic *Leishmania* should allow visualization of genetic exchange in the sand fly (*7*). If experimental species crosses can routinely be established, it should allow mapping of key phenotypic determinants of virulence, pathogenesis, and drug resistance.

PHOTO CREDITS: M. YEO (FLUORESCENT *LEISHMANIA*); AUDIO VISUAL, LSHTM/WELLCOME IMAGES (SAND FLY)

References and Notes

1. H. W. Murray, J. D. Berman, C. R. Davies, N. G. Saravia, *Lancet* **366**, 1561 (2005).
2. J. Lukes *et al.*, *Proc. Natl. Acad. Sci. U.S.A.* **104**, 9375 (2007).
3. N. S. Akopyants *et al.*, *Science* **324**, 265 (2009).
4. J. Heitman, *Curr. Biol.* **16**, R711 (2006).
5. L. Jenni *et al.*, *Nature* **322**, 173 (1986).
6. M. Tibayrenc, F. J. Ayala, *Parasitol. Today* **7**, 228 (1991).
7. W. Gibson, L. Peacock, V. Ferris, K. Williams, M. Bailey, *Parasit. Vectors* **1**, 4 (2008).
8. M. W. Gaunt *et al.*, *Nature* **421**, 936 (2003).
9. D. Nolder *et al.*, *Am. J. Trop. Med. Hyg.* **76**, 573 (2007).
10. P. Volf *et al.*, *Int. J. Parasitol.* **37**, 589 (2007).
11. J. M. Schwenkenbecher *et al.*, *Int. J. Parasitol.* **36**, 237 (2006).
12. M. Yeo *et al.*, *Int. J. Parasitol.* **35**, 225 (2005).
13. J. P. Boyle *et al.*, *Proc. Natl. Acad. Sci. U.S.A.* **103**, 10514 (2006).
14. M. K. Poxleitner *et al.*, *Science* **319**, 1530 (2008).
15. We thank M. D. Lewis for constructive suggestions on the manuscript, and the Wellcome Trust and EC contract INCO-CT2005-015407 for financial support.

10.1126/science.1172789

EVOLUTION

Symmetry in Turns

A model explains how animals maneuver during hovering and slow flight.

Bret W. Tobalske

Being earthbound save for the ability to fly airplanes and helicopters, humans stand in awe of animals that power their own movement through the air by flapping their wings, and of the spectacular maneuvers that some of these animals can achieve. Imagine a common housefly flying in tight, erratic circles as it attempts to escape from a room or a hummingbird diving and turning to chase a competitor away from a backyard feeder. One might expect these extreme maneuvers to be accompanied by pronounced asymmetries in the way animals move their wings. Yet, evidence from insects (*1*, *2*), birds (*3*, *4*), and bats (*5*) suggests that aerial maneuvers are routinely accomplished through relatively subtle changes in wing motion. On page 252 of this issue, Hedrick *et al.* provide further insight into this phenomenon (*6*). The results will inform all future research into maneuvering flight in animals and biomimetic flying robots.

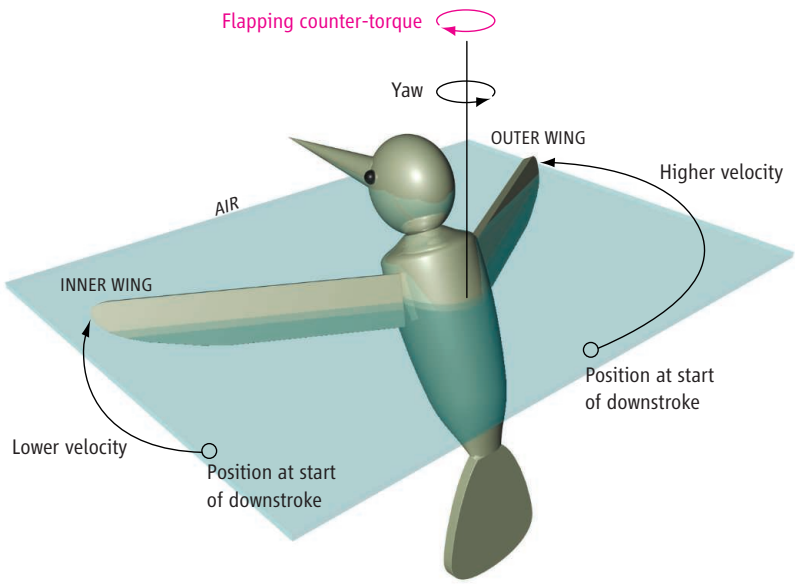

Flapping counter-torque during a yaw maneuver. The hovering bird is engaged in downstroke and is yawing counterclockwise about a vertical axis. Coupling the overall rotation of the body with symmetric motion of the wings causes the outside wing to move faster than the inside wing relative to air. The outer wing thus generates greater aerodynamic force, and a net flapping counter-torque (red) decreases the rate of yaw (*6*).

The authors show that flying animals arrest yaw (rotation about a vertical axis; see the figure) during hovering and slow flight by spinning about a vertical axis, without asymmetry in their wing movement. Holding both wings with the same posture, and flapping them back and forth in the same way relative to their body, are sufficient to stop the spinning. The authors refer to the underlying phenomenon as "flapping counter-torque."

To understand the importance of this result, consider the array of solutions that flying animals have at their disposal to modulate aerodynamic forces (lift and drag) and inertia (mass and its distribution). Animals may vary the velocity of their wings by increasing the frequency and amplitude of their wingbeat, alter the path of wing movement relative to the body, or twist the whole wing to alter the angle at which it meets the air. Birds or bats may also use their muscles and internal skeletal elements to alter wing curvature, surface area, or long-axis twist (*1*–*8*). Testing which—if any—of these features are being altered requires multiple, synchronized high-speed video recordings to reconstruct motion in all three dimensions.

Once a yaw is initiated, either by a force external to the animal (for example, from a gust of wind) or by an asymmetry in force production created by the animal's wings, some form of force asymmetry is necessary to arrest the yaw. If yaw is occurring counterclockwise as in the figure, a net clockwise torque (force times distance from the axis of rotation) is required to stop the yaw. Hedrick *et al.* develop a mathematical model that predicts how symmetrical wing flapping can create such a torque.

In their model, during downstroke (see the figure), both wings move at the same velocity relative to the bird, but in terms of global motion relative to Earth and air, the outside (right) wing moves faster than the inside (left) wing, because the angular velocity of the body adds to the angular velocity of the outside wing and subtracts from the angular velocity of the inside wing. Because lift and drag on the wings are proportional to velocity squared (*9*), the outer wing exerts an exponentially larger force on the air. The orientation of net force is nearly perpendicular to the upper surface of each wing (*2*), and the difference in force between the wings generates a net clockwise torque that decelerates the angular velocity of the body. The process is reversed during upstroke (see Hedrick *et al.* for details).

Hedrick *et al*. use the predictions of yaw deceleration from the above model to test the model's validity against an alternative model that incorporates active modulation of wing posture and motion. They then compare the predictions of both models to video recordings of maneuvers in four species of insects, two bird species, and a bat. According to their model, symmetrical flapping causes an exponential rate of decay in yaw velocity, whereas active modulation of wing posture and motion creates a linear rate of decay in yaw. All animals exhibit exponential decay in yaw.

The fact that the flapping counter-torque model is robust over a wide range of body size indicates that it represents a universal model. This advances our understanding, because previously it was thought that maneuvers in small insects would be dominated by skin friction due to the viscosity ("stickiness") of the air (*2*) and in larger birds and the bats by wing and body inertia (*3*, *4*). The relative contribution of inertial force over viscous force is expressed as a Reynolds number: The higher this number, the greater the extent to which body and wing inertia dominate aerodynamics (*9*). The largest bird Hedrick *et al*. studied has a Reynolds number 148 times as large as that of the smallest insect in their sample; yet each used the same mechanism—flapping counter-torque—to arrest their yaw.

Hedrick *et al.* hypothesize that flapping counter-torque may simplify the neural input that would otherwise be required to recover from perturbations during flight. This predic-

Field Research Station at Fort Missoula, Division of Biological Sciences, University of Montana, Missoula, MT 59812, USA. E-mail: bret.tobalske@mso.umt.edu

CREDIT: ADAPTED BY P. HUEY/*SCIENCE*

Published by AAAS

tion may lead to new research into the neuromuscular control of aerial maneuvers in animals (*3*, *4*) and will aid efforts to engineer controllers and actuators that effect wing movement in biomimetic flying robots (*10*). Passive stability during flapping may thus be analogous to a process in terrestrial locomotion in which neural input and passive dynamics interact to augment stability (*11*).

A major goal of functional morphology and comparative biomechanics is to understand how animal design relates to movement, ecology, and behavior. Thus, it is also important that Hedrick *et al.* show that animals with wings that are large relative to their body size decrease yaw velocity more quickly than animals with proportionally small wings. Hypotheses about maneuverability and ecomorphology in birds and bats have been dominated by the assumptions of fixed-wing, gliding aerodynamics (*12*). It has been recognized for some time that flapping must be integrated with such models (*3*), and the model of Hedrick *et al*. is a vital step in this direction.

Yaw during hovering and slow flight is just one type of maneuver; an almost limitless array of combinations of yaw, pitch, roll, and flight velocity are available to flying animals. Now that technology has developed to the point where detailed measurements of flapping maneuvers have become feasible (*1*–*8*), a world of comparative research is opening in which the flapping counter-torque model can be used to test the functional significance of flapping motions in maneuvering dynamics.

References

1. L. Lehmann, M. Dickinson, *J. Exp. Biol.* **204**, 627 (2001).
2. S. Fry, R. Sayaman, M. Dickinson, *Science* **300**, 495 (2003).
3. D. Warrick, M. Bundle, K. Dial, *Integr. Comp. Biol*. **42**, 141 (2002).
4. T. Hedrick, A. Biewener, *J. Exp. Biol*. **210**, 1897 (2007).
5. J. Iriarte-Diaz, S. Swartz, *J. Exp. Biol.* **211**, 3478 (2008).
6. T. L. Hedrick, B. Cheng, X. Deng, *Science* **324**, 252 (2009).
7. B. Tobalske *et al*., *J. Exp. Biol*. **210**, 2368 (2007).
8. D. Riskin *et al.*, *J. Theor. Biol*. **254**, 604 (2008).
9. S. Vogel, *Life in Moving Fluids: The Physical Biology of Flow* (Princeton Univ. Press, Princeton, NJ, ed. 2, 1994).
10. J. Zufferey. *Bio-Inspired Flying Robots: Experimental Synthesis of Autonomous Indoor Flyers* (EFPL Press, Lausanne, 2008).
11. R. Full *et al*., *Integr. Comp. Biol.* **42**, 149 (2002).
12. U. Norberg, J. Rayner, *Philos. Trans. R. Soc. London B Biol. Sci.* **316**, 335 (1987).

10.1126/science.1172839

GENOMICS

Green Evolution, Green Revolution

The genomes of two species of green algae provide clues to how green plants evolved.

John M. Archibald

The trees and plants that color our continents are more closely related to aquatic microorganisms—unicellular algae, in particular—than they are to the animals and fungi with which they cohabit. The smallest of these algae, called picophytoplankton, are individually miniscule (less than 2 μm in diameter) but collectively massive in ecological and evolutionary importance. On page 268 of this issue, Worden *et al.* (*1*) present the genome sequences of two such microbes, which belong to the green algal lineage *Micromonas*. Their analyses provide crucial insights into the plasticity of the eukaryotic genome over short evolutionary time scales and also shed light on the genetic "toolkit" that may have been present in the ancestors of today's land plants and green algae.

We are in the midst of a revolution in our exploration of the hidden microbial majority on Earth. Even the tiniest of cells can now be probed, poked, and sorted, and, with a bit of effort, subjected to DNA sequence analysis (*2*). In the case of photosynthetic eukaryotes, two microalgal genome sequences were available in 2004 (the diatom *Thalassiosira* and the red alga *Cyanidioschyzon*); by early 2009, almost a dozen had been sequenced (*3*). Several of these sequences are derived from organisms within the green lineage, such as the model lab alga *Chlamydomonas* (*4*), providing valuable reference points for comparison to the genomes of land plants like *Arabidopsis* (*5*).

Green photosynthetic eukaryotes are divided into two branches, chlorophytes and streptophytes (see the figure). The streptophyte branch is composed of land plants and their closest relatives, such as stoneworts (*6*) and the aquatic unicell *Mesostigma* (*7*, *8*). Molecular data [for example, (*9*)] show that the prasinophytes are the earliest offshoots of the chlorophyte branch; in the eyes of many, these organisms represent our best guess as to what the ancestor of green eukaryotic life looked like (*10*). It has long been hoped that a solid understanding of prasinophyte biology would open a window on the chlorophyte-streptophyte common ancestor.

The first prasinophyte genomes to be sequenced were from a pair of *Ostreococcus* species (*11*, *12*), the reining champions of eukaryotic cellular miniaturization (*13*). *Ostreococcus* genomes, too, are tiny: Just ~13

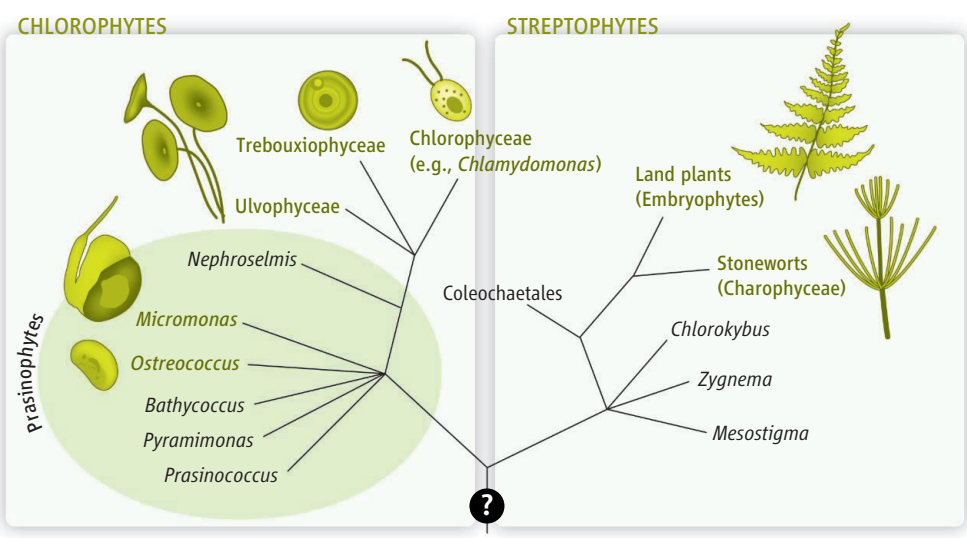

Green revolution. This evolutionary tree depicts a consensus view of the green tree of life, based on (*10*) and with consideration of new data, for example, from (*8*). By sequencing the genomes of two prasinophytes, Worden *et al.* (*1*) expand our knowledge of the genes present in the ancestors of land plants and green algae.

CREDIT: ADAPTED BY P. HUEY/*SCIENCE*

The Canadian Institute for Advanced Research, Program in Integrated Microbial Biodiversity, Department of Biochemistry and Molecular Biology, Dalhousie University, Halifax, Nova Scotia B3H 1X5, Canada. E-mail: john.archibald@dal.ca

million base pairs in size and with ~8000 genes, they are clearly the product of reductive evolution (*14*). In the case of *Micromonas*, Worden *et al.* now show that bigger is better. The authors sequenced the genomes of strains CCMP1545 and RCC299, isolated from temperate and tropical oceans, respectively (*1*). Although modest by eukaryotic standards, the *Micromonas* genomes are less streamlined than those of *Ostreococcus*. Both are ~20 million base pairs in size and possess ~10,000 genes. Comparison of the *Micromonas* genomes to one another, to those of *Ostreococcus* (*11*, *12*), and to other algae, plants, and nonphotosynthetic eukaryotes provides fascinating insights into how green plants evolved.

Of particular note among the 1384 genes shared by both *Micromonas* strains but absent in *Ostreococcus* is an impressive suite of transcription factor genes, the origins of some of which can now reasonably be moved to the common ancestor of chlorophytes and streptophytes. Compared with *Ostreococcus*, *Micromonas* has a richer set of nutrient transporter gene families (most of which are also found in land plants); *Micromonas* also contains a more complex suite of genes potentially involved in combating reactive oxygen species and heavy metals. *Micromonas* thus appears to be the more flexible of the two in terms of environmental "adaptability," which could explain its broader global distribution (*1*). Both *Micromonas* and *Ostreococcus* are clearly sexual: A slew of conserved meiosis-specific genes exist in all four genomes, and the presence of hydroxyproline-rich glycoprotein genes suggests—by analogy to *Chlamydomonas*—the existence of a (yet to be observed) sex-related, thick-walled stage of their life cycle (*1*). The prasinophytes are thus a lot more complex than previously believed.

The two *Micromonas* strains analyzed by Worden *et al.* are morphologically indistinguishable from one another and were previously assumed to be members of the same genus and species (their 18*S* rRNA sequences are ~97% identical), yet CCMP1545 and RCC299 share only 90% of their genes. Phylogenomic analysis reveals that many genes that occur in one *Micromonas* genome, but not the other, are very similar to those found in organisms as evolutionarily distant as animals, fungi, and bacteria (*1*). One interpretation is that such genes are the product of horizontal gene transfer, through which an organism incorporates genetic material from an unrelated or distantly related species; this process is gaining increasing acceptance as a real force in eukaryotic genome evolution (*15*).

The two *Micromonas* genomes also have unexpectedly different gene and genome structures. For example, CCMP1545 genes have on average more and larger spliceosomal introns than those of RCC299, many of which contain novel intronic repeats dubbed "introner elements." These elements make up 9% of the CCMP1545 genome but are absent from RCC299 (*1*). Understanding the importance of these strain-specific differences in gene and genome structure and content will go a long way toward understanding the differences in their biology and ecology.

It is exciting to think that some of the smallest eukaryotes on our planet can provide key insights into the early history of multicellular green plants. Worden *et al*. have made a substantial contribution to this story, laying the foundation for further comparative genomic analyses on a much broader diversity of plants and algae. Dozens of lineages up and down the green line are ripe for genome sequencing, and if the past few years are any indication, we will have answers sooner rather than later.

References

1. A. Z. Worden *et al.*, *Science* **324**, 268 (2009).
2. D. Vaulot, W. Eikrem, M. Viprey, H. Moreau, *FEMS Microbiol. Rev.* **32**, 795 (2008).
3. M. S. Parker, T. Mock, E. V. Armbrust, *Ann. Rev. Genet.* **42**, 619 (2008).
4. S. S. Merchant *et al.*, *Science* **318**, 245 (2007).
5. The *Arabidopsis* Genome Initiative, *Nature* **408**, 796 (2000).
6. K. G. Karol, R. M. McCourt, M. T. Cimino, C. F. Delwiche, *Science* **294**, 2351 (2001).
7. B. Marin, M. Melkonian, *Protist* **150**, 399 (1999).
8. N. Rodríguez-Ezpeleta *et al*., *Mol. Biol. Evol*. **24**, 723 (2007).
9. L. Guillou *et al.*, *Protist* **155**, 193 (2004).
10. L. A. Lewis, R. M. McCourt, *Am. J. Bot.* **91**, 1535 (2004).
11. E. Derelle *et al.*, *Proc. Natl. Acad. Sci. U.S.A.* **103**, 11647 (2006).
12. B. Palenik *et al.*, *Proc. Natl. Acad. Sci. U.S.A.* **104**, 7705 (2007).
13. C. Courties, A. Vaquer, M. Troussellier, J. Lautier, *Nature* **370**, 255 (1994).
14. P. J. Keeling, *Trends Genet.* **23**, 151 (2007).
15. P. J. Keeling, J. D. Palmer, *Nat. Rev. Genet.* **9**, 605 (2008).

10.1126/science.1172972

CANCER

Puzzling Patterns of Predisposition

Mutations in a gene that encodes a metabolic enzyme have been linked to certain brain tumors, but is the gene a tumor suppressor or an oncogene?

Patrick J. Pollard and Peter J. Ratcliffe

Following Theodor Boveri's seminal observation of abnormal chromosomal constitution in malignant tumors, successive advances in genetic analysis have shed new light on the cause of cancer. The latest of these, high-throughput DNA sequencing, is now providing an unprejudiced picture of cancer-associated mutations across the genome. The most intriguing are mutations in genes of known biological function but with previously unsuspected links to cancer. Thus, the recent identification of mutations in a specific isoform of the enzyme isocitrate dehydrogenase (IDH1) in glioblastoma multiforme (a malignant human brain tumor) has generated widespread interest (*1*). On page 261 of this issue, Zhao *et al.* (*2*) propose a mechanism through which this enzyme promotes oncogenesis.

Heterozygous IDH1 mutations have been identified in up to 80% of certain types of glioblastoma multiforme (*1*, *3*–*5*). Remarkably, the mutations are confined to a single residue, Arg^{132}. Although the majority are $Arg^{132} \rightarrow$ His substitutions, five other exchanges (to Ser, Cys, Gly, Val, and Leu) have been observed. Although heterozygous mutation at a single site might suggest dominant gain of function, six dissimilar substitutions would be surprising for such a mechanism. This has engendered a lively debate as to whether *IDH1* is an atypical tumor suppressor gene (in which a mutation causes loss of function) or an oncogene (in which a mutation causes gain of function) (*6*).

IDH1 is one of three isocitrate dehydrogenases that catalyze the oxidative decarboxylation of isocitrate to α-ketoglutarate (α-KG). IDH1 and IDH2 require nicotinamide adenine dinucleotide phosphate (NADP) as co-substrate, whereas IDH3 requires nicotinamide adenine dinucleotide (NAD). IDH2 and IDH3

Henry Wellcome Building for Molecular Physiology, University of Oxford, Oxford OX3 7BN, UK. E-mail: pjr@well.ox.ac.uk

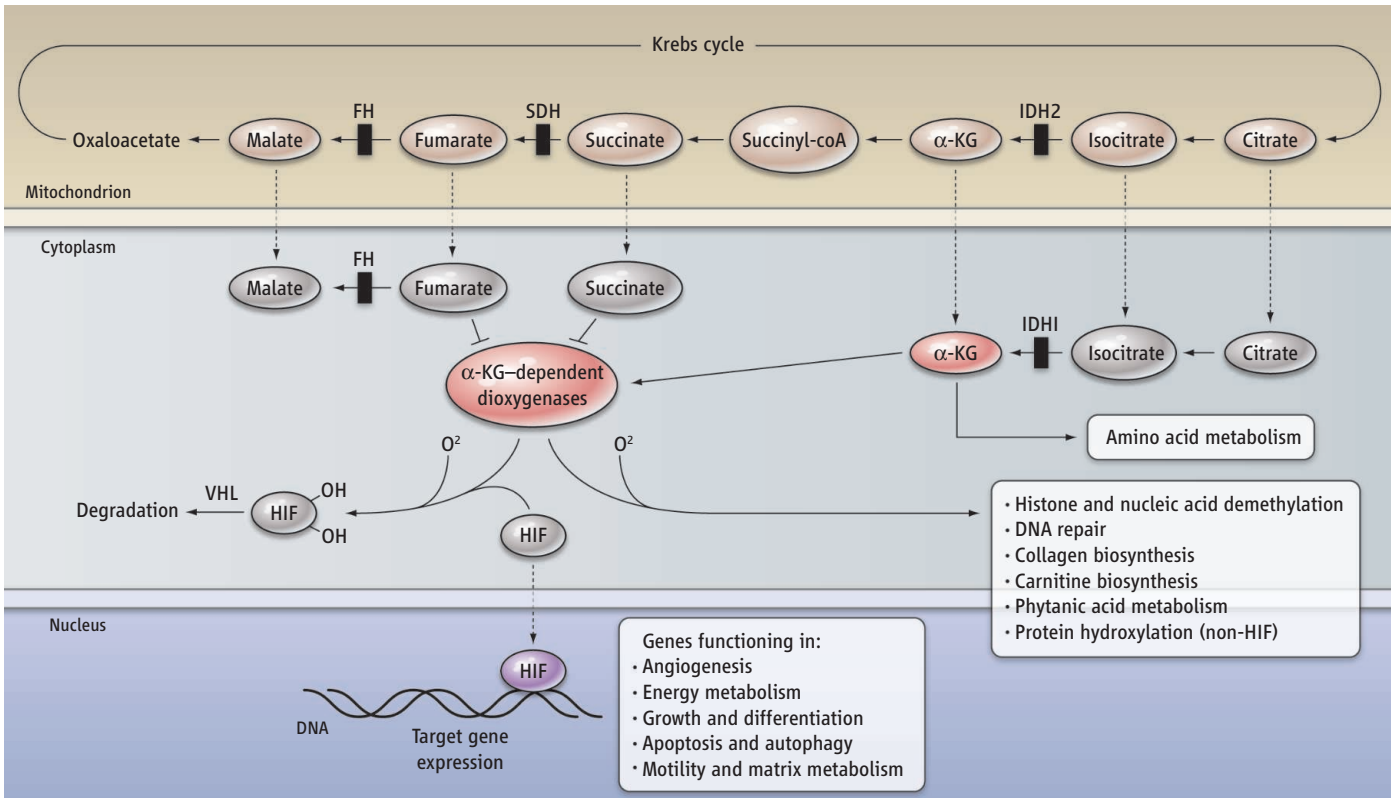

Routes to HIF activation. Depletion of cytosolic α-KG impairs the activity of α-KG–dependent dioxygenases that hydroxylate the transcription factor HIF and trigger its degradation by VHL. HIF hydroxylation is also inhibited by fumarate and succinate, which accumulate after FH and SDH inactivation. α-KG–dependent dioxygenases that function in other processes may be inhibited in a similar manner.

are mitochondrial enzymes that function in the Krebs cycle, the series of chemical reactions that generates the substrates for cellular respiration (see the figure). By contrast, IDH1 is located in the cytosol and peroxisomes, where it supplies NADPH (the reduced form of NADP) for biosynthetic and other reactions. Both NADPH and α-KG are metabolites in many cellular processes, providing a range of possibilities for the oncogenic or tumor suppressor actions of IDH1.

Zhao *et al.* show that tumor-associated mutations exert a dominant inactivating effect on IDH1 and propose an oncogenic mechanism based on the activation of hypoxia inducible factor (HIF), the key transcriptional pathway directing cellular responses to hypoxia. Mutant IDH1 enzyme is shown to dimerize with wild-type enzyme to produce an inactive product. The authors propose that disruption of Arg^{132} prevents cooperative conformational changes that activate the enzyme upon isocitrate binding. Expression of mutant enzyme in cells caused a decrease in the amount of α-KG. This reduction inhibits the activity of certain enzymes of the α-KG–dependent dioxygenase family that catalyze hydroxylation of HIF to cause its degradation. Thus, a decrease in α-KG increases HIF activity. In support of the proposed oncogenic mechanism, the authors show that HIF is indeed up-regulated in glioblastomas bearing IDH1 mutations.

This hypothesis fits well with the postulated tumor suppressor actions of certain Krebs cycle enzymes—succinate dehydrogenase (SDH) and fumarate hydratase (FH) (*7*). In tumors associated with mutations in *SDH* and *FH*, inactivation of these enzymes leads to accumulation of succinate or fumarate. These metabolites are proposed to exit the mitochondrion and compete with cytosolic α-KG to inhibit the HIF hydroxylases, thus activating oncogenic HIF pathways (see the figure). Linking *IDH1* into this unifying hypothesis is appealing, as several HIF target gene products promote tumor growth. If correct, the explanation of Zhao *et al.* adds substantially to the "α-KG hypothesis" of HIF activation. SDH is a mitochondrial enzyme, whereas FH is both mitochondrial and cytosolic. By contrast, HIF hydroxylation is extramitochondrial. In tissues bearing mutations in the genes encoding SDH, FH, and IDH2, Krebs cycle metabolites exit the mitochondrion to affect HIF hydroxylation, but inactivation of these enzymes will also have effects on mitochondrial metabolism that offer alternative explanations for both oncogenesis and activation of HIF (*7*). The study by Zhao *et al.* indicates that disruption of an extramitochondrial process is sufficient for HIF activation and oncogenesis.

Nonetheless, there are caveats. Zhao *et al.* do not directly test the role of HIF activation in tumors with mutations in *IDH1*, nor has this been directly tested in *SDH* or *FH*-associated tumors. Many other processes that are dependent on isocitrate and α-KG (or NADP and NADPH) may be perturbed, not least the numerous enzymes in the same α-KG–dependent dioxygenase family as the HIF hydroxylases (*8*). Many of these, such as the Jumonji-domain histone demethylases, have credible functions in oncogenesis, and dysregulation might contribute to tumor predisposition (*9*). Moreover, tumor predispositions conferred by mutations in *IDH1*, *SDH*, or *FH* are very different. Although *IDH1* has not been analyzed in paragangliomas or renal cancers of the type associated with *SDH* and *FH* mutations, families with mutations in *SDH* and *FH* are not known to be predisposed to glioblastoma multiforme. It is thus difficult to understand how activation of HIF, a transcription factor that operates in all cells, could be responsible for such different and restricted patterns of tumor predisposition.

However, emerging data in von Hippel–Lindau disease, an inherited cancer syndrome that disrupts HIF degradation, suggest an

intriguing possibility. Mutations in the tumor suppressor gene *VHL* that are associated with qualitatively different tumor predispositions (pheochromocytoma versus clear cell renal carcinoma) appear to be associated with quantitative differences in impairment of HIF regulation (*10*–*12*). Conceivably, matching of cellular context to a relatively precise, quantitatively restricted, level of HIF activation (that is the consequence of an IDH1 Arg^{132} mutation) is necessary for glioblastoma multiforme predisposition. If true, then alteration of such a balance, through metabolic interventions that target α-KG, might offer a therapeutic or preventive strategy.

Finally, although Zhao *et al.* provide an explanation for dominant mutational inactivation of IDH1, they do not completely explain why the pathogenic effects are restricted to Arg^{132}. Other arginine residues (Arg^{100} and Arg^{109} in human IDH1) are implicated in isocitrate binding (*13*), and in recombinant porcine IDH1, mutations at all these sites are inactivating (*14*). Perhaps the proposed disruption of subunit cooperation is restricted to Arg^{132} mutations, or Arg^{132} mutations in some way favor the heterodimerization that is required for dominant inactivation. Alternatively, Arg^{132} mutations might have some quantitatively specific effect on enzyme inhibition that is necessary for oncogenic predisposition.

On the other hand, could there be a primary genetic explanation? Mutational predisposition at CG dinucleotides can explain the common $Arg^{132} \rightarrow$ His substitution but not all of the other mutations. Moreover, Yan *et al.* recently sequenced the homologous exon of the *IDH2* gene in tumors that did not contain an *IDH1* mutation, and found nine mutations at the equivalent Arg^{172}, a residue that is encoded by a codon not containing the CG dinucleotide (*3*). This mutation was shown to be inactivating, although neither dominant inactivation nor effects on HIF were tested. Further studies to test this and other (non–disease-associated) mutations in the model proposed by Zhao and colleagues should be of great interest.

References

1. D. W. Parsons *et al.*, *Science* **321**, 1807 (2008).
2. S. Zhao *et al.*, *Science* **324**, 261 (2009).
3. H. Yan *et al.*, *N. Engl. J. Med.* **360**, 765 (2009).
4. F. E. Bleeker *et al.*, *Hum. Mutat.* **30**, 7 (2009).
5. J. Balss *et al.*, *Acta Neuropathol.* **116**, 597 (2008).
6. C. B. Thompson, *N. Engl. J. Med.* **360**, 813 (2009).
7. E. Gottlieb, I. P. Tomlinson, *Nat. Rev. Cancer* **5**, 857 (2005).
8. C. Loenarz, C. J. Schofield, *Nat. Chem. Biol.* **4**, 152 (2008).
9. Y. Shi, J. R. Whetstine, *Mol. Cell* **25**, 1 (2007).
10. W. G. Kaelin Jr., *Nat. Rev. Cancer* **8**, 865 (2008).
11. L. Li *et al.*, *Mol. Cell. Biol.* **27**, 5381 (2007).
12. K. Knauth, C. Bex, P. Jemth, A. Buchberger, *Oncogene* **25**, 370 (2006).
13. X. Xu *et al.*, *J. Biol. Chem.* **279**, 33946 (2004).
14. S. Soundar, B. L. Danek, R. F. Colman, *J. Biol. Chem.* **275**, 5606 (2000).

10.1126/science.1173362

APPLIED PHYSICS

Laser Beams Take a Curve

Complex energy flows within laser beams can cause them to curve as they travel.

Jérôme Kasparian and Jean-Pierre Wolf

The properties usually associated with laser beams are illustrated by laser pointers, which are monochromatic (red or green), coherent (they create speckle patterns), and directional (the beam travels in a straight line). However, the advent of laser sources that emit ultrashort laser pulses has changed this simple picture: These sources are broadband and may maintain coherence for very short times—just for one or a few cycles of the electric field. These sources are so intense that, when traveling through a medium such as air, they can ionize atoms and create plasmas. On page 229 of this issue, Polynkin *et al.* (*1*) exploit linear optical effects of laser beams with complex profiles, as well as nonlinear effects that arise at high intensities, to create laser beams that can form plasma channels whose paths curve as they propagate.

Laser beams with complex profiles (that have multiple maxima and minima and are not a single peak) can curve in part because energy can flow between components within these beams. Polynkin *et al.* use a beam profile based on the Airy function, which has its own history in optics—it was introduced in the study of rainbows. A two-dimensional (2D) Airy beam (*2*, *3*) (see the figure, panel A) can be prepared by inserting an active element such as a matrix of liquid crystals oriented so as to tailor the distribution of phase in the plane perpendicular to the beam. This Airy profile is asymmetrical and its intensity is strongly localized in a main peak on one side of the beam profile.

As the beam propagates, interferences between the phases in different locations in the beam profile impose a curved trajectory to the main peak in the Airy profile. This interference effect is linear—it depends neither on the beam intensity nor on interactions with the propagation medium. Viewed head on, the pulse would appear to swing from the left and back to the right. However, the beam's center of mass still propagates on a straight line (the red line in panel A) because the energy fraction contained in the long trail on the other side of the beam balances the main Airy peak.

A further remarkable property of the Airy beam is that it is "self-healing": If part of the beam hits an opaque object, energy flows from the rest of the beam profile and reconstructs the original asymmetric pattern (*4*). A similar self-healing effect occurs in high-intensity laser beams that form self-guided plasma channels, also called filaments (*5*–*8*). A dynamic balance develops between the nonlinear optical Kerr effect, which changes the refractive index of its propagation medium to create a virtual converging lens, and diffraction by the self-generated plasma, which creates long plasma channels. If a laser filament impinges on a particle, the scattered light is released into the periphery of the profile, where it contributes to the optical Kerr effect, thereby reconstructing the filament shortly after the interaction (*9*). This self-healing capability may allow high-intensity laser beams to access remote locations and to be transmitted through clouds and turbulence, opening the way to atmospheric applications (*8*, *10*).

Polynkin *et al.* combined the complex profile of an Airy beam with nonlinear optical effects to create plasma channels that can turn and follow the shape (or "caustic") shown in panel A of the figure; the plasma forms only in the high-intensity region of the main peak. A key issue is whether the natural (linear) energy flow (see the figure, panel B) that displaces the transverse beam will dominate the nonlinearly induced energy flow from the optical Kerr effect, which attracts energy toward the plasma filament (see the figure, panel C) and feeds it during its propagation.

GAP-Biophotonics, University of Geneva, 20, rue de l'École de Médecine, 1211 Geneva 4, Switzerland. E-mail: jerome.kasparian@unige.ch; jean-pierre.wolf@unige.ch

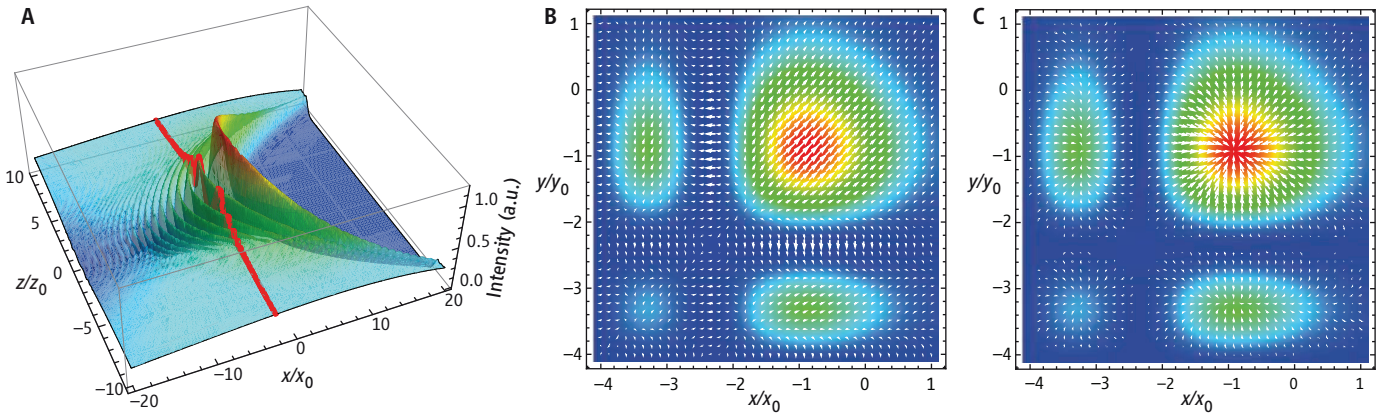

Laser beams taking turns. (**A**) A laser pulse with an Airy profile propagates in the *z* direction (normalized units). The main peak emerges from an initially broad profile, accelerates toward the exterior of the beam while progressively growing up to $z = 0$, and then loses intensity until it is absorbed in a resurgent broad maximum. The red line is the straight trajectory of the beam's center of gravity. (**B** and **C**) Energy flows in the curving beams of Polynkin *et al*. (B) Linear and (C) nonlinear (Kerr effect) energy flow (white arrows) across the beam profile. The same normalized color scale as in (A) is used to illustrate a 2D Airy beam (damping coefficient $a = 0.1$; $z = 0$). While the linear Airy flow pushes the main peak of the profile toward the top-right corner of the graph, independently from the incident intensity, the Kerr effect tends to attract the energy toward this main peak, with an efficiency proportional to the local intensity. The competition between the two processes causes deformations of the plasma channels generated in Airy beams at high intensity.

At moderate intensities, the transverse energy flux is dominated by the Airy regime, but at higher intensities, the Kerr contribution establishes an attractor at the beam's main peak, and tends to let the beam move straight rather than follow the Airy caustic. However, the curved plasma channels observed by Polynkin *et al.*—both in their experiments and in the numerical integration of the nonlinear Schrödinger equation—show that such a regime is not reached in the filaments in gases, where the intensity ranges from 10^{13} to 10^{14} W/cm^2 (*11*).

Thus, the Airy regime will dominate in most realistic experimental conditions in air. In particular, the observed curved plasma channel compares well to the electron density that would be generated by the intensity of a linearly propagating Airy beam. This density can be estimated as the eighth power of the intensity profile, which takes into account the ionization of oxygen driven by multiple absorption of photons (*11*). However, the longitudinal asymmetry of the curved plasma channel and the bifurcations observed both experimentally and numerically by Polynkin *et al.* show that the Kerr effect cannot be fully neglected at this intensity level.

Because the trajectory of the curved plasma channels roughly follow that of the Airy beam, their length and curvature suffer from the same limitations related to the intensity drop of the main peak along its propagation path. The maximum achievable deviation from a straight path scales linearly with the initial beam size w_0, but the propagation distance required to reach a given deviation scales with w_0^2. Sending a macroscopic Airy beam around a corner thus appears difficult. For example, an Airy beam with a main peak of w_0 = 1-cm width and an optimal value of the confinement factor *a* (in this case, 0.05) would need to propagate more than 2.8 km before reaching its maximum deviation of only 24 cm.

Nevertheless, Airy beams carrying high intensities provide a wealth of attractive applications at smaller geometrical scales. Self-bent beams could be used to manufacture curved waveguides in transparent bulk media, in a way similar to permanent optical waveguides inscription in fused silica using filaments (*6*). The ability of controlling curvature would allow for the realization of complex guiding structures in three dimensions, with applications such as wavelength division multiplexers, beam splitters, and couplers. A beam main peak of ~10 μm could be deviated by ~25 times its size, meaning that it would have moved off a straight trajectory by 250 μm after less than 3-mm propagation.

A further striking advantage of Airy-driven curved propagation, compared to Kerr-driven propagation, is its applicability in vacuum. A curved beam in vacuum, especially at high intensity, could open new ways of achieving long interaction lengths with particle beams, acceleration of protons and electrons on controlled trajectories, or efficient coupling with beams of x-rays or gamma-rays.

The use of Airy beams in the context of high-power pulses and self-channeling further builds on a recent trend to apply specific beam shapes, such as X-waves (*12*), Bessel beams (*13*), or axially or radially polarized beams (*14*), to exploit their remarkable properties already developed in the linear regime. Depending on the specific beam shape considered, such properties may include nondiffractiveness, self-healing, transverse acceleration, or the generation of a zero electric field at the beam center. When these methods are used with higher-power sources, nonlinear effects such as self-guiding further extend their scope for applications. Examples include tailoring the spectrum of the "white light" generated in the filaments for atmospheric remote sensing, or using filaments and their associate plasma to divert lightning strikes from sensitive targets, such as airports and industrials plants (*15*).

References and Notes

1. P. Polynkin, M. Kolesik, J. V. Moloney, G. A. Siviloglou, D. N. Christodoulides, *Science*, **324**, 229 (2009).
2. M. V. Berry, N. L. Balazs, *Am. J. Phys.* **47**, 264 (1979).
3. I. M. Besieris, A. M. Shaarawi, *Opt. Lett.* **32**, 2447 (2007).
4. J. Broky, G. A. Siviloglou, A. Dogariu, D. N. Christodoulides, *Opt. Express* **16**, 12880 (2008).
5. S. L. Chin *et al.*, *Can. J. Phys.* **83**, 863 (2005).
6. A. Couairon, A. Mysyrowicz. *Phys. Rep.* **441**, 47 (2007)
7. L. Bergé, S. Skupin, R. Nuter, J. Kasparian, J. P. Wolf, *Rep. Prog. Phys.* **70**, 1633 (2007).
8. J. Kasparian, J.-P. Wolf, *Opt. Express* **16**, 466 (2008).
9. F. Courvoisier *et al.*, *Appl. Phys. Lett.* **83**, 213 (2003).
10. J. Kasparian *et al.*, *Science* **301**, 61 (2003).
11. J. Kasparian, R. Sauerbrey, S. L. Chin, *Appl. Phys. B* **71**, 877 (2000).
12. D. Faccio *et al.*, *Phys. Rev. Lett.* **96**, 193901 (2006).
13. P. Polesana, M. Franco, A. Couairon, D. Faccio, P. Di Trapani, *Phys. Rev. A* **77**, 043814 (2008).
14. R. Martínez-Herrero, P. M. Mejías, S. Bosch, *Opt. Commun.* **281**, 3046 (2008).
15. J. Kasparian *et al.*, *Opt. Express* **16**, 5757 (2008).

16. This work was supported by the Swiss NSF, contract 200021-116198/1.

10.1126/science.1172244

Eppendorf & Science Prize for

Neurobiology

$25,000 Prize

Get recognized!

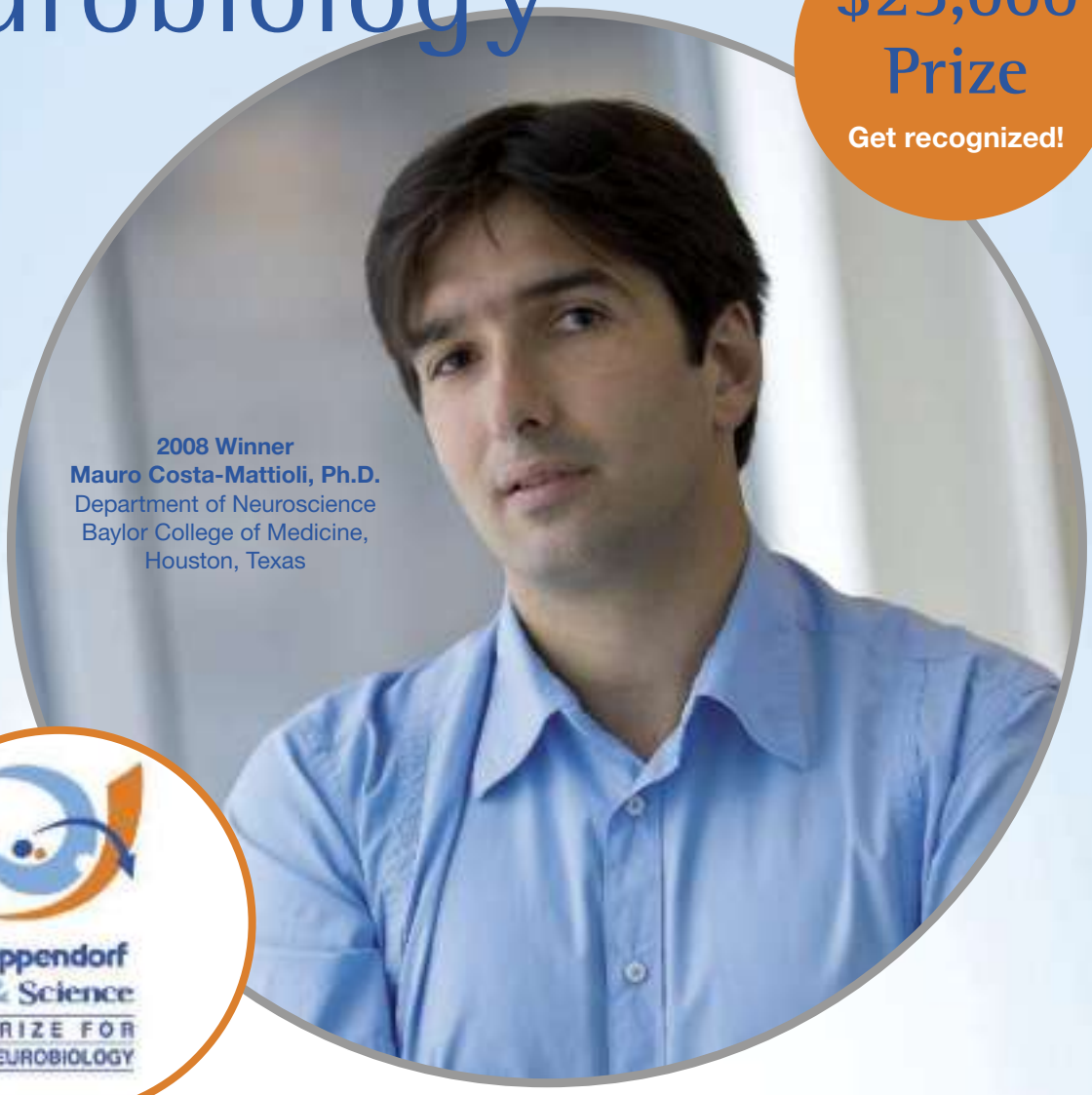

2008 Winner
Mauro Costa-Mattioli, Ph.D.
Department of Neuroscience
Baylor College of Medicine,
Houston, Texas

eppendorf & Science PRIZE FOR NEUROBIOLOGY

Deadline for entries
June 15, 2009

For more information
www.eppendorf.com/prize

This annual international research prize recognizes accomplishments in neurobiology research based on methods of molecular and cell biology. The winner and finalists are selected by a committee of independent scientists, chaired by the Editor-in-Chief of *Science*. Past winners include postdoctoral scholars and assistant professors.

To be eligible, you must be 35 years of age or younger. If you´re selected as this year´s winner, you will receive $25,000, have your work published in the prestigious journal *Science* and be invited to visit Eppendorf in Hamburg, Germany.

eppendorf
In touch with life

Science
AAAS

Kurstin Roe Photography

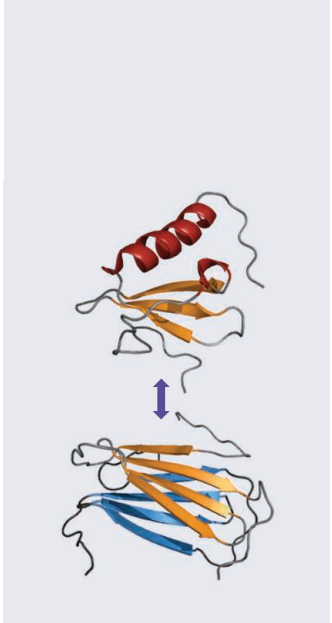

INTRODUCTION

Proteins in Motion

THREE YEARS AGO, A SPECIAL ISSUE OF *SCIENCE* (14 APRIL 2006) FOCUSED ON NEW tools used to observe proteins at work. The view that has emerged is that of an intricate ballet: Individual proteins are in constant motion, sampling an ensemble of different conformations and perhaps changing interaction partners as they play their part in a particular biological process.

How do these dynamics affect function? The conformational space that a protein can explore can be described by an energy landscape, in which different conformations are populated based on their energies, and rates of interconversion are dependent on the energy barriers between states. The landscape, and thus the relative populations of conformational states, can be modulated, for example, by interactions with other proteins or by covalent modifications such as phosphorylation. Smock and Gierasch (p. 198) present examples that illustrate how these dynamic properties allow proteins to transmit signals by acting as switches and transducers. Factors that modulate the energy landscape might also disrupt protein function. Traditional structure-based drug design has focused on targeting a static active site. More opportunities for drug discovery come from considering the entire free-energy landscape of a protein. Lee and Craik (p. 213) provide examples of allosterically active drugs that are either on the market or in late clinical testing. These lay the groundwork for future efforts to discover drugs that act by trapping proteins in an inactive state; such drugs can act to inhibit enzyme activity or to inhibit an interaction on a signaling pathway.

The proficiency and specificity of proteins are characteristics that might reasonably be associated with a lack of versatility, but proteins also adapt, as evidenced by the serious problem of drug resistance. Tokuriki and Tawfik (p. 203) suggest that the conformational diversity of proteins makes them evolvable. Minor conformers may mediate alternate functions, and mutations could shift the conformational equilibrium to favor these conformers and so increase the level of the alternate function. The scale at which protein dynamics influence function goes beyond the molecular and cellular levels to the tissue level. Engler *et al.* (p. 208) describe how dynamic cell-cell and cell–extracellular matrix adhesion complexes respond to soluble factors and to mechanical cues to form and maintain differentiated tissues.

In Presentations, Perspectives, Meeting Reports, and Research Articles, *Science Signaling* (www.sciencemag.org/sciext/proteindynamics) highlights conformational changes in G protein–coupled receptor signaling (Houslay) and allosteric regulation in immune cell signaling (Chakraborty *et al.*), as well as providing insight into how pathogens exploit host protein interactions to their advantage (Liu *et al.*) and mechanisms by which the subcellular trafficking of proteins can influence cellular behavior (Pouille *et al.* and Dustin).

As progress continues in identifying proteomes and mapping interaction networks, the challenge is to also understand the molecular-level protein dynamics that allow proteins to act as receivers, switches, and relays and facilitate communication from the subcellular level through to the cell and tissue levels.

– VALDA J. VINSON

CREDIT: TOKURIKI AND TAWFIK

Protein Dynamics

CONTENTS

Reviews

Perspective

See also related online material at www.sciencemag.org/sciext/proteindynamics

Science

Published by AAAS

REVIEW

Sending Signals Dynamically

Robert G. Smock and Lila M. Gierasch

Proteins mediate transmission of signals along intercellular and intracellular pathways and between the exterior and the interior of a cell. The dynamic properties of signaling proteins are crucial to their functions. We discuss emerging paradigms for the role of protein dynamics in signaling. A central tenet is that proteins fluctuate among many states on evolutionarily selected energy landscapes. Upstream signals remodel this landscape, causing signaling proteins to transmit information to downstream partners. New methods provide insight into the dynamic properties of signaling proteins at the atomic scale. The next stages in the signaling hierarchy—how multiple signals are integrated and how cellular signaling pathways are organized in space and time—present exciting challenges for the future, requiring bold multidisciplinary approaches.

Transmission of signals between cells, within cells, and from the extracellular environment to the cellular interior is essential to life. In recent years, we have gained tremendous knowledge of the interacting networks that act as communication pathways for cellular signaling, culminating with extensive maps of "interactomes" based on genetic and physical interaction data [e.g., (*1*)]. Yet we know far less about how signals are passed from one component of a network to another. This puzzle can be viewed at the level of the protein machines that make up signaling networks: How does information, generally mediated by a binding interaction or a covalent modification, get relayed to the downstream member of the pathway?

It is increasingly apparent that signaling relies on the intrinsic dynamic properties of proteins and that proteins relay signals by shifting among different fluctuating energy states in response to one or more inputs. This emerging view of signaling raises many compelling questions: What is the genetic information that encodes the functionally productive dynamic properties of a protein? How do individual protein domains cooperate to form signaling pathways? How are signals integrated in multicomponent interconnecting networks? How do the dynamics of signaling proteins ultimately determine the response times of cells to signals and the time scales for signal propagation? We are beginning to develop the methods and principles to address these questions, but many challenges lie ahead. Our ability to develop therapeutic modulators of signaling and to reengineer cellular communication pathways will rely on progress in this fascinating but complex arena.

The intrinsic motions of proteins are determined by the covalent and noncovalent restraining forces that hold them together. The result is a symphony of dynamic modes oscillating at frequencies from picoseconds to milliseconds or even seconds. Tweaking a protein by a binding interaction or chemical modification alters this symphony, either gently changing its pitch or abruptly shifting the collective harmony. Just as the ability of a protein to fold is now understood to be best described by an "energy landscape," which maps the many states that a folding protein can visit as it samples conformational space en route to its native structure, so also is the ability of a signaling protein to respond to signals and pass them on dependent on the features of the energy landscape. The functional states crucial to signaling are in the lower energy regions of the overall folding landscape (Fig. 1). In both folding and signaling, the conformational states of a protein are populated to varying extents according to their energies, and rates of interconversions between states are governed by the heights of energy barriers between them.

Both the energetically favored structures of a given protein and its dynamic properties, including both amplitudes and frequencies of fluctuations between states, are encoded in its sequence and are subject to evolutionary pressures. Understanding how a given protein can transmit signals entails a full elaboration of its energy landscape and how this landscape is modulated by interactions with other proteins, peptides, or smaller ligands, as well as by covalent modifications such as phosphorylation. Thus, a static image of a protein, such as that from x-ray crystallography, is an extremely helpful starting point, but we must learn about the ensemble of accessible states in order to gain deeper insight into functions. For example, as simple a function as oxygen binding to hemoglobin requires a conformational change to enable oxygen entry and egress, which was noted by biophysicists as soon as they saw the structure (*2*).

It is considerably more difficult to fully describe the energy landscapes of proteins—both the extent of their sampling of different structures and the rates of this sampling—than it is to determine a single structure. Fortunately, research on protein dynamics and how functions of proteins relate to their movements has expanded greatly in recent years (*3*). Methodological advances that enable increasingly deep understanding of protein dynamics are emerging, concomitant with an enhanced awareness of complex interacting pathways in cellular physiology. Experimental methods that shed light on the dynamic properties of proteins are most informative in relatively narrow frequency ranges, and the methods applied to a given system must be matched to the underlying processes. Biological signal transmission occurs over a wide range of time scales. The fastest events are those triggered by light or electrical stimuli, which can take place on the femtosecond to picosecond time scales. Large-scale conformational rearrangements occur much more slowly, from milliseconds to seconds. Cellular networks of signals comprise molecular binding events, which may be transient or stable, and thus may prolong the time scale of signaling well beyond seconds.

The realization of the importance of dynamics to protein function is not new; major figures in biophysics recognized that protein motions were essential to function a half century ago (*4*–*7*). But progress in computational simulations of protein dynamics (*8*), in nuclear magnetic resonance (NMR) [in particular, relaxation dispersion (*9*)], and in single-molecule spectroscopy (*10*) has enabled the description of several signaling events in great depth on time scales from picoseconds to milliseconds. Together with an explosion of biological knowledge about complex signaling networks, these techniques offer an unprecedented opportunity for major advances in understanding. Below, we use several recently studied signaling systems to illustrate how the intrinsic dynamic properties of proteins allow them to act as switches and transducers in response to incoming signals and to thereby mediate signal transmission.

Incoming Signals Remodel Energy Landscapes

Signals can be transmitted by a shift in the equilibrium population of states for a protein with a rugged energy landscape (*7*). The "new view" of allostery (*11*) encapsulates the ideas of dynamics and postulates that the protein populates ensembles of many conformations at all times, fluctuating among these conformations. The interaction with a signaling partner remodels the landscape and consequently shifts the population distribution in such a way as to bias toward a particular downstream event.

How does a binding signal alter the energy landscape and lead to a productive signaling response? A central mechanism appears to rely on plasticity within an individual protein signaling domain—in other words, the existence of alternative residue packing networks with coupled dynamic motions. Extensive study of different examples of the widespread PDZ signaling

Department of Biochemistry and Molecular Biology and Department of Chemistry, University of Massachusetts, Amherst, MA 01003, USA. E-mail: gierasch@biochem.umass.edu (L.M.G.); rsmock@student.umass.edu (R.G.S.)

domain has identified potential intramolecular structural and dynamic pathways that appear to connect incoming signals, notably binding to recognition motifs present on upstream partner signaling molecules, to downstream partners. In their many different cellular contexts, PDZ domains function to transduce these binding events into favorable domain-domain assembly of complexes.

The correlation of evolutionary conservation among PDZ domains pointed to a spatially contiguous set of residues as candidates for transmission of functional signals (*12*), and other methods including NMR dynamics analysis (*13*, *14*), thermal fluctuation analysis of crystal structures (*15*), and computational simulations of correlated motions (*14*, *16*, *17*) found similar networks (Fig. 2). Intriguingly, in one example (the second PDZ domain of human tyrosine phosphatase 1E), the network of residues showing similar binding-induced dynamic changes did not coincide with the set of residues that undergoes structural changes between ligand-bound and free states (*14*). An in-depth analysis of the dynamics time scales of another PDZ domain (from mouse tyrosine phosphatase BL) showed interconversion between different allosteric states to be relatively slow (microseconds to milliseconds). By contrast, a different PDZ domain (human PSD-95 PDZ3) lacked the dynamic network (*18*). These results, together with recent analysis using double-mutant cycles, support the notion that different PDZ domains evolve to have different dynamic properties tailored to their specific functions. In this case, PSD-95 PDZ3 functions as a rigid protein interaction domain (*19*).

Whereas intramolecular signal transmission in PDZ domains seems to arise from a combination of structural changes and dynamic fluctuations, other domains rely more exclusively on dynamics for signaling (*20*). For example, the phosphotyrosine-binding domain of insulin receptor substrate–1 (IRS-1) binds to the autophosphorylated state of hormone-activated insulin receptor to mediate downstream signaling. A detailed NMR dynamics analysis revealed only subtle conformational changes between free IRS-1 and IRS-1 bound to a phosphotyrosine-containing peptide (*21*). Rather, a cluster of dynamically perturbed residues was found to connect the peptide-binding site to a distal surface, where the subsequent downstream signaling interaction was postulated to occur. In another example (*22*), binding of one cyclic adenosine monophosphate (cAMP) to CAP, a homodimeric cAMP-binding transcriptional activator, reduced the affinity for the second cAMP without any alteration in the overall structure of the subunit but with enhancement of its overall mobility on a microsecond to millisecond time scale. By contrast, binding of the second ligand led to rigidification (Fig. 1B). The authors provide a compelling case that the altered dynamics and consequent entropy costs explain the observed negative cooperativity in cAMP binding with no change in the average structure of the CAP protein.

Biological signaling requires the integration of multiple inputs: Multiple interactions can be modulated within the same molecule by coupling the remodeling influences of more than one ligand. For example, calmodulin, a central player in intracellular calcium signaling, regulates a wide array of downstream partner proteins in response to calcium concentration. A recent NMR study showed that binding to different target regulatory domains alters calmodulin internal dynamics to differing extents and "tunes" affinity through conformational entropy (*23*). Moreover, calmodulin signaling is dependent on its rugged energy landscape with multiple low-energy valleys and consequent ability to undergo substantial conformational rearrangement. The relatively small calmodulin molecule links two calcium-binding EF hands by a long helix that has the capacity to fold back on itself in a hinge-like motion. A recent study (*24*) computationally elaborated the ensembles of structures sampled by calmodulin in its free and calcium-bound states and showed, by incorporating NMR-derived distances and orientation parameters, how this ligand alters dynamics locally (i.e., within the EF hand subdomains) (Fig. 3A). These local events increase the affinity for downstream signaling molecules,

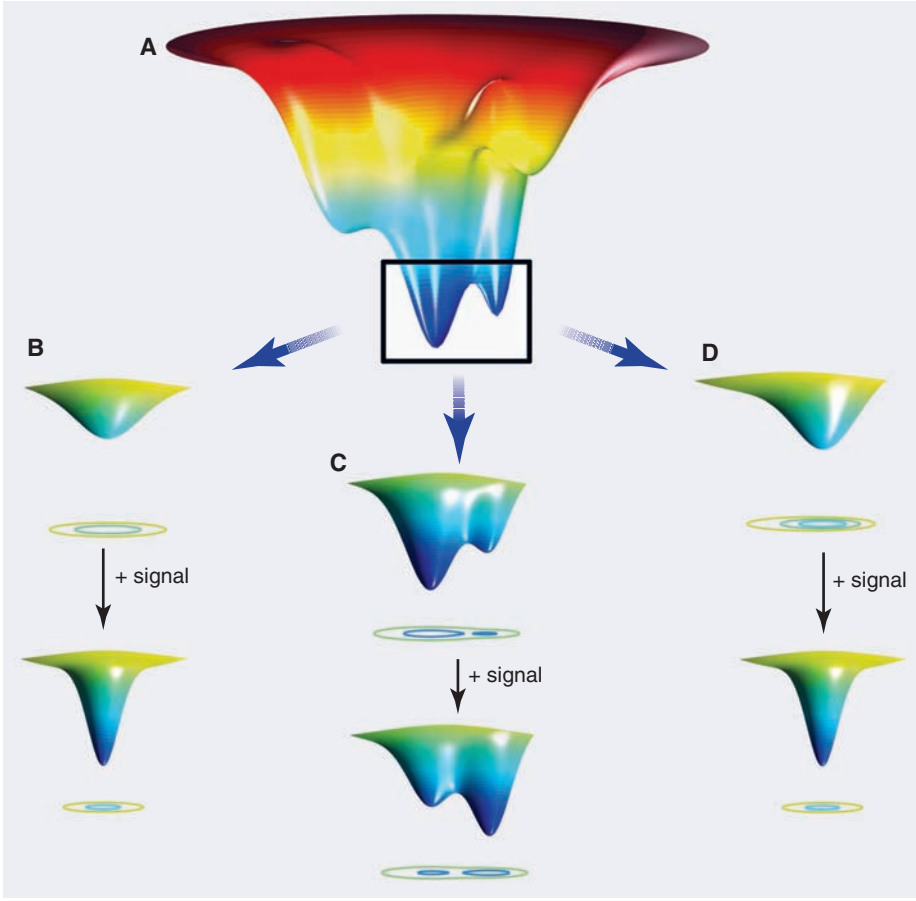

Fig. 1. Energy landscapes can be remodeled in several ways to alter protein dynamics and enable them to communicate signaling information. (**A**) Schematic illustration of the energy landscape available to a protein from higher energy (red) to lower energy (blue). Folding to the native state occurs as the large ensemble of non-native states moves down the energy funnel to the native state. The boxed region encloses conformational states that are energetically accessible and will be sampled under physiological conditions, given thermal fluctuations. (**B**) One way that a signal can remodel the energy landscape is to narrow the size of the ensemble of states in a single energy well. This reduces the dynamics of the protein, leading to a structural rigidification of the same average conformation. (**C**) Alternatively, a protein may exist in equilibrium between two distinct conformational states, and an incoming signal can alter the relative energies of the two states, leading to a redistribution of their occupancies. (**D**) A slight variation on (C) may occur if the sampling of a higher-energy state in the absence of ligand provides a partial pathway toward a signal-induced conformation, as shown by partially overlapping wells of the two states. In the landscape shown, the higher-energy state is narrowed and shifted somewhat in structure upon interaction with a signal.

such as myosin light chain kinase, which first binds the C-terminal calcium-bound EF hand. This binding in turn predisposes the N-terminal domain to form additional contacts, thus causing the overall molecular hinge to close. The result is a clamping of the partner molecule between the two halves of calmodulin. The findings are consistent with previous NMR (*25*) and single-molecule fluorescence results (*26*); together with other recent studies of this system (*27*, *28*), they illustrate how the intrinsic dynamics of a molecule such as calmodulin can lead to multistep coupled allosteric signaling events.

Autoinhibition via a Reversible Intramolecular "Latch"

Several signaling proteins are autoinhibited via internal domain-domain interactions. An upstream signal, such as a binding or phosphorylation event, leads to destabilization of the internal contacts, releasing the autoinhibition and enabling downstream events. In a landscape view, the inhibited signaling protein populates predominantly the autoinhibited state but visits occasionally excited states where inhibition is relieved. The ability of ligands to modulate this equilibrium and the dynamic nature of the response to a signal have now been quantitatively established for the human proto-oncogene Vav, which relays signals from cell surface receptors to modulate intracellular events, by combined use of NMR relaxation methods and biochemical assays (*29*). In this case, autoinhibition occurs because an acidic region (the "latch," termed Ac) binds as a helix to the guanine nucleotide exchange factor (GEF) substrate-binding site of the Vav Dbl homology (DH) domain (Fig. 3B). An excited state, in which the acidic helix is displaced, was sampled on the microsecond to millisecond time scale in the absence of any upstream signal. Phosphorylation of a single tyrosine in Ac (Tyr^{174}) catalyzed by an upstream kinase led to release of Ac binding and a shift of the population to the state that was previously infrequently visited (Fig. 1C). Strikingly, Tyr^{174} is not accessible in the inhibited state of Vav DH. Thus, the population of the excited state limits the rate of phosphorylation; moreover, for the mutant proteins that were amenable to this measurement, the excited-state population also paralleled their ability to activate the downstream GEF. When phosphorylated, the Ac region lacks stable secondary structure and is quite flexible. The Ac of Vav epitomizes "intrinsically disordered regions" (IDRs), which have evolved to be devoid of stable structure and often play key roles in signaling (see below) (*30*).

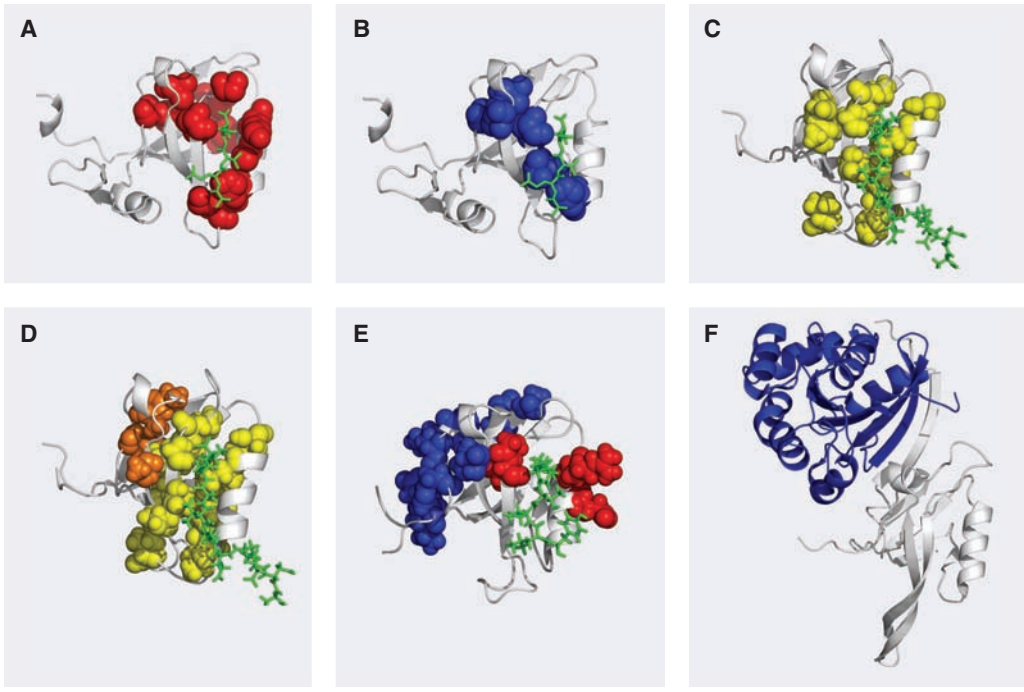

Fig. 2. Potential pathways of signal transmission within isolated PDZ domains. Similar networks linking the peptide-binding site (bound peptide shown in green sticks) to distal surfaces have been identified in PDZ domains by a number of approaches. (**A**) Patterns of evolutionarily coupled residues conserved among PDZ family members (shown in red spacefill) connect the peptide-binding site to a distal surface of the domain (*12*). (**B**) A network of residues identified by analysis of thermal fluctuations in PDZ-domain crystal structures is shown in blue spacefill, with the bound peptide in green sticks (*15*). (**C**) A pathway comprising residues in a PDZ domain, showing dipeptide-induced changes in their side-chain dynamics, is shown in yellow spacefill, with the peptide ligand in green sticks. (*13*) (**D**) A dynamic network identified by a molecular dynamics simulation restrained by experimental parameters (*14*) is shown in spacefill. Unexpectedly, one portion of the network shows enhanced flexibility upon peptide binding (orange) and, conversely, another region (red near the peptide binding pocket) shows reduced dynamics. (**E**) Domain-domain interaction between two PDZ domains appears to make use of the same basic pathways identified within an isolated PDZ domain. Residues shown as blue spheres were directly implicated in interdomain interactions in a phosphotyrosine phosphatase BL PDZ domain, and a set distal to these showed increased dynamics (red spheres) (*42*). (**F**) The interdomain interface identified in a crystal structure (PDB code 1NF3) of a complex of the regulatory Cdc42 (blue cartoon) and the Par-6 PDZ domain (white cartoon) also coincides with the surface of the PDZ domain that is connected to the peptide binding site by many of the identified intradomain networks.

Autoinhibition-based switches can be regulated extrinsically, as by phosphorylation of the Vav Ac domain, or intrinsically by the timing of a conformational change required to release the "latch." The Crk protein, an intracellular regulator of the tyrosine kinase Abl, comprises an Src homology 2 (SH2) domain followed by two SH3 domains separated by a 50–amino acid linker. The N-terminal SH3 domain of Crk binds proline-rich motifs in target proteins but is autoinhibited by interaction with the C-terminal SH3 domain. This inhibition is dependent on the Gly^{237}-Pro^{238} peptide bond within the linker adopting the cis isomeric state (*31*). A slow isomerization to the trans form (on a time scale of seconds) releases the interdomain linker and opens the N-terminal SH3 domain polyproline II ligand-binding site to partner interactions. Although these downstream aspects remain unknown, the cis-trans equilibrium may be regulated by Abl-mediated phosphorylation of a tyrosine near the key Gly^{237}-Pro^{238} bond in the linker, and the rate of interconversion between cis and trans forms can be catalyzed by prolyl isomerases. In turn, regulated access to this latter enzyme could afford yet another layer of dynamic regulation.

Disordered Regions Are Built-In Dynamic Switches

A large fraction of the exons in the human genome carry the signature amino acid composition and patterns predicted to fall into the class of IDRs [or IDPs (intrinsically disordered proteins)], and these regions are frequently reported to function as dynamic entities in signaling (*30*, *32*–*34*). By negative design, these regions retain the ability to interact with multiple recognition sites, typically

in alternative conformations. Some IDRs have the intrinsic ability to serve as molecular recognition features. In some cases, such as the Vav Ac described above, these regions may interact with another domain or protein in a stable secondary structure some of the time, and may then switch to another state that is either disordered or bound to a second binding partner. Their binding affinities are governed by competing entropic contributions (the costs of ordering the region upon binding) and enthalpic contributions (the favorable interactions formed). In addition to their malleable nature, IDRs provide geometric flexibility, allowing domain movements and serving as variable-length dynamic tethers.

The ability of IDRs to bind multiple partners leads to functional diversity in signaling cascades, as illustrated by the IDR-containing cell cycle regulator p21 (*35*) (Fig. 3C). Additionally, in this same group of cell cycle regulators, p27 illustrates that IDRs can bridge across long distances in complexes, in this case between a site on cyclin-dependent kinase (Cdk)–and one on cyclin A (*36*). Evidence from NMR suggests that binding to IDRs may occur stepwise, facilitating a "fly-casting" search, whereby multiple weak binding events favor initial complex formation (*37*, *38*) (Fig. 3D). Subsequent "Velcro"-like multivalent binding using several interactions at once leads to stable complexes. This coupling of binding and folding is accompanied by an entropically uphill "disorder-to-order" transition. In an alternative manifestation of multivalent binding, the recognition of the Cdk inhibitor Sic1 by its receptor, Cdc4, occurs via binding of several different sites on Sic1 to one site on the receptor, in a fluctuating dynamic equilibrium (*39*) (Fig. 3E). In this example, linking several weakly binding sites on one dynamic ligand maintains its receptor in an activated state. Clearly, the requirements for any given signaling interaction can be "tuned" by means of dynamic and intrinsically unstructured binding motifs.

Switchable Domain-Domain Interactions

Signaling network complexity can be achieved by flexibly linking domains and coupling signal-induced intradomain structural and dynamic responses to overall domain-domain rearrangements. This strategy accounts for the "Lego"-like evolutionary diversification of signaling pathways by recurrent use of the same switchable modules (*40*, *41*). This hierarchical buildup of signaling complexity is exemplified by the PDZ domains described above, which exist in combinations in many signaling proteins (Fig. 2). Their responses to signals can be altered by their context. For example, the first PDZ domain of mouse phosphotyrosine phosphatase BL (which contains five PDZ domains) modulates the

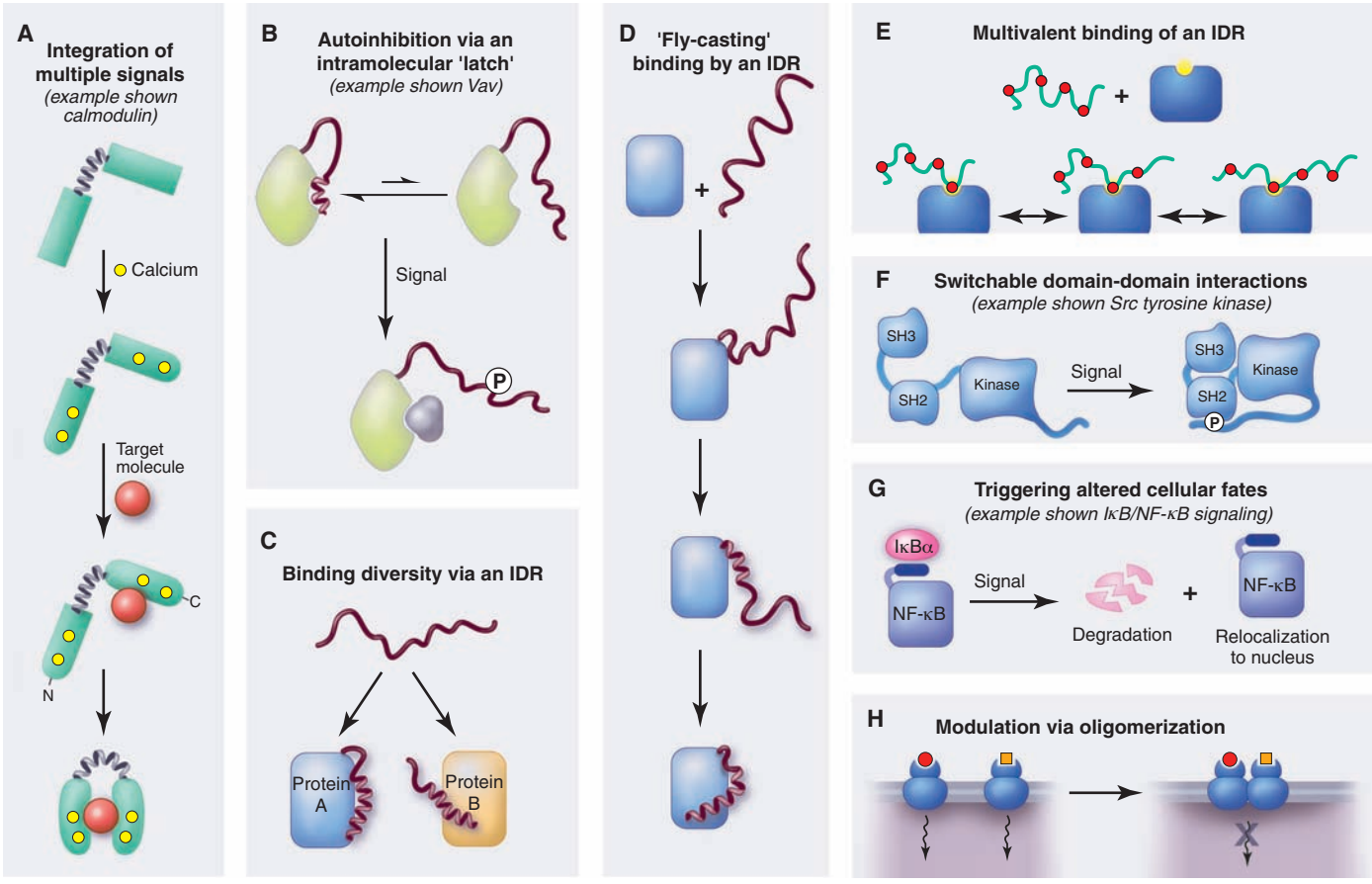

Fig. 3. Examples of how proteins take advantage of intrinsic dynamic properties to respond to an incoming signal. (**A**) Multiple signals can be integrated to create a response. Here, in the case of calmodulin, first calcium (yellow circles) is sensed by binding to the EF hand subdomains, which favors binding to a target molecule such as myosin light chain kinase (red circle). Binding of the target to one site on calmodulin leads to enhanced likelihood of binding to a second binding site (*24*). (**B**) Intramolecular autoinhibition can occur such that a downstream target interaction site is occluded. Opening of the autoinhibitory domain (here shown for Vav) can be favored by an upstream signal such as phosphorylation (*29*). (**C**) An intrinsically disordered region (IDR) can confer binding diversity on a signaling protein, enabling two targets to be recognized (*35*). (**D**) IDRs also enable a "fly-casting" mechanism of binding by allowing stepwise association with a target (*37*). (**E**) In some cases, multivalent binding can be mediated by an IDR that harbors several potential binding sites (small red circles) that each transiently occupy a single site on the target (*39*). (**F**) Dynamic domain-domain rearrangements can be triggered by signals such as phosphorylation (*45*). (**G**) Disruption of complexes can reveal signals for any of several downstream outcomes, such as relocalization in the cell and degradation (*47*). (**H**) Receptor complexes enable the possibility of higher-order modulation of responses to two different signaling ligands (shown as red circle and yellow square) (*50*).

peptide affinity and specificity of its second PDZ domain through an interdomain interaction site that is consistent with the intradomain networks discussed above (*42*). Similarly, the *Drosophila* cell polarity protein Par-6 is regulated by the Rho guanosine triphosphatase (GTPase) Cdc42 via binding of Cdc42 to a CRIB domain adjacent to the Par-6 PDZ domain. Cdc42-CRIB activation of the PDZ domain occurs with pronounced rigidification of CRIB and CRIB-PDZ contacts on the opposite side from the PDZ ligand-binding site, consistent with the signaling pathways observed for isolated PDZ domains. This indirect domain-domain rearrangement changes the conformation of the PDZ domain, increasing its affinity for peptide and triggering subsequent cell polarity signaling (*43*). PDZ conformational switching has also recently been implicated in the INAD scaffold protein of the *Drosophila* visual photoreceptor (*44*); this protein was previously thought to be a passive organization template. The new data show that INAD PDZ5 acts as a redox switch, switching an internal cysteine pair to an oxidized state in a light-dependent manner to regulate the binding of target proteins and promote signaling, although the mechanistic details of signal transduction are unclear.

Incoming signals can also promote assembly and disassembly of multiple domains (Fig. 3F). Src tyrosine kinase SH2 and SH3 domains undergo reversible assembly and disassembly in a dynamic equilibrium that is dependent in part on binding of a phosphotyrosine from the adjacent kinase domain. Binding of the phosphorylated kinase segment to the SH2 domain favors SH2-SH3 assembly and inactivates the kinase. When the kinase is activated (and the tyrosine is not phosphorylated), the SH2-SH3 tandem domains are uncoupled from one another. They nonetheless fluctuate between the assembled and disassembled arrangements. The interdomain linker is crucial to this fluctuating equilibrium, as mutation of the linker can lead to constitutive activation (*45*). Apparently, the interdomain linker biases substates populated in the active form of Src kinase so as to reduce conformational search in assembly-mediated inactivation (Fig. 1D). Switchable domain-domain associations involving the interdomain linker are also exemplified by transmembrane C-cadherin proteins, which function in cell adhesion during development (*46*). Binding of calcium rigidifies flexible segments between cadherin repeats, altering their dynamics and mechanical properties and increasing the availability of adhesive contacts.

Modulation of dynamics and domain arrangements from incoming signals can lead to altered cellular localization and enhanced degradation (Fig. 3G). The NF-κB transcription factor is normally bound to the inhibitory protein IκBα, which partially occludes a NF-κB nuclear localization sequence, resulting in dynamic shuttling between the cytoplasm (predominantly) and the nucleus. Relief of inhibition occurs through phosphorylation, ubiquitination, and consequent degradation of IκBα, which results in localization of NF-κB exclusively to the nucleus and transcriptional activation of target genes, including IκBα, which acts via negative feedback. Several of IκBα's ankyrin repeat domains rigidify upon binding to NF-κB, but there is an increase in flexibility in the central repeats (*47*). The IκB–NF-κB signaling module has emerged as a paradigm for linkage of regulation of gene expression to temporal responses of a signal transduction network, and its behavior has been mathematically modeled by several groups (*48*). An exciting future prospect is the correlation of the molecular dynamic properties of its components to the signaling dynamics of the entire system.

Wholesale Intermolecular Reorganization: Switchable Oligomerization and Arrays

Cellular networks display yet higher levels of organization. Recent studies show that oligomerization and array formation of signaling molecules, and of transmembrane receptors in particular, can have important functional consequences in several systems. Arrays of transmembrane receptors can integrate a spectrum of coincident extracellular signals, and the dynamics of formation and disassociation of the arrays will alter the cell's response to the multiple inputs. Examples are provided by bacterial chemotactic receptors, which cluster in heterogeneous arrays, "sniffing" the extracellular environment for any of several chemotactic signals and altering cell motility. The intracellular response elements are in large measure shared among the chemotactic receptors, even though they respond to different extracellular ligands. A recent elegant study shows clearly that clustering density has a marked effect on intracellular kinase and methylation activities (*49*).

The superfamily of heterotrimeric guanine nucleotide–binding protein (G protein)–coupled receptors (GPCRs), which comprises many subclasses that respond to specific ligands and perform a myriad of signaling functions, can show even greater functional diversity through multimerization. Cross-talk between the monomers within homodimers of GPCRs has been described, and newly discovered functional consequences of assemblies of different GPCRs are emerging. In one case, the binding of morphine to the μ-opioid receptor induces conformational change in a bound α_{2A}-adrenergic receptor, which in turn inhibits activation of its associated G protein and downstream signaling under conditions that would promote signaling in the absence of either morphine or receptor dimerization (*50*) (Fig. 3H). A fascinating extension of this theme involves association of various receptor types into a higher-order functional mosaic: Functional clustering of cannabinoid, dopamine, and adenosine receptors was indicated by the observation that ligands for the adenosine receptors modulated interactions between the cannabinoid and dopamine receptors (*51*). Such observations underscore the complexity of functional relationships in signal integration and propagation.

Another example of modulation via oligomerization was recently described for the Wiskott-Aldrich syndrome protein (WASP) family (*52*), members of which control actin dynamics through stimulation of Arp 2/3 complexes. The WASP VCA domain is responsible for the Arp 2/3 interaction but is normally intramolecularly inhibited by association with an adjacent GTPase-binding domain (GBD). This autoinhibition is allosterically relieved by a variety of WASP activators, which disrupt the interdomain contacts and free the VCA domain for its downstream interactions. WASP dimerization greatly enhances the affinity of the VCA domain for Arp2/3, leading to localized signal amplification. Dimerization is postulated to be favored by higher-order effects (such as interaction with multivalent WASP-binding partners) or by membrane clustering mediated by binding to regions enriched in phosphatidylinositol 4,5-bisphosphate. Interestingly, WASP and the related family member WAVE can heterodimerize in some cooperative processes, enabling yet more complex signal integration via allosteric and oligomeric mechanisms and increasing the capacity of the system to receive and integrate a greater variety of signals.

Perspective: From Atomic-Resolution Domain Dynamics to Complex Signaling Networks

Cells and organisms are processing and reacting to many signals at all times. The integration of many signals by complex networks is central to balancing needs and coordinately regulating a multitude of biochemical pathways. We have attempted to illustrate how the fundamental dynamic properties of signaling proteins may enable them to mediate these complex signaling tasks. New advances are offering greater insight into intrinsic dynamic properties of small protein modules and how binding events and covalent modifications influence them. Concurrently, explosive progress in the identification of components in signaling networks and the mapping of their interactions provides a tantalizing challenge for the future: Can we connect the atomic-scale descriptions of protein dynamics to the higher-level interdomain and intermolecular communication events that make up a signaling network?

Paradigms for how proteins act as receivers, switches, relays, and nodes in pathways are emerging. A hint of how higher-level organization of signaling components can lead to integration of signals and coordinated modulation of responses has been provided in a few cases. However, there remains a huge gap between the molecular level and the cellular or intercellular

level of signaling. This gap is spatial (cellular distances are on the scale of micrometers; protein movements are measured in angstroms), organizational (compartmentalization and orderly arrangements of pathways are essential to life), temporal (molecular movements occur in picoseconds to seconds, whereas cellular communication may persist substantially longer), and combinatorial (the sheer numbers of cell types, proteins, small molecules, stimuli, etc., and the multiplicity of their functional relationships with each other lead to extraordinary numbers of possibilities). The challenge to bridge this gap will require powerful new methods, interdisciplinary strategies, and creative, bold minds. We are encouraged by efforts to apply information theory to quantitatively interpret signal transmission (*53*), by multiscale modeling to bridge the molecular simulations to biochemical networks (*54*), and by whole-cell mapping of signaling protein dynamics (*55*, *56*). A holistic picture of the entire orchestra of dynamic contributions to cellular signaling can now begin to be envisioned.

References and Notes

1. H. Yu *et al.*, *Science* **322**, 104 (2008); published online 21 August 2008 (10.1126/science.1158684).
2. M. F. Perutz, F. S. Mathews, *J. Mol. Biol.* **21**, 199 (1966).
3. K. Henzler-Wildman, D. Kern, *Nature* **450**, 964 (2007).
4. K. Linderstrom-Lang, J. Schellman, in *The Enzymes*, P. Boyer, Ed. (Academic Press, New York, 1959), vol. 1, pp. 443–510.
5. A. Ansari *et al.*, *Proc. Natl. Acad. Sci. U.S.A.* **82**, 5000 (1985).
6. H. Frauenfelder, S. G. Sligar, P. G. Wolynes, *Science* **254**, 1598 (1991).
7. G. Weber, *Biochemistry* **11**, 864 (1972).
8. P. Sherwood, B. R. Brooks, M. S. Sansom, *Curr. Opin. Struct. Biol.* **18**, 630 (2008).
9. A. Mittermaier, L. E. Kay, *Science* **312**, 224 (2006).
10. C. Bustamante, *Annu. Rev. Biochem.* **77**, 45 (2008).
11. J. F. Swain, L. M. Gierasch, *Curr. Opin. Struct. Biol.* **16**, 102 (2006).
12. S. W. Lockless, R. Ranganathan, *Science* **286**, 295 (1999).
13. E. J. Fuentes, C. J. Der, A. L. Lee, *J. Mol. Biol.* **335**, 1105 (2004).
14. A. Dhulesia, J. Gsponer, M. Vendruscolo, *J. Am. Chem. Soc.* **130**, 8931 (2008).
15. N. Ota, D. A. Agard, *J. Mol. Biol.* **351**, 345 (2005).
16. P. De Los Rios *et al.*, *Biophys. J.* **89**, 14 (2005).
17. Y. Kong, M. Karplus, *Proteins Struct. Funct. Bioinf.* **74**, 145 (2009).
18. S. Gianni *et al.*, *Structure* **14**, 1801 (2006).
19. C. N. Chi *et al.*, *Proc. Natl. Acad. Sci. U.S.A.* **105**, 4679 (2008).
20. C. J. Tsai, A. del Sol, R. Nussinov, *J. Mol. Biol.* **378**, 1 (2008).
21. V. A. Jarymowycz, M. J. Stone, *Biochemistry* **47**, 13371 (2008).
22. N. Popovych, S. Sun, R. H. Ebright, C. G. Kalodimos, *Nat. Struct. Mol. Biol.* **13**, 831 (2006).
23. K. K. Frederick, M. S. Marlow, K. G. Valentine, A. J. Wand, *Nature* **448**, 325 (2007).
24. J. Gsponer *et al.*, *Structure* **16**, 736 (2008).
25. K. P. Hoeflich, M. Ikura, *Cell* **108**, 739 (2002).
26. C. K. Johnson, *Biochemistry* **45**, 14233 (2006).
27. J. P. Junker, F. Ziegler, M. Rief, *Science* **323**, 633 (2009).
28. S. Tripathi, J. J. Portman, *Proc. Natl. Acad. Sci. U.S.A.* **106**, 2104 (2009).
29. P. Li, I. R. S. Martins, G. K. Amarasinghe, M. K. Rosen, *Nat. Struct. Mol. Biol.* **15**, 613 (2008).
30. A. K. Dunker, I. Silman, V. N. Uversky, J. L. Sussman, *Curr. Opin. Struct. Biol.* **18**, 756 (2008).
31. P. Sarkar, C. Reichman, T. Saleh, R. B. Birge, C. G. Kalodimos, *Mol. Cell* **25**, 413 (2007).
32. A. K. Dunker *et al.*, *BMC Genomics* **9** (suppl. 2), S1 (2008).
33. A. K. Dunker, V. N. Uversky, *Nat. Chem. Biol.* **4**, 229 (2008).
34. M. Fuxreiter *et al.*, *Nat. Chem. Biol.* **4**, 728 (2008).
35. R. W. Kriwacki, L. Hengst, L. Tennant, S. I. Reed, P. E. Wright, *Proc. Natl. Acad. Sci. U.S.A.* **93**, 11504 (1996).
36. C. A. Galea *et al.*, *J. Mol. Biol.* **376**, 827 (2008).
37. K. Sugase, H. J. Dyson, P. E. Wright, *Nature* **447**, 1021 (2007).
38. D. Eliezer, A. G. Palmer 3rd, *Nature* **447**, 920 (2007).
39. T. Mittag *et al.*, *Proc. Natl. Acad. Sci. U.S.A.* **105**, 17772 (2008).
40. J. E. Dueber, B. J. Yeh, R. P. Bhattacharyya, W. A. Lim, *Curr. Opin. Struct. Biol.* **14**, 690 (2004).
41. T. Pawson, P. Nash, *Science* **300**, 445 (2003).
42. L. C. van den Berk *et al.*, *Biochemistry* **46**, 13629 (2007).
43. F. C. Peterson, R. R. Penkert, B. F. Volkman, K. E. Prehoda, *Mol. Cell* **13**, 665 (2004).
44. P. Mishra *et al.*, *Cell* **131**, 80 (2007).
45. J. D. Faraldo-Gómez, B. Roux, *Proc. Natl. Acad. Sci. U.S.A.* **104**, 13643 (2007).
46. M. Sotomayor, K. Schulten, *Biophys. J.* **94**, 4621 (2008).
47. S.-C. Sue, C. Cervantes, E. A. Komives, H. J. Dyson, *J. Mol. Biol.* **380**, 917 (2008).
48. R. Cheong, A. Hoffmann, A. Levchenko, *Mol. Syst. Biol.* **4**, 192 (2008).
49. T. Y. Besschetnova *et al.*, *Proc. Natl. Acad. Sci. U.S.A.* **105**, 12289 (2008).
50. J. P. Vilardaga *et al.*, *Nat. Chem. Biol.* **4**, 126 (2008).
51. D. Marcellino *et al.*, *Neuropharmacology* **54**, 815 (2008).
52. S. B. Padrick *et al.*, *Mol. Cell* **32**, 426 (2008).
53. T. Lenaerts *et al.*, *BMC Struct. Biol.* **8**, 43 (2008).
54. M. Stein, R. R. Gabdoulline, R. C. Wade, *Curr. Opin. Struct. Biol.* **17**, 166 (2007).
55. J. M. Ankers, D. G. Spiller, M. R. White, C. V. Harper, *Curr. Opin. Biotechnol.* **19**, 375 (2008).
56. T. D. Pollard, *Biochem. Soc. Trans.* **36**, 425 (2008).

57. Supported by NIH grants GM027616 and OD000945 (L.M.G.).

10.1126/science.1169377

REVIEW

Protein Dynamism and Evolvability

Nobuhiko Tokuriki and Dan S. Tawfik*

The traditional view that proteins possess absolute functional specificity and a single, fixed structure conflicts with their marked ability to adapt and evolve new functions and structures. We consider an alternative, "avant-garde view" in which proteins are conformationally dynamic and exhibit functional promiscuity. We surmise that these properties are the foundation stones of protein evolvability; they facilitate the divergence of new functions within existing folds and the evolution of entirely new folds. Packing modes of proteins also affect their evolvability, and poorly packed, disordered, and conformationally diverse proteins may exhibit high evolvability. This dynamic view of protein structure, function, and evolvability is extrapolated to describe hypothetical scenarios for the evolution of the early proteins and future research directions in the area of protein dynamism and evolution.

Proteins are proficient, accurate, and specific. These characteristics generally correlate with a lack of versatility; however, proteins also exhibit a marked ability to acquire new functions and structures. The evidence for the evolutionary adaptability of proteins is compelling, not only in the vast range of proteins that have presumably diverged from a few common ancestors, but also in recent evolutionary events such as the emergence of drug resistance and enzymes that degrade chemicals that appeared on this planet only a few decades ago.

Department of Biological Chemistry, Weizmann Institute of Science, Rehovot 76100, Israel.

*To whom correspondence should be addressed. E-mail: tawfik@weizmann.ac.il

What are the features that make proteins evolvable? Evolution acts by enriching preexisting diversities. Proteins conforming to the traditional view of absolute functional specificity, and only one well-defined structure are therefore not likely to readily respond to new selection pressures. However, a "new view" of proteins as an ensemble of alternative substructures, or conformers, in equilibrium with their so-called "native state" currently prevails [the new view was originally proposed by R. L. Baldwin and K. A. Dill in relation to protein folding and was later extended to describe native state ensembles (*1*)]. The new view is more consistent with evolutionary adaptability and is extended here to an avant-garde view of protein dynamism and evolvability.

Conformational variability, or dynamism, is an inherent property of any polymeric chain. The conformational diversity observed in proteins ranges from fluctuations of side chains and movements of active-site loops to secondary structure exchanges and rearrangements of the entire protein fold. Alternate structural conformers can mediate alternate folds and functions (*1*, *2*). Such structural and functional diversity is the foundation of "protein evolvability," defined as the abil-

ity of proteins to rapidly adopt (i.e., within a few sequence changes) new functions within existing folds or even adopt entirely new folds.

Functional promiscuity seems to be the starting point for divergence of new functions. Mutations can shift the equilibrium toward alternative functions and structures and therefore make up the raw material on which selection acts. Here, we discuss mechanisms that enable proteins to accumulate a larger number of mutations and thereby facilitate their adaptation. We also outline possible scenarios for the evolution of the earliest proteins by drawing parallels from RNA and protein folding intermediates, and we speculate what their properties could teach us about primordial protein forms. As there are only few well-characterized examples of recent adaptations and the ancient ones are challenging to track (*3*), we outline possible mechanisms and driving forces for the divergence of new functions and folds that mostly remain in the realm of theory and need to be experimentally substantiated, as discussed in the last section.

Local, Active-Site Flexibility Mediates Promiscuity and Evolvability

Active-sites loops are flexible, and their sampling of conformational ensembles at different time scales and magnitudes is related to catalysis and regulation (*4*, *5*). The enzymatic chemistry occurs within rigid, preorganized sites, but other steps (such as product release) may determine the enzymatic turnover rate and could be facilitated by conformational rearrangements. The same flexibility that is required for catalysis can provide the basis for functional diversity and the route to evolutionary divergence of new functions. Many proteins exhibit multiple cellular functions, and enzymes promiscuously catalyze reactions other than the ones they originally evolved to catalyze (*6*). This promiscuity and multispecificity could be ascribed to various ligands or substrates, shifting the equilibrium in favor of those minor conformations in the ensemble that bind them (*1*) (Fig. 1).

Earlier examples of multispecificity include an antibody that was shown to exist, before ligand addition, in equilibrium between several different binding site conformers. These conformers enabled the binding of two unrelated ligands, each of which could shift the equilibrium in favor of a different conformer (*7*). Recently, a nuclear magnetic resonance study of ubiquitin revealed an ensemble of conformers that are nearly identical to complexes of ubiquitin with 46 different partners (*8*). This inherent flexibility enables ubiquitin to bind multiple partners in a specific manner while fixing one out of many alternative conformations. Such conformationally plastic yet specific binding modes are also seen in T cell receptors and in "fuzzy complexes" where multiple conformations, or even complete disorder, prevail (*9*). Examples of flexible enzymes include a cytochrome P450 that displays a wide range of different active-site conformations that bind and transform a wide diversity of substrates (Fig. 2A) (*10*). Loop flexibility also enables domain repositioning in iron regulatory protein 1, where one conformer binds mRNA to repress translation or degradation and the other binds an iron-sulfur cluster and becomes an aconitase enzyme (*11*).

There seems to be a correlation between the degree of conformational diversity and promiscuity. In P450s, for example, the relatively rigid CYP2A6 exhibits narrow substrate specificity, whereas CYP3A4, the most promiscuous CYP known, exhibits the highest flexibility (*12*). In antibodies, increased affinity for a ligand gives decreased binding-site flexibility (*13*). Directed evolution experiments yield new enzymatic specificities by introducing mutations into inherently flexible active-site loops (*14*). These mutations are generally destabilizing (*14*), suggesting an increase in configurational entropy and active-site flexibility so that the new specificity comes from increasing a latent promiscuous function (*15*). Similarly, mutations acquired by selecting for one promiscuous function often induce broad specificity and allow other unselected substrates to be accommodated (*6*), possibly by allowing new degrees of freedom to active-site loops (*15*) (Fig. 1). Though the above suggests that more flexible active sites are more promiscuous and more evolvable, a link between active-site flexibility and evolvability is yet to be established. Similarly, a role of promiscuous ligand and substrate binding, or reaction, in providing a starting point for new gene functions has been only implicated in few instances (*16*–*18*) and needs to be more broadly established.

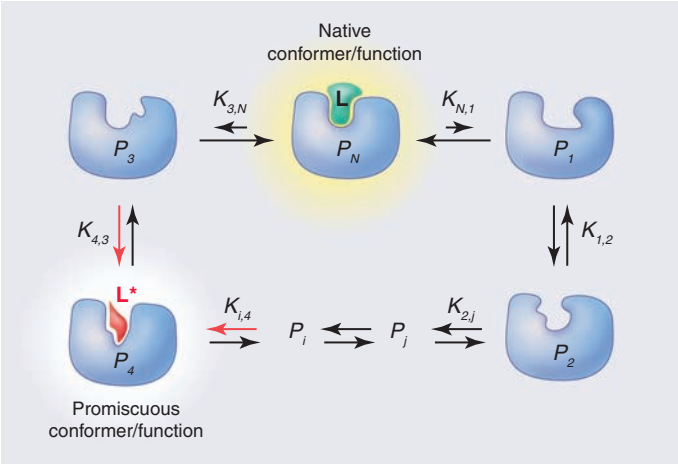

Fig. 1. The dynamics of protein structure and function and protein evolvability. The model assumes that proteins exist as an ensemble of conformations, the dominant one being the native state (P_N, interacting with the native ligand L). The alternative conformers relate to structural variations spanning from side-chain roatmers and active-site loop rearrangements to more profound fold transitions. Minor conformers (e.g., P_4) may mediate alternative functions, such as the promiscuous interaction with L^* (where L^* is a ligand that the protein did not evolve to bind). Mutations can gradually alter this equilibrium such that scarcely populated conformers become more favorable with substantial effects on the corresponding promiscuous function (e.g., an increase in occupancy of P_4 from 0.01 to 0.1 can yield a 10-fold increase in the overall level of promiscuous function). The relative occupancy of the native conformer would be hardly affected (e.g., from 0.5 to ≥0.41, leading to <20% loss of the native function). Similarly, higher specificity could evolve via mutations that reduce the occupancy of certain promiscuous conformers. This model also accounts for weak negative tradeoffs between the existing and evolving functions and the evolutionary potential of neutral mutations.

Global Conformational Diversity and the Evolution of New Folds

Beyond the alternative side-chain rotamers and loop conformations described above (local flexibility), global structural rearrangements and fold transitions within the same sequence have also been observed (*2*, *19*). For example, lymphotactin exists in equilibrium between two different folds (Fig. 2B) (*20*), and Mad 2 is a homodimer that adopts two different β-sheet organizations (*21*).

Theoretical studies have also addressed the issue of fold transitions by mapping networks of sequence-fold spaces, primarily in RNA where secondary structures are accurately predicted (*22*), but also with lattice protein models (*23*). Each fold makes up a neutral network—a set of sequences that adopt the same structure (and presumably the same function) and are connected by single point mutations. Individual neutral networks are connected to one another at certain transition points (sequences) and can therefore be smoothly traversed by single mutational steps. This idea was demonstrated by isolating two ribozymes with different folds and functions that are connected by single point mutations and an intermediate that equilibrates between the two (*24*). In vitro evolution showed that a few mutations could convert one function into another while inducing a new fold (*25*). Similarly drastic transitions of fold and function are rarely demonstrated with proteins, as their folds are far more complex (the RNA-protein analogy is discussed in the last section of this review). One example is a 28–amino acid cysteine-rich domain, where one mutation resulted

in an equilibrium between the original fold and the fold of another naturally occurring domain; another mutation completed this transition (Fig. 2C) (*26*) [see also recent reviews (*2*, *19*)].

Other examples of conformational switches in natural proteins include prions that exist in a soluble form and aggregated amyloid form, and a myriad of intermediate oligomeric forms. Intrinsically disordered proteins (IDPs) make up another class of proteins where large structural transitions occur. Typically, order and tight packing are observed only when the ligand is bound (coupled binding-folding), and even then, other parts may remain disordered (*9*, *27*). IDPs are considered as a separate class of proteins with specific sequence compositions and functions that correlate with their unusual properties. Nevertheless, coupled binding and folding might have played a role in the evolution of the first protein forms and may be important in major fold transitions. Notably, order-disorder is not an all-or-nothing property. Short disordered segments are commonly observed within otherwise ordered proteins [and are often involved in function (*9*)], and relatively low degrees of order seem to characterize certain protein classes such as viral proteins (*28*). In fact, partial order may endow high tolerance to sequence changes and higher evolvability.

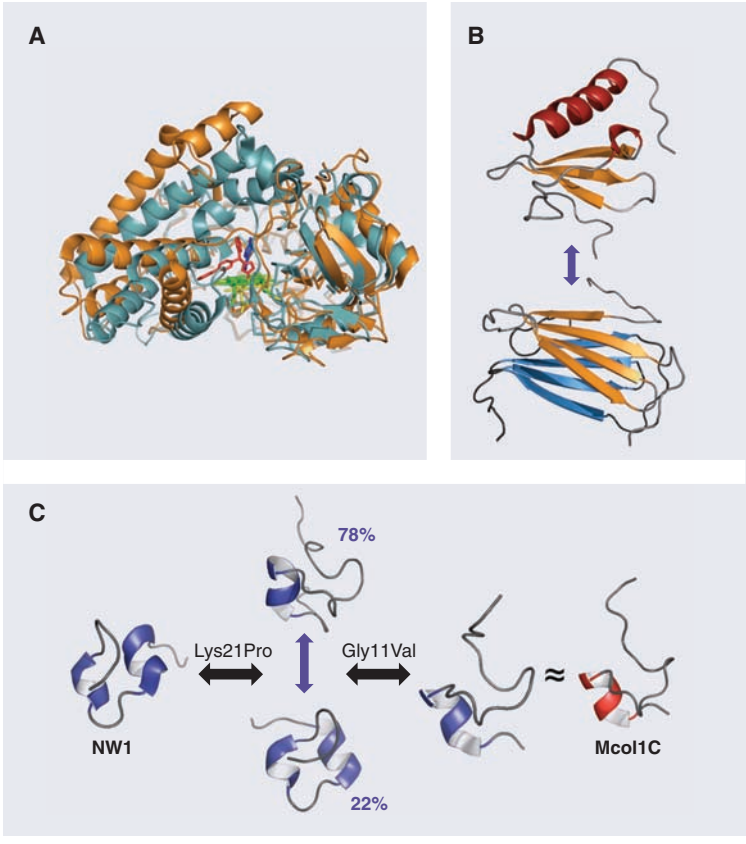

Fig. 2. Examples of conformational diversity. (**A**) Local conformational changes mediate an enzyme's broad substrate specificity. The open conformation of P450-CYP2B4 (orange) occurs with a large substrate (bifonazole, illustrated in red), and the closed one (light blue) occurrs with the smaller 4-(4-chlorophenyl) imidazole (darker blue) (*10*). (**B**) Metamorphic proteins. Lymphotactin exists in equilibrium between a beta-alpha mononer (top) and an all-beta dimer (bottom) (*20*). (**C**) Transition folds. Two different topologies (mediated by three different disulfide bridges) are found in two naturally occurring cysteine-rich domains (NW1 and Mcol1C) that show almost no sequence identity beyond the conserved cysteines. Conversion between these topologies was demonstrated via one mutation $Lys^{21} \rightarrow Pro^{21}$ (K21P) that afforded an intermediate that equilibrates between the two topologies, and a second mutation $Gly^{11} \rightarrow Val^{11}$ (G11V) completed the transition (*26*).

Protein Evolvability and the Effects of Mutations

Evolution is the fixation of sequence changes, or mutations, that are often associated with functional changes and adaptation to new environments (adaptive mutations). However, mutations could also occur, and even fixate, with no apparent effects, as described by Kimura's neutral theory. A related issue is that evolvability has two contradictory components. Organisms, genes, and their encoded proteins are constantly exposed to mutations, and proteins whose neutrality or robustness (i.e., the ability to accommodate mutations without loss of structure and function) is limited may cause fitness losses at the organismal level. Yet because mutations generally accumulate one at a time, to adapt, the function and structure of a protein should change in response to few mutations (plasticity). Neutrality implies that mutations have no effect, whereas plasticity demands large effects of mutations on protein function and structure. Can the neutrality-plasticity dichotomy be reconciled (*29*)? Here we discuss this conundrum in relation to the functional and structural dynamism of proteins.

Contrary to the above dichotomy, comparisons of protein folds indicate that more neutral protein folds (folds that show higher sequence diversity) also exhibit higher functional diversification (*30*). How could that be? Gene duplication, relief of selection from the redundant copy, and accumulation of a large number of mutations before the acquisition of a new function is one possibility, but the abundance of deleterious mutations leading to rapid nonfunctionalization make this scenario unfavorable (*31*). Another explanation is that mutations can exhibit substantial effects on promiscuous protein functions but have minor effects on the native one (*6*). Likewise, mutations that initially appeared as neutral in a given environment (as polymorphism, or even fixed in a population) can facilitate future adaptations under changing circumstances (*29*) by altering latent promiscuous functions and conformers (Fig. 1) (*23*, *32*). Promiscuous conformers and functions can be also regarded as phenotypic variations. As is the case with regulatory networks, physiological adaptations such as the use of a promiscuous function in response to environmental changes, might correlate with changes that occur in response to mutations (evolutionary adaptations) (*33*). That said, tradeoffs between existing and evolving protein functions (as well as between correlated physiological and evolutionary adaptations) are far from being fully understood, and many other mechanisms operate in addition to the simplistic models described here.

Another aspect that relates to the neutrality-plasticity dichotomy is the structural characteristics of highly evolvable proteins. Traditionally, neutrality correlates with high thermodynamic stability (*34*). More than 80% of deleterious mutations relate to loss of protein stability, and the concomitant decline in the levels of soluble, functional protein. Thus, high stability (and, in particular, high thermodynamic stability owing to a more stable native state) correlates with well-packed, highly compact structures with increased tolerance to mutations (Fig. 3) (*35*). In cases such as the immunoglobulin fold, tight packing and highly robust scaffolds are combined with pronounced function and sequence diversity achieved primarily via changes in surface loops (e.g., antibody complementarity determining region loops). This separation of a tightly packed scaffold and floppy active site is also seen in many enzyme families (e.g., TIM barrels) and could simultaneously promote neutrality (via a robust scaffold) and plasticity (via loop changes).

However, most proteins exhibit limited stability (*34*), even (or especially) when placed under high mutational rates. Proteins from RNA viruses, where mutations rates are ~10^6-fold higher than in bacteria and eukarya, exhibit structural features that correlate with low stability:

namely, loose packing, low compactness, and a tendency to local disorder. These features may indicate an alternative mode of tolerating mutations because individual mutations lead to smaller stability losses due to weak interresidue contacts (*28*). This alternative mode of protein robustness is also supported by the observation that folds exhibiting the highest diversity in sequence and function show a higher tendency for disorder (*30*). Many IDPs show high rates of sequence diversification, and RNAs highly evolvable character arises from a small number of long-range tertiary contacts. Hence, higher evolvability might also correlate with loose packing (low degree of tertiary interactions), low compactness, and disorder (local or global). However, although higher neutrality of disordered regions has been recorded (*36*), their ability to rapidly evolve new functions and structures (plasticity) is yet to be established. The inevitable outcome of low stability could be partially compensated for by coupling function to folding or by destabilization of the unfolded state (negative design), rather than by high stability of the folded, native state (Fig. 3).

The Evolution of Early Protein Folds—Speculations and Future Directions

As described above, the concepts of conformational diversity and functional promiscuity can be applied to describe how new proteins diverged from existing ones, gradually (through sequential mutations) and smoothly (through functional intermediates) (*1*, *2*, *23*). These concepts can be extended to the evolution of primordial protein precursors, an issue that is still in the realm of speculation and hypotheses.

The size of sequence space of biopolymers (n^L, where n is the number of monomer types, and L is chain length) can be daunting ($20^{100} \approx 10^{130}$ sequence permutations for a 100–amino acid polypeptide). It makes the emergence of sequences with function a highly improbable event, despite considerable redundancy (many sequences giving the same structure and function). The higher evolvability of RNA compared with that of proteins is partly due to a vastly smaller sequence space ($n = 4$, as opposed to 20). However, functional proteins can be obtained with minimal sets of as few as nine amino acids (*37*). Short polypeptides ($L < 30$) assembled as homo- or hetero-oligomers, can enhance function by avidity effects. Oligomerization, or even ordered β sheet–based aggregates (*38*), could also promote the stability and solubility of emerging folds by burying exposed hydrophobic surfaces. Oligomeric interfaces may have composed the first binding and active sites (as is the case in numerous modern proteins). Duplication and fusion could then have resulted in larger, single-domain, monomeric proteins. The internal symmetry of about half of the known folds and the isolation of putative oligomeric precursors for highly symmetrical folds such as β propellers support this hypothesis (*39*).

Another obstacle regarding the evolution of the first proteins (and enzymes in particular) is that function depends on a relatively structured native state, but structure itself provides no selective advantage. A scenario that function was selected for, and structure coevolved, is therefore likely (*40*) (Fig. 4A). Assuming that partially ordered polypeptides made up the first evolutionary intermediates, two scenarios could be proposed (Fig. 4B). In a manner similar to Haeckel's principle that ontogeny recapitulates phylogeny, folding intermediates may reflect the nature of evolutionary intermediates. Proteins fold by diverse pathways. In some cases, a nucleus of secondary structure (that can partly exist in the unfolded state) is followed by tertiary long-range contacts. Alternatively, folding may begin with a seed of hydrophobic core via long-range interactions, followed by the formation of secondary structure (*41*). There are potential pros and cons and anecdotal evidence supporting these scenarios. Molten globules that resemble advanced folding intermediates can exhibit enzymatic function (*42*). Secondary structure elements such as α helices and β strands seem to evolve by simple patterning of polar and nonpolar amino acids (*37*). The sequence constraints for β-strand formation in particular are very minimal (*38*). A key to RNA evolvability seems to be a range of stable, easily exchangeable secondary structure elements, with only few and much weaker long-range tertiary interactions. On the other hand, tertiary interactions can be crucial because elements of tertiary structure in the form of 20– to 30–amino acid–long loops closed by hydrophobic interactions were identified as the potential seeds of protein folds (*43*).

Overall, the dynamism of protein structure and function provides the grounds for evolutionary adaptations (whether they are new functions in existing folds or the emergence of completely new proteins) with the variety of models described here. However, key insights regarding protein evolution are still needed. How did the early protein forms evolve, and how do substantial fold transitions occur? Does global structural flexibility (and partial or complete disorder) provide higher evolvability of fold (Fig. 4)? And, conversely, does local flexibility of active-site loops, combined with a robust well-packed scaffold, promote functional changes within the same fold? High flexibility and large ensembles of alternative conformers are likely to result in lower activity, so do evolvability and activity tradeoff? Are, for example, viral enzymes, more evolvable and

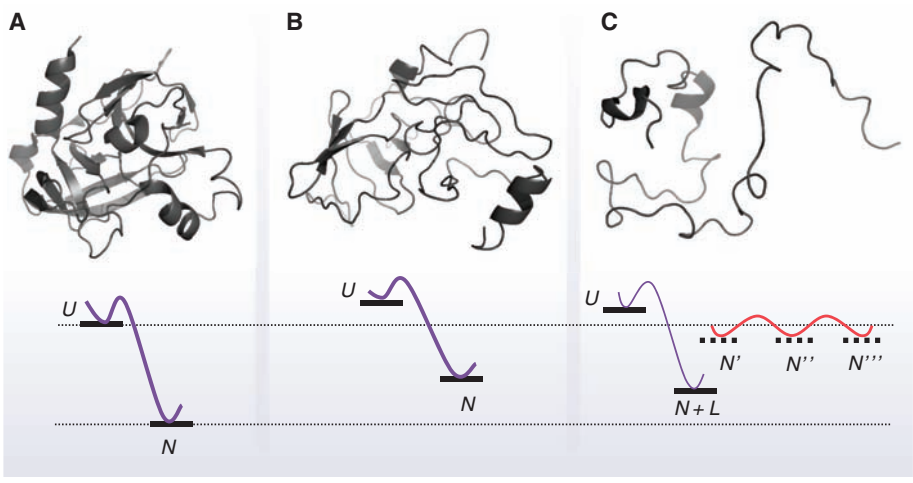

Fig. 3. Protein structure, stability, and evolvability. The figure depicts three stereotypes along an entire spectrum of packing orders. (**A**) Tightly packed, highly ordered, and compact proteins. An intense network of interresidue contacts makes the native state (*N*) highly favored and provides high stability [large energy difference between *U* (unfolded state) and *N*]. Such folds tolerate destabilizing mutations owing to an excess of stability that could be sacrificed without compromising their structural integrity. (**B**) Loosely packed proteins show lower degrees of interresidue contacts, fewer well-defined secondary structure elements (strands and helices), and higher fractions of loops and disordered segments. Therefore, the native state exhibits higher free energy, although the overall stability could be partly regained by destabilization of the unfolded state. Despite low stability, mutations are tolerated because sequence changes in weakly interacting residues cause smaller stability losses (*28*). (**C**) Disordered proteins adopt a defined structure only when in complex (*N* + *L*), but even then, their bound states are fairly loose with few long-range tertiary interactions. Their native state is composed of an ensemble of different conformers of similar energy (*N*′, *N*′′, etc.), and they are highly amenable to sequence changes (*27*).

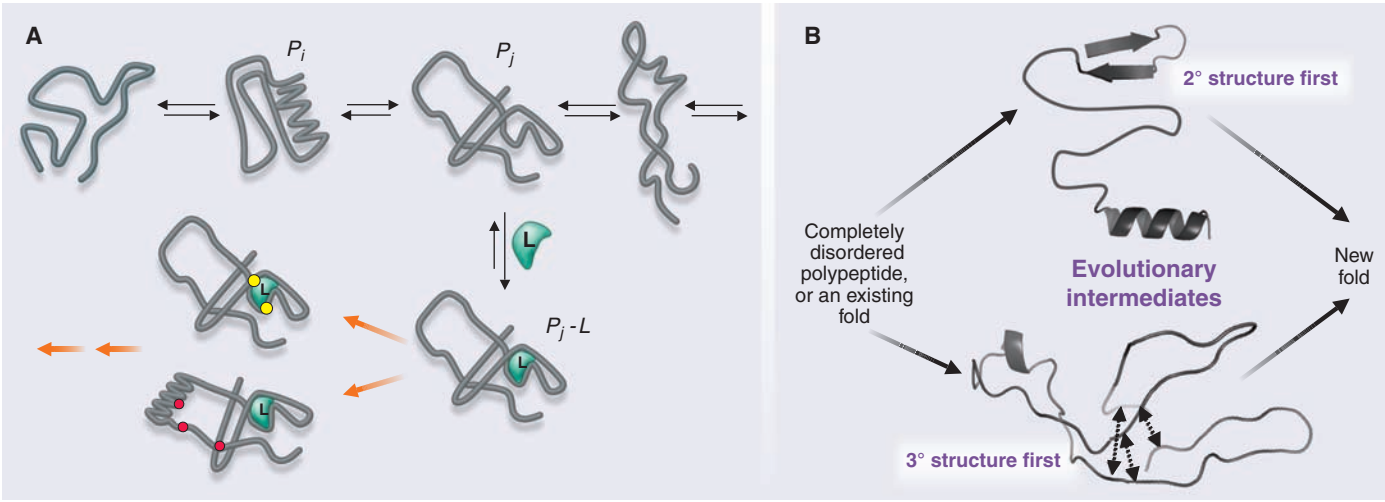

Fig. 4. Putative scenarios for the evolution of the primordial proteins. (**A**) Coevolution of fold and function via conformational selection from a repertoire of disordered polypeptides (P_i, P_j, etc.). Binding of a ligand (*L*) or substrate shifts the equilibrium in favor of a given conformer (P_j). Subsequent mutations (orange arrows) provide higher levels of function by stabilizing the functional conformer (thus evolving a fold, shown with red dots) and by altering the ligand contacting residues (yellow dots). (**B**) Evolutionary intermediates leading from a disordered protein to a folded one may resemble folding intermediates: 2° structure first involves the emergence of some secondary structure elements followed by the evolution of tertiary, long-range contacts and a fully folded protein. 3° structure first involves the formation of a rudimentary hydrophobic core by virtue of closing loops with a length of 20 to 30 amino acids (*43*), followed by the evolution of secondary structure.

hence less proficient than their highly ordered, well-packed orthologs? Is evolvability, therefore, an evolvable trait (*44*)? Traits such as functional promiscuity and conformational flexibility are inherent and need not be (and probably never were) selected for. Other traits such as robustness to mutations may have resulted from environmental, rather than genetic, pressures (*45*). It could be, however, that by virtue of their evolutionary history, certain classes of enzymes are more evolvable than others. Secondary metabolism is constantly responding to environmental changes, whereas core metabolism remained largely unchanged. Are secondary metabolism enzymes more flexible, more evolvable, and generally less proficient? Theory and simulations, perhaps of close-to-actual protein structures rather than lattice models, could help to address these questions, as can experiments, including in vitro evolution experiments that enable the actual reconstruction of evolutionary processes. The latter can use entirely random sequences as starting points (*46*) but could be better guided by bioinformatics (*47*), including phylogenies of large and prevalent superfamilies and folds that may have appeared first. The experimental reconstruction of the emergence of these rudimentary protein folds (and of function) from relatively simple and short polypeptides and insights regarding the intermediates along the route present a major challenge for future research.

References and Notes

1. L. C. James, D. S. Tawfik, *Trends Biochem. Sci.* **28**, 361 (2003).
2. S. Meier, S. Özbek, *Bioessays* **29**, 1095 (2007).
3. A. M. Dean, J. W. Thornton, *Nat. Rev. Genet.* **8**, 675 (2007).
4. K. A. Henzler-Wildman *et al.*, *Nature* **450**, 913 (2007).
5. N. M. Goodey, S. J. Benkovic, *Nat. Chem. Biol.* **4**, 474 (2008).
6. O. Khersonsky, C. Roodveldt, D. S. Tawfik, *Curr. Opin. Chem. Biol.* **10**, 498 (2006).
7. L. C. James, P. Roversi, D. S. Tawfik, *Science* **299**, 1362 (2003).
8. O. F. Lange *et al.*, *Science* **320**, 1471 (2008).
9. P. Tompa, M. Fuxreiter, *Trends Biochem. Sci.* **33**, 2 (2008).
10. B. K. Muralidhara, L. Sun, S. Negi, J. R. Halpert, *J. Mol. Biol.* **377**, 232 (2008).
11. W. E. Walden *et al.*, *Science* **314**, 1903 (2006).
12. J. Skopalík, P. Anzenbacher, M. Otyepka, *J. Phys. Chem. B* **112**, 8165 (2008).
13. I. F. Thorpe, C. L. Brooks, *Proc. Natl. Acad. Sci. U.S.A.* **104**, 8821 (2007).
14. N. Tokuriki, F. Stricher, L. Serrano, D. S. Tawfik, *PLoS Comput. Biol.* **4**, e1000002 (2008).
15. Y. H. Chen, J. Delmas, J. Sirot, B. K. Shoichet, R. Bonnet, *J. Mol. Biol.* **348**, 349 (2005).
16. L. Afriat, C. Roodveldt, G. Manco, D. S. Tawfik, *Biochemistry* **45**, 13677 (2006).
17. J. T. Bridgham, S. M. Carroll, J. W. Thornton, *Science* **312**, 97 (2006).
18. D. W. Brown, M. R. Schaab, W. R. Birmingham, R. N. Armstrong, *Biochemistry* **48**, 1847 (2009).
19. A. Andreeva, A. G. Murzin, *Curr. Opin. Struct. Biol.* **16**, 399 (2006).
20. R. L. Tuinstra *et al.*, *Proc. Natl. Acad. Sci. U.S.A.* **105**, 5057 (2008).
21. M. Mapelli, L. Massimiliano, S. Santaguida, A. Musacchio, *Cell* **131**, 730 (2007).
22. L. W. Ancel, W. Fontana, *J. Exp. Zool.* **288**, 242 (2000).
23. R. Wroe, H. S. Chan, E. Bornberg-Bauer, *HFSP J.* **1**, 79 (2007).
24. E. A. Schultes, D. P. Bartel, *Science* **289**, 448 (2000).
25. E. A. Curtis, D. P. Bartel, *Nat. Struct. Mol. Biol.* **12**, 994 (2005).
26. S. Meier *et al.*, *Curr. Biol.* **17**, 173 (2007).
27. H. J. Dyson, P. E. Wright, *Nat. Rev. Mol. Cell Biol.* **6**, 197 (2005).
28. N. Tokuriki, C. J. Oldfield, V. N. Uversky, I. N. Berezovsky, D. S. Tawfik, *Trends Biochem. Sci.* **34**, 53 (2009).
29. A. Wagner, *Nat. Rev. Genet.* **9**, 965 (2008).
30. E. Ferrada, A. Wagner, *Proc. Biol. Sci.* **275**, 1595 (2008).
31. S. Bershtein, D. S. Tawfik, *Mol. Biol. Evol.* **25**, 2311 (2008).
32. G. Amitai, R. D. Gupta, D. S. Tawfik, *HFSP J.* **1**, 67 (2007).
33. R. Milo, J. H. Hou, M. Springer, M. P. Brenner, M. W. Kirschner, *Proc. Natl. Acad. Sci. U.S.A.* **104**, 16998 (2007).
34. M. A. DePristo, D. M. Weinreich, D. L. Hartl, *Nat. Rev. Genet.* **6**, 678 (2005).
35. E. Bornberg-Bauer, H. S. Chan, *Proc. Natl. Acad. Sci. U.S.A.* **96**, 10689 (1999).
36. C. J. Brown *et al.*, *J. Mol. Evol.* **55**, 104 (2002).
37. Y. Wei, M. H. Hecht, *Protein Eng. Des. Sel.* **17**, 67 (2004).
38. A. Corazza *et al.*, *Proteins* **62**, 64 (2006).
39. I. Yadid, D. S. Tawfik, *J. Mol. Biol.* **365**, 10 (2007).
40. T. Yomo, S. Saito, M. Sasai, *Nat. Struct. Biol.* **6**, 743 (1999).
41. V. Daggett, A. R. Fersht, *Trends Biochem. Sci.* **28**, 18 (2003).
42. K. Vamvaca, I. Jelesarov, D. Hilvert, *J. Mol. Biol.* **382**, 971 (2008).
43. E. N. Trifonov, I. N. Berezovsky, *Curr. Opin. Struct. Biol.* **13**, 110 (2003).
44. D. J. Earl, M. W. Deem, *Proc. Natl. Acad. Sci. U.S.A.* **101**, 11531 (2004).
45. J. A. de Visser *et al.*, *Evol. Int. J. Org. Evol.* **57**, 1959 (2003).
46. A. D. Keefe, J. W. Szostak, *Nature* **410**, 715 (2001).
47. V. Anantharaman, L. Aravind, E. V. Koonin, *Curr. Opin. Chem. Biol.* **7**, 12 (2003).

48. We gratefully acknowledge financial support from the Israel Science Foundation and the European Union MiFEM network. We thank M. Fuxreiter, L. James, and R. Milo for their insightful comments.

10.1126/science.1169375

REVIEW

Multiscale Modeling of Form and Function

Adam J. Engler,[1] Patrick O. Humbert,[2] Bernhard Wehrle-Haller,[3] Valerie M. Weaver[4,5]*

Topobiology posits that morphogenesis is driven by differential adhesive interactions among heterogeneous cell populations. This paradigm has been revised to include force-dependent molecular switches, cell and tissue tension, and reciprocal interactions with the microenvironment. It is now appreciated that tissue development is executed through conserved decision-making modules that operate on multiple length scales from the molecular and subcellular level through to the cell and tissue level and that these regulatory mechanisms specify cell and tissue fate by modifying the context of cellular signaling and gene expression. Here, we discuss the origin of these decision-making modules and illustrate how emergent properties of adhesion-directed multicellular structures sculpt the tissue, promote its functionality, and maintain its homeostasis through spatial segregation and organization of anchored proteins and secreted factors and through emergent properties of tissues, including tension fields and energy optimization.

Morphogenesis is the process whereby a complex living system is created from individual components that are systemically developed to yield a functionally stable unit with a defined form and function. As proposed by Edelman and colleagues (*1*), topobiology is the process that sculpts and maintains differentiated tissues and is acquired by the energetically favored segregation of cells through heterologous cellular interactions. That "tissue affinity" is the primary morphogenetic driver was first demonstrated by Townes and Holtfreter, who showed that disaggregated amphibian cells self-organize into tissue structures with distinct cell fates (*2*). This concept was confirmed by the identification of cell adhesion molecules, which facilitate the assembly of multiprotein "signaling modules" that mediate, integrate, and stabilize multicellular interactions (*3*). Phenotypic cues mediated through gradients of secreted "soluble" factors such as fibroblast growth factor, transforming growth factor–β (TGFβ), and Wnt also control tissue patterning by activating genetic programs such as HOX gene clusters, thereby inducing and maintaining cellular identity and directing higher-order tissue architecture (*4*). Tensile forces also govern the self-organization of heterologous cellular interactions during embryogenesis and modulate tissue movements in development by altering the activity of critical transcriptional regulators such as twist, implicating physical cues as key morphometric integrators (*5*, *6*). Indeed, composition and topology of the extracellular matrix (ECM) stroma, which is secreted and modified by cells as they develop, changes throughout morphogenesis and directly regulates cell and tissue fate by inducing signaling within cells through specific matrix adhesion receptors to modify cytoskeletal organization and cell shape (*7*). Soluble factors such as hepatocyte growth factor and TGFβ also modulate cell fate either by directly destabilizing multicellular tissue organization through Rho guanosine triphosphatase (GTPase)–dependent actomyosin contractility (*8*) or by changing ECM composition and posttranslational processing through altered transcription to stiffen the matrix (*9*). Thus, while morphogenesis might depend upon cell adhesion, it is orchestrated by a highly coordinated series of events that are initiated by soluble factors that activate cellular signaling at the adhesions and that are integrated by mechanical cues operating at the molecular, cellular, and tissue level. Here, we discuss how topobiological cues are arranged from the molecular to the organism level based on the repetitive use of basic conserved "decision-making modules" (Fig. 1 and Table 1). We describe how these decision-making modules not only orchestrate rapid and highly adaptive changes in nonstructured masses of cells as they mature into highly defined tissues and organs but also are dynamic—displaying exquisite sensitivity to mechanical cues and undergoing reciprocal state transitions that permit the fine tuning of the organism. Finally, we speculate how emergent properties of organized multicellular tissues dictate specialized functions and modulate the functional integrity of cell and tissue fate so that altered expression, organization, or structure of any of these decision-making modules

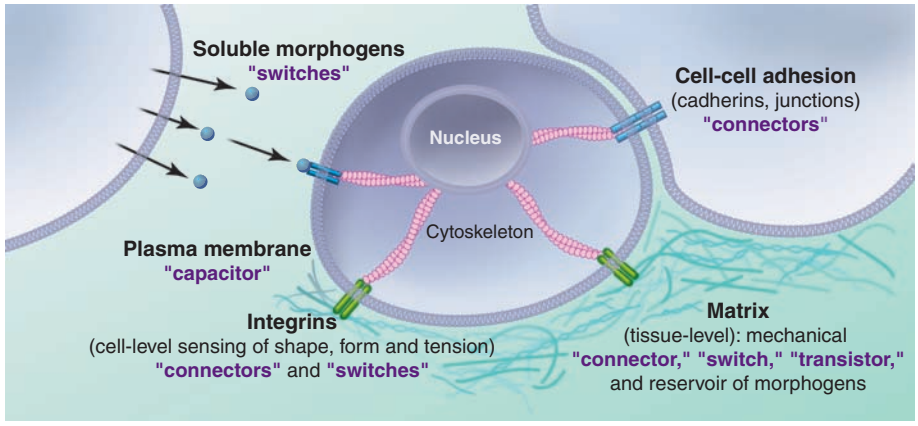

Fig. 1. Basic biological modules operate in tissues at multiple length scales. Variations and repetitions of the critical biological modules through many length scales and systems allow the formation and maintenance of increasingly complex multicellular structures with highly evolved functions. Different elements can "connect" one cell to its neighbor by homophilic receptors such as cadherins. Other connectors, such as integrins, mechanically link cells to the extracellular matrix, a three-dimensional (3D) scaffold to which different cell types can adhere. This mechanical connection allows the contraction or cell shape change of one cell to be transmitted by matrix fibrils through the cytoskeleton to a cohort of cells embedded in the same matrix, amplifying small perturbations to cause the matrix to act as a "transistor." Upon matrix binding, conformational changes within integrin adhesions recruit adapter proteins, which modify the cytoskeleton and act as individual switches to control adhesion, migration, and the like. Cytokine stimulation can also act as a switch, turning on and off to fine-tune cellular behavior. The plasma membrane with its intracellular recycling and storage compartment consists of a reservoir of receptors, the dynamic reshuffling of which controls the degree of signaling by acting as a capacitor. Complex interactions and repetitions of these modules through various length scales is the critical mechanism controlling morphogenesis and form.

[1]Department of Bioengineering, University of California, San Diego, La Jolla, CA 92093, USA. [2]Cell Cycle and Cancer Genetics Laboratory, Research Division, Peter MacCallum Cancer Center, Melbourne, Victoria, Australia. [3]Department of Cell Physiology and Metabolism, Centre Medical Universitaire, 1211 Geneva 4, Switzerland. [4]Center for Bioengineering and Tissue Regeneration and Department of Surgery, University of California, San Francisco (UCSF), San Francisco, CA 94143, USA. [5]Department of Anatomy, Department of Bioengineering and Therapeutic Sciences, Center for Regenerative Medicine and UCSF Comprehensive Cancer Center, San Francisco, CA 94143, USA.

*To whom correspondence should be addressed. E-mail: Valerie.weaver@ucsfmedctr.org

will alter cell and tissue architecture and perturb homeostasis and ultimately lead to disease.

Phenotypic Complexity Through Modular Sensors, Transistors, and Amplifiers

The first niche requirement for a multicellular organism is the development of cell-cell adhesions, which act as "connector" modules that define which cells will adhere to each other as they segregate. These modules are also the nucleation point for signaling molecules and cytoskeletal elements that regulate cell and tissue shape and function, giving them "switchlike" properties. A myriad of cell-cell adhesion molecules have evolved and have gained increasing complexity to facilitate cell-cell adhesion based on conserved components consisting of cytoplasmic, transmembrane, and 3 to 5 repeated extracellular domains, such as in neural cell adhesion molecules, that homotypically bind to each other. Evolution of these repeated domains has precisely set cell-cell spacing and has also regulated the amount of force that the bond can resist (*10*). Nevertheless, as exemplified by the ability of classic cadherins to link the actin cytoskeleton and adjacent cells, the major function of these modules is to mediate the efficient segregation of heterogeneous cell populations into distinct entities (*11*). This task is achieved by constant actomyosin-mediated pushing and pulling and the initiation of signaling that optimizes connections among neighboring cells and leads to phenomena such as cell compaction, as occurs at the blastula stage during embryogenesis. Thus, cell compaction is determined by the strength and number of connectors expressed on the cell surface and is likely dictated by the tension induced at the cellular and tissue levels. For example, cortical tension enhances the strength of cell adhesion in zebrafish such that the distinct germ layers display differing adhesion strengths (*6*). Assuming equal module density, the number of engaged connectors and the overall energy dynamics of the system will enable cells to determine whether they are sitting within or at the periphery of a given cell mass and will dictate the ultimate stability, size, and shape of the multicellular structure. Cellular rearrangements and coordinated tissue migration are also guided by the extracellular milieu of the tissue. Thus, the assembled ECM at the exterior of the blastula provides a qualitatively different anchorage site for the actin cytoskeleton that permits the differentiation of cell-cell from cell-ECM interactions (*12*). Integrins, which comprise the best characterized class of cell-ECM adhesion molecules, are heterodimeric transmembrane proteins that upon activation bind to specific ECM sites. After their binding, integrins recruit a host of structural and signaling modules, such as talin and Rho GTPases, respectively, to the plasma membrane, thereby responding to matrix tension and reciprocally exerting contractility at the cell periphery (*13*, *14*). Similar conserved modules occur in cell-cell adhesions, where structural and signaling modules act to hold cells together and communicate with the transcriptional apparatus in the nucleus to which the cellular cytoskeleton is tethered. Although they contain similar modules, integrin-matrix adhesions segregate from cadherins to define multicellular properties such as cell and tissue polarity. Thus, mice lacking β1 integrin fail to deposit ECM (e.g., laminin) at the blastula surface, leading to developmental arrest after implantation (*15*) that can be rescued by coating the blastula with purified laminin (*16*). In this manner, coordinated and dynamic interactions between cell-cell and cell-ECM are thought to direct multicellular tissue development. Nevertheless, how these events are executed and integrated at the tissue level is poorly understood and remains an area of intense investigation.

Table 1. Other examples of basic biological modules that could regulate form and function.

Module	Type	Major concept	References
Switch	Soluble morphogen	Spatial modulation of growth factor receptors in oogenesis	(*66*, *67*)
		Morphogen regulation of PCP	(*68*, *69*)
	Focal adhesion	Force-dependent signaling of adhesion complexes	(*70*, *71*)
Connector	Cell-cell binding	Adherens junctions and β-catenin in nonmetazoans	(*72*)
		Cell sorting and segregation scales with cadherin levels	(*73*)
		Peripheral myosin regulates cell intercalation	(*74*)
	Focal adhesion	Molecular clutch hypothesis for focal adhesions	(*75*, *76*)
Capacitor	Plasma membrane	Lipid raft-induced membrane curvature	(*77*)
Transistor	ECM	Storage of growth factors to guide tissue development and direct cancer progression	(*78*, *79*)

Phenotype Is Dominant over Genotype: Clues from the Evolution of Cell-Cell Interactions

Reciprocal and dynamic cell-cell and cell-ECM adhesion communication is essential for multicellular tissue morphogenesis and homeostasis. Consistently, mechanisms intersecting at different length scales have evolved to facilitate this dialogue. These mechanisms act locally at adhesions through competitive associations between conserved signaling complexes and function globally to efficiently transmit information from the cellular to the tissue level by directed cytoskeletal remodeling and cellular and tissue tension. For instance, blastula assembly is followed by blastocoel cavity formation and the assembly of a fibrillar fibronectin matrix, both of which are regulated by the integrin-linked kinase (ILK)/pinch/parvin complex (*17*). Consistently, blastocoel formation fails in ILK-null embryos (*18*), and inhibition of fibronectin-integrin interactions inhibits the epithelial-mesenchymal transition that is critical for gastrulation (*19*). Although the processes occur at dramatically different length scales, both require specific gene expression (e.g., Rho GTPase) and activation to drive tension-dependent processes—for example, cell-cell adhesion maturation and focal adhesion assembly—and act by initiating actin remodeling (*3*).

Cell-cell and cell-ECM modules share many conserved features; however, they have also evolved fundamental differences that optimize environmental responses and permit fine-tuning of the multicellular organism throughout its life span. Whereas adherens junctions are tightly regulated by receptor number and density to maximize structural variability, integrins evolved to transduce environmental cues, thereby maximizing survival advantage and adaptability for the organism (Fig. 1). Indeed, homotypic adhesion systems appeared in primitive organisms such as the *Dictyostelium* fruiting body to maintain its integrity through aggregation. *Dictyostelium* use at least two independent homotypic adhesion systems that are related to metazoan adhesion molecules (*20*): the Cadherin super family member DdCAD-1 and the immunoglobulin-like domain protein gp80. These connector modules have weak interactions that allow dynamic rearrangement to cluster, sort, stream migrate, and maintain the rigidity of the organism. A fundamental feature of these early adhesion molecules is their enrichment at filipodial extensions, which, together with actin, form transient spot adhesions required for their initial clustering. These molecules are then rapidly replaced with adhesion plaque proteins such as the glycosylphosphatidylinositol-anchored protein gp80, which establishes more stable cell contacts that act as storage modules through associations with lipid-rich membrane micro domains. Although similar principles operate in higher organisms to facilitate multicellular integrity, the nature of the adhesions has become more complex so that spot-like junctions have been extended into beltlike structures such as those found in adherens and in occluding, tight, and septate junctions in higher organisms (*21*). A common framework for these diverse junctional complexes is that they all are organized into large complexes made up of highly clustered modules that, through adaptor proteins, i.e., "switch" modules, initiate signaling cascades,

and act as connector modules to strengthen the cytoskeletal link in response to increasing tension. Whether adhesion or signaling function came first for this class of cell adhesion complexes is still a matter of contention, but it is now clear that similar downstream signaling components are used by both cadherins and junctional complexes. Yet, while the modular nature of these switches is undisputed, the molecular and physical factors that regulate their function remain unknown.

Phenotype Is Dominant over Genotype: Clues from the Evolution of Cell-Matrix Interactions

Modern heterodimeric integrins developed to link the onset of multicellular structures with the appearance of a stable form in metazoans such as *Dictyostelium discoideum,* where they developed as specialized sensory modules to regulate adhesion, survival, and phagocytosis (*22*, *23*). These primitive integrin-like proteins called "sib receptors" contain several conserved motifs identical to β integrins, in addition to having tandem NPXY repeat motifs in the cytoplasmic tail (*22*), suggesting that sib is a cation-dependent, low-affinity receptor for exposed acidic residues in extracellular proteins. Sib also appears to act as a mechanical connector to the actin cytoskeleton through the recruitment of FERM domain–containing proteins such as talin (*22*). In addition to a mechanical role, sib's recruitment into the phagocytic cup, as with integrin clustering in the membrane for metazoans, likely serves as an important signaling transistor for prey recognition and feeding stimulation (*13*). Thus, integrins evolved to permit organisms to respond rapidly to biochemical and physical cues from their microenvironment with specialized features that include adhesion to substrate, active mobility, and detection and capture of prey by phagocytosis (Fig. 2) (*24*–*39*).

Organism	Feeding	Mobility	Adhesion & scaffold
Bacteria	Passive (food absorption & assimilation	Swimming Chemotaxis	Polysaccharide-based biofilm formation (*24*)
Fungi	Passive	Pseudohyphal growth	GPI-anchored (*25*) cell-cell & cell-substrate receptors (*26*)
Amoebozoa	Active "hunting" β-integrin-like (sib)-dependent phagocytosis	Migration (β-integrin-like (sib)-dependent)	Cellulose-based, cysrich & laminin-like ECM (*27*) β-integrin-like & paxillin-dependent (*28, 29*)
Choanoflagellates *M. brevicollis*	Passive	Swimming (no adhesion)	Collagens, laminins but no β-integrin (*30*)
Porifera	Filtration	Sessile (secretion of ECM-like scaffold)	Collagens (*31*) α & β-integrins (*32, 33*)
Placozoans *T. adhaerens*	Active (extra-organismal gastric cavity)	Migration on surfaces	Collagens, laminins, fibrin, no visible ECM scaffold α & β-integrins (*34*)
Cnidariens	Active "hunting" (gastric cavity)	Sessile (polyp) Swimming (medusae)	Collagens, laminins, ECM scaffold (*35*) α & β-integrins (*36*)
Nematodes Echinoderms Arthropodes Chordates Vertebrates (gastrulation)	Active "hunting" (gastric cavity)	Specific organelles for mobility	Collagens, laminins, α & β-integrins (*37, 38*) fibronectin, tenascins (from chordates on) (*39*)

Fig. 2. Functional evolution of adhesion-dependent form and function, from bacteria to vertebrates. Although the mechanisms for replication are directly linked to the multiplication and management of the genetic information, the capacity to form complex multilayer organisms is likely based on the evolutionary advantage to adhere to new environments and survive in potentially hostile environments. Although bacteria and fungi use rather simple strategies to create multicellular structures, the evolution of "hunters," such as amoeba, introduced new dynamic and controllable cell-cell and cell-substrate adhesion systems, such as integrins, allowing the capture of prey and formation of complex multicellular structures. In parallel, the evolution from polysaccharide- or cellulose-based to protein-based extracellular scaffold increased the versatility of cell-to-substrate adhesion systems. Interestingly, the emergence of integrin α/β-heterodimers correlates with the appearance of metazoans (dashed line), indicating that the intracellular perception of the extracellular scaffold is critical to the stable generation of form and function. Details can be found in (*24*–*39*).

A second distinguishing feature of integrin-matrix adhesion modules is their ability to function as molecular switches through adaptor molecules that are activated to initiate a cascade of downstream events that amplify the original signal. When compared with adenosine triphosphate–driven signaling enzymes, such as kinases that are typical of this type of switch module, the function of adapter proteins in cell adhesions may, at least at first glance, seem neither similar nor switchlike. However, many adapter proteins bind to both a cytoskeletal protein and an integrin-based adhesion protein to form a complex, where stability of the adapter protein is greatly increased by the initial binding reaction and subsequent change in conformation, for example, vinculin (*40*). Structural changes, such as those brought on by forces imposed on the adapter protein (*41*), could liberate additional protein-protein interaction sites in a cooperative manner, and the immediate influx of new binding opportunities for signaling molecules could switch on previously dormant cell behaviors and alter properties like cell shape. Another efficient way to create a switch module for adhesion is to limit protein-protein interactions by immobilizing individual binding partners to a surface. Adsorption-limited diffusion of the binding partners restricts the conformational changes that would inactivate the connector module in examples that range from the rapid rise of phosphatidylinositol biphosphate in the plasma membrane that stabilizes the integrin/talin complex (*42*) to the regulation of cell motility by ECM sheets like basement membrane (*43*). For protein interactions, receptor-like protein tyrosine phosphatase–α binding to α_v integrin acts as a switch to form the nucleation site for a focal adhesion. One characteristic aspect of this switch is its response to the external application of force, resulting in new protein-protein binding sites, such as with the Src family kinase Fyn (*44*). In fact, integrin receptors themselves react in response to force by increasing their binding affinities to ligands through conformational changes (*45*), resulting in the formation of a catch bond that holds under force and gets released in the absence of force (*46*). An analogy to an old fashioned "finger trap" is perhaps insightful: force-dependent integrin extension acts to increase affinity, much like the pulling force by fingers stuck in the trap further tightens the trap on the fingers. Given their shape and functional differences with lower organisms as well as cell-cell proteins, this is perhaps suggestive of the evolutionary force behind integrin-driven tissue morphogenesis, which relies heavily on its binding partner, the ECM, to aid in the drive to undergo morphogenesis.

These integrin features enable the organism to discriminate noise from critical external cues as well as ensure a quick response to these stimuli, both necessary elements required for multicellular organisms to maintain their survival advantage in a rapidly changing environment.

Accordingly, cells use both cadherins and integrins to assemble into multicellular tissues, to distinguish and rapidly respond to external cues, and to amplify the signal to launch an appropriate and coordinated response. Tissues achieve this task by a series of evolutionarily conserved modules that are initiated through the adhesion sensor, transduced through a series of molecular switches, and propagated through amplifiers (*21*, *47*, *48*) (Fig. 3).

Signaling in Context: Emergent Properties of Complex Systems

Multicellular organisms require stable adhesion between neighboring cells and coordination of cell behaviors through cell-cell signaling to develop shape and compartmentalize function into tissues. The first coordinated event to occur in metazoa is gastrulation, which imparts a body pattern. Given the level of reorganization required to establish the resulting form (*49*), it is evolutionarily advantageous to ensure tighter regulation and spatial arrangement of proliferative ectodermal cells covering the embryo versus motile, involuting cells during gastrulation. The impetus to rearrange and expand the multiple layers of tissue, however, may be due to the microtubule organizing center having competing roles in motility and cell division (*50*). As a result, metazoans employ additional cell-cell adhesion-based mechanisms to control the identity and spatial distribution of differentiated cells, including cell polarity, tension, and morphogen gradients, rather than relying on proliferation alone. Cell polarity refers to the asymmetric distribution of cell constituents and organelles, and, if coordinated through cell-cell connectors, cell orientation can effect tissue-wide polarity, known as planar cell polarity (PCP), using a highly conserved set of polarity protein complexes (*51*). This behavior is likely to have arisen from unicellular organisms that would distribute unequally damaged cell components to bypass senescence (*52*). The advent of stable connector modules such as adherens or tight junctions further contributed to the development of apical-basal membrane segregation, permitting the establishment of cell sheets as well as outside and inside separation of an organism. Orientated cell division and polarized cell shape changes, such as those seen in the convergence and extension phase of gastrulation, can also be used to rotate the body axis out of the plane of a tissue, to contribute to the differential spatial orientation of cells, and to establish anisotropic mechanical properties (*49*). The latter of these characteristics can establish differences in ECM properties by secretion or cross-linking, setting up spatially controlled matrix topography and elasticity, both of which are known regulators of differentiation (*53*, *54*). Interplay among polarity, ECM, and adhesions has also been shown in mammary acini, where increased matrix elasticity altered tensional homeostasis, perturbed tissue polarity, and promoted a malignant phenotype (*55*). Polarity, however, should be thought of not just in terms of how it modulates matrix and restricts secretion but also how it changes the context of signaling; for example, loss of Scribble in mammary epithelia can block morphogenesis and induce dysplasia by disrupting cell polarity and inhibiting apoptosis (*56*). Cells organized into polarized tissue structures respond very differently to external signaling cues than do cell sheets or isolated cells (*57*). In fact, by forcing a polarized tissue structure on both normal and teratocarcinoma cells, the signaling milieu that the cells inhabit can give rise to animals that retain tumor cells but exhibit no detectable tumor phenotype (*58*). These observations argue that additional emergent properties arise in polarized tissue structures that regulate cell and tissue behavior.

In addition to polarity, positional information within the organism and tissue also need to be programmed after initial cell segregation. Body plan axis and length, for example, are regulated by morphogen gradients, where local signal concentrations define the coordinates for each cell, based on source distance (*59*). Progenitor cell phenotype can be regulated by these gradients, where cells from one location transplanted to another will express the phenotype of the new niche (*4*). In fact, nodal gradients in the developing embryo even modulate the development of tension in the blastula (*6*). Mechanoregulation of homeostasis by morphogen gradients likely continues through gastrulation, the formation of organs, and internal assembly, because evidence shows that they can direct cells to stop proliferating to maintain size (*60*), as well as cease migration (*11*) once cells are appropriately segregated.

Morphogen gradients are not always present in nonstereotyped organs such as the heart or mammary acini, where homeostasis is maintained by a balance between matrix compliance and cell tension in a manner that may parallel proposed intracellular tension balances, such as with the concept of tensegrity (*61*). This argues for a set of newly emerging properties that can shape tissue and organ level form and function. Recent evidence implicates tension as such a regulator, not only to shape cell form as previously shown but also to control tissue formation (*62*). As mammary acini secrete milk proteins, this generates outward pressure on the cells, tensing their adhesive modules and forcing them into a spherical structure, which maximizes their surface area to volume ratio so that they hold as much fluid as possible while at the same time minimizing the energetics of the system to promote stability. When tension is misregulated at this length scale, as with constitutively active Rho, it can shift the acinar force balance to compromise morphogenesis and integrity and induce a cancer-like phenotype. As a

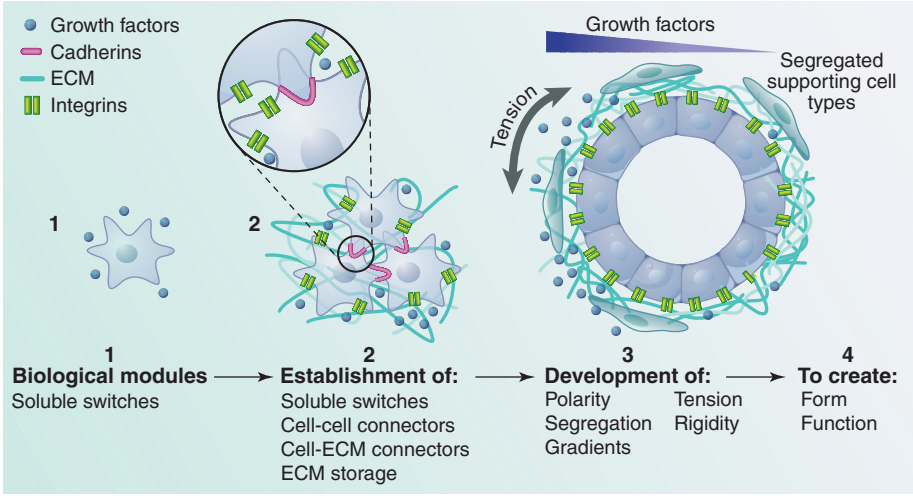

Fig. 3. Tensional homeostasis and emergent properties of multicellular systems. At a single-cell level, filopodial projections probe the cellular environment while cells secrete and ingest growth factors that act as switches to turn on behaviors. With the onset of multicellular aggregates, adhesive "connectors," for example, cadherins, form and link the lamellopodia to a lattice of individual actin filaments within the cell, permitting adhesion to and migration on surfaces or dense fibrillar network. Whereas these structures can contribute to cell sheets such as an epithelial cell layer adhered to a basement membrane, the development of segregated adhesion structures establishes cell polarity, morphogen gradients signal to cells to regulate cell coordinates within the body plan, and actomyosin-based contractions allow cells to integrate within a 3D environment in a particular structure. Within this framework, the continuous contraction against a compliant ECM maintains tensional homeostasis to create form and function through the incorporation of all of these conserved modules.

disease parallel to this, breast cancer is characterized by increased matrix stiffness and cell contractility, altered rheology, and changes in cell shape and tissue architecture (*55*). In addition to these force-induced changes in cell and tissue behavior, matrix stiffness and elevated cell tension stimulate excessive fibronectin production that compromises tissue integrity and perturbs tissue polarity (*63*), illustrating how cell and matrix tension operate at multiple length scales to influence malignancy. Conversely, normal acinar morphology can be a powerful tumor suppressor, preventing expression of the malignant phenotype even in cells with a multitude of genomic alterations, including amplifications in key oncogenes (*64*). Heart looping also appears to be force sensitive, such that a threefold gradient in matrix deposition corresponds to a similar gradient in stiffness for the inner versus outer curvature of the heart tube. As hemodynamic forces differentially press against the softer basal wall, it induces cell shape changes that create the looped form of the embryonic heart (*65*). Altered differences in matrix gradients could easily upset how cells at the outer curve extend by changing the cell tension that cells along the curve can generate (*7*). The underpinnings of tension-driven regulation may rest in clarifying why changing membrane tension or curvature induced by matrix or shape perturbations can exert such a profound effect on the lineage specification of stem cells (*14*, *54*). Although tissue development and homeostasis clearly require reciprocal cross-talk between the cell and its extracellular matrix mediated through dynamic adhesion interactions (*64*), scaling up these cell-ECM changes to tissue level behaviors, much like has been done with morphogen gradients and polarity, will greatly advance our understanding of these modules and their economies of scale.

Unresolved Issues?

Although emergent properties of multicellular tissues and signaling modules clearly regulate processes such as gastrulation and acini formation, it is not clear how these morphogenetic events shape an organ, tissue, or cell at large distances where diffusion of morphogens may be limited, direct cell-cell contacts are out of range, and the matrix is discontinuous. Do processes that sculpt multicellular tissues and maintain homeostasis at short length scales and acute time frames operate similarly in the organism at larger length scales in complex tissues or organ systems with multiple cell types and variable chronologies? For some of the open developmental questions posed above, modular analogies (Fig. 1) perhaps improve our ability to describe the toolbox of tissue homeostasis and clarify the circuitry rules required to use them, i.e., combining connectors in series. However, much of our circuitry diagram is missing, and key integrators that operate at multilength scales and that retain the molecular memory necessary for the long-term viability and adaptability demanded of complex organisms have yet to be identified. The solution to understanding how this enormous task is achieved likely rests on discovering new modules and alternate signaling paradigms. Nevertheless, it is clear that without including a comprehensive description of all the environmental players and clarifying their interrelations—for example, matrix, cadherins, and integrins—an explanation of the origin of form and function will remain incomplete.

References and Notes

1. G. M. Edelman, *Topobiology: An Introduction to Molecular Embryology* (Basic Books, New York 1988).
2. P. Townes, J. Holtfreter, *J. Exp. Zool.* **128**, 53 (1955).
3. E. Brouzes, E. Farge, *Curr. Opin. Genet. Dev.* **14**, 367 (2004).
4. F. V. Mariani, G. R. Martin, *Nature* **423**, 319 (2003).
5. N. Desprat, W. Supatto, P. A. Pouille, E. Beaurepaire, E. Farge, *Dev. Cell* **15**, 470 (2008).
6. M. Krieg *et al.*, *Nat. Cell Biol.* **10**, 429 (2008).
7. C. M. Nelson *et al.*, *Proc. Natl. Acad. Sci. U.S.A.* **102**, 11594 (2005).
8. J. de Rooij, A. Kerstens, G. Danuser, M. A. Schwartz, C. M. Waterman-Storer, *J. Cell Biol.* **171**, 153 (2005).
9. K. M. Heinemeier *et al.*, *J. Physiol.* **582**, 1303 (2007).
10. C. P. Johnson, I. Fujimoto, C. Perrin-Tricaud, U. Rutishauser, D. Leckband, *Proc. Natl. Acad. Sci. U.S.A.* **101**, 6963 (2004).
11. B. M. Gumbiner, *Cell* **84**, 345 (1996).
12. T. Rozario, B. Dzamba, G. F. Weber, L. A. Davidson, D. W. Desimone, *Dev. Biol.* **327**, 386 (2008).
13. S. Miyamoto, S. K. Akiyama, K. M. Yamada, *Science* **267**, 883 (1995).
14. R. McBeath, D. M. Pirone, C. M. Nelson, K. Bhadriraju, C. S. Chen, *Dev. Cell* **6**, 483 (2004).
15. L. E. Stephens *et al.*, *Genes Dev.* **9**, 1883 (1995).
16. S. Li *et al.*, *J. Cell Biol.* **157**, 1279 (2002).
17. S. Li *et al.*, *J. Cell Sci.* **118**, 2913 (2005).
18. T. Sakai *et al.*, *Genes Dev.* **17**, 926 (2003).
19. T. Darribere, J. E. Schwarzbauer, *Mech. Dev.* **92**, 239 (2000).
20. C. H. Siu, T. J. Harris, J. Wang, E. Wong, *Semin. Cell Dev. Biol.* **15**, 633 (2004).
21. C. R. Magie, M. Q. Martindale, *Biol. Bull.* **214**, 218 (2008).
22. S. Cornillon *et al.*, *EMBO Rep.* **7**, 617 (2006).
23. A. L. Hughes, *J. Mol. Evol.* **52**, 63 (2001).
24. C. Ryder, M. Byrd, D. J. Wozniak, *Curr. Opin. Microbiol.* **10**, 644 (2007).
25. F. Li, S. P. Palecek, *Microbiology* **154**, 1193 (2008).
26. A. Halme, S. Bumgarner, C. Styles, G. R. Fink, *Cell* **116**, 405 (2004).
27. L. Eichinger *et al.*, *Nature* **435**, 43 (2005).
28. S. Cornillon, R. Froquet, P. Cosson, *Eukaryot. Cell* **7**, 1600 (2008).
29. T. Bukahrova *et al.*, *J. Cell Sci.* **118**, 4295 (2005).
30. N. King *et al.*, *Nature* **451**, 783 (2008).
31. J. Y. Exposito *et al.*, *J. Biol. Chem.* **283**, 28226 (2008).
32. Z. Pancer, M. Kruse, I. Muller, W. E. Muller, *Mol. Biol. Evol.* **14**, 391 (1997).
33. D. L. Brower, S. M. Brower, D. C. Hayward, E. E. Ball, *Proc. Natl. Acad. Sci. U.S.A.* **94**, 9182 (1997).
34. M. Srivastava *et al.*, *Nature* **454**, 955 (2008).
35. J. Heino, M. Huhtala, J. Kapyla, M. S. Johnson, *Int. J. Biochem. Cell Biol.* **41**, 341 (2009).
36. B. A. Knack *et al.*, *BMC Evol. Biol.* **8**, 136 (2008).
37. N. H. Brown, *Matrix Biol.* **19**, 191 (2000).
38. C. A. Whittaker *et al.*, *Dev. Biol.* **300**, 252 (2006).
39. R. P. Tucker, R. Chiquet-Ehrismann, *Int. J. Biochem. Cell Biol.* **41**, 424 (2009).
40. H. Chen, D. M. Cohen, D. M. Choudhury, N. Kioka, S. W. Craig, *J. Cell Biol.* **169**, 459 (2005).
41. C. P. Johnson, H. Y. Tang, C. Carag, D. W. Speicher, D. E. Discher, *Science* **317**, 663 (2007).
42. C. Cluzel *et al.*, *J. Cell Biol.* **171**, 383 (2005).
43. M. Paulsson, *Crit. Rev. Biochem. Mol. Biol.* **27**, 93 (1992).
44. G. von Wichert *et al.*, *J. Cell Biol.* **161**, 143 (2003).
45. J. Zhu *et al.*, *Mol. Cell* **32**, 849 (2008).
46. J. C. Friedland, M. H. Lee, D. Boettiger, *Science* **323**, 642 (2009).
47. V. M. Bowers-Morrow, S. O. Ali, K. L. Williams, *Biol. Rev. Camb. Philos. Soc.* **79**, 611 (2004).
48. N. King, C. T. Hittinger, S. B. Carroll, *Science* **301**, 361 (2003).
49. R. Keller, L. A. Davidson, D. R. Shook, *Differentiation* **71**, 171 (2003).
50. N. King, *Dev. Cell* **7**, 313 (2004).
51. P. A. Lawrence, G. Struhl, J. Casal, *Nat. Rev. Genet.* **8**, 555 (2007).
52. I. G. Macara, S. Mili, *Cell* **135**, 801 (2008).
53. M. J. Dalby *et al.*, *Nat. Mater.* **6**, 997 (2007).
54. A. J. Engler, S. Sen, H. L. Sweeney, D. E. Discher, *Cell* **126**, 677 (2006).
55. M. J. Paszek *et al.*, *Cancer Cell* **8**, 241 (2005).
56. L. Zhan *et al.*, *Cell* **135**, 865 (2008).
57. V. M. Weaver *et al.*, *Cancer Cell* **2**, 205 (2002).
58. B. Mintz, K. Illmensee, *Proc. Natl. Acad. Sci. U.S.A.* **72**, 3585 (1975).
59. J. Jaeger *et al.*, *Nature* **430**, 368 (2004).
60. D. Rogulja, C. Rauskolb, K. D. Irvine, *Dev. Cell* **15**, 309 (2008).
61. D. E. Ingber, *Sci. Am.* **278**, 48 (1998).
62. C. M. Nelson, M. J. Bissell, *Annu. Rev. Cell Dev. Biol.* **22**, 287 (2006).
63. C. M. Williams, A. J. Engler, R. D. Slone, L. L. Galante, J. E. Schwarzbauer, *Cancer Res.* **68**, 3185 (2008).
64. V. M. Weaver *et al.*, *J. Cell Biol.* **137**, 231 (1997).
65. E. A. Zamir, V. Srinivasan, R. Perucchio, L. A. Taber, *Ann. Biomed. Eng.* **31**, 1327 (2003).
66. S. Y. Shvartsman, C. B. Muratov, D. A. Lauffenburger, *Development* **129**, 2577 (2002).
67. H. Strutt, D. Strutt, *Curr. Biol.* **13**, 1451 (2003).
68. K. Amonlirdviman *et al.*, *Science* **307**, 423 (2005).
69. U. Weber, C. Pataki, J. Mihaly, M. Mlodzik, *Dev. Biol.* **316**, 110 (2008).
70. A. del Rio *et al.*, *Science* **323**, 638 (2009).
71. B. Geiger, J. P. Spatz, A. D. Bershadsky, *Nat. Rev. Mol. Cell Biol.* **10**, 21 (2009).
72. M. J. Grimson *et al.*, *Nature* **408**, 727 (2000).
73. R. A. Foty, M. S. Steinberg, *Dev. Biol.* **278**, 255 (2005).
74. C. Bertet, L. Sulak, T. Lecuit, *Nature* **429**, 667 (2004).
75. C. E. Chan, D. J. Odde, *Science* **322**, 1687 (2008).
76. M. L. Gardel *et al.*, *J. Cell Biol.* **183**, 999 (2008).
77. T. Baumgart, S. T. Hess, W. W. Webb, *Nature* **425**, 821 (2003).
78. A. R. Small *et al.*, *J. Theor. Biol.* **252**, 593 (2008).
79. X. Wang, R. E. Harris, L. J. Bayston, H. L. Ashe, *Nature* **455**, 72 (2008).

80. We apologize to the many authors whose work is not cited due to space limitations. This work was supported by grants NIH R01-CA078731, Department of Defense Era of Hope Breast Cancer Research Grant W81XWH-05-1-330, Department of Energy A107165, and California Institute for Regenerative Medicine RS1-00449 to V.M.W.; American Heart Association 0865150F to A.J.E.; the Australian NHMRC, CCV, Prostate Cancer Foundation of Australia; the AICR UK and NHMRC Career Development Award to P.O.H.; and the Swiss National Science Foundation and Nevus Outreach to B.W.-H.

10.1126/science.1170107

PERSPECTIVE

Trapping Moving Targets with Small Molecules

Gregory M. Lee and Charles S. Craik*

Structure-based drug design traditionally uses static protein models as inspirations for focusing on "active" site targets. Allosteric regulation of biological macromolecules, however, is affected by both conformational and dynamic properties of the protein or protein complex and can potentially lead to more avenues for therapeutic development. We discuss the advantages of searching for molecules that conformationally trap a macromolecule in its inactive state. Although multiple methodologies exist to probe protein dynamics and ligand binding, our current discussion highlights the use of nuclear magnetic resonance spectroscopy in the drug discovery and design process.

Normal biological processes generally rely on a finely tuned network of dynamic macromolecular interactions that allow signals to transfer throughout the cell. Misregulation of these signaling complexes often ends in disease states. For example, misregulated protein-protein interactions lead to unchecked cellular signaling in multiple forms of cancer. In fact, many proteins that are intrinsically unstructured or have domains that fold into regular structural motifs upon binding to their partner proteins can be linked to human diseases (*1*, *2*).

To control the activity of these complexes in a disease state, efforts generally focus on small-molecule ligands that competitively bind to a particular catalytic or active site, using a static model of the complex as a starting point. This method has identified and validated a multitude of viable active-site therapeutics in use today. However, as reflected by the high failure rate of new drug compounds (only an estimated 8% of phase I clinical therapeutics eventually gain Food and Drug Administration approval, at a conservative cost of $800 million per drug), many efforts are unsuccessful and often targets are abandoned once they are deemed undruggable (*3*). Focusing on active-site inhibitors limits the number of potential sites that can be targeted by therapeutics. Expanding the search for inhibitors that bind beyond the active site, or even at protein complex interfaces, offers "more shots on goal" for a particular target. These allosteric effectors can initiate a cascade of changes that alter macromolecular activity (*4*–*6*).

The energetics of macromolecular complexes involve enthalpic and entropic properties that govern activity by influencing the conformational rigidity and flexibility of macromolecules within the complex. The main theories linking allosteric regulation to alterations in protein conformation and dynamics, and ultimately protein function, usually focus on the protein folding or ligand binding free-energy landscape (*7*). The Monod-Wyman-Changeux (MWC) symmetrical model of allostery states that an unbound, or "apo," target protein exists in an equilibrium that thermodynamically favors one of two distinct conformational states and that ligand binding initiates an interconversion between these two states in a concerted manner (*8*). Conversely, the Koshland-Nemethy-Filmer (KNF) induced-fit model of allostery suggests that conformational changes within the target protein propagate sequentially through the system after ligand binding (*9*). In other words, the unbound target protein is a static structure, and protein dynamics are induced.

More current theories extend the MWC two-state model and posit that in their apo form, proteins sample multiple preexisting conformations, the majority of which are minor populations (*10*, *11*). A dynamic free-energy landscape with shallow energy wells and transition barriers would allow the target protein to sample the conformation appropriate for efficient ligand-binding interactions (Fig. 1). Upon ligand binding to a minor populated state, the dynamic free-energy landscape would alter and shift the equilibrium to favor that bound conformational state (*7*, *11*). The concept of allostery can be extended to include such conformational trapping, which might shift the equilibrium away from the active state. In some cases, allosteric effects may involve perturbations in protein dynamics only in the absence of a conformational change, suggesting that ligand binding can be solely due to alterations in entropic factors (*12*).

Allosteric sites might also display more selectivity than active sites. More important, in contrast to competitive inhibitors, which generally focus on a single conformational binding state, different allosteric inhibitors could target multiple conformational states. This in turn provides more opportunities to inhibit the same macromolecular target. By targeting multiple sites on a particular macromolecule, rather than focusing on a single active site, allosteric therapeutics would encounter less drug resistance due to mutations within the receptor. Resistance to allosteric inhibitors can also eventually occur, but combination therapy against the same target helps alleviate this situation. An example of this type of combination therapy is found in the highly active antiretroviral treatment drug cocktail for AIDS (*13*).

Several allosterically active drugs are either on the market or in late clinical testing stages. One example is imatinib (Gleevec), discussed below. Other examples include non-nucleoside inhibitors that target HIV reverse transcriptase (*14*) and herpesvirus C polymerase (*15*). These inhibitor classes act by restricting conformational mobility in regions of the enzymes required for catalytic activity. Though preclinical, allosteric inhibitors of caspases (dimeric complexes implicated in inflammation and apoptosis) were shown to trap the enzyme in an inactive zymogen conformational state (*16*). X-ray crystallography, nuclear magnetic resonance (NMR), and computational studies of HIV protease have shown "closed" and "open" flap conformations, which help regulate substrate access to the catalytic site (*17*). Inhibitors that restrict the motion of these dynamic flaps have potential for regulating the enzymatic activity of a well-validated target at a nonactive site.

Small-molecule inhibitors may also regulate protein-protein interactions by restricting conformational mobility. Because of the larger and flatter surfaces associated with protein-protein interaction sites, discovering small-molecule compounds that disrupt protein complexes is more difficult than discovering those that bind to a monomeric target with well-defined binding pockets (*18*). Most protein-protein interactions exhibit nanomolar to millimolar binding affinities, and finding the "high-hanging fruit" that capture dynamic macromolecules in their inactive state remains a pathway of high potential (*18*, *19*). Herpesvirus proteases represent a homodimeric enzyme family, members of which are attractive targets for controlling several human viral pathogens with small-molecule compounds (*20*). Each monomer contains two flexible helices at the dimer interface undergoing a conformational disorder-to-order transition that is critical for regulating enzymatic activity (*21*). Small molecules that capture an inactive conformation of the monomer and disrupt dimerization may provide new opportunities to make this previously intractable target druggable.

Although there are several methods to discover inhibitors that target dynamic proteins, NMR is particularly suited to sampling multiple time frames in order to characterize protein motion and is a powerful technique for detecting conformational changes in proteins and protein complexes on a per-residue basis [see supporting online material (SOM)] (*22*). Traditionally, NMR studies were

Department of Pharmaceutical Chemistry, University of California, San Francisco (UCSF), 600 16th Street, Box 2280, San Francisco, CA 94158–2280, USA.

*To whom correspondence should be addressed. E-mail: craik@cgl.ucsf.edu

relegated to studying proteins smaller than 20 to 30 kD. However, recent advances in NMR methodologies can now probe conformational and dynamic properties of protein complexes approaching 1 MD (*23*). Collectively, NMR data can derive information reflecting the ligand-binding energetics of a particular complex. For example, differences in protein conformation upon the addition of a small druglike molecule reflect enthalpic changes, whereas differences in dynamic properties indicate entropic changes (*24*).

Conformational changes in proteins labeled with ^{15}N and/or ^{13}C stable isotopes can be detected by two-dimensional heteronuclear single-quantum coherence (HSQC) spectroscopy, with extensions that allow applications to larger proteins (*23*). Upon ligand binding, cross peaks representing residues in or near binding sites will be perturbed, either by shifting locations or broadening out. These data are mapped onto a protein structure, providing a "fingerprint" and allowing easy differentiation between competitive and allosteric-site binders (Fig. 1). By the same principle, protein dynamics in the absence and presence of small-molecule ligands can be compared. This experiment is the basis for the well-established and widely used structure-activity relationship (SAR)–by–NMR technique (*25*), which combines NMR and fragment-based approaches for drug design and development. NMR can be used to quantitatively measure the binding affinities of ligands with submicromolar to millimolar dissociation constant values. An extension of the SAR-by-NMR technique that holds potential for semi–high-throughput ligand screening involves the simultaneous acquisition of multiple target protein spectra by differential labeling. NMR spectral editing techniques deconvolute the spectra to separate the data of the individual proteins, allowing determination of which, if any, targets interact with the ligand (*26*, *27*).

A combination of NMR spectroscopy and x-ray crystallography showed how imatinib (Gleevec) allosterically inhibits the ABL tyrosine kinase associated with chronic myelogenous leukemia. Second-generation ABL inhibitors currently on the market include dasatinib (Sprycel) and nilotinib (Tasigna). Proliferation assays involving Bcr-ABL–expressing cells indicated imatinib median inhibitory concentration (IC_{50}) values of 260 nM, with higher potencies reported for nilotinib (13 nM) and dasatinib (0.8 nM) (*28*). Enzyme activity is regulated by a structural motif that places the catalytic residues in an orientation required for efficient substrate phosphorylation. This motif contains an α helix and two loops: the phosphate-binding (P) and activation (A) loops, with the A loop adopting two major conformers corresponding to the active and inactive states (*29*).

Although classified as competitive adenosine triphosphate inhibitors, x-ray crystallography studies of ABL-imatinib and ABL-nilotinib complexes indicate that ligand binding induces an allosteric reorientation of the A loop to its inactive state. Conversely, and counter to activity studies, complexes of ABL-dasatinib and two investigational compounds display the active conformation in their crystal structures (*29*). Recent NMR data confirm the x-ray crystallography data and suggest that the A loop of the protein is still conformationally dynamic. Corresponding residues within all the ABL-inhibitor complexes display peak broadening and indicate that dasatinib imparts enhanced backbone dynamics relative to imatinib/nilotinib and that it is able to sample both the active and inactive ABL loop conformations (*29*). This suggests that the major effect on enzyme

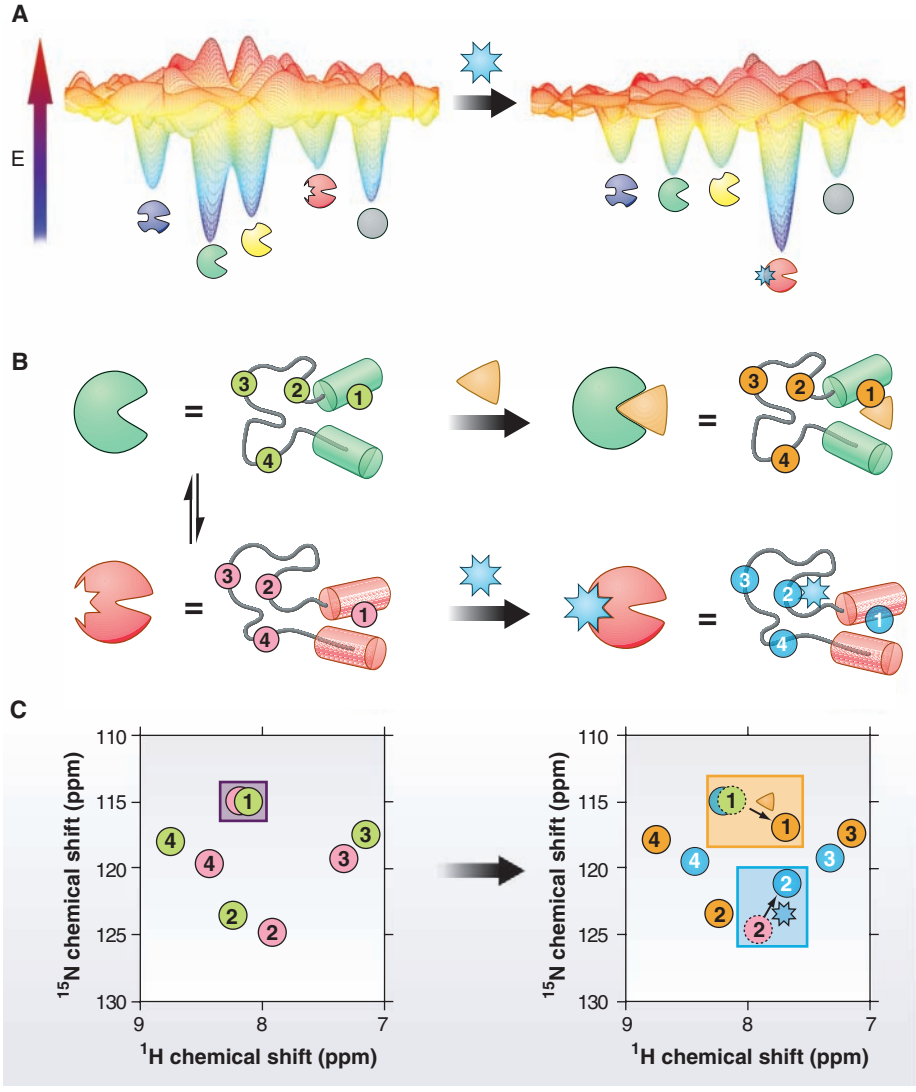

Fig. 1. (**A**) Shallow wells and transitional barriers of a dynamic free-energy landscape allow a macromolecule to sample multiple preexisting conformational states, corresponding to the catalytically active (green) and inactive (blue, red, yellow, and gray) forms. The global energy minimum shifts to favor the inactive conformation (red) when an inhibitor (cyan star) binds to an allosteric site. (**B**) The active (green) and inactive (red) conformations schematically represent a small enzyme, consisting of a flexible loop connecting two helices. Both conformations are in equilibrium while the enzyme is in the apo state. A native substrate (orange triangle) binds to the active site located between the two helices. Alternatively, a small molecule (cyan star) binds to a region within the flexible loop of the inactive conformer, allosterically inhibiting the enzyme. (**C**) Overlaid theoretical ^{15}N-HSQC spectra display peaks corresponding to backbone amides of residues in selected regions of the enzyme, numbered 1 to 4. Green and pink peaks represent the apo active and inactive conformers (left); orange and cyan peaks represent the bound active and inactive conformers (right), respectively. As depicted, peak 1 of the active and inactive conformations is located in the same helix of both conformations and is superimposible (purple box), whereas peaks 2 to 4 correspond to regions within the flexible loop region. Upon native substrate binding at the active site, only peak 1 of the active conformation shifts to a new location (orange box). Similarly, only peak 2 of the inactive conformation (cyan box) is perturbed when a small-molecule inhibitor binds at an allosteric site.

activity is conformationally based. Future drug discovery efforts can benefit from the HSQC fingerprints of the active and inactive loop conformations, by identifying promising new leads that impart diagnostic spectral signatures.

In addition to quickly mapping ligand-binding–induced conformational changes of a macromolecule, NMR also detects disruptions in protein complexes by taking advantage of the overall dynamics of large oligomeric complexes. A protein that displays sharp resonances in its monomeric state would exhibit extensive peak broadening once it became part of a larger macromolecular complex. If a small molecule disrupts these complexes, the protein would exhibit an HSQC spectrum closely associated with its monomeric state (*30*). A major advantage of this technique is that it does not require protein resonance assignments. Additionally, these assays are able to identify which protein partner binds to the small molecule. If the small molecule strongly associates with one of the protein partners, the final HSQC spectrum also acts as a starting point for further SAR-by-NMR studies.

This dynamic property of protein complexes for detecting small-molecule ligands that disrupt protein-protein interactions was demonstrated with the well-studied p53-MDM2 complex (*31*). Activity of p53 is intimately involved with suppressing tumor growth and proliferation in a number of cancer types; unchecked p53-MDM2 binding results in the misregulation of p53 activity. Binding competition experiments were reported with nutlin-3 (SOM) (*30*), a member of the nutlin family that inhibits p53-MDM2 binding with an IC_{50} value of 90 nM (*32*). This affinity is comparable to that observed for p53-MDM2 binding as determined with the use of peptide analogs and surface plasmon resonance (*33*). The N-terminal domain of p53 displays a dramatic disorder-to-order transition. In the apo state, it is intrinsically unstructured, whereas in complex with MDM2, it folds into an α helix. Meanwhile, the apo form of MDM2 contains a short N-terminal "lid" region, which exists in slow exchange between a conformationally dynamic open (minor) state and a more structured helical closed (major) state closely associated with the p53-binding cleft of MDM2 (*34*). An examination of the backbone dynamics of the lid indicates higher conformational mobility in the p53-MDM2 dimer relative to the apo MDM2 and MDM2–nutlin-3 complex (*34*). Nutlin-3 does not conformationally trap an inactive state of either MDM2 or p53. However, these initial studies lay the groundwork for future drug discovery efforts, which may lead to compounds that trap either protein in an inactive state.

Protein-protein interactions involving cAMP response element–binding protein (CREB) and CREB-binding protein (CBP) also illustrate the use of NMR for screening small-molecule conformational traps in a more highly conformationally dynamic complex. CREB is involved with cellular signaling, and misregulation of its activity is associated with various neurological disorders and cancers, whereas CBP is classified as a coactivator protein. Interactions between the two proteins are governed by the KID domain of CREB and the KIX domain of CBP. The KID domain is unfolded in its apo state but forms two helices when bound to KIX (*35*). Similarly, the KIX domain exhibits lowly populated conformers in its apo state, becoming less dynamic upon binding to KID (*36*).

Previous inhibition studies primarily focused on short peptides that competitively associated with the shallow hydrophobic KID-binding cleft of KIX (*37*). However, NMR screening of 762 preselected small-molecule ligands demonstrated that protein-protein interactions of this complex can be regulated by trapping an inactive conformer (*38*). Mapping the HSQC spectral differences onto the structures indicated that two of these compounds bound to sites in the KIX domain that were distal to the KID-binding pocket. Residues of the KID-binding cleft display smaller perturbations, indicating that these small molecules trap the KIX domain in a conformation which is unable to effectively bind KID (*38*). Though still preclinical, these compounds, which exhibited fluorescence-based inhibition constant values in the micromolar range (*38*), highlight the possibility of making a challenging target amenable to drug intervention.

Along with the realization that biological macromolecules exist in binding free-energy landscapes (*39*) comes a myriad of opportunities for drug discovery. Target receptors that were biologically validated but then deemed undruggable are now more attractive. In some cases, the less tractable targets, such as complexes involving protein-protein interactions, can be reconsidered or, as in the case of human herpesvirus proteases, even resurrected. The greater selectivity of these allosteric inhibitors we refer to as conformational traps could bode well for compounds facing the gauntlet of factors, such as efficacy, pharmacokinetics, and toxicity, that result in the staggering attrition rate of current clinical lead compounds in the drug pipeline. Similarly, issues surrounding any drug lead such as sufficient affinity, ligand efficiency, binding free energy per atom, absorption, and permeability must be addressed. Integration of multiple methodologies such as NMR spectroscopy and computational modeling (*40*) to complement the current approaches of rational drug design is needed. This will substantially increase the chances of effectively hitting a given target to antagonize or agonize its activity.

References and Notes

1. H. J. Dyson, P. E. Wright, *Nat. Rev. Mol. Cell Biol.* **6**, 197 (2005).
2. V. N. Uversky, C. J. Oldfield, A. K. Dunker, *Annu. Rev. Biophys.* **37**, 215 (2008).
3. C. T. Caskey, *Annu. Rev. Med.* **58**, 1 (2007).
4. D. Kern, E. R. Zuiderweg, *Curr. Opin. Struct. Biol.* **13**, 748 (2003).
5. K. Henzler-Wildman, D. Kern, *Nature* **450**, 964 (2007).
6. N. M. Goodey, S. J. Benkovic, *Nat. Chem. Biol.* **4**, 474 (2008).
7. C. J. Tsai, B. Ma, R. Nussinov, *Proc. Natl. Acad. Sci. U.S.A.* **96**, 9970 (1999).
8. J. Monod, J. Wyman, J. P. Changeux, *J. Mol. Biol.* **12**, 88 (1965).
9. D. E. Koshland, G. Nemethy, D. Filmer, *Biochemistry* **5**, 365 (1966).
10. G. Weber, *Biochemistry* **11**, 864 (1972).
11. C. J. Tsai, S. Kumar, B. Ma, R. Nussinov, *Protein Sci.* **8**, 1181 (1999).
12. C. J. Tsai, A. del Sol, R. Nussinov, *J. Mol. Biol.* **378**, 1 (2008).
13. J. L. Martinez-Cajas, M. A. Wainberg, *Drugs* **68**, 43 (2008).
14. S. Martins, M. J. Ramos, P. A. Fernandes, *Curr. Med. Chem.* **15**, 1083 (2008).
15. R. De Francesco, A. Carfi, *Adv. Drug Deliv. Rev.* **59**, 1242 (2007).
16. J. M. Scheer, M. J. Romanowski, J. A. Wells, *Proc. Natl. Acad. Sci. U.S.A.* **103**, 7595 (2006).
17. V. Hornak, C. Simmerling, *Drug Discov. Today* **12**, 132 (2007).
18. J. A. Wells, C. L. McClendon, *Nature* **450**, 1001 (2007).
19. M. R. Arkin, J. A. Wells, *Nat. Rev. Drug Discov.* **3**, 301 (2004).
20. L. M. Babe, C. S. Craik, *Cell* **91**, 427 (1997).
21. A. M. Nomura *et al.*, *Nat. Struct. Mol. Biol.* **12**, 1019 (2005).
22. D. D. Boehr, H. J. Dyson, P. E. Wright, *Chem. Rev.* **106**, 3055 (2006).
23. R. Sprangers, A. Velyvis, L. E. Kay, *Nat. Methods* **4**, 697 (2007).
24. K. K. Frederick, M. S. Marlow, K. G. Valentine, A. J. Wand, *Nature* **448**, 325 (2007).
25. S. B. Shuker, P. J. Hajduk, R. P. Meadows, S. W. Fesik, *Science* **274**, 1531 (1996).
26. A. P. Golovanov, R. T. Blankley, J. M. Avis, W. Bermel, *J. Am. Chem. Soc.* **129**, 6528 (2007).
27. L. R. Masterson, M. Tonelli, J. L. Markley, G. Veglia, *J. Am. Chem. Soc.* **130**, 7818 (2008).
28. T. O'Hare *et al.*, *Cancer Res.* **65**, 4500 (2005).
29. N. Vajpai *et al.*, *J. Biol. Chem.* **283**, 18292 (2008).
30. L. D'Silva *et al.*, *J. Am. Chem. Soc.* **127**, 13220 (2005).
31. C. Q. Hu, Y. Z. Hu, *Curr. Med. Chem.* **15**, 1720 (2008).
32. L. T. Vassilev *et al.*, *Science* **303**, 844 (2004).
33. M. Pazgier *et al.*, *Proc. Natl. Acad. Sci. U.S.A.* **106**, 4665 (2009).
34. S. A. Showalter *et al.*, *J. Am. Chem. Soc.* **130**, 6472 (2008).
35. K. Sugase, H. J. Dyson, P. E. Wright, *Nature* **447**, 1021 (2007).
36. P. Schanda, B. Brutscher, R. Konrat, M. Tollinger, *J. Mol. Biol.* **380**, 726 (2008).
37. H. M. Volkman, S. E. Rutledge, A. Schepartz, *J. Am. Chem. Soc.* **127**, 4649 (2005).
38. J. L. Best *et al.*, *Proc. Natl. Acad. Sci. U.S.A.* **101**, 17622 (2004).
39. G. M. Verkhivker *et al.*, *Curr. Opin. Struct. Biol.* **12**, 197 (2002).
40. D. L. Mobley, K. A. Dill, *Structure*, in press.

41. This research was supported in part by grants from the NIH (grant 1R01A1067423) and the HIV Accessory and Regulatory Complex Center (grant P50 GM082250). G.M.L. is a recipient of the 2007–2008 UCSF-Gladstone Institute for Virology & Immunology/Center for AIDS Research Clinical Science Pilot Award (grant P30-AI027763). We also thank K. Dill, J. Gross, D. Hostetter, and T. Shahian for discussion and proofreading of this manuscript.

Supporting Online Material

www.sciencemag.org/cgi/content/full/324/5924/213/DC1
SOM Text
References

10.1126/science.1169378

NEW JERSEY COMMISSION ON BRAIN INJURY RESEARCH GRANT AVAILABILITY

1. Individual Research Grants not to exceed $495,000 over 3 years.

2. Multi Investigator Research Grants not to exceed $1,980,000 over 3 years.

3. Postdoctoral/Graduate Student Fellowship Research Grants:
- **Postdoctoral Fellowship grants not to exceed a $162,000 stipend over 3 years based on the postgraduate level of experience.**
- **Graduate Student Fellowship Research Grants not to exceed a $72,000 stipend over 3 years.**

4. Pilot Research Grants not to exceed $165,000 over 2 years.

Application forms and details contact: www.nj.gov/health/njcbir

New Jersey Commission on Brain Injury Research
PO Box 360
Market and Warren Streets
Trenton, New Jersey 08625-0360
Tel: 609-633-6465
E-mail: njcbir@doh.state.nj.us

Letter of Intent deadline: June 1, 2009
Closing date for applications: September 1, 2009

Exomic Sequencing Identifies *PALB2* as a Pancreatic Cancer Susceptibility Gene

Siân Jones,[1,2] Ralph H. Hruban,[2,3] Mihoko Kamiyama,[3] Michael Borges,[3] Xiaosong Zhang,[1,2] D. Williams Parsons,[1,2] Jimmy Cheng-Ho Lin,[1,2] Emily Palmisano,[2] Kieran Brune,[2] Elizabeth M. Jaffee,[2,3] Christine A. Iacobuzio-Donahue,[2,3] Anirban Maitra,[2,3] Giovanni Parmigiani,[2,3] Scott E Kern,[2,3] Victor E. Velculescu,[1] Kenneth W. Kinzler,[1] Bert Vogelstein,[1,2] James R. Eshleman,[2,3]* Michael Goggins,[2,3,4]* Alison P. Klein[2,3]*†

There is considerable debate about the value of personal genome sequencing (*1*). In addition to the five individuals whose genomes have been sequenced in their entirety, 68 patients have been evaluated for tumor-specific mutations in all exons of protein-coding genes (exomic sequencing). This coincidentally yielded information about germline sequence variations in these individuals (*2*–*4*). To explore the utility of such information, we evaluated a pancreatic cancer patient (Pa10) whose tumor DNA had been sequenced in (*4*). This patient had familial pancreatic cancer, as defined by the fact that his sister also had developed the disease.

Among the 20,661 coding genes analyzed (*5*), we identified 15,461 germline variants in Pa10 not found in the reference human genome. Of these, 7318 were synonymous, 7721 were missense, 64 were nonsense, 108 were at splice sites, and 250 were small deletions or insertions (54% in-frame). Past studies have shown that tumors arising in patients with a hereditary predisposition harbor no normal alleles of the responsible gene: One allele is inherited in mutant form, often producing a stop codon, and the other (wild-type) allele is inactivated by somatic mutation during tumorigenesis. In Pa10, only three genes met these criteria: *SERPINB12*, *RAGE*, and *PALB2*. Of these, we considered *PALB2* to be the best candidate because germline stop codons in *SERPINB12* and *RAGE*, but not in *PALB2*, are relatively common in healthy individuals and because germline *PALB2* mutations have previously been associated with breast cancer predisposition and Fanconi anemia (*6*), although the function of the gene is not well understood. Pa10 harbored a germline deletion of 4 base pairs (TTGT at ~172 to 175) that produced a frameshift at codon 58; the pancreatic cancer that developed in Pa10 had also somatically acquired a transition mutation (C to T) at a canonical splice site for exon 10 (IVS10+2).

To determine whether *PALB2* mutations occur in other patients with familial pancreatic cancer, we sequenced this gene in a cohort of 96 familial pancreatic cancer patients, 90 of whom were of Caucasian ancestry. Sixteen of these patients had one first-degree relative with pancreatic cancer, and 80 had at least two additional relatives, at least one of whom was first degree, with the disease. Truncating mutations were identified in three of the 96 patients, each producing a different stop codon (Fig. 1). The average age of onset of pancreatic cancer in these families was 66.7 years, similar to the mean age of onset of 65.3 years in the families without *PALB2* mutations. We determined the germline sequence of an affected brother in one of these kindreds, and he harbored the same stop codon. Truncating mutations in *PALB2* are rare in individuals without cancer; none were reported among 1084 normal participants in a previous study that used a cohort of similar ethnicity to ours (*7*). Although some families we identified with a *PALB2* stop mutation had a history of both breast and pancreatic cancer, breast cancer was not observed in all families (pedigrees in fig. S1). From these data, *PALB2* appears to be the second most commonly mutated gene for hereditary pancreatic cancer. The most commonly mutated gene is *BRCA2* (*8*), whose protein product is a binding partner for the *PALB2* protein (*9*).

In summary, through complete, unbiased sequencing of protein-coding genes we have identified a gene responsible for a hereditary disease. This approach is independent of classical methods for gene discovery, such as linkage analysis, which can be challenging in the absence of large families with monogenic diseases. We predict that variations of the approach described here will soon become a standard tool for the discovery of disease-related genes.

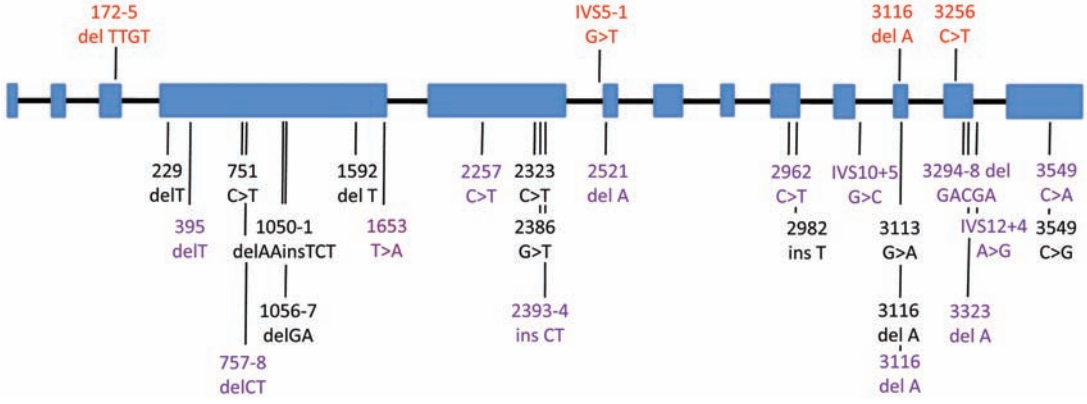

Fig. 1. Location of mutations in the *PALB2* gene. Exons are represented as blue boxes and introns as black lines (not to scale). Mutations previously identified in patients with familial breast cancer or Fanconi anemia are shown in black or purple, respectively. Germline mutations identified in patients with familial pancreatic cancer are shown above the gene in red.

References and Notes

1. A. L. McGuire, M. K. Cho, S. E. McGuire, T. Caulfield, *Science* **317**, 1687 (2007).
2. L. D. Wood *et al.*, *Science* **318**, 1108 (2007); published online 11 October 2007 (10.1126/science.1145720).
3. D. W. Parsons *et al.*, *Science* **321**, 1807 (2008); published online 4 September 2008 (10.1126/science.1164382).
4. S. Jones *et al.*, *Science* **321**, 1801 (2008); published online 4 September 2008 (10.1126/science.1164368).
5. Materials and methods are available as supporting material on *Science* Online.
6. C. Turnbull, N. Rahman, *Annu. Rev. Genomics Hum. Genet.* **9**, 321 (2008).
7. N. Rahman *et al.*, *Nat. Genet.* **39**, 165 (2007).
8. A. Maitra, R. H. Hruban, *Annu. Rev. Pathol.* **3**, 157 (2008).
9. B. Xia *et al.*, *Mol. Cell* **22**, 719 (2006).
10. Supported by the Sol Goldman Pancreatic Cancer Research Center; the Lustgarten Foundation for Pancreatic Cancer Research; the Virginia and D. K. Ludwig Fund for Cancer Research; NIH grants CA62924, CA123483, and RO1CA97075; and the Michael Rolfe Pancreatic Cancer Foundation.

Supporting Online Material

www.sciencemag.org/cgi/content/full/1171202/DC1
Materials and Methods
Fig. S1
References

21 January 2009; accepted 20 February 2009
Published online 5 March 2009;
10.1126/science.1171202
Include this information when citing this paper.

[1]Ludwig Center for Cancer Genetics and Therapeutics and Howard Hughes Medical Institute, Baltimore, MD 21231, USA. [2]Department of Oncology, The Sol Goldman Pancreatic Cancer Research Center, The Johns Hopkins Medical Institutions, Baltimore, MD 21231, USA. [3]Department of Pathology, The Sol Goldman Pancreatic Cancer Research Center, The Johns Hopkins Medical Institutions, Baltimore, MD 21231, USA. [4]Department of Medicine, The Sol Goldman Pancreatic Cancer Research Center, The Johns Hopkins Medical Institutions, Baltimore, MD 21231, USA.

*These authors contributed equally to this work.
†To whom correspondence should be addressed. E-mail: aklein1@jhmi.edu

Genome-Wide Analysis in Vivo of Translation with Nucleotide Resolution Using Ribosome Profiling

Nicholas T. Ingolia,* Sina Ghaemmaghami,† John R. S. Newman, Jonathan S. Weissman

Techniques for systematically monitoring protein translation have lagged far behind methods for measuring messenger RNA (mRNA) levels. Here, we present a ribosome-profiling strategy that is based on the deep sequencing of ribosome-protected mRNA fragments and enables genome-wide investigation of translation with subcodon resolution. We used this technique to monitor translation in budding yeast under both rich and starvation conditions. These studies defined the protein sequences being translated and found extensive translational control in both determining absolute protein abundance and responding to environmental stress. We also observed distinct phases during translation that involve a large decrease in ribosome density going from early to late peptide elongation as well as widespread regulated initiation at non–adenine-uracil-guanine (AUG) codons. Ribosome profiling is readily adaptable to other organisms, making high-precision investigation of protein translation experimentally accessible.

The ability to monitor the identity and quantity of proteins that a cell produces would inform nearly all aspects of biology. Microarray-based measurements of mRNA abundance have revolutionized the study of gene expression (*1*). However, for several reasons there is a critical need for techniques that directly monitor protein synthesis. First, mRNA levels are an imperfect proxy for protein production because mRNA translation is subject to extensive regulation (*2*–*4*). Second predicting the exact protein product from the transcript sequence is not possible because of effects such as internal ribosome entry sites, initiation at non-AUG codons, and nonsense readthrough (*5*, *6*). Finally, programmed ribosomal pausing during protein synthesis is thought to aid the cotranslational folding and secretion of some proteins (*7*–*9*).

Polysome profiling, in which mRNAs are recovered from translating ribosomes for subsequent microarray analysis, can provide a useful estimate of protein synthesis (*10*). However, this approach suffers from limited resolution and accuracy. Additionally, upstream open reading frames (uORFs)—short translated sequences found in the 5′ untranslated region (5′UTR) of many genes—result in ribosomes that are bound to an mRNA and yet are not translating the encoded gene (*11*). Advances in quantitative proteomics circumvent some of these problems (*2*, *3*), but there currently are substantial limits on their ability to independently determine protein sequences and measure low-abundance proteins.

The position of a translating ribosome can be precisely determined by using the fact that a ribosome protects a discrete footprint [~30 nucleotides (nt)] on its mRNA template from nuclease digestion (*12*). We reasoned that advances in deep-sequencing technology, which make it possible to read tens of millions of short (~35 base pairs) DNA sequences in parallel (*13*), would allow the full analysis of ribosome footprints from cells. Here, we present a ribosome-profiling strategy that is based on the deep sequencing of ribosome-protected fragments and provides comprehensive high-precision measurements of in vivo translation with subcodon precision.

Quantifying RNA with deep sequencing. To establish ribosome profiling as a quantitative tool for monitoring translation, we needed to implement three steps: (i) robustly generate ribosome-protected mRNA fragments ("footprints") whose sequences indicate the position of active ribosomes; (ii) convert these RNA footprints into a library of DNA molecules in a form that is suitable for deep sequencing with minimal distortion; and (iii) measure the abundance of different footprints in this library by means of deep sequencing. We first established that counting the number of times a sequence is read by a deep-sequencing experiment provides a quantitative measurement of its abundance in a complex library (fig. S1) (*14*). We then optimized nuclease conditions for obtaining ribosome footprints from in vivo translating ribosomes (fig. S2, A and B). Finally, we tested various strategies for preparing sequencing libraries from a pool of randomly fragmented yeast mRNAs, reasoning that the abundance of different fragments of the same mRNA should be comparable. Using this benchmark, we optimized a strategy, outlined in Fig. 1A, that avoided RNA ligases that typically are used in previous approaches for converting small RNAs to DNA (*15*) because they caused large distortions in the distribution of RNA species (figs. S3 and S4) (*16*).

We performed deep sequencing on a DNA library that was generated from fragmented total mRNA in order to measure abundances of different transcripts (table S1), focusing on 5295 genes that were relatively free of repetitive sequences and overlapping transcribed features (*14*). We conceptually divided each coding sequence (CDS) into two regions of equal length. The number of reads aligning to these two regions thus represents independent measurements of the abundance of the full-length mRNA before fragmentation. The error between these two counts only slightly exceeded the theoretical minimum dictated by sampling statistics (Fig. 1B), demonstrating the accuracy and sequence independence of our library-generation strategy. The mRNA density measurements were highly reproducible [correlation coefficient (R^2) = 0.98; SD in log ratio between biological replicates corresponded to a 1.2-fold change] (fig. S5). Our measurements also agreed well with previous microarray-based measurements of mRNA abundance (R^2 = 0.66) (fig. S6) (*17*, *18*). A particular advantage of our strategy for quantitating mRNA levels is that it retained strand information and, by fragmenting messages to a small uniform size, minimized distortions caused by RNA secondary structure, allowing accurate quantifications of specific subregions (for example, individual exons) of transcripts.

Monitoring ribosome position with single-codon resolution with deep sequencing. We sequenced 42 million fragments that were generated by using the ribosome protection assay on the budding yeast *Saccharomyces cerevisiae* (*14*). 7.0 million (16%) of sequencing reads aligned to CDSs, whereas most of the remainder were derived from ribosomal RNA (rRNA) (table S1). Because most contaminating rRNA is derived from a few specific sites, it should be straightforward to remove them by means of subtractive hybridization before sequencing.

Along a given message, we found that the positions of the 5′ ends of the footprint fragments started abruptly 12 to 13 nt upstream of the start codon, ended 18 nt upstream from the stop codon, and showed a strong 3-nt periodicity (Fig. 2, A and B). Thus, coverage by ribosome footprints defines the sequence being translated. The high precision of ribosome positions allowed us to monitor the reading frame being translated. For example, 75% of the 28-nt oligomer ribosome-protected fragments started on the first nucleotide of a codon (Fig. 2C). Although each individual footprint provides imperfect statistical evidence of the ribosome position, averaging multiple codons allows unambiguous determination of the reading frame. This should enable genome-wide studies of programmed frameshifting and readthrough of stop codons (*5*).

Department of Cellular and Molecular Pharmacology, Howard Hughes Medical Institute, University of California, San Francisco, and California Institute for Quantitative Biosciences, San Francisco, CA 94158, USA.

*To whom correspondence should be addressed. E-mail: ingolia@cmp.ucsf.edu

†Present address: Institute for Neurodegenerative Diseases, University of California, San Francisco, San Francisco, CA 94158, USA.

Genome-wide measurements of translation. We next sought to use ribosome profiling data to quantify the rate of protein synthesis. We estimated protein expression from the density of ribosome footprints (*14*), although further improvements could incorporate variations in the speed of translation along a message (see below). From 7.0 million footprint sequences, we were able to measure the translation of 4648 of 5295 genes with a precision (fig. S7) and reproducibility comparable with our mRNA abundance measure (R^2 = 0.98; ~20% error between biological replicates) (Fig. 2D).

Comparing the rate of translation with mRNA abundance from the same samples revealed a roughly 100-fold range of translation efficiency (as measured by the ratio of ribosome footprints to mRNA fragments) between different yeast genes, in addition to a subset of transcripts that were translationally inactive (Fig. 2E and fig. S8A). Thus, differences in translational efficiency, which are invisible to mRNA abundance measurements, contribute substantially to the dynamic range of gene expression (table S2).

The rate of protein synthesis is expected to be a better predictor of protein abundance than measurements of mRNA levels. Indeed, estimates of the absolute abundance of proteins from proteome-wide mass spectrometry had a correlation coefficient of R^2 = 0.42 with our translation-rate measurements versus R^2 = 0.17 with our mRNA abundance (fig. S9) (*19*). Differences in protein stability contribute to the imperfect correlation between the rate of a protein's synthesis and its steady-state levels. Thus, comparison between changes in synthesis measured by ribosome profiling and abundance measured by mass spectrometry should reveal examples of the regulated degradation of proteins (*19*).

Ribosome profiling reveals different phases of translation. Previous polysome studies found that shorter genes tended to have a higher ribosome density (*10*). We saw a similar, though weaker, trend and an overall agreement between ribosome profiling and polysome profiling (figs. S8B and S10). This phenomenon was surprising because it suggested that the rate of translation initiation was sensitive to the total length of the gene, thus causing shorter messages to be better translated. Alternatively, there may be a higher ribosome density in a region of constant length at the start of each gene, which would contribute a larger fraction of the total ribosome occupancy for shorter genes. However, a previous study found no evidence for higher ribosome density at the 5′ end of six individual mRNAs (*20*).

Our genome-wide position-specific measurements of ribosome occupancy let us test this possibility more broadly. An averaging over hundreds of well-translated genes revealed considerably greater (approximately threefold) ribosome density for the first 30 to 40 codons (Fig. 2F), which after 100 to 200 codons relaxed to a uniform

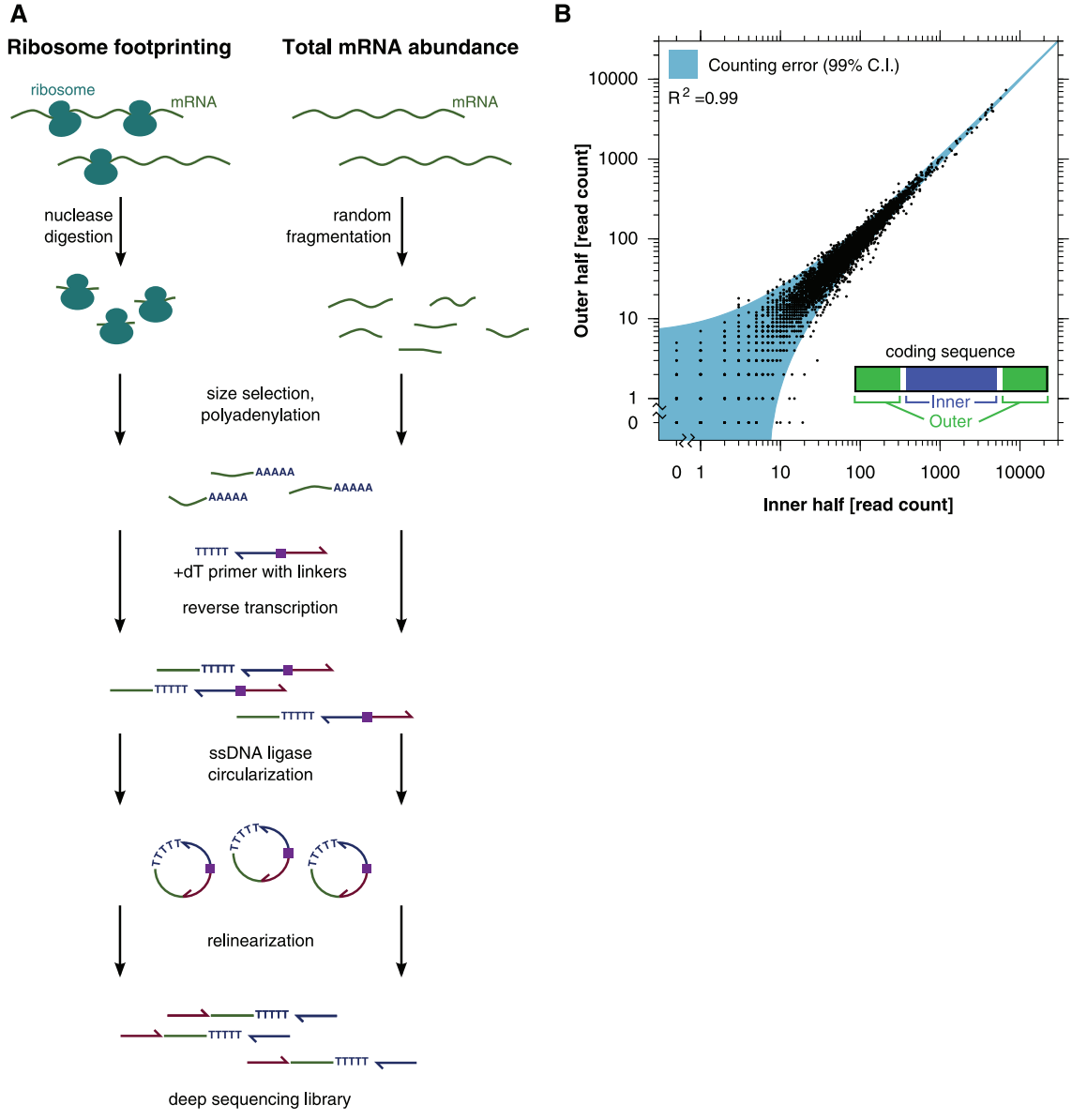

Fig. 1. Quantifying mRNA abundance and ribosome footprints by means of deep sequencing. (**A**) Schematic of the protocol for converting ribosome footprints or randomly fragmented mRNA into a deep-sequencing library. (**B**) Internal reproducibility of mRNA-abundance measurements. CDSs were conceptually divided as shown, and the mRNA counts on the two regions are plotted. The error estimate is based on the χ^2 statistic.

density that persisted until translation termination (fig. S11A). The excess of ribosomes at the start of genes explained the higher ribosome density on shorter genes and was not an artifact of immobilizing ribosomes with cycloheximide treatment or stalled ribosomes on the 5′ end of genes (fig. S12). Elevated 5′ ribosome density appears to be a general feature of translation that is independent of the length of the CDS, its translation level, and the presence of an N-terminal signal sequence (fig. S11, B to D). Correcting the estimate of protein-synthesis rates for this effect substantially improved the correlation with protein abundance (R^2 = 0.60 versus R^2 = 0.42) (fig. S13). This argues that the decrease in ribosome density along a transcript results from either increases in the rate of translation elongation and/or premature translation termination.

Codon-specific measurements of ribosome positions. Ribosome profiling reports on the precise positions of ribosomes, making it possible to delineate what parts of a transcript are being decoded. Almost all (98.8%) of the ribosome footprints in our data set mapped to protein-coding regions. Nonetheless, this left 56,105 unexplained footprints, which probably represent true translation events because they copurified with the 80*S* ribosomes. Furthermore, they were far more common in the 5′UTRs (Fig. 3A), whereas we expect background resulting from the spurious capture of RNAs to be evenly distributed across transcripts. Introns and 3′UTRs, in particular, typically had less than 1% of the ribosome density seen in a CDS (fig. S14), and most had no observed footprints. The absence of reads in unspliced introns indicates that the intronic regions detected from mRNA sequencing experiments (*21*) are rarely translationally active; thus, ribosome profiling can simplify the analysis of expression of spliced genes.

In contrast, about one quarter of the 5′UTRs showed substantial translational activity, in many cases comparable to that of CDSs (Fig. 3B). One source of translation in 5′UTRs is the presence

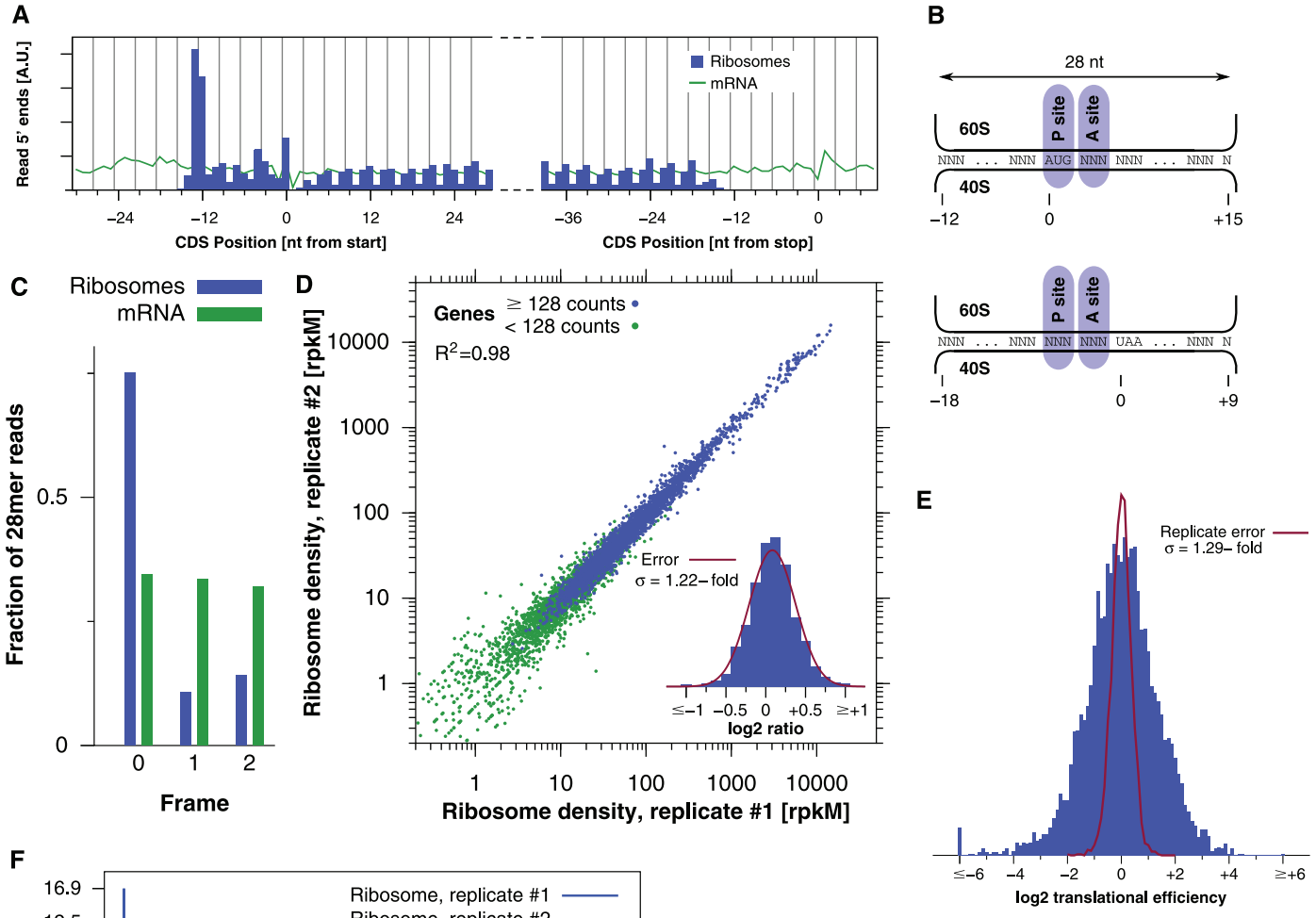

Fig. 2. Ribosome footprints provide a codon-specific measurement of translation. (**A**) Total number of ribosome footprints falling near the beginning or end of CDSs. (**B**) The offset between the start of the footprint and the P- and A-site codons at translation initiation and termination (*34*). (**C**) Position of 28-nt ribosome footprints relative to the reading frame. (**D**) Ribosome footprint densities in two complete biological replicates. Density in terms of reads per kilobase per million (rpkM) is corrected for total reads and CDS length (*21*). (Inset) Histogram of log2 ratios between replicates for genes with low counting statistics error (fig. S7) along with the normal error curve (mean = 0.084, SD = 0.291 in log2 units; σ is SD expressed as a fold change). (**E**) Histogram of translational efficiency, the ratio of ribosome footprint density to mRNA density. The error shows actual ratios between biological replicates (SD = 0.367 in log2 units). (**F**) Read density as a function of position. Well-expressed genes were each individually normalized and then averaged with equal weight (*14*).

of uORFs, short translated reading frames upstream of the CDS that can play an important role in translational regulation (*11*). We identified 1048 candidate uORFs in the yeast genome on the basis of the presence of an upstream AUG codon (table S3) (*22*, *23*). We focused on the 86 upstream AUG codons in the most abundant messages (*14*), in which we could reliably quantify even low levels of translation. Among this set, only 20 of the uORFs were well-translated, a prominent example being *ICY1* (Fig. 3C and table S4). More broadly, among all annotated 5′UTRs we found evidence for the translation of 153 uORFs (table S5), fewer than 30 of which had previously been experimentally evaluated.

Nonetheless, these uORFs account for only a fraction of the 706 genes in which we found substantial translation in the 5′UTR. Some genes, such as *PRE2* and *PDR5*, had a discrete region of ribosome density that was terminated by a stop codon but lacked an AUG codon (Fig. 3D and fig. S15). In both cases, the translated region could be accounted for by initiation at a UUG codon. There are two known examples in which translation initiates at a non-AUG codon in yeast, the tRNA synthetases *GRS1* (*24*) and *ALA1* (*25*), and both are apparent in our data (fig. S16). Initiation at non-AUG codons is strongly dependent on the surrounding sequence context (*26*), in contrast to canonical initiation in yeast (*27*), and the non-AUG initiation sites in *PRE2* and *PDR5* both match an experimentally verified strong initiation sequence (*26*).

On the basis of this finding, we searched for other candidate non-AUG initiation sites where a codon with a single mismatch against AUG had a favorable initiation context (*14*). Most of these start sites would lead to short uORFs, as seen in *PRE2* and *PDR5*, although there was

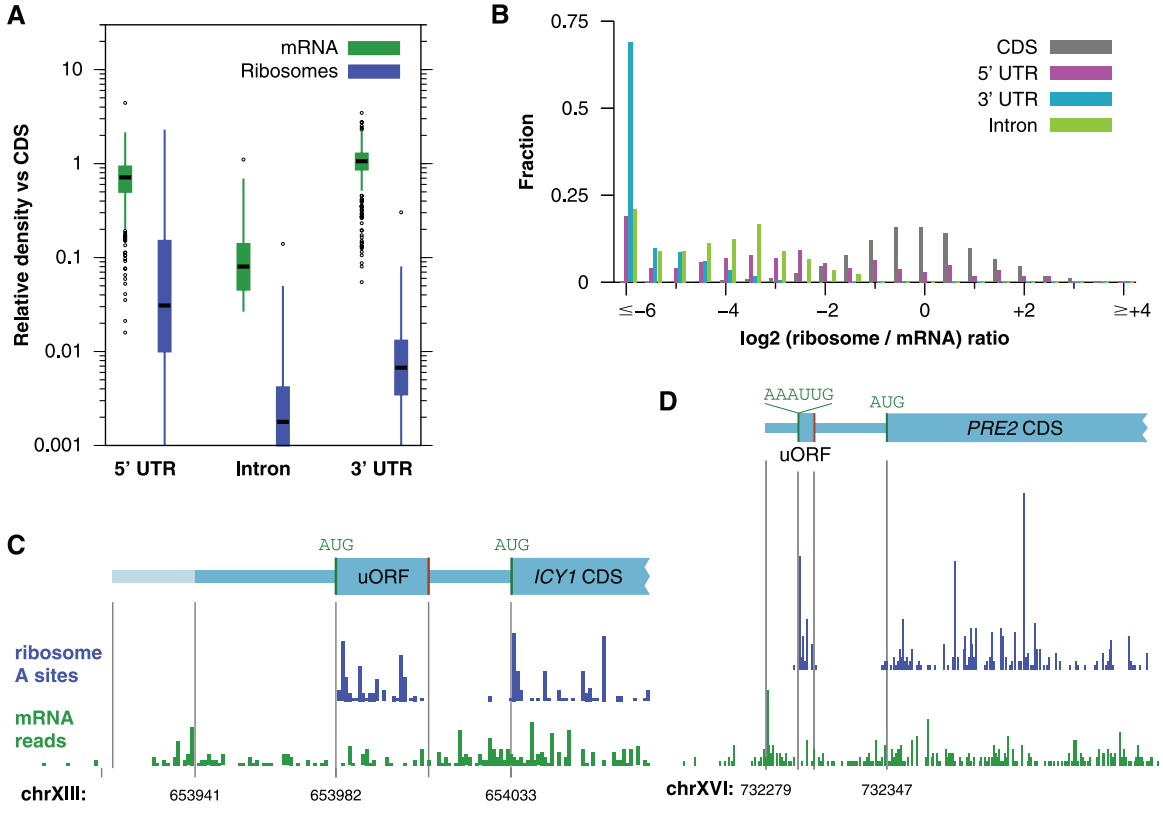

Fig. 3. Ribosome occupancy of upstream open-reading frames and other sequences. (**A**) Density of mRNA fragments and ribosome footprints on non–protein-coding sequences relative to the associated CDS. (**B**) Histogram of translational efficiencies for different classes of sequences. (**C**) Ribosome and mRNA density showing the uORF in the *ICY1* 5′UTR. (**D**) Ribosome and mRNA density showing non-AUG uORFs in the *PRE2* 5′ UTR. The proposed AAAUUG translational initiation site is shown along with the subsequent open reading frame and stop codon (indicated by a vertical line).

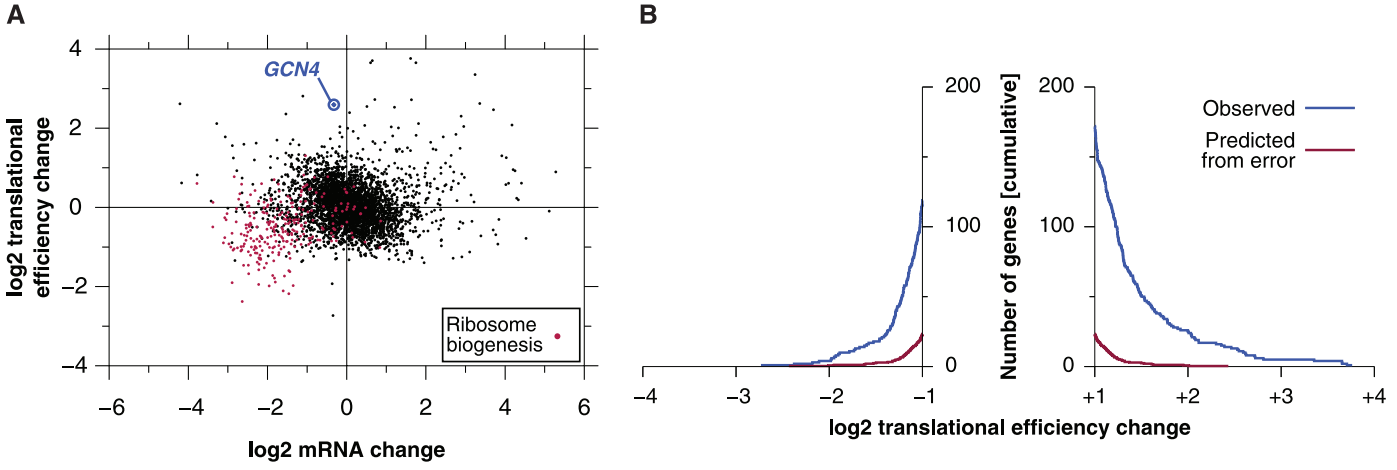

Fig. 4. Translational response to starvation. (**A**) Changes in mRNA abundance and translational efficiency in response to starvation. (**B**) Distribution of translational efficiency changes in response to starvation. Measurement error was estimated from the actual distribution of ratios between biological replicates. A false discovery rate threshold of 10% corresponds to a twofold change in translational efficiency.

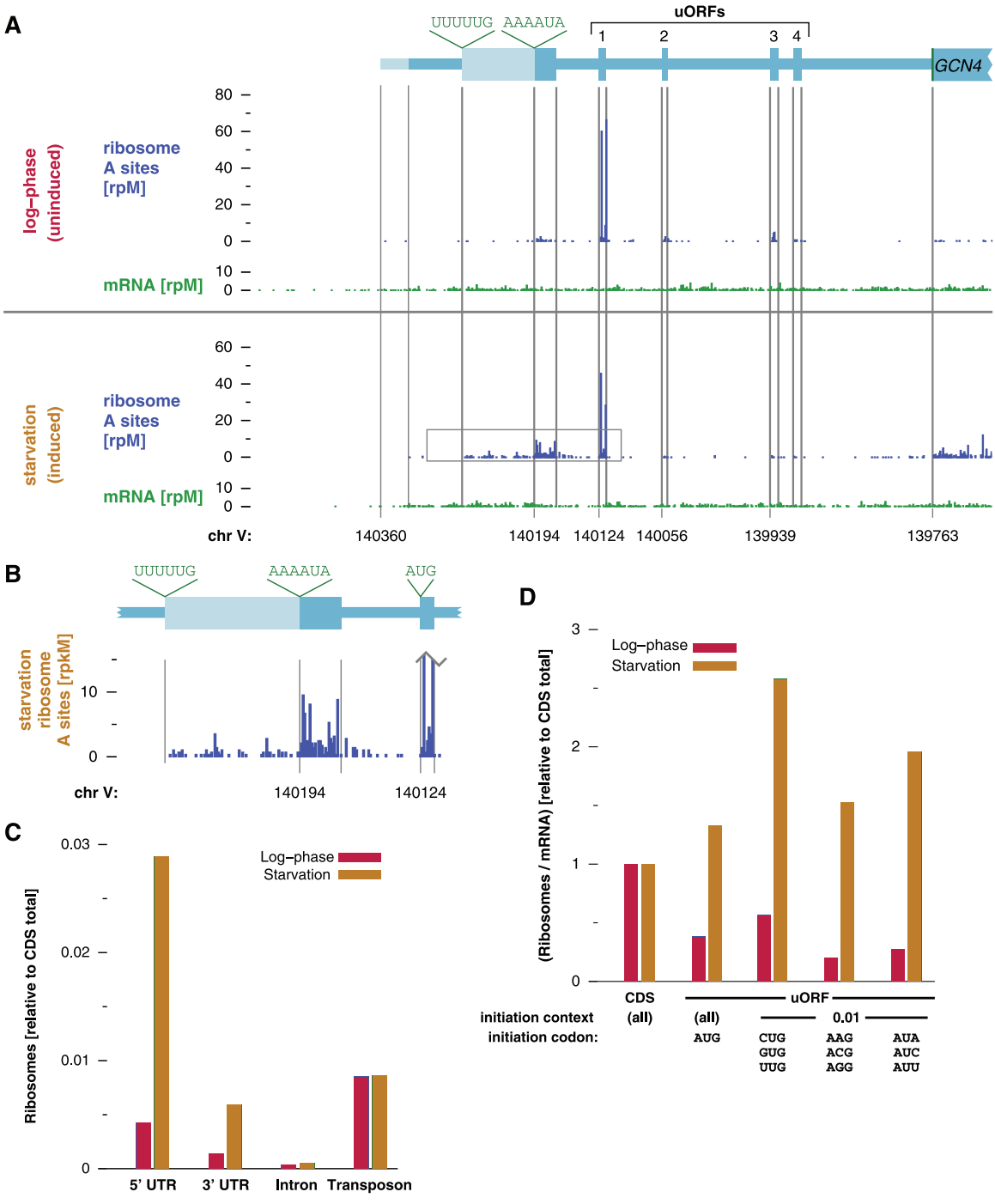

Fig. 5. Changes in 5′UTR translation during starvation. (**A**) Ribosome and mRNA densities in the *GCN4* 5′UTR in repressive and inducing conditions. The four known uORFs are indicated along with the proposed initiation sites for upstream translation. (**B**) Non-AUG uORF upstream of *GCN4*. Shown is an enlargement of the gray boxed area in (A). (**C**) Ribosome occupancy of noncoding sequences. The number of ribosome footprints mapping to different classes of regions is shown relative to the number of CDS reads. (**D**) Aggregate translational efficiency of uORFs (*14*).

evidence for N-terminal extensions in a few genes, including the cyclin *CLB1* (fig. S17). In aggregate, these 1615 predicted uORFs had a much greater (approximately threefold) translational efficiency than other regions of 5′UTRs, particularly when the start codon differed from AUG at the first position (approximately sixfold; see below). We found a strong bias for 28-nucleotide oligomer footprints to align with the predicted reading frame just downstream of these non-AUG initiation sites, which is similar to the effect we saw in protein-coding genes (fig S18).

Furthermore, when elongation was not inhibited, ribosome footprints were depleted from 5′UTRs just as they were from the beginning of protein-coding genes, indicating that they were active ribosomes capable of runoff elongation (fig. S19). Overall, we found 143 non-AUG uORFs with evidence of translation (table S6), which account for 20% of 5′UTR ribosome footprints. Thus, there is pervasive initiation at specific, favorable, non-AUG sites.

Translational responses to starvation. The ability to evaluate rates of translation as well as mRNA abundance with high precision enables quantitative measurements of translational regulation. Acute amino acid starvation in yeast produces substantial transcriptional and translational changes (*28*), including a global decrease in translational initiation (*29*). We subjected yeast to 20 min of amino acid deprivation and made ribosome-footprint and mRNA-abundance measurements (fig. S20). We then compared starvation and log-phase growth measurements for the 3769 genes for which statistical counting error did not compromise our ability to detect translational regulation (Fig. 4A and fig. S7). One-third of the genes showed changes in relative translational efficiency upon starvation (fig. S21), with 291 strongly affected (greater than twofold) genes (Fig. 4B and table S7). Forty-three of the 111 down-regulated genes ($P < 10^{-40}$) are involved in

ribosome biogenesis (Fig. 4A and table S8), a process that is repressed at many different levels in response to stresses such as starvation (*30*, *31*).

The fraction of each gene's mRNA that is associated with polysomes had previously been used to provide a semiquantitative measurement of translational efficiency (*32*). Many ribosome biogenesis transcripts leave the polysome fraction in response to starvation, in agreement with our observations, and changes in polysome association were significantly correlated with changes in translation that were measured with ribosome profiling (up-regulated genes, $P < 10^{-12}$ and down-regulated genes, $P < 10^{-6}$) (fig. S22). Ribosome profiling also allowed us to detect the sevenfold translational induction of *GCN4*, a well-studied and translationally regulated gene (*29*) whose response to starvation was not detected by the earlier polysome studies (*32*).

The regulation of *GCN4* translation results from four uORFs in its 5′UTR [reviewed in (*29*)]. During log-phase growth, we saw translation of *GCN4* uORF 1, along with some translation of uORFs 2 to 4, but very little translation of the main *GCN4* CDS (Fig. 5A). This pattern of ribosome occupancy is consistent with the standard model of *GCN4* 5′UTR function, in which uORF 1 is constitutively translated but permissive for downstream reinitiation. In log-phase growth, reinitiation occurs at uORFs 2 to 4 rather than at *GCN4* itself. Upon starvation, however, reinitiation bypasses uORFs 2 to 4 and reaches the main CDS, thereby relieving the translational repression of *GCN4*. Indeed, we saw a decrease in ribosome occupancy of the repressive uORFs as well as an increase in translation of the protein-coding region upon starvation. Unexpectedly, we also observed additional translation in the 5′UTR upstream of the characterized uORFs. This region was detectably translated even in log-phase growth, and its translation was greatly enhanced under starvation (Fig. 5B). Most translation in this region started from a noncanonical AAA*AUA* site, although there was also initiation from an upstream in-frame noncanonical UUU*UUG* site. Sequences overlapping this region are required for proper translational regulation by uORF 1 (*33*), which supports the idea of these non-AUG uORFs having a functional role.

More broadly, during starvation we found a large (sixfold) increase in the fraction of ribosome footprints derived from 5′UTRs but little change in introns (Fig. 5C). There was also a less pronounced increase in ribosome occupancy of 3′UTRs, although the overall density remained low. The non-AUG uORFs showed a particularly dramatic increase in ribosome occupancy during starvation, apparently exceeding the translation not only of canonical AUG uORFs but of the CDSs themselves (Fig. 5D). Non-AUG uORFs upstream of genes such as *GLN1* and *PRE9*, which were marginally translated during log-phase growth, had much higher ribosome densities after starvation (figs. S23 and S24). However, even in the case of *GLN1*, it is clear that no single uORF can account for the entire distribution of ribosomes on the 5′UTR. Instead, there is a more general change in the stringency of initiation codon selection that favors certain noncanonical start sites but has broader effects as well (fig. S25). The initiation factor eIF2α, whose phosphorylation mediates the effect of starvation on translation (*29*), also has a prominent role in initiator codon selection (*34*) and thus may contribute to this relaxation.

Perspective. Ribosome profiling greatly increases our ability to quantitatively monitor protein production, as is underscored by our considerably improved predictions of protein abundance. This technique should become a central tool in the repertoire available for studying the internal state of cells. The basic strategy is readily adaptable to other organisms, including mammals, and it can allow tissue-specific translational profiling by using the restricted expression of epitope-tagged ribosomes (*35*). Immediate applications of ribosome profiling include studies of the translational control of gene expression and molecular characterization of disease states such as cancer, in which associated cellular stress will probably directly affect translation (*36*). Additionally, the ability to determine precisely what regions of a message are being decoded should greatly aid efforts to experimentally define the full proteome of complex organisms such as humans.

Our approach also allows in-depth analysis of the process of translation in vivo. For example, ribosome profiling revealed an unanticipated complexity to translation that leads to differences in ribosome density along the length of CDSs. This presumably reflects differences in the functional states of the ribosome that affect its rate of elongation or processivity. The switch from the early to the late elongation phase begins with the first emergence of the nascent peptide from the ribosome, allowing interactions between the nascent chain and molecular chaperones (*37*). Measurements of the effects of starvation on translational activity also revealed widespread and regulated initiation at non-AUG codons, suggesting a new effect of the well-studied eIF2α-mediated stress response. Finally, high-resolution gene-specific ribosome density profiles will enable efforts to explore how variations in the rate of translation, as well as effects such as ribosomal pausing, modulate protein synthesis and folding.

References and Notes

1. P. O. Brown, D. Botstein, *Nat. Genet.* **21**, 33 (1999).
2. D. Baek *et al.*, *Nature* **455**, 64 (2008).
3. M. Selbach *et al.*, *Nature* **455**, 58 (2008).
4. N. Sonenberg, A. G. Hinnebusch, *Mol. Cell* **28**, 721 (2007).
5. O. Namy, J. P. Rousset, S. Napthine, I. Brierley, *Mol. Cell* **13**, 157 (2004).
6. C. Touriol *et al.*, *Biol. Cell* **95**, 169 (2003).
7. A. A. Komar, T. Lesnik, C. Reiss, *FEBS Lett.* **462**, 387 (1999).
8. A. K. Lakkaraju, C. Mary, A. Scherrer, A. E. Johnson, K. Strub, *Cell* **133**, 440 (2008).
9. S. L. Wolin, P. Walter, *EMBO J.* **7**, 3559 (1988).
10. Y. Arava *et al.*, *Proc. Natl. Acad. Sci. U.S.A.* **100**, 3889 (2003).
11. H. A. Meijer, A. A. Thomas, *Biochem. J.* **367**, 1 (2002).
12. J. A. Steitz, *Nature* **224**, 957 (1969).
13. D. R. Bentley *et al.*, *Nature* **456**, 53 (2008).
14. Materials and methods are available as supporting material on *Science* Online.
15. E. Berezikov, E. Cuppen, R. H. Plasterk, *Nat. Genet.* **38** (suppl.), S2 (2006).
16. E. Romaniuk, L. W. McLaughlin, T. Neilson, P. J. Romaniuk, *Eur. J. Biochem.* **125**, 639 (1982).
17. F. C. Holstege *et al.*, *Cell* **95**, 717 (1998).
18. U. Nagalakshmi *et al.*, *Science* **320**, 1344 (2008).
19. L. M. de Godoy *et al.*, *Nature* **455**, 1251 (2008).
20. Y. Arava, F. E. Boas, P. O. Brown, D. Herschlag, *Nucleic Acids Res.* **33**, 2421 (2005).
21. A. Mortazavi, B. A. Williams, K. McCue, L. Schaeffer, B. Wold, *Nat. Methods* **5**, 621 (2008).
22. C. Vilela, J. E. McCarthy, *Mol. Microbiol.* **49**, 859 (2003).
23. Z. Zhang, F. S. Dietrich, *Curr. Genet.* **48**, 77 (2005).
24. K. J. Chang, C. C. Wang, *J. Biol. Chem.* **279**, 13778 (2004).
25. H. L. Tang *et al.*, *J. Biol. Chem.* **279**, 49656 (2004).
26. S. J. Chen, G. Lin, K. J. Chang, L. S. Yeh, C. C. Wang, *J. Biol. Chem.* **283**, 3173 (2008).
27. H. Yoon, T. F. Donahue, *Mol. Microbiol.* **6**, 1413 (1992).
28. A. G. Hinnebusch, *Microbiol. Rev.* **52**, 248 (1988).
29. A. G. Hinnebusch, *Annu. Rev. Microbiol.* **59**, 407 (2005).
30. P. Jorgensen *et al.*, *Genes Dev.* **18**, 2491 (2004).
31. J. A. Pleiss, G. B. Whitworth, M. Bergkessel, C. Guthrie, *Mol. Cell* **27**, 928 (2007).
32. J. B. Smirnova *et al.*, *Mol. Cell. Biol.* **25**, 9340 (2005).
33. C. M. Grant, P. F. Miller, A. G. Hinnebusch, *Nucleic Acids Res.* **23**, 3980 (1995).
34. L. D. Kapp, J. R. Lorsch, *Annu. Rev. Biochem.* **73**, 657 (2004).
35. M. Heiman *et al.*, *Cell* **135**, 738 (2008).
36. M. Holcik, N. Sonenberg, *Nat. Rev. Mol. Cell Biol.* **6**, 318 (2005).
37. R. J. Nelson, T. Ziegelhoffer, C. Nicolet, M. Werner-Washburne, E. A. Craig, *Cell* **71**, 97 (1992).

38. We thank C. Chu, J. deRisi, and K. Fischer for help with sequencing; D. Bartel, H. Guo, D. Herschlag, J. Hollien, S. Luo, and G. Schroth for helpful discussions of RNA methods; P. Walter and T. Aragon for the use of a density gradient fractionator; the 2008 Woods Hole Physiology course students for data analysis; and members of the Weissman lab, L. Lareau, and T. Ingolia for critical commentary on the manuscript. Sequencing data have been deposited in the National Center for Biotechnology Information's Gene Expression Omnibus (www.ncbi.nlm.nih.gov/geo/) under accession number GSE13750. This investigation was supported by a NIH P01 grant (AG10770) and a Ruth L. Kirschstein National Research Service Award (GM080853) (to N.T.I.) and by the Howard Hughes Medical Institute (to J.S.W.). N.T.I. and J.S.W. are the inventors on a patent application, assigned to the Regents of the University of California, on the ribosome profiling and sequencing library generation techniques described in this work. S.G. and J.R.S.N. developed a microarray-based approach that served as a proof of principle for the present studies; N.T.I. and J.S.W. designed the experiments; N.T.I. performed the experiments and analyzed the data; and N.T.I. and J.S.W. interpreted the results and wrote the manuscript.

Supporting Online Material

www.sciencemag.org/cgi/content/full/1168978/DC1
Materials and Methods
Figs. S1 to S25
Tables S1 to S8
References

25 November 2008; accepted 30 January 2009
Published online 12 February 2009;
10.1126/science.1168978
Include this information when citing this paper.

Elastic Shear Anisotropy of Ferropericlase in Earth's Lower Mantle

Hauke Marquardt,[1*] Sergio Speziale,[1] Hans J. Reichmann,[1] Daniel J. Frost,[2] Frank R. Schilling,[1†] Edward J. Garnero[3]

Seismic shear anisotropy in the lowermost mantle most likely results from elastic shear anisotropy and lattice preferred orientation of its constituent minerals, including perovskite, post-perovskite, and ferropericlase. Measurements of the elastic shear anisotropy of single-crystal $(Mg_{0.9}Fe_{0.1})O$ up to 69 gigapascals (GPa) show that it increased considerably across the pressure-induced spin transition of iron between 40 and 60 GPa. Increasing iron content further enhances the anisotropy. This leads to at least 50% stronger elastic shear anisotropy of (Mg,Fe)O in the lowermost mantle compared to MgO, which is typically used in geodynamic modeling. Our results imply that ferropericlase is the dominant cause of seismic shear anisotropy in the lower mantle.

The lower mantle, which is dominated by an assemblage of (Mg,Fe)O ferropericlase and $(Mg,Fe,Al)(Si,Al)O_3$ perovskite [or post-perovskite (ppv) at the base of the lower mantle (*1*, *2*)], constitutes more than 50% of Earth's volume and plays a pivotal role in the evolution and present-day dynamics of our planet. Seismic shear anisotropy is a key feature within many regions of the lowermost mantle (the D″ layer) (*3*–*8*), which likely results from lattice preferred orientation (LPO) coupled with strong elastic anisotropy of lower-mantle minerals (*6*, *7*, *9*–*11*). An understanding of the mineral properties and their deformation behavior that lead to seismic anisotropy can elucidate information on mantle flow in these regions (*5*–*7*). It has been proposed that ppv (*1*, *2*) may cause seismic anisotropy in D″; however, ppv is probably a poor match to the seismic observations (*12*, *13*). It has been shown that LPO of ferropericlase leads to $V_{SH} > V_{SV}$ anisotropy (where V_{SH} and V_{SV} are the velocities of the horizontally and vertically polarized seismic shear waves, respectively) in horizontal shear (*10*); this is qualitatively consistent with seismic observations (*4*, *6*, *9*), but the contribution of (Mg,Fe)O to seismic shear anisotropy is uncertain given the small volume abundance of (Mg,Fe)O in the lower mantle (~20 vol. %).

The elastic anisotropy of ferropericlase had been determined at low pressures (*14*–*16*) or for pure MgO (*11*, *17*, *18*). In addition to the effect of Fe-Mg substitution, the spin-pairing transition of Fe^{2+} in ferropericlase (*19*) at pressures of the lower mantle affects single-crystal elastic constants (*20*), as well as bulk elastic properties (*21*–*23*). Recently, the single-crystal elastic properties of $(Mg_{0.94}Fe_{0.06})$ were measured to 60 GPa (*20*) by impulsive stimulated light scattering. That study resolved the longitudinal elastic stiffness constant c_{11}, but did not sufficiently constrain c_{12} and c_{44} (where c_{ij} are the elements of the second-order elastic stiffness tensor) for shear anisotropy to be distinguished from that of MgO.

To quantify the effect of iron content and iron spin state on the elastic shear anisotropy of (Mg,Fe)O, we performed high-pressure Brillouin scattering measurements on single-crystal $(Mg_{0.9}Fe_{0.1})O$, which was grown in a multianvil apparatus at 24 GPa and 1800°C in an Fe foil capsule (*24*) to minimize the amount of ferric iron (*25*) and associated defects. Brillouin spectroscopy was performed to 69 GPa in the diamond-anvil cell, where different pressure-transmitting media were used in different experimental runs (table S1). Information on the high-pressure density of our sample, which is needed to relate measured velocities to elastic moduli, was obtained independently from x-ray powder diffraction measurements at beamline I15 at Diamond Light Source, UK (fig. S4).

In our experiments (Fig. 1), the shear wave propagating in the [001] direction was fastest at room pressure, but its velocity remained almost constant with pressure, whereas the velocity of the shear wave along [011], polarized along [0-11], strongly increased with pressure. This led to an inversion of the fastest propagation direction at about 18 GPa. The pressure derivative of the shear wave velocity along [011] clearly increased at ~45 GPa, a pressure that corresponds to the onset of the spin transition in Fe^{2+} (*22*). The shear wave velocity along [001] was only slightly affected by the change in electronic configuration of Fe^{2+} and showed a weak depression.

The Voigt-Reuss-Hill averaged shear velocity of $(Mg_{0.9}Fe_{0.1})O$ calculated from the Brillouin data (Fig. 2) is in agreement with previous studies on (Mg,Fe)O with a variety of iron contents (*11*, *14*, *17*, *20*, *23*) that were conducted using different techniques. An increase in the mole fraction of iron causes a decrease in the average shear velocity (v_s). The pressure derivative of the shear wave velocity (dv_s/dP) decreased with increasing pressure up to ~50 GPa, where dv_s/dP steeply increased. This increase can be assigned to the spin transition of Fe^{2+} in ferropericlase, but our data do not show a clear depression in v_s associated with the spin transition, as reported in (*20*). The influence of iron on v_s becomes less pronounced once iron assumes the low-spin state.

The addition of iron increased the elastic shear anisotropy of both high-spin (HS) and low-spin (LS) (Mg,Fe)O with respect to MgO throughout the pressure regime of the lower mantle (Fig. 3). The substitution of 10% of the magnesium ions

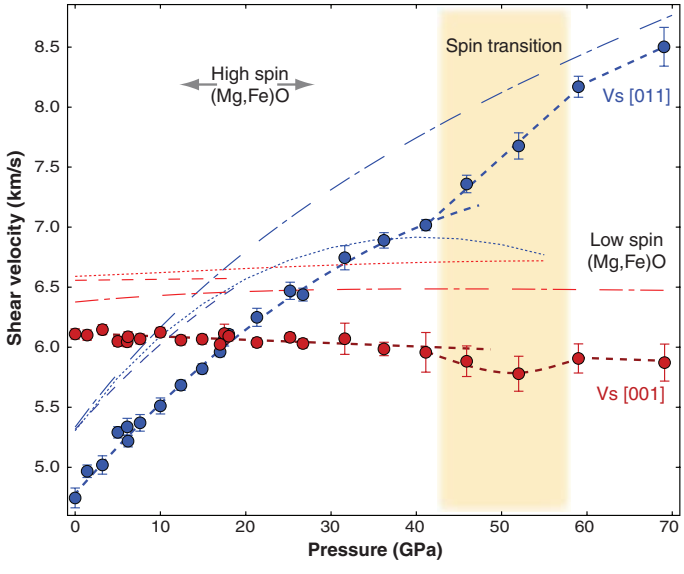

Fig. 1. Maximum and minimum shear velocities in $(Mg_{0.9}Fe_{0.1})O$ as a function of pressure. Shear velocities were measured in the (100) plane at different angles (at least seven directions) at each pressure and inverted for the two effective elastic shear constants $(c_{11} - c_{12})/2$ and c_{44}, which were used to calculate maximum and minimum shear velocity. Uncertainties are based on the propagation of the uncertainties in every measured velocity, taking into account the positions of Stokes and anti-Stokes peaks, their uncertainties, and the broadness of the peaks. The thin dashed, dotted, and dash-dotted lines are calculated from experimental (*17*, *18*) and computational (*11*) data of MgO.

[1]GFZ German Research Centre for Geosciences, Telegrafenberg, 14473 Potsdam, Germany. [2]Bayerisches Geoinstitut, Universität Bayreuth, 95440 Bayreuth, Germany. [3]School of Earth and Space Exploration, Arizona State University, Box 871404, Tempe, AZ 85287, USA.

*To whom correspondence should be addressed. E-mail: hama@gfz-potsdam.de

†Karlsruhe Institute of Technology, IBF, 76131 Karlsruhe, Germany.

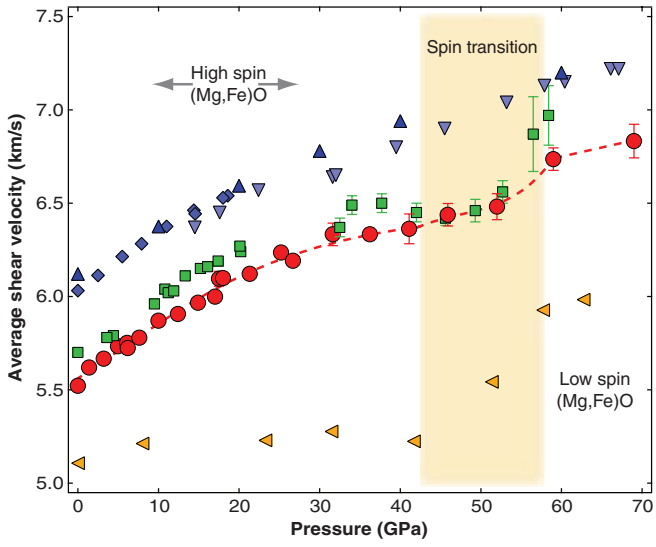

Fig. 2. Increasing iron content in (Mg,Fe)O ferropericlase causes marked differences in average shear velocities. Average velocities for $(Mg_{0.9}Fe_{0.1})O$ obtained in this study by using Brillouin spectroscopy are shown as red circles. Experimental results for single-crystal MgO (*17*) (blue diamonds) and polycrystalline MgO (*32*) (blue inverse triangles), $(Mg_{0.94}Fe_{0.06})O$ (*14*, *20*) (green squares), and $(Mg_{0.75}Fe_{0.25})O$ (*23*) (yellow left-pointing triangles), along with computational data for MgO (*11*) (blue triangles), are shown for comparison.

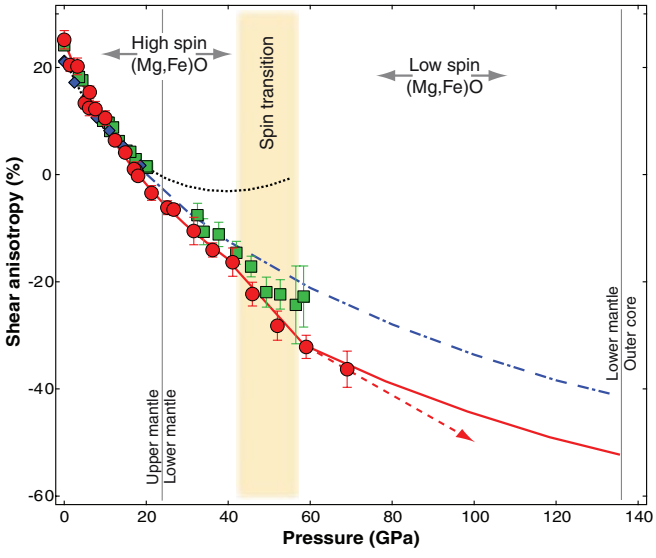

Fig. 3. Shear anisotropy of (Mg,Fe)O as a function of pressure. The shear anisotropy is defined as $(v_{s[001]} - v_{s[011]})/[(v_{s[001]} + v_{s[011]})/2]$. At pressures corresponding to those of the lower mantle, $(Mg_{0.9}Fe_{0.1})O$ (red circles) is elastically more anisotropic than iron-free MgO (blue symbols). The dashed arrow indicates that the pressure derivative of the anisotropy of ferropericlase might even be larger than for MgO; this would further increase the anisotropy difference in the lowermost mantle. Experimental data of MgO (*17*) (blue diamonds) were extrapolated (dash-dotted line) by using the pressure derivative predicted by a computational study of MgO (*11*). The only available experimental data on MgO at lower mantle pressures (*18*) (dark dotted line) show a different trend above ~20 GPa than other results, possibly caused by the limited number of measured directions (*24*). Data for $(Mg_{0.94}Fe_{0.06})O$ (*14*, *20*) (green squares) are also plotted for comparison.

by iron not only caused an increase in anisotropy at room pressure, but also resulted in a larger pressure derivative to the anisotropy. A considerable increase in elastic shear anisotropy across the HS-LS transition was observed.

The increase in elastic anisotropy at ambient pressure cannot be explained by the size of iron (a transition metal) as in the case of alkaline-earth oxides (*26*). It can, instead, be attributed to the asymmetric electronic density distribution associated with Fe^{2+} in the HS state (*27*) that produces an increase of c_{12} (the constant that relates axial strain to orthogonal stress). The effect of pressure is to diminish the anisotropy of the 3d electron density distribution of Fe^{2+} that, combined with the negligible pressure dependence of c_{44} (Fig. 1 and fig. S2), causes a steep pressure derivative of the elastic anisotropy. With the onset of the spin transition, the 3d-electron density distribution of Fe^{2+} changes to a more symmetric configuration (*25*, *27*), causing a decrease in c_{12} and an increase of c_{11} in the LS phase.

The pressure dependence of the elastic anisotropy of LS $(Mg_{0.9}Fe_{0.1})O$ appears to be similar to that of MgO (*11*), but is shifted toward higher anisotropy (i.e., absolute value of anisotropy). This probably reflects differences in metal-oxygen bonding strength and the size difference between Mg and Fe. The difference between the elastic anisotropy of MgO and LS $(Mg_{0.9}Fe_{0.1})O$ is distinct, indicating that the HS-LS transition leads to a strong directionally dependent change in the elastic properties (Fig. 1). Assuming that the pressure dependence of the elastic anisotropy of LS $(Mg_{0.9}Fe_{0.1})O$ is identical to that of MgO, we extrapolated our data to the pressure corresponding to that of the core-mantle boundary (Fig. 3).

To evaluate the impact of our results on modeling of the elastic anisotropy of the lower mantle, we calculated the resulting maximum elastic shear anisotropy for a simplified model lower-mantle assemblage of ~80 vol. % $MgSiO_3$ and ~20 vol. % $(Mg_{0.8}Fe_{0.2})O$ (*24*). Our results show that the elastic shear anisotropy of (Mg,Fe)O strongly depends on the iron content and that ~20

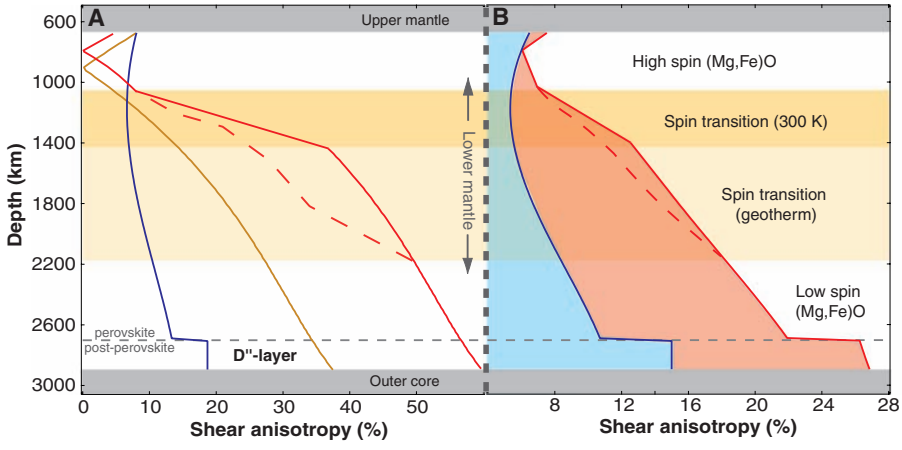

Fig. 4. Maximum shear anisotropy of major lower-mantle phases along a model geotherm. The shear polarization anisotropy is defined as $(v_{s,max} - v_{s,min})/[(v_{s,max} + v_{s,min})/2]$, where $v_{s,max}$ and $v_{s,min}$ are maximum and minimum shear velocity in a given direction. (**A**) The maximum single-crystal polarization anisotropy of the two major components of Earth's lower mantle. The shear anisotropy of MgO (gold) and $MgSiO_3$ (blue) were calculated with available computational data at high pressure and temperature. The elastic anisotropy of $(Mg_{0.8}Fe_{0.2})O$ (red), a model mantle composition, was linearly scaled from the data of MgO and $(Mg_{0.9}Fe_{0.1})O$, corrected for temperature (*24*). The expected broadening of the spin transition region (dashed lines) with temperature was estimated from experimental data on $(Mg_{0.75}Fe_{0.25})O$ (*33*). (**B**) The anisotropies of the single phases were weighted by their volume abundance in the lower mantle (*24*), where the shaded areas illustrate the maximum possible contributions of perovskite (blue) and ferropericlase (red), a situation in which all the crystals of the same mineral phase have the same orientation.

vol. % of $(Mg_{0.8}Fe_{0.2})O$ contribute about equally to the overall possible seismic shear anisotropy as ~80 vol. % $MgSiO_3$ (Fig. 4). Because (Mg,Fe)O is a much weaker phase (*28*), it will accommodate most of the strain (*29*); it should, therefore, develop a much stronger texture than $(Mg,Fe)SiO_3$ (*13*). Thus, it is likely that LPO of (Mg,Fe)O dominates seismic anisotropy in the lower mantle. Strong partitioning of iron into ferropericlase, suggested by experiments (*19*, *30*), may favor even stronger anisotropy from (Mg,Fe)O. However, consensus on the partitioning behavior of iron under lower-mantle conditions has not been reached (*30*, *31*).

If LPO of ferropericlase dominates lower-mantle anisotropy, seismic anisotropy could also be present above the D″ discontinuity in regions where deformation is dominated by dislocation creep at very high strain levels (*6*, *9*). The rapid spreading of seismic receivers around the world will allow us to better quantify the depth distribution of anisotropy in the lower mantle.

References and Notes

1. M. Murakami, K. Hirose, K. Kawamura, N. Sata, Y. Ohishi, *Science* **304**, 855 (2004).
2. A. R. Oganov, S. Ono, *Nature* **430**, 445 (2004).
3. T. Lay, Q. Williams, E. J. Garnero, *Nature* **392**, 461 (1998).
4. E. J. Garnero, V. Maupin, T. Lay, M. J. Fouch, *Science* **306**, 259 (2004).
5. M. Panning, B. Romanowicz, *Science* **303**, 351 (2004).
6. A. K. McNamara, P. E. van Keken, S.-I. Karato, *Nature* **416**, 310 (2002).
7. J. Wookey, S. Stackhouse, J. M. Kendall, J. Brodholt, G. D. Price, *Nature* **438**, 1004 (2005).
8. J. M. Kendall, P. G. Silver, *Nature* **381**, 409 (1996).
9. H. R. Wenk, S. Speziale, A. K. McNamara, E. J. Garnero, *Earth Planet. Sci. Lett.* **245**, 302 (2006).
10. D. Yamazaki, S.-i. Karato, *Phys. Earth Planet. Inter.* **131**, 251 (2002).
11. B. B. Karki, R. M. Wentzcovitch, S. de Gironcoli, S. Baroni, *Science* **286**, 1705 (1999).
12. S. Merkel *et al.*, *Science* **316**, 1729 (2007).
13. R. M. Wentzcovitch, T. Tsuchiya, J. Tsuchiya, *Proc. Natl. Acad. Sci. U.S.A.* **103**, 543 (2006).
14. J. M. Jackson *et al.*, *J. Geophys. Res.* **111**, B09203 (2006).
15. S. D. Jacobsen *et al.*, *J. Geophys. Res.* **107**, 2037 (2002).
16. H. J. Reichmann, S. V. Sinogeikin, J. D. Bass, *Am. Mineral.* **93**, 1306 (2008).
17. S. V. Sinogeikin, J. D. Bass, *Phys Earth Planet. Inter.* **120**, 43 (2000).
18. C.-S. Zha, H.-k. Mao, R. J. Hemley, *Proc. Natl. Acad. Sci. U.S.A.* **97**, 13494 (2000).
19. J. Badro *et al.*, *Science* **300**, 789 (2003).
20. J. C. Crowhurst, J. M. Brown, A. F. Goncharov, S. D. Jacobsen, *Science* **319**, 451 (2008).
21. J.-F. Lin *et al.*, *Nature* **436**, 377 (2005).
22. S. Speziale *et al.*, *Proc. Natl. Acad. Sci. U.S.A.* **102**, 17918 (2005).
23. J.-F. Lin *et al.*, *Geophys. Res. Lett.* **33**, L22304 (2006).
24. Materials and methods are available as supporting material on *Science* online.
25. H. Keppler, I. Kantor, L. Dubrovinsky, *Am. Mineral.* **92**, 433 (2007).
26. T. Tsuchiya, K. Kawamura, *J. Chem. Phys.* **114**, 10086 (2001).
27. T. Tsuchiya, R. M. Wentzcovitch, C. R. S. da Silva, S. de Gironcoli, *Phys. Rev. Lett.* **96**, 198501 (2006).
28. S.-i. Karato, *Phys Earth Planet. Inter.* **55**, 234 (1989).
29. K. Madi, S. Forest, P. Cordier, M. Boussuge, *Earth Planet. Sci. Lett.* **237**, 223 (2005).
30. M. Murakami, K. Hirose, N. Sata, Y. Ohishi, *Geophys. Res. Lett.* **32**, L03304 (2005).
31. Y. Kobayashi *et al.*, *Geophys. Res. Lett.* **32**, L19301 (2005).
32. M. Murakami, Y. Ohishi, N. Hirao, K. Hirose, *Earth Planet. Sci. Lett.* **277**, 123 (2009).
33. J.-F. Lin *et al.*, *Science* **317**, 1740 (2007).

34. We thank J.-F. Lin, S. Jahn, T. Duffy, M. Koch-Müller, R. Jeanloz, K. Hartmann, and two anonymous reviewers for helpful comments and ideas on the project and the manuscript; A. Kurnosov for gas-loading at Bayerisches Geoinstitut, H. Wilhelm for assistance at the Diamond Light Source; and M. Gottschalk and T. Boffa Ballaran for single-crystal x-ray diffraction. E.J.G. acknowledges support from NSF grant EAR-0711401.

Supporting Online Material

www.sciencemag.org/cgi/content/full/324/5924/224/DC1
Materials and Methods
Figs. S1 to S5
Table S1
References

4 December 2008; accepted 16 February 2009
10.1126/science.1169365

A Great Earthquake Rupture Across a Rapidly Evolving Three-Plate Boundary

Kevin P. Furlong,[1]* Thorne Lay,[2] Charles J. Ammon[1]

On 1 April 2007 a great, tsunamigenic earthquake (moment magnitude 8.1) ruptured the Solomon Islands subduction zone at the triple junction where the Australia and Solomon Sea–Woodlark Basin plates simultaneously underthrust the Pacific plate with different slip directions. The associated abrupt change in slip direction during the great earthquake drove convergent anelastic deformation of the upper Pacific plate, which generated localized uplift in the forearc above the subducting Simbo fault, potentially amplifying local tsunami amplitude. Elastic deformation during the seismic cycle appears to be primarily accommodated by the overriding Pacific forearc. This earthquake demonstrates the seismogenic potential of extremely young subducting oceanic lithosphere, the ability of ruptures to traverse substantial geologic boundaries, and the consequences of complex coseismic slip for uplift and tsunamigenesis.

Great earthquakes typically involve sudden sliding between two tectonic plates, and the largest events are located in subduction zones where an oceanic plate thrusts into the mantle below an overriding plate. In a few locations, a boundary between two oceanic plates impinges on a subduction zone, causing both plates to descend beneath the overriding plate, but at different rates and directions. This is the situation that led to the great moment magnitude M_w 8.1 Solomon Islands earthquake of 1 April 2007 [8.47°S, 157.04°E, 20:39:58.7 UTC (*1*)], which ruptured the megathrust between the overriding Pacific plate (PaP) and the independently subducting Australia (AuP) and Solomon Sea–Woodlark Basin (SWP) plates (Fig. 1). The inferred rupture area along the San Cristobal and New Britain trenches, as indicated by aftershocks (*1*), patterns of uplift/subsidence (*2*–*4*), and preliminary rupture analysis (*5*, *6*), straddles the down-dip extension of the Simbo transform fault that separates the SWP from the AuP; thus, the earthquake ruptured across the SWP-AuP plate boundary. The rupture generated a large local tsunami, and about 50 lives were lost and more than 9000 people displaced.

Before the 2007 event, this triple junction region, where the three plates meet, had low seismic activity and no record of large interplate events (*7*); thus, pre-event seismicity, or other available geologic and tectonic data, provided limited constraint on the subduction zone geometry. The region above the down-dip extension of the Simbo Fault is a localized region of rapid Holocene uplift (*8*). The age of lithosphere currently subducting along the trench varies from ~0.5 to 3.5 million years old, and it has been speculated that such young, hot lithosphere will not produce large earthquakes. Here we describe the 2007 earthquake rupture to address how, before the earthquake, strain was distributed between the subducting and overriding plates.

Before ~0.5 million years ago (Ma), the easternmost segment of the Woodlark Basin spreading ridge was subducting beneath the western margin of the Solomon Islands (Fig. 1), and the ridge-trench triple junction migrated northwesterly at ~110 to 120 mm/year. The differences in plate subduction rates and directions produced a slab window, which today lies beneath the southern New Georgia Islands. The SWP subducts at 135 mm/year (N45°E), whereas the AuP subducts at 97 mm/year (N70°E) (*8*, *9*). The near-total cessation of spreading on the most trenchward section of the Woodlark Basin ridge at ~0.5 Ma (*8*, *9*) and the formation of the right-lateral

[1]Department of Geosciences, The Pennsylvania State University, State College, PA 16802 USA. [2]Department of Earth and Planetary Sciences, University of California, Santa Cruz, CA 95064, USA.

*To whom correspondence should be addressed. E-mail: kevin@geodyn.psu.edu

strike-slip Simbo transform fault caused the Ghizo lithospheric fragment (Fig. 1) to be transferred from the SWP to the AuP. The Simbo transform now accommodates ~60 mm/year plate motion between SWP and AuP, and the new triple junction formed by the Simbo transform and the trench migrates southeastward at ~110 mm/year (fig. S1).

Teleseismic body waves and short-arc Rayleigh waves (R1) were collected to characterize the mainshock rupture. Azimuthal variations of the R1 source time functions (STFs) (*10*) constrain the average rupture length and rupture velocity. Figure 2 shows the R1 STFs, which are narrow (~50 s) in the rupture direction and broad (~180 s) in the opposite direction (*11*). The systematic duration variation is consistent with unilateral rupture parallel to the trench axis with an average rupture speed of 2.5 ± 0.4 km/s. The STFs suggest a seismic moment of 2.5×10^{21} N·m (M_w = 8.2), somewhat larger than the global centroid-moment tensor (GCMT) estimate, which has an unusually large (37°) dip (*5*). A large aftershock is evident in the STFs ~7 min after the mainshock. This M_w = 6.6 event initiated ~200 km to the northwest of the mainshock hypocenter (7.17°S, 155.78°E, 20:47:31.3 UTC).

We computed finite-fault models for relatively uniform azimuthal distributions of teleseismic *P* and *SH* waves, using a least-squares inversion (*12*) with prescribed fault orientation, specified rupture velocity V_r, and variable subfault rake and source time function (*11*). Our preferred solution is for a fault strike of 305° ± 5°, dip of 25° ± 5°, and V_r = 2.5 ± 0.4 km/s (Fig. 3). The main effect of variations in rupture velocity is a simple stretching of the slip zone (fig. S3). The basic solution is stable with respect to changes in fault dip (fig. S4), strike (fig. S5) and data subsets (fig. S6).

The slip model shows two main patches of slip at shallow depth along strike, with a systematic 36° difference in rake between the patches (the near-epicentral patch has an average rake of 49 ± 11°, and the northwestern patch has a rake of 85 ± 15°). A third region of deeper slip with rake varying between values for the two shallow patches is located ~100 km from the hypocenter. The body waves also indicate predominantly unilateral rupture, with a total duration of about 100 s and seismic moment M_o = 1.87×10^{21} N·m (M_w = 8.1). The basic slip attributes are consistent with those indicated by rapid studies (*5*, *6*).

The distinct directions of coseismic slip in the major slip regions define separate domains of interseismic strain accumulation. The position of this transition on the slab interface (Fig. 4) is consistent with the expected down-dip extent of the Simbo fault if it developed ~0.5 Ma. The consistency between the shallow earthquake slip directions and current relative plate motions for the two plate pairs delineates the region of the subducted Ghizo fragment that has been transferred from the SWP to the AuP. The gradual transition in fault slip between AuP-PaP and SWP-PaP relative motion directions down-dip of the subducted Simbo fault suggests that the subducted slab is still at least partially connected in that region, leading to complexity in the strain accumulation and coseismic release.

The limited depth extent of rupture in the southeastern main rupture patch (AuP-PaP interaction) is compatible with the extreme youth of the subducted plate and the extent and location of the slab window that developed during ridge subduction before 0.5 Ma (Fig. 1). The relatively small coseismic slip along the megathrust near the subducted Simbo fault is enigmatic, particularly given the appreciable uplift associated with this earthquake (*2*–*4*) in the region and the similar patterns of Holocene uplift (*8*) above the subducted transform fault.

There are two end-member scenarios for interseismic and coseismic elastic strain accumulation and release in subduction zones. In the "slab deformation" model, all interseismic elastic deformation occurs within the subducting slab—i.e., there is no deformation of a rigid upper plate. Under this assumption, all coseismic recovery would involve displacement of the slab. In the "upper plate deformation" model, the overriding plate accumulates all of the interseismic deformation, and thus coseismic displacements all occur within the upper plate. This latter case would produce more surface uplift and potentially be more tsunamigenic than the former. Subduction

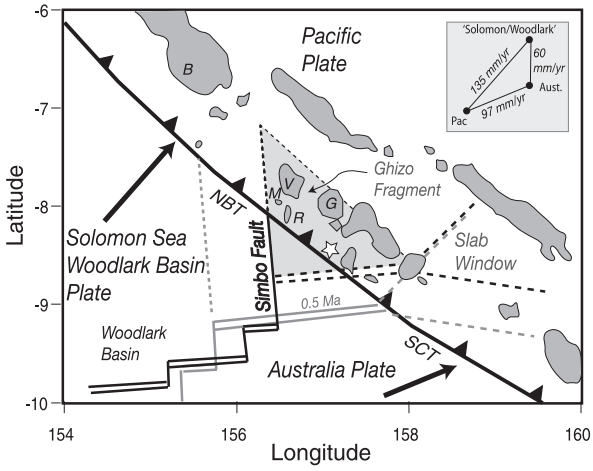

Fig. 1. Plate tectonic setting and recent tectonic evolution of the rupture area of the 1 April 2007, M_w 8.1 earthquake (epicenter shown by star). Plate boundary structures at ~0.5 Ma, including the incipient Simbo transform fault and the slab window produced by the subduction of the actively spreading Woodlark spreading ridge, are shown by gray lines. Black lines show present plate boundary structures. The shaded triangular region (Ghizo Fragment) maps the extent of subducted oceanic lithosphere that may have been transferred from the SWP to the AuP with the formation of the Simbo transform at ~0.5 Ma. Following Tregoning *et al*. (*17*), we consider the Woodlark Basin and Solomon Sea to comprise a single tectonic unit, the Solomon Sea–Woodlark Basin plate (SWP). The arrows show plate motions of the SWP and AuP relative to the PaP. The inset shows the plate motion velocity triangle in the earthquake rupture area. Locations labeled on map: SCT, San Cristobal trench; NBT, New Britain trench; B, Bougainville; M, Mbava; V, Vella Lavella; R, Ranongga; and G, Ghizo.

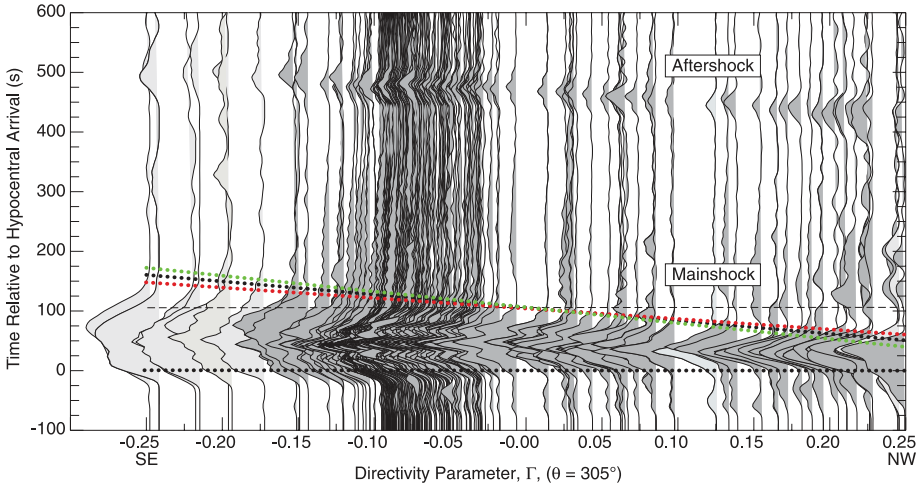

Fig. 2. R1 Rayleigh wave effective source time functions (STFs) plotted as a function of directivity parameter, Γ (*18*), assuming a rupture propagation azimuth of 305°. STFs along the direction of rupture (positive Γ) are shorter in duration, indicating predominantly unilateral rupture in the direction 305°. Fitting a line along the ends of the STFs, projected to limiting values of Γ (±0.25 s/km), allows one to estimate the minimum (52 s), maximum (182 s), and average (117 s) STF durations; each of these values has about ±10 s uncertainty due to scatter in the STFs. Lines indicate the onset, average, and end times of the STFs. STFs for a large aftershock about 7 min after the mainshock are apparent.

zone behavior likely falls somewhere between these two end-members, and normally seismologic observations are unable to distinguish in what domain a particular subduction plate boundary resides. If the Solomon subduction regime lies on the slab deformation end of the spectrum, then the coseismic slip behavior would require sympathetic or triggered slip on the subducted Simbo fault during the event and/or loading of the Simbo Fault. Neither appears to be the case (fig. S8).

Rather, the seismic cycle behavior of the Solomon subduction regime is consistent with that expected in the upper plate deformation model. Before the event, Global Positioning System displacements for the AuP, just to the south of the rupture region, indicated unimpeded motion of Australia with respect to the Pacific (*13*), implying little if any strain accumulation in the subducting Australia plate. Patterns of uplift associated with the earthquake (*2*, *3*) and the locations of maximum local tsunami run-up (*3*, *4*, *14*) are consistent with coseismic shortening in the upper plate in the transition zone between the two domains of interplate displacements (Fig. 4). The uplift, which may have been coseismic or rapid postseismic deformation, was observed on a suite of islands in the arc-trench region (*2*–*4*)—Ranongga, Mbava, and Vella Lavella—that overlie the location of the subducted Simbo transform and Simbo Ridge. Previously this near-trench uplift was attributed to uniform slip of 5 m over a narrow rectangular fault (*2*), but the more complex fault rupture pattern shown in Fig. 3 and in particular the relative minimum in fault slip right in the vicinity of the subducted Simbo transform suggest that an alternative mechanism, other than subduction of the bathymetry feature along the Simbo fault, may be needed to account for the uplift pattern.

Models of uplift driven by the observed pattern of coseismic slip show an increase in local uplift of >30% in that region (*15*). Similarly, the localization of maximum tsunami run-ups in that region (*3*, *4*) may represent the amplifying effects of the localized uplift (if coseismic) and/or reflect a constructive interference of waves produced by the two distinct patches of moment release. The lack of near-trench islands elsewhere along the margin hampers our ability to assess whether the uplift and tsunami run-ups observed on Ranongga are typical along the rupture zone. The existence of Ranongga (and associated islands) and the longer-term patterns of rapid uplift, >3 mm/year in the Holocene (*8*), for nearby islands implies that this region represents a relative maximum in near-trench uplift. As shown schematically in Fig. 4, under the assumption that this event represents an upper plate deformation case, our rupture model for the 2007 event indicates that this rapid uplift is a region of local along-arc convergence within the Pacific forearc between that overlying the southeastern rupture patch and the forearc overlying the northwestern rupture zone. This complex rupture pattern coupled with an upper plate–dominated deformation regime increases the seismic hazard in such areas.

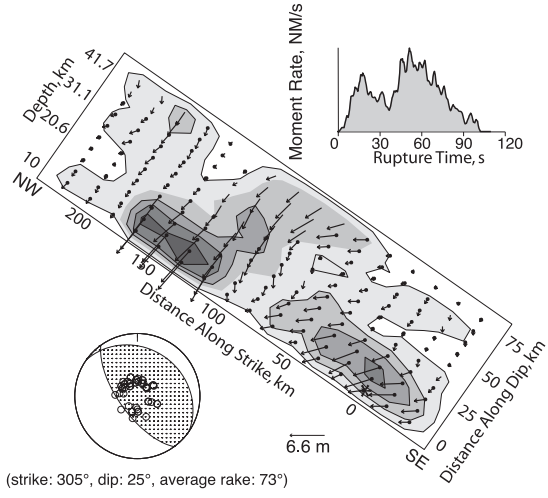

Fig. 3. Summary of the finite slip model for the mainshock obtained from inversion of *P* and *SH* waves. The model shows a source focal mechanism for the average fault orientation; the rupture surface with slip vectors indicating the sense of motion of the PaP relative to the SWP and AuP, with 1-m slip contour intervals; and the moment rate function, which indicates seismic energy release as a function of time. The seismic moment estimate, M_o, gives M_w = 8.1. The rupture velocity assumed in the inversion, V_r, is 2.5 km/s.

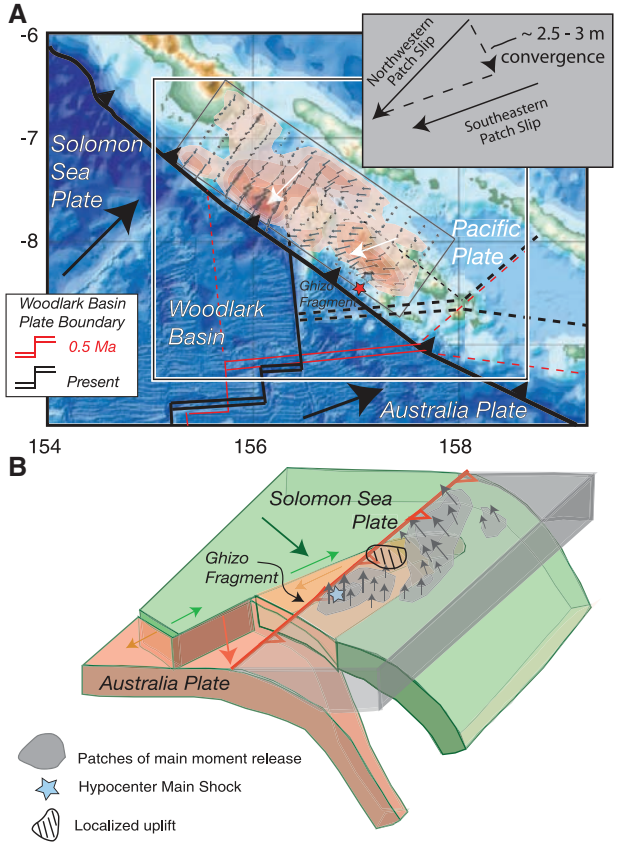

Fig. 4. Comparison of the earthquake slip model with the plate tectonic setting of the region. (**A**) Map view of the rupture model, which spans the region from the subducted (extinct) Woodlark spreading center to the initial location (at 0.5 Ma) of the Simbo transform triple junction. Inset shows kinematic relations between the slip along the two main patches of moment release, resulting in approximately 2.5 to 3.0 m of shortening within the overriding Pacific plate in the region of maximum observed uplift. (**B**) Three-dimensional view of rupture along the subduction interface. Coseismic slip on the southern patch of moment release suggests that region is fully connected to the Australia plate. Slip within the shallow northwestern patch suggests SWP affinities. The location of expected intraplate shortening during the coseismic slip within the Pacific plate is shown.

References and Notes

1. U. S. Geological Survey, http://earthquake.usgs.gov/eqcenter/eqinthenews/2007/us2007aqbk/ (2007).
2. F. W. Taylor *et al.*, *Nat. Geosci.* **1**, 253 (2008).
3. B. G. McAdoo *et al.*, *Eos Trans. AGU* **89**, 169 (2008).
4. H. M. Fritz, N. Kalligeris, *Geophys. Res. Lett.* **35**, L01607 (2008).
5. G. Ekström, M. Nettles, http://neic.usgs.gov/neis/eq_depot/2007/eq_070401_aqbk/neic_aqbk_hrv.html (2007).
6. C. Ji, http://earthquake.usgs.gov/eqcenter/eqinthenews/2007/us2007aqbk/finite_fault.php (2007).
7. T. Lay, H. Kanamori, *Phys. Earth Planet. Inter.* **21**, 283 (1980).
8. P. Mann, F. W. Taylor, M. B. Lagoe, A. Quarles, G. Burr, *Tectonophysics* **295**, 259 (1998).
9. K. A. W. Crook, B. Taylor, *Mar. Geophys. Lett.* **16**, 65 (1994).
10. C. J. Ammon, A. A. Velasco, T. Lay, *Geophys. Res. Lett.* **33**, L14314 10.1029/2006GL026303 (2006).
11. Additional details of the processing steps are available as supporting material on *Science* Online.
12. M. Kikuchi, H. Kanamori, www.eri.u-tokyo.ac.jp/ETAL/KIKUCHI/ (2003).
13. P. Tregoning, F. Tan, J. Gilliland, H. McQueen, K. Lambeck, *Geophys. Res. Lett.* **25**, 3627 (1998).
14. M. A. Fisher *et al.*, *Sci. Tsunami Hazards* **26**, 3 (2007).

15. Simple boundary element models using the average slip in the two main patches of the finite fault model produce a pattern of localized uplift in the region of convergence between the two slip domains that is >30% larger than at comparable distances from the trench along-strike. The lack of uplift and other slip observations away from the exposed islands preclude more detailed modeling at present.
16. A. M. Dziewonski, D. L. Anderson, *Phys. Earth Planet. Inter.* **25**, 297 (1981).
17. P. Tregoning *et al.*, *J. Geophys. Res.* **103**, 12181 (1998).
18. The directivity parameter, $\Gamma = \cos(\phi_{sta} - \phi_{rup})/c$, where ϕ_{sta} is the station azimuth, ϕ_{rup} is a unilateral rupture azimuth, and c is a reference phase velocity [c is chosen as 4.0 km/s, the phase velocity for 80-s-period Rayleigh waves for model PREM (*16*)].
19. The Incorporated Research Institutions for Seismology data management center provided the broadband seismic data. We thank C. Biryol and S. L. Beck for sharing a preprint manuscript and H. Kanamori for discussions about surface wave STFs and slip inversions. This work was supported in part by NSF under grant EAR0635570 (T.L.). We thank three anonymous reviewers for comments on the manuscript.

Supporting Online Material

www.sciencemag.org/cgi/content/full/324/5924/226/DC1
Methods
Figs. S1 to S11
Table S1
References

21 October 2008; accepted 26 February 2009
10.1126/science.1167476

Curved Plasma Channel Generation Using Ultraintense Airy Beams

Pavel Polynkin,[1]* Miroslav Kolesik,[1] Jerome V. Moloney,[1,2] Georgios A. Siviloglou,[3] Demetrios N. Christodoulides[3]

Plasma channel generation (or filamentation) using ultraintense laser pulses in dielectric media has a wide spectrum of applications, ranging from remote sensing to terahertz generation to lightning control. So far, laser filamentation has been triggered with the use of ultrafast pulses with axially symmetric spatial beam profiles, thereby generating straight filaments. We report the experimental observation of curved plasma channels generated in air using femtosecond Airy beams. In this unusual propagation regime, the tightly confined main intensity feature of the axially nonsymmetric laser beam propagates along a bent trajectory, leaving a curved plasma channel behind. Secondary channels bifurcate from the primary bent channel at several locations along the beam path. The broadband radiation emanating from different longitudinal sections of the curved filament propagates along angularly resolved trajectories.

The initial observation of plasma channel generation by intense femtosecond laser pulses in air (*1*) paved the way for a series of fundamental studies in the field of extreme nonlinear optics of gaseous media. Continued interest in the subject is fueled by various potential applications such as remote spectroscopy (*2*), generation of terahertz waves (*3*, *4*), compression of ultrashort laser pulses down to few optical cycles (*5*), and atmospheric science (*6*).

During propagation of an ultraintense and ultrashort laser pulse in a transparent gaseous medium, the defocusing effect of the plasma generated via multiphoton ionization prevents the beam from the self-focusing collapse to a singularity. The hot core of the beam, composed of the high-intensity laser field and the generated plasma, is referred to as the filament. Filaments are typically ~100 μm in diameter and exhibit self-guided, subdiffractive propagation over long distances (*7*–*9*).

One of the important attributes of laser-induced filaments is the forward emission of broadband light, the very property that enables various remote-spectroscopy applications (*2*). This so-called conical emission carries information concerning pulse dynamics, which can be deduced by analyzing the associated angularly resolved spectra in the far field (*10*).

In early studies of femtosecond laser filamentation initiated by ultrashort pulses with Gaussian (*1*) or flat-top (*11*) spatial beam profiles or more complex waveforms such as Bessel (*12*, *13*) and hollow ring beams (*14*), the beams were axially symmetric. Consequently, the plasma channels were always generated along straight lines. Analysis of the conical radiation emanating from straight filaments is complicated by the fact that emissions originating from different longitudinal sections of the beam overlap in the observation plane.

In this study, we used femtosecond pulses with the transverse spatial beam profile in the form of a two-dimensional (2D) Airy function, the so-called Airy beams (*15*, *16*), for the initiation of filamentation. Generation of Airy beams relies on the fact that the Airy function $\mathrm{Ai}(x/x_0)$ and the complex exponential $\exp[i(\beta K)^3/3]$ form a Fourier transform pair, where x and K are conjugate variables and x_0 and β are appropriate scale factors. Thus a plane wave can be converted into an Airy beam by applying a cubic phase modulation followed by a spatial Fourier transformation through focusing with a lens (*15*). Airy beams are not axially symmetric and exhibit the following two unusual characteristics: (i) They remain approximately diffraction-free. (ii) Their main intensity features tend to freely self-bend (or transversely accelerate) during propagation (*15*–*18*). In fact, these beams follow parabolic trajectories in a way analogous to the ballistics of projectiles moving under the action of gravity (*17*). On the other hand, the "center of gravity" of an Airy beam moves along a straight path, in agreement with Ehrenfest's momentum theorem (*17*, *19*). In principle, Airy wave packets can be synthesized simultaneously in both space and time resulting in nondispersive and spatially localized temporal waves or optical bullets that are impervious to both dispersion and diffraction (*16*, *20*).

When intense femtosecond Airy beams are used for initiation of the filamentation, an unusual propagation regime results, in which the binding strength between the filamented beam core and its remaining quasi-linear part can be manipulated by varying the transverse acceleration of the Airy pattern. The generated plasma channel is curved,

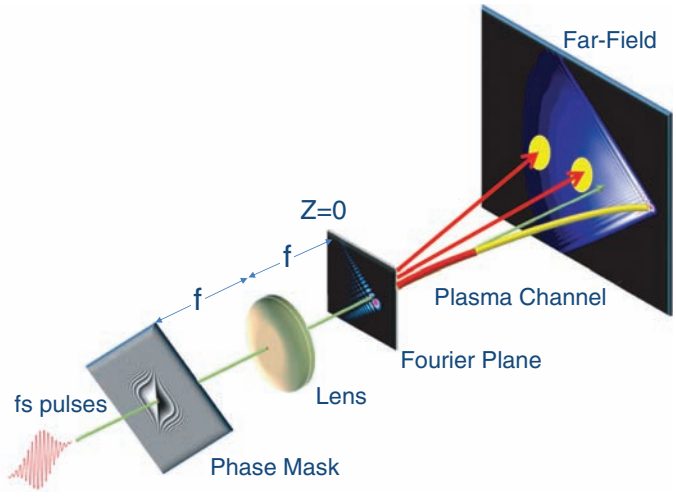

Fig. 1. Experimental setup. The continuous wave visible laser beam that we used as a spatial reference has a much smaller size than that of the phase mask. The reference beam experiences a negligible wavefront modulation and propagates along a straight line.

[1]College of Optical Sciences, University of Arizona, Tucson, AZ 85721, USA. [2]Department of Mathematics, University of Arizona, Tucson, AZ 85721, USA. [3]Center for Research and Education in Optics and Lasers–College of Optics and Photonics, University of Central Florida, Orlando, FL 32816, USA.

*To whom correspondence should be addressed. E-mail: ppolynkin@optics.arizona.edu

and such an arrangement acts as a streak camera by projecting the broadband emission from different longitudinal sections of the filament along angularly separated paths, resulting in the spatial separation of this emission in the far field.

In the experimental setup (Fig. 1), 35-fs laser pulses are generated by a multistage Ti:sapphire system having a clean Gaussian spatial mode profile. The laser output is passed through a transparent phase mask that imposes a 2D cubic phase pattern onto the beam. This wavefront is subsequently focused, and the spatial Fourier image of the field is formed at the focal plane of the lens. The transverse dimension of the resulting Airy beam can be scaled, and the corresponding acceleration can be varied with lenses that have different focal lengths.

To simulate beam propagation numerically, we used a pulse propagator code based on the unidirectional pulse propagation equation (*21*). The model used accounts for linear diffraction, group velocity dispersion, and Kerr effect, as well as for plasma generation via multiphoton ionization and the associated beam defocusing.

The experimentally measured parabolic trajectory of the dominant intensity feature of the beam is shown for two different focusing lenses (Fig. 2A). The beam deflection with respect to a straight reference beam propagating along the optical axis is plotted as a function of the propagation distance. From the scaling properties of Airy beams, the lens with shorter focal length yields a faster self-deflection rate (as expected), and the ratio of these two accelerations is approximately equal to the inverse ratio of the two focal lengths cubed.

We consider only the $f = 75$ cm case (here, f is the focal length of the lens) where the transverse acceleration is more pronounced. The plasma density along the beam path was measured by a capacitor-based plasma probe (*12*) with a longitudinal resolution of 5 mm (Fig. 2B). It is evident that the generated plasma channel remains longitudinally continuous (within the spatial resolution of the probe) for all three values of the pulse energy. The plasma channel starts to form before the Fourier plane, and the length of the channel grows with increasing pulse energy. For comparison, the plasma density generated from the filamentation of the corresponding Gaussian beam (when the phase mask is removed) is also shown. In this latter case, the generated plasma is more dense, but the plasma channel is shorter compared to that generated

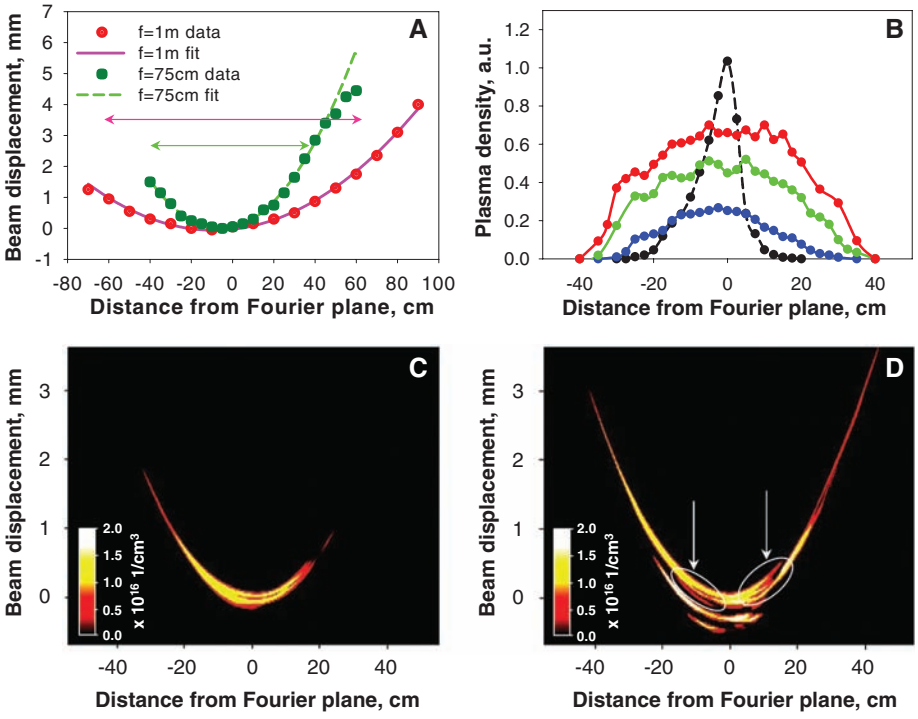

Fig. 2. (**A**) Deflection of a femtosecond Airy beam with 5-mJ pulse energy for two different focusing lenses with focal lengths equal to 75 cm and 1 m. Fitting the data with parabolas yields the beam acceleration parameters 1.3×10^{-3} mm/cm^2 and 4.0×10^{-4} mm/cm^2 for lenses with $f = 75$ cm and 1 m, respectively. Horizontal arrows show the approximate extent of the generated plasma channels in these two cases. (**B**) Linear plasma density along the filament for $f = 75$ cm focusing and different pulse energies: 5 mJ (blue), 10 mJ (green), and 15 mJ (red). The black dashed curve shows plasma density (scaled down by a factor of 3) with the phase mask removed at 10-mJ pulse energy. (**C**) Results of numerical simulations for the peak free-electron density in plane of curvature of the Airy beam for 5-mJ pulses. The generated plasma channel is continuous and smooth. (**D**) Same as in (C) but for 10-mJ pulses. Secondary lobes of the Airy beam start generating their own plasma channels, and the main channel develops bifurcations along the propagation path. Locations of the two most pronounced bifurcations are indicated with arrows.

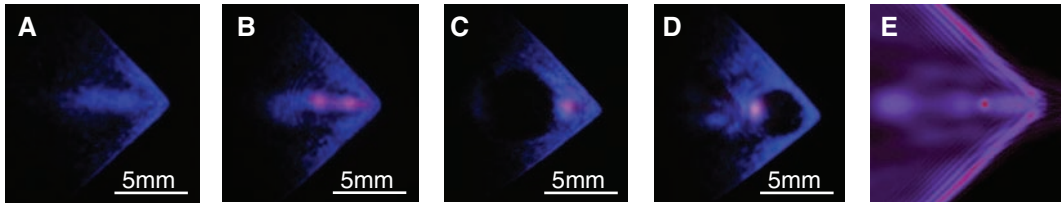

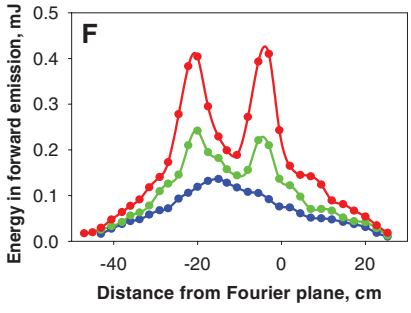

Fig. 3. (**A** to **D**) Photographs of the far-field emission patterns at different pulse energies. The forward emission pattern is elliptical for 5-mJ pulses (A) and breaks into two spots for higher-energy pulses [10 mJ, (B)]. Each of the two spots can be selectively blocked by masking the tip of the Airy beam at $z = -20$ cm (C) and $z = 0$ (D). (**E**) Numerically simulated far-field emission pattern for 10-mJ pulses showing breakup of the forward emission into multiple isolated spots. (**F**) Intensity distribution of the forward emission along the filament, for different values of pulse energy: 5 mJ (blue), 7.5 mJ (green), and 10 mJ (red). At energies above 5 mJ, the distribution develops two peaks that are consistent with two spots in the photographs of emission patterns.

by an Airy beam of the same transverse size and pulse energy. The generation of extended filaments by Airy beams is a direct consequence of their diffraction-free nature.

In Fig. 2, C and D, we show simulation results for the plasma density generated by the accelerating beam for different values of pulse energy. The color-coded plots show the peak free electron density in the plane of the curved laser beam. According to these simulations, above a certain pulse-energy threshold, the continuous curved plasma channel develops bifurcations or split-off channels. The locations of these bifurcations are indicated by white arrows in Fig. 2D. The split-off channels do not extend far and die out without the support of the accelerating beam. In addition, at high energies, the secondary lobes of the Airy beam generate their own local plasma channels that are weaker and shorter than the primary channel generated by the dominant lobe of the beam.

According to the dynamic spatial replenishment theory (*7*), the length of a plasma channel approximately scales with the extent of the linear focus zone of the laser beam. For Airy beams generated from Gaussian beams via cubic phase modulation and focusing, the distance from the focal plane of the lens over which the peak intensity drops to the exp(–2) level can be estimated by $z_0 \approx 2.8\,\Phi_{tot}^{1/3} W_A^2/\lambda$, where Φ_{tot} is the total phase imposed by the cubic phase mask across the full exp(–2) intensity width of the incident Gaussian beam, W_A is the full width at half maximum (FWHM) of the main lobe of the generated Airy pattern at the focal plane of the lens, and λ is the optical wavelength (*22*). The length of the generated plasma channel can be roughly estimated as twice this distance ($2z_0$). The transverse deflection Δ of the dominant lobe of the beam as a function of distance z is approximately described by $\Delta(z) = 0.037\,\lambda^2 z^2/W_A^3$. In the experiment, $\Phi_{tot} \approx 180$ rad, $W_A = 132$ μm, and the center wavelength of the laser source is 0.8 μm. With these parameters, the total length of the generated plasma channel is estimated to be $2z_0 \approx 69$ cm, and in this case the beam acceleration rate is $\Delta(z)/z^2 \approx 1.04 \times 10^{-3}$ mm/cm^2. These values are in good agreement with the experimental data and simulations shown in Fig. 2. Note that an equivalent Gaussian beam with FWHM equal to W_A would decay to the exp(–2) level, due to diffraction, after propagating a distance of about one third of z_0.

Photographs of the beam along with the forward emission from the generated filament (Fig. 3, A to D) were taken on a weakly fluorescent screen placed 50 cm away from the Fourier plane, shortly after the plasma channel ceased. At this distance, the beam pattern differs substantially from a 2D Airy function because of both the finite beam size and distortions resulting from filamentation. The forward emission from different longitudinal segments of the filament is spatially resolved along the horizontal direction. At a low pulse energy (5 mJ; Fig. 3A), the pattern of emission is a horizontal ellipse, indicative of a continuous bent plasma channel. As the energy is increased (10 mJ; Fig. 3B), the far-field emission pattern breaks into two spots. Because of the self-healing properties of Airy beams (*23*, *24*), each spot can be selectively blocked without affecting the other one by masking the tip of the Airy pattern at an appropriate location along the propagation direction. In other words, the Airy pattern can regenerate itself during propagation, even if a portion of it has been blocked.

Numerical simulations qualitatively reproduce the observed emission pattern broken into multiple spots at high pulse energies (Fig. 3E).

The energy distribution of the forward emission by the filament (Fig. 3F) was recorded by measuring the pulse energy passing through a 5-mm circular aperture placed 3 m after the Fourier plane. The aperture's position is traced to the exact location along the plasma channel from which the forward emission originated, as schematically shown in Fig. 1. What facilitates this mapping is the fact that the light beam and the associated plasma channel self-bend along a predictable trajectory. The transition from the continuous emission at low pulse energies to the lumped emission into well-defined spots at high energies is evident. This type of diagnostics is impossible with standard axially symmetric optical beams (producing straight plasma channels) because the emissions from different longitudinal sections of the filament would overlap in the far field.

The data shown in Fig. 3F is consistent with the results of the plasma-density simulations that show the formation of two secondary filaments that branch out from the primary filament at high pulse energy. These split-off filaments leave their marks in the spatially resolved forward emission.

The above experimental and numerical data are in agreement with the analysis of burn patterns on an aluminum foil taken at different locations along the beam path. At a low pulse energy (5 mJ; Fig. 4, A to C), no apparent satellite beam develops in the transverse beam plane. For a higher energy (10 mJ; Fig. 4, D to F), a satellite beam develops, and at z = 15 cm, this satellite lags the accelerating primary beam by ~1 mm. This distance is much larger than the transverse separation between the lobes of the Airy beam in the filamentation zone, therefore the satellite cannot be produced by the beam's secondary lobes. Instead, the satellite spot is most likely produced by the forward radiation from a secondary filament that has bifurcated from the primary curved filament. The 1-mm distance between the satellite spot and the dominant lobe of the beam at z = 15 cm is consistent with the data on the angularly resolved forward emission shown in Fig. 3F, as well as with the simulation results of Fig. 2D that

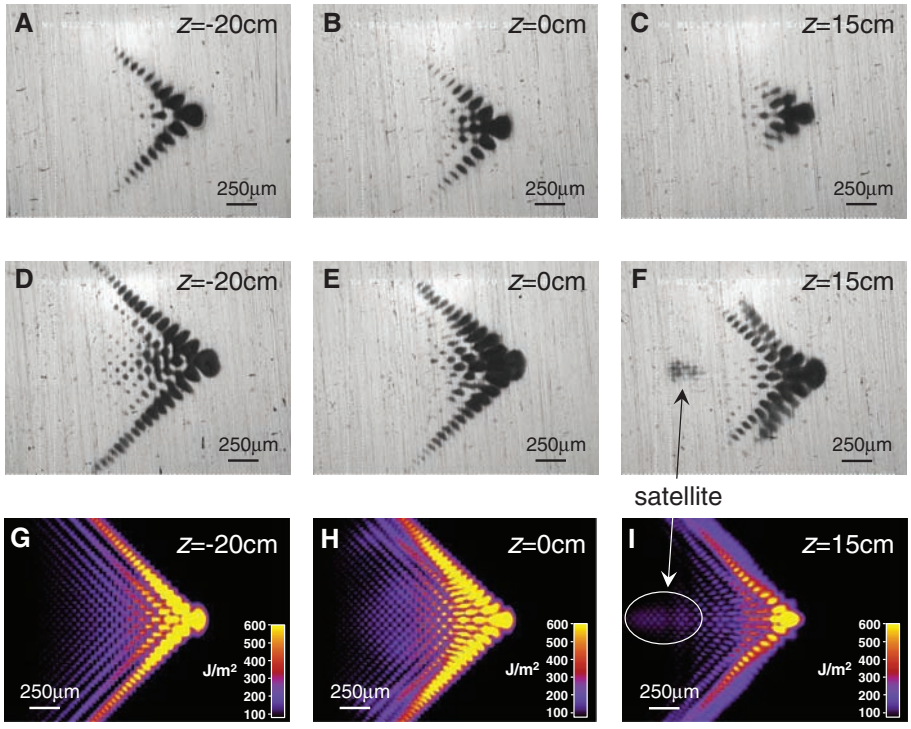

Fig. 4. Near-field beam patterns at different locations along the propagation direction. (**A** to **C**) Burn patterns on an aluminum foil for 5-mJ pulses. No apparent satellite is formed in the transverse plane during propagation. (**D** to **F**) Same as in (A) to (C) but for 10-mJ pulses. The beam undergoes a nonlinear reshaping, and a satellite spot appears that is indicated by the arrow in image F. (**G** to **I**) Numerically simulated near-field intensity profiles for 10-mJ pulses. Both the whisker-shaped ghost beam and the faint satellite are visible in (I).

shows the first branching-off event occurring at $z \approx -20$ cm. In both low- and high-energy cases, a complex nonlinear reshaping of the Airy wave packet takes place in which the high-intensity beam core develops a whiskerlike ghost beam that exhibits slightly faster acceleration compared to the primary Airy beam. The ghost beam is clearly visible in the high-intensity case. The beam reshaping features are well reproduced by the simulations that show both the whiskerlike structure and the faint satellite developing on propagation (Fig. 4, G to I).

The above observations suggest that the dominant lobe of the Airy beam acts as a "light bullet," an intense concentration of electromagnetic energy that travels along a curved trajectory and leaves a bent plasma channel behind. This wave packet is ~130 μm in diameter, 10 μm long (corresponding to the 35-fs-long pulse), and carries ~30% of the total energy of the laser pulse. Under these conditions, the wave packet's trajectory deviates from a straight line by over 2 mm, which is much larger than its size in both the transverse and longitudinal dimensions. For high pulse energies, secondary bullets bifurcate from the primary one but they quickly die out. The highly nonlinear propagation regime of the intense femtosecond Airy wave packet resembles that of a spatio-temporal soliton wave. What makes it markedly different is the fact that the Airy wave packet propagates along a curved trajectory, whereas known solitons in uniform media propagate along straight paths.

References and Notes

1. A. Braun *et al*., *Opt. Lett.* **20**, 73 (1995).
2. Q. Luo *et al*., *Appl. Phys. B* **82**, 105 (2006).
3. A. Proulx, A. Talebpour, S. Petit, S. L. Chin, *Opt. Commun.* **174**, 305 (2000).
4. C. D'Amico *et al*., *Phys. Rev. Lett.* **98**, 235002 (2007).
5. C. P. Hauri *et al*., *Appl. Phys. B* **79**, 673 (2004).
6. J. Kasparian *et al*., *Opt. Express* **16**, 5757 (2008).
7. M. Mlejnek, E. M. Wright, J. V. Moloney, *Opt. Lett.* **23**, 382 (1998).
8. J. Kasparian *et al*., *Science* **301**, 61 (2003).
9. A. Couairon, A. Mysyrowicz, *Phys. Rep.* **441**, 47 (2007).
10. D. Faccio *et al*., *Phys. Rev. Lett.* **96**, 193901 (2006).
11. S. Tzortzakis *et al*., *Opt. Lett.* **25**, 1270 (2000).
12. P. Polynkin *et al*., *Opt. Express* **16**, 15733 (2008).
13. S. Akturk, B. Zhou, M. Franco, A. Couairon, A. Mysyrowicz, *Opt. Commun.* **282**, 129 (2009).
14. M. Châteauneuf, S. Payeur, J. Dubois, J.-C. Kieffer, *Appl. Phys. Lett.* **92**, 091104 (2008).
15. G. A. Siviloglou, J. Broky, A. Dogariu, D. N. Christodoulides, *Phys. Rev. Lett.* **99**, 213901 (2007).
16. G. A. Siviloglou, D. N. Christodoulides, *Opt. Lett.* **32**, 979 (2007).
17. G. A. Siviloglou, J. Broky, A. Dogariu, D. N. Christodoulides, *Opt. Lett.* **33**, 207 (2008).
18. M. V. Berry, N. L. Balazs, *Am. J. Phys.* **47**, 264 (1979).
19. I. M. Besieris, A. M. Shaarawi, *Opt. Lett.* **32**, 2447 (2007).
20. P. Saari, *Opt. Express* **16**, 10303 (2008).
21. M. Kolesik, J. V. Moloney, M. Mlejnek, *Phys. Rev. Lett.* **89**, 283902 (2002).
22. See supporting material on *Science* Online.
23. J. Broky, G. A. Siviloglou, A. Dogariu, D. N. Christodoulides, *Opt. Express* **16**, 12880 (2008).
24. J. Baumgartl, M. Mazilu, K. Dholakia, *Nat. Photonics* **2**, 675 (2008).

25. This work was supported by the U.S. Air Force Office of Scientific Research through grants FA9550-07-1-0010 and FA9550-07-1-0256. The contribution of G.A.S. and D.N.C. was partially supported by Lockheed Martin Corporation. We thank T.-M. O. Crust for stimulating discussions and D. Hansen and T. Milster for fabricating cubic phase masks used in the experiments.

Supporting Online Material

www.sciencemag.org/cgi/content/full/324/5924/229/DC1
Materials and Methods
SOM Text
References

9 December 2008; accepted 23 February 2009
10.1126/science.1169544

Solar Power Wires Based on Organic Photovoltaic Materials

Michael R. Lee, Robert D. Eckert, Karen Forberich, Gilles Dennler, Christoph J. Brabec, Russell A. Gaudiana*

Organic photovoltaics in a flexible wire format has potential advantages that are described in this paper. A wire format requires long-distance transport of current that can be achieved only with conventional metals, thus eliminating the use of transparent oxide semiconductors. A phase-separated, photovoltaic layer, comprising a conducting polymer and a fullerene derivative, is coated onto a thin metal wire. A second wire, coated with a silver film, serving as the counter electrode, is wrapped around the first wire. Both wires are encased in a transparent polymer cladding. Incident light is focused by the cladding onto to the photovoltaic layer even when it is completely shadowed by the counter electrode. Efficiency values of the wires range from 2.79% to 3.27%.

The use of organic and hybrid solar cells, based on nanostructured bulk heterojunction composites, represents a general approach toward flexible solar cells with reduced costs and size (*1*–*8*). The photoactive layer, as reported by Sariciftci *et al*. (*9*–*11*), consists of a conducting polymer and a solubilized fullerene derivative PCBM [(6,6)-phenyl-C_{61} butyric acid methyl ester]. These components, which are for the most part insoluble in one another, can be dissolved in a mutual solvent. When the resulting homogenous solution is coated as a thin layer on a substrate, the polymer and fullerene partially phase separate into intertwined wormlike or channel-like domains. This morphology creates an extremely high surface between the polymer phase (the electron donor) and the fullerene phase (the electron acceptor) that enhances the efficiency of electron collection.

If the cross-sectional dimension of the channels is in the range from 20 to 50 nm, excitons produced in the polymer phase, upon absorption of incident radiation, diffuse to the interface with the fullerene phase. At this interface, an electron from the excited state of the polymer is transferred to the fullerene phase. The hole, or cation, on the polymer chain, from which the electron was ejected, migrates to the secondary electrode by an electron/hole exchange mechanism between neighboring polymer chains. The electron in the fullerene phase hops from one fullerene molecule to another as it moves toward the primary electrode. The electrons flow from the primary electrode to an external load and reenter the cell via the secondary electrode. At the interface with the secondary electrode, each hole residing on the polymer chain picks up an electron, which converts it back to its ground state, thus completing the electrical circuit.

Theoretical studies have shown that the most recent generation of bulk heterojunction composites has an efficiency potential >10% for single junction devices (*12*) and 15% for dual junction (tandem) devices (*13*) that absorb in two different wavelengths, e.g., the visible and the near infrared.

One of the major difficulties with organic photovoltaics (OPV) wire technology is the thinness of the photoactive coatings, which can lead to shorting between the electrodes if their surface features exceed the combined layer thickness. Consequently, a wire core is required with a smooth surface in order to eliminate shorts resulting from large surface spikes. In addition, an n-type carrier counter electrode that is both highly conductive and optically transparent has not been reported. Even indium-tin oxide coatings with a resistivity as low as 10 ohm/cm^2 cannot transport the photocurrent generated with 1 sun irradiance over more than 10 to 15 mm without incurring electrical losses. Thus, we use one wire as the primary electrode for collecting electrons generated by the active layer, and we successively coat all three of the photocell layers, for example, the electron transport layer, the photoactive layer, and the hole transport layer, in sequence on top of one another, placing layer upon layer around the core wire. Each of the coatings

Konarka Technologies, Incorporated, Lowell, MA 01852, USA.

*To whom correspondence should be addressed. E-mail: rgaudiana@konarka.com

is deposited by drawing the core wire through a series of coating cups and drying ovens. The secondary electrode, for example, the counter electrode wire, is then wrapped under tension around the coated core wire. The idea that a second wire can be used to conduct electrons, provided that it contacts the surface of the primary wire along its entire length, is a key concept for making practical PV wires. Lastly, the wires are coated with a photocurable, transparent, protective polymer cladding.

Several attempts to make PV active wires or fibers have appeared in the recent literature. The organic-based fibers suffer from poor performance, for example, <1% efficiency, because of the use of thin, coated electrodes (*14*, *15*). Double wire-based dye-sensitized titania cells suffer from cracking with only 1% elongation and slight bending (*16*–*18*).

To begin the process of building an OPV wire, a stainless steel wire, which serves as the primary electrode, is coated with the photoactive layers. Stainless steel (ultrasmooth, 316 grade) exhibits a very useful combination of properties. It has high break strength, for example, 470 g, at small diameters (100 μm) and good conductivity (resistance = 94 ohm/m). The electrons generated by the photoactive layer at any location must travel no more than 100 nm before reaching the primary electrode. However, the holes on the polymers chains of the very thin active layer and hole transport layer on the core wire (circumference = 314 μm; the diameter of the primary electrode wire is 100 μm; see Fig. 1) must travel at most 157 μm to reach any point on the outer circumference where they come into contact with the secondary wire. Hence, a coating with a resistivity of 1 kohm/cm^2 is sufficient for efficient charge collection. The use of a highly conductive poly(3,4-ethylenedioxylenethiophene) (conductivity ~ 10 S/cm) hole transport layer can easily fulfill this requirement, and its transmission is >85% in the visible region of the spectrum. The coaxially wound counter electrode is also stainless steel (370 ohm/m, 50 μm). It is coated with a thin layer of silver paste, comprising both platelike and irregularly shaped silver particles, which improves the conductivity and acts as a smoothing layer. The coating is applied to the wire by drawing it through a coating cup and then drying at 120°C, where a uniform, 25-μm-thick conductive sheath of silver

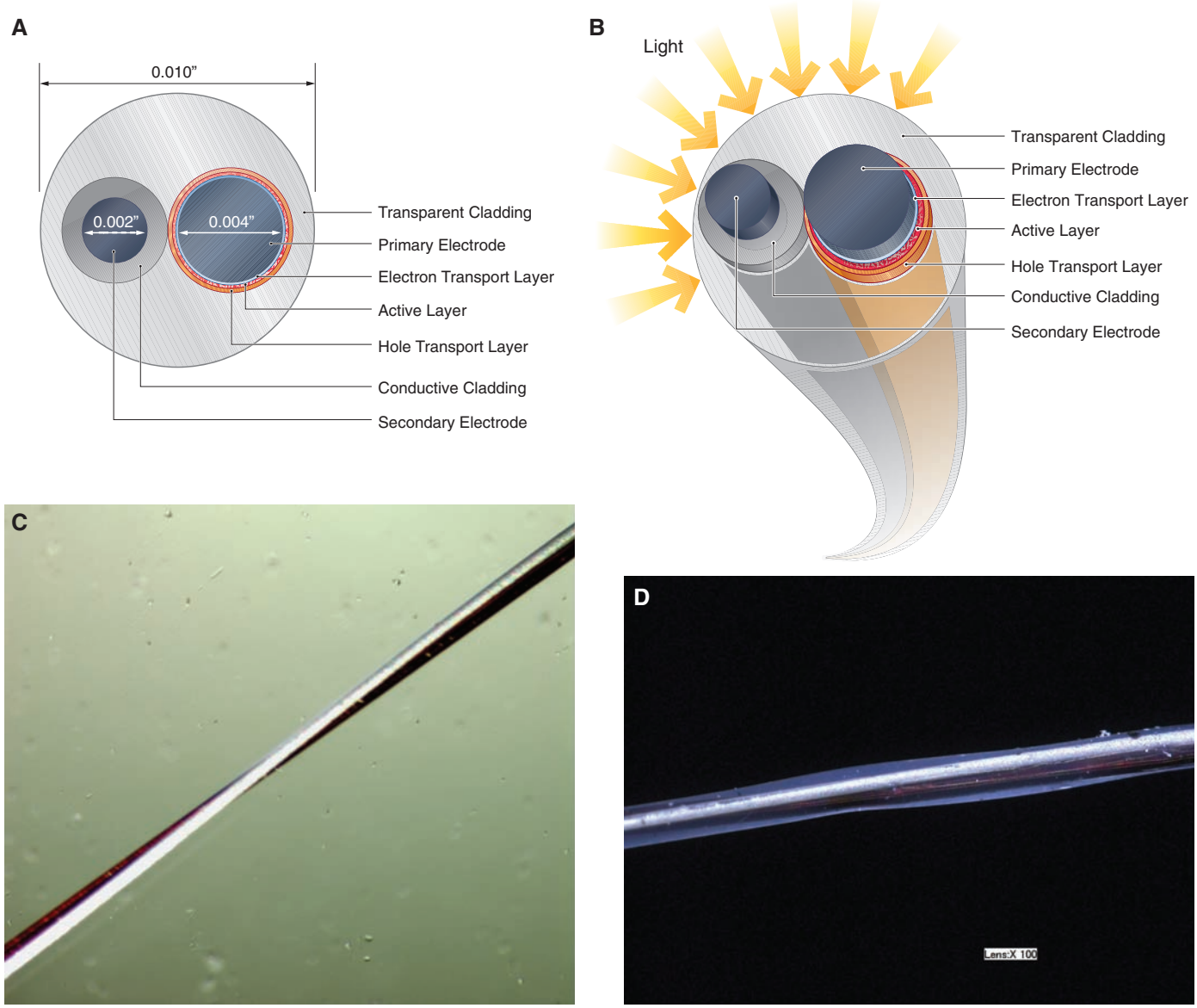

Fig. 1. (**A**) End-on schematic view of an OPV wire with the dimensions of the electrode wires and the coated layers; the photoactive layers on the primary electrode are not drawn to scale. (**B**) Schematic of a complete fiber showing the potential for shadowing by the secondary electrode. (**C**) Optical microscope picture of the silver-coated, secondary electrode wire (white) wrapped around the coated, primary electrode wire before cladding. (**D**) Digital microscope picture of a polymer-clad double wire.

forms around the wire. The resistance of a 1-m-long wire is 115 ohms, which makes it nearly as conductive as the primary wire. The wire is taken up on a spool before joining it to the primary wire.

The PV layers are coated successively on one another by means of a series of vertically aligned coating cups containing the coating solutions of each successive layer. The coating speeds range from 10 feet/min (3.048 m/min) to as high as 50 feet/min (15.24 m/min). Each coating cup has a hole in the bottom; the diameter of the hole is slightly larger than the diameter of the wire, which allows the wire to pass through without touching the walls of the orifice. In this process, the primary wire is drawn through a cup containing an isopropanol solution of tetra(*n*-butyl)titanate, after which it immediately enters an oven (90° to 100°C), which drives off the solvent. This process forms a smooth, thin, robust layer of TiO_x that serves as the electron transport layer.

Next the coated wire is drawn through a second coating cup containing a solution of the active layer, which in these examples is a 1:0.8 (weight/weight) mixture of poly(3-hexyl-2,5-thiophene) (P3HT, Merck KGaA, Darmstadt, Germany) and [(6,6)-phenyl-C_{61} butyric acid methyl ester] ($PC_{61}BM$, Solenne BV, Groningen, Netherlands). This coating is then dried in a second oven set at 120°C. The procedure is repeated for the hole transport layer, that is, the electron blocking layer, which is typically poly(3,4-ethylenedioxylenethiophene)–polystyrne sulfonate (PEDOT·PSS, Baytron P HC V4, H. C. Stark, Newton, Massachusetts) or one of its analogs (Fig. 1).

The physical and electrical contact between the two wires was accomplished by wrapping the secondary electrode wire around the coated primary wire in a precisely controlled manner by means of a rotating stage on which the spool of secondary wire is mounted. This process is similar to that used in commercial wire winding operations. One compete wrap is accomplished only every 1.25 cm. An optical microscope image (Fig. 1C) shows the white secondary electrode wire wrapped around the reddish-brown primary wire. Electrical contact is maintained because the wrapped pair was kept under tension while pulling them through a coating cup containing a solventless, liquid, photocurable epoxide. Immediately upon exiting the coating cup, the wires enter an ultraviolet irradiation chamber, which rapidly polymerizes and hardens the cladding (Fig. 1D). The process for generating photoactive, clad wires has been developed to the point where it is now capable of routinely producing several hundred feet of PV wire for any given experiment (fig. S2D).

The photovoltaic performance of the OPV wire was determined in a manner similar to that used for flat cells and modules. Lengths of wire, ranging from 5 to 30 cm cut from the large spool, were placed in a calibrated solar simulator with an irradiance of 100 mW/cm^2 at AM 1.5. Raw data from the solar simulator were corrected for the spectral mismatch of P3HT/PCBM via external quantum efficiency measurements, which resulted in ~5% deviation to the true AM 1.5 values. The instrument was also cross-calibrated by remeasuring organic solar cells that were earlier certified by the National Renewable Energy Laboratory and the National Institute of Advanced Industrial Science and Technology. The area of the wire was taken as its length multiplied by the

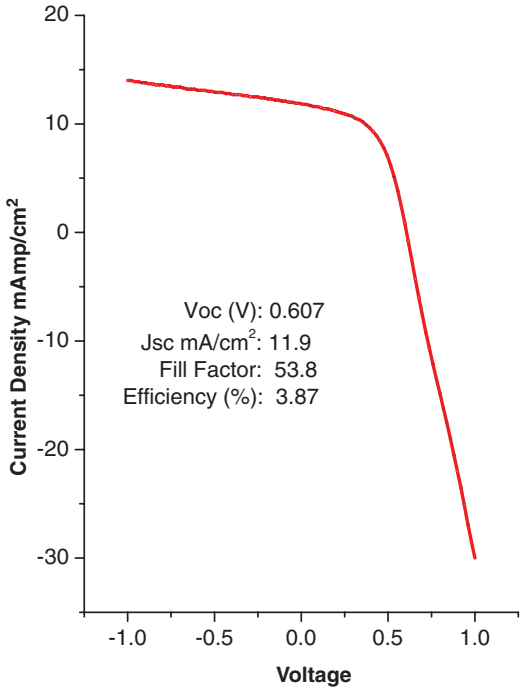

Fig. 2. *I-V* curve for a PV wire with the best performance observed thus far. J_{sc} indicates short circuit current.

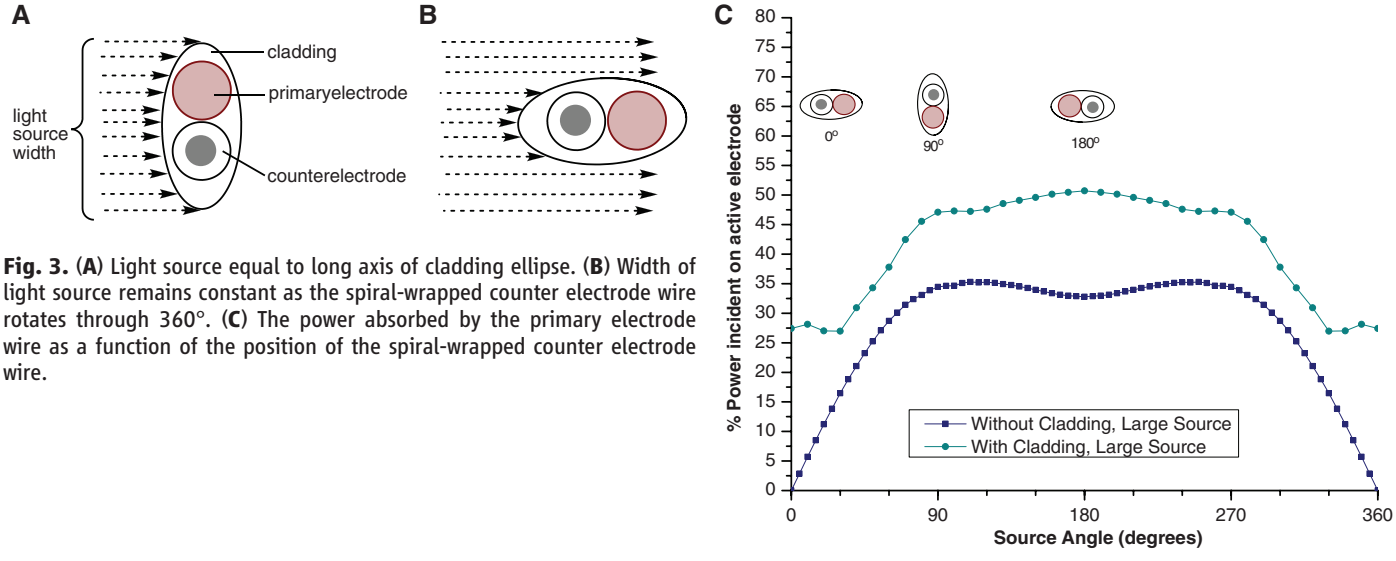

Fig. 3. (**A**) Light source equal to long axis of cladding ellipse. (**B**) Width of light source remains constant as the spiral-wrapped counter electrode wire rotates through 360°. (**C**) The power absorbed by the primary electrode wire as a function of the position of the spiral-wrapped counter electrode wire.

diameter of the primary electrode wire, for example, 100 μm, which is the projected area. No corrections are made for optical losses resulting from reflections from the curved air/cladding interface or the curvature of the primary wire or for shadowing from the spiral-wrapped secondary electrode wire, which is estimated to be 32% (Fig. 1C). This number was obtained by calculating the projection of the secondary electrode wire on the primary electrode wire at the currently used pitch. Shadowing of the primary wire may be altered by simply changing the pitch of the secondary electrode. Current-voltage (*I-V*) curves of 50 wire samples selected randomly from these long wires taken from many experimental spools exhibit an average efficiency of 2.99% (range from 2.79 to 3.27%). When the counter electrode is positioned completely behind the primary wire relative to the incident radiation, for example, no shadowing, the efficiency reaches 3.87%; an *I-V* curve of one of the latter is shown in Fig. 2.

Many of the wire cell parameters are equivalent typically to those exhibited by flat cells. In the best cell, the open circuit voltage (V_{oc}) is >0.6 mV, and the short circuit current density is 11.9 mA/cm^2. The current density in high-performance flat cells with the same materials in the active layer is usually in the range of 10 to 11 mA/cm^2; the highest reported is 11.5 mA/cm^2 (*19*). The origin of this unexpectedly high value exhibited by the wire is related to the optics of the double wire system. The efficiency of the wire is reduced because of the fill factor (FF = 53.8%), which in flat cells is typically around 60%. The lower value here is likely the result of incomplete contact between the wires.

The optical properties of the cladding along with the geometry of this coaxial wire system were examined in order to gain insight into the origin of the unexpectedly high current density. Ray tracing analysis was performed in order to evaluate the amount of light incident on the active layer coated wire when it is shadowed to various levels by the spiral-wrapped counter electrode wire (Fig. 3). The geometry of the model used for this analysis comprises two circular cylinders, representing the electrode wires, embedded in an elliptical cylinder of transparent cladding (refractive index = 1.49); this is an accurate representation of the shape of polymer cladding at any position along the wires. Light striking the primary electrode is assumed to be completely absorbed, whereas the silver-coated counter electrode acts as a diffuse reflector; the silver coating has a measured diffuse reflectivity ranging from 42 to 54% across the visible spectrum. Because the counter electrode wire is spirally wound around the primary electrode wire, shadowing of the latter ranges from complete shadowing to no shadowing. In this model, the width of the light source is held constant and set equal to the long axis of the ellipse. The estimated percent of the power absorbed by the primary electrode is a function of the position of the counter electrode.

When the counter electrode completely shadows the primary (e.g., 0°), the cladding focuses the incident light onto the primary wire, which allows it to capture 30% of the incident radiation (green line) compared with 0% without the cladding (blue line). At 180°, where the primary electrode faces the incident light source, the cladding focuses the light and improves incident power absorption by 18% compared with the unclad fiber, for example, 51% versus 33%, respectively. At angles between 0°, 180°, and 360° (especially between 100° to 140° and 220° to 260°), the power produced by the primary wire is partially from light reflected from the counter electrode. For the clad wires, this effect is evidenced by the shoulders in the same range of angles. The results clearly indicate that shadowing by the counter electrode is partially compensated by the lensing effect of the cladding and, to a lesser but nonnegligible extent, by diffuse reflection from the counter electrode.

Another approach to estimating the potential of this coaxial wire system is to determine the number of photons striking the active layer. We consider only two parameters: (i) the refractive index of the cladding and (ii) the distance of the point of incidence from the center of the fiber core. The photon count can be calculated by geometric optics; the transmission coefficients of the rays at the air-cladding interface were determined via the Fresnel formulas. We can estimate efficiency by plotting the light management factor in the photovoltaic wire as a function of the refractive index and the ratio of the primary wire diameter to the cladding diameter (Fig. 4). This factor is defined as the number of photons incident on the active layer of the wire with cladding, divided by the number of photons for a wire without cladding. When the ratio of the diameters is taken as 0.5, for example, the wire core is 100 μm, and the cladding is 200 μm; a cladding with a refractive index of 1.6 gives a light management factor of 1.42, which means that it can enhance the number of photons impinging the photoactive wire by more than 40% relative to a cladding with a refractive index of 1.4. A larger cladding with a higher refractive index could potentially capture energy that would otherwise be lost.

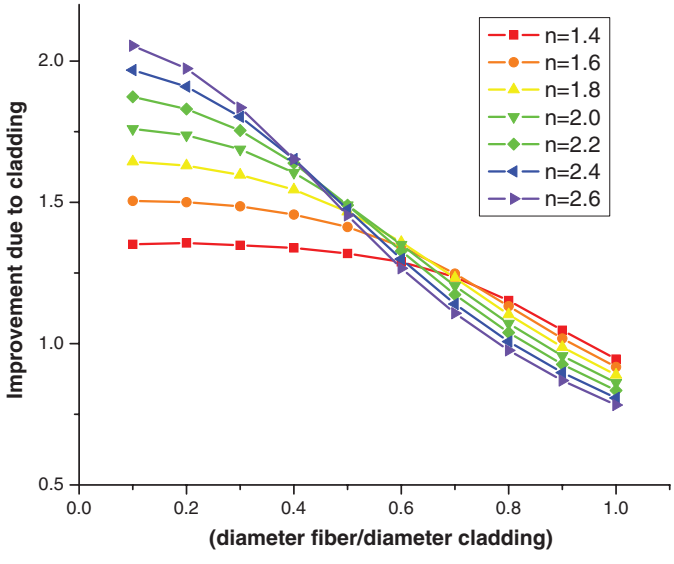

Fig. 4. Enhancement factor for the J_{sc} for different values of the refractive index of the OPV fiber and the ratio of the diameter of fiber and cladding.

References and Notes

1. G. Yu, J. Gao, J. C. Hummelen, F. Wudl, A. J. Heeger, *Science* **270**, 1789 (1995).
2. G. Yu, A. Gang, A. J. Heeger, *Synth. Met.* **85**, 1183 (1997).
3. L. Schmidt-Mende *et al.*, *Science* **293**, 1119 (2001).
4. Y. Kim *et al.*, *Nat. Mater. Lett.* **5**, 197 (2006).
5. J. Y. Kim *et al.*, *Science* **317**, 222 (2007).
6. J. Peet *et al.*, *Nat. Mater.* **6**, 497 (2007).
7. B. O'Regan, M. Graetzel, *Nature* **353**, 737 (1991).
8. W. U. Huynh, J. J. Dittmer, A. P. Alivisatos, *Science* **295**, 2425 (2002).
9. N. S. Sariciftci, L. Smilowitz, A. J. Heeger, F. Wudl, *Science* **258**, 1474 (1992).
10. N. S. Sariciftci, A. J. Heeger, U.S. Patent 5,454,880 (1994).
11. N. S. Sariciftci, A. J. Heeger, U.S. Patent 5,331,183 (1992).
12. M. C. Scharber *et al.*, *Adv. Mater.* **18**, 789 (2006).
13. G. Dennler *et al.*, *Adv. Mater.* **20**, 579 (2008).
14. J. Liu, M. A. G. Namboothiry, D. L. Carroll, *Appl. Phys. Lett.* **90**, 133515 (2007).
15. B. O'Connor, K. P. Pipe, M. Shtein, *Appl. Phys. Lett.* **92**, 193306 (2008).
16. J. Ramier *et al.*, *Thin Solid Films* **516**, 1913 (2008).
17. J. Ramier *et al.*, *Renewable Energy* **33**, 314 (2008).
18. X. Fan *et al.*, *Adv. Mater.* **20**, 592 (2008).
19. M. D. Irwin, D. B. Buchholz, A. W. Hains, R. P. H. Chang, T. J. Marks, *Proc. Natl. Acad. Sci. U.S.A.* **105**, 2783 (2008).

20. We would like to thank the ARMY Soldier Center (Natick, MA) for their support of this work. We acknowledge the following related patents, PCT/US2006/039364 and U.S. Patent 6,913,713.

Supporting Online Material

www.sciencemag.org/cgi/content/full/1168539/DC1
Materials and Methods
Figs. S1 and S2

14 November 2008; accepted 23 February 2009
Published online 12 March 2009;
10.1126/science.1168539
Include this information when citing this paper.

Running Droplets of Gallium from Evaporation of Gallium Arsenide

J. Tersoff,[1]* D. E. Jesson,[2]* W. X. Tang[2]

High-temperature annealing of gallium arsenide in vacuum causes excess evaporation of arsenic, with accumulation of gallium as liquid droplets on the surface. Using real-time in situ surface electron microscopy, we found that these droplets spontaneously run across the crystal surface. Running droplets have been seen in many systems, but they typically require special surface preparation or gradient forces. In contrast, we show that noncongruent evaporation automatically provides a driving force for running droplets. The motion is predicted and observed to slow and stop near a characteristic temperature, with the speed increasing both below and above this temperature. The same behavior is expected to occur during the evaporation of similar III-V semiconductors such as indium arsenide.

Spontaneous motion on surfaces has long held a special fascination; the "camphor dance" of a camphor particle on water was widely discussed as early as the 19th century. A number of recent papers have provided examples of spontaneous motion along with an improved understanding of the underlying mechanisms (*1*–*6*), especially for liquid droplets on solid surfaces. Thermal or chemical gradients can drive droplet motion (*5*, *6*), but the more interesting case is where the surface is uniform until the droplet breaks the symmetry by its own motion (*1*–*4*). Generally some special preparation of the system is required, and the motion may be self-limiting as the moving droplet irreversibly alters the surface.

Using in situ surface electron microscopy, we observed that running droplets of Ga occur spontaneously during annealing of gallium arsenide (GaAs) (001) in a vacuum (Langmuir evaporation), with no special surface preparation. This motion continued even after evaporation of hundreds of atomic layers of the crystal. Moreover, we show that this behavior is a general consequence of the evaporation process, resulting from the disequilibrium between the Ga droplet and the surrounding surface. There is a congruent evaporation temperature T_c where the surface and droplet are in equilibrium, near which the motion slows and eventually stops.

[1]IBM Research Division, T. J. Watson Research Center, Yorktown Heights, NY 10598, USA. [2]School of Physics, Monash University, Victoria 3800, Australia.

*To whom correspondence should be addressed. E-mail: tersoff@us.ibm.com (J.T.); david.jesson@sci.monash.edu.au (D.E.J.)

GaAs is the most widely used compound semiconductor, and evaporation is commonly used for cleaning GaAs (001) wafers (*7*, *8*). The formation of Ga droplets during evaporation has been studied for decades (*9*–*14*), and recently Ga droplets have been applied in nanofabrication via droplet epitaxy (*15*–*18*).

We annealed (001)-oriented undoped GaAs samples within our ultrahigh-vacuum surface electron microscope. Images were obtained in mirror electron microscopy (MEM) mode (*19*), which is ideally suited to imaging real-time changes in surface morphology. After sample degassing, the surface oxide was removed by flashing to 600°C and annealing at 580°C for 2 hours (*20*). Upon heating the sample to 640°C, we observed the expected formation and growth of liquid Ga droplets due to excess evaporation of As. We also observed that the Ga droplets moved laterally, which was unexpected.

An example of the initial droplet motion is shown in Fig. 1. The epitaxy-ready surface (*20*) has a slight roughness, and as the droplet moves, it leaves behind a smooth trail. The initial motion has a stick-slip character, as seen in movie S1. Motion occurs independent of sample preparation or surface roughness, and persists even after evaporation of hundreds of atomic layers of GaAs. Droplets move preferentially along the [110] direction, but equally in both directions, ruling out thermal gradient effects. The forces on a droplet derive from interfacial energies, which in turn depend on local chemical potentials (*21*, *22*). We therefore consider the thermodynamics of the GaAs surface during evaporation and how it relates to droplet motion.

The GaAs surface can be characterized by its surface Ga chemical potential μ_s. The sum $\mu_{Ga} + \mu_{As}$ is fixed by equilibrium with the GaAs crystal (*21*, *22*). In congruent evaporation at a given temperature T, μ_s finds a steady-state value where Ga and As evaporate at equal rates. With increasing T, μ_s increases and eventually reaches the Ga liquidus value μ_L for that T (*10*). This defines the upper limit T_c for congruent evaporation. Above T_c, $\mu_s > \mu_L$, so excess Ga can begin to collect as liquid droplets rather than all evaporating. These droplets are expected to stay close to equilibrium with the GaAs crystal at the liquidus value μ_L. For attachment-limited Ga transport, the surface is characterized by a uniform value of μ_s that depends on T, and $\mu_s \neq \mu_L$ except at $T = T_c$.

A Ga droplet on a planar GaAs surface is shown schematically in Fig. 2A. The net inward force per length applied to the drop at any point on the contact line is $\gamma_{ls} - \gamma_{vs}$, where γ_{vs} and γ_{ls} are the energies of the vacuum-solid and liquid-solid interfaces, respectively. (The force vector from the liquid surface tension γ_{vl} sums to zero around the contact line, and so does not contribute to the net force on the droplet.) As μ_s changes with T, so do other surface properties: the Ga coverage, the surface structure, and in particular the surface free energy. We therefore write $\gamma_{vs(s)}$ to denote the surface free energy at μ_s. The dependence of $\gamma_{vs(s)}$ and of Ga coverage on μ_s have been studied using ab initio methods (*21*, *22*).

In a symmetric situation, this inward force vector has equal magnitude around the entire perimeter, so it integrates to zero total force on the drop. However, if the droplet is displaced to the left (e.g., by a thermal fluctuation), we have the situation in Fig. 2, B and C. On the right, fresh surface is created as the interface is exposed. Because the droplet serves as the reservoir for Ga during this process, the fresh surface on the right is at μ_L, not at μ_s as on the left. We denote the corresponding surface free energy $\gamma_{vs(L)}$. Only after the droplet moves away can the exposed surface start to gain or lose net Ga by diffusion and evaporation, evolving toward the same nonequilibrium $\gamma_{vs(s)}$ as the surrounding surface.

Integrating the force vector around the perimeter, the total net force on the droplet is

$$F_{tot} = (\gamma_{vs(s)} - \gamma_{vs(L)})d \qquad (1)$$

where d is the droplet diameter. If $\gamma_{vs(s)} > \gamma_{vs(L)}$, the force is in the direction of the displacement.

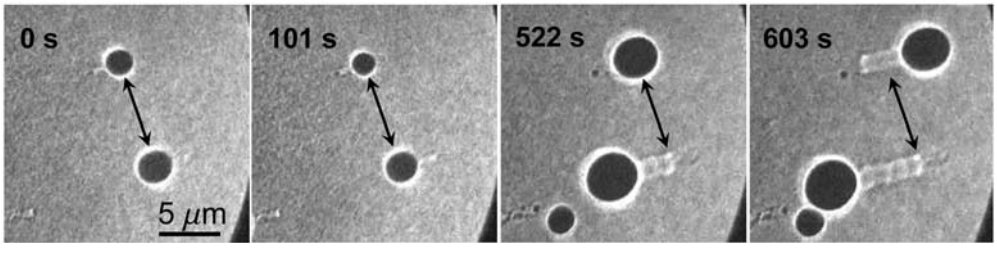

Fig. 1. MEM images (taken from movie S1) of surface dynamics of Ga droplets at 660°C. The droplet appears in MEM as a uniform dark disc somewhat larger than the actual droplet, surrounded by a concentric bright ring (*19*, *20*). The reference arrow indicates the positions of two droplets that are stationary at the beginning of the sequence. With time, droplets grow in size and begin to move, usually in [110] directions as shown here.

In this case the droplet will run freely across the surface, provided the force is large enough. But if $\gamma_{vs(s)} < \gamma_{vs(L)}$, the droplet will remain stationary. We therefore need to understand how $\gamma_{vs(s)}$ depends on temperature via μ_s.

Ahead of the moving droplet, the surface has the structure corresponding to μ_s, which has excess surface Ga density n_s (*21*, *22*). However, as this surface is covered by the drop, the reservoir for its excess Ga is the droplet at μ_L. As a result, the nonequilibrium surface free energy $\gamma_{vs(s)}$ in Eq. 1 is

$$\gamma_{vs(s)} = E_s(\mu_s) - n_s\mu_L \qquad (2)$$

where $E_s(\mu_s)$ is the energy of the surface at μ_s (*21*, *22*). Expanding to lowest order in $T - T_c$ (and correspondingly in $\mu_s - \mu_L$), we find that $\mu_s - \mu_L$ is linear in $T - T_c$ (reflecting the evaporation kinetics), and $\gamma_{vs(s)}$ is quadratic in $\mu_s - \mu_L$ (reflecting the thermodynamics). Thus, $\gamma_{vs(s)} = \gamma_{vs(L)} + \alpha(T - T_c)^2$ and

$$F_{tot} = \alpha(T - T_c)^2 d \qquad (3)$$

where the coefficient α involves both thermodynamic and kinetic properties of the surface (*20*).

This is a surprising prediction; according to Eq. 3, motion is expected at temperatures well above or well below T_c, but not very close to T_c. To test this, we measured the droplet velocity versus temperature. By first heating above T_c to form droplets, and then cooling to the desired T, we can study droplet motion even below T_c. At each T the droplet velocity is averaged over many minutes.

The results are shown in Fig. 3. There is a range of about 20°C where the droplets do not move at all over this time scale. Outside of this range the droplets move, and their average velocity increases with either increasing or decreasing temperature. Moreover, the temperature at which motion ceases is clearly set by T_c; the moving droplets at higher T grow visibly with time, whereas the moving droplets at lower T shrink visibly, as in Fig. 3A. This temperature dependence provides decisive confirmation of the unanticipated mechanism driving droplet motion here.

Phenomenologically, we can describe the time-averaged stick-slip motion as a damped response to F_{tot}, plus an effective "friction" (i.e., a force opposite to the direction of motion and independent of velocity). Then from Eq. 3 the velocity becomes

$$v \sim m\alpha(T - T_c)^2 - v_f \qquad (4)$$

where m represents the mobility (inverse damping), and v_f is the friction term. Note that $v = 0$ when $(T - T_c)^2 < v_f/m\alpha$. When the range of T is large, it becomes necessary to include cubic and higher terms in the power-law expansion about T_c (*20*).

With this simple model, we can fit the data well using Eq. 4 extended to cubic order, as shown in Fig. 3B. The fit by itself is not remarkable because we have four parameters (T_c, v_f, and the quadratic and cubic coefficients), but it confirms the validity of our interpretation. The basic prediction of $v \propto (T - T_c)^2$ captures the overall behavior, with the fitted value of T_c agreeing well with the boundary between growing and shrinking droplets. The deviations of the data from this simple picture can be understood in terms of small corrections from "friction" and from higher-order terms in the expansion about T_c.

As a further test that the behavior is intrinsic and independent of surface preparation, we have examined the behavior at a much later stage where hundreds of atomic layers of GaAs have evaporated, and no trace remains of the original surface or its preparation. The droplets move in the ±[110] directions, and more rapidly than on the initial surface, as seen in movie S2. A time sequence is shown in fig. S1. We confirmed that the droplets move more slowly near T_c than at either higher or lower temperatures. However, we were never able to arrest the motion entirely, which suggests that the friction seen on the initial surface may be associated with the slight roughness of this surface.

The roughness of the initial surface must increase its surface energy; the motion of the drop leaves behind a smoothed surface, reducing the energy. This should provide an additional roughness-derived force for motion. Indeed, on the initial surface we never saw a drop reverse direction and move onto the smoothed surface. This contrasts with the steady-state behavior after prolonged evaporation (movie S2), where droplets readily reverse direction. Apparently the roughness-derived force is strong enough to break the symmetry, but it is clearly a weak effect relative to the evaporation-derived force, because it is not strong enough by itself to overcome the friction in Eq. 4.

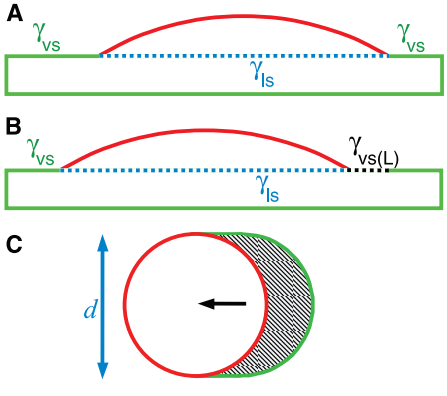

Fig. 2. Schematic of liquid droplet on planar surface. (**A**) Cross section, with surface and interface energies γ indicated. (**B**) Same after displacing droplet to the left, exposing a region with different chemical potential and hence different γ. (**C**) Top view [smaller scale than (A) and (B)]. Black arrow indicates direction of displacement, and d is the droplet diameter. Cross-hatching indicates the freshly exposed region at $\gamma_{vs(L)}$.

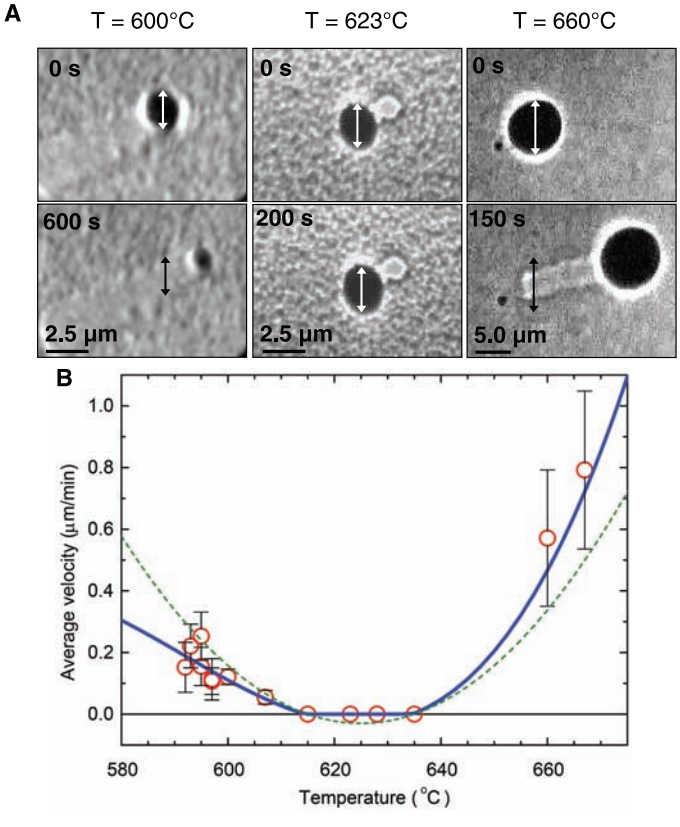

Fig. 3. Droplet motion on the epitaxy-ready GaAs (001) surface. (**A**) Image pairs at successive times for three temperatures T as indicated; the center image pair is near T_c. Arrows are reference marks for comparing position and diameter at two times. The droplet is seen to move and shrink below T_c and to move and grow above T_c. Near T_c there is no visible motion or size change. (**B**) Average velocity versus T. The solid line is the truncated-cubic fit described in the text; the dashed line is the quadratic term alone, extracted from the fit. Error bars show root-mean-square scatter of multiple measurements at the same T.

The mechanism we have described requires only a few general materials characteristics, in particular that at temperatures where a liquidus exists, the more slowly evaporating component accumulates as a liquid on the surface. Therefore, comparable behavior is expected in other III-V semiconductors such as InAs (*23*) and perhaps in many other systems. Evaporation is used in the cleaning of GaAs, and Ga droplets are central to droplet epitaxy (*15*–*18*). The intrinsic droplet motion observed here may therefore have important technological consequences and may open up new extensions for the droplet epitaxy technique.

References and Notes

1. C. D. Bain, G. D. Burnett-Hall, R. R. Montgomerie, *Nature* **372**, 414 (1994).
2. F. D. Dos Santos, T. Ondarçuhu, *Phys. Rev. Lett.* **75**, 2972 (1995).
3. A. K. Schmid, N. C. Bartelt, R. Q. Hwang, *Science* **290**, 1561 (2000).
4. Y. Sumino, N. Magome, T. Hamada, K. Yoshikawa, *Phys. Rev. Lett.* **94**, 068301 (2005).
5. M. K. Chaudhury, G. M. Whitesides, *Science* **256**, 1539 (1992).
6. K. Ichimura, S.-K. Oh, M. Nakagawa, *Science* **288**, 1624 (2000).
7. K. Iizuka *et al.*, *J. Cryst. Growth* **150**, 13 (1995).
8. N. Isomura, S. Tsukamoto, K. Iizuka, Y. Arakawa, *J. Cryst. Growth* **301-302**, 26 (2007).
9. J. R. Arthur, *J. Phys. Chem. Solids* **28**, 2257 (1967).
10. J. Y. Tsao, *Materials Fundamentals of Molecular Beam Epitaxy* (Academic Press, San Diego, CA, 1993).
11. M. Zinke-Allmang, L. C. Feldman, W. van Saarloos, *Phys. Rev. Lett.* **68**, 2358 (1992).
12. C. T. Foxon, J. A. Harvey, B. A. Joyce, *J. Phys. Chem. Solids* **34**, 1693 (1973).
13. T. D. Lowes, M. Zinke-Allmang, *J. Appl. Phys.* **73**, 4937 (1993).
14. C. Chatillon, D. Chatain, *J. Cryst. Growth* **151**, 91 (1995).
15. T. Mano *et al.*, *Nano Lett.* **5**, 425 (2005).
16. S. Huang *et al.*, *Appl. Phys. Lett.* **89**, 031921 (2006).
17. M. Yamagiwa *et al.*, *Appl. Phys. Lett.* **89**, 113115 (2006).
18. Ch. Heyn *et al.*, *Phys. Rev. B* **76**, 075317 (2007).
19. S. A. Nepijko, N. N. Sedov, G. Schönhense, *J. Microsc.* **203**, 269 (2001).
20. See supporting material on *Science* Online.
21. E. Kaxiras, Y. Bar-Yam, J. D. Joannopoulos, K. C. Pandey, *Phys. Rev. B* **35**, 9625 (1987).
22. G.-X. Qian, R. M. Martin, D. J. Chadi, *Phys. Rev. B* **38**, 7649 (1988).
23. J.-Y. Shen, C. Chatillon, *J. Cryst. Growth* **106**, 543 (1990).

24. We thank R. Mackie for technical support. Supported by Australian Research Council grants DP0556492 and DP0985290 (D.E.J., W.X.T.).

Supporting Online Material

www.sciencemag.org/cgi/content/full/324/5924/236/DC1
Materials and Methods
SOM Text
Fig. S1
Movies S1 and S2
References

9 December 2008; accepted 10 February 2009
10.1126/science.1169546

Total Synthesis of (+)-11,11'-Dideoxyverticillin A

Justin Kim, James A. Ashenhurst, Mohammad Movassaghi*

The fungal metabolite (+)-11,11'-dideoxyverticillin A, a cytotoxic alkaloid isolated from a marine *Penicillium* sp., belongs to a fascinating family of densely functionalized, stereochemically complex, and intricate dimeric epidithiodiketopiperazine natural products. Although the dimeric epidithiodiketopiperazines have been known for nearly 4 decades, none has succumbed to total synthesis. We report a concise enantioselective total synthesis of (+)-11,11'-dideoxyverticillin A via a strategy inspired by our biosynthetic hypothesis for this alkaloid. Highly stereo- and chemoselective advanced-stage tetrahydroxylation and tetrathiolation reactions, as well as a mild strategy for the introduction of the epidithiodiketopiperazine core in the final step, were developed to address this highly sensitive substructure. Our rapid functionalization of the advanced molecular framework aims to mimic plausible biosynthetic steps and offers an effective strategy for the chemical synthesis of other members of this family of alkaloids.

The fungal metabolite (+)-11,11'-dideoxyverticillin A (**1**, Fig. 1) (*1*) is a member of the epidithiodiketopiperazine alkaloids, a large family of natural products that has received substantial attention from the scientific community for its rich biological activity and complex molecular architecture (*2*–*7*). The dimeric subset of alkaloids to which the title compound belongs has been known for nearly 4 decades with the isolation of (+)-chaetocin A (**2**) (*8*) and (+)-verticillin A (**3**) (*9*). Reflective of the daunting challenges posed by molecular structures replete with sterically congested stereogenic centers and highly acid-, base-, and redox-sensitive functional groupings (*5*), no dimeric epidithiodiketopiperazine alkaloid has yet succumbed to total synthesis. Herein we describe a concise strategy for the enantioselective total synthesis of the dimeric epidithiodiketopiperazine alkaloid (+)-**1**. Our biosynthetically inspired synthesis features stereo- and chemoselective advanced-stage tetrahydroxylation and tetrathiolation reactions, providing a generalizable solution to the epidithiodiketopiperazine substructure found in the broader family of these alkaloids.

At the outset of our synthetic studies, structural similarities among members of this alkaloid family combined with Kirby's radio-labeled amino acid feeding experiments and his hypothesis for gliotoxin biosynthesis (*10*) prompted us to consider the possibility that the epidisulfides of (+)-**1** are assembled by enzymes that exploit the inherent chemistry of dimeric diketopiperazines. Our retrosynthetic analysis of (+)-**1** imitates a plausible biosynthetic sequence of events linking dimeric epidithiodiketopiperazines to common α-amino acid precursors (Fig. 2). We envisioned preparation of (+)-**1** by mild oxidation of the tetrathiol **5**, which could be accessed via stereoselective tetrathiolation of an octacyclic tetraol **6**. In contrast to a previous biosynthetic hypothesis for monomeric epidithiodiketopiperazines invoking thiolation via an N-hydroxylation–dehydration sequence (*11*), we speculated that a postdimerization C_α-hydroxylation would enable substrate-directed hemiaminal thiolation through the intermediacy of an acyliminium ion. Intermediate **7**, which we hypothesized to arise from a dimerization event, could be assembled from the readily available *cyclo*-dipeptide **8** by using the concise cobalt-mediated dimerization strategy reported from our laboratories (*12*, *13*). The imposing challenges associated with quadruple C_α-methine hydroxylation of **7** and the tetrathiolation of inter-

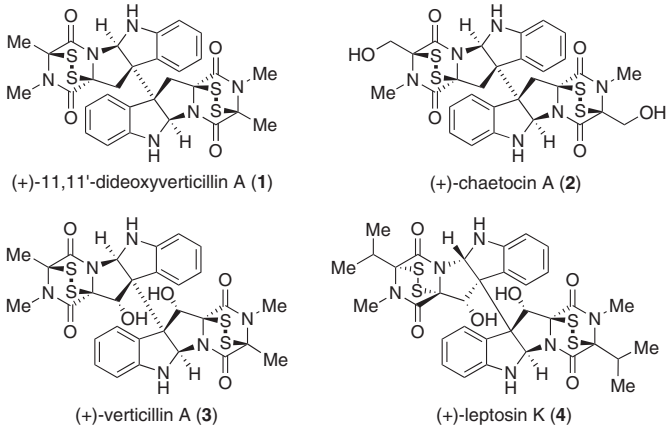

Fig. 1. The molecular structure of (+)-11,11'-dideoxyverticillin A (**1**) and representative dimeric epidithiodiketopiperazine alkaloids.

Department of Chemistry, Massachusetts Institute of Technology, Cambridge, MA 02139, USA.

*To whom correspondence should be addressed. E-mail: movassag@mit.edu

mediate **6** notwithstanding, the need for absolute and relative stereochemical control (Fig. 2) of the six tetrasubstituted carbons of (+)-**1** posed noteworthy strategic concerns. We envisioned the introduction of the C3 and the C3′ vicinal quaternary stereocenters as a prelude to stereochemical control of the four thiolated-carbon stereogenic centers of (+)-**1** in a strategy reminiscent of Seebach's self-reproduction of chirality (*14*). Such a final-stage tetrathiolation followed by immediate disulfide formation would obviate the need to mask the notoriously sensitive epidithiodiketopiperazine functional grouping in the early stages of the synthesis.

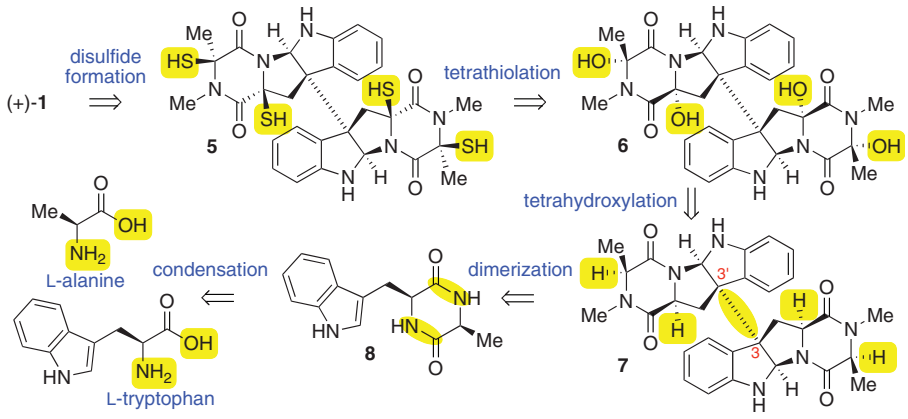

Fig. 2. Retrosynthetic analysis of (+)-11,11'-dideoxyverticillin A (**1**) based on a biosynthetic hypothesis.

The dimeric diketopiperazine (+)-**13** was assembled in six steps from commercially available amino acid derivatives (Fig. 3) [supporting online material (SOM) text]. The sequential treatment of amide (–)-**9** with trifluoroacetic acid followed by cyclization with morpholine readily afforded access to the desired *cis*-diketopiperazine (–)-**10** in 84% yield (>20 g). Exposure of *cyclo*-L-tryptophan-L-alanine (–)-**10** to molecular bromine in acetonitrile at 0°C furnished the desired monomeric tetracyclic bromide (+)-**11** in 76% isolated yield (SOM text). Treatment of tetracyclic bromide (+)-**11** with methyl iodide and potassium carbonate gave the base-sensitive dimerization precursor (+)-**12** in 77% yield (*15*). Reductive dimerization of the tertiary benzylic bro-

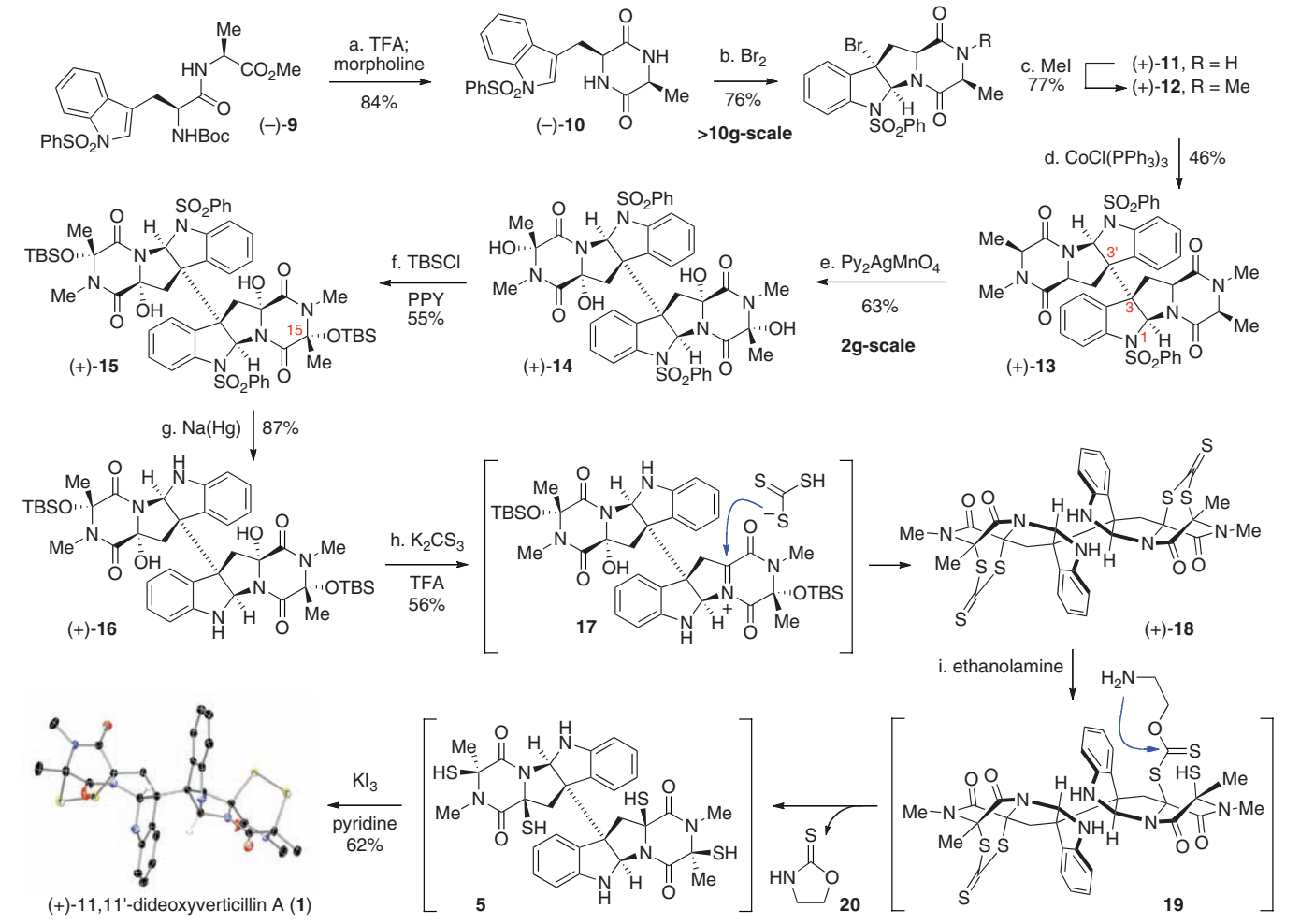

Fig. 3. Concise enantioselective total synthesis of (+)-11,11'-dideoxyverticillin A (**1**). Isolated yields are given for each step. Reaction conditions are as follows: (a) trifluoroacetic acid (TFA), dichloromethane (CH_2Cl_2), 23°C, 4 hours; *tert*-butanol (^tBuOH), morpholine, 23°C, 48 hours. (b) Br_2, acetonitrile (MeCN), 0°C, 5 min. (c) methyl iodide (MeI), K_2CO_3, acetone, 23°C, 5 days. (d) tris(triphenylphosphine)cobalt(I) chloride [$CoCl(PPh_3)_3$], acetone, 23°C, 30 min. (e) bis(pyridine)silver(I) permanganate (Py_2AgMnO_4), CH_2Cl_2, 23°C, 2 hours. (f) *tert*-butyl(chloro)dimethylsilane (TBSCl), PPY 5 mole %, triethylamine (Et_3N), *N*,*N*-dimethyl formamide (DMF), 23°C, 30 min. (g) 5% Na(Hg), NaH_2PO_4, methanol (MeOH), 23°C. (h) K_2CS_3, TFA, CH_2Cl_2, 23°C, 28 min. (i) ethanolamine, acetone, 23°C; KI_3, pyridine, CH_2Cl_2, 23°C. The thermal ellipsoid representation of synthetic (+)-**1** from x-ray crystallographic analysis is shown with most hydrogens omitted for clarity.

mide (+)-**12** with tris(triphenylphosphine)cobalt(I) chloride in acetone provided the key dimeric octacyclic intermediate (+)-**13** in 46% yield (*16*). Preference for cis-fusion on 5,5-ring systems made this an effective strategy for simultaneously securing the two vicinal C3 and C3′ quaternary stereocenters (*12*). This chemistry is amenable to multigram scale synthesis of (+)-**13** (e.g., 43% yield on 8 g scale).

Guided by our biosynthetic hypothesis for late-stage functionalization of the diketopiperazines (i.e., **7**→**5**, Fig. 2), we sought methods for C_α-oxidation of the dimeric octacycle (+)-**13**. Initially, we focused on the oxidation of the readily accessible enol tautomers or corresponding enolates of (+)-**13** (SOM text). Unfortunately, these strategies were plagued by formation of partially oxidized and diastereomeric products in addition to substantial competing decomposition. Likewise, a variety of soft-enolization and electrophilic amide activation strategies failed to provide the necessary C_α-methine oxidation. Although we ultimately developed conditions for dihydroxylation (or didehydrogenation) of a model monomeric tetracyclic diketopiperazine **21** (Fig. 4A) along with its conversion to the corresponding monomeric epidithiodiketopiperazine **23** (SOM text), none of these methodologies proved effective when applied to the more-challenging dimeric octacyclic bisdiketopiperazine (+)-**13**, likely because of additional modes of C3–C3′ bond fragmentation and/or unfavorable interactions between the tetracyclic subunits.

Careful analysis of the bond dissociation energies (*17*) involved in our successful radical-based abstraction of C_α-methines in the model tetracycle **21** (SOM text) suggested weak C_α–H bonds resulting from stabilization of the ensuing C_α-radicals in diketopiperazines. Thus, the use of mild oxidants typically reserved for hydrogen atom abstraction from formyl groups became a focus of our efforts in pursuit of an effective strategy for single-step tetrahydroxylation of dimeric octacycle (+)-**13**. After extensive experimentation, we found that the treatment of the diketopiperazine **21** with tetra-*n*-butylammonium permanganate (3.0 equiv) (*18*) in pyridine at 23°C for 2 hours provided the desired tetracyclic diol **22** in 78% yield primarily as one diastereomer. Application of these conditions to the oxidation of the more-challenging dimeric octacycle (+)-**13** resulted in 40% yield of the desired tetraol as a complex mixture of hemiaminal diastereomers. Because this tetrahydroxylation was fraught with competing epimerization of C_α-methines and incomplete oxidation leading to complex product mixtures (SOM text), we sought to refine this reaction.

Further studies revealed that bis(pyridine)-silver(I) permanganate (Py_2AgMnO_4) (*19*) oxidized dimeric octacycle (+)-**13** selectively and efficiently. Under optimal conditions, treatment of dimer (+)-**13** with Py_2AgMnO_4 (4.8 equiv) in dichloromethane at 23°C for 2 hours afforded the desired dimeric octacyclic tetraol (+)-**14** in 63% yield as a single diastereomer (Fig. 3). The high level of diastereoselection (SOM text) is consistent with a fast abstraction-rebound mechanism (*20*, *21*), as suggested by hydroxylation of the radical-clock hydantoin **24** (74%) (Fig. 4A) and x-ray diffraction analysis of tetraol (+)-**14**. Oxidation of the corresponding *cyclo*-D-Trp-L-Ala derivatives under these conditions resulted only in oxidation at the alanine C_α(L-Ala)-methines, leaving the C_α(D-Trp)-methines unchanged (SOM text). This observation, which has important consequences for the choice of natural or unnatural amino acid precursors, is attributed to a nonoptimal conformation of the C–H bond for abstraction and/or the sterically disfavored approach of the oxidant from the concave face of the 5,5-ring system.

The dimeric octacyclic tetraol (+)-**14** proved highly acid- and base-sensitive. Its treatment with Brønsted acids led to formation of tetraene **26** (Fig. 4B) (*22*), whereas its exposure to base resulted in either decomposition or conversion to hemiaminal diastereomers (SOM text). The high sensitivity of tetraol (+)-**14** to base may be attributed to reversible ring opening at the C15-aminal, allowing deleterious side reactions of the alpha-keto amide derivative **27** (Fig. 4B). Unexpectedly, even dissolution of (+)-**14** in methanol at ambient temperature led to slow decomposition.

With multigram access to dimeric octacyclic tetraol (+)-**14**, we focused on its conversion to alkaloid (+)-**1**. Removal of the benzenesulfonyl groups with sodium amalgam in methanol buffered with dibasic sodium phosphate unveiled an unstable diaminotetrahemiaminal **28** (Fig. 4C). Immediate exposure of this labile compound to condensed hydrogen sulfide at –78°C with a Lewis acid (*6*), followed by warming, resulted in formation of the corresponding tetrathiol **29** as a mixture of hemithioaminal diastereomers. Oxidation of the crude mixture of tetrathiols with potassium triiodide resulted in (+)-11,11'-dideoxyverticillin A (**1**), albeit in low overall yields (2 to 15%, three steps) from tetraol (+)-**14**.

The fragility of tetraol (+)-**14** and derivatives **28** and **29**, the poor mass balance of this capricious three-step sequence, and our preference to avoid the use of pressurized toxic hydrogen sulfide led us to seek a superior strategy for the synthesis of the epidithiodiketopiperazine substructure of this family of alkaloids. After substantial experimentation, we realized that a simple tactical conversion of the tetraol (+)-**14** to the diol (+)-**15** (Fig. 3) imparted considerable stability to this structure, consistent with prevention of an undesired diketopiperazine ring opening. The use of Fu's (*R*)-(+)-4-pyrrolidinopyridinyl(pentamethylcyclopentadienyl)-iron (PPY) catalyst (5 mole %) (*23*) was optimal

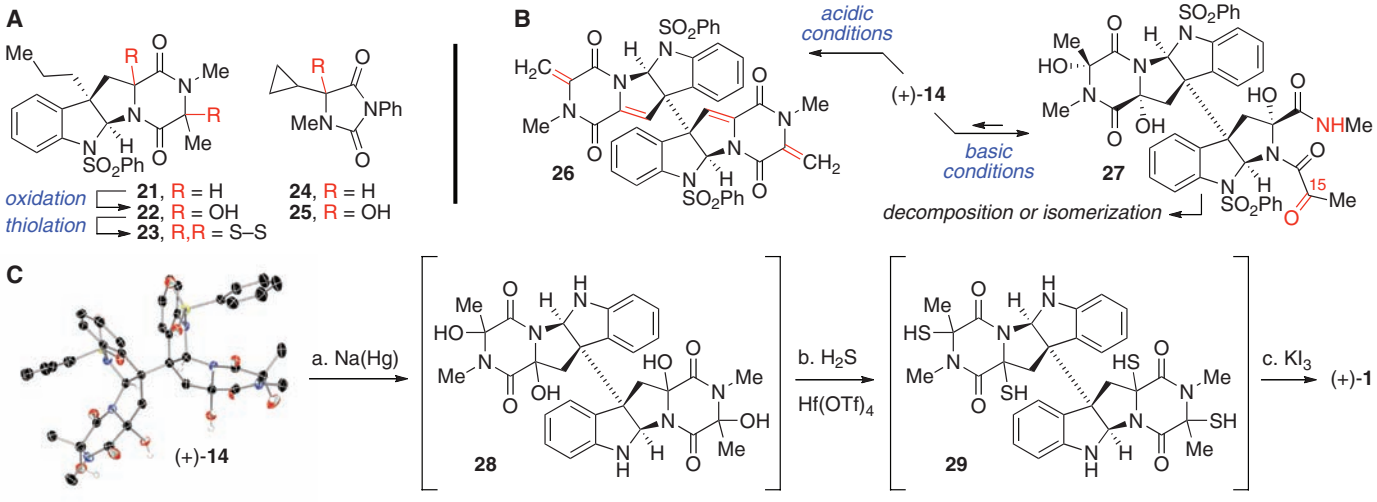

Fig. 4. Key observations enabling our first-generation synthesis of (+)-11,11'-dideoxyverticillin A (**1**). (**A**) Functionalization of exploratory models. (**B**) Sensitivity of dimeric octacyclic tetraol (+)-**14** to both acidic and basic conditions. (**C**) Thermal ellipsoid representation of (+)-**14**. Synthesis of alkaloid (+)-**1** from dimeric tetraol (+)-**14**. Conditions: (a) 5% Na(Hg), Na_2HPO_4, MeOH, 23°C. (b) H_2S, CH_2Cl_2, hafnium(IV) trifluoromethanesulfonate [$Hf(OTf)_4$], –78→23°C, 14 hours. (c) KI_3, pyridine, CH_2Cl_2, 23°C, 2 to 15% for three steps.

for the selective derivatization of both alanine-derived hemiaminals of (+)-**14** (SOM text). Treatment of a methanolic solution of diol (+)-**15** containing monobasic sodium phosphate with sodium amalgam cleanly unveiled the stable diaminodiol (+)-**16** in 87% yield as a surrogate for our hypothetical biosynthetic intermediate **6** (Fig. 2).

At this juncture, we envisioned that coordinating the introduction of the two sulfur atoms on each diketopiperazine ring would provide greater stereochemical control and structural stability. Inspired by the Woodward-Prévost cis-dihydroxylation of alkenes with carboxylate ions (*24*) and cognizant of the observation from Kishi's seminal synthesis of gliotoxin that epidithiodiketopiperazines are acutely sensitive toward basic, reductive, oxidative, and strongly acidic conditions (*5*), we reasoned that the use of a trithiocarbonate (*25*) would deliver a sulfurated product poised for mild unveiling of the targeted tetrathiol at an advanced stage. In the event, treatment of diaminodiol (+)-**16** with potassium trithiocarbonate and trifluoroacetic acid in dichloromethane resulted in rapid formation and isolation of the desired dimeric bisdithiepanethione (+)-**18** in 56% yield (*26*) (SOM text), likely via kinetic trapping of iminium ion **17** followed by intramolecular dithiepanethione formation. In this single operation, four carbon-oxygen bonds are exchanged for four carbon-sulfur bonds, the stereochemistry at all four tertiary thiols is secured, and the targeted *cis*-dithiodiketopiperazine substructure of **5** is attained.

Addition of ethanolamine to a solution of bisdithiepanethione (+)-**18** at 23°C rapidly afforded the proposed biosynthetic precursor diaminotetrathiol **5** (*27*), which is subject to mild oxidation to (+)-**1** upon exposure to air (SOM text). Under optimized conditions, after the formation of diaminotetrathiol **5**, partitioning of the reaction mixture between aqueous hydrochloric acid and dichloromethane and immediate addition of potassium triiodide to the organic layer provided (+)-11,11'-dideoxyverticillin A {$[\alpha]_D^{21} = +590$ (*c* 0.30, $CHCl_3$); for lit. $[\alpha]_D^{21} = +624.1$ (*c* 0.3, $CHCl_3$); where α is the specific rotation and c is concentration in g/100 ml} in 62% yield as a colorless solid. All spectroscopic data for (+)-**1** matched those reported in the literature (*1*). Furthermore, we unambiguously secured the structure of synthetic (+)-**1** by crystallographic analysis.

This concise strategy for the synthesis of (+)-**1** required a carefully choreographed sequence of events. In this sequence, the inherent chemistry of intermediates was maximally used in generation of chemical complexity and stereochemical control. For example, unveiling of the aniline nitrogen (N1) of (+)-**13** followed by attempted tetrahydroxylation led to complete decomposition under a variety of conditions. The challenges associated with the high sensitivity of (+)-**13** toward epimerization at the L-amino acid–derived C_α-stereocenters was compounded by the requirement for oxidation before epimerization (*vide supra*). Furthermore, thiolation of the oxidized diketopiperazines at an earlier stage led to substantial reductive cleavage or elimination of the sensitive carbon-sulfur bonds during subsequent transformations. These key insights guided our described strategy, whereby the conversion of diaminodiol (+)-**16** to dimeric dithiepanethione (+)-**18** enabled tetrathiolation with concomitant inversion of all four C_α-stereocenters, allowing rapid epidithiodiketopiperazine formation.

Collectively, our observations on the inherent reactivity of these structures hint at a plausible biosynthetic sequence for alkaloid (+)-**1** (Fig. 2). Whereas the viability of the proposed biosynthetic intermediates is supported through chemical synthesis, the successful implementation of our synthetic strategy offers a potential roadmap to the function of enzymes involved in the biosynthesis of epidithiodiketopiperazine alkaloids. For instance, Howlett's studies of the epidithiodiketopiperazine biosynthetic gene clusters (*28*, *29*) have identified genes encoding proteins with unassigned function that have sequence homology to cytochrome P450 mono-oxygenases. The mechanistic semblance of our permanganate diketopiperazine hydroxylation to the well-studied C–H abstraction-hydroxylation of substrates by P450 oxygenases (*30*, *31*) prompts consideration of the involvement of these genes in the C_α-oxidation of the diketopiperazine core.

Alkaloid (+)-**1** potently inhibits the tyrosine kinase activity of the epidermal growth factor receptor (median inhibitory concentration = 0.14 nM), exhibits antiangiogenic activity, and has efficacy against several cancer cell lines (*32*–*34*). The strategy and methodologies described here are expected to yield ready access to related compounds and provide an inroad to further biological studies. In this report, we have attempted to capture the power of biosynthetic considerations as a guiding principle for synthetic planning and as an inspiration for the development of new reactions.

References and Notes

1. B. W. Son, P. R. Jensen, C. A. Kauffman, W. Fenical, *Nat. Prod. Res.* **13**, 213 (1999).
2. D. M. Gardiner, P. Waring, B. J. Howlett, *Microbiology* **151**, 1021 (2005).
3. Y. Kishi, T. Fukuyama, S. Nakatsuka, *J. Am. Chem. Soc.* **95**, 6490 (1973).
4. R. M. Williams, W. H. Rastetter, *J. Org. Chem.* **45**, 2625 (1980).
5. T. Fukuyama, S. Nakatsuka, Y. Kishi, *Tetrahedron* **37**, 2045 (1981).
6. For other representative syntheses of epidithiodiketopiperazines, see (*35*) and references cited therein.
7. For a recent total synthesis of a sulfur containing diketopiperazine, see (*36*).
8. D. Hauser, H. P. Weber, H. P. Sigg, *Helv. Chim. Acta* **53**, 1061 (1970).
9. K. Katagiri, K. Sato, S. Hayakawa, T. Matsushima, H. Minato, *J. Antibiot. (Tokyo)* **23**, 420 (1970).
10. G. W. Kirby, D. J. Robins, in *The Biosynthesis of Mycotoxins: A Study in Secondary Metabolism*, P. S. Steyn, Ed. (Academic Press, New York, 1980), p. 301.
11. J. D. Herscheid, R. J. Nivard, M. W. Tijhuis, H. P. Scholten, H. C. Ottenheijm, *J. Org. Chem.* **45**, 1880 (1980).
12. M. Movassaghi, M. A. Schmidt, *Angew. Chem. Int. Ed.* **46**, 3725 (2007).
13. M. Movassaghi, M. A. Schmidt, J. A. Ashenhurst, *Angew. Chem. Int. Ed.* **47**, 1485 (2008).
14. D. Seebach, M. Boes, R. Naef, W. B. Schweizer, *J. Am. Chem. Soc.* **105**, 5390 (1983).
15. Sensitivity of diketopiperazine (+)-**11** to epimerization at the tryptophan-derived C_α-methine is highlighted by isolation of the corresponding diastereomer of **12** in 11% yield.
16. The major isolable side product is the C3-reduction product. Although the use of tetrahydrofuran (THF) as solvent provided a higher yield of dimer (+)-**13** (52%) on <1 g scale, the yields of larger scale reactions (>1 g scale) in THF were lower (40%).
17. A. Rauk *et al.*, *Biochemistry* **38**, 9089 (1999).
18. T. Sala, M. V. Sargent, *J. Chem. Soc. Chem. Commun.* **1978**, 253 (1978).
19. H. Firouzabadi, B. Vessal, M. Naderi, *Tetrahedron Lett.* **23**, 1847 (1982).
20. K. A. Gardner, J. M. Mayer, *Science* **269**, 1849 (1995).
21. T. Strassner, K. N. Houk, *J. Am. Chem. Soc.* **122**, 7821 (2000).
22. All attempts at the conversion of tetraene **26** to **1** based on the chemistry developed (fig. S5) in the synthesis of **23** failed, highlighting the additional challenges of the dimeric series.
23. J. C. Ruble, G. C. Fu, *J. Am. Chem. Soc.* **120**, 11532 (1998).
24. R. B. Woodward, F. V. Brutcher, *J. Am. Chem. Soc.* **80**, 209 (1958).
25. E. Cuthbertson, D. D. MacNicol, P. R. Mallinson, *Tetrahedron Lett.* **16**, 1345 (1975).
26. In addition to the desired (+)-(11*S*,11'*S*,15*S*,15'*S*)-**18**, the corresponding (11*R*,11'*S*,15*R*,15'*S*)-**18a** and (11*R*,11'*R*,15*R*,15'*R*)-**18b** diastereomers were also isolated (**18**:**18a**:**18b**, 25:7:1). Exposure of any diastereomer to the reaction conditions does not result in equilibration.
27. The expected 1,3-oxazolidine-2-thione (**20**) was observed in the product mixture.
28. E. M. Fox, B. J. Howlett, *Mycol. Res.* **112**, 162 (2008).
29. D. M. Gardiner, B. J. Howlett, *FEMS Microbiol. Lett.* **248**, 241 (2005).
30. H. Chen, B. K. Hubbard, S. E. O'Connor, C. T. Walsh, *Chem. Biol.* **9**, 103 (2002).
31. A. Schoendorf, C. D. Rithner, R. M. Williams, R. B. Croteau, *Proc. Natl. Acad. Sci. U.S.A.* **98**, 1501 (2001).
32. Y.-X. Zhang *et al.*, *Anticancer Drugs* **16**, 515 (2005).
33. Y. Chen *et al.*, *Biochem. Biophys. Res. Commun.* **329**, 1334 (2005).
34. Y. Chen, Z. Miao, W. Zhao, J. Ding, *FEBS Lett.* **579**, 3683 (2005).
35. L. E. Overman, T. Sato, *Org. Lett.* **9**, 5267 (2007).
36. Z. Wu, L. J. Williams, S. J. Danishefsky, *Angew. Chem. Int. Ed.* **39**, 3866 (2000).

37. M.M. is an Alfred P. Sloan Research Fellow and a Beckman Young Investigator. J.K. and J.A.A. acknowledge predoctoral (National Defense Science and Engineering Graduate) and postdoctoral [Fonds québécois de la recherche sur la nature et les technologies (FQRNT)] fellowships, respectively. We thank P. Müller for assistance with x-ray structures of (+)-**1** and (+)-**14**. We acknowledge generous support from Amgen, AstraZeneca, Boehringer Ingelheim, GlaxoSmithKline, Merck, and Lilly. Structural parameters for (+)-**1** and (+)-**14** are freely available from the Cambridge Crystallographic Data Centre under CCDC-719219 and CCDC-719218, respectively.

Supporting Online Material

www.sciencemag.org/cgi/content/full/324/5924/238/DC1
Materials and Methods
SOM Text
Figs. S1 to S5
Tables S1 to S14
References

12 January 2009; accepted 23 February 2009
10.1126/science.1170777

Pulsatile Stimulation Determines Timing and Specificity of NF-κB–Dependent Transcription

Louise Ashall,[1]* Caroline A. Horton,[1]* David E. Nelson,[1]* Pawel Paszek,[1]* Claire V. Harper,[1] Kate Sillitoe,[1] Sheila Ryan,[1] David G. Spiller,[1] John F. Unitt,[2] David S. Broomhead,[3] Douglas B. Kell,[4] David A. Rand,[5] Violaine Sée,[1] Michael R. H. White[1]†

The nuclear factor κB (NF-κB) transcription factor regulates cellular stress responses and the immune response to infection. NF-κB activation results in oscillations in nuclear NF-κB abundance. To define the function of these oscillations, we treated cells with repeated short pulses of tumor necrosis factor–α at various intervals to mimic pulsatile inflammatory signals. At all pulse intervals that were analyzed, we observed synchronous cycles of NF-κB nuclear translocation. Lower frequency stimulations gave repeated full-amplitude translocations, whereas higher frequency pulses gave reduced translocation, indicating a failure to reset. Deterministic and stochastic mathematical models predicted how negative feedback loops regulate both the resetting of the system and cellular heterogeneity. Altering the stimulation intervals gave different patterns of NF-κB–dependent gene expression, which supports the idea that oscillation frequency has a functional role.

Eukaryotic cells interpret multiple signals to coordinate the activity of transcription factors, which modulate the expression of target genes. Nuclear factor κB (NF-κB) signaling in many mammalian cell types regulates responses to pathogens and stresses (*1*). NF-κB, most commonly comprising a dimer of RelA and p50, is bound in the cytoplasm of unstimulated cells by inhibitor of nuclear factor κB (IκB) proteins. Stimulation by cytokines such as tumor necrosis factor–α (TNFα) activates the IκB kinase (IKK) complex that phosphorylates IκB proteins, leading to IκB degradation and NF-κB translocation into the nucleus. Activated NF-κB regulates transcription from promoter regions of approximately 300 genes, including those encoding cytokines and several NF-κB family members that can feedback to regulate the system (*2*). Signaling through NF-κB can regulate diverse cellular outcomes, including cell death or division (*3*). How such a diversity of responses is generated has remained unclear.

Real-time fluorescence imaging and mathematical modeling have shown that the activity of the NF-κB system can be oscillatory (*4*). This raised the possibility that, such as with calcium (*5*), this signaling pathway might use oscillation frequency as one component of the cellular signal that controls innate immunity and cell fate. After stimulation with TNFα, target gene expression can be regulated by negative feedback loops that modulate the cytoplasmic-nuclear translocation of NF-κB (*4*). One of these feedbacks is mediated by IκBα, which upon binding to NF-κB in the nucleus shuttles the NF-κB protein complex back to the cytoplasm. These oscillations have been observed in single cells expressing the fluorescently labeled NF-κB subunit RelA and IκBα (*4*, *6*, *7*) and also through bulk cell electrophoretic mobility shift assay (EMSA) analysis in IκBε and IκBε-IκBβ knockout mouse embryonic fibroblasts (MEFs) (*8*, *9*).

Single-live-cell fluorescent imaging has demonstrated NF-κB oscillations in various cell types (*4*, *6*). SK-N-AS neuroblastoma cells showed particularly robust oscillations in response to TNFα simulation after transient (*4*) or stable transfection with a vector expressing RelA fused to the *Discosoma sp.* red fluorescent protein dsRed-Express (RelA-dsRedxp) (Fig. 1, A and B). Oscillations were unlikely to be the result of RelA overexpression, because stably transfected cells expressed nearly physiological amounts of the fusion protein [relative level of 0.91 ± 0.04 (SD, $n = 6$ replicates) compared with endogenous protein in untransfected control (*7*)]. In contrast to the conclusions of other reports (*9*, *10*), we observed oscillations in the translocation of RelA-dsRedxp fusion protein in single transiently transfected MEFs (Fig. 1, C to E). These data [as well as bulk cell chromatin immunoprecipitation (ChIP) assays (fig. S1)] suggest that oscillations are a normal response to TNFα stimulation.

In an inflammatory tissue, cells receive pulsatile signals such as TNFα from neighboring cells

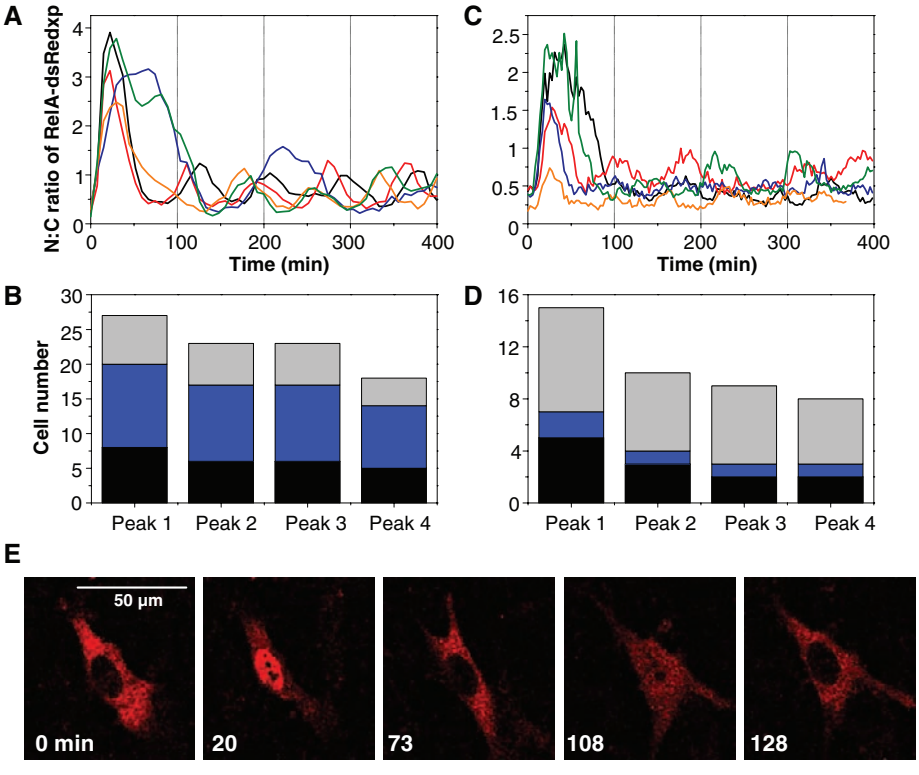

Fig. 1. RelA oscillations at the single-cell level. (**A** and **C**) Time course of the ratio of nuclear to cytoplasmic localization (N:C) of RelA-dsRedxp in (A) SK-N-AS (stably transfected) and (C) MEF (transiently transfected) cells. Single-cell dynamics are shown by differently colored lines. (**B** and **D**) The number of cells (separate experiments are represented by different colors) showing RelA-dsRedxp translocations in (B) stably transfected SK-N-AS (imaged for at least 350 min; 0 cells failed to respond) and (D) transiently transfected MEF cells (imaged for at least 250 min; 1 cell failed to respond). (**E**) Time-lapse confocal images of a typical RelA-dsRedxp-transfected MEF cell after TNFα stimulation.

[1]Centre for Cell Imaging, School of Biological Sciences, Bioscience Research Building, Crown Street, Liverpool, L69 7ZB, UK. [2]Molecular Biology Department, AstraZeneca R&D Charnwood, Bakewell Road, Loughborough, Leicestershire, LE11 5RH, UK. [3]School of Mathematics, The Alan Turing Building, The University of Manchester, Oxford Road, Manchester, M13 9PL, UK. [4]Manchester Centre for Integrative Systems Biology, School of Chemistry, and Manchester Interdisciplinary Biocentre, University of Manchester, 131 Princess Street, Manchester, M1 7DN. [5]Warwick Systems Biology, Coventry House, University of Warwick, Coventry CV4 7AL, UK.

*These authors contributed equally to this work.
†To whom correspondence should be addressed. E-mail: mwhite@liv.ac.uk

(*11*, *12*). To mimic this, we exposed cells to 5-min pulses of TNFα at various intervals, followed by a wash-off. When stimulated at 200-min intervals, RelA-dsRedxp fusion protein expressed in SK-N-AS cells showed synchronous translocations from the cytoplasm to the nucleus and back of equal magnitude in response to each successive pulse (Fig. 2, A and B, and fig. S4). In contrast, whereas stimulation at 100- or 60-min intervals also caused synchronous cell responses, there was significant reduction in the magnitude of RelA-dsRedxp fusion protein translocation (Fig. 2, A and B). These data indicate that the system completely resets between 100 and 200 min after each stimulus. Western blot analysis of synchronized cell populations supported the hypothesis that the cycles of RelA-dsRedxp fusion protein translocation were associated with cycles of phosphorylation at Ser^{32} and degradation of IκBα (Fig. 2C and fig. S5). Analysis of the amounts of Ser^{32}-phospho-IκBα, relative to total IκBα levels, confirmed that the failure to reset was quantitatively reflected by the phosphorylation of IκBα (Fig. 2, C and D, and fig. S6). Cycles of phosphorylation and dephosphorylation of RelA at Ser^{536} were consistent with RelA being phosphorylated in the cytoplasm and dephosphorylated in the nucleus (*4*).

The inability of available model structures (*7*, *8*, *13*, *14*) to provide a single parameter set that could simulate the observed behavior for all

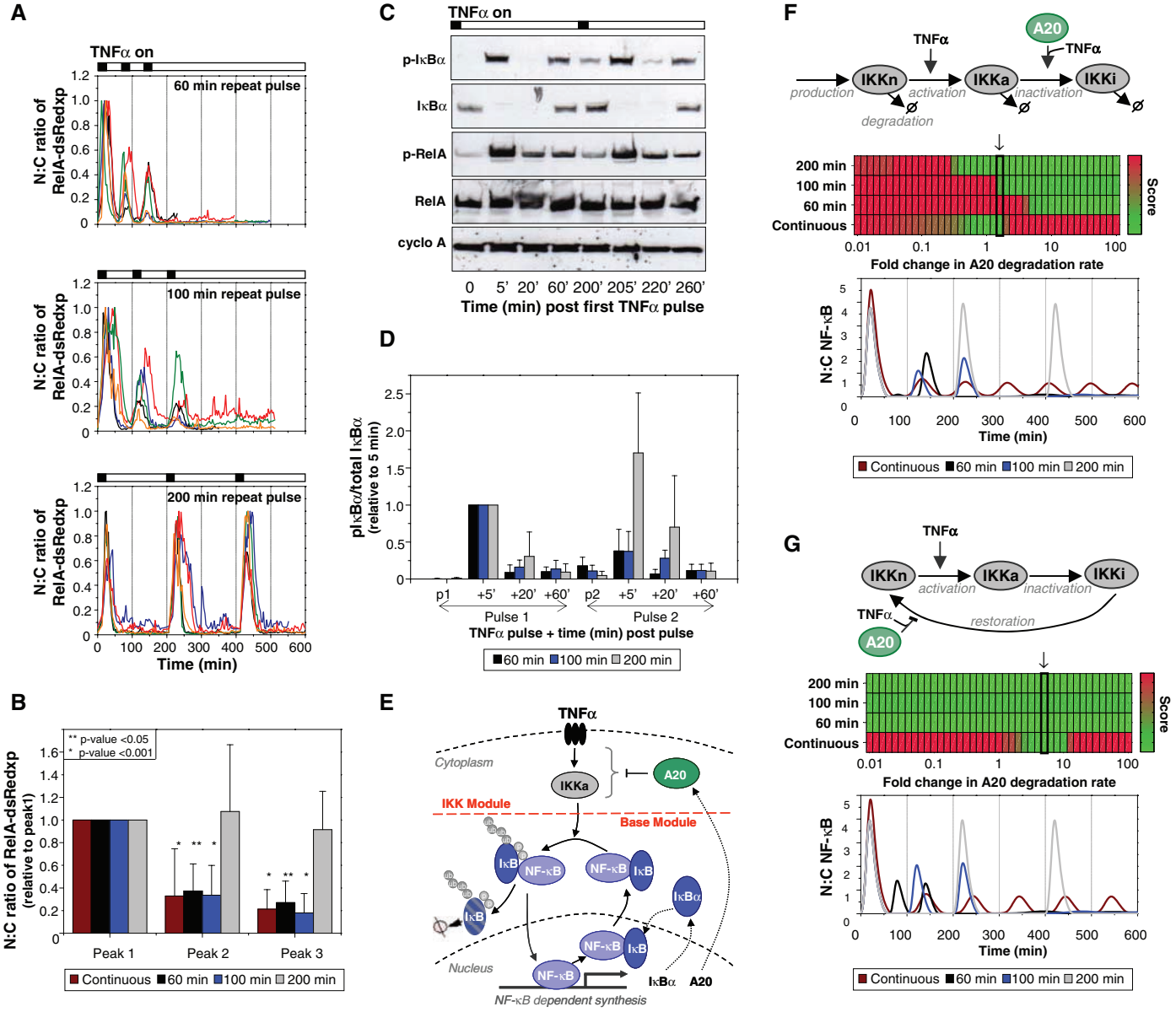

Fig. 2. Response of SK-N-AS cells to various TNFα pulse frequencies. (**A**) Time course of RelA-dsRedxp N:C ratio in transiently transfected cells pulsed three times with TNFα for 5 min at intervals of 60, 100, or 200 min (five typical cells shown for each). RelA-dsRedxp N:C ratio was normalized to peak 1 intensity. (**B**) Amplitude of successive peaks of RelA-dsRedxp localization after pulses or continuous exposure of cells to TNFα. Results were normalized to the amplitude of peak 1 (+SD). Asterisks indicate *P* values for a one-sample Wilcoxon test for peak amplitude equal to 1. (**C**) Western blot of Ser^{32} phospho-IκBα (p-IκBα), IκBα, Ser^{536} phospho-RelA (p-RelA), RelA, and cyclophilin A (cyclo A) amounts in cells stimulated with TNFα pulses 200 min apart. (**D**) Ratio of p-IκBα/total IκBα (relative to that recorded at t = 5 min) in cells stimulated 60, 100, and 200 min apart (+SD) [data based on (C)] (fig. S4). p1 and p2 indicate time after pulse 1 or 2 for each stimulation protocol. (**E**) Two-feedback NF-κB signaling pathway showing IKK and the base module. (**F** and **G**) Computational analysis of existing (F) (*21*) and proposed (G) IKK structures. Heat maps [poor (red) to good (green)] represent the ability of the model to quantitatively fit the experimental data for a range of selected parameter values (table S5). A20 degradation rate (c4) was varied on a logarithmic scale two orders of magnitude above and below 0.0009 s^{-1}. The best fit is highlighted and the corresponding simulated N:C ratio shown (F and G, bottom) for all TNFα stimulation conditions; c4 = 0.00143 s^{-1} in (F) and c4 = 0.0045 s^{-1} in (G).

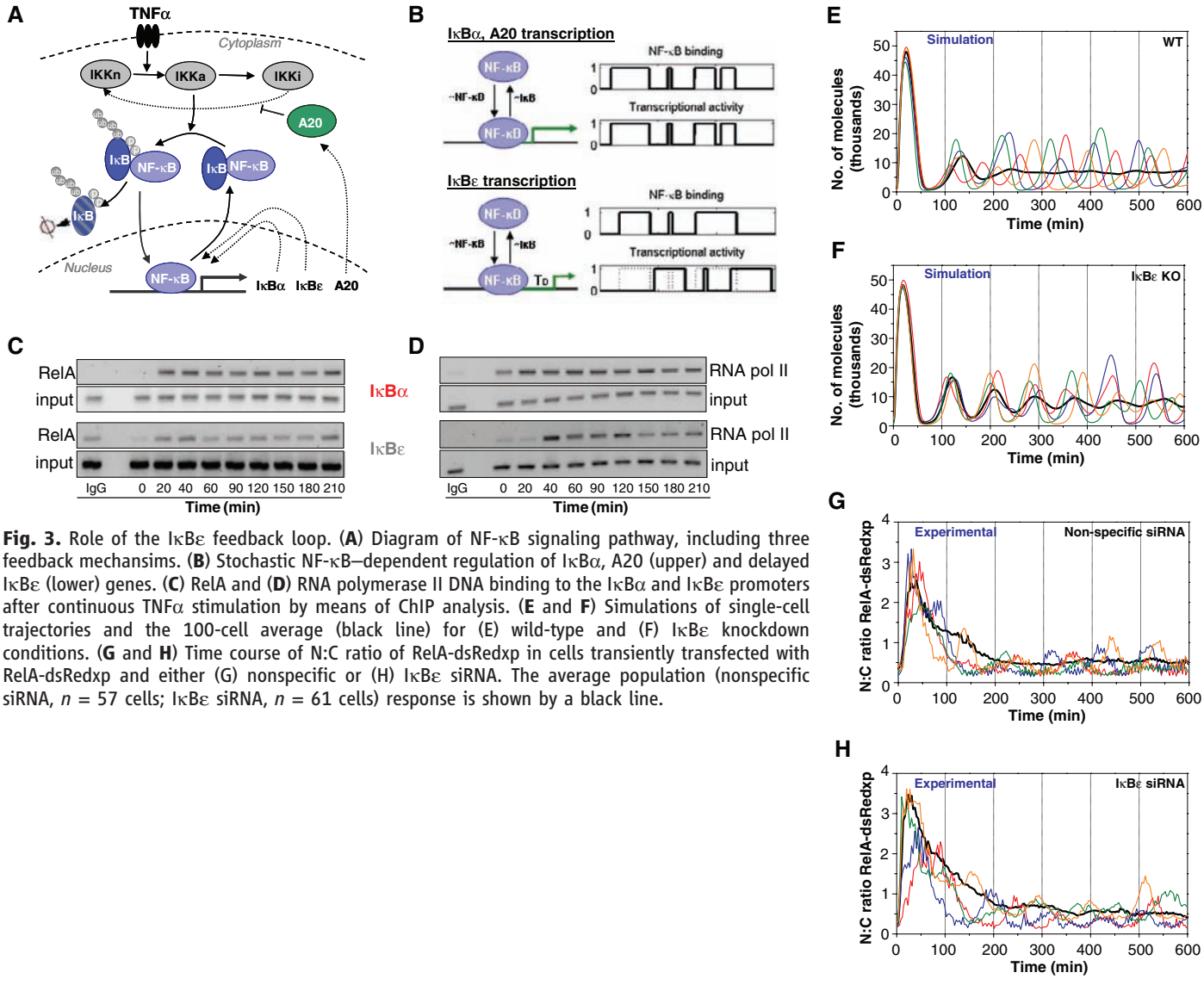

Fig. 3. Role of the IκBε feedback loop. (**A**) Diagram of NF-κB signaling pathway, including three feedback mechansims. (**B**) Stochastic NF-κB–dependent regulation of IκBα, A20 (upper) and delayed IκBε (lower) genes. (**C**) RelA and (**D**) RNA polymerase II DNA binding to the IκBα and IκBε promoters after continuous TNFα stimulation by means of ChIP analysis. (**E** and **F**) Simulations of single-cell trajectories and the 100-cell average (black line) for (E) wild-type and (F) IκBε knockdown conditions. (**G** and **H**) Time course of N:C ratio of RelA-dsRedxp in cells transiently transfected with RelA-dsRedxp and either (G) nonspecific or (H) IκBε siRNA. The average population (nonspecific siRNA, n = 57 cells; IκBε siRNA, n = 61 cells) response is shown by a black line.

the tested TNFα stimulation conditions demonstrated a need for model refinement (Fig. 2, E to G). We used the experimentally observed limited IκBα phosphorylation, which is associated with reduced NF-κB translocation level at higher pulse frequencies (Fig. 2, B and D), to constrain simulated IKK activity. The core NF-κB–IκBα network used a similar structure to that of previous models (Fig. 2E), although multiple model parameters were modified partly on the basis of cell-specific measurements (table S1). Model simulations using the existing IKK network structure (*14*) (Fig. 2F) failed to recapitulate experimental conditions because the repeated pulse stimulation required sufficient IKK activity to degrade almost all IκBα; however, persisting oscillations observed with continual TNFα were sensitive to high IKK activity (figs. S8 and S9). Using a scoring function to compare model performance with all experimental data (table S5), we composed a new deterministic model with a modified network structure of IKK and A20 NF-κB inhibitory protein interactions (Fig. 2G and fig. S10). The chosen model represented the simplest structure that included IKK state recycling (*15*) and was able to use a single parameter set to reproduce all of the experimental data. The A20 feedback loop was assumed to include other related negative feedback inhibitors, such as Cezanne (*16*) and Cylindromatosis (CYLD) (*17*), which together may limit the reactivation of IKK. The model predicted a low stability of A20, which could be compatible with a key regulatory factor being the ubiquitin-editing activity of A20 rather than its protein concentration. A20 activity may be linked to processes upstream of IKK (*18*), or IKK-mediated phosphorylation of A20 may inhibit IKK activity (*19*).

Persistent bulk cell oscillations have been observed after continuous TNFα by using EMSA assays of MEFs from IκBε-deficient or combined IκBε-IκBβ–deficient animals (*8*, *9*). Although deterministic simulation was appropriate for the work described above, the heterogeneous nature of single-cell responses to continuous TNFα stimulation in wild-type cells cannot be elucidated in this manner. Stochastic models (*20*, *21*) have been used to propose that cell-to-cell heterogeneity arises through intrinsic, stochastic, transcriptional variability because there are only two copies of the IκBα and A20 feedback genes (*21*). We developed a new hybrid, stochastic, three-feedback model on the basis of the deterministic model structure described above, which considered delayed stochastic transcription from the IκBε gene and stochastic transcription of the IκBα and A20 genes (Fig. 3, A and B). ChIP analysis confirmed that RelA binds to the IκBα and IκBε promoters in SK-N-AS cells within 20 min after TNFα stimulation (Fig. 3C). In contrast, RNA polymerase II was bound to the IκBα promoter before stimulation, whereas binding to the IκBε promoter was delayed (Fig. 3D), perhaps as a result of chromatin remodeling. The three-feedback stochastic model predicted persistent oscillations of similar amplitude in both wild-type (Fig. 3E) and IκBε-deficient (Fig. 3F) cells after stimulation. Furthermore, stochastic variation from delayed IκBε feedback may generate enhanced cell-to-cell heterogeneity

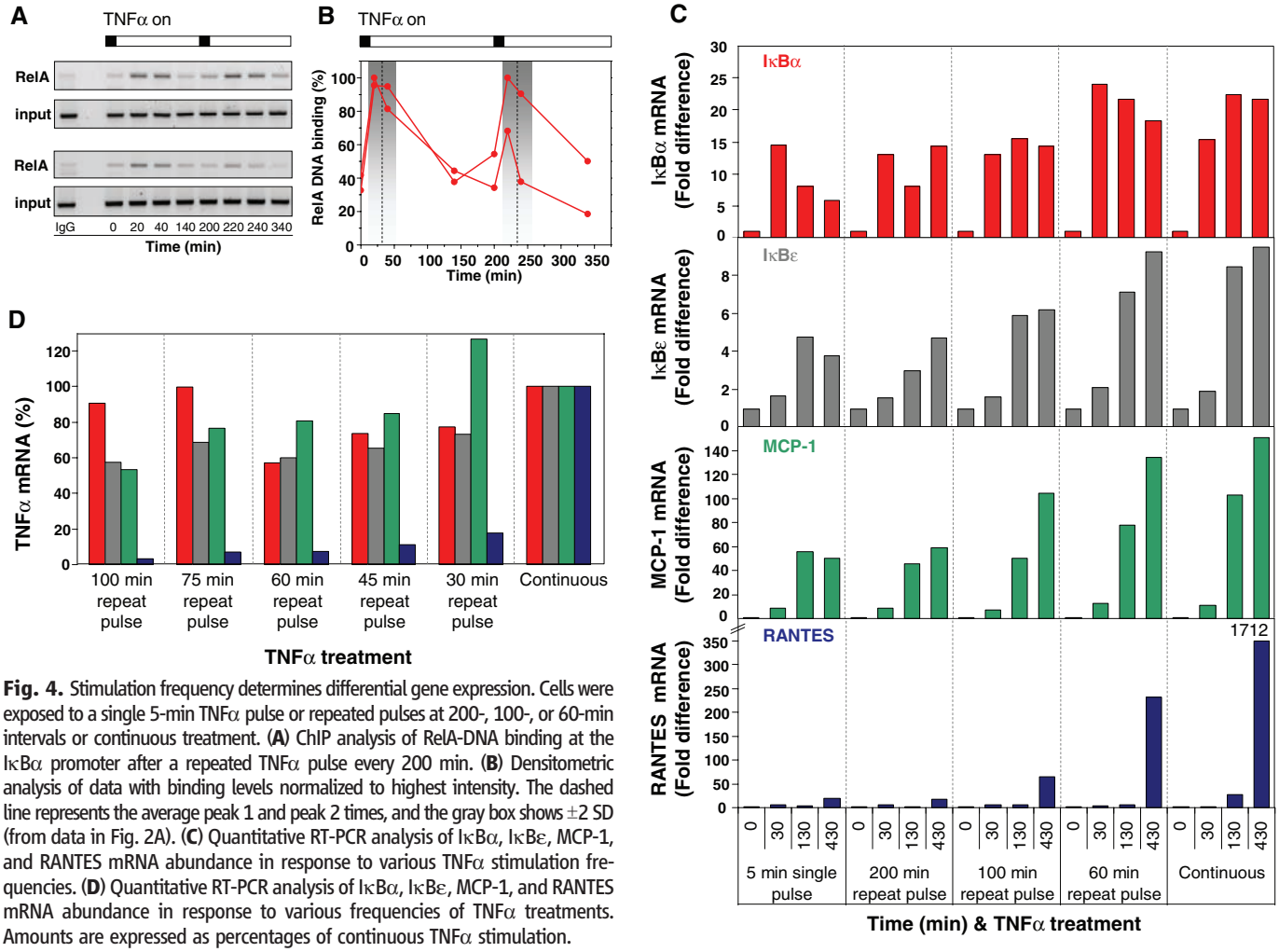

Fig. 4. Stimulation frequency determines differential gene expression. Cells were exposed to a single 5-min TNFα pulse or repeated pulses at 200-, 100-, or 60-min intervals or continuous treatment. (**A**) ChIP analysis of RelA-DNA binding at the IκBα promoter after a repeated TNFα pulse every 200 min. (**B**) Densitometric analysis of data with binding levels normalized to highest intensity. The dashed line represents the average peak 1 and peak 2 times, and the gray box shows ±2 SD (from data in Fig. 2A). (**C**) Quantitative RT-PCR analysis of IκBα, IκBε, MCP-1, and RANTES mRNA abundance in response to various TNFα stimulation frequencies. (**D**) Quantitative RT-PCR analysis of IκBα, IκBε, MCP-1, and RANTES mRNA abundance in response to various frequencies of TNFα treatments. Amounts are expressed as percentages of continuous TNFα stimulation.

in wild-type cells as compared with that in IκBε-deficient cells. The lack of IκBε feedback could therefore generate increased cell-to-cell homogeneity, which was predicted to be detectable as oscillations at the average population level (Fig. 3F). Experimental small interfering RNA (siRNA) depletion of IκBε feedback in SK-N-AS cells (Fig. 3H) had no effect on oscillation amplitude (Fig. 3G), which contradicts the prediction that IκBε feedback might dampen oscillations in wild-type cells (*9*). Although IκBε-deficient MEFs showed homogeneous cell-to-cell oscillations, the stochastic three-feedback model predicted that this effect would not occur in cells overexpressing RelA by as little as twofold [as in our siRNA knockdown experiments (fig. S15)]. Therefore, the three-feedback stochastic model was able to simulate and predict key aspects of the available experimental data.

To assess the functional importance of oscillation timing in TNFα-induced NF-κB signaling in single cells, we used quantitative reverse transcription polymerase chain reaction (RT-PCR) to measure the time course of transcription from a set of early, middle, and late NF-κB–dependent endogenous genes in response to various durations and frequencies of TNFα treatment. ChIP analyses after repeated 100- and 200-min pulses showed cycles of DNA binding (Fig. 4, A and B, and fig. S23). Over a 430-min time course, we observed successively later peaks in the mRNA transcription of four representative genes in response to TNFα stimulation (from early to late: IκBα, IκBε, MCP-1, RANTES) (Fig. 4C) (*8*, *22*). Although IκBα responded equally to a 5-min single pulse of TNFα and to pulses at 200-min intervals, later genes showed reduced responses, and the gene encoding the RANTES chemokine exhibited almost no response. There was an increase in late transcript abundance in which stimuli were applied at 100-min intervals, which was even more marked when the cells were stimulated at shorter intervals (Fig. 4D). Thus, varying frequencies of NF-κB nuclear entry result in the differential regulation of particular downstream genes.

In this study, we used combined experimental and computational studies to explain the source of cellular heterogeneity and show that oscillations are an important characteristic of the response of NF-κB to TNFα. Cells in inflammatory tissues may experience varying cytokine stimulation. In response to timed fluctuations in TNFα stimulation, the NF-κB response can become homogeneous and can be driven at differing frequencies. Such varying frequencies in stimulation resulted in altered gene-expression profiles, specifically affecting the abundance of late gene transcription. These results therefore support the idea of oscillatory dynamics having a key functional role in this important stress-response system. The recent observation that the yeast calcium–regulated transcription factor Crz1 also controls gene expression through nuclear translocation frequency (*23*) suggests that this behavior may be a property of other important signaling pathways, such as p53 (*24*).

References and Notes

1. M. S. Hayden, S. Ghosh, *Cell* **132**, 344 (2008).
2. A. Hoffmann, D. Baltimore, *Immunol. Rev.* **210**, 171 (2006).
3. N. D. Perkins, *Nat. Rev. Mol. Cell Biol.* **8**, 49 (2007).
4. D. E. Nelson *et al.*, *Science* **306**, 704 (2004).
5. M. J. Berridge, M. D. Bootman, H. L. Roderick, *Nat. Rev. Mol. Cell Biol.* **4**, 517 (2003).
6. S. Friedrichsen *et al.*, *Endocrinology* **147**, 773 (2006).
7. D. E. Nelson *et al.*, *Science* **308**, 52b (2005).
8. A. Hoffmann, A. Levchenko, M. L. Scott, D. Baltimore, *Science* **298**, 1241 (2002).
9. J. D. Kearns, S. Basak, S. L. Werner, C. S. Huang, A. Hoffmann, *J. Cell Biol.* **173**, 659 (2006).
10. D. Barken *et al.*, *Science* **308**, 52a (2005).
11. M. W. Covert, T. H. Leung, J. E. Gaston, D. Baltimore, *Science* **309**, 1854 (2005).

12. S. L. Werner, D. Barken, A. Hoffmann, *Science* **309**, 1857 (2005).
13. A. E. Ihekwaba *et al.*, *Syst. Biol. (Stevenage)* **152**, 153 (2005).
14. T. Lipniacki, P. Paszek, A. R. Brasier, B. Luxon, M. Kimmel, *J. Theor. Biol.* **228**, 195 (2004).
15. H. Hacker, M. Karin, *Sci. STKE* **2006**, re13 (2006).
16. K. Enesa *et al.*, *J. Biol. Chem.* **283**, 7036 (2008).
17. E. Trompouki *et al.*, *Nature* **424**, 793 (2003).
18. S. C. Sun, *Nat. Rev. Immunol.* **8**, 501 (2008).
19. J. E. Hutti *et al.*, *Mol. Cell. Biol.* **27**, 7451 (2007).
20. F. Hayot, C. Jayaprakash, *J. Theor. Biol.* **240**, 583 (2006).
21. T. Lipniacki, P. Paszek, A. R. Brasier, B. A. Luxon, M. Kimmel, *Biophys. J.* **90**, 725 (2006).
22. B. Tian, D. E. Nowak, A. R. Brasier, *BMC Genomics* **6**, 137 (2005).
23. L. Cai, C. K. Dalal, M. B. Elowitz, *Nature* **455**, 485 (2008).
24. G. Lahav *et al.*, *Nat. Genet.* **36**, 147 (2004).
25. We thank N. Perkins for reading the manuscript and D. Jackson, M. Kimmel, and T. Lipniacki for discussion. The work was supported by Biotechnology and Biological Sciences Research Council (BBSRC) grants BBD0107481, BBF0059381, BBC0082191, and BBC0071581; BBSRC studentships to L.A. and K.S. (AstraZeneca Collaborative Awards in Science and Engineering); and Medical Research Council grant G0500346. C.V.H. holds a Professor John Glover Memorial Research Fellowship; D.A.R. held an Engineering and Physical Sciences Research Council Senior Fellowship [EP/C544587/1, GR/S29256/01 and European Union (BioSim Network contract 005137)]; D.B.K. holds a Royal Society/Wolfson Merit Award; and V.S. holds a BBSRC David Phillips Research Fellowship (BBC5204711). Hamamatsu Photonics and Carl Zeiss Limited provided training and technical support.

Supporting Online Material

www.sciencemag.org/cgi/content/full/324/5924/242/DC1
Materials and Methods
Figs. S1 to S32
Tables S1 to S8
References

19 August 2008; accepted 29 December 2008
10.1126/science.1164860

Antibody Recognition of a Highly Conserved Influenza Virus Epitope

Damian C. Ekiert,[1] Gira Bhabha,[1] Marc-André Elsliger,[1] Robert H. E. Friesen,[2] Mandy Jongeneelen,[2] Mark Throsby,[2] Jaap Goudsmit,[2] Ian A. Wilson[1,3]*

Influenza virus presents an important and persistent threat to public health worldwide, and current vaccines provide immunity to viral isolates similar to the vaccine strain. High-affinity antibodies against a conserved epitope could provide immunity to the diverse influenza subtypes and protection against future pandemic viruses. Cocrystal structures were determined at 2.2 and 2.7 angstrom resolutions for broadly neutralizing human antibody CR6261 Fab in complexes with the major surface antigen (hemagglutinin, HA) from viruses responsible for the 1918 H1N1 influenza pandemic and a recent lethal case of H5N1 avian influenza. In contrast to other structurally characterized influenza antibodies, CR6261 recognizes a highly conserved helical region in the membrane-proximal stem of HA1 and HA2. The antibody neutralizes the virus by blocking conformational rearrangements associated with membrane fusion. The CR6261 epitope identified here should accelerate the design and implementation of improved vaccines that can elicit CR6261-like antibodies, as well as antibody-based therapies for the treatment of influenza.

Over the past century, three human influenza A pandemics (1918 H1N1 Spanish, 1957 H2N2 Asian, and 1968 H3N2 Hong Kong) have killed ~50 million to 100 million people worldwide. Each pandemic virus was derived, at least in part, from an avian influenza virus by direct interspecies transmission or exchange of genetic material between avian and human viruses (*1*–*4*). In each case, an HA envelope glycoprotein was acquired that was antigenically distinct from the HAs of the human viruses in circulation at that time. HA is the primary target of neutralizing antibodies and rapidly and continuously accumulates mutations to escape recognition by the immune system. In pandemic years, HAs are shuffled from the vast reservoir of 16 HA subtypes in avian viruses into a circulating human virus to evade prevailing immunity in the human population. Thus, although many factors likely contribute to virulence and transmissibility, immune evasion is critical for the rapid spread of pandemic and epidemic viruses.

Several small molecules are in use for treatment of influenza. Most notable are neuraminidase (NA) inhibitors, oseltamivir (Tamiflu) and zanamivir (Relenza), which prevent release of nascent virions, and amantadine (*5*), which interferes with the M2 channel proton conducting activity. However, excessive use leads to resistant viruses (*6*–*8*) that often show surprisingly little attenuation from the escape mutations, thereby contributing to rapid spread worldwide (*6*). Recently, a binding pocket was characterized on the HA for the fusion inhibitor tert-butyl hydroquinone (TBHQ) (*9*), which shows great promise but is still in the early stages of development. Consequently, vaccination remains the most effective countermeasure against influenza virus.

Current trivalent influenza vaccines elicit a potent neutralizing antibody response to the vaccine strains and closely related isolates but rarely extend to more diverged strains within a subtype or to other subtypes (*10*). Selection of the appropriate vaccine strains presents many challenges and frequently results in suboptimal protection (*11*, *12*). Furthermore, predicting the subtype and clade of the next pandemic virus, including when and where it will arise, is currently impossible. A vaccine that stimulates production of antibodies capable of neutralizing multiple influenza A subtypes would eliminate much of the guesswork associated with strain selection and impede emerging pandemic viruses. Although a few rare antibodies with broad, heterosubtypic patterns of neutralization have been reported, their epitopes remain obscure and have hampered attempts at rational vaccine design (*13*–*15*).

Antibody CR6261 was isolated from the immune repertoire of a healthy, vaccinated individual by using phage display selection on recombinant H5 HA (*15*). Despite no known exposure to H5 viruses, several clones capable of neutralizing H5 viruses were obtained. Human immunoglobulin G1 (IgG1) CR6261 neutralizes multiple influenza subtypes, including H1, H2, H5, H6, H8, and H9, and protects mice from lethal challenge with H1N1 and H5N1 viruses when administered up to 5 days postinfection (*15*). To characterize the CR6261 epitope on the HA and the mechanism of neutralization, we determined crystal structures of CR6261 Fab in complex with HAs from the human 1918 H1N1 pandemic virus (A/South Carolina/1/1918; SC1918/H1) and from a highly pathogenic avian H5N1 virus (A/Vietnam/1203/2004; Viet04/H5).

The SC1918/H1 and Viet04/H5 HA ectodomains were expressed in baculovirus, and Fab CR6261 was expressed in mammalian cells (*16*). Cocrystal structures were determined at 2.2 Å and 2.7 Å resolution by molecular replacement (table S1) (*17*) and revealed three antibodies bound per HA trimer (Fig. 1). Both HAs are very similar to their unliganded structures (fig. S1) (*18*–*20*). Each HA polypeptide is proteolytically cleaved during viral maturation to two disulfide-linked chains, HA1 and HA2. HA1 consists primarily of the membrane-distal receptor binding and vestigial esterase domains, but its N- and C-terminal regions extend toward the viral membrane and are intertwined with the exterior surface of HA2. HA2 constitutes the core fusion machinery in the stalk region and is dominated by the long, central CD helix (residues 75 to 126) that forms a trimeric coiled-coil and the shorter A helix (residues 38 to 58) that packs against the central helical bundle (*21*). Exposure to low pH leads to major structural rearrangements in HA2 that facilitate membrane fusion (*22*, *23*).

[1]Department of Molecular Biology, The Scripps Research Institute, 10550 North Torrey Pines Road, La Jolla, CA 92037, USA. [2]Crucell Holland BV, Archimedesweg 4-6, 2301 CA Leiden, Netherlands. [3]The Skaggs Institute for Chemical Biology, The Scripps Research Institute, 10550 North Torrey Pines Road, La Jolla, CA 92037, USA.

*To whom correspondence should be addressed. E-mail: wilson@scripps.edu

Interpretable density is observed for HA1(11–325) and HA2(1–172) (SC1918/H1) and HA1(11–324) and HA2(1–177) (Viet04/H5) [H3 numbering (*22*, *24*)]. The N-terminal fusion peptide in HA2 is embedded in the hydrophobic pocket between adjacent HA2 subunits (fig. S2), indicating that both HAs are in their prefusion states. Unlike other structurally characterized neutralizing antibodies, CR6261 binds at the membrane proximal end of each HA, roughly parallel to the plane of the viral envelope (Fig. 2A) (*25*–*28*), within ~25 Å of the bilayer. CR6261 interacts primarily with the HA2 A helix but also contacts HA1 residues in the stem region. The epitope and the Fab variable domains are well ordered in both complexes (fig. S3), but the Fab constant domains in the SC1918/H1 complex are partially disordered (*29*). Unexpectedly, the Fab interaction is mediated exclusively by the heavy chain (Fig. 2B) (*30*). Furthermore, the relatively modest buried surface area [680 $Å^2$ on HA (70% HA2), 624 $Å^2$ on the Fab, and 116 van der Waals contacts] presents fewer possibilities for escape mutations, particularly for highly conserved epitopes that are functionally important, and may also reduce the ability of masking glycans to interfere with antibody binding. Consistent with this notion, a universally conserved glycan on HA2 Asn^{154} lies directly between the CR6261 light chain variable region (V_L) and the HA (Fig. 2B and fig. S4) (*31*). The selection of heavy chain–dominant antibodies may also be enhanced as a consequence of the large, diverse repertoire that can be accessed from the combinatorial pairings of heavy and light chains in the construction of phage libraries (*32*, *33*).

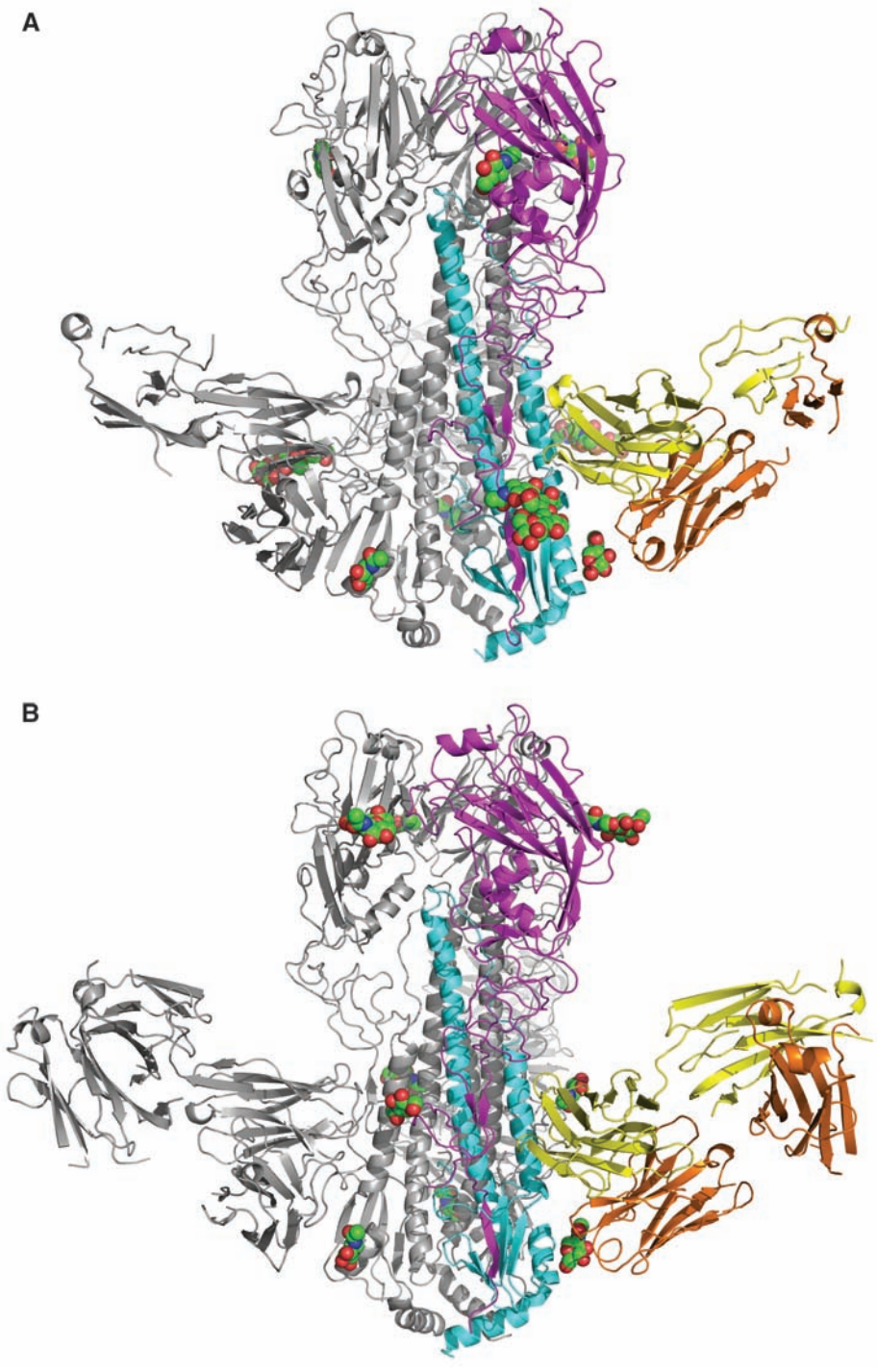

Fig. 1. Crystal structures of broadly neutralizing antibody CRF6261 in complex with SC1918/H1 and Viet04/H5 HAs. (**A**) The trimeric CRF6261-SC1918/H1 complex. One HA/Fab protomer is colored with HA1 in purple, HA2 in cyan, Fab heavy chain in yellow, and Fab light chain in orange; the other two HA monomers and Fabs in the trimer are colored in gray for clarity. Glycans are depicted as their component atoms (carbon in green, oxygen in red, and nitrogen in blue) with their van der Waals radii. (**B**) The trimeric CRF6261-Viet04 complex, colored as in (A). The HA1 globular heads are located at the top of the figure, and the membrane-proximal stem is at the bottom, where the Fab is bound.

The CR6261-SC1918/H1 interaction is depicted in Fig. 3, A to C, in which eight hydrogen bonds are formed with HA2 (table S2), five of which involve recognition of the A helix by the heavy chain complementarity determining region 1 (HCDR1), primarily by the main chain (*34*). In contrast, CR6261 makes mainly nonpolar contacts with HA1 that can be grouped into two distinct clusters within the hydrophobic groove at the junction between the A helix and HA1 (Fig. 3, B and C, and table S3). The first region consists of HA1 Val^{40}, Leu^{42}, and Leu^{292}, along with HA2 Thr^{49}, Val^{52}, and Ile^{56} from the membrane-distal end of the A helix, which interact with HCDR1 Pro^{28} and Phe^{29}. In addition, Phe^{74} in framework region 3 (FR3), reminiscent of HV4 in T cell receptors (TCRs) (*35*), interacts with this first hydrophobic patch, likely because of the binding interactions being focused exclusively on the heavy chain. The second cluster, close to the membrane-proximal end of the A helix, includes His^{18} and His^{38} from HA1 and Trp^{21}, Thr^{41}, and Ile^{45} from HA2, which interact with the conserved hydrophobic tip of HCDR2 (Ile^{53} and Phe^{54}), and Tyr^{98} from HCDR3.

To reveal the basis for cross-neutralization of the H5 subtype, we determined the structure of CR6261 with Viet04/H5 HA. Overall, the CR6261-Viet04/H5 interface is only slightly more restricted (Fig. 3, D to F, and tables S2 and S3) with six H bonds to HA2 (*36*). However, five of the six H bonds to the A helix are retained with Viet04/H5, highlighting the importance of the conserved A helix recognition as the major determinant of specificity. An additional H bond is formed between HA1 Ser^{291} and Asp^{72} (FR3). Thus, a somewhat peripheral contact with a homo-

typic antigen (SC1918/H1) is converted to a more direct and specific one with the heterotypic HA (Viet04/H5). Otherwise, the interactions with the two hydrophobic clusters at the junction of the A helix with HA1 are qualitatively similar, with similar van der Waals contacts (104 to 122 for the two independent complexes) in the H5 interaction (total buried surface of 1220 to 1256 Å^2; 640 to 656 Å^2 for the HAs and 580 to 600 Å^2 for Fabs).

It is interesting to note that many broadly neutralizing antibodies, including CR6261, have preferentially selected the Ig V_H1–69 germline segment that codes for a conserved hydrophobic tip on HCDR2. CR6261 was isolated along with other independent VDJ recombinants, of which 12/13 broadly neutralizing clones were derived from V_H1–69 (*15*). Similarly, many CD4-induced antibodies that target HIV-1 gp120 also use V_H1–69 (*37*–*39*). Structures of several Ig V_H1–69–derived Fabs with their antigens show that their HCDR2 tips frequently interact with solvent-exposed hydrophobic clusters that may require electroneutral interactions (*37*, *38*). Indeed, CR6261 HCDR2 is directed into a hydrophobic pocket adjacent to the A helix in both structures (fig. S5), which differs from that proposed from docking and mutational studies (*15*, *40*). Furthermore, HCDR1, which makes the most critical contacts with the highly conserved A helix, is also germline-encoded (*41*), although somatic mutations in the V_H1–69 framework also make important contributions to binding (*42*). Perhaps more unusually, HCDR3 contributes relatively little, in contrast to its usual dominant role in antigen recognition (*43*). Thus, CR6261 binds with nanomolar affinity primarily by using the germline-encoded CDRs defined by Ig V_H1–69 and complementary mutations in the framework regions with only a small contribution from HCDR3 and none from the light chain (*15*).

Most neutralizing antibodies against influenza HA recognize epitopes in the hypervariable regions that surround the receptor binding site and interfere with binding to host cells (Fig. 2A) (*25*, *27*, *28*, *44*, *45*). However, a few rare antibodies likely interfere with membrane fusion (*13*, *46*). CR6261 does not inhibit agglutination of erythrocytes in vitro, suggesting that it might act by inhibiting membrane fusion (*15*). Thus, we assayed the ability of CR6261 to prevent conversion of SC1918/H1 and Viet04/H5 HAs to the postfusion state upon exposure to low pH (*47*, *48*). Both HAs are readily converted to their protease-susceptible, postfusion form at pH 4.9 or 5.3 but not at pH 8.0 (Fig. 4, A and B, lanes 7 to 9). CR6261 Fab prevents conversion of both HAs to their postfusion conformations (Fig. 4, A and B, lanes 10 to 12).

Acidification of endosomal compartments during endocytosis of influenza virus particles results in major structural rearrangements in HA2, leading to fusion of the viral envelope with internal, host cell membranes (*23*). Most notably, low pH exposure converts the connecting segment between the A and CD helices to an additional α-helical segment, extending the central HA2 trimeric coil toward the target endosomal membrane and dragging the A helix and the N-terminal fusion peptide along with it (Fig. 4, E and F). Subsequent HA2 rearrangements are thought to bring the viral and target membranes into close proximity for fusion (*23*, *49*). The SC1918/H1 HA in complex with CR6261 is essentially identical to the unliganded, prefusion HA structure (fig. S1), despite the crystals being grown at pH 5.3, well below the pH of membrane fusion. Exposure of SC1918/H1 HA to a range of pH conditions resulted in a dose-response curve with a pH of 5.76 for 50% conversion in 1 hour (95% confidence interval, 5.70 to 5.82; Fig. 4C). Because crystals did not appear for 2 to 3 days at pH 5.3, SC1918 HA would have been expected to adopt a postfusion conformation in the crystals. Therefore, CR6261 appears to neutralize the virus by stabilizing the prefusion state and preventing the pH-dependent fusion of viral and cellular membranes.

In addition to its key role in receptor binding, HA1 is believed to act as a latch that locks HA2 in its prefusion conformation and prevents premature triggering of the fusion machinery. Around pH 7, the HA1 globular heads tightly pack atop HA2. However, pre- and postfusion structures

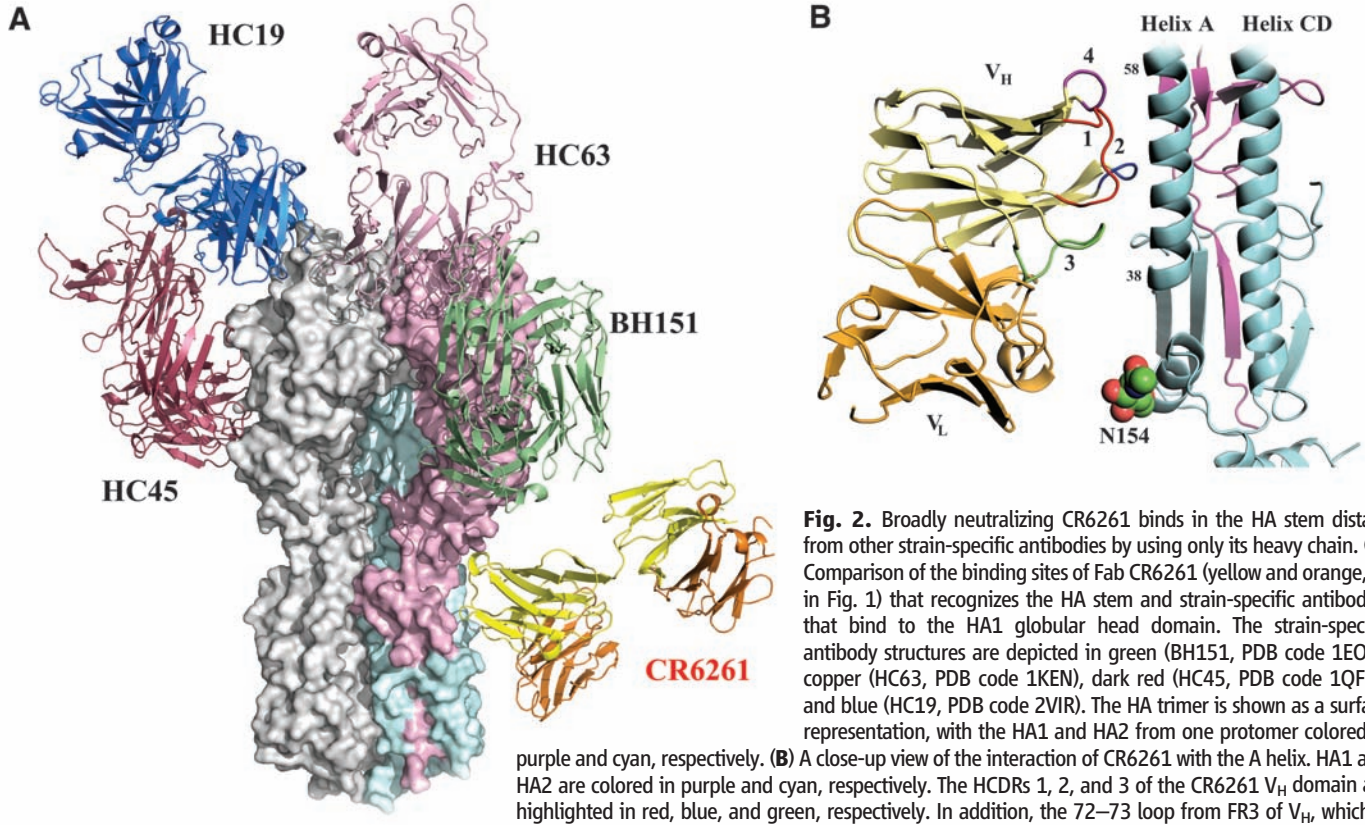

Fig. 2. Broadly neutralizing CR6261 binds in the HA stem distant from other strain-specific antibodies by using only its heavy chain. (**A**) Comparison of the binding sites of Fab CR6261 (yellow and orange, as in Fig. 1) that recognizes the HA stem and strain-specific antibodies that bind to the HA1 globular head domain. The strain-specific antibody structures are depicted in green (BH151, PDB code 1EO8), copper (HC63, PDB code 1KEN), dark red (HC45, PDB code 1QFU), and blue (HC19, PDB code 2VIR). The HA trimer is shown as a surface representation, with the HA1 and HA2 from one protomer colored in purple and cyan, respectively. (**B**) A close-up view of the interaction of CR6261 with the A helix. HA1 and HA2 are colored in purple and cyan, respectively. The HCDRs 1, 2, and 3 of the CR6261 V_H domain are highlighted in red, blue, and green, respectively. In addition, the 72–73 loop from FR3 of V_H, which is structurally analogous to the CDR HV4 of a TCR, is indicated in purple. CDR1 runs along the side of the A helix, interacting with five consecutive helical turns. In contrast, the light chain makes no contacts with the HA and is separated from the nearest HA side chain by ~8 Å. The N-linked carbohydrate attached to Asn^{154} (N154) that prevents the light chain from making contact with the HA is shown in red (oxygen) and green (carbon) balls.

reveal that the HA1 heads must disassemble from the central threefold axis to initiate refolding of HA2 during membrane fusion (Fig. 4, E and F). The electron density maps for CR6261-Viet04/H5 (crystals grown at pH 6.4) are consistent with a rigid molecule in a single conformation. However, although the SC1918/H1 maps (crystals grown at pH 5.3) are also excellent throughout the HA2/HA1 stem and Fab variable domains, they deteriorate toward the globular heads containing the receptor binding site at the membrane-distal end of the trimer (fig. S6) (*50*). Therefore, we conclude the HA1 heads are flexible and adopt multiple conformations in our crystals, with a pivot axis running roughly through Val^{56} and Glu^{271} of HA1 in the base of the vestigial esterase domain (*51*). This pivot is suggestively located in the region where HA1 would be expected to peel away from HA2 during the fusion process and may indicate that the low pH has loosened the HA1 interdomain associations. Because CR6261 lies just below the hinge, it is well positioned to act as a molecular buttress to oppose the dissociation of the HA1 heads and inhibit membrane fusion. Consistent with this hypothesis, CR6261 Fab neutralizes virus as potently as intact IgG, suggesting that cross-linking adjacent HA protomers and interference by the Fc region are not critical for inhibition.

To understand why subtypes such as H3 and H7 are not neutralized by CR6261, we conducted an extensive analysis of all nonredundant influenza A HA sequences in the National Center for Biotechnology Information (NCBI) Flu database (*52*, *53*). Given its prominent role, we first examined A helix conservation. The CR6261 binding surface on the A helix is almost invariant across all 16 subtypes, including H3 (Fig. 4D), whereas the opposite face of the helix, buried in the trimer interface, is more variable. A single polymorphism corresponding to Asn^{49} in H3 (Thr in most other subtypes) would still permit hydrogen bonding interactions with the backbone of HCDR1 Arg^{30} (*54*). Thus, to explain the low reactivity of CR6261 with H3 HA, we expanded our analysis to include the surrounding residues. Once again, most nearby residues were similar between SC1918/H1 and H3 HAs. However, whereas HA1 residues 38 and 40 of SC1918/H1 were His and Val, respectively, the same positions in H3 were Asn and Thr. Therefore, Asn^{38} is subject to N-linked glycosylation, as observed in H3 HA crystal structures (*22*, *28*). Because His^{38} lies near the center of the epitope and makes direct contact with the Fab heavy chain in the H1 and H5 complex structures, Asn^{38} glycosylation would almost certainly abolish CR6261 binding to H3 HAs. Indeed, introduction of this glycosylation site in an H5 HA reduced CR6261 binding by ~70% (*15*). The masking and unmasking of protein epitopes by carbohydrate to evade immune recognition play a major role in evolution of viral glycoproteins such as HA and HIV-1 gp120 (*22*, *45*, *55*). Asn^{38} and Thr^{40} in HA1 occurs only in the H3, H7, H10, and H15 subtypes (fig. S7) (*56*) and correlates with lack of CR6261 binding or neutralization with H3, H7, and H10 isolates (*15*). Thus, neutralization breadth of CR6261 is determined in large part by whether glycosylation is present at Asn^{38}, although isolate-specific variation in other residues proximal to the epitope may also influence the interaction. Notwithstanding, CR6261 can likely neutralize isolates from 12 of the 16 influenza A subtypes: H1, H2, H4 to H6, H8, H9, H11 to H14, and H16.

In light of the persistent threat posed by zoonotic influenza viruses, such as H5N1, H7N7, and H9N2 bird flus, and the three major pandemics in the last century, a vaccine that can provide heterosubtypic immunity would be a tremendous advance for public health. Furthermore, rational vaccine design, using potent and broadly neutralizing antibodies as a guide, is increasingly seen as the most promising solution to combat the immense diversity in certain pathogens, such as HIV-1 (*57*, *58*). Immunization with

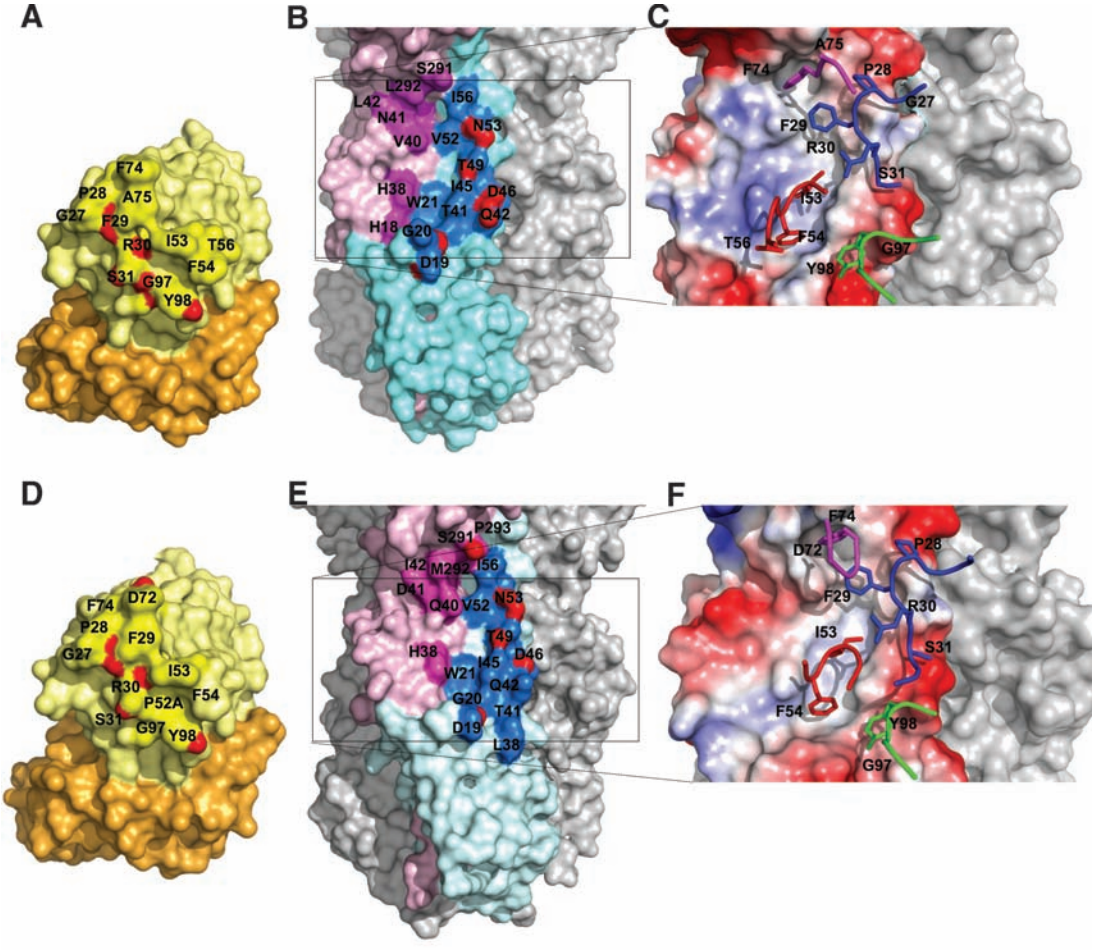

Fig. 3. Interaction of CR6261 with SC1918/H1 and Viet04/H5 HA illustrating the neutralizing epitope. Surface representations of the interaction of CR6261 with SC1918/H1 (**A** to **C**) and Viet04/H5 (**D** to **F**). The coloring in (A), (B), (D), and (E) corresponds to Fig. 1, with interacting epitope residues highlighted in a darker shade. Atoms making polar contacts are highlighted in red. (C) and (F) depict the electrostatic potential surface of the epitope on the HA (red, negative; blue, positive; and gray, neutral) with HCDRs 1, 2, 3, and FR3 (CDR "HV4") represented as sticks and colored blue, red, green, and purple, as in Fig. 2. Key interacting residues on the antibody and the HA are indicated on the top of the surface with labels (*63*).

HIV-1 and influenza leads to a robust response against hypervariable loops and regions of the envelope glycoproteins and elicitation of neutralizing antibodies. However, these hypervariable regions are generally not functionally important, and a virus can readily escape antibody binding. Occasionally, antibodies may be found that recognize highly conserved epitopes on the envelope proteins that are critical for viral entry. For HIV-1, three such classes of antibodies include b12 (which recognizes the gp120 CD4 binding site), 2G12 (conserved carbohydrate clusters on gp120), and 2F5 and 4E10 [membrane proximal regions of gp41 (*58*, *59*) that are more akin to CR6261]. For influenza, only a handful of such broadly neutralizing antibodies have been described. Most notably, a mouse monoclonal antibody C179 was reported to neutralize H1, H2, and H5 subtypes (*13*, *60*) —and, more recently, two reports describing broadly neutralizing human antibodies against H1 and H5 HA (*14*, *15*)—that may well map to the same or similar epitope as CR6261. Although CR6261 recognizes a conformational epitope between HA1 and HA2, it consists of two component parts: (i) the A helix, which accounts for most of the interacting surface and most of the polar contacts, and (ii) the HA1 region adjacent to the A helix, which makes primarily hydrophobic contacts with CR6261. Thus, it may only be necessary to mimic the A helix as a linear peptide in any rationally designed antigen (*61*). Innovative strategies may be required to improve its immunogenicity because the epitope is not particularly exposed in intact virus, although it is certainly antigenic because it reacts with high affinity to CR6261.

The conservation of this epitope suggests a critical role in membrane fusion. In late stages of fusion, the HA2 C terminus rearranges (Fig. 4, E and F) and makes extensive contacts with the A helix. In particular, the residues that mediate all of the hydrogen bonds between the A helix and CR6261 form hydrogen bonds and a salt bridge to this HA2 C-terminal H segment in the postfusion conformation (Fig. 4G), strongly suggesting that the CR6261 epitope is important in the membrane fusion process. Thus, identifica-

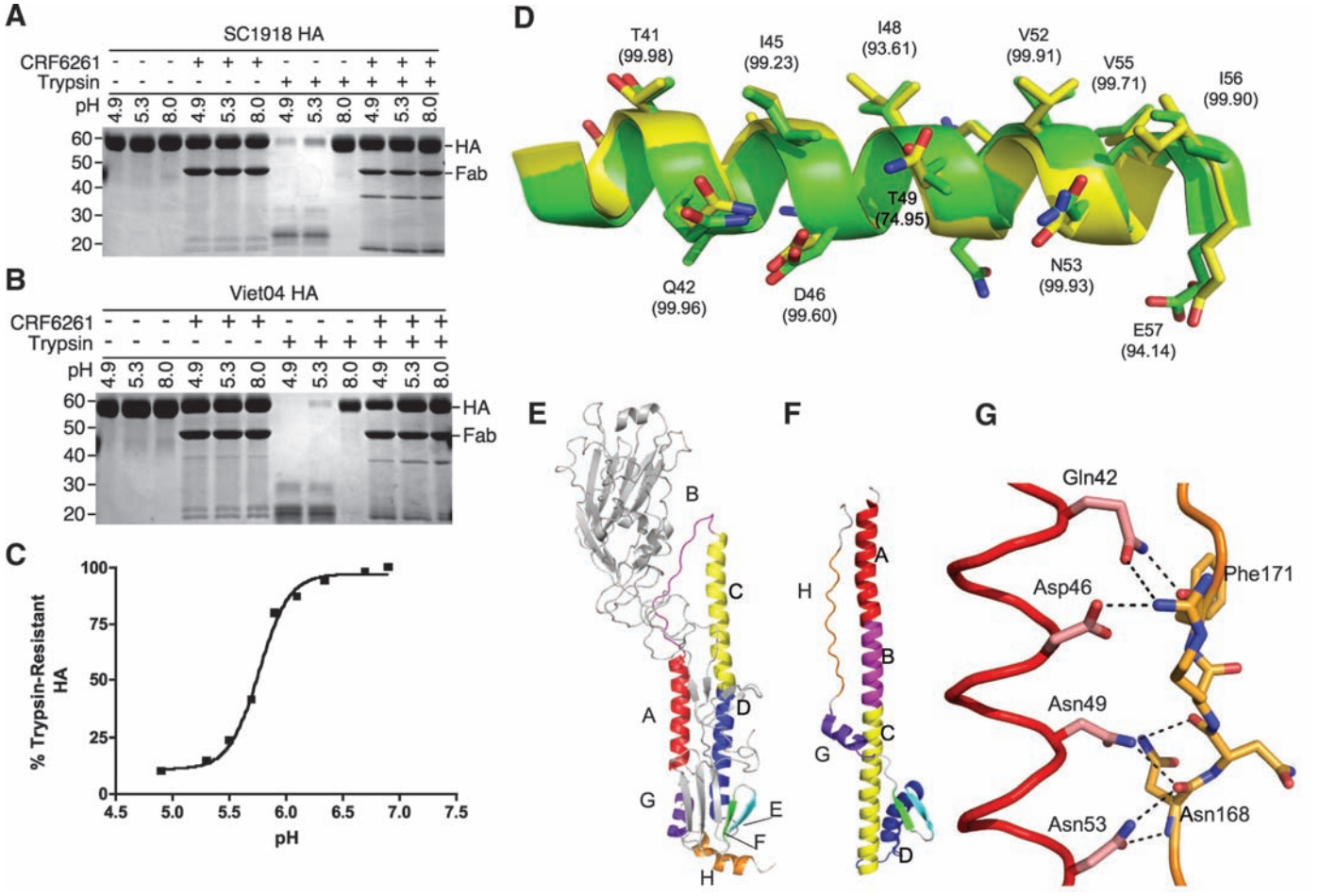

Fig. 4. CR6261 recognizes a functionally conserved epitope in the stalk region and inhibits the pH-induced conformational changes in the SC1918/H1 and Viet04/H5 HAs. CR6261 protects SC1918/H1 (**A**) and Viet04/H5 (**B**) HAs from the pH-induced protease sensitivity associated with membrane fusion. Exposure to low pH renders the SC1918/H1 and Viet04/H5 HAs sensitive to trypsin digestion (lanes 7 and 8 versus 9), but CR6261 prevents conversion to the protease susceptible conformation (lanes 10 to 12). The CR6261-SC1918-H1 crystals were grown at pH 5.3, which also indicates that CR6261 blocks the extensive pH-induced conformational changes. (**C**) Titration of SC1918-H1 trypsin resistance versus varying pH treatments (followed by neutralization to pH 8.0). The pH resulting in 50% conversion to protease sensitive conformation is 5.76 (95% confidence interval, 5.70 to 5.82). (**D**) Superposition of the A helix from SC1918/H1 (green) and an H3 HA (yellow, PDB code 2VIU) reveals that the CR6261-interacting surface is highly conserved among all subtypes. Helix positions are labeled (*63*) according to the SC1918/H1 sequence, with the percent similarity across all subtypes (H1 to H16, from an analysis of 5261 sequences) indicated in parentheses. (**E** and **F**) HA2 undergoes a dramatic and irreversible conformational change between the pre- and postfusion states. This results in the translocation of the A helix (red) from its initial position near the viral envelope (E) toward the target membrane at the opposite end of the HA trimer (F). The zipping-up of coil H along the outside of the A and B helices is thought to drive the fusion reaction. The orientation of helix C (yellow) is roughly identical in (E) and (F). (**G**) Polar residues on the CR6261-interacting surface of the A helix form a network of interactions with coil H in the postfusion state. These residues are well positioned to play a critical role in the late stages of membrane fusion, explaining the exceptional conservation the CR6261 epitope on the A helix.

tion of the CR6261 epitope provides a lead for the design of antivirals and takes an important step toward the development of a durable and cross-protective "universal" vaccine against influenza A.

References and Notes

1. J. R. Schafer *et al*., *Virology* **194**, 781 (1993).
2. A. H. Reid, T. G. Fanning, J. V. Hultin, J. K. Taubenberger, *Proc. Natl. Acad. Sci. U.S.A.* **96**, 1651 (1999).
3. Y. Kawaoka, S. Krauss, R. G. Webster, *J. Virol.* **63**, 4603 (1989).
4. W. J. Bean *et al*., *J. Virol.* **66**, 1129 (1992).
5. J. Beigel, M. Bray, *Antiviral Res.* **78**, 91 (2008).
6. A. C. Lowen, P. Palese, *Infect. Disord. Drug Targets* **7**, 318 (2007).
7. R. A. Bright, D. K. Shay, B. Shu, N. J. Cox, A. I. Klimov, *JAMA* **295**, 891 (2006).
8. M. Kiso *et al*., *Lancet* **364**, 759 (2004).
9. R. J. Russell *et al*., *Proc. Natl. Acad. Sci. U.S.A.* **105**, 17736 (2008).
10. The most common vaccine formulations contain influenza A H1N1 and H3N2 and influenza B components.
11. S. Salzberg, *Nature* **454**, 160 (2008).
12. *MMWR Morb. Mortal. Wkly. Rep.* **57**, 393 (2008).
13. Y. Okuno, Y. Isegawa, F. Sasao, S. Ueda, *J. Virol.* **67**, 2552 (1993).
14. A. K. Kashyap *et al*., *Proc. Natl. Acad. Sci. U.S.A.* **105**, 5986 (2008).
15. M. Throsby *et al*., *PLoS One* **3**, e3942 (2008).
16. The complex was generated by using a slight stoichiometric excess of antibody to HA (~3:1) to saturate the potential binding sites on the HA trimer and then purified by gel filtration.
17. Materials and methods are available as supporting material on *Science* Online.
18. J. Stevens *et al*., *Science* **312**, 404 (2006); published online 15 March 2006 (10.1126/science.1124513).
19. S. J. Gamblin *et al*., *Science* **303**, 1838 (2004); published online 5 February 2004 (10.1126/science.1093155).
20. S. Yamada *et al*., *Nature* **444**, 378 (2006).
21. The helices are designated A and CD (Fig. 4, E and F) in accordance with the nomenclature established in (*23*).
22. I. A. Wilson, J. J. Skehel, D. C. Wiley, *Nature* **289**, 366 (1981).
23. P. A. Bullough, F. M. Hughson, J. J. Skehel, D. C. Wiley, *Nature* **371**, 37 (1994).
24. Whereas baculovirus-expressed HAs lacking a polybasic cleavage site are typically secreted in the uncleaved form (HA0), treatment with trypsin yields the fusion-competent HA1/HA2. In our crystals, both HAs have been cleaved to HA1 and HA2. CR6261 binds to both cleaved and uncleaved HA.
25. D. Fleury, R. S. Daniels, J. J. Skehel, M. Knossow, T. Bizebard, *Proteins* **40**, 572 (2000).
26. C. Barbey-Martin *et al*., *Virology* **294**, 70 (2002).
27. D. Fleury *et al*., *Nat. Struct. Biol.* **6**, 530 (1999).
28. D. Fleury, S. A. Wharton, J. J. Skehel, M. Knossow, T. Bizebard, *Nat. Struct. Biol.* **5**, 119 (1998).
29. This disorder is presumably because of the well-established flexibility of the constant domains relative to the variable domains, the paucity of crystal contacts to the constant region, and the insertion of four extra residues in the light-chain elbow region. Indeed, we ultimately succeeded in building about 35 residues each of C_H1 and C_L in the region closest to the elbow. A comparison of the CR6261 Fabs from the Viet04/H5 structure with those from the SC1918/H1 structure revealed a ~13° rotation of the constant domains with respect to the variable domains between the two structures.
30. The closest distance is about 8 Å. To our knowledge, broadly neutralizing antibody b12, which targets HIV-1 gp120, is the only other example of a noncamelid or shark antibody that makes absolutely no light chain interactions with its protein antigen (*39*). Whether heavy chain–only binding correlates with the potency and cross-reactivity of antibodies, such as CR6261 and b12, is provocative but not yet proven (*15*, *37*).
31. We found that 5241 of 5261 HA protein sequences have a glycosylation consensus motif (Asn-Xaa-Ser/Thr) at position 154 of HA2. Although only the first one to two sugar residues are well ordered in our crystals, the entire glycan is presumably much larger and would likely interfere with light-chain interactions with the HA protein surface in the orientation adopted by CR6261. Details of the sequence data set used can be found in (*52*) and in (*17*).
32. The isolation of heavy chain dominant binders may be enhanced in phage display by the separation and random repairing of heavy and light chains during library preparation. This is expected to favor heavy chains that can bind antigen with little or no contribution from the light chain.
33. R. A. Lerner, *Angew. Chem. Int. Ed. Engl.* **45**, 8106 (2006).
34. Four of these five H bonds are mediated by the HCDR1 backbone, with the hydroxyl of Ser^{31} making the only polar side chain contact. A sixth H bond to the A helix is formed between the backbone amide of Tyr^{98} from HCDR3 and Gln^{42} (table S2).
35. K. C. Garcia *et al*., *Science* **274**, 209 (1996).
36. Asp^{19} is unchanged in the CR6261-Viet04/H5 complex and accepts a single H bond via its backbone carbonyl group. However, in CR6261-SC1918/H1, the density maps indicate some flexibility in this region that would allow Asp^{19} to rotate and reach over to H-bond with Thr56OG1, replacing the existing water-mediated H bond with $Ile^{18}O$.
37. C. C. Huang *et al*., *Proc. Natl. Acad. Sci. U.S.A.* **101**, 2706 (2004).
38. M. A. Luftig *et al*., *Nat. Struct. Mol. Biol.* **13**, 740 (2006).
39. T. Zhou *et al*., *Nature* **445**, 732 (2007).
40. In other previously characterized structures, $V_H(1–69)$ restriction was proposed to result from the role of the unique protruding hydrophobic HCDR2 in anchoring HCDR3 interaction rather than in preserving precise molecular interactions (*37*).
41. CDR definitions after (*62*).
42. These mutations are Thr^{28}→Pro^{28} and Ser^{30}→Arg^{30} in the FR1 loop directly preceding HCDR1 and Ser^{74}→Phe^{74} mutation in FR3.
43. M. M. Davis, *Semin. Immunol.* **16**, 239 (2004).
44. W. Gerhard, J. Yewdell, M. E. Frankel, R. Webster, *Nature* **290**, 713 (1981).
45. D. C. Wiley, I. A. Wilson, J. J. Skehel, *Nature* **289**, 373 (1981).
46. C. Barbey-Martin *et al*., *Virology* **294**, 70 (2002).
47. J. J. Skehel *et al*., *Proc. Natl. Acad. Sci. U.S.A.* **79**, 968 (1982).
48. The HA prefusion state is highly protease-resistant, whereas the postfusion state is much more susceptible to protease degradation (*47*).
49. J. Chen, J. J. Skehel, D. C. Wiley, *Proc. Natl. Acad. Sci. U.S.A.* **96**, 8967 (1999).
50. Despite considerable efforts to reposition HA1, including rigid body refinement of various subdomains, simulated annealing, and manual rebuilding, no improvement of fit was achieved for the membrane-distal portion of HA. More details can be found in (*17*).
51. The best fit of HA1 to the density results in a 2 Å radial displacement of the receptor binding site compared with its location in the unliganded form.
52. Description of the analyzed sequence data set: A total of 5261 clones comprising all full-length, nonredundant influenza A HA protein sequences were analyzed. Only lab strains were excluded from the analysis, to avoid the effects of any mutations involved in adaption to culture in vitro. The data set included 854 H1, 125 H2, 1582 H3, 144 H4, 1384 H5, 261 H6, 359 H7, 17 H8, 334 H9, 59 H10, 71 H11, 25 H12, 26 H13, 2 H14, 5 H15, and 13 H16 sequences. Details of the methods used for analysis are available in (*17*). Sequences were retrieved on 14 January 2009 from www.ncbi.nlm.nih.gov/genomes/FLU/FLU.html.
53. Our analysis included a total of 5261 protein sequences, encompassing all 16 subtypes and isolates from all species, including humans.
54. Although we cannot rule out the possibility that the slightly larger Asn could result in unfavorable interactions between the Fab, sufficient space is available to accommodate the Asn side chain.
55. P. D. Kwong *et al*., *Nature* **393**, 648 (1998).
56. We predict that 2004 of 2005 clones are glycosylated on the basis of the presence of an Asn-Xaa-Ser/Thr motif at residues 38 to 40 (in 1581/1582 H3, 359/359 H7, 59/59 H10, and 5/5 H15 clones). Only a single H3 clone [A/New York/252/1999(H3N2)] lacked the consensus sequence. In contrast, not a single glycosylation motif was present in 3256 clones from the H1, H2, H4 to H6, H8, H9, H11 to H14, and H16 subtypes (fig. S7).
57. B. D. Walker, D. R. Burton, *Science* **320**, 760 (2008).
58. D. R. Burton, R. L. Stanfield, I. A. Wilson, *Proc. Natl. Acad. Sci. U.S.A.* **102**, 14943 (2005).
59. M. B. Zwick, D. R. Burton, *Curr. HIV Res.* **5**, 608 (2007).
60. Y. A. Smirnov *et al*., *Acta Virol.* **43**, 237 (1999).
61. Whereas polar interactions impose charge, spatial, and steric constraints on an interacting surface, hydrophobic interactions are less specific but provide binding energy. For example, formation of a hydrogen bond to a particular donor requires a suitable acceptor group ("charge") to be placed on a particular position of the interaction surface and in a particular orientation (spatial), and the interacting residues and their neighbors must be able to physically accommodate the interacting residues (steric). In contrast, it is relatively likely that two or more aliphatic side chains will end up in close proximity and be able to exclude solvent. Thus, although the hydrophobic interactions with HA1 may help to stablize CR6261 binding to HA and increase the free energy of binding, the polar interactions with conserved residues in the A helix are probably most critical for the specific recognition of multiple HA subtypes.
62. C. Chothia *et al*., *J. Mol. Biol.* **227**, 799 (1992).
63. Single-letter abbreviations for the amino acid residues are as follows: A, Ala; C, Cys; D, Asp; E, Glu; F, Phe; G, Gly; H, His; I, Ile; K, Lys; L, Leu; M, Met; N, Asn; P, Pro; Q, Gln; R, Arg; S, Ser; T, Thr; V, Val; W, Trp; and Y, Tyr.

64. This work was supported in part by NIH grant AI-058113 (I.A.W.) and a predoctoral fellowship from the Achievement Rewards for College Scientists Foundation (D.C.E.) and the Skaggs Institute. The Joint Center for Structural Genomics (JCSG) is supported by NIH National Institute of General Medical Sciences (NIGMS) (U54 GM074898). The GM/CA CAT 23-ID-B beamline has been funded in whole or in part with federal funds from National Cancer Institute (Y1-CO-1020) and NIGMS (Y1-GM-1104). Use of the Advanced Photon Source (APS) was supported by the U.S. Department of Energy, Basic Energy Sciences, Office of Science, under contract no. DE-AC02-06CH11357. The content is solely the responsibility of the authors and does not necessarily represent the official views of NIGMS or the NIH. The authors thank H. Tien and D. Marciano of the Robotics Core at the JCSG for automated crystal screening; C. Ogata and the staff of the APS GM/CA CAT 23-ID-B for beamline support; X. Dai and R. Stanfield for excellent assistance with data collection and processing and analyses; R. Pejchal, M. Crispin, M. Wormald, and D. Wolan for valuable comments; and R. Lerner for insightful discussion. This is publication 19980 from the Scripps Research Institute. Coordinates and structure factors are deposited in the Protein Data Bank (PDB) (3GBN and 3GBM for CR6261-SC1918/H1 and CR6261-Viet04/H5, respectively).

Supporting Online Material

www.sciencemag.org/cgi/content/full/1171491/DC1
Materials and Methods
Figs. S1 to S7
Tables S1 to S3
References

27 January 2009; accepted 19 February 2009
Published online 26 February 2009;
10.1126/science.1171491
Include this information when citing this paper.

Wingbeat Time and the Scaling of Passive Rotational Damping in Flapping Flight

Tyson L. Hedrick,[1]* Bo Cheng,[2] Xinyan Deng[2]*

Flying animals exhibit remarkable capabilities for both generating maneuvers and stabilizing their course and orientation after perturbation. Here we show that flapping fliers ranging in size from fruit flies to large birds benefit from substantial damping of angular velocity through a passive mechanism termed flapping counter-torque (FCT). Our FCT model predicts that isometrically scaled animals experience similar damping on a per-wingbeat time scale, resulting in similar turning dynamics in wingbeat time regardless of body size. The model also shows how animals may simultaneously specialize in both maneuverability and stability (at the cost of efficiency) and provides a framework for linking morphology, wing kinematics, maneuverability, and flight dynamics across a wide range of flying animals spanning insects, bats, and birds.

Flying animals of all sizes exhibit a surprising degree of maneuverability, and animals ranging in size from fruit flies (*1*) to pigeons (*2*) have been the subject of detailed analyses of maneuvering kinematics. Many studies have also considered stability and control in animal flight, both from a neural standpoint (*3*, *4*) and in broader analyses incorporating both neural and physical inputs (*5*–*7*). This body of work provides the opportunity to examine the scaling of maneuvering capability with body size and determine whether animals of different sizes and phylogenetic groups use similar or different mechanisms to accomplish maneuvers.

We focus our comparison on a particular type of maneuver: low-speed yaw turns of 60° or more (Fig. 1), because these have been most widely recorded in freely flying animals. Rotational maneuvers such as yaw turns necessarily include both an angular acceleration phase, where the animal begins turning, and an angular deceleration phase, where the animal slows and ends the rotation. In the acceleration phase, the animal must actively produce an aerodynamic torque through some type of flapping or body asymmetry. However, the animal might then decelerate by either actively producing a torque in the opposite direction (*1*) or simply allowing friction to passively damp out its rotational velocity, coasting to a halt. Because the moment of inertia is proportional to mass to the five-thirds power (mass$^{5/3}$), large animals such as birds are likely to require active deceleration whereas smaller animals such as flies are often modeled with substantial fluid drag (*8*), which might allow passive deceleration, although a recent report emphasizes active deceleration in these animals as well (*1*). However, other recent analyses of yaw turns in insects (*9*) and banked turns in birds (*10*) emphasized the importance of a form of aerodynamic damping related to symmetric wing motion, raising the possibility that passive damping is important at many size scales.

Damping from wing motion arises as follows: Consider an animal engaged in symmetric hovering or low-speed flight (Fig. 2, A and B). Previous experiments have shown that during downstroke, net aerodynamic forces are directed upward and posteriorly; in upstroke, in animals with an aerodynamically active upstroke, the forces are directed upward and anteriorly (*11*, *12*). However, when the animal experiences whole-body rotation (for example, about an axis normal to the plane of flapping), net wing velocity is enhanced on the outside wing during downstroke and on the inside wing during upstroke (*2*). This net velocity asymmetry, which arises when the animal is flapping symmetrically, gives rise to a force asymmetry (and therefore a torque) that acts to slow the animal's rotation (Fig. 2, C and D). We refer to this form of damping as FCT because it depends on flapping and acts counter to the direction of body rotation. Below, we explore the scaling implications of FCT by postulating a simple equation modeling FCT and a second equation modeling active torque generation via asymmetric flapping, the expected deceleration method for large animals because of the rapid increase in moment of inertia with body size. We use these two equations to develop alternative predictions of the rotational deceleration dynamics for flying animals and then compare the predictions to measurements of yaw turning in four species of insects and three species of vertebrates across six orders of magnitude in body mass (from 1×10^{-4} to 285 g). The results of the comparison are consistent with FCT but not with an active deceleration via asymmetric flapping.

The rotational damping due to FCT arises from the difference in velocity between the inside and outside wings (Fig. 2, C and D). Thus, FCT is the result of (velocity due to flapping – velocity due to body rotation)^2 on one wing minus (velocity due to flapping + velocity due to rotation)^2 on the other wing, multiplied by the determinants of aerodynamic force: air density; wing size and shape; and where flapping velocity is determined by amplitude, frequency, and trajectory. Angular deceleration resulting from FCT is therefore

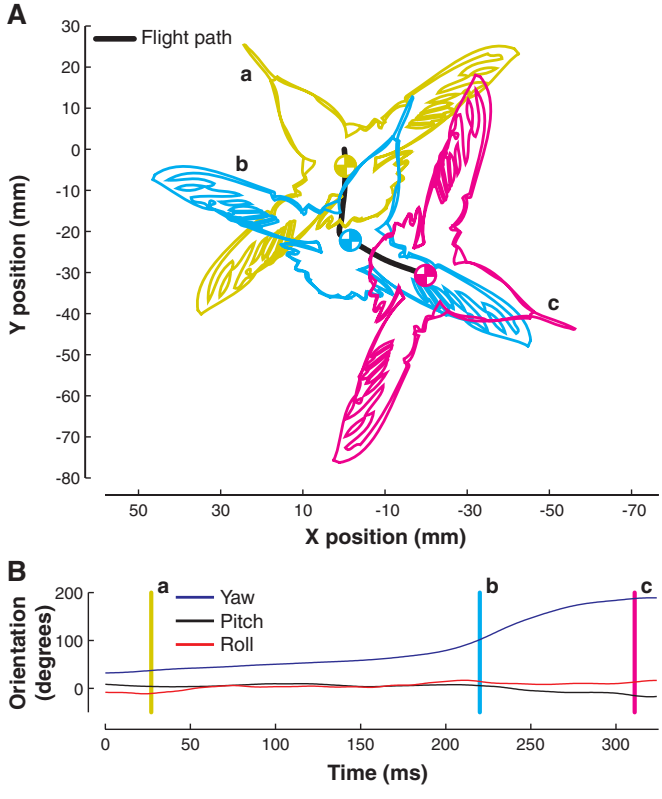

Fig. 1. A sharp yaw turn performed by a hovering ruby-throated hummingbird. (**A**) The hummingbird's position and orientation in the horizontal (*x*-*y*) plane at three different times during the turn, viewed from above the bird, looking down. The +*z* axis points into the page and toward the ground, parallel to gravity. The hummingbird yaws to its right, corresponding to a clockwise motion on the figure between stages a, b, and c. The hummingbird is to scale, but the wing position in the figure does not indicate the actual wing position. In addition to the horizontal movement depicted here, the hummingbird descended 25 mm during the recording. (**B**) The hummingbird's yaw, pitch, and roll orientation through time. The vertical lines a, b, and c indicate the time represented by each of the outline figures in (**A**).

[1]Department of Biology, University of North Carolina at Chapel Hill, Chapel Hill, NC 27599, USA. [2]Department of Mechanical Engineering, University of Delaware, Newark, DE 19716, USA.

*To whom correspondence should be addressed. E-mail: thedrick@bio.unc.edu (T.L.H.); deng@udel.edu (X.D.)

proportional to angular velocity and inversely proportional to the animal's moment of inertia. These factors may be expressed concisely by the following ordinary differential equation

$$\dot{\omega}_{FCT} = -\omega \frac{\rho R^4 \bar{c} \hat{r}_3^3(S) \Phi n \overline{C_F \sin(\alpha)(d\hat{\varphi}/d\hat{t})}}{I} \quad (1)$$

where $\dot{\omega}_{FCT}$ is angular deceleration due to FCT, ω is angular velocity, $\overline{C}_F$ is the mean aerodynamic resultant force coefficient, α is the spanwise rotation angle of the wing, ρ is air density, R is wing length, $\bar{c}$ is the average wing chord, $\hat{r}_3(S)$ is the nondimensional third moment of area, Φ is wing stroke amplitude, n is wingbeat frequency, $(d\hat{\phi}/d\hat{t})$ is the nondimensional wing angular velocity, and I is the animal's moment of inertia. All symbols are as per Ellington (*13*). See appendix A in (*14*) for background on this equation.

An alternative to deceleration by FCT, active torque generation by asymmetric flapping, depends on the degree of functional asymmetry between the two wings; deceleration due to asymmetric flapping may be written as

$$\dot{\omega}_a = (\gamma - 1) \frac{\rho R^4 \bar{c} \hat{r}_3^3(S) \Phi^2 n^2 \overline{C_F \sin(\alpha)(d\hat{\varphi}/d\hat{t})^2}}{8I} \quad (2)$$

where γ is the magnitude of the asymmetry, ranging from 0 to 1, with 1 indicating no asymmetry. Unlike FCT, active deceleration is not related to body angular velocity. See appendix B in (*14*) for additional details on this formulation.

It is known that the dimensions of flying animals scale at near isometry, with wing length and chord proportional to mass$^{1/3}$ and moment of inertia proportional to mass$^{5/3}$ (*15*). Wingbeat frequency is known to scale as mass$^{-0.24}$ for insects and hummingbirds, but the fit is poor and there is substantial variation within a given size range (*16*). Therefore, after assuming isometric scaling and eliminating nonvarying and nondimensional terms from Eqs. 1 and 2, we are left with the following proportionalities

$$\dot{\omega}_{FCT} \propto -\omega \Phi n \quad (3)$$

$$\dot{\omega}_a \propto (\gamma - 1) \Phi^2 n^2 \quad (4)$$

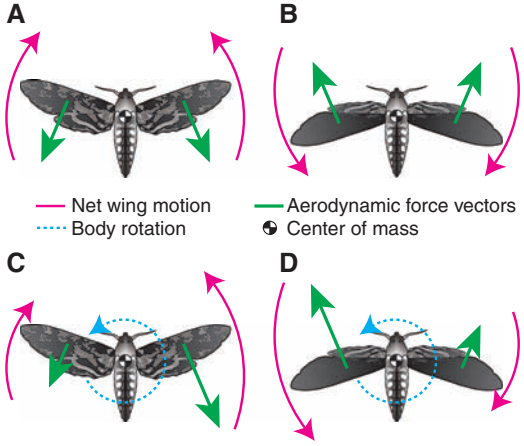

Fig. 2. FCT arises when overall body rotation interacts with symmetric wing motion. (**A**) and (**B**) show the aerodynamic forces experienced by a flying animal in upstroke (A) and downstroke (B). (**C**) and (**D**) show how wing motion and aerodynamic forces are modified by overall body rotation. The now asymmetric aerodynamic forces provide a torque counter to the body rotation.

Table 1. Morphological data and predictions from the active and passive deceleration hypotheses along with the measurements. I'_{zz}, moment of inertia of the animal in the stroke plane frame yaw axis; $t_{1/2}(N)$, half-life as a function of number of wingbeats. See (*14*) for details of the FCT and active deceleration predictions as well as the sources of the morphological and kinematic data. Active deceleration predictions are for the time required to decelerate to one-half of peak velocity, making them directly comparable to the FCT predictions. We used a γ of 0.944, based on an arithmetic solution of Eq. 2 to the fruit fly data. See (*14*) for results scaling γ to body size or other factors. For both sets of predictions, we assume that $\overline{C_F \sin(\alpha)(d\hat{\phi}/d\hat{t})}$ is equal to 6.0 and $\overline{C_F \sin(\alpha)(d\hat{\phi}/d\hat{t})^2}$ is equal to 31.3 for all species.

Species	Morphology							FCT passive deceleration predictions		Active deceleration predictions		Measurements	
	Mass (g)	I'_{zz} (N·m s^2)	R (mm)	$\bar{c}$ (mm)	n (Hz)	Φ (°)	$\hat{r}_3(S)$ (–)	$t_{1/2}(t)$ (ms)	$t_{1/2}(N)$ (wingbeats)	$t_{1/2}(t)$ (ms)	$t_{1/2}(N)$ (wingbeats)	$t_{1/2}(t)$ (ms)	$t_{1/2}(N)$ (wingbeats)
Fruit fly (*Drosophila melanogaster*)	9.6 ± 2.7 × 10^{-4}	2.72 × 10^{-13} –	2.39 ± 0.08	0.80 ± 0.02	218 ± 7	140 ± 10	0.59	9.2 ± 1.5	2.00 ± 0.32	10.4 ± 2.3	2.22 ± 0.48	10.36	2.2
Stalk-eyed fly (*Cyrtodiopsis dalmanni*)	7.0 ± 1.0 × 10^{-3}	1.60 × 10^{-11} –	4.46 ± 0.14	0.94 ± 0.08	170 ± 8	140* ± 10	0.64	38.0 ± 11.1	6.47 ± 1.85	55.1 ± 11.8	9.35 ± 1.82	35.68	5.6
Bluebottle fly (*Calliphora vicina*)	6.2 × 10^{-2} ± 5.0 × 10^{-3}	2.81 × 10^{-10} –	9.2 ± 0.5	3.14 ± 0.5	143 ± 9	138 ± 15	0.59	17.2 ± 11.7	2.43 ± 1.63	30.8 ± 15.0	4.32 ± 2.01	14.31	2.1
Hawkmoth (*Manduca sexta*)	1.62 ± 0.33	2.43 × 10^{-7} –	48.8 ± 2.1	18.6 ± 1.6	26 ± 2	98 ± 4	0.56	28.4 ± 6.6	0.74 ± 0.16	166.1 ± 46.3	4.31 ± 1.02	19	0.5†
Hummingbird (*Archilochus colubris*)	3.17 ± 0.15	3.58 × 10^{-7} –	45.0 ± 4.7	11.8 ± 2.0	48.7 ± 9.1	134 ± 7.2	0.57	33.8 ± 26.1	1.64 ± 1.13	184.1 ± 180.2	8.86 ± 6.12	45	2.0†
Fruit bat (*Cynopterus brachyotis*)	35.1 ± 1.8	4.12 × 10^{-5} –	150 ± 14	83 ± 14	11.1 ± 0.6	141 ± 14	0.54	22.0 ± 12.3	0.24 ± 0.14	415.4 ± 256.5	4.60 ± 2.77	17	0.2†
Cockatoo (*Eolophus roseicapillus*)	285.9 ± 14.4	1.29 × 10^{-3} –	347 ± 8	118 ± 4	7.1 ± 1.1	99 ± 16.4	0.58	30.3 ± 6.4	0.22 ± 0.02	945.4 ± 392.5	6.72 ± 1.37	40	0.3†

*A wingbeat amplitude measure was not available for the stalk-eyed fly; *Drosophila* kinematics were substituted. †The measurement of half-life in wingbeats uses the animal's exact wingbeat frequency when available.

where $\dot{\omega}$ is body angular deceleration due to FCT or active (a) means, ω is body angular velocity, Φ is wingbeat amplitude, n is wingbeat frequency, and γ is the magnitude of asymmetry in flapping. Wingbeat amplitude is not known to vary widely or systematically among species, whereas wingbeat frequency varies over two orders of magnitude (*15*) and from 218 to 7.1 Hz in the species examined here. Thus, variation in these equations among different species is dominated by variation in wingbeat frequency.

These equations summarize two distinct modes by which flying animals might reduce their angular velocity at the end of a maneuver. Yaw deceleration dominated by FCT would exhibit exponential decay (Eqs. 1 and 3 and eqs. S19 to S23), a pattern observed in early studies of fruit fly turning (*17*, *18*) and ascribed to body friction. For animals of approximately isometric dimensional scaling, similar wingbeat amplitudes, and similar aerodynamic force coefficients, Eq. 3 also implies that normalizing time by wingbeat frequency should result in similar wingbeat time dynamics regardless of body size (eq. S23). Deceleration due to the simple model of asymmetric flapping (Eqs. 2 and 4) is linear and occurs at a rate that varies with the square of flapping frequency.

We tested predictions of turning dynamics arising from these two modes against data from seven different animals executing low-speed yaw turns (Fig. 1 and Table 1). See appendix C in (*14*) for a description of the various sources of these data, both in the literature and from previously unreported experiments.

Unsurprisingly, given the considerable range of species examined, the different animals exhibited widely divergent yaw turning performance (Fig. 3A and Table 1), slowing down at very different rates. However, in contrast to their differences in deceleration rate, the fruit fly, stalk-eyed fly, bluebottle fly, and hummingbird all exhibited similar peak yaw rates of approximately 1600° s^{-1}. This does not appear to reflect a mechanical limitation, because Eq. 2 indicates that these animals should have greatly different capabilities for active torque generation and even different ratios of active torque to FCT (Eq. 5). It may reflect neurophysiological limitations on the rate at which flying animals can acquire and process sensory information for flight control (*19*).

The measured duration of yaw rate half-life during deceleration was similar to that predicted by the FCT passive deceleration model (Eq. 1, Table 1, and Fig. 3D). The deceleration rate, measured as the time to decelerate to one-half the peak yaw rate, was not similar to that predicted for active torque generation (Eq. 2 and Table 1). Furthermore, the prediction that approximately isometric animals should have similar rotational deceleration dynamics in wingbeat time was also supported (Fig. 2B). This prediction is specific to isometrically scaled animals; the data reveal two such groups with similar dynamics. Fruit flies, bluebottle flies, and hummingbirds have similar scaling of wing and body dimensions (table S1) and all exhibited a deceleration half-life of about two wingbeats. Hawkmoths, bats, and cockatoos all have wings approximately twice as large relative to body weight as those of the aforementioned group and all exhibited half-lives of less than a wingbeat. The stalk-eyed fly has a moment of inertia out of proportion to body size due to its unusual eye position (*20*) and had a half-life of about six wingbeats.

Our FCT model predicts yaw turn deceleration dynamics across seven phylogenetically and morphologically dissimilar flying animals spanning six orders of magnitude in body mass (Fig. 3), using only morphological and kinematic inputs, supporting FCT as a unifying principle central to the dynamics of flying animals across a large size range. Our results do not agree with a model based on deceleration via torque generation by asymmetric flapping. However, interspecific or temporal variation in asymmetry (γ) could produce the observed results—a perfectly valid although less parsimonious possibility. However, the appropriate variation in γ cannot be produced by scaling it from any of the measured morphological parameters [appendix D in (*14*) and fig. S3].

In addition to providing a framework for assessing animal flight dynamics, FCT also provides insights into form/function relationships. For example, maneuverability and stability are often cast in opposition to one another, but some factors that enhance maneuverability would also enhance FCT, a form of passive stability. The scaling of rotational maneuverability may be approximated by the same equation we use to estimate the scaling of deceleration via active torque generation (Eq. 2). Thus, increases in wingbeat frequency (n) in particular improve both an animal's aerodynamic capacity for torque generation

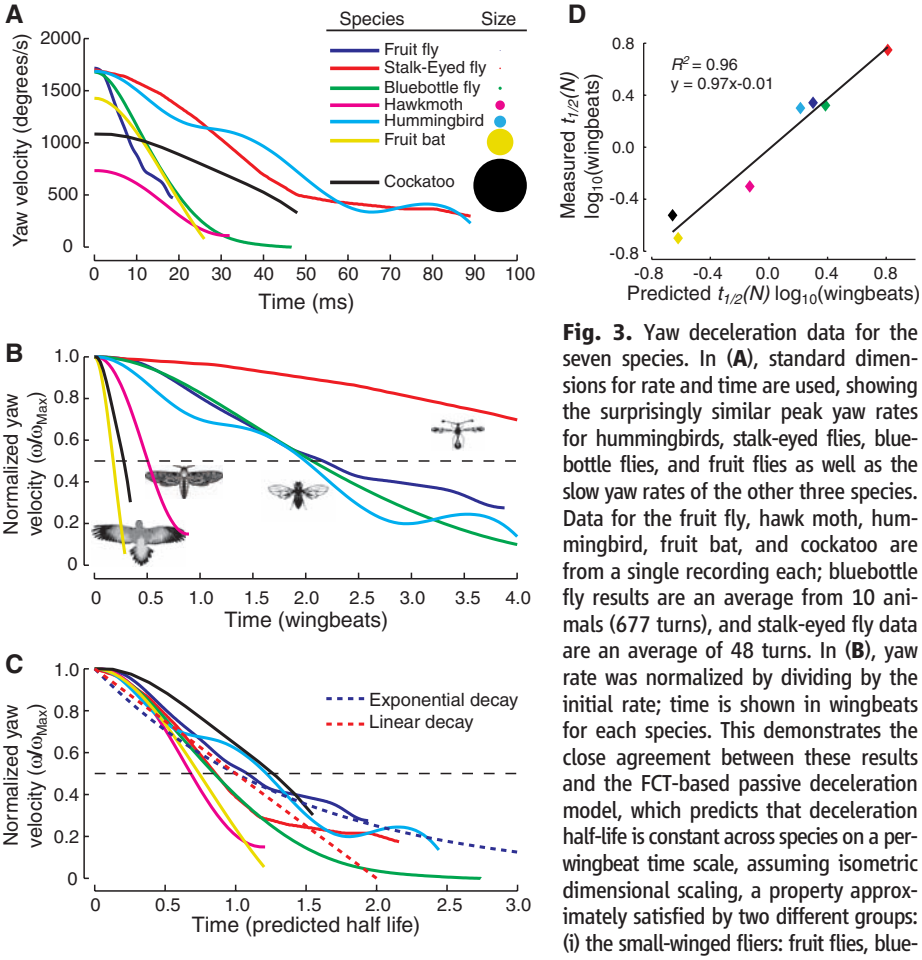

Fig. 3. Yaw deceleration data for the seven species. In (**A**), standard dimensions for rate and time are used, showing the surprisingly similar peak yaw rates for hummingbirds, stalk-eyed flies, bluebottle flies, and fruit flies as well as the slow yaw rates of the other three species. Data for the fruit fly, hawk moth, hummingbird, fruit bat, and cockatoo are from a single recording each; bluebottle fly results are an average from 10 animals (677 turns), and stalk-eyed fly data are an average of 48 turns. In (**B**), yaw rate was normalized by dividing by the initial rate; time is shown in wingbeats for each species. This demonstrates the close agreement between these results and the FCT-based passive deceleration model, which predicts that deceleration half-life is constant across species on a per-wingbeat time scale, assuming isometric dimensional scaling, a property approximately satisfied by two different groups: (i) the small-winged fliers: fruit flies, bluebottle flies, and hummingbirds; and (ii) the large-winged fliers: hawk moths, bats, and cockatoos. See table S1 for a comparison of wing and body scaling among these species. In (**C**), yaw rate is normalized as in (B) and time is normalized to the predicted half-life of each species (Table 1). Ideal exponential decay (FCT) and linear decay (asymmetric flapping) curves are also shown. (**D**) compares the predicted and measured yaw deceleration half-life across the seven species. $t_{1/2}(N)$, half-life as a function of number of wingbeats. As expected, there was a strong relationship between predicted and measured values, and the least-squares regression slope is similar to 1.0 and the regression intercept close to 0, showing that the FCT model accurately predicts deceleration half-life for this group of species, despite the wide range of body sizes, differences in body and wing morphology, and phylogenetic distance.

and the magnitude of FCT. Because active torque is proportional to n^2 and passive torque to n, the ratio of active to passive torque increases as n increases (Eq. 5), even while both quantities increase individually

$$\frac{\dot{\omega}_a}{\dot{\omega}_{FCT}} = -(\gamma - 1)\frac{\Phi n\,\overline{(d\hat{\varphi}/d\hat{t})}}{8\omega} \qquad (5)$$

The increase in the ratio indicates an enhanced capability for active maneuvers and active stabilization, whereas the increase in FCT adds to passive stability. Thus, increasing wingbeat frequency enhances both maneuverability and stability. Hummingbirds provide an interesting example; males typically have greater wingbeat frequencies (*21*) and smaller body sizes as compared to females of the same species, potentially conferring a benefit in maneuverability and therefore an advantage in display flights (*22*) as well as greater stability when experiencing an external perturbation. These benefits are not without cost, because increasing wingbeat frequency increases the inertial and profile power requirements of flapping flight.

Finally, the success of our FCT model in predicting yaw deceleration dynamics implies that passive damping may be important to flight control in flying animals across a wide range of body sizes. For example, if a steadily flapping animal experiences a brief perturbation in midstroke, by the time it is prepared to execute a corrective wingbeat, FCT will have eroded much of the effect of the perturbation, regardless of the wingbeat frequency employed by the animal. Thus, FCT provides open loop stability for some aspects of animal flight, reducing its neuromuscular and neurosensory requirements. These are not eliminated, because FCT results in asymmetric forces from symmetric flapping, implying that the animal's muscles must generate asymmetric forces and suggesting neural regulation to enforce symmetry. Furthermore, FCT does not address all the stability problems faced by flying animals. This study is limited to yaw dynamics in hovering or slow-speed flight; FCT is likely to be influential in fast forward flight, but no data are available to test such predictions. More important, a full description of body dynamics involves many factors beyond FCT and includes modes such as pitching and longitudinal dynamics known to be inherently unstable in open loop conditions (*23*, *24*) and subject to active control (*25*, *26*). Finally, yaw damping due to FCT is a feature of flapping flight that is not found in human-made fixed-wing or rotary-wing flyers and may lead to improvements in the stability and maneuverability of biomimetic micro–air vehicles.

References and Notes

1. S. N. Fry, R. Sayaman, M. H. Dickinson, *Science* **300**, 495 (2003).
2. D. R. Warrick, K. P. Dial, *J. Exp. Biol.* **201**, 655 (1998).
3. M. F. Land, T. S. Collett, *J. Comp. Physiol. A* **89**, 331 (1974).
4. J. W. S. Pringle, in *Insect Flight*, M. Abercrombie, P. B. Medawar, G. Salt, M. M. Swann, V. B. Wigglesworth, Eds. (Cambridge Monographs in Experimental Biology, Cambridge Univ. Press, London, 1957), pp. 86–118.
5. G. K. Taylor *et al.*, *J. Exp. Biol.* **211**, 258 (2008).
6. G. K. Taylor, *Biol. Rev. Camb. Philos. Soc.* **76**, 449 (2001).
7. H. Wagner, *Philos. Trans. R. Soc. London Ser. B* **312**, 527 (1986).
8. N. Boeddeker, M. Egelhaaf, *J. Exp. Biol.* **208**, 1563 (2005).
9. T. Hesselberg, F.-O. Lehmann, *J. Exp. Biol.* **210**, 4319 (2007).
10. T. L. Hedrick, A. A. Biewener, *J. Exp. Biol.* **210**, 1897 (2007).
11. S. P. Sane, *J. Exp. Biol.* **206**, 4191 (2003).
12. J. R. Usherwood, C. P. Ellington, *J. Exp. Biol.* **205**, 1565 (2002).
13. C. P. Ellington, *Philos. Trans. R. Soc. London Ser. B* **305**, 41 (1984).
14. See supporting material on *Science* Online.
15. C. H. Greenewalt, *Smithson. Misc. Collect.* **144**, 1 (1962).
16. R. Dudley, *The Biomechanics of Insect Flight. Form, Function, Evolution* (Princeton Univ. Press, Princeton, NJ, 2000).
17. M. Mayer, K. Vogtmann, B. Bausenwein, R. Wolf, M. Heisenberg, *J. Comp. Physiol. A* **163**, 389 (1988).
18. H. H. Bülthoff, T. Poggio, C. Wehrhahn, *Z. Naturforsch. C* **35**, 811 (1980).
19. G. K. Taylor, H. G. Krapp, in *Insect Mechanics and Control*, J. Casas, S. J. Simpson, Eds. (Academic Press, London, 2007), vol. 34, pp. 231–316.
20. G. Ribak, J. Swallow, *J. Comp. Physiol. A* **193**, 1065 (2007).
21. T. A. Hunter, J. Picman, *Condor* **107**, 570 (2005).
22. F. G. Stiles, D. L. Altshuler, R. Dudley, *Auk* **122**, 872 (2005).
23. G. K. Taylor, A. L. R. Thomas, *J. Theor. Biol.* **214**, 351 (2002).
24. M. Sun, J. K. Wang, *J. Exp. Biol.* **210**, 2714 (2007).
25. G. K. Taylor, A. L. R. Thomas, *J. Exp. Biol.* **206**, 2803 (2003).
26. X. Deng, L. Schenato, S. S. Sastry, *IEEE Trans. Robotics* **22**, 789 (2006).

27. We thank A. Biewener of Harvard University and S. Swartz and K. Breuer of Brown University for providing the hummingbird and fruit bat data. This work was funded in part by NSF grant 0732267 (Division of Integrative Organismal Systems) to T.L.H. and NSF grant 0545931 (Division of Information and Intelligent Systems) to X.D.

Supporting Online Material

www.sciencemag.org/cgi/content/full/324/5924/252/DC1
SOM Text
Figs. S1 to S3
Table S1
References
Appendices A to D

12 November 2008; accepted 20 February 2009
10.1126/science.1168431

Coding-Sequence Determinants of Gene Expression in *Escherichia coli*

Grzegorz Kudla,[1]* Andrew W. Murray,[2] David Tollervey,[3] Joshua B. Plotkin[1]†

Synonymous mutations do not alter the encoded protein, but they can influence gene expression. To investigate how, we engineered a synthetic library of 154 genes that varied randomly at synonymous sites, but all encoded the same green fluorescent protein (GFP). When expressed in *Escherichia coli*, GFP protein levels varied 250-fold across the library. GFP messenger RNA (mRNA) levels, mRNA degradation patterns, and bacterial growth rates also varied, but codon bias did not correlate with gene expression. Rather, the stability of mRNA folding near the ribosomal binding site explained more than half the variation in protein levels. In our analysis, mRNA folding and associated rates of translation initiation play a predominant role in shaping expression levels of individual genes, whereas codon bias influences global translation efficiency and cellular fitness.

The theory of codon bias posits that preferred codons correlate with the abundances of iso-accepting tRNAs (*1*, *2*) and thereby increase translational efficiency (*3*) and accuracy (*4*). Recent experiments have revealed other effects of silent mutations (*5*–*7*). We synthesized a library of green fluorescent protein (GFP) genes that varied randomly in their codon usage, but encoded the same amino acid sequence (*8*). By placing these constructs in identical regulatory contexts and measuring their expression, we isolated the effects of synonymous variation on gene expression.

The GFP gene consists of 240 codons. For 226 of these codons, we introduced random silent mutations in the third base position, while keeping the first and second positions constant (Fig. 1A). The resulting synthetic GFP constructs differed by up to 180 silent substitutions, with an average of 114 substitutions between pairs of constructs (Fig. 1B and figs. S1 and S2). The range of third-position GC content (GC3) across the library of constructs encompassed virtually all (99%) of the GC3 values among endogenous *Escherichia coli* genes, and the variation in the codon adaptation index (CAI) (*9*) contained most (96%) of the CAI values of *E. coli* genes (Fig. 1).

We expressed the GFP genes in *E. coli* using a T7-promoter vector, and we quantified expression by spectrofluorometry. Fluorescence levels varied 250-fold across the library, and they were highly reproducible for each GFP construct (Spearman $r = 0.98$ between biological replicates) (fig. S3). Fluorescence variation was consistent across a broad range of experimental conditions (fig. S4).

[1]Department of Biology and Program in Applied Mathematics and Computational Science, The University of Pennsylvania, Philadelphia, PA 19104, USA. [2]Department of Molecular and Cellular Biology, Harvard University, Cambridge, MA 02138, USA. [3]Wellcome Trust Centre for Cell Biology and Centre for Systems Biology, University of Edinburgh, Edinburgh EH9 3JR, UK.

*Present address: Wellcome Trust Centre for Cell Biology, University of Edinburgh, Edinburgh EH9 3JR, UK.
†To whom correspondence should be addressed. E-mail: jplotkin@sas.upenn.edu

An alternative plasmid with bacterial promoter reduced overall expression levels, but the correlation between the two expression systems remained high ($r = 0.9$) (fig. S4). A similar pattern of fluorescence variation was observed in fluorescence-activated cell sorting measurements (fig. S5). Because the encoded protein sequence was identical for all genes, we attributed fluorescence variation to differences in protein levels. This was confirmed by strong correlations between fluorescence and total GFP levels in Western blots (fig. S5) and Coomassie staining ($r = 0.9$, $P < 10^{-15}$).

To test the theory that *E. coli* translation rates and eventual protein levels depend on the concordance between codon usage and cellular tRNA abundances (*10*–*12*), we compared codon usage to fluorescence among the 154 synonymous GFP variants. Notably, neither of the two most common measures of codon bias, the CAI or the frequency of optimal codons (*3*), was significantly correlated with fluorescence levels ($r = 0.14$, $P = 0.09$, and $r = 0.11$, $P = 0.16$, respectively) (Fig. 2A). Moreover, some of the most highly expressed genes featured low CAI and vice versa.

Although codon adaptation near the 5′ terminus is considered particularly important for expression (*12*, *13*), the CAI value of the first 42 bases in a GFP gene was not significantly correlated with the gene's fluorescence intensity ($r = 0.1$, $P = 0.2$). Similarly, the number of rare codons (sites with CAI < 0.1) in a sequence was not significantly correlated with fluorescence ($r = -0.02$, $P = 0.7$), and neither was the number of pairs of consecutive rare codons ($r = -0.14$, $P = 0.09$). Although specific consecutive codon pairs have been proposed to influence translation (*14*, *15*), the frequency of such rare pairs in a gene was not significantly correlated with its fluorescence ($r = 0.07$, $P = 0.35$) (*8*).

Statistical analyses of which nucleotide positions influenced gene expression (fig. S6) indicated the importance of local sequence patterns, as opposed to global codon bias. This pattern is consistent with studies of base content (*16*, *17*), which suggest that mRNA structure may shape expression levels (*18*–*21*). Therefore, for each GFP construct, we computed the predicted minimum free energy associated with the secondary structure of its entire mRNA or specific regions of its mRNA. The folding energy of the entire mRNA was not significantly correlated with fluorescence ($r = 0.16$, $P = 0.051$), but the folding energy of the first third of the mRNA was strongly correlated: mRNAs with stronger structure produced lower fluorescence ($r = 0.60$, $P < 10^{-15}$). A moving window analysis identified a region, from nucleotide (nt) –4 to +37 relative to start, for which predicted folding energy explained 44% of the variation in fluorescence levels across the GFP library ($r = 0.66$, $P < 10^{-15}$) (Fig. 2B). The same folding energies explained 59% of fluorescence variation when constructs were expressed using a bacterial promoter ($r = 0.77$, $P < 4 \times 10^{-16}$) (fig. S7). mRNA folding also correlated with fluorescence in a separate analysis of GFP constructs differing by single mutations (*8*).

The strong correlation between mRNA folding and fluorescence suggests the simple mechanistic explanation that tightly folded messages obstruct translation initiation and thereby reduce protein synthesis (*22*). Predicted mRNA structures for highly expressed GFPs characteristically contained many unpaired nucleotides near the start codon, whereas constructs expressed at low levels featured long hairpin loops (Fig. 2B and fig. S8), consistent with known obstructions to initiation (*22*). The region of strongest correlation between folding energy and expression did not overlap with the Shine-Dalgarno (SD) sequence, which suggested that SD occlusion by secondary structure (*22*, *23*) did not play a major role in inhibiting expression, probably because our constructs contained no noncoding mutations. By contrast, the region of strongest effect overlapped

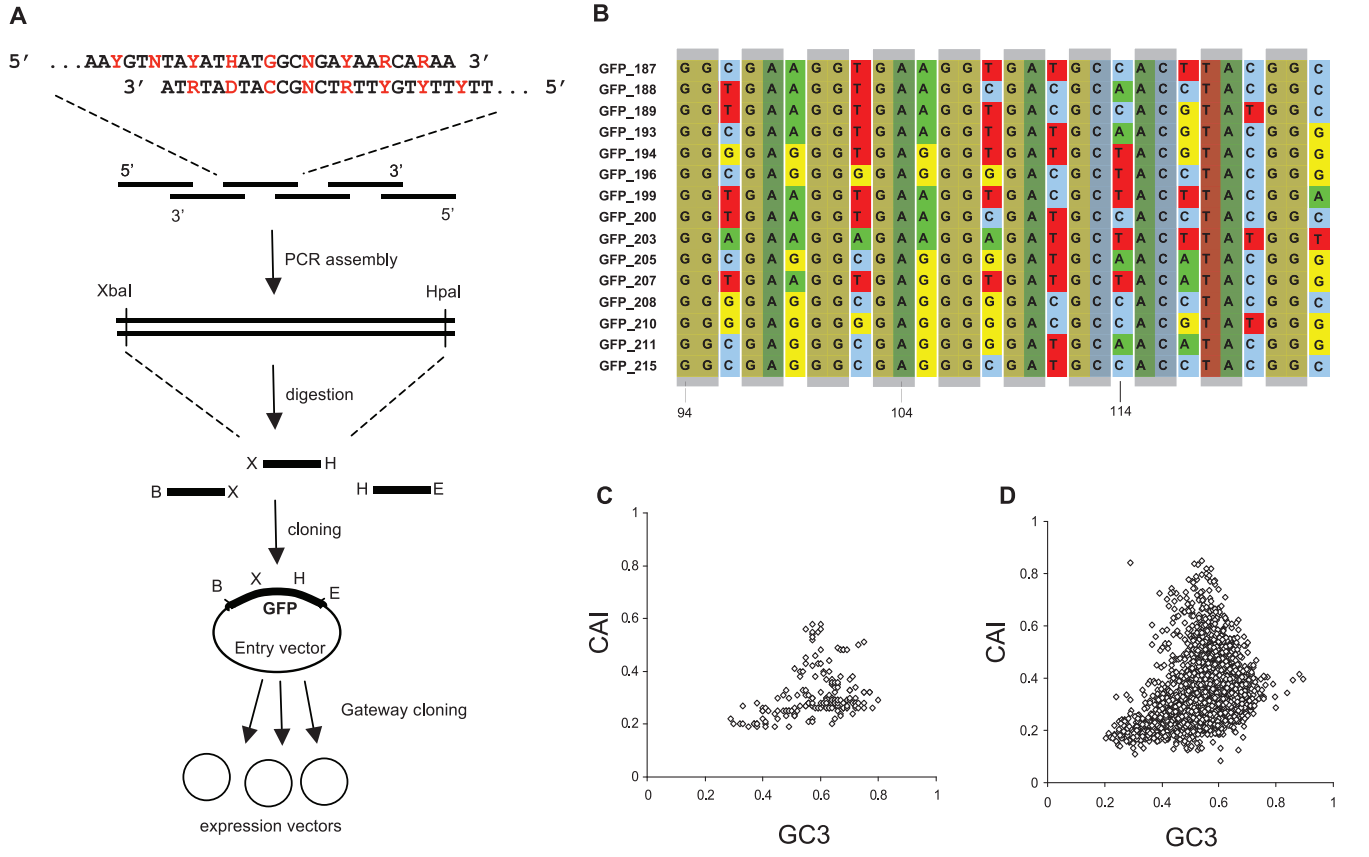

Fig. 1. Synthetic library of GFP genes with randomized codon usage. (**A**) Degenerate oligonucleotides were mixed and assembled by polymerase chain reaction. Fragments were then cloned, sequenced, and assembled into complete GFP genes. Red indicates third-codon positions. Degenerate symbols are as follows: D (A or G or T); H (A or C or T); N (A or C or G or T); R (A or G); and Y (C or T). (**B**) Example alignment illustrating sequence diversity among 15 synthetic genes. Shaded boxes indicate first and second codon positions, which are conserved across the library. (**C** and **D**) The distribution of GC3 and CAI among the 154 synthetic GFP genes (C) is representative of the diversity among the 4288 endogenous *E. coli* genes (D).

significantly with the 30-nt ribosome–binding site centered around the start codon (Fig. 2C).

In a multiple regression, mRNA folding energy near the start codon (nt –4 through +37) explained nearly 10 times as much variation in expression levels as any other predictor variable, including the global GC content, CAI, the number of rare-codon sites or consecutive pairs, the length of the longest rare-codon stretch, the number of predicted transcription termination signals, the propensity for conformation changes into Z-DNA, and the number of predicted ribonuclease (RNase) E cleavage sites (*8*). RNase E cleavage sites tended to reduce expression, as expected (*24*), and explained 4.7% of fluorescence variation.

Although global GC content was not significantly correlated with fluorescence ($r = –0.031$, $P = 0.7$), GC content near the start codon was strongly correlated. But this was likely mediated by mRNA secondary structure; GC content was itself correlated with folding energy, and folding energy explained 10 times as much variation in fluorescence as was explained by GC content (*8*).

GFP mRNA levels, as quantified by Northern blotting, varied across the library, but the extent of mRNA variation was three times smaller than that of corresponding fluorescence variation. We also observed 3′-truncated mRNA species that differed among GFP variants, which likely reflected different stabilities of mRNA degradation intermediates (fig. S9). mRNA levels were highly correlated with fluorescence ($r = 0.53$) and also with folding energy near the start codon ($r = 0.33$). These relations are consistent with the hypothesis that secondary structure influences both mRNA and protein levels through occlusion of ribosome subunit binding. Reduced ribosome binding increases mRNA exposure to nuclease digestion, which in turn decreases stability (*25*).

Bacterial growth rates were strongly influenced by the codon usage of the expressed GFP construct (*8*). Elevated CAI was correlated with faster growth ($r = 0.54$, $P < 9 \times 10^{-13}$), whereas 5′ mRNA folding energy showed no significant correlation with growth ($r = 0.12$, $P = 0.15$). These results support the hypothesis that low codon adaptation in an overexpressed gene decreases cellular fitness (*16*), probably because retarded elongation sequesters ribosomes on the GFP mRNA and thereby hinders translation of essential mRNAs. The growth rate data could alternatively be explained by the hypothesis that high codon adaptation reduces the rate of deleterious protein misfolding (*6*, *26*, *27*). Although we do not rule out this possibility, in our experiments CAI was not correlated with the degree of misfolding, whether it was quantified by the ratio of Coomassie to fluorescence or by the ratio of mRNA to fluorescence (*8*).

Our findings lead to the following prediction: Adding a stretch of codons with weak mRNA structure to the 5′ end of a gene with originally strong structure should increase expression, even if the additional codons have low CAI. To test this prediction, we fused a 28-codon tag to the 5′ terminus of 72 GFP constructs. The tagged constructs, which featured weak mRNA secondary structure and low CAI (*8*), produced consistently high expression, including those GFPs poorly expressed in nontagged form (Fig. 3). These results suggest that endogenous *E. coli* genes may have undergone selection for weak 5′ secondary structure. Consistent with this hypothesis, we found that the predicted secondary structures for the 4294 *E. coli* genes are significantly weaker near their start codons (nt –4 to +37) than immediately downstream (nt +38 to +79; Wilcoxon $P < 10^{-15}$).

Here, we have systematically quantified the effects of synonymous nucleotide variation on gene expression in *E. coli*, on the basis of unbiased sequences that control for regulatory context. The data reveal a predominant role for mRNA structure around the ribosomal binding site in shaping mRNA and protein levels. By contrast,

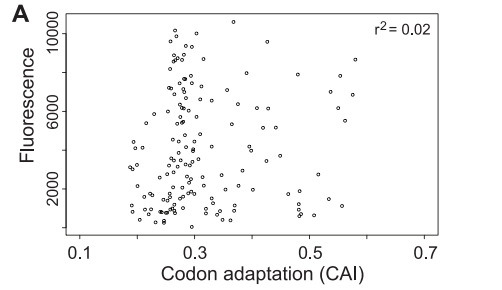

Fig. 2. The determinants of gene expression. (**A**) Codon adaptation was not significantly correlated with fluorescence among the 154 GFP constructs ($r = 0.14$, $P = 0.09$). (**B**) Predicted 5′ mRNA folding energy was strongly correlated with fluorescence ($r = 0.66$, $P < 10^{-15}$). For each construct, folding energy was calculated in a window spanning positions –4 to +37 relative to translation start; two sample structures are shown. (**C**) Sliding window analysis of mRNA folding and fluorescence. Local mRNA folding energies were calculated in a sliding window of length 42 nt. The significance of the correlation between local folding energy and fluorescence (negative $\log_{10} P$ value) is plotted as a function of window position along the sequence. Note the overlapping locations of the 30-nt ribosome–binding site (blue bar) and the window of strongest correlation between folding energy and fluorescence (partially overlapping red bar, nt –4 through nt +37).

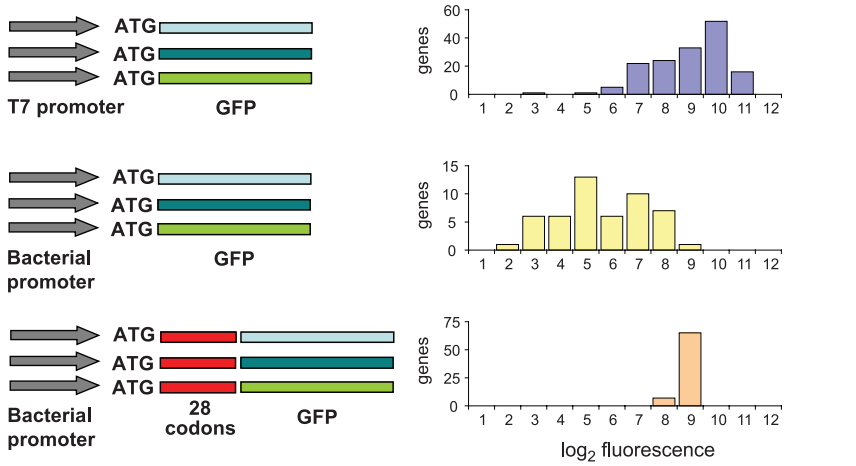

Fig. 3. Expression levels of alternative GFP constructs. The distribution of $\log_2$ normalized fluorescence levels for (**top**) pGK8 (T7 promoter, no leader sequence), (**middle**) pGK14 (P_{BAD} bacterial promoter, no leader sequence) and (**bottom**) pGK16 (trp-lac bacterial promoter, 28-codon leader sequence) expression vectors. Fluorescence varied substantially when expressed using T7 or bacterial promoter. The addition of a 28-codon leader sequence with low secondary structure produced uniformly high expression levels.

neither local nor global codon bias had significant effects on mRNA or protein levels. This finding is consistent with the view that translation initiation, not elongation, is rate-limiting for gene expression (*28*), but it seems to contradict the well-known correspondence between codon bias and expression level for endogenous genes (*11*, *29*). There is a simple explanation to this apparent contradiction, which reverses the arrow of causality between codon adaptation and gene expression. In one view, high CAI induces strong protein expression (*10*–*12*), whereas we argue that strong expression induces selection for high CAI. Unlike genome-wide correlations between CAI and expression levels [e.g. (*11*)], our analyses control for noncoding regulation and, thus, can distinguish between these two alternatives.

We propose that the correspondence between codon adaptation and expression level among endogenous *E. coli* genes arises from selection to make translation efficient at a global level, rather than at the level of individual genes. High CAI increases the elongation rate, but because initiation is rate-limiting in translation, elongation rate does not significantly affect expression. On the other hand, rapid elongation sequesters fewer ribosomes on the message, thereby increasing the total rate of protein synthesis and accelerating cell growth. A similar model for codon preference has been proposed by Andersson and Kurland (*16*). Well-adapted codons could also confer a metabolic advantage by reducing the load of misfolded proteins (*26*, *27*). In either case, increasing a gene's codon adaptation should not increase its expression. High codon adaptation in a gene should, however, improve cellular fitness to an extent that depends on its expression level.

References and Notes

1. E. Zuckerkandl, L. Pauling, *J. Theor. Biol.* **8**, 357 (1965).
2. T. Ikemura, *Mol. Biol. Evol.* **2**, 13 (1985).
3. T. Ikemura, *J. Mol. Biol.* **151**, 389 (1981).
4. H. Akashi, *Genetics* **136**, 927 (1994).
5. J. L. Parmley, L. D. Hurst, *Bioessays* **29**, 515 (2007).
6. C. Kimchi-Sarfaty *et al*., *Science* **315**, 525 (2007).
7. A. G. Nackley *et al*., *Science* **314**, 1930 (2006).
8. Materials and methods are available as supporting material on *Science* Online.
9. P. M. Sharp, W. H. Li, *Nucleic Acids Res.* **15**, 1281 (1987).
10. C. Gustafsson, S. Govindarajan, J. Minshull, *Trends Biotechnol.* **22**, 346 (2004).
11. G. Lithwick, H. Margalit, *Genome Res.* **13**, 2665 (2003).
12. A. H. Rosenberg, E. Goldman, J. J. Dunn, F. W. Studier, G. Zubay, *J. Bacteriol.* **175**, 716 (1993).
13. E. I. Gonzalez de Valdivia, L. A. Isaksson, *Nucleic Acids Res.* **32**, 5198 (2004).
14. S. Boycheva, G. Chkodrov, I. Ivanov, *Bioinformatics* **19**, 987 (2003).
15. J. R. Coleman *et al*., *Science* **320**, 1784 (2008).
16. S. G. Andersson, C. G. Kurland, *Microbiol. Rev.* **54**, 198 (1990).
17. A. Eyre-Walker, M. Bulmer, *Nucleic Acids Res.* **21**, 4599 (1993).
18. M. N. Hall, J. Gabay, M. Debarbouille, M. Schwartz, *Nature* **295**, 616 (1982).
19. K. E. Griswold, N. A. Mahmood, B. L. Iverson, G. Georgiou, *Protein Expr. Purif.* **27**, 134 (2003).
20. G. Qing, B. Xia, M. Inouye, *J. Mol. Microbiol. Biotechnol.* **6**, 133 (2003).
21. J. Duan *et al*., *Hum. Mol. Genet.* **12**, 205 (2003).
22. M. Kozak, *Gene* **361**, 13 (2005).
23. M. H. de Smit, J. van Duin, *Proc. Natl. Acad. Sci. U.S.A.* **87**, 7668 (1990).
24. E. A. Mudd, H. M. Krisch, C. F. Higgins, *Mol. Microbiol.* **4**, 2127 (1990).
25. I. Iost, M. Dreyfus, *EMBO J.* **14**, 3252 (1995).
26. D. A. Drummond, J. D. Bloom, C. Adami, C. O. Wilke, F. H. Arnold, *Proc. Natl. Acad. Sci. U.S.A.* **102**, 14338 (2005).
27. N. Stoletzki, A. Eyre-Walker, *Mol. Biol. Evol.* **24**, 374 (2007).
28. N. Jacques, M. Dreyfus, *Mol. Microbiol.* **4**, 1063 (1990).
29. S. Ghaemmaghami *et al*., *Nature* **425**, 737 (2003).

30. We thank A. Helwak, J. Lucks, P. Sharp, L. Hurst, and members of the Plotkin and Tollervey laboratories for conceptual input; and A. Heath (Sigma), A. Aitken, J. Skerker, T. Shimizu, I. Iost, and J. Han for reagents, protocols, and equipment. Support provided by the Burroughs Wellcome Fund, James S. McDonnell Foundation, Penn Genome Frontiers Institute, and Defense Advanced Research Projects Agency "FunBio Program" HR0011-05-1-0057 (J.B.P.); Foundation for Polish Science and European Molecular Biology Organization (G.K.); Wellcome Trust/BBSRC grant BB/DO19621/1 (D.T.).

Supporting Online Material

www.sciencemag.org/cgi/content/full/324/5924/255/DC1
Materials and Methods
Figs. S1 to S9
References
List of Oligonucleotides

23 December 2008; accepted 17 February 2009
10.1126/science.1170160

Leucine-Rich Repeat Protein Complex Activates Mosquito Complement in Defense Against *Plasmodium* Parasites

Michael Povelones, Robert M. Waterhouse, Fotis C. Kafatos, George K. Christophides*

Leucine-rich repeat–containing proteins are central to host defense in plants and animals. We show that in the mosquito *Anopheles gambiae*, two such proteins that antagonize malaria parasite infections, LRIM1 and APL1C, circulate in the hemolymph as a high-molecular-weight complex held together by disulfide bridges. The complex interacts with the complement C3-like protein, TEP1, promoting its cleavage or stabilization and its subsequent localization on the surface of midgut-invading *Plasmodium berghei* parasites, targeting them for destruction. LRIM1 and APL1C are members of a protein family with orthologs in other disease vector mosquitoes and appear to be important effectors in innate mosquito defenses against human pathogens.

Anopheline mosquitoes are the vectors of malaria that is caused by protozoan *Plasmodium* parasites and claims the lives of 1 to 3 million people annually (*1*). Parasites enter female mosquitoes during blood feeding and develop into ookinetes that on traversing the midgut epithelium and encountering the hemolymph are attacked by the mosquito immune system (*2*). A few survive to transform into oocysts, which generate sporozoites capable of reinfecting humans.

The *Anopheles gambiae* leucine-rich repeat (LRR)–containing protein LRIM1 is a potent *Plasmodium berghei* antagonist that is also involved in phagocytosis of bacteria and melanization of parasites and Sephadex beads (*3*–*5*). Since the discovery of LRIM1, two other LRR proteins, APL1 (*6*) and LRRD7 (*7*), have been shown to limit *Plasmodium* infection. LRIM1 and APL1 (also called LRIM2) also mediate *Plasmodium* lysis and melanization in *Anopheles quadriannulatus* species A, contributing to the natural refractory phenotype of these mosquitoes to parasites (*8*). The *APL1* locus encompasses three distinct yet highly similar genes, which originate from recent duplications. Of these, *APL1C* is the sole *P. berghei* antagonist; *APL1A* and *B* do not influence infection intensities (*9*).

We used single and double gene knockdowns (KDs) to compare the quantitative effects of *LRIM1* and *APL1* on *P. berghei* infections in susceptible *A. gambiae* and obtained an increase by a factor of ~50 in parasite infection intensities and no significant difference between double and single KDs (Fig. 1A). Quantitative real-time polymerase chain reaction confirmed equal and efficient silencing of *LRIM1* and *APL1* (using primers amplifying all three *APL1* genes) and no detectable cross-silencing (fig. S1). The known role of *LRIM1* in melanization (*3*, *4*) prompted us to examine whether *APL1* is also required in this immune reaction. We silenced *LRIM1* and *APL1* in *A. gambiae* L3-5 mosquitoes, which melanize virtually all invading *P. berghei* ookinetes (*10*). Indeed, both KDs produced identical phenotypes: no melanization and an increase by a factor of ~80 in live oocyst numbers (Fig. 1, B and C). Thus, in both *Plasmodium*-susceptible and -refractory mosquitoes, the effects of *LRIM1* and *APL1* are qualitatively and quantitatively indistinguishable, suggesting that the two genes function in a single genetic pathway that is disrupted by silencing either gene alone.

Sequencing multiple *LRIM1* and *APL1C* cDNA clones from adult female mosquitoes verified their strong similarities in gene architecture.

Division of Cell and Molecular Biology, Department of Life Sciences, Imperial College London, Exhibition Road, London SW7 2AZ, UK.

*To whom correspondence should be addressed. E-mail: g.christophides@imperial.ac.uk

Each gene encompasses a short first exon separated from a long second exon by a short intron. Their deduced amino acid sequences also show striking structural similarities: signal peptides indicating secretory proteins; N-terminal regions with 10 and 12 predicted LRR repeats for LRIM1 and APL1C, respectively; and C-terminal regions with two closely spaced coiled-coil domains (Fig. 2A). The LRR domains are flanked at their C termini by a cysteine-rich region. In addition, both proteins have consensus sites for putative N-linked glycosylation. The N-terminal region of the mature APL1C encompasses multiple repeats of the consensus amino acid sequence Pro-Ala-Asn-Gly-Gly-Leu (PANGGL). These repeats are not found in LRIM1 or any other *A. gambiae* protein. Preliminary data indicate that laboratory *A. gambiae* colonies have *APL1C* alleles encoding variable numbers of these repeats.

We generated antibodies against LRIM1 and APL1C peptides (orange lines in Fig. 2A) and found that they specifically recognize single protein bands of the predicted sizes in mosquito hemolymph: 55 kD and 80 kD, respectively (Fig. 2B). Peptide *N*-glycosidase F (PNGase-F) treatment increased the band mobility, indicating that both proteins are N-glycosylated. Because LRIM1 and APL1C contain several cysteine residues, we used Western blot analysis of hemolymph to examine whether they exist in disulfide-bonded complexes. Under nonreducing conditions, both antibodies detected major protein bands of similar molecular weights of ~260 kD, which resolved into the expected monomers under reducing conditions (Fig. 2C). These data indicated that LRIM1 and APL1C are either in the same complex or in different complexes with fortuitously identical molecular weights.

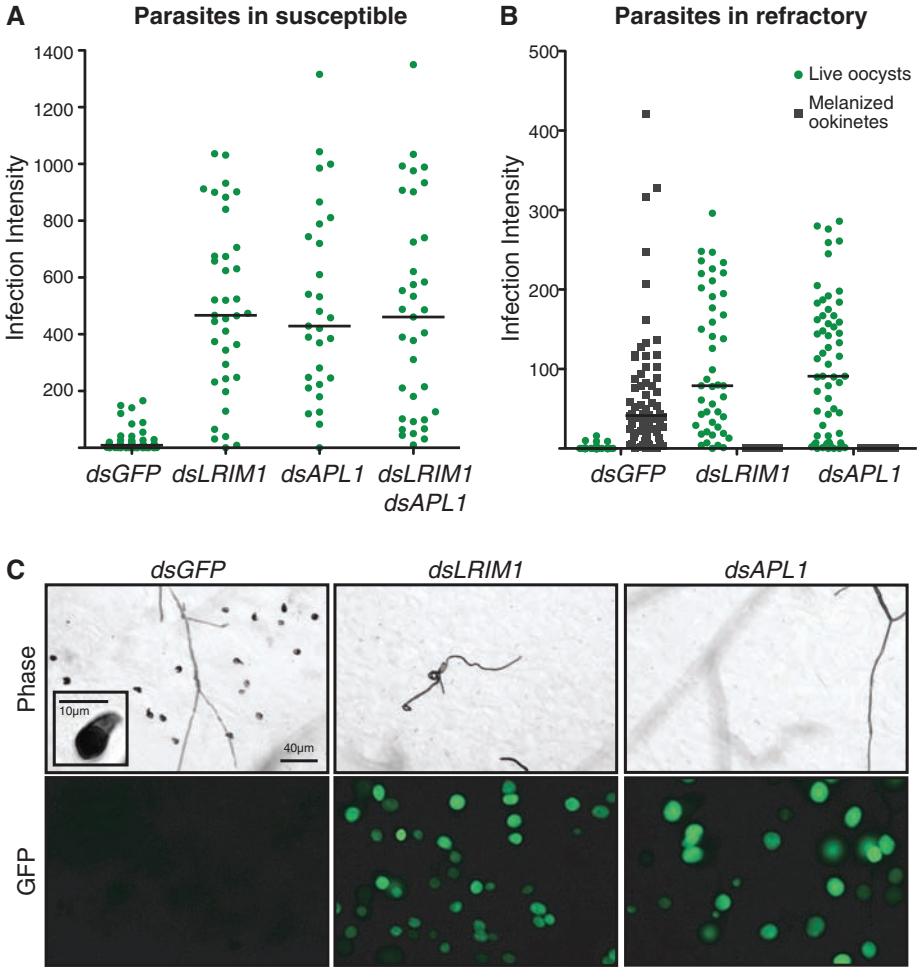

Fig. 1. Silencing of *LRIM1* and *APL1* together has the same effect on midgut infections of GFP-expressing *P. berghei* as silencing either gene alone. Experiments were performed 7 days after infection, with injection of *dsGFP* serving as the control. Horizontal lines indicate the median. (**A**) Oocyst numbers in susceptible mosquitoes. Whether injected together or separately, *dsLRIM1*- and *dsAPL1*-treated mosquitoes show a significant ($P < 0.001$) increase of oocyst numbers compared with the control, but no difference between them. (**B**) Live oocysts (green dots) and melanized ookinetes (gray squares) in refractory mosquitoes. Both the increase in live and the decrease in melanized parasites in *dsLRIM1*- and *dsAPL1*-injected mosquitoes are significant ($P < 0.001$) compared with the control. (**C**) Phase contrast (top row) and fluorescent (bottom row) photomicrographs of parasites in the midguts of refractory mosquitoes after injection of dsRNA. Inset in the control shows a melanized ookinete at higher magnification.

We used APL1C antibody to immunoprecipitate the 260-kD APL1C-containing hemolymph complex, which was then analyzed by Western blot (Fig. 2D). LRIM1 was found to be part of this complex when assayed under nonreducing conditions and migrated at the monomer's size of 55 kD under reducing conditions. These data suggest that LRIM1 and APL1C are partners in a disulfide-bonded complex.

Next, we investigated what effect removing either component would have on the formation of the complex. Neither the complex nor the monomers were detectable in hemolymph after depletion of either protein alone (Fig. 2E), indicating that formation of the complex is required for secretion of these proteins. Taken together, these data demonstrate that the LRIM1/APL1C complex is the only hemolymph form of the two proteins.

We used affinity purification to investigate whether the LRIM1/APL1C complex interacts with other secreted proteins. Because such interactions would be expected to be dynamic and transient, we used hemocyte-like *A. gambiae* Sua4.0 cells that possess immune properties, such as phagocytosis of bacteria and induction of immune genes (*11*, *12*), to circumvent the problem of limited amounts of hemolymph extracts. Cells were cotransfected with transgenic *LRIM1* and *APL1C* carrying C-terminal 10x His-tags or with control *GFP* (green fluorescent protein), expressed via constitutive promoters, and then allowed to condition serum-free medium for 3 days. Capture using the His-tag revealed that, as in hemolymph, $LRIM1^{HIS}$ and $APL1C^{HIS}$ in conditioned medium are detected in the 260 kD complex (Fig. 3A). Additional complexes containing $LRIM1^{HIS}$ or $APL1C^{HIS}$ as well as $LRIM1^{HIS}$ and $APL1C^{HIS}$ monomers were also detected. This secretion pattern is not due to tagging or overexpression but is an intrinsic property of cultured cells (fig. S2).

Silver staining of captured proteins revealed three additional, prominent protein bands (Fig. 3A). Two of these had molecular weights that matched the cleaved form of another important *P. berghei* antagonist, the complement C3-like molecule TEP1 (*13*). TEP1 is secreted into the hemolymph as a 165-kD precursor (TEP1-F) and then processed by an unidentified mechanism to generate an 80-kD C-terminal fragment (TEP1-C) that bears a reactive thioester motif (*14*, *15*). Through the thioester, TEP1 opsonizes bacteria, promoting their phagocytosis (*5*, *14*). It also localizes to the surface of ookinetes during midgut invasion, targeting them for lysis or melanization (*13*). The indistinguishable loss-of-function phenotypes of TEP1 and LRIM1 (*16*) on *P. berghei* infections led us to investigate whether either of these two bands corresponds to TEP1. Indeed, there was a selective enrichment of TEP1-C in the material cocaptured with $LRIM1^{HIS}/APL1C^{HIS}$ compared with the control (Fig. 3A). This indicates that the complex interacts with TEP1 and may be involved in TEP1 processing.

To address this, we probed the hemolymph of *LRIM1* and *APL1* KD mosquitoes with TEP1

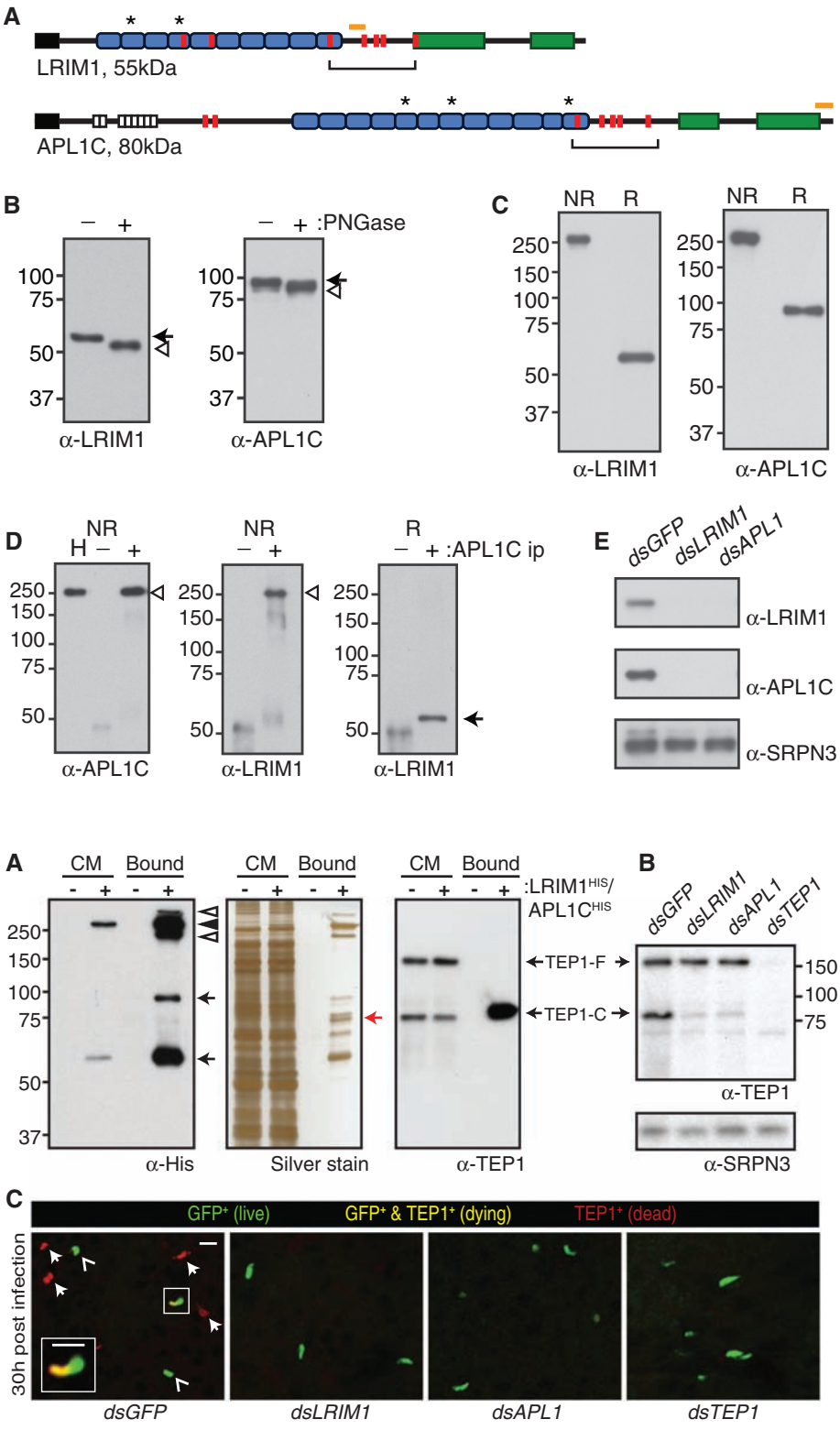

Fig. 2. LRIM1 and APL1C circulate in the hemolymph as a disulfide-bonded multimeric complex. (**A**) Schematic representation and predicted molecular weights of the LRIM1 and APL1C proteins. Features: asterisk, predicted N-linked glycosylation site; red line, cysteine residue; black bracket, conserved cysteine-rich region. Colored boxes: black, signal peptide; white, PANGGL repeats; blue, LRR repeats; green, coiled-coil domain. Orange horizontal lines show the location of peptides used to generate antibodies. (**B**) LRIM1 and APL1C Western blots of hemolymph before (–) and after (+) treatment with PNGase-F. Arrows indicate the position of the endogenous proteins, and open arrowheads indicate deglycosylated forms. (**C**) LRIM1 and APL1C Western blots of hemolymph under nonreducing (NR) and reducing (R) conditions. (**D**) LRIM1 coimmunoprecipitates with the APL1C complex. Hemolymph (H) was used for immunoprecipitation with an antibody against APL1C (+) or mock treated (–). Left and middle panels show Western blot analysis of samples run under NR conditions and probed with APL1C and LRIM1 antibodies, respectively. Right panel shows Western blot under R conditions, probed with LRIM1 antibody. Immunoprecipitated complex detected with APL1C antibody (white arrowhead), LRIM1 antibody (white arrowhead), and LRIM1 monomer (arrow) are indicated. (**E**) Silencing by injection of either *dsLRIM1* or *dsAPL1* results in specific loss of the LRIM1/APL1C complex from the hemolymph compared with control (*dsGFP*). Probing with SRPN3 served as a loading control. The LRIM1 and APL1C blots were cropped at the position of the complex because no other bands were detected.

Fig. 3. The LRIM1/APL1C complex interacts with TEP1-C. (**A**) *A. gambiae* cultured cells were cotransfected with transgenes for $LRIM1^{HIS}$ and $APL1C^{HIS}$ (+) or *GFP* (–) as a control. His-tagged proteins were affinity purified from conditioned medium (CM). Starting CM and captured (Bound) samples were analyzed by Western blot with antibodies to His (left panel) or TEP1 (right panel), or silver stained (middle panel). Black arrows, $LRIM1^{HIS}$ and $APL1C^{HIS}$ monomers; black arrowhead, $LRIM1^{HIS}/APL1C^{HIS}$ complex; white arrowheads, alternative $LRIM1^{HIS}$ and $APL1C^{HIS}$ complexes; red arrow, putative TEP1-C bands; black double arrows, TEP1-F and TEP1-C. (**B**) TEP1 Western blot of hemolymph extracted from *dsGFP*-, *dsLRIM1*-, *dsAPL1*- and *dsTEP1*-injected mosquitoes. Probing with SRPN3 served as a loading control. (**C**) Confocal analysis of TEP1 immunolocalization (red) in midgut epithelia from susceptible mosquitoes 30 hours after infection with GFP-expressing *P. berghei* (green). A mixture of live (GFP^+, open arrows), dead ($TEP1^+$, white arrows), and dying (GFP^+ and $TEP1^+$, box and inset) parasites are detected in control-injected (*dsGFP*) mosquitoes. In contrast, no dead or dying parasites were observed in mosquitoes injected with *dsLRIM1*, *dsAPL1*, or *dsTEP1* in three independent experiments. Scale bars in *dsGFP* panel and inset are 10 μm.

antibody. A decrease was detected in the abundance of TEP1-C in KDs compared with *GFP* double-stranded RNA (dsRNA)–treated controls (Fig. 3B). Thus, the LRIM1/APL1C complex appears to be involved in TEP1 processing in the mosquito hemolymph. However, the lack of a parallel increase in TEP1-F may alternatively indicate that the complex is required for the stabilization of TEP1-C in the mosquito hemolymph. This might serve to prevent the reactive TEP1-C from nonspecific interaction with self-surfaces and/or to direct TEP1-C to foreign surfaces during infection.

Binding of TEP1 to invading parasites is proposed to mediate their killing through a complement-like pathway (*2*). To investigate whether TEP1 binding is affected by the loss of the LRIM1/APL1C complex, we immunolocalized TEP1 on GFP-expressing *P. berghei* ookinetes

30 hours after infection of mosquitoes lacking LRIM1, APL1, or TEP1. As reported previously (*16*), three distinct classes of parasites were observed in the midguts of control mosquitoes: live (GFP positive), dead (TEP1 positive), and dying (GFP and TEP1 positive). In contrast, TEP1-positive parasites were never detected in *LRIM1* or *APL1* KD mosquitoes (Fig. 3C), despite the presence of TEP1-F in the hemolymph. Lack of TEP1 parasite staining was as complete as in TEP1 KD mosquitoes, which entirely lack TEP1 in the hemolymph. These data demonstrate that the LRIM1/APL1C complex is necessary for TEP1-mediated parasite killing during midgut invasion and indicate that TEP1 binds parasites only after it is processed.

The *APL1* locus has been implicated in mosquito resistance to the human malaria parasite, *Plasmodium falciparum* (*6*), and TEP1 has been shown to act against *P. falciparum* in laboratory infections (*7*). Mosquito defense against *Plasmodium* is likely to be influenced by vector/parasite coevolution and adaptation; thus, the observation that LRIM1 did not affect *P. falciparum* in experimental field infections (*17*) may suggest that parasites have evolved to evade this pathway. Proteins such as the fibrinogen-related FBN9 (*18*) or other LRR proteins may provide alternative mechanisms for TEP1-mediated parasite killing.

Bioinformatic searches for proteins related to LRIM1 and APL1C using their shared structural features (signal peptide, LRRs, cysteine pattern, and coiled-coils) (see supporting online material) detected more than 20 *LRIM*-like genes in each of the available mosquito genomes—*A. gambiae*, *Aedes aegypti*, and *Culex quinquefasciatus*—but not in any other species (table S1). Several of these genes were previously implicated in *A. gambiae* immune responses (*3*, *6*, *7*, *9*, *19*). Phylogenetic analysis in conjunction with pairwise comparisons, examination of orthologous genomic neighborhoods, and protein domain analysis revealed four distinct LRIM subfamilies (figs. S3 and S4). Thus, LRIM1 and APL1C are members of a family of putative recognition receptors, which appears to be unique and greatly expanded in mosquitoes. Nevertheless, structural integrity of both LRRs and coiled-coils rests with only a few key amino acids, allowing considerable sequence variation that may hinder identification of functional equivalents in other organisms.

The versatile LRR motif mediates recognition of diverse pathogen-associated molecules in host innate defense in plants and animals (*20*). For example, the repertoire of variable lymphocyte receptor (VLR) antibodies in jawless vertebrates is generated by combinatorial assembly of LRR modules instead of immunoglobulin segments as in jawed vertebrates (*21*). Similarly to LRIM1/APL1C, the VLR antibodies are secreted as disulfide-linked multimers (*22*).

LRIMs form a family of mosquito LRR receptors with putative roles in defense against human and animal pathogens. LRIM1 and APL1C exist as a complex that mediates immunity against malaria parasites through activation of mosquito complement. The multimeric nature of the complex indicates the potential to bind multiple targets similarly to mammalian multisubunit receptors that robustly activate complement, that is, immunoglobulin M, lectin, and C1q. Bound LRIM1/APL1C complex may then undergo conformational changes inducing the recruitment of additional cascade components, such as a TEP1-activating protease. In-depth study of these interactions will provide insights into complement activation in mosquitoes and tools toward blocking disease transmission.

References and Notes

1. R. W. Snow, C. A. Guerra, A. M. Noor, H. Y. Myint, S. I. Hay, *Nature* **434**, 214 (2005).
2. S. A. Blandin, E. Marois, E. A. Levashina, *Cell Host Microbe* **3**, 364 (2008).
3. M. A. Osta, G. K. Christophides, F. C. Kafatos, *Science* **303**, 2030 (2004).
4. E. Warr, L. Lambrechts, J. C. Koella, C. Bourgouin, G. Dimopoulos, *Insect Biochem. Mol. Biol.* **36**, 769 (2006).
5. L. F. Moita *et al.*, *Immunity* **23**, 65 (2005).
6. M. M. Riehle *et al.*, *Science* **312**, 577 (2006).
7. Y. Dong *et al.*, *PLoS Pathog.* **2**, e52 (2006).
8. T. Habtewold, M. Povelones, A. M. Blagborough, G. K. Christophides, *PLoS Pathog.* **4**, e1000070 (2008).
9. M. M. Riehle *et al.*, *PLoS One* **3**, e3672 (2008).
10. F. H. Collins *et al.*, *Science* **234**, 607 (1986).
11. G. Dimopoulos, A. Richman, H. M. Muller, F. C. Kafatos, *Proc. Natl. Acad. Sci. U.S.A.* **94**, 11508 (1997).
12. H. M. Muller, G. Dimopoulos, C. Blass, F. C. Kafatos, *J. Biol. Chem.* **274**, 11727 (1999).
13. S. Blandin *et al.*, *Cell* **116**, 661 (2004).
14. E. A. Levashina *et al.*, *Cell* **104**, 709 (2001).
15. R. H. Baxter *et al.*, *Proc. Natl. Acad. Sci. U.S.A.* **104**, 11615 (2007).
16. C. Frolet, M. Thoma, S. Blandin, J. A. Hoffmann, E. A. Levashina, *Immunity* **25**, 677 (2006).
17. A. Cohuet *et al.*, *EMBO Rep.* **7**, 1285 (2006).
18. Y. Dong, G. Dimopoulos, *J. Biol. Chem.* www.jbc.org/cgi/doi/10.1074/jbc.M807084200. Published online 4 February 2009.
19. R. Aguilar *et al.*, *Insect Biochem. Mol. Biol.* **35**, 709 (2005).
20. T. Nurnberger, F. Brunner, B. Kemmerling, L. Piater, *Immunol. Rev.* **198**, 249 (2004).
21. Z. Pancer *et al.*, *Nature* **430**, 174 (2004).
22. B. R. Herrin *et al.*, *Proc. Natl. Acad. Sci. U.S.A.* **105**, 2040 (2008).

23. The authors thank A. C. Koutsos for generating the LRIM1 antibody and sharing it before publication and F. M. Ausubel for critically reviewing the manuscript. Fluorescence microscopy was performed at the Imperial College Facility for Imaging by Light Microscopy imaging facility. This work was supported by a Wellcome Trust Program grant (GR077229/Z/05/Z), an NIH Program Project (2PO1AI044220-06A1), and a Biotechnology and Biological Sciences Research Council grant (BB/E002641/1). R.M.W. was supported by a Wellcome Trust Ph.D. fellowship.

Supporting Online Material

www.sciencemag.org/cgi/content/full/1171400/DC1
Materials and Methods
Figs. S1 to S4
Table S1
References

26 January 2009; accepted 24 February 2009
Published online 5 March 2009;
10.1126/science.1171400
Include this information when citing this paper.

Glioma-Derived Mutations in *IDH1* Dominantly Inhibit IDH1 Catalytic Activity and Induce HIF-1α

Shimin Zhao,[1,2] Yan Lin,[1]* Wei Xu,[1,2]* Wenqing Jiang,[1,2]* Zhengyu Zha,[1] Pu Wang,[1,2] Wei Yu,[1,2] Zhiqiang Li,[4] Lingling Gong,[5] Yingjie Peng,[6] Jianping Ding,[6] Qunying Lei,[1,3] Kun-Liang Guan,[1,3,7]† Yue Xiong[1,2,8]†

Heterozygous mutations in the gene encoding isocitrate dehydrogenase-1 (*IDH1*) occur in certain human brain tumors, but their mechanistic role in tumor development is unknown. We have shown that tumor-derived *IDH1* mutations impair the enzyme's affinity for its substrate and dominantly inhibit wild-type IDH1 activity through the formation of catalytically inactive heterodimers. Forced expression of mutant *IDH1* in cultured cells reduces formation of the enzyme product, α-ketoglutarate (α-KG), and increases the levels of hypoxia-inducible factor subunit HIF-1α, a transcription factor that facilitates tumor growth when oxygen is low and whose stability is regulated by α-KG. The rise in HIF-1α levels was reversible by an α-KG derivative. HIF-1α levels were higher in human gliomas harboring an *IDH1* mutation than in tumors without a mutation. Thus, IDH1 appears to function as a tumor suppressor that, when mutationally inactivated, contributes to tumorigenesis in part through induction of the HIF-1 pathway.

Gliomas are the most common type of human brain tumors and can be classified based on clinical and pathological criteria into four grades. The grade IV glioma, commonly known as glioblastoma multiforme (GBM), has one of the worst prognoses among all types of human tumors and can develop either de novo (primary GBM) or through progression from low-grade tumors (secondary GBM). Although pathologically indistinguishable, primary and secondary GBM exhibit distinct patterns of cancer gene alterations (*1*). A recent cancer genome sequencing project revealed that the gene encoding *IDH1* is somatically mutated predominantly in secondary GBM (*2*). Three subsequent studies of targeted *IDH1* gene sequencing confirmed this finding, together identifying *IDH1* mutations in more than 70% of secondary GBM or low-grade gliomas but

infrequently in primary GBM (about 5%) (*3*–*5*). Notably, all of the *IDH1* mutations identified to date produce a single amino acid substitution at Arg^{132} (R132) and no obvious inactivating (frameshift or protein-truncation) mutations were found. This observation, together with the fact that the tumors do not show loss-of-heterozygosity (LOH), has led to speculation that R132 mutations lead to oncogenic activation of the enzyme.

IDH enzymes catalyze the oxidative decarboxylation of isocitrate (ICT) to produce α-KG. The human genome has five *IDH* genes coding for three distinct IDH enzymes whose activities are dependent on either nicotinamide adenine dinucleotide phosphate ($NADP^+$-dependent IDH1 and IDH2) or nicotinamide adenine dinucleotide (NAD^+-dependent IDH3). Both IDH2 and IDH3 enzymes are localized in the mitochondria and participate in the citric acid (TCA) cycle for energy production, whereas IDH1 is localized in the cytoplasm and peroxisomes (*6*). The R132 residue is conserved in all $NADP^+$-dependent IDHs.

To explore the functional impact of the tumor-associated mutations at R132, we performed modeling studies based on the previously reported human cytosolic IDH1 crystal structure (*7*). Among all residues involved in binding with ICT, the side chain of R132 uniquely forms three hydrogen bonds with both the α- and β-carboxyl groups of the substrate ICT, whereas other residues involved in ICT binding form no more than two hydrogen bonds (Fig. 1A). Substitution of R132 with any one of the six amino acids observed in gliomas (His, Ser, Gly, Cys, Val, and Leu) would impair interactions of the enzyme with ICT both sterically and electrostatically. Representative modeling of H132, which corresponds to the most prevalent *IDH1* mutation in human gliomas, is shown in Fig. 1A. We determined the in vitro enzymatic activities of three tumor-derived IDH1 mutants, R132H, R132C and R132S, expressed in transformed human embryonic kidney (HEK) 293T cells and found that all three mutants have a greater than 80% reduction in activity as compared with the wild-type (WT) IDH1 (Fig. 1B). Analysis of recombinant IDH1 mutant proteins purified from *Escherichia coli* likewise displayed little activity in vitro compared with wild-type controls (Fig. 1B). Kinetic analyses of recombinant IDH1 proteins revealed that all three mutant IDH1s had a dramatically reduced affinity for ICT: The Michaelis constants (K_ms) of $IDH1^{R132C}$, $IDH1^{R132S}$, and $IDH1^{R132H}$ for ICT were increased by factors of 60, 70, and 94, respectively (Fig. 1C). In contrast, the K_m for $NADP^+$ and the maximum velocity (V_{max}) were not appreciably altered (Fig. 1C). Similarly, mutation of an arginine residue in pig mitochondrial IDH2 equivalent to R132 in human IDH1 caused a dramatic increase in K_m for isocitrate (by a factor of 165), with minimal effect on V_{max} (*8*). Because the normal cellular concentration of ICT is 20 to 30 μM (*9*), which is lower than the K_m of the IDH1 mutants, the mutant enzymes are likely to have limited activity under physiological conditions. Together, these structural and biochemical analyses indicate that the tumor-associated *IDH1* mutations inactivate the enzyme.

Given that IDH1 normally functions as a homodimer, we hypothesized that the mutant IDH1 molecules in tumor cells form heterodimers with wild-type molecules and, in so doing, dominantly inhibit the activity of wild-type IDH1. To test this hypothesis, we coexpressed His-tagged wild-type and FLAG-tagged R132H mutant *IDH1* in *E. coli* and isolated the heterodimer by sequential affinity purification using first nickel resin and then FLAG beads. Formation of either WT:WT homodimer or WT:R132H heterodimer was confirmed by gel filtration (fig. S1). As expected, the WT:WT homodimers were fully active and the R132H:R132H homodimers were nearly completely inactive (Fig. 2A). Notably, the WT:R132H heterodimer exhibited only 4% of the activity shown by the wild-type enzyme when assayed with limited ICT concentration (Fig. 2A). Normally, IDH1 can adopt at least three distinct conformations during catalysis: a quasi-open conformation when it is in a complex with $NADP^+$, a quasi-closed conformation when it is in a complex with ICT, and a closed conformation when it is in a complex with both $NADP^+$ and ICT (fig. S2A) (*7*). The two IDH1 subunits act in a cooperative manner and undergo conformational changes in a concerted way. Our modeling study suggests that the impairment in enzyme binding with ICT conferred by the R132 mutation in one subunit might also impair the binding of ICT to the second wild-type subunit. As a result, both subunits would be locked in an unliganded or quasi-open ($NADP^+$-bound) conformation, thereby inhibiting catalytic activity (Fig. 2B for the close-up of the catalytic active site) (fig. S2, B and C). Consistent with this model, we found that the wild-type IDH1 exhibits a sigmoidal curve of cooperative binding to ICT, whereas the WT:R132H heterodimer displayed a hy-

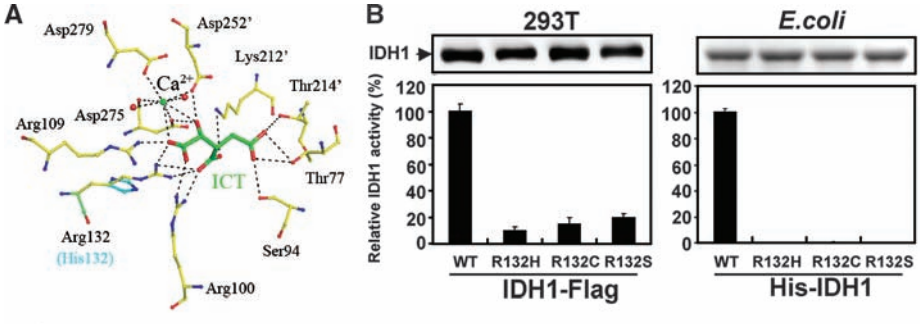

C

IDH1	WT	R132H	R132S	R132C
Km isocitrate (μM)	6.2 ± 1	582.4 ± 56.1	434.1 ± 12.2	368.6 ± 20.6
Km $NADP^+$ (μM)	7.3 ± 0.6	12.2 ± 3.8	14.4 ± 2.2	6.8 ± 2.0
Vmax μmol.min^{-1}.mg^{-1}	56.9 ± 6.6	31.9 ± 3.2	48.0 ± 1.8	57.5 ± 5.7

Fig. 1. Tumor-derived IDH1 mutants have reduced catalytic activity because of impaired isocitrate binding. (**A**) Structural modeling predicts that mutation of R132 in IDH1 would weaken hydrogen bonding of the enzyme to ICT. Shown is a view of the catalytic active site of human IDH1 bound with $NADP^+$ (omitted for clarity), ICT (green), and Ca^{2+}. The residues interacting with ICT from the adjacent subunit are labeled with an apostrophe. Hydrogen-bonding interactions are indicated with dashed lines. Simulated H132 mutation (cyan) is superimposed on R132. (**B**) Tumor-derived IDH1 mutants have reduced catalytic activity in vitro. Left, FLAG-tagged wild-type and mutant IDH1 were expressed in HEK293T cells, purified by immunoprecipitation and eluted by FLAG peptide; right, HIS-tagged wild-type and mutant IDH1 were expressed in *E. coli* and purified by nickel resin. Specific IDH1 activities for all proteins were measured in the presence of $NADP^+$ (10 μM) and ICT (30 μM), with the presence of 2 mM Mn^{2+}. Shown are mean values of triplicate experiments ±SD. (**C**) Kinetic parameters of wild-type and mutant IDH1. Shown are mean values of duplicate experiments ±SD.

[1]Molecular and Cell Biology Laboratory, Institute of Biomedical Sciences, Fudan University, 130 Dong-An Road, Shanghai 200032, China. [2]School of Life Sciences, Fudan University, 220 Han-Dan Road, Shanghai 200433, China. [3]Department of Biological Chemistry, School of Medicine, Fudan University, 130 Dong-An Road, Shanghai 200032, China. [4]Department of Neurosurgery, Zhongnan Hospital, Wuhan University, Wuhan 430071, China. [5]Department of Pathology, Zhongnan Hospital, Wuhan University, Wuhan 430071, China. [6]State Key Laboratory of Molecular Biology, Institute of Biochemistry and Cell Biology, Shanghai Institute for Biological Sciences, Chinese Academy of Sciences, 320 Yue-Yang Road, Shanghai 200031, China. [7]Department of Pharmacology and Moores Cancer Center, University of California San Diego, La Jolla, CA 92093, USA. [8]Department of Biochemistry and Biophysics, Lineberger Comprehensive Cancer Center, University of North Carolina at Chapel Hill, NC 27599, USA.

*These authors contributed equally to this work.
†To whom correspondence should be addressed. E-mail: kuguan@ucsd.edu (K.-L.G.); yxiong@email.unc.edu (Y.X.)

perbolic curve with a much higher K_m (Fig. 2C), indicating that the heterodimer not only loses affinity but also cooperativity toward ICT.

We next investigated whether loss of IDH1 activity would alter cellular levels of α-KG, the product of IDH1 catalysis. We used RNA interference to down-regulate endogenous *IDH1* and determined the α-KG levels in U-87MG human glioblastoma cells. Two independent short hairpin RNAs (shRNAs) decreased *IDH1* mRNA by more than 75% and reduced cellular α-KG levels by up to 50% (fig. S3). Expression of the IDH1^{R132H} mutant at a level similar to the endogenous protein (fig. S4A) in the cytoplasm of U-87MG cells caused a dose-dependent reduction of α-KG levels (Fig. 2D) (fig. S4, A and B). Together, these data indicate that tumor-derived mutant IDH1 dominantly inhibits the wild-type IDH1 by forming a catalytically inactive heterodimer, resulting in a decrease of cellular α-KG.

Because α-KG is required by prolylhydroxylases (PHD), enzymes that hydroxylate and promote the degradation of hypoxia-inducible

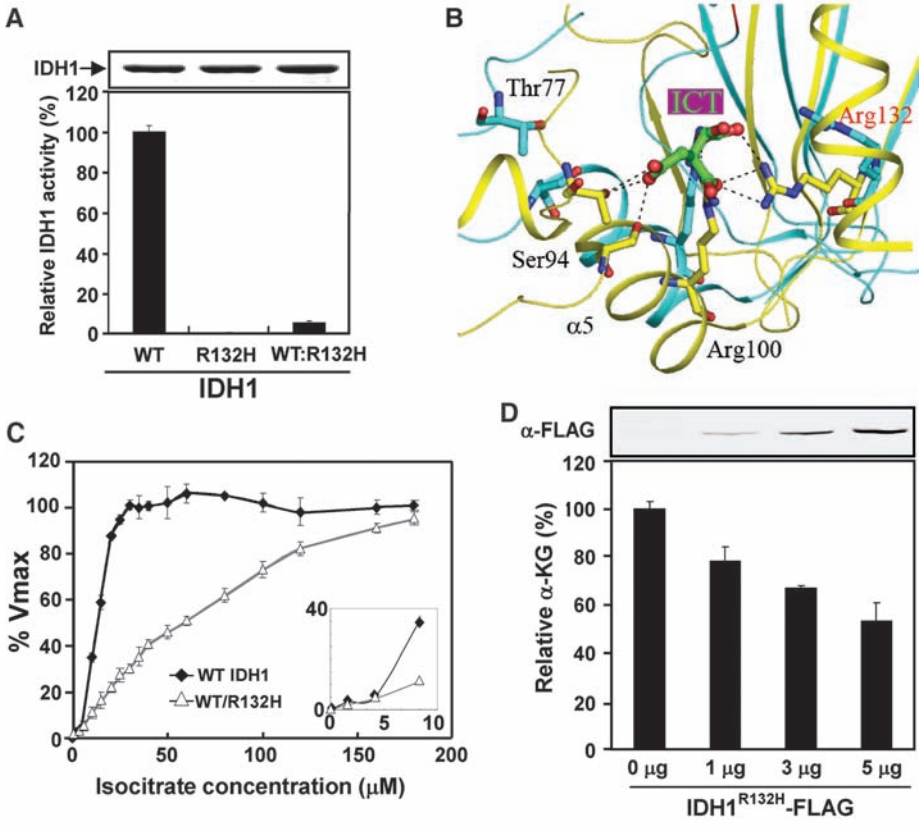

Fig. 2. The R132H mutation dominantly inhibits IDH1 activity and reduces cellular levels of α-KG. (**A**) The WT:R132H heterodimer of IDH1 has low specific activity. The specific activities of WT:WT, R132H:R132H, and WT:R132H dimers were measured under conditions of $NADP^+$ (10 μM), ICT (30 μM), and 2 mM $MnCl_2$. Activities were normalized by protein levels, and wild-type activity was arbitrarily set as 100%. Shown are mean values of triplicate experiments ±SD. (**B**) A close-up view showing the conformational differences between the IDH1-$NADP^+$ and IDH1-$NADP^+$-ICT complexes at the active site. The enzyme adopts a quasi-open conformation in the IDH1-$NADP^+$ complex (cyan) and a closed conformation in the IDH1-$NADP^+$-ICT complex (yellow). The bound ICT and the side chains of several residues in IDH1 involved in ICT binding are shown. (**C**) The WT:R132H heterodimer loses cooperative binding to ICT. The activities of the WT:WT and WT:R132H enzymes were assayed with increasing concentrations of ICT in the presence of 100 μM $NADP^+$ and 2 mM Mn^{2+}. Shown are mean values of duplicate assays ±SD. The inset is an expanded view showing the IDH1 activities at lower isocitrate concentrations. (**D**) Cellular α-KG levels decrease with increasing IDH1^{R132H} expression. The upper panel is a Western blot showing expression levels of the transfected IDH1^{R132H} mutant in U-87MG cells. The α-KG level in cells transfected with empty vector was set as 100%, and this value was used to calculate the relative α-KG level in cells transfected with different amounts of IDH1^{R132H} mutant. Shown are mean values of triplicate assays ±SD.

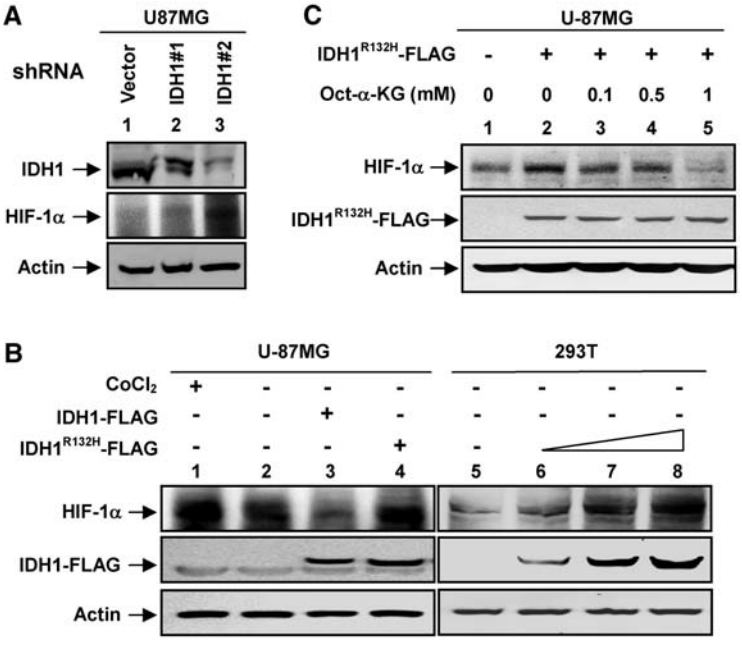

Fig. 3. α-KG mediates the HIF-1α induction in cells with a decreased IDH1 activity. (**A**) *IDH1* knockdown elevates HIF-1α levels in U-87MG glioblastoma cells. IDH1 and HIF-1α protein levels were determined by Western blotting from stable U-87MG cells transduced with empty retrovirus or retrovirus expressing different shRNAs silencing *IDH1*. (**B**) Ectopic expression of the *IDH1*^{R132H} mutant elevates HIF-1α levels in U-87MG and HEK293T cells. The *IDH1*^{R132H} mutant was overexpressed in U-87MG or HEK293T cells, and protein levels were detected by Western blot. $CoCl_2$-treated cells (a mimetic of hypoxia) and cells overexpressing wild-type *IDH1* were also included as controls. (**C**) A cell-permeable α-KG derivative blocks HIF-1α induction in cells expressing *IDH1*^{R132H}. The U-87MG cells were transfected with *IDH1*^{R132H}, and different concentrations of octyl-α-KG ester were added to each transfected cell for 4 hours. HIF-1α protein levels were assayed by Western blot.

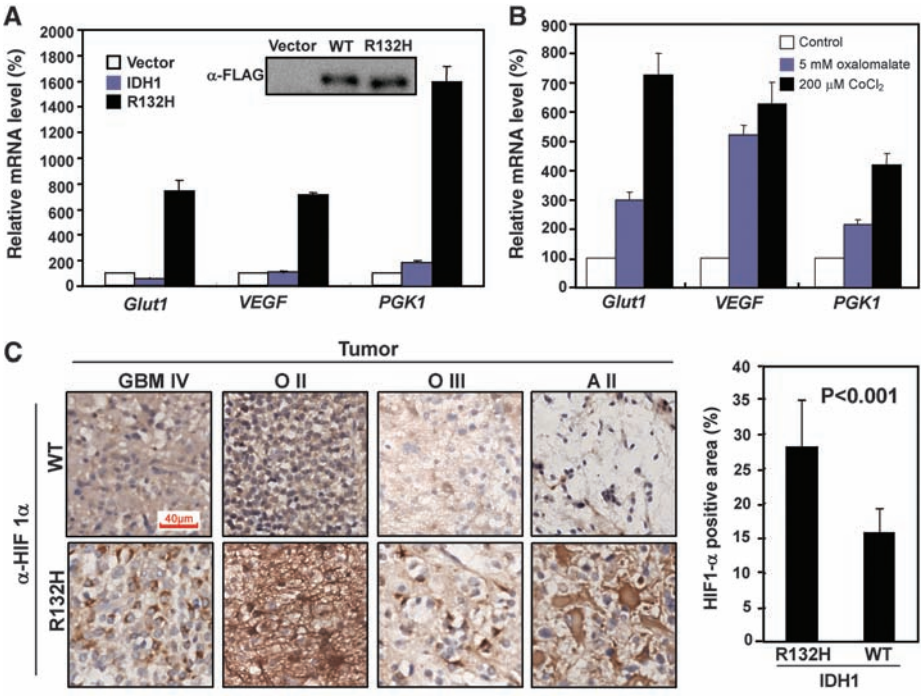

Fig. 4. IDH1 activity affects the levels of HIF-1α and HIF-1α target genes in gliomas and cultured cells. (**A**) Overexpression of the *IDH1*^{R132H} mutant in U-87MG cells stimulates expression of HIF-1α target genes (*Glut1, VEGF*, and *PGK1*) as assayed by QPCR. Shown are mean values of triplicate assays ±SD. (**B**) Inhibition of IDH1 by oxalomalate activates HIF-1α target genes. U-87MG cells were either untreated (control), treated with 5 mM oxalomalate, an IDH1 inhibitor, or treated with $CoCl_2$, a hypoxia mimetic. HIF-1α target gene mRNAs were determined. Shown are mean values of triplicate assays ±SD. (**C**) Immunohistochemistry of HIF-1α was carried out in 12 human gliomas with wild-type *IDH1* and 8 gliomas of similar grade harboring a mutated *IDH1* allele. Shown are side-by-side comparisons of four gliomas representing different types or grades. Scale bar, 40 μM. Five fields (~173 μm^2 each) were randomly selected from each sample for quantification of HIF-1α-positive staining area. Statistical analysis was performed using seven *IDH1* wild-type and seven *IDH1*-mutated gliomas.

factor 1α (HIF-1α), we hypothesized that decreased IDH1 activity might stabilize HIF-1α and increase its steady-state levels. We found that HIF-1α protein levels in U-87MG cells were elevated in response to shRNA-mediated knockdown of *IDH1* (Fig. 3A). Conversely, overexpression of wild-type IDH1 reduced HIF-1α protein levels in HeLa (fig. S5A) and U-87MG cells (Fig. 3B). Notably, overexpression of *IDH1*^{R132H} mutant increased HIF-1α protein levels in U-87MG and HEK293T cells (Fig. 3B). These results suggest that IDH1 regulates HIF-1α levels by controlling the level of α-KG. We tested this hypothesis by treating cells with octyl-α-KG, a cell-permeable derivative of α-KG that upon entering the cells is converted into α-KG after hydrolysis of the ester group (*10*). We found that octyl-α-KG suppressed the HIF-1α induction caused by either *IDH1* knockdown in HeLa cells (fig. S5B) or overexpression of *IDH1*^{R132H} mutant in U-87MG cells (Fig. 3C). We therefore conclude that a reduction in IDH1 activity produces a reduction in α-KG levels that in turn can lead to stabilization of HIF-1α.

We next determined whether inhibition of IDH1 enzyme activity leads to up-regulated expression of HIF-1α target genes. HIF-1α is a key component of HIF-1, a transcription factor that senses low cellular oxygen levels and that regulates the expression of genes implicated in glucose metabolism, angiogenesis, and other signaling pathways that are critical to tumor growth. Quantitative real-time fluorescence polymerase chain reaction (QPCR) of mRNAs corresponding to three well-established HIF-1α target genes, glucose transporter 1 (*Glut1*), vascular endothelial growth factor (*VEGF*), and phosphoglycerate kinase (*PGK1*) showed that *IDH1* knockdown induced the expression of these HIF-1α target genes (fig. S6A). Moreover, expression of the *IDH1*^{R132H} mutant, but not wild-type *IDH1*, strongly induced HIF-1α target gene expression (Fig. 4A). Oxalomalate, a competitive inhibitor of IDH1 (*11*) (fig. S6B), also induced expression of these HIF-1α target genes (Fig. 4B).

Finally, we determined whether *IDH1* mutations correlate with elevated levels of HIF-1α in human gliomas. In a collection of 26 glioma samples, we identified 8 tumors that contained the R132H mutation in one allele of *IDH1* (table S1) (fig. S7A). Using immunohistochemistry, we compared HIF-1α expression in gliomas with and without *IDH1* mutations. We found that 8 tumors harboring the R132H mutation showed a statistically stronger HIF-1α signal than did 12 tumors that did not harbor this mutation (Fig. 4C). In *IDH1* mutated tumors, 28.1 ± 6.7% of the cells stained positive for HIF-1α, whereas in tumors with wild-type *IDH1*, only 15.8 ± 3.5% of the cells stained positive ($P < 0.001$) (Fig. 4C). *IDH1*-mutated gliomas also exhibited an increase in VEGF levels compared with gliomas without *IDH1* mutation of similar type and grade (fig. S7B).

In summary, we have shown that *IDH1* is likely to function as a tumor suppressor gene rather than as an oncogene. The glioma-associated mutations dominantly inhibit the activity of wild-type IDH1 through heterodimer formation (fig. S8). *IDH1* gene mutations in gliomas exhibit two unique features: the lack of LOH and the lack of apparent inactivating mutations such as frameshift or truncations. Our findings help to explain both features, as dominant inhibition would eliminate the selection pressure to mutate or lose the remaining wild-type allele (LOH) and frameshift or premature termination would likely generate IDH1 fragments unable to dimerize with and inhibit the wild-type IDH1 protein.

The link between *IDH1* and HIF-1α highlights an emerging theme in which mutationally altered metabolic enzymes are thought to contribute to tumor growth by stimulating the HIF-1α pathway and tumor angiogenesis. The genes encoding two TCA enzymes, fumarate hydratase (*FH*) and succinate dehydrogenase (*SDH*), have been found to sustain loss-of-function mutations in certain human tumors, which likewise correlate with an increase in HIF-1α levels (*10*, *11*). In addition to affecting PHD, an alteration in α-KG might contribute to tumorigenesis by affecting other dioxygenases that use α-KG as a substrate. IDH1 also catalyzes the production of NADPH; thus, it is possible that a reduction in NADPH levels resulting from IDH1 mutation contributes to tumorigenesis through effects on cell metabolism and growth. Several dozen anticancer agents directly targeting HIF-1α are under development or being tested (*12*). Our finding that an α-KG derivative can reverse the induction of HIF-1α levels in cultured cells expressing mutant *IDH1* suggests that drugs mimicking α-KG may merit exploration as a therapy for gliomas that harbor an *IDH1* mutation.

References and Notes

1. F. B. Furnari *et al.*, *Genes Dev.* **21**, 2683 (2007).
2. D. W. Parsons *et al.*, *Science* **321**, 1807 (2008).
3. J. Balss *et al.*, *Acta Neuropathol.* **116**, 597 (2008).
4. F. E. Bleeker *et al.*, *Hum. Mutat.* **30**, 7 (2009).
5. H. Yan *et al.*, *N. Engl. J. Med.* **360**, 765 (2009).
6. B. S. Winkler, N. DeSantis, F. Solomon, *Exp. Eye Res.* **43**, 829 (1986).
7. X. Xu *et al.*, *J. Biol. Chem.* **279**, 33946 (2004).
8. S. Soundar, B. L. Danek, R. F. Colman, *J. Biol. Chem.* **275**, 5606 (2000).
9. K. R. Albe, M. H. Butler, B. E. Wright, *J. Theor. Biol.* **143**, 163 (1990).
10. E. D. MacKenzie *et al.*, *Mol. Cell. Biol.* **27**, 3282 (2007).
11. O. C. Ingebretsen, *Biochim. Biophys. Acta* **452**, 302 (1976).

12. G. L. Semenza, *Drug Discov. Today* **12**, 853 (2007).
13. We thank members of the Fudan Molecular and Cell Biology Laboratory for valuable input; Y. Liu, X. Liu, and H. Zhu for assistance with histology; Z. Bao, L. Yang, Q. Shi, and G. Zhao for clinical samples; and S. Jackson for reading the manuscript. This work is supported by the 985 program from the Chinese Ministry of Education, State Key Development Programs of China (2009CB918401, 2006CB806700), National 863 Program of China (2006AA02A308), China NSF grants (30600112 and 30871255) and Shanghai Key Basic Research Projects (06JC14086, 07PJ14011, and 08JC1400900), and NIH grants (to K.-L.G. and Y.X.). Y. Xiong, K.-L. Guan, and S. Zhao are applying for a patent related to the work on permeable alpha-ketogluterate.

Supporting Online Material
www.sciencemag.org/cgi/content/full/324/5924/261/DC1
Materials and Methods
Figs. S1 to S8
Table S1

15 January 2009; accepted 10 March 2009
10.1126/science.1170944

Demonstration of Genetic Exchange During Cyclical Development of *Leishmania* in the Sand Fly Vector

Natalia S. Akopyants,[1]* Nicola Kimblin,[2]* Nagila Secundino,[2] Rachel Patrick,[2] Nathan Peters,[2] Phillip Lawyer,[2] Deborah E. Dobson,[1] Stephen M. Beverley,[1]† David L. Sacks[2]†‡

Genetic exchange has not been shown to be a mechanism underlying the extensive diversity of *Leishmania* parasites. We report here evidence that the invertebrate stages of *Leishmania* are capable of having a sexual cycle consistent with a meiotic process like that described for African trypanosomes. Hybrid progeny were generated that bore full genomic complements from both parents, but kinetoplast DNA maxicircles from one parent. Mating occurred only in the sand fly vector, and hybrids were transmitted to the mammalian host by sand fly bite. Genetic exchange likely contributes to phenotypic diversity in natural populations, and analysis of hybrid progeny will be useful for positional cloning of the genes controlling traits such as virulence, tissue tropism, and drug resistance.

Parasitic protozoa of the genus *Leishmania* cause a spectrum of human diseases that pose serious public health challenges for prevention, diagnosis, and treatment. The diversity of *Leishmania* species, with more than 20 currently recognized, is thought to have arisen by gradual accumulation of divergent mutations rather than by sexual recombination. Tibayrenc *et al*. (*1*) have reported strong linkage disequilibrium in several *Leishmania* species and proposed that these parasites are essentially clonal. This notion must be reconciled, however, with the accumulating examples of naturally occurring strains that share genotypic markers from two recognized species and thereby provide circumstantial evidence for sexual recombination (*2*–*4*). Genetic exchange has been documented for the other trypanosomatids that cause human disease. Hybrid genotypes were observed in tsetse flies during cotransmission of two strains of *Trypanosoma brucei* (*5*) and in mammalian cells after coinfection with two clones of *Trypanosoma cruzi* differing in drug-resistance markers (*6*). Using drug resistance markers, we provide evidence for genetic exchange in *Leishmania major* and discuss the implications of these findings to *Leishmania* biology and experimental analysis.

[1]Department of Molecular Microbiology, Washington University School of Medicine, St. Louis, MO 63110, USA. [2]Laboratory of Parasitic Diseases, National Institute of Allergy and Infectious Diseases, NIH, Bethesda, MD 20892, USA.

*†These authors contributed equally to this work.
‡To whom correspondence should be addressed. E-mail: dsacks@nih.gov

One parental clone, LV39c5(HYG), was derived from strain LV39 clone 5 (MHOM/SU/59/P) and was heterozygous for an allelic replacement of the *LPG5A* on chromosome 24 by a hygromycin B–resistance cassette (*LPG5A*/*LPG5A*::Δ*HYG*) (*7*). The second parental clone, FV1(SAT), was derived from NIH Friedlin clone V1 (MHOM/IL/80/FN) and bore a heterozygous nourseothricin–resistance (*SAT*) marker, integrated along with a linked firefly luciferase (*LUC*) reporter gene into one allele of the ~24 rRNA cistrons located on chromosome 27 (*8*) (+/*SSU*::*SAT-LUC*). These strains were chosen as they are phenotypically identical to their respective parental wild-type (WT) virulent *L. major*, whereas the markers were chosen because they are functionally independent (*9*). The target gene modifications were chosen because they caused no effect on normal growth in vitro or in mouse infections (*10*), and epistatic interactions were not anticipated between these alleles.

Multiple attempts to generate hybrid parasites resistant to both antibiotics during *in vitro* coculture of the parental lines were unsuccessful (*11*). The parental clones were tested for their ability to generate parasites resistant to both drugs during coinfection in the sand fly. The growth of each parental line in *Phlebotomus duboscqi,* a natural vector of *L. major*, is shown in fig. S1. Promastigotes of each parent survived the initial period of blood-meal digestion and excretion (days 1 to 6) and underwent metacyclogenesis at a comparable frequency (20 to 60%), although the FV1(SAT) parent established and maintained a higher intensity of infection by a factor of 3 to 4. The parental clones were tested for their ability to generate doubly drug–resistant parasites during coinfection in the sand fly. Flies were fed through a membrane on mouse blood containing 3 and 1×10^6/ml of the LV39c5(HYG) and FV1(SAT) lines, respectively, each obtained from log-phase cultures and extensively washed to remove antibiotics. A total of 102 flies from four independent coinfection experiments were dissected 13 to 16 days postinfection; at this time, they harbored mature infections with an average of 39,400 ± 14,700 promastigotes per midgut. Flies cannot be maintained under aseptic conditions, and more than half of the cultures established from the midgut parasites were lost to fungal contamination during the subsequent 1 to 2 weeks of culture. In the remaining cultures, 12 (26%) grew out promastigotes that were resistant to both drugs. Clonal lines were generated from nine of the doubly drug–resistant populations, and the genotypes and phenotypes of one or two clones from each culture were determined (summarized in Table 1).

Polymerase chain reaction (PCR) tests with primers specific for the parental markers showed that all doubly drug–resistant clones tested contained both the *HYG* and *SAT* drug-resistance genes (Fig. 1A, Table 1, and table S3). Controls showed that the marker loci had not rearranged during hybrid formation but had maintained their location within the *LPG5A* or *SSU* rRNA loci, respectively (fig. S2). These data indicated that the doubly drug–resistant clonal lines were genetic hybrids. To confirm that hybrid formation was compatible with transmission to the mammalian host, coinfected sand flies were allowed to bite and to induce lesions in BALB/c mice. Two doubly drug–resistant clonal lines, designated 6.16.E8 and 6.14.F9, were recovered from the eight dermal lesions examined and were found to be similar to those directly recovered from insects, as discussed below (Table 1). Coinjection of both parental lines into mouse ears by needle never led to the recovery of doubly drug–resistant parasites from the 20 dermal lesions examined, each containing $>2.4 \times 10^7$ amastigotes, which suggested that the hybrids selected after transmission by the coinfected sand flies were generated in the fly and not in the mammalian host.

We examined the segregation of loci not linked to chromosomes 24 and 27, the location of the *HYG* and *SAT* markers, respectively. We used single-nucleotide polymorphisms (SNPs) developed from comparisons of the terminal ~30-kb chromosomal regions encompassing the *SCG* genes located on *L. major* chromosomes 2,

7, 21, 25, 31, 35, and 36 in the WT parent of LV39c5(HYG). *SCG*s make up a family of polymorphic telomeric galactosyltransferases (*12*), but genes internal to these showed SNPs occurring at an overall frequency of ~0.15%, consistent with other estimates of strain variation (*13*, *14*). For each chromosome, SNPs from one to two loci, located from 8.5 to 23 kb inwards of the telomeric *SCG*s (*12*) (tables S1 and S2), were analyzed by a combination of SNP-CAPS (*15*) [SNP genotyping combined with cleaved amplified polymorphic site analysis (CAPS)] and/or direct sequencing. Each parent was homozygous for every marker tested, and all 18 progeny showed clearly that they had inherited both parental alleles (Fig. 1B and Table 1). This provides evidence that each progeny clone inherited a full set of chromosomes from each parent and were thus full genome hybrids.

In 7 out of 18 hybrid progeny clones, the relative ratio of the parental alleles seen in SNP-CAPS digestions differed from the expected 1:1. Instead, in each case the most intense bands or sequencing trace peaks were those associated with the LV39c5 parent, a finding seen at all loci and in all lines tested (Fig. 1B, fig. S3, and Table 1). One possibility is the occurrence of triploid offspring, bearing two chromosomal complements from one parent (LV39) and one from the other (FV1). The DNA contents of the progeny clones were measured relative to those of the parents by flow cytometry, and the profiles compared with 2*n* and 4*n* lines studied previously (*16*). Although the parents and most hybrids showed 2*n* DNA contents, the seven hybrids detected above showed 3*n* DNA content (Fig. 2 and Table 1); intermediate DNA content was not observed. Thus, although all doubly drug–resistant lines were full genome hybrids, a significant fraction appeared to be triploid rather than diploid and had inherited two genomic complements from the LV39 and one from FV1 parents. Similarly, for four of the 2*n* lines (1.16.A1, 1.16.C4, 5.12.D9, and 5.12.F11), the segregation of chromosome 31 markers appeared to differ from the expected 1:1 ratio, with the LV39c5 parent again predominating in sequencing and/or SNP-CAPs analysis of the hybrids (Table 1). This may arise from the finding that *Leishmania* chromosomes are occasionally aneuploid (*17*), which includes tetrasomy of *Leishmania* chromosome 31 in the parental lines studied here. Potentially, tetrasomy may affect mitotic inheritance and segregation, as seen in autotetraploid or allotetraploid species (*18*). This was not pursued further in this study.

SNP markers were identified to determine the inheritance of mitochondrial maxicircle formed of kinetoplast DNA (kDNA) (Fig. 1C, Table 1, and tables S1 to S3). In contrast to the chromosomal DNA, maxicircle markers demonstrated clear and consistent uniparental inheritance, with 6 of the progeny clones having maxicircle kDNA exclusively from the LV39c5(HYG) and 12 inheriting maxicircle kDNA exclusively from FV1(SAT) (Table 1 and Fig. 1C). These markers allowed us to establish that two clonal lines arising from the same fly that had identical nuclear markers were in fact different (4.9.C8/C6 and 4.3.A12/G12) (Table 1). kDNA minicircles were not examined.

Several studies were undertaken to compare the progeny clones for parental phenotypic traits. Metacyclic promastigotes of the FV1 line react with monoclonal antibody (mAb) 3F12, which recognizes the abundant surface lipophosphoglycan (LPG) and other phosphoglycans expressing mono–β-galactose–modified repeat units terminating with β(1,2)arabinose residues. The same antibody fails to bind to LV39c5 metacyclics, owing to differences in the β-galactose chain length (*19*). Metacyclic promastigotes purified from all progeny clones displayed strong reactivity with mAb 3F12, as determined by surface agglutination of live parasites (fig. S4A). Thus, the mono-galactosylated 3F12 trait appeared to be inherited as a dominant trait. Another dominant trait is the "clumpy" appearance of LV39c5(HYG) when grown in standard culture medium, in contrast to FV1(SAT), which grows as individual cells. All hybrid offspring appeared clumpy (fig. S4B).

It is noteworthy that the parental clones differ in a virulence trait defined as the time required

Table 1. Summary of phenotype and genotype data for parental and progeny clones. Hybrid lines nomenclature: experiment number.fly number.clone name, and for 6.14.F9 and 6.16.E8, experiment number.ear lesion number.clone name. Virulence profile: fast (f) or slow (s). Maxicircle inheritance: F, FV1(SAT) SNP pattern; L, LV39c5(HYG) SNP pattern. Chromosomal analysis: SEQ, ratio of parental SNP peaks by sequence analysis; CAPS, cleaved and amplified polymorphic site analysis; and H, hybrid. The six chromosomes are 2, 7, 21, 25, 35, and 36. Chromosome 31 is tetrasomic.

Cell line	Virulence profile	Maxicircle inheritance	3F12 antibody	Clumping	Ploidy	Chromosomal analysis			
						Six chromosomes		Chr 31	
						SEQ	CAPS	SEQ	CAPS
FV1(SAT)	f	F	+	–	2*n*				
LV39.5c5(HYG)	s	L	–	+	2*n*				
1.10.B12	ND	L	+	+	2*n*	1:1	H	1:1	H
1.10.D9	ND	L	+	+	2*n*	1:1	H	1:1	H
1.16.A1	f	F	+	+	2*n*	1:1	H	L > F	H
1.16.C4	ND	F	+	+	2*n*	1:1	H	L > F	H
4.3.A12	f	F	+	+	2*n*	1:1	H	1:1	H
4.3.G12	ND	L	+	+	2*n*	1:1	H	1:1	H
4.7.A3	f	F	+	+	2*n*	1:1	H	1:1	H
5.12.D9	ND	F	+	+	2*n*	1:1	H	L > F	H
5.12.F11	s	F	+	+	2*n*	1:1	H	L > F	H
5.22.A10	f	F	+	+	2*n*	1:1	H	1:1	H
6.14.F9	f	F	+	+	2*n*	1:1	H	1:1	H
1.14.B11	s	L	+	+	3*n*	L > F	H	L > F	H
1.14.E10	ND	L	+	+	3*n*	L > F	H	L > F	H
4.9.C8	s	L	+	+	3*n*	L > F	H	L > F	H
4.9.E6	s	F	+	+	3*n*	L > F	H	L > F	H
4.17.A3	s	F	+	+	3*n*	L > F	H	L > F	H
4.17.F4	ND	F	+	+	3*n*	L > F	H	L > F	H
6.16.E8	s	F	+	+	3*n*	L > F	H	L > F	H

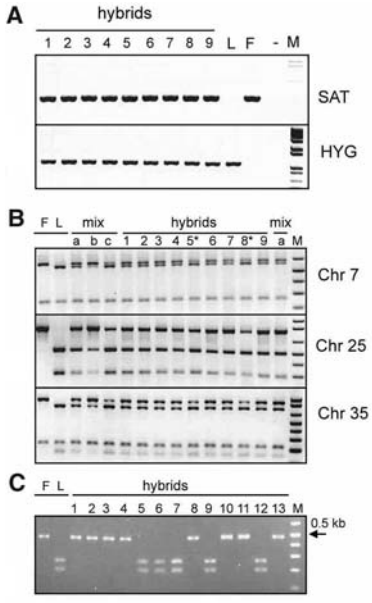

Fig. 1. Genotyping of hybrid *Leishmania*. (**A**) PCR for parental selectable drug markers *SAT* and *HYG*. Samples are F, FV1(SAT); L, LV39c5(HYG); M, 1 kb plus marker (Invitrogen, Carlsbad, CA); -, no template control, 1, 1.10.B12; 2, 1.10.D9; 3, 4.3.G12; 4, 4.3.A12; 5, 1.14.E10; 6, 5.12.D9; 7, 5.12.F11; 8, 1.14.B11; and 9, 5.22.10. (**B**) SNP-CAPS analysis for loci on chromosomes 7, 25, and 35. F, L and M are as in (**A**). Mix a, b, and c, parental templates mixed in different ratios (1:1, 3:1, or 1:3 F:L, respectively). DNA content analysis showed that hybrids 5 and 8 are 3*n* (marked by an asterisk), and the remainder shown are 2*n* progeny. (**C**) SNP-CAPS analysis of maxicircle. Digestion with Bfa I of the ND5–divergent region PCR product is shown. Hybrids tested are 1, 4.7.A3; 2, 4.17.A3; 3, 4.9.E6; 4, 4.17.F4; 5, 1.10.B12; 6, 1.10.D9; 7, 4.3.G12; 8, 4.3.A12; 9, 1.14.E10; 10, 5.12.D9; 11, 5.12.F11; 12, 1.14.B11; and 13, 5.22.10.

for the emergence of lesions in susceptible BALB/c mice (Fig. 3). After subcutaneous foot-pad inoculation of 10^4 metacyclic promastigotes, purified in each case from stationary cells freshly transformed from lesion amastigotes, five of the progeny clones displayed lesion progression as fast or faster than the FV1(SAT) parent, whereas another five of the progeny showed lesion development as slow or slower than the LV39c5(HYG) parent. These data indicate that despite the low nucleotide heterozygosity typically found in *L. major* (*14*), there is sufficient variation in one or both parental clones for distinct virulence phenotypes to emerge. The most parsimonious explanation is that either "slow" or "fast" growth is inherited as a dominant trait and that one or both parental clones are heterozygous for the gene(s) controlling this trait.

All five triploid lines tested exhibited the "slow virulence" trait, which occurred in only one out of eight of the diploid lines. There may be a reduction in virulence associated with polyploidy that accounts for the failure to detect polyploid lines in field isolates. In contrast, no significant association was seen with the maxicircle genotype and virulence or ploidy (Table 1).

Leishmania can undergo genetic exchange during growth and development in the sand fly vector and can transmit infectious-stage hybrid progeny to a mammalian host. Based on the analysis of 18 hybrid clones representing a minimum of 11 independent crosses, the findings argue for inheritance of at least one full set of chromosomes from each parent, accompanied by independent, uniparental inheritance of the maxicircle kDNA derived from one parent. The inheritance patterns of nuclear DNA fit a Mendelian model of meiosis of the parental strains followed by fusion of the haploid cells. However, alternative mechanisms, modeled after the tetraploid sexual cycle described in *Saccharomyces cerevisiae* (*20*), could involve fusion of parental diploid cells, followed by meiosis and intracellular fusion of haploid nuclei (*21*, *22*). Triploid offspring have also been seen in trypanosome crosses and have been attributed to incomplete meiotic division and fusion of haploid and diploid nuclei (fig. S5) (*21*, *23*). In trypanosomes as well, maxicircle kDNA was initially thought to be inherited uniparentally; however, later studies showed it to be inherited biparentally, but subsequently to segregate out during mitosis, leading to fixation (*24*). It is possible that mixed maxicircle genotypes might have also been present in earlier generations of the *Leishmania* crosses than were examined here.

The frequency of genetic exchange involving these two parental clones would appear to be rare (~2.5×10^{-5} or less, after correcting for recovery of only doubly drug–resistant offspring). Consistent with this, most clonal lines from a single infected fly were identical, although two flies yielded offspring with different maxicircle genotypes, which suggested two independent crossing events. Whether the frequency observed in the FV1 × LV39c5 cross here is typical for other *Leishmania* strains or species remains to be determined. The low frequency agrees with the general sense that gene exchange must occur rarely, as deduced from observed heterozygosities and linkage disequilibrium in natural populations (*1*).

Despite the infrequency of gene exchange experimentally or in nature, there are many examples of hybrid genotypes observed in field isolates involving most *Leishmania* species (*2*–*4*, *25*–*27*). Potentially, these hybrids arose from rare "mating" events, yielding offspring with a strong selective advantage, such as seen in *Toxoplasma gondii* (*28*), and suggested by the clonal propagation of an emergent hybrid mucosal strain in Peru (*3*). Given the rarity with which mixed infections in flies are likely to occur, in conjunction with the low frequency of hybridization that we have observed in coinfected flies, any successful new genotype would be expected to propagate clonally.

Although rare in nature, the frequency of experimental hybrid formation is sufficient to enable its use as an experimental tool. Our studies show segregation of "virulence traits" in the FV1 × LV39c5 crosses studied here, and through positional cloning, the genes responsible may be identified. Future studies will explore the possibilities of carrying out backcrosses, as well as crosses between species, and of developing SNP tools for genetic linkage analysis.

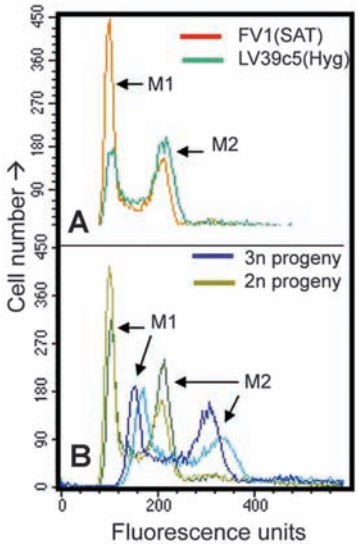

Fig. 2. DNA contents of parental and 2*n* and 3*n* progeny clones. DNA content was measured in log phase cells by flow cytometry after staining RNase-treated permeabilized cells with propidium iodide. (**A**) Parental lines: FV1(SAT), red, and LV39c5(HYG), green. (**B**) Representative 2*n* (green, 4.3.G12 and 1.10.D9) and 3*n* (blue, 1.14.E10 and 4.9.C8) progeny. M1 refers to cells in the G_1/G_0 phase of the cell cycle and M2 refers to cells in G_2/M phase. Small differences in the M_1/M_2 ratio reflect minor differences in cellular growth rate and growth phase and are not significant nor found in other studies of these lines.

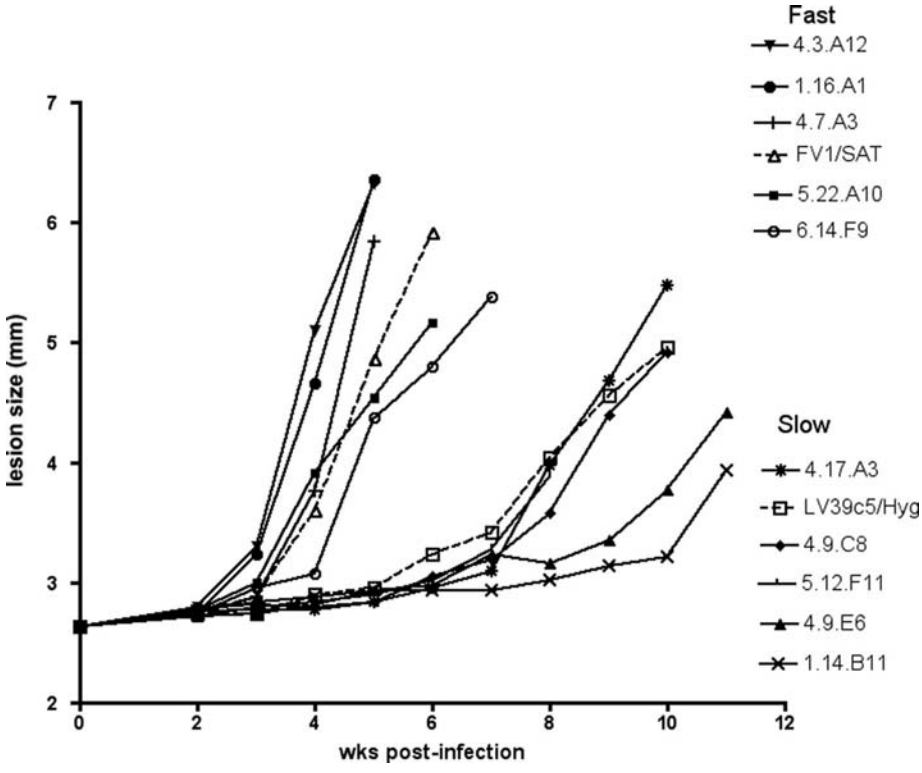

Fig. 3. Lesion formation in BALB/c mice by parental and hybrid progeny clones. Mice were infected in the hind foot pad by subcutaneous inoculation of 10^4 metacyclic promastigtoes. Results are representative of three independent experiments.

References and Notes

1. M. Tibayrenc, S. Ben Abderrazak, F. Guerrini, A. Banuls, *Arch. Inst. Pasteur Tunis* **70**, 375 (1993).
2. J. M. Kelly, J. M. Law, C. J. Chapman, G. J. Van Eys, D. A. Evans, *Mol. Biochem. Parasitol.* **46**, 253 (1991).
3. D. Nolder, N. Roncal, C. R. Davies, A. Llanos-Cuentas, M. A. Miles, *Am. J. Trop. Med. Hyg.* **76**, 573 (2007).
4. C. Ravel *et al.*, *Int. J. Parasitol.* **36**, 1383 (2006).
5. L. Jenni *et al.*, *Nature* **322**, 173 (1986).
6. M. W. Gaunt *et al.*, *Nature* **421**, 936 (2003).
7. A. A. Capul, T. Barron, D. E. Dobson, S. J. Turco, S. M. Beverley, *J. Biol. Chem.* **282**, 14006 (2007).
8. S. Martinez-Calvillo *et al.*, *Mol. Biochem. Parasitol.* **116**, 147 (2001).
9. P. B. Joshi, J. R. Webb, J. E. Davies, W. R. McMaster, *Gene* **156**, 145 (1995).
10. A. A. Capul, S. Hickerson, T. Barron, S. J. Turco, S. M. Beverley, *Infect. Immun.* **75**, 4629 (2007).
11. Materials and methods are available as supporting material on *Science* Online.
12. D. E. Dobson, L. D. Scholtes, P. J. Myler, S. J. Turco, S. M. Beverley, *Mol. Biochem. Parasitol.* **146**, 231 (2006).
13. J. Lukes *et al.*, *Proc. Natl. Acad. Sci. U.S.A.* **104**, 9375 (2007).
14. A. C. Ivens *et al.*, *Science* **309**, 436 (2005).
15. T. Thiel, R. Kota, I. Grosse, N. Stein, A. Graner, *Nucleic Acids Res.* **32**, e5 (2004).
16. A. K. Cruz, R. Titus, S. M. Beverley, *Proc. Natl. Acad. Sci. U.S.A.* **90**, 1599 (1993).
17. C. Ravel, P. Dubessay, P. Bastien, J. M. Blackwell, A. C. Ivens, *Parasitol. Today* **14**, 301 (1998).
18. M. E. Moody, L. D. Mueller, D. E. Soltis, *Genetics* **134**, 649 (1993).
19. D. E. Dobson *et al.*, *J. Biol. Chem.* **278**, 28840 (2003).
20. M. D. Rose, *Annu. Rev. Cell Dev. Biol.* **12**, 663 (1996).
21. W. Gibson, L. Garside, M. Bailey, *Mol. Biochem. Parasitol.* **51**, 189 (1992).
22. J. Heitman, *Curr. Biol.* **16**, R711 (2006).
23. M. Hope *et al.*, *Mol. Biochem. Parasitol.* **104**, 1 (1999).
24. C. M. Turner, G. Hide, N. Buchanan, A. Tait, *Exp. Parasitol.* **80**, 234 (1995).
25. J. C. Dujardin *et al.*, *Acta Trop.* **59**, 293 (1995).
26. J. M. Schwenkenbecher *et al.*, *Int. J. Parasitol.* **36**, 237 (2006).
27. I. L. Mauricio, M. K. Howard, J. R. Stothard, M. A. Miles, *Parasitology* **119**, 237 (1999).
28. M. E. Grigg, S. Bonnefoy, A. B. Hehl, Y. Suzuki, J. C. Boothroyd, *Science* **294**, 161 (2001).

29. This research was supported in part by the Intramural Research Program of the NIH, National Institute of Allergy and Infectious Diseases (NIAID), and in part by NIAID grant support (S.M.B., D.E.D., and N.S.A. A1029646 and A1020941). We thank K. Owens for inventorying and shipping parasite strains; K. Beacht for mouse infection studies; and M. Grigg, L. Miller, and A. Sher for critical review of the manuscript. Maxicircle sequences have been submitted to GenBank and had been assigned accession numbers FJ349262 to FJ349263 (12*S* rRNA) and FJ349264 to FJ349265 (Divergent region).

Supporting Online Material

www.sciencemag.org/cgi/content/full/324/5924/265/DC1
Materials and Methods
Figs S1 to S5
Tables S1 to S3
References

8 December 2008; accepted 18 February 2009
10.1126/science.1169464

Green Evolution and Dynamic Adaptations Revealed by Genomes of the Marine Picoeukaryotes *Micromonas*

Alexandra Z. Worden,[1]* Jae-Hyeok Lee,[2]† Thomas Mock,[3]†‡ Pierre Rouzé,[4]† Melinda P. Simmons,[1]† Andrea L. Aerts,[5] Andrew E. Allen,[6] Marie L. Cuvelier,[1,7] Evelyne Derelle,[8] Meredith V. Everett,[7] Elodie Foulon,[9] Jane Grimwood,[5,10] Heidrun Gundlach,[11] Bernard Henrissat,[12] Carolyn Napoli,[13] Sarah M. McDonald,[1] Micaela S. Parker,[3] Stephane Rombauts,[4] Aasf Salamov,[5] Peter Von Dassow,[9] Jonathan H. Badger,[6] Pedro M. Coutinho,[11] Elif Demir,[1] Inna Dubchak,[5] Chelle Gentemann,[14] Wenche Eikrem,[15] Jill E. Gready,[16] Uwe John,[17] William Lanier,[18] Erika A. Lindquist,[5] Susan Lucas,[5] Klaus F. X. Mayer,[10] Herve Moreau,[8] Fabrice Not,[9] Robert Otillar,[5] Olivier Panaud,[19] Jasmyn Pangilinan,[5] Ian Paulsen,[20] Benoit Piegu,[19] Aaron Poliakov,[5] Steven Robbens,[4] Jeremy Schmutz,[5,10] Eve Toulza,[21] Tania Wyss,[22] Alexander Zelensky,[23] Kemin Zhou,[5] E. Virginia Armbrust,[3] Debashish Bhattacharya,[18] Ursula W. Goodenough,[2] Yves Van de Peer,[4] Igor V. Grigoriev[5]

Picoeukaryotes are a taxonomically diverse group of organisms less than 2 micrometers in diameter. Photosynthetic marine picoeukaryotes in the genus *Micromonas* thrive in ecosystems ranging from tropical to polar and could serve as sentinel organisms for biogeochemical fluxes of modern oceans during climate change. These broadly distributed primary producers belong to an anciently diverged sister clade to land plants. Although *Micromonas* isolates have high 18*S* ribosomal RNA gene identity, we found that genomes from two isolates shared only 90% of their predicted genes. Their independent evolutionary paths were emphasized by distinct riboswitch arrangements as well as the discovery of intronic repeat elements in one isolate, and in metagenomic data, but not in other genomes. Divergence appears to have been facilitated by selection and acquisition processes that actively shape the repertoire of genes that are mutually exclusive between the two isolates differently than the core genes. Analyses of the *Micromonas* genomes offer valuable insights into ecological differentiation and the dynamic nature of early plant evolution.

Ancestral green algae were of fundamental importance to the eukaryotic greening that shaped the geochemistry of our planet. This process began over a billion years ago when a cyanobacterium was captured by a heterotrophic protist and incorporated as an endosymbiont, giving rise to the first eukaryotic alga (*1*). The extant Prasinophytae retain characteristics that are believed to have been present in the last common ancestor of green algae (chlorophytes) and land plants (streptophytes, including charophyte algae) (*2*). Most prasinophytes within the monophyletic marine order Mamiellales (Fig. 1A and fig. S1), such as *Micromonas*, are tiny (≤2 μm in diameter) and known as picoeukaryotes. *Micromonas* is a motile unicell, with a single chloroplast and mitochondrion (Fig. 1A, inset), first reported as a dominant phytoplankter in the 1950s (*3*) and now recognized as having a global distribution (Fig. 1B) (*4*).

Today's oceans contain a polyphyletic diversity of algae, some with plastids that share ancestry with land plants (green algae) and others (chromalveolates) that are derived from red algae through secondary or tertiary (eukaryotic-eukaryotic) endosymbioses (*5*, *6*). Unlike most episodic chromalveolate bloomers and the freshwater green alga *Chlamydomonas* (*7*), the Mamiellales have reduced genomes, as first shown in *Ostreococcus* (*8*, *9*). *Ostreococcus* has a narrower environmental distribution than *Micromonas* (Fig. 1B) and a smaller genome (12 to 13 Mb containing only ~8000 genes). Open-ocean bacteria, including SAR11 and *Prochlorococcus* (*10*, *11*), show similar patterns of cell size and genome minimization. Conditions favoring picophytoplankton growth, such as increased stratification, less mixing, and reduced nutrient concentrations in ocean surface waters, are predicted climate change outcomes, and thus picoeukaryote dynamics may be useful ecosystem indicators.

We sequenced the nuclear genomes of *Micromonas* isolates RCC299 and CCMP1545 (Table 1 and figs. S2 and S3) (*12*). These isolates are from distant ocean provinces and fall into distinct phylogenetic clades that can co-occur (Fig. 1) (*12*, *13*) but are generally considered a single species (*Micromonas pusilla*). Transmission electron microscopy revealed no morphological differences (*12*), and 18*S* ribosomal DNA (rDNA) identity was high (97%). Surprisingly, only 90% of their 10,056 (RCC299) and 10,575 (CCMP1545) predicted genes (table S1) were shared (Fig. 2A). In contrast, *Ostreococcus lucimarinus* and *O. tauri* share 97% of cataloged genes (*12*), and yeast genera can share ~95% of homologs (*14*). The divergence we observed between the *Micromonas* isolates supports their classification as distinct species.

Synteny, GC content, and codon usage pointed to a shared evolutionary history for RCC299 and

CCMP1545 but underscored their genomic divergence [supporting online material (SOM) text S1]. Each genome contained a region that had 14% lower than average GC content, composing 7% (RCC299) and 8% (CCMP1545) of the genome (figs. S3 and S4), which also had higher transcriptional activity (SOM text S1). Similar regions in *Ostreococcus* (*8*, *9*) form smaller genome proportions. DNA alignment between RCC299 and CCMP1545 low-GC regions was poor, protein colinearity was absent, and codon usage was different, in contrast to normal GC chromosomes (figs. S4 to S6).

Two major evolutionary themes emerged from our analyses. First, the common ancestor of the Mamiellales had already undergone genomic reduction, highlighted by their organellar genomes (SOM text S2, fig. S7, and tables S2 to S4). Second, *Micromonas* appeared to be less derived than *Ostreococcus*, rendering insights into the genetic composition of the proto-prasinophyte (the common ancestor of plants and prasinophytes) and specialization in extant species. Most "core" nucleus-encoded genes (genes common to the four Mamiellales genomes) were found to have known functions (Fig. 2, A and B) in key pathways (SOM text S3 to S6, tables S5 to S9, and fig. S8), such as photosynthesis, and included selenoproteins (SOM text S3 and table S10). A significant proportion of genes grouped with land plants (Fig. 2C). Core genes branching with chromalveolates (mostly diatoms and brown algae) (Fig. 2C) presumably reflected losses (or extensive divergence) in other green lineage organisms and red algae or perhaps horizontal gene transfer (HGT).

The proto-prasinophyte features we discovered in *Micromonas* included transcription factors that probably belong to the "basal green toolkit" (SOM text S7, figs. S9 to S11, and table

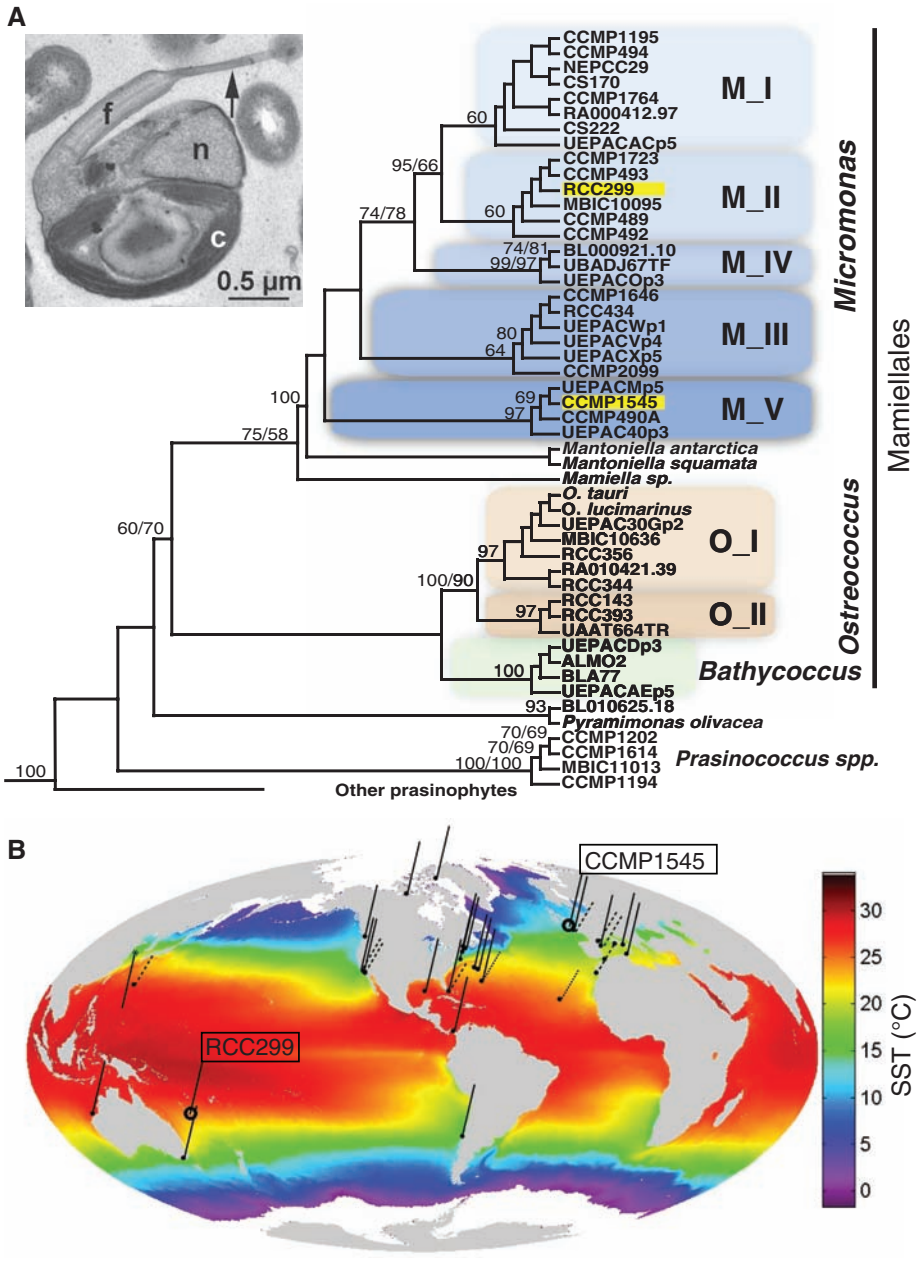

Fig. 1. *Micromonas* phylogeny and distribution. (**A**) A consensus neighbor-joining (NJ) distance 18*S* rRNA gene tree illustrating the distinct *Micromonas* clades (*12*). Bootstrap values represent a percent of 1000 replicates (NJ), and where provided the second value represents the maximum-likelihood bootstrap percentages. The genome isolates sequenced in this work are highlighted (yellow). The previously sequenced *Ostreococcus tauri* and *O. lucimarinus* neighbor each other in clade O_I. The relationship to plants and other photosynthetic lineages is shown in fig S1. (Inset) *Micromonas* thin section showing the nucleus (n), chloroplast (c), flagellum (f), and mucronate extension (the thin tip at the end of the flagellum, indicated by the arrow). (**B**) Mean sea surface temperature (SST) for 2006 measured with global high-resolution SST (GHRSST) blended infrared and microwave SSTs, and locations where *Micromonas* (solid lines and circles around the isolates used in this work) and *Ostreococcus* (dashed lines) 18*S* rDNA sequences have been recovered. *Micromonas* appeared in all temperature regimes.

[1]Monterey Bay Aquarium Research Institute, Moss Landing, CA 95039 USA. [2]Department of Biology, Washington University at St. Louis, St. Louis, MO 63130, USA. [3]School of Oceanography, University of Washington, Seattle, WA 98195, USA. [4]Department of Plant Systems Biology, Flanders Institute for Biotechnology (VIB) and Department of Molecular Genetics, Ghent University, 9052 Gent, Belgium. [5]U.S. Department of Energy (DOE) Joint Genome Institute (JGI), Walnut Creek, CA 94598, USA. [6]J. Craig Venter Institute, San Diego, CA 92121, USA. [7]Rosenstiel School of Marine and Atmospheric Science, University of Miami, Miami, FL 33149, USA. [8]Observatoire Océanologique, CNRS–Université Pierre et Marie Curie, 66651 Banyuls sur Mer, France. [9]Station Biologique de Roscoff, CNRS–Université Pierre et Marie Curie, Roscoff Cedex, France. [10]Stanford Human Genome Center, Stanford University School of Medicine, Palo Alto, CA 94304, USA. [11]Institute of Bioinformatics and System Biology, German Research Center for Environmental Health, 85764 Neuherberg, Germany. [12]Architecture et Fonction des Macromolécules Biologiques, Universities of Aix-Marseille I and II, Marseille 13288, France. [13]Biology Institute, University of Arizona, Tucson, AZ 85719, USA. [14]Remote Sensing Systems, Santa Rosa, CA 95401, USA. [15]Avdeling for Marinbiologi og Limnologi, University of Oslo, Oslo N-0316, Norway. [16]Division of Molecular Bioscience, College of Medicine, Biology and the Environment, Australian National University, Canberra ACT 2601, Australia. [17]Alfred Wegener Institute for Polar and Marine Research, Am Handelshafen, Bremerhaven 27570, Germany. [18]Department of Biology, University of Iowa, Iowa City, IA 52242, USA. [19]Laboratoire Genome et Development des Plantes Université de Perpignan, 66860 Perpignan, France. [20]Department of Chemistry and Biomolecular Sciences, Macquarie University, New South Wales 2109, Australia. [21]Ecosystèmes Lagunaires, Université Montpellier II, F-34095 Montpellier Cedex 05, France. [22]Department of Biology, University of Miami, Miami, FL 33149, USA. [23]Department of Genetics, Erasmus Medical Center, Rotterdam 3015 CE, Netherlands.

*To whom correspondence should be addressed. E-mail: azworden@mbari.org

†These authors contributed equally to this work.

‡Present address: School of Environmental Sciences, University of East Anglia, Norwich NR4 7TJ, UK.

S11). For example, early-branching land plants encode most higher-plant transcription factor families except for the YABBY family (*15*), which was therefore posited to be evolutionarily associated with the development of leaves. However, we found YABBY in *Micromonas*, although it is absent from *Chlamydomonas* and *Ostreococcus*, indicating that it was part of the basal toolkit (fig. S11). We also found diversified homeodomains (fig. S12 and table S12) that are relevant to the evolution of green regulatory networks.

Although prasinophytes are often considered asexual, our observations indicated that the proto-prasinophyte was sexual. First, meiotic-specific and non-meiotic representatives of the *RECA-RAD51*, *TOP6A/SPO11*, and *MUTS* gene families were found (SOM text S5 and table S13). Second, the low-GC regions showed features of sex chromosomes, including RWP-RK transcription factor family genes (SOM text S7 and table S14). Third, numerous Mamiellales genes encoded hydroxyproline-rich glycoproteins (HRGP) (SOM text S6, table S15, and fig. S13), which are cell-wall components in *Chlamydomonas* and plants (*16*). Like the many carbohydrate-active enzymes (SOM text S6 and table S17), this was unexpected because cell walls have not been observed in *Micromonas* or *Ostreococcus* (Fig. 1A, inset) (*4*). In *Chlamydomonas*, one HRGP gene set is expressed only after sexual fusion to produce a thick adhesive zygote wall (*17*). *Micromonas* may behave similarly. Collectively, these data indicate the occurrence of sexual differentiation and the formation of a resistant life-cycle stage.

Fourteen percent of genes were shared between RCC299 and CCMP1545 but not with *Ostreococcus* (Fig. 2, SOM text S3 and S8, table S18, and fig. S14). Shared enzymes for the synthesis and remodelling of peptidoglycan in the plastid provided new insight into the evolutionary history of the ancestral cyanobacterial endosymbiont (SOM text S6) (*18*, *19*). The shared genes also showed more rapid evolutionary rates than core genes (fig. S15), indicating that they escaped constraints acting on the Mamiellales core but still probably play important roles, given their presence in both isolates. Moreover, a larger proportion of "unique" genes (used here to mean genes mutually exclusive between RCC299 and CCMP1545) branched with opisthokont or bac-

Table 1. Characteristics of the *Micromonas* genomes.

Characteristic	CCMP1545	RCC299
Genome size (Mb)	21.9	20.9
G+C (%)	65	64
Number of genes	10,575	10,056
Gene size (bp)	1,557	1,587
Multiexon genes (%)	50	37
Introns (per gene)	0.90	0.57
Intron length (bp)	187	163

Table 2. Genes with associated TPP riboswitches in RCC299, CCMP1545, and *Ostreococcus* (both *O. tauri* and *O. lucimarinus*). The position of the riboswitch relative to the gene is indicated in the columns headed "Riboswitch." DC, domain containing; NF, not found with protein-protein basic local alignment search tool (BLASTP) or protein-nucleotide six-frame translation (TBLASTN). See SOM text S15 for gene descriptions. Protein IDs refer to JGI genome browser protein IDs.

	RCC299			CCMP1545			*Ostreococcus*		
Gene name	Protein ID	Riboswitch 5′	Riboswitch 3′	Protein ID	Riboswitch 5′	Riboswitch 3′	Presence	Riboswitch 5′	Riboswitch 3′
NMT1	102273	no	yes	58387	no	no	NF	-	-
FOLR-like	106264	no	yes	NF	-	-	NF	-	-
EFG-DC	56895	no	yes	NF	-	-	NF	-	-
SSSF-F	NF	-	-	48760	yes	yes	yes	yes	no
SSSF-P	NF	-	-	60112	yes	yes	yes	yes	no

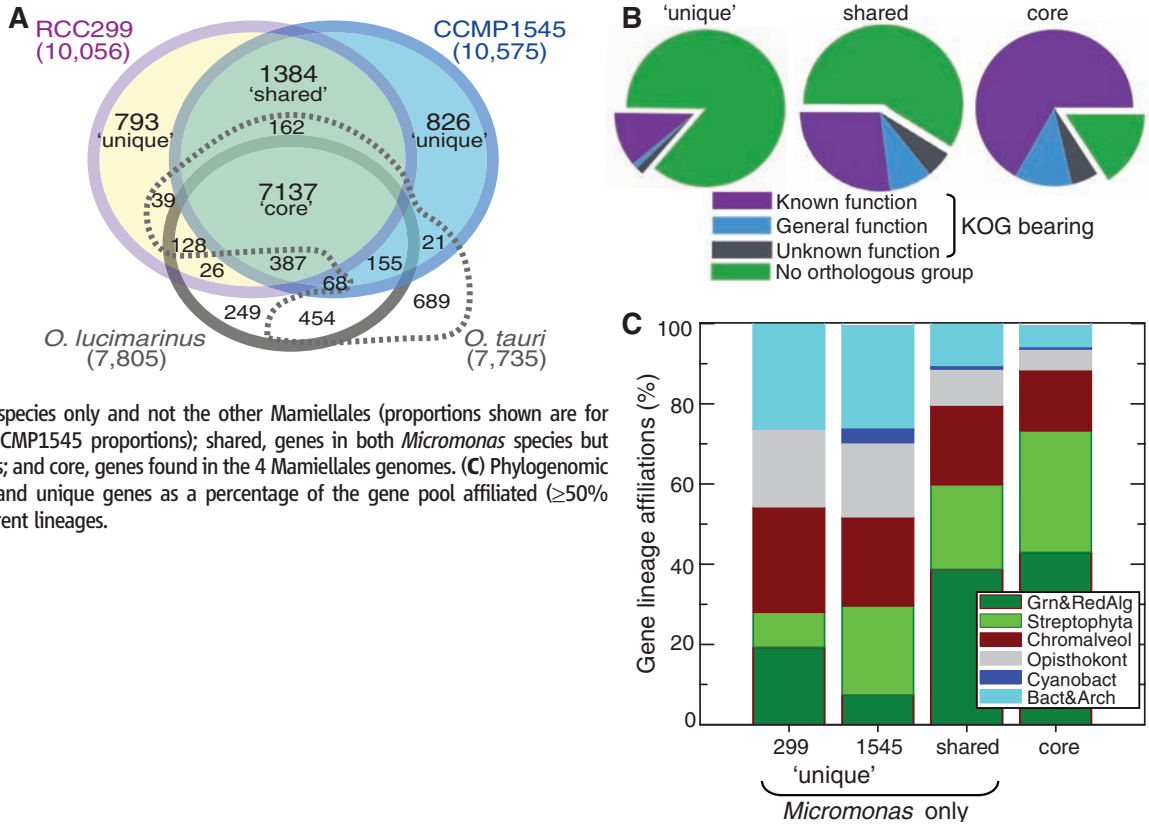

Fig. 2. Comparison of Mamiellales gene complements. (**A**) Venn diagram comparing RCC299 and CCMP1545, *O. tauri* and *O. lucimarinus* gene complements. Circle sizes roughly represent relative numbers of genes in each genome. (**B**) Proportions of genes within eukaryotic orthologous groups (KOGs) and without KOG placement for the gene pools: unique, genes in one *Micromonas* species only and not the other Mamiellales (proportions shown are for RCC299; see fig. S14 for CCMP1545 proportions); shared, genes in both *Micromonas* species but neither *Ostreococcus* species; and core, genes found in the 4 Mamiellales genomes. (**C**) Phylogenomic profiling for core, shared, and unique genes as a percentage of the gene pool affiliated (≥50% bootstrap values) with different lineages.

terial lineages (Fig. 2C), which is consistent with acquisition by means of HGT. Many were of unknown function (Fig. 2B) but may provide useful indicator information. Following early genome reduction, fundamentally different selection/acquisition processes acting on the unique genes appear to have promoted differentiation.

Marked differences in nutrient transport were seen as compared with that in other green-lineage organisms. Between the *Micromonas* species, 52 of the 59 transporter gene families common to land plants were present as well as several transporter gene families found in marine chromalveolates but not in other green-lineage members (SOM text S9 and table S19). Both *Micromonas* spp. had more transporter families represented and higher numbers of transporters than *Ostreococcus*, although CCMP1545 was missing specific transporter gene families, including some related to nitrogen uptake (SOM text S9 and table S19). These differences possibly reflected environmental parameters; for instance, RCC299 is from highly oligotrophic waters, in which nutrient scavenging is essential.

We explored other genomic features related to competition and mortality that influence community structure (SOM text S10 to S13 and figs. S16 to S18). Two types of carbon-concentrating mechanisms (CCM) were identified (SOM text S12 and figs. S17 and S18) that can alleviate CO_2 limitation during blooms. The more unusual *Micromonas* CCM, a C_4-like carbon fixation pathway, includes a nicotinamide adenine dinucleotide phosphate–dependent malic-enzyme (NADP-ME) that is targeted to the plastid lumen, an atypical localization that probably reduces CO_2 leakage (SOM text S12). Because C_4-like pathways have now been identified in the four Mamiellales genomes and in diatoms (SOM text S12), they may represent a fairly basic necessity rather than a rare form of optimization in a few taxa. Both *Micromonas* species appeared to have more robust defenses against heavy-metal toxicity and reactive-oxygen species (SOM text S13 and table S20) than *Ostreococcus*. The larger *Micromonas* genome sizes may thus facilitate broader physiological response capabilities than the *Ostreococcus* genomes.

We found few (CCMP1545) (table S21) or no (RCC299) recognizably functional transposable elements (TEs). Most eukaryotes, including *Ostreococcus* (*9*), contain many TEs, and TE content is positively correlated with genome size above an ~10 Mb threshold (*20*, *21*). Any relic or degenerate TEs in *Micromonas* had low similarity to known TEs, and structural features of class II elements were not found. GC bias was thought responsible for the high proportion of TEs in the low-GC regions of *Ostreococcus* and for loss of synteny in these regions (*9*). However, the low-GC regions of *Micromonas*, although rearranged (fig. S5), had few simple repeats, con-

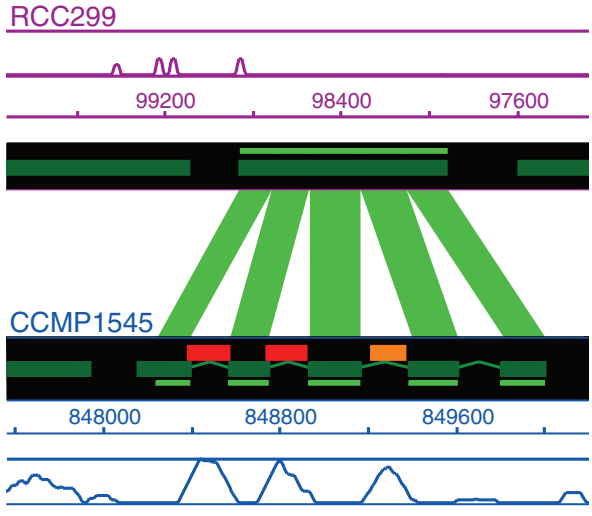

Fig. 3. Depiction of *Micromonas* orthologs with and without IEs. Single-exon (horizontal dark green bars represent exons) RCC299 [JGI protein identification (ID) 84234, chromosome 8] corresponds to a multi-exon gene in CCMP1545 (JGI protein ID 70142, scaffold 11). Different IE elements are shown (red and orange) within introns (horizontal light green lines). Diagonally oriented green lines show syntenic relationships by connecting exons with >70% nucleotide identity [minimum 100 base pairs (bp)]. Purple (RCC299, reversed orientation) and blue (CCMP1545) curves and peaks represent 16-nucleotide oligomer frequencies.

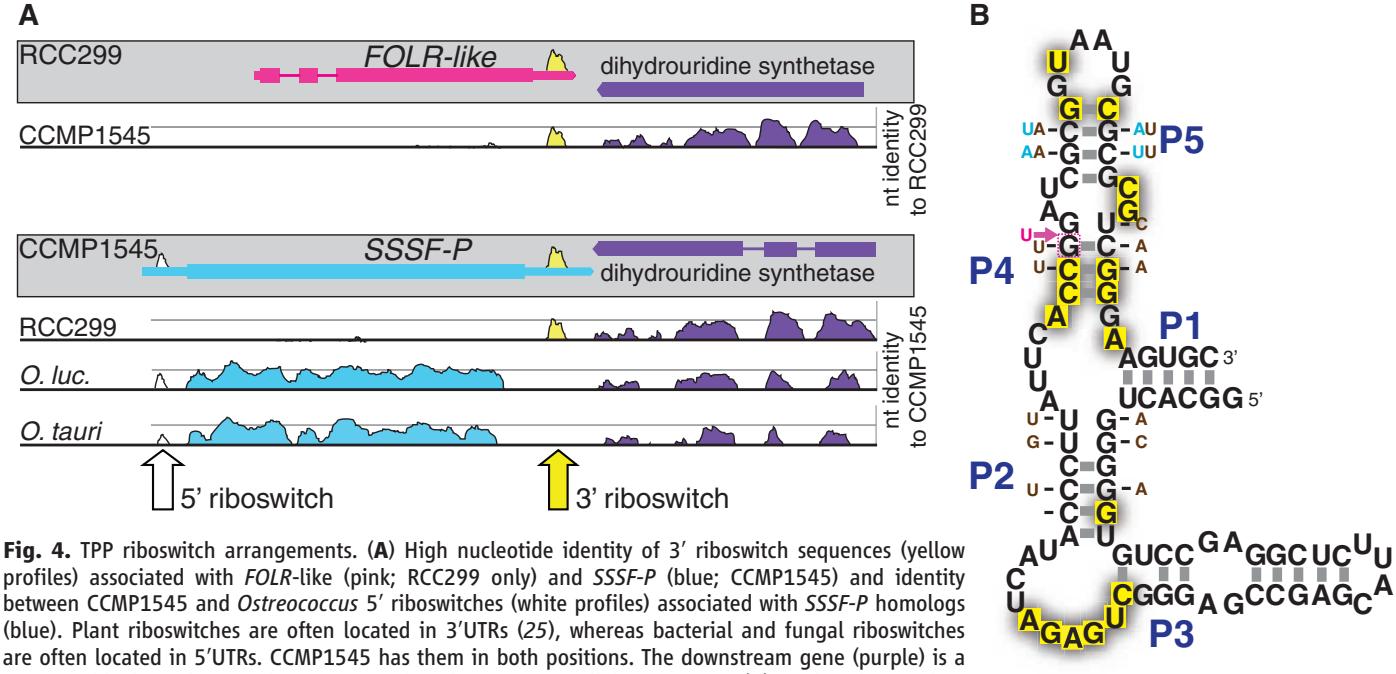

Fig. 4. TPP riboswitch arrangements. (**A**) High nucleotide identity of 3′ riboswitch sequences (yellow profiles) associated with *FOLR*-like (pink; RCC299 only) and *SSSF-P* (blue; CCMP1545) and identity between CCMP1545 and *Ostreococcus* 5′ riboswitches (white profiles) associated with *SSSF-P* homologs (blue). Plant riboswitches are often located in 3′UTRs (*25*), whereas bacterial and fungal riboswitches are often located in 5′UTRs. CCMP1545 has them in both positions. The downstream gene (purple) is a putative dihydrouridine synthase conserved in the four Mamiellales genomes. (**B**) Predicted secondary structure of *FOLR*-like–associated riboswitch showing the positions that are conserved among a range of organisms, particularly plants (yellow background), and a conserved position in all known plant riboswitches but not conserved in *Micromonas* (pink boxed U). Nucleotides adjacent to P2, P4, and P5 regions reflect differences in the CCMP1545 *SSSF-P* 3′ riboswitch (blue) and CCMP1545 *SSSF-F* 5′ riboswitch (brown). Differences in the more variable P1 and P3 are not marked in order to maintain the figure's simplicity.

tained only potential relic TEs, and showed high transcriptional activity (theoretically facilitating TE insertion) (SOM text S1), which suggests TE activity/propagation is actively hindered.

We discovered intronic repeat sequences in CCMP1545 that were absent from RCC299 and other published genomes (SOM text S14, tables S22 and S23, and figs. S19 to S22). These abundant introner elements (IEs) were located within introns, extended nearly to donor and acceptor sites (Fig. 3 and fig. S21), and lacked known TE characteristics (*22*). RCC299 genes generally had fewer introns than IE-bearing CCMP1545 homologs (Fig. 3), and CCMP1545 had a higher overall intron frequency (Table 1). The 9904 IEs fell into four heterogeneously distributed subfamilies (fig. S22 and table S22), making up 9% of the genome. We also found IEs in Sargasso Sea metagenome data (*23*) that have flanking coding domains with a high similarity to CCMP1545 but lower similarity to RCC299. *Micromonas* 18*S* rDNA sequences in the same metagenome data belong to uncultured clade M_IV (Fig. 1A) (*13*). Given the extent of genome reduction, the abundance of IE suggests that they are functional or resistant to purging.

Putative RNA interference (RNAi) components also differed between the *Micromonas* species (SOM text S4 and table S6). Only RCC299 had an argonaute-encoding gene. A version of argonaute is also found in *Chlamydomonas* and plants but not *Ostreococcus*. DEAD box and SDE3 gene analyses provided circumstantial evidence for a diverged RCC299 RNA helicase. Argonaute can act to combat TE invasion (*24*), which is notable given that RCC299 had no recognizable TEs or IEs.

Both *Micromonas* spp. had putative thiamine pyrophosphate (TPP) riboswitches, untranslated mRNAs that regulate gene expression by means of metabolite binding (*25*, *26*). These were not associated with homologous genes nor with known thiamine-biosynthesis–related genes, except for *N-myristoyltransferase 1* (*NMT1*) (Table 2 and SOM text S15). CCMP1545 riboswitches were located at both gene ends (Fig. 4A), an arrangement never before seen, and formed two divergent groups: 5′ riboswitches shared with *Ostreococcus* and 3′ riboswitches shared with RCC299 (Fig. 4B). A conserved 3′ riboswitch was shared between *folate receptor* (*FOLR*)–like (RCC299) and *SSSF-P* (CCMP1545), even though these genes were not held in common; yet *Ostreococcus* also had *SSSF-P* and a 5′ riboswitch (Fig. 4A). Only one of the seven *Micromonas* riboswitches was associated with a multi-exon gene (*FOLR*-like). Thus, it appears that the putative riboswitches in *Micromonas* act akin to bacterial riboswitches and lack the spliceosomal functions that evolved in other eukaryotes (*26*).

Deficiencies in the thiamine-biosynthesis pathway (*27*, *28*) were notable (SOM text S15). However, comparison with other lineages indicated the *Micromonas* riboswitch-containing genes represent ancient thiamine-pathway components. We identified TPP riboswitches associated with *SSSF-P* in SAR11 bacteria, which also lack classical thiamine-biosynthesis genes (*10*), and with *SSSF-F* in *Chlamydomonas* and *Volvox*. The functional importance of the gene-riboswitch associations is supported by the same gene-riboswitch pairings being found in these disparate lineages (SOM text S15).

The *Micromonas* genomes reveal features of the ancestral algae that initiated the billion-year trajectory of the green lineage and the greening of Earth. Their divergence, combined with acquisition strategies that are consistent with HGT, highlight the dynamic nature of marine protistan evolution and provide a springboard for unraveling functional aspects of phytoplankton populations. The challenge now is to identify biogeochemically important features within this natural diversity and apply them in assessing ecological transformations caused by environmental change.

References and Notes

1. J. D. Hackett *et al.*, *Mol. Biol. Evol.* **24**, 1702 (2007).
2. L. A. Lewis, R. M. McCourt, *Am. J. Bot.* **91**, 1535 (2004).
3. E. W. Knight-Jones, P. R. Walne, *Nature* **167**, 445 (1951).
4. A. Z. Worden, F. Not, in *Microbial Ecology of the Oceans,* D. L. Kirchman, Ed. (Wiley, Hoboken, NJ, 2008), pp. 159–205.
5. A. Reyes-Prieto, A. P. Weber, D. Bhattacharya, *Annu. Rev. Genet.* **41**, 147 (2007).
6. C. E. Lane, J. M. Archibald, *Trends Ecol. Evol.* **23**, 268 (2008).
7. S. S. Merchant *et al.*, *Science* **318**, 245 (2007).
8. E. Derelle *et al.*, *Proc. Natl. Acad. Sci. U.S.A.* **103**, 11647 (2006).
9. B. Palenik *et al.*, *Proc. Natl. Acad. Sci. U.S.A.* **104**, 7705 (2007).
10. S. J. Giovannoni *et al.*, *Science* **309**, 1242 (2005).
11. G. Rocap *et al.*, *Nature* **424**, 1042 (2003).
12. Materials and methods are available as supporting material on *Science* Online.
13. A. Z. Worden, *Aquat. Microb. Ecol.* **43**, 165 (2006).
14. C. Hall, S. Brachat, F. S. Dietrich, *Eukaryot. Cell* **4**, 1102 (2005).
15. S. K. Floyd, J. L. Bowman, *Int. J. Plant Sci.* **168**, 1 (2007).
16. J. H. Lee, S. Waffenschmidt, L. Small, U. Goodenough, *Plant Physiol.* **144**, 1813 (2007).
17. U. Goodenough, H. Lin, J. H. Lee, *Semin. Cell Dev. Biol.* **18**, 350 (2007).
18. T. Cavalier-Smith, *Trends Plant Sci.* **5**, 174 (2000).
19. G. I. McFadden, *Curr. Opin. Plant Biol.* **2**, 513 (1999).
20. B. Gaut, J. Ross-Ibarra, *Science* **320**, 484 (2008).
21. M. Lynch, *The Origins of Genome Architecture* (Sinauer, Sunderland, MA 2007).
22. T. Wicker *et al.*, *Nat. Rev. Genet.* **8**, 973 (2007).
23. J. Venter *et al.*, *Science* **304**, 66 (2004).
24. A. A. Aravin, G. J. Hannon, J. Brennecke, *Science* **318**, 761 (2007).
25. A. Wachter *et al.*, *Plant Cell* **19**, 3437 (2007).
26. M. T. Cheah, A. Wachter, N. Sudarsan, R. R. Breaker, *Nature* **447**, 497 (2007).
27. M. T. Croft, M. Moulin, M. E. Webb, A. G. Smith, *Proc. Natl. Acad. Sci. U.S.A.* **104**, 20770 (2007).
28. D. DellaPenna, R. L. Last, *Science* **320**, 479 (2008).
29. P. Deschamps *et al.*, *Genetics* **178**, 2373 (2008).

30. We thank the Culture Collection for Marine Phytoplankton and Roscoff Culture Collection for providing isolates, in particular F. LeGall, A. Houdan, and D. Vaulot. We also thank R. Gausling, C. Perle, Q. Ren, D. Root, L. Stal, J. Van Wye, T. Weissman, R.M. Welsh, and U. Wollenzien. F. Partensky, N. Simon, P. Deschamps, and S. Ball facilitated chloroplast and starch (*29*) annotations; C. Rancurel and B. Cantarel assisted with carbohydrate-active enzymes (with CNRS funding). We are grateful to S. Giovannoni for thoughtful criticism of the manuscript and overall enthusiasm. Genome sequencing was performed under the DOE Biological and Environmental Research Program contracts DE-AC02-05CH11231, DE-AC52-07NA27344, DE-AC02-06NA25396, and DEFC02-99ER62873. U.W.G. and J.-H.L. were funded by NSF Molecular and Cellular Biosciences (MCB) grant 0326829. Funding carrying the project from inception to completion was provided by a Young Investigator in Marine Microbiology award to A.Z.W. from the Gordon and Betty Moore Foundation with additional funds from NSF MCB grant 0429359 and the Lucille and David Packard Foundation. A.Z.W. coordinated the project and annotation; A.Z.W. and U.W.G. wrote the manuscript with input and sections from J.-H.L., T.M., P.R., and M.P.S. (joint second authors are listed in alphabetical order), and Y.V.P. and D.B. performed intellectually based editing to which S. Rombauts and M.S.P. contributed; I.V.G. coordinated the sequencing and analysis at JGI. A.L.A., A.E.A., M.L.C., E. Derelle, M.V.E., E.F., J.G., H.G., B.H., C.N., S.M.M., M.S.P., S. Rombauts, A.S., and P.V.D. also made substantial contributions (listed in alphabetical order). J.H.B. and A.E.A. constructed the phylogenomic analysis tool. A.Z.W., E.V.A., K.F.X.M., U.W.G., and Y.V.P. supervised analyses; A.Z.W. conceived the study with input from D.B., H.M., and E.V.A. All others contributed as members of the *Micromonas* genome consortium or JGI sequencing and are listed in alphabetical order. RCC299 and CCMP1545 assemblies and annotations are available at www.jgi.doe.gov/MicromonasRCC299 and www.jgi.doe.gov/MicromonasCCMP1545, respectively. Genome assemblies together with predicted gene models and annotations were deposited at DNA Data Bank of Japan/European Molecular Biology Laboratory/GenBank under the project accession numbers ACCO00000000 and ACCP00000000 for RCC299 and CCMP1545, respectively.

Supporting Online Material

www.sciencemag.org/cgi/content/full/324/5924/268/DC1
Materials and Methods
SOM Text
Figs. S1 to S22
Tables S1 to S25
References

14 October 2008; accepted 23 February 2009
10.1126/science.1167222

Call for Papers

Submit your research now to be one of the first to be considered for publication in the inaugural issue of *Science Translational Medicine!*

Science Translational Medicine, to be published online weekly beginning in the fourth quarter 2009, focuses on the conversion of basic biomedical research into practical applications, thus bridging the research-to-application gap.

The editors of ***Science Translational Medicine*** are accepting manuscripts for review in the following areas:
cancer, cardiovascular disease, metabolism/diabetes/obesity, neuroscience/neurology/psychiatry, immunology/vaccines, infectious diseases, policy, behavior, bioengineering, physics, chemical genomics/drug discovery, imaging, applied physical sciences, medical nanotechnology, drug delivery, biomarkers, gene therapy/regenerative medicine, toxicology and pharmacokinetics, data mining, cell culture, animal, and human studies, medical informatics, and other interdisciplinary approaches to medicine.

Review the information for authors at http://sciencemag.org/marketing/stm/papers.dtl

Submit your research at www.submit2scitranslmed.org

For more information, contact Editor Katrina Kelner, Ph.D. at scitranslmededitors@aaas.org

Science Translational Medicine
AAAS

Integrating Medicine and Science

www.ScienceTranslationalMedicine.org

SANGER WHO?

SEQUENCING THE NEXT GENERATION

In November 2008 Elaine Mardis of Washington University in St. Louis and colleagues published the complete genome sequence of an individual with acute myeloid leukemia. Coming just a few years after the decade-long, multibillion dollar Human Genome Project, the paper was remarkable on several levels. For one thing, the team sequenced two human genomes, both cancerous and normal, some 140 billion bases in all. More impressive, though, was what the study omitted: the 50 human genomes Mardis sequenced that year (albeit not as deeply) for the 1,000 Genomes Project. "It's like a whole new world," she says. Welcome to the sequencing frontier. **By Jeffrey M. Perkel**

Elaine Mardis's acute myeloid leukemia work comprised about nine months of collecting 32-base snippets at the rate of about a billion bases per instrument every five days, with five instruments running in parallel, she says. "That seemed like a huge amount [of sequence] at the time," she recalls.

The instruments in question, **Illumina** Genome Analyzers, are one of a cadre of so-called next-generation DNA sequencers. Over the past five years they have wrested control of the high-end sequencing market from the once-dominant Sanger dideoxy sequencing chemistry and its workhorse, the 3730xl from **Applied Biosystems** (now part of **Life Technologies,** formerly **Invitrogen**).

Yet today, says Mardis, those heady gigabase-a-week days seem "sort of like 'ho hum, that took a really long time.'"

Adam Lowe, Illumina's director of life science product marketing, estimates that his company's user base "generates about a thousand gigabases per week," he says, or about 20 times the size of Genbank in 2005.

Harvard University geneticist and next-gen pioneer George Church says the rate of technical improvement in the sequencing arena is unprecedented, about 10-fold per year, and far outpaces Moore's Law. Illumina reads are now at 75 bases standard, and have been pushed as far as 250 with overlapping paired-end reads (about 40 gigabases per run). Life Technologies has doubled the throughput on its next-gen SOLiD instrument every quarter. At those levels, says Mardis, the study that took some "90-ish" Illumina runs to accomplish in 2008 would require just six or eight today.

Such is life on genomics' bleeding edge. Rising from relative obscurity in 2005 to *Science's* Breakthrough of the Year in 2007, the next-gen sequencing industry now sports five commercial offerings, with several others nearing release. Employing different strategies and addressing different applications, each promises previously unimaginable data output.

Unsurprisingly, the technology is attracting attention. "People can't seem to get enough of it," says Church. "When you get a factor of 10,000 [improvement] in four years, people eventually notice."

Out with the Old...

Prior to 2005, almost all DNA sequencing used a variant of the chemistry first described in 1977 by Fred Sanger.

Sanger's methodology coopts the normal process of DNA synthesis by blocking the growth of new DNA chains using a sort of molecular brake called a continued >

"It's like a whole new world."

Look for these **Upcoming** Articles

Molecular Diagnostics — May 8

Nucleic Acid Purification and Manipulation — May 15

Technologies for Gene Transfer — June 19

Inclusion of companies in this article does not indicate endorsement by either AAAS or Science, *nor is it meant to imply that their products or services are superior to those of other companies.*

"The applications tend to break apart on read length dependency versus tag density."

dideoxynucleotide terminator. The resulting pool of molecules, which on average will terminate at every position, can then be sequenced chromatographically, originally on large polyacrylamide gels, and later in hair-thin capillaries.

The ABI 3730 ran 96 capillaries in parallel, each capable of producing between 500 and 1000 bases of high-quality data per run. At that rate, says Mardis, the system could produce about 1.2 megabases per day. Compare that to the gigabase throughputs being generated on new equipment, and it's clear why sequencing centers are mothballing their old equipment.

But throughput isn't the only factor; Sanger sequencing is labor-intensive and expensive. DNA to be sequenced first must be cloned, and the resulting libraries maintained. That requires instrumentation and labor, not to mention lab real estate.

New sequencing technologies employ completely different paradigms. All avoid size-separation in favor of strategies in which fragmented DNA is immobilized in a fixed position and repeatedly interrogated, like an iterative microarray assay. Most, but not all, use polymerase chain reaction to amplify that DNA; **Helicos Biosciences, Pacific Biosciences,** and **ZS Genetics** actually read single molecules instead. **454 Life Sciences** (part of **Roche Applied Science**), Illumina, Helicos, and Pacific Biosciences use DNA polymerase to drive their sequencing reactions, but Polonator (**Dover Systems**), SOLiD (Life Technologies), and **Complete Genomics** sequence with DNA ligase, and ZS Genetics uses electron microscopy. And whereas most reactions are synchronous—that is, sequential, with a single base interrogated at a time at each position—454 and Pacific Biosciences generate asynchronous reads, such that individual reactions run at their own rates and are not synchronized to one another.

The Longest Read

In 454's process the DNA to be sequenced is fragmented into 500-to-1,000-base-pair pieces and capped on each end with adaptors. The fragments are then amplified on bead surfaces via emulsion PCR (emPCR), a massively parallel strategy that separately amplifies each fragment inside an aqueous microdroplet in oil emulsion to create a sort of run-time sequencing library. Michael Egholm, chief technology officer and vice president of research and development at 454 Life Sciences calls emPCR one of "several key innovations" at the heart of the company's success.

Following amplification, the emulsion is broken and the beads placed into the wells of a PicoTiterPlate (PTP), a 6-by-6-cm support of some 3.5 million packed optical fibers etched with wells on one side. "We deposit the beads in each of these [fibers], and cleverly, the holes on the end of the optical fibers are such that there's only room for one bead," says Egholm. The result: an immobilized array of 3.5 million beads, each containing millions of identical DNA fragments. Each bead is what Church calls a polony, or polymerase colony.

The sequence itself is read via pyrosequencing, which monitors base-incorporation via the resulting release of pyrophosphate. Pyrosequencing converts that pyrophosphate into ATP, which in turn drives luciferase. As a result, a burst of light is produced whenever a new base is incorporated.

In 454's Genome Sequencer FLX, this process occurs in a flow cell. Basically, each base is flowed sequentially over the PTP – first A, then C, then G, then T. If the next base in the template is a G, the polymerase must wait until dCTP flows in. At that point, it will incorporate the base and release pyrophosphate, resulting in a flash of light whose intensity is directly proportional to the number of bases added (CCC will yield light three times as intense as C alone). That light is picked up by the optical fibers and transmitted to a camera, which reads the reaction.

Illumina and Helicos don't use pyrosequencing, yet their processes are largely similar, except the amplification (in the case of Illumina's technology) occurs directly on the flow cell rather than on beads, and the synthesis uses fluorescently labeled, reversible terminators; the reactions thus pause after each incorporation event (as if using a sort of Sanger sequencing 2.0). Helicos eliminates the amplification step, using what it terms true single molecule sequencing.

On the other hand 454 uses only standard DNA building blocks. As a result, says Egholm, it is both fast and free of background. "It's almost biblical, there's light and then there's no light," he says. And, producing by far the longest reads of any next-gen instrument, between 400 and 500 bases per bead, Egholm says the FLX can sequence 50 million bases per hour.

The Power of the Short Read

With read lengths approaching those of the 3730, 454 far outpaces the 125 bases Illumina is rolling out, not to mention the SOLiD's 75, Complete Genomics' 70, or the Polonator's 26. As such, it has become the de facto choice for metagenomics, immunogenomics, viral profiling, whole-transcript sequencing, and especially de novo genome sequencing. The technology has been used to sequence and assemble the *Arabidopsis* and *Drosophila* genomes from scratch—but not the human; when James Watson's DNA was decoded in April 2008, that was resequencing, aligning reads to the preexisting reference framework made possible by the Human Genome Project.

On the other hand, the FLX's 1.25 million reads is a mere fraction of what other instruments can produce. The Polonator yields 200 million to 400 million mappable reads and the SOLiD about 750 million. At the February 2009 Advances in Genome Biology and Technology (AGBT) meeting, Illumina presented data suggesting it could generate 520 million mappable reads per paired-end run. At those levels, a whole different set of applications opens up, including digital RNA profiling, targeted resequencing, and polymorphism discovery.

"The applications tend to break apart on read length dependency versus tag density," says Kevin McKernan, senior director of scientific operations for SOLiD at Life Technologies. At the **Broad Institute of Harvard and MIT,** whose 40 3730s, 20 Genome Analyzers, 10 FLXs, 8 SOLiDs, and one Polonator churned out 3 *petabases* of sequence in 2008, the SOLiD tackles "applications that require tons of data," such as polymorphism discovery and tumor profiling, says continued >

Congratulations

to the 2009 AAAS Student Poster Competition Winners

AAAS recognizes the winners of the 2009 Student Poster Competition that took place at the AAAS Annual Meeting in Chicago. Their work in a variety of fields displayed originality and understanding that set them apart from their colleagues. First-place winners receive cash prizes thanks to the generous support of Subaru of America, Inc.

BRAIN AND BEHAVIOR

Winner (tie): Diane Livio, University of California, Irvine
The Strength of Sexual Imprinting Effects in Zebra Finch (Taeniopygia guttata) *Populations*

Winner (tie): Maira Soto, University of California, Irvine
Characterization of Novel Human Beta-defensins

ENVIRONMENT AND ECOLOGY

Winner: Rebecca Aicher, University of California, Irvine
Soil Nitrogen Affects Convergence in Community Composition in California Grasslands

Honorable Mention: Jaquan Horton, University of California, Irvine
Tough Guts?: The Material Properties of Teleost Intestinal Tissues

MATH, TECHNOLOGY, AND ENGINEERING

Winner: Ross Barnowski, University Michigan, Ann Arbor
Remote Detection of Radioactive Plumes Using Millimeter Wave Technology

Honorable Mention: Alejandro Campos, University of Rochester
Advances in Dust Detection and Removal for Tokamaks

MEDICINE AND PUBLIC HEALTH

Winner: Eric Howell, Texas Tech University
Chemotherapeutic Challenge of the Chernobyl Rodent Apodemus flavicollis

Honorable Mention: Arun Paul, Rosalind Franklin University of Medicine and Sciences
Therapeutic Potential of COX Inhibitors in Treating Kaposi's Sarcoma Herpes Virus (KSHV) Associated Body Cavity B Cell Lymphoma (BCBL)

MOLECULAR AND CELLULAR

Winner (tie): Kathleen Mettel, University of Illinois, Urbana-Champaign
Plasticity in the Auditory Thalamus Following Exposure to Complex Acoustic Sequences

Winner (tie): Nagaraj Kerur, Rosalind Franklin University of Medicine and Science
KSHV Infection Induces Inflammasome in Human Monoctytic THP1 Cells

Honorable Mention: Adriana Garcia, University of California, Irvine
18F-fallypride MicroPET Imaging To Monitor Pancreatic Beta Cell Loss in Diabetes Mellitus

PHYSICAL SCIENCES

Winner: Patrick Brown, University of Notre Dame
Vertically-Aligned Carbon Nanotube Growth for Energy Storage Applications

Honorable Mention: Amanda David and Agustin Diaz, University of Puerto Rico, Rio Piedras
Encapsulation of Insulin into Inorganic Layered Nanomaterials Envisioned as a Drug Delivery System

SOCIAL SCIENCES

Winner: Vanashri Nargund, Indiana University
The Influence of Secondary Science Teachers' Beliefs on Classroom Instruction in India

Bookmark www.aaas.org/meetings for details on the 2010 AAAS Annual Meeting, 18-22 February. The Poster Submission site opens on 20 July 2009.

The Student Poster Competition recognizes the individual efforts of undergraduate and graduate students working toward a degree. Posters are judged at the meeting. Winners in each category receive a cash award, framed certificate, and AAAS membership. Postdoctoral scholars who hold a doctoral degree are not eligible to enter.

Full abstracts can be viewed at
www.aaas.org/meetings

AAAS
ADVANCING SCIENCE, SERVING SOCIETY

Chad Nusbaum, co-director of the institute's genome sequencing and analysis program.

The SOLiD, along with the Polonator and Complete Genomics' process, is based on sequencing by ligation, a strategy Church first successfully demonstrated in 2005 on *E. coli*.

The process, Church explains, "is directly mappable to sequencing by polymerase. In both cases you've got a template and a primer. In one case polymerase adds a mononucleotide, and in the other case ligase adds an oligonucleotide 6-to-9 bases long, where one of the bases is keyed to the color."

In general, given a primer-template pair, you add a pool of short oligonucleotides whose sequence is completely random, except that one base corresponds to the fluorescent dye attached to the molecule; you then let ligase make the base call.

Say you are using six-base-long oligos and interrogating base No. 3. Of the 4,096 possible hexamers, 1,024 have an A at position 3 and a corresponding color, 1,024 have a C at that position and a different color, and so on. Only that one oligo whose sequence precisely matches the template will bind strongly enough to be ligated, so that, when the unbound molecules are washed away, the reaction will glow a uniform color. Then, to read the next base, simply denature the primer-template pair, add new primer, and repeat.

One advantage of this approach is that, unlike polymerase-based methods, the bases may be read out of order, thereby eliminating polymerase-induced errors. "In a way, it's better than the polymerase, where you go sequentially, in the sense that there's a certain element of random access to this," Church says. Another advantage: unlike with polymerases, ligase can sequence in both the 5'-to-3' and 3'-to-5' directions.

But ligation strategies also produce extremely short fragments, which must then be aligned to a reference. Complete Genomics generates 70 bases by reading a few bases from each of eight start sites; the Polonator interrogates 26 bases by reading two sets each of six and seven bases, respectively, from either end of a longer DNA fragment (a strategy called paired-end sequencing, also supported by Illumina and Life Technologies, which improves the mappability of short sequences by adding phase information). Life Technologies actually garners the longest contiguous reads of any ligation strategy – up to 75 bases, according to data presented at AGBT—by reading two bases at a time at five-base increments, resetting, and repeating the process with a one-base frameshift.

The Next Next-Generation?

Other companies are pushing alternate strategies. Like Helicos, Pacific Biosciences is pursuing single molecule sequencing. The company arrays DNA polymerases on the surface of a plate, relying on zero mode waveguides to isolate the individual enzymes and watch as they add base after fluorescent base using a highly multiplexed confocal fluorescence microscope built for the purpose, says founder and chief technical officer Stephen Turner.

"The differentiation with Pacific Biosciences [compared to other polymerase-based strategies] is that we don't stop the action of the polymerase," says Turner. "We let it go at its native speed, and we watch in real time and simply record the activity of the polymerase."

The technology potentially could produce reads far longer than 454's. The company announced at AGBT the sequencing of the *E. coli* genome with reads averaging 586 bases and as long as 2,805; a commercial launch is planned for 2010.

ZS Genetics literally reads sequences using transmission electron microscopy (EM). A DNA-copying step is used to substitute the normal bases of DNA with variants containing proton-rich atoms (such as 5-bromo-dCTP), which then are visualized directly in the EM. Though still in development, says William Glover III, company president and vice president of research and development, "We expect to have, when we launch, in the range of five-to-8,000-base pair reads or better."

Whatever the future, next-generation sequencing has entered the scientific zeitgeist. It has its own X-Prize challenge, and garnered two spots in *The Scientist* magazine's 2008 top 10 technologies list. Knome is actively selling consumer genomics at $99,500 apiece, while Complete Genomics talks of sequencing one million human genomes in the next five years. Church's Personal Genome Project has signed up some 10,000 volunteers to have their genomes sequenced and released into the public domain.

Meanwhile, technology development continues on the *next* next-gen, based on such ideas as nanopores and fluorescence resonance energy transfer between nucleotide and polymerase.

That's not to say Sanger chemistry is disappearing; some applications simply don't need next-gen throughput. And with their on-the-fly library generation, next-gen strategies don't support clone reanalysis. Though the need likely exists for multiple technologies (say, long versus short reads) what remains to be seen is whether the market exists for so many competing technologies. One thing is certain: at the current pace of development, 2009 should be a very interesting year.

Jeffrey M. Perkel is a freelance science writer based in Pocatello, Idaho.

DOI: 10.1126/science.opms.p0900033

Featured Participants

Applied Biosystems (Life Technologies)
www.appliedbiosystems.com

Broad Institute of Harvard and MIT
www.broad.mit.edu

Complete Genomics
www.completegenomics.com

Dover Systems
www.polonator.org

Harvard University
www.harvard.edu

Helicos Biosciences
www.helicosbio.com

Illumina
www.illumina.com

Invitrogen (Life Technologies)
www.invitrogen.com

Pacific Biosciences
www.pacificbiosciences.com

Roche Applied Science
www.roche-applied-science.com

ZS Genetics
www.zsgenetics.com

New Products

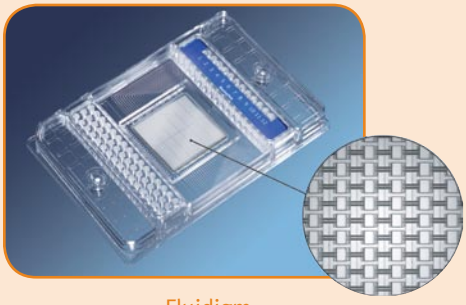

Fluidigm
For information +33-44-259-3861
www.fluidigm.com

Digital Array

The Fluidigm 12.765 Digital Array is for performing simple, fast, and reliable high throughput polymerase chain reaction (PCR) applications, including target quantitation, copy number variation, and mutation detection. The 12.765 Digital Array is an integrated fluidic circuit that makes use of a network of integrated channels and valves to divide a mixture of sample and PCR reagents into 765 replicates. The chip is specially designed to quantify target sequences accurately and to detect low-abundance targets that differ by only a base-pair from the wild-type sequence. These targets can be difficult to detect with conventional assays. Because it requires just four simple steps, the array transforms digital PCR into a straightforward, routine approach for applications that demand extreme accuracy.

Sequence Enrichment

The Sequence Enrichment Solution for targeted sequencing of the human genome enables the high-resolution analysis of genetic variation between individuals within populations at a superior level. It improves sample uniformity and reduces the selection bias typically associated with targeted sequences. It includes the RDT 1000 system, which generates picoliter-volume discrete polymerase chain reactions in droplets at the rate of 10 million per hour. It amplifies hundreds to thousands of genomic loci with high specificity and uniformity. The Sequence Enrichment Solution also includes Custom-Order Content for DNA Primer Libraries, which enable the amplification of hundreds to thousands of genomic loci in a single tube.

RainDance Technologies
For information 781-861-6300
www.RainDancetech.com

Sequence Chemistry Kits

New sequencing chemistry kits and complementary software for the Genome Analyzer enable researchers to generate 40 percent more reads per run and extend read length to more than 75 base pairs. The Mate Pair Library Preparation Kit provides support for generating longer insert paired-end libraries and complements Illumina's existing short-end paired libraries. These new products enable researchers to generate 10 to 15 gigabases of high-quality data per run, more than doubling the output of the Genome Analyzer. The mate pair library kits and long paired-end reads improve the ability of Illumina sequencers to sequence complementary DNA libraries and even open the possibility of de novo sequencing of complex organisms. The flexible mate pair technique also allows researchers to generate paired-end insert libraries measuring two to five kilobases in order to more comprehensively catalog large structural variations.

Illumina
For information 858-332-4055
www.illumina.com

SNP and INDEL Detection Module

A new module for NextGENe software is designed for use with the Roche Applied Science Genome Sequencer FLX System to identify single nucleotide polymorphisms (SNPs) and sequence insertions and deletions (INDELs). The module addresses the homopolymer-based errors of the FLX system by making use of the system's high coverage to statistically polish and correct the inherent system errors. NextGENe's alignment tool can accurately align reads with long INDELs and identify them as mutations. Another detection application can identify SNPs by accurately aligning sample reads with a reference. The sequence alignment tool also provides information about amino acid changes, exon-intron boundaries, copy numbers, and methylation sites.

SoftGenetics
For information 814-237-9340
www.softgenetics.com

Genomics Workstation

The Zephyr Genomics Workstation is an easy-to-use, powerful automation tool for molecular biology applications. The workstation includes preinstalled methods for automating many widely used nucleic acid purification chemistries, as well the manufacturer's methods for routine applications such as polymerase chain reaction setup and sample normalization. This capability removes sample preparation bottlenecks in next generation sequencing, microRNA analysis, genotyping, and gene expression studies. The system also includes several features to minimize common errors and simplify operation, such as a graphical user interface, partial tip loading, and an ultrasonic detector. The interface guides the user through method selection and proper deck setup, eliminating many of the common errors associated with high throughput processing. It can process as few as eight and as many as 96 samples simultaneously.

Caliper Life Sciences
For information 877-522-2447
www.caliperLS.com

Correction: An image that appeared on page 1570 of the Technology Feature in the December 12, 2008, issue of *Science* (volume 322) was not correctly credited. The image credit should have read: Top and bottom, image courtesy of R&D Systems, Inc.; Middle, image courtesy of Cell Signaling Technology.

Electronically submit your new product description or product literature information! Go to **www.sciencemag.org/products/newproducts.dtl** for more information.

Newly offered instrumentation, apparatus, and laboratory materials of interest to researchers in all disciplines in academic, industrial, and governmental organizations are featured in this space. Emphasis is given to purpose, chief characteristics, and availabilty of products and materials. Endorsement by *Science* or AAAS of any products or materials mentioned is not implied. Additional information may be obtained from the manufacturer or supplier.

POSITIONS OPEN

SCRIPPS FLORIDA

FACULTY POSITIONS
Department of Neuroscience

The Scripps Florida campus of The Scripps Research Institute (TSRI) is seeking outstanding applicants for tenure-track faculty positions in the Department of Neuroscience at its newly opened, state-of-the-art campus in Jupiter, Florida. TSRI applies integrative molecular genetic, biochemical, biophysical, chemical biology, cell biology, anatomical, and behavioral approaches to elucidate the cellular, molecular, physiological, and systems mechanisms underlying brain function. Collaborations with TSRI's Translational Research Institute allow for the development and testing of novel therapeutics.

The Department of Neuroscience is seeking highly qualified, interactive, and extramurally funded investigators who will bring and initiate creative research programs. Areas of focus for the current search include learning and memory, diseases of learning and memory, sleep research, mechanisms of action for anesthetics, and drug development in these areas. The unique cores at Scripps Florida, including high throughput genomic screening, proteomics, crystallography, pharmacokinetics, medicinal chemistry, and an ultrahigh throughput small molecule facility, offer enabling resources for research in these areas.

Appointments are available at all levels. TSRI offers very attractive startup packages and an outstanding intellectual environment for fostering top-tier basic and translational research. In addition, the Max Planck Florida Institute, the first Max Planck Institute in the United States, is under construction adjacent to Scripps Florida, and will offer state-of-the-art bioimaging capabilities.

Interested candidates should submit their curriculum vitae, a synopsis of their past, current, and proposed research, and complete contact information for at least three professional references as a single PDF file to:

Dr. Ronald L. Davis, Chairman,
Department of Neuroscience
c/o Hollie Alkema
E-mail: hollie@scripps.edu
The Scripps Research Institute, Scripps Florida
130 Scripps Way, Jupiter, FL 33458

TULANE NATIONAL PRIMATE RESEARCH CENTER

The Division of Bacteriology and Parasitology of the Tulane National Primate Research Center (TNPRC) wishes to recruit a **RESEARCH SCIENTIST** to coordinate the analysis of various DNA microarray data emanating from its DNA Microarray and Expression Core.

You should have a Master's degree in biology, bioinformatics, or biostatistics with hands-on, documented experience in high-dimensional DNA microarray data analysis, using such tools as Spotfire, R, and S+.

Job duties: (1) Develop protocols for the bioinformatic and biostatistical analysis of DNA microarray data. (2) Under direct oversight of his/her supervisor, will analyze the microarray data generated by the TNPRC DNA Microarray and Expression Core, for the benefit of a diverse range of principal investigators. (3) Perform regular data analysis quality control measures and develop new algorithms and analysis methods using the data generated by the core.

To be considered, please apply online at **website: http://www.profilesams.com** using **job number 102763,** or send curriculum vitae and the names of three individuals who may be contacted for references to: **Deepak Kaushal, Ph.D., Director, DNA Microarray and Expression Core, Division of Bacteriology and Parasitology, Tulane National Primate Research Center, 18703 Three Rivers Road, Covington, LA 70433. E-mail: dkaushal@tulane.edu.**

Tulane University is an Affirmative Action and Equal Opportunity Educator and Employer. Women and minorities are strongly encouraged to apply.

POSITIONS OPEN

UNIVERSITY OF SOUTH CAROLINA

seniorsmart.

The SeniorSMART™ Endowed Chair in Memory and Brain Health: SmartBRAIN™

The University of South Carolina (USC) invites applications for the Endowed Chair in Memory and Brain Health: SmartBRAIN™ **(website: http://www.seniorsmart.org).** The SmartBRAIN™ initiative will focus on developing methods to promote brain health and reduce the impact of age-associated diseases such as Alzheimer's, Parkinson's, and stroke. SmartHOME®, SmartWHEELS®, and SmartBRAIN™ comprise SeniorSMART™, a South Carolina Center for Economic Excellence (SCCEE) (**website: http://www.sccoee.org**) that is being developed among three academic partners (Clemson University, the Medical University of South Carolina, and the University of South Carolina) and two hospital systems (Greenville Hospital System University Medical Center and Palmetto Health). The SmartBRAIN™ initiative will work closely with the Brain Imaging Center of Economic Excellence (**website: http://www.bicoee.org**). The SmartBRAIN™ Endowed Chair will be based in the USC School of Medicine at the rank of **ASSOCIATE PROFESSOR** or **PROFESSOR,** with opportunity for joint appointment in other academic units at the University of South Carolina and its partners.

The successful applicant will have an M.D. and/or Ph.D. degree, a demonstrated track record in interdisciplinary scholarly productivity, and programmatic support from competitive extramural funding sources. Extensive experience in the broad field of neuroscience is essential. Familiarity with the mechanisms for enhancing research value through economic development (e.g., intellectual property, interaction with relevant businesses, translational research activities, et cetera) is an important attribute that will build on the SCCEE program.

Further information is on the **website: http://www.seniorsmart.org.** Address specific inquiries to **G. Paul Eleazer, M.D.**, Chair of Search Committee for SmartBRAIN™.

How to apply: All applications should be submitted electronically to **e-mail: smartbrain@uscmed.sc.edu.** Applications should include (a) curriculum vitae, (b) a list of three to five references, and (c) a letter summarizing applicant qualifications, current research activities and interests, potential for realized economic value from the research, and the candidate's qualifications to exert a leadership role.

The University of South Carolina does not discriminate in educational or employment opportunities or decisions for qualified persons on the basis of race, color, religion, sex, national origin, age, disability, sexual orientation, or veteran status.

RESEARCH ASSISTANT PROFESSOR

Applications are invited for Research Assistant Professor in immunology. Requires a Ph.D. in immunology or related area with postdoctoral research experience and excellent publication record. Apply with curriculum vitae and three references to: **Dr. Mitzi Nagarkatti, Chair, Department of Pathology, Microbiology and Immunology, University of South Carolina School of Medicine, Columbia, SC 29208** or **e-mail: rapimmuno@uscmed.sc.edu.**

University of South Carolina, Columbia is an Equal Opportunity, Affirmative Action Employer and encourages applications from women and minorities.

U.S. Environmental Protection Agency
Office of Research and Development

HIGH-LEVEL CAREER OPPORTUNITIES

EPA's Office of Research and Development (ORD) is seeking internationally recognized scientists to fill **three** positions in the National Risk Management Research Laboratory (NRMRL). One position (01) is located in Ada, Oklahoma and two positions (02, 03) are located in Cincinnati, Ohio. NRMRL's leadership in science and engineering is recognized throughout EPA and the environmental community as the source of responsive, objective solutions to complex, multidisciplinary environmental problems. More information about NRMRL can be found at **www.epa.gov/nrmrl/**.

ORD plans to fill these positions using EPA's Title 42 Authority, which offers up to 5-year renewable appointments at highly competitive, market-based salaries. The positions are part of a larger EPA effort to use state-of-the-science approaches and technologies in its mission of protecting human health and the environment. The ideal candidates will have a doctoral-level degree and extensive specialized experience. Positions and major duties include:

NRMRL-09-42-01 Director, Ground Water and Ecosystems Restoration Division (Interdisciplinary- Biologist, Engineer, Physical Scientist, Chemist)

- Establishing and leading a research program in the area of chemical, physical, and biological processes and kinetics of contaminant behavior in the subsurface; the interface between biogeochemical cycling in subsurface and surface environments; and the ecosystem level processes and kinetics that control water quality at a watershed level.

NRMRL-09-42-02 Director, Sustainable Technology Division (Interdisciplinary- Economist, Engineer, Physical Scientist, Chemist)

- Establishing and leading a research program on sustainability that includes science-based decision support systems for addressing the ecological integrity of natural and built environments, and analyzing environmental, societal and economic impacts of energy production and use systems such as biofuels, and new materials such as nanotechnology products, from a life cycle point of view.

NRMRL-09-42-03 Director, Water Supply and Water Resources Division (Interdisciplinary- Biologist, Engineer, Physical Scientist, Chemist)

- Establishing and leading a technically complex national research program to develop improved methods for drinking water treatment and distribution, protection of source waters, control of urban wet weather pollution and environmental management of watersheds.

Responsibilities for all positions include providing hands-on leadership of ORD's research programs, serving as a senior spokesperson/representative, identifying collaborative opportunities with outside organizations, and playing a vital leadership role within NRMRL.

Salary and Benefits: Salary is up to $200,000 per annum, dependent upon qualifications, experience, and other factors. The selected applicant will be eligible for full benefits including health and life insurance, retirement, vacation and sick leave.

How to Apply: Send the following information: (a) a cover letter (1-2 pages), with information about your interest in applying and your research goals; (b) curriculum vitae; (c) the names of three references; (d) citizenship status; (e) compensation requirements; and (f) a list of the types and quantities of resources anticipated to perform the job (e.g., staff, equipment, supplies, software, space). **Candidates must reference the specific vacancy number(s) of the position(s) for which they are applying.**

Applications should be mailed to the attention of: **Ms. Dorothy Carr, U.S. EPA, MD-C639-02, RTP, NC 27711** or sent via email to **title42@epa.gov** by **June 8, 2009**. For additional information, **Ms. Carr** can also be reached at **(800) 433-9633**. Technical questions regarding **NRMRL-09-42-01** may be addressed to **Dr. Herbert Fredrickson** at **(513) 569-7402**. Technical questions pertaining to **NRMRL-09-42-02** and **NRMRL-09-42-03** may be addressed to **Dr. Subhas Sikdar** at **(513) 569-7528**. Additional information about the positions is available at **http://www.epa.gov/ORD/NRMRL/jobs/index.html**.

The U.S. Environmental Protection Agency is an Equal Opportunity Employer.

University of Zurich

The Institute of Physical Chemistry at the University of Zurich is looking for scientists to fill the following positions as soon as possible:

1 PhD position
Chemist/Biochemist

Study of molecular interactions between proteins and surfaces

1 Postdoctoral position
Chemist/Material Scientist

Development of nanostructured superhydrophobic and superoleophobic surfaces

2 PhD positions
Chemist/Material Scientist

Development of nanostructured superhydrophobic and superoleophobic surfaces

1 Postdoctoral position
Chemist/Physicist

Ultrasensitive fluorescence detection and nanoscopy

We are searching highly motivated, enthusiastic and independent employees with passion for science for our team. Very good studies results are required.

We offer outstanding working conditions, a high quality of life in Zurich, an adequate salary and conditions of employment of the Kanton Zurich.

Please send your complete application documents by e-mail only to: application.seeger@pci.uzh.ch

Prof Dr. Stefan Seeger, University of Zurich, Institute of Physical Chemistry

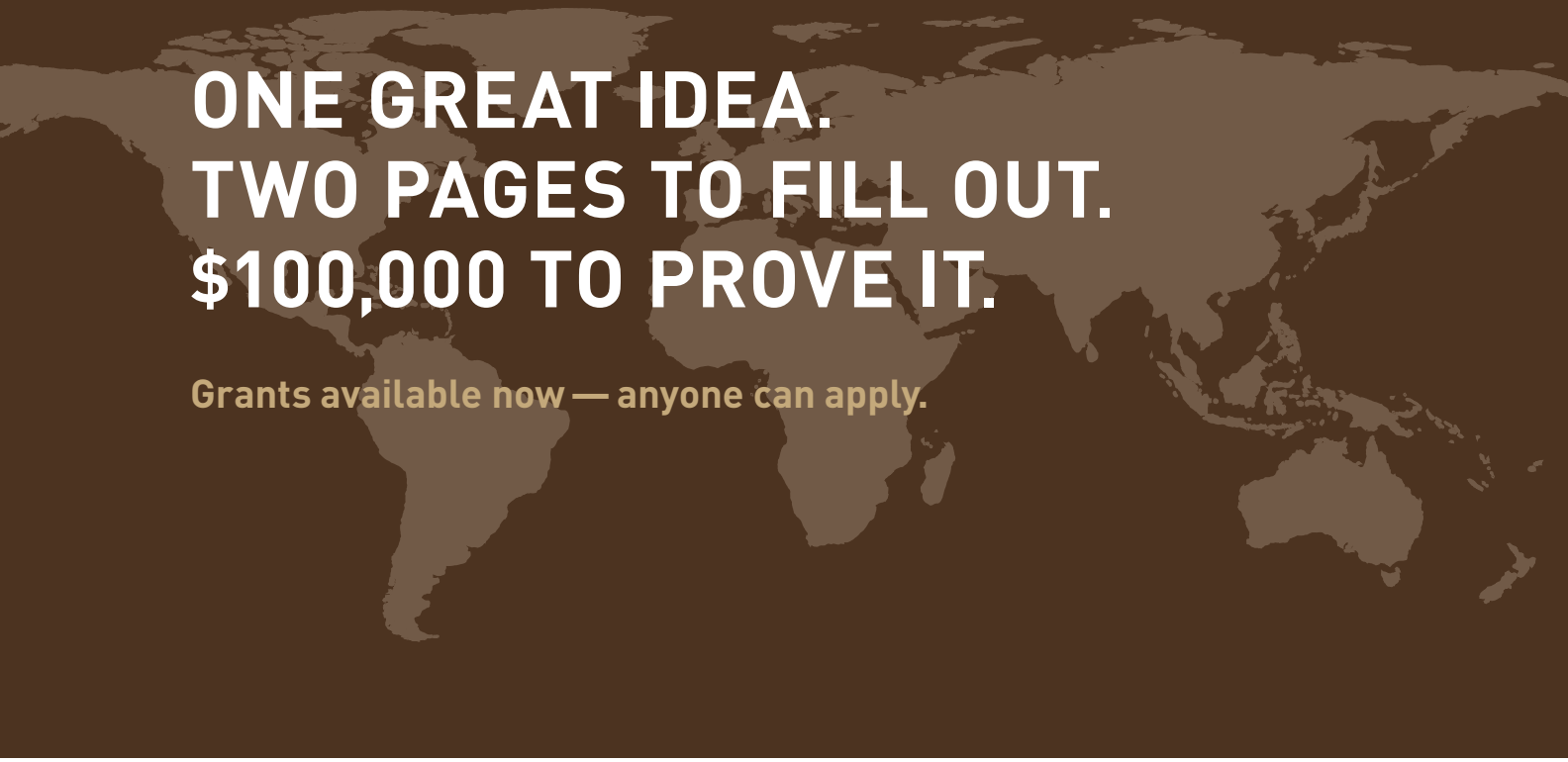

ONE GREAT IDEA.
TWO PAGES TO FILL OUT.
$100,000 TO PROVE IT.

Grants available now — anyone can apply.

The Bill & Melinda Gates Foundation seeks bold ideas from innovative thinkers to solve the greatest challenges in global health.

As part of our Grand Challenges Explorations initiative, grants of $100,000 are awarded two times a year. Projects that show great promise have the opportunity to receive a subsequent grant of $1 million or more.

Proposals will be accepted March 31 through May 28, 2009.

Please visit www.grandchallenges.org/explorations for Round 3 topics and complete application materials.

BILL & MELINDA GATES *foundation*

Grand Challenges | EXPLORATIONS

KOÇ UNIVERSITY

DEAN • School of Medicine

Koç University invites applications and nominations for the position of the Dean of the School of Medicine (KUSOM), with the appointment effective as early as September 2009. Koç University is a private, nonprofit institution of higher education, founded in 1993. Koç University is on a state-of-the-art campus at Rumeli Feneri, overlooking the Black Sea, close to the city of Istanbul. The University is committed to the pursuit of excellence in both research and teaching. Its aim is to provide world class education and research opportunities to a high quality group of students by distinguished faculty. The medium of instruction is English. Currently, Koç University offers degrees in the Colleges of Administrative Sciences and Economics, Sciences, Humanities and Social Sciences, Engineering, and Law as well as the School of Nursing. More detailed information about Koç University can be found at the web site: **http://www.ku.edu.tr**

The School of Medicine is a new school. As an integral part of the University, its mission is to educate the future leaders of the medical profession who have the highest professional standards, who have a strong foundation in the scientific basis of medicine, who can apply that knowledge to the prevention and treatment of disease, and who are highly skilled in providing the best care to patients. The School was established to respond to the societal needs and to fulfill the commitment of the University to medicine, life sciences and related fields.

The Dean will report to the Provost and the President. The qualifications for the position include:

- A distinguished research record in basic medical and/or medical sciences with a commitment to medical education and clinical care;
- Demonstrated ability for organizational and interpersonal skills;
- Turkish citizenship.

The Dean will manage and direct the academic and administrative operations of KUSOM. In this capacity the major responsibilities of the Dean include:

- Design and implementation of the medical curriculum that is consistent with the educational philosophy of the University in general;
- Recruiting faculty, staff and students;
- Development of the research programs and infrastructure;
- Faculty appointments, evaluations, and promotions;
- Work closely with the Vehbi Koç Foundation;
- Work closely with the Higher Educational Council, medical institutions and healthcare organizations;
- Management of School of Medicine finances;
- Limited teaching.

The compensation package is competitive. All information on candidates will be kept confidential.

Review of applications will start immediately and continue until the position is filled. Candidates should submit their letter, a list of references, curriculum vitae and further inquiries to:

Professor Yaman Arkun
Chair of Dean Search Committee, Provost
Koç University
Rumeli Feneri Yolu
34450 Sarıyer, Istanbul, Turkey
Phone: 90-212-338 1313 Fax: 90-212-338 1205
E-mail: yarkun@ku.edu.tr

Assistant Professor, Structural Biology
Children's Hospital Boston
Harvard Medical School

The Program in Cellular and Molecular Medicine at Children's Hospital Boston in partnership with the Department of Biological Chemistry and Molecular Pharmacology (BCMP) at Harvard Medical School is recruiting tenure track faculty at the rank of Assistant Professor. Our Program (also known as the Immune Disease Institute) is highly interactive and offers outstanding opportunities for collaboration and technical support. The successful candidate will be offered a competitive start-up package. He/she will direct an independent research laboratory and his/her work will complement and enhance the efforts of our distinguished faculty in cell biology, immunology, inflammation, vascular biology, infectious disease and cancer. This is part of a major initiative in structural biology involving several recruits, space in a new building on Longwood Avenue, and substantial new funding.

We are seeking a candidate who integrates macromolecular structure and biological function, especially someone who works on fundamental problems involving signal transmission in extracellular and cytoplasmic environments and across cell membranes. Approaches using molecular dynamics and spectroscopy, protein structure prediction and design, X-ray crystallography, electron microscopy, single molecule studies, and innovative light microscopy will be of special interest. The structural biology initiative will be able to draw on available resources at Children's Hospital and the HMS Center for Molecular and Cellular Dynamics (CMCD).

Please forward a cover letter requesting consideration by the search committee, curriculum vitae, reprints of key publications, letters separately sent from three referees, and a two-page statement of research interests including previous contributions and future research plans, no later than **May 1, 2009** to: **Timothy A. Springer and Stephen C. Harrison, Search Chairs, 3 Blackfan Circle – room 3103, Boston, MA 02115; recruitment@idi.harvard.edu.**

Children's Hospital Boston and Harvard Medical School are Affirmative Action/Equal Opportunity Employers. Women and minority candidates are strongly encouraged to apply.

WORKING AT THE UNIVERSITY OF GENEVA

The **FACULTY OF SCIENCE** invites applications for

ASSISTANT or ASSOCIATE or FULL PROFESSOR
in Plant Molecular Biology
(www.unige.ch/sciences/biologie/index.html)

We seek applicants with a record of excellence in research, who have proven their ability to develop and apply novel concepts in the general area of plant molecular biology. The successful candidate is expected to lead a strong, independent research program, attract external funding and contribute to teaching at the graduate and undergraduate levels. Special consideration given to scientists studying important biological problems using novel multidisciplinary approaches.

ACADEMIC TITLE REQUIRED: Ph.D. degree or equivalent.

STARTING DATE: 1st January 2010 at the earliest.

Candidate files including a curriculum vitae, a publication list, a summary of past and future research interests and names and addresses of three potential referees must be addressed **by May 29th**, **2009** to : Décanat de la Faculté des sciences, 30, Quai Ernest-Ansermet, CH-1211 Genève 4 or by e-mail to gaelle.auge@unige.ch and from whom additional information can be obtained regarding the responsibilities of the post and other conditions.

The University of Geneva is an Equal Opportunity Employer and encourages applications from female candidates.

UNIVERSITÉ DE GENÈVE

Food and Drug Administration

COMMISSIONER'S Fellowship Program

Protecting The Public Health Through Science and Regulation

The FDA offers a two-year Fellowship Program, which provides an opportunity for health professionals and scientists to receive training and experience at the FDA.

You Can Make A Difference

The FDA Commissioner's Fellowship Program is designed to attract top-notch health professionals and scientists. The Fellows train minutes from the nation's Capital at FDA's new state-of-the-art White Oak campus in Silver Spring, Maryland or at other FDA facilities. Fellows will be exposed to the regulatory processes necessary to ensure that our drugs, biologics, food, cosmetics, and devices are safe for use.

Coursework and Preceptorship

The Fellowship Program combines rigorous didactic coursework with the development of a hypothesis-driven, regulatory science research project. The coursework is designed to provide an in-depth understanding of the science behind regulatory review, encompassing the activities of the FDA across foods, drugs, biologics, devices, and cosmetics. Coursework during the two years includes public policy, FDA law, epidemiology, clinical trials, and statistics. Under the guidance of an FDA senior scientist committed to mentoring, Fellows will explore a specific aspect of FDA regulatory science. The experience can be in a biology, physics or engineering lab, in a clinical review team, in biostatistics, informatics, epidemiology, risk analysis or other aspects of FDA science.

Benefits

We offer an excellent benefits package including health insurance, retirement plan, and vacation.

Eligibility Requirements

Applicants must have a Doctoral level degree (M.D., D.O., D.D.S., D.P.M., D.V.M., Pharm.D., or Ph.D.) to be eligible. Applicants with a B.S./B.A. or M.S./M.A. in an engineering discipline are eligible. Candidates must be a U.S. Citizen, a non-citizen national of the U.S., or have been admitted to the U.S. for permanent residence before the program start date. Applicants cannot be current FDA employees or FDA contractors (such as ORISE fellows).

Application Process

To apply, and for further information about the FDA Commissioner's Fellowship Program, please visit **www.fda.gov/commissionersfellowships/default.htm**.

FDA is an Equal Opportunity Employer and is a smoke-free environment.

dkfz. DEUTSCHES KREBSFORSCHUNGSZENTRUM IN DER HELMHOLTZ-GEMEINSCHAFT

MAX-PLANCK-GESELLSCHAFT

The Max Planck Institute for Metals Research together with the German Cancer Research Center seeks a creative researcher eager to develop a highly innovative

Independent Junior Research Group

at the frontier of biophysical and biomedical science. Ideally, the group will focus on the deconvolution of the complex interdependencies of local biochemical and biophysical processes upon cancer cell invasion by innovative bio- or nano-technological approaches. Applicants should have a strong background in biophysics as well as the cellular and molecular biology of cancer.

The successful candidate will be given ample resources to establish and direct an independent research program. For this purpose, he or she will be guaranteed funding to recruit and lead a team of researchers, for operating expenses, scientific collaboration, and technical as well as secretarial support.

The successful candidate will start a five-year contract between July and October 2009. The payment corresponds to the W2 level on the German university scale, equivalent to an Assistant or Associate Professorship.

Applicants should have completed a doctoral degree in the past decade. They should have an outstanding record in the above mentioned fields.

The Max Planck Society and the German Cancer Research Center is committed to employing more handicapped individuals and to increasing the share of women in areas where they are underrepresented, and therefore expressly encourages applications from such qualified individuals.

The applicant should submit a three to five page description of a research program, along with a work plan, a complete CV, and three personal references.

Please send applications by May 16, 2009 to geschaeftsstelle@mf.mpg.de by e-mail.

Max-Planck-Institut für Metallforschung
Geschäftsstelle. Heisenbergstr. 3, 70569 Stuttgart
Telefon: 0711/ 689-1931

Postdoctoral Associate AKAP Biology

Stony Brook University is looking to fill a postdoctoral associate position for those holding a Ph.D./ D.Sc. or equivalent in the Biological Sciences.

Required: Experience in cell signaling including microscopy/imaging of autofluorescent proteins, siRNA techniques, overexpression techniques. The structure and function of A-kinase anchoring proteins (i.e., gravin and AKAP79) will be explored at the cellular level using molecular biological, proteomics, FRET/BRET, and imaging techniques. **Preferred:** Prior experience in cell signaling analyses, GFP-tagged molecule localization, and FRET/BRET and up to two years of full-time postdoctoral training.

For a full position description, visit *www.stonybrook.edu/jobs* (Ref. # HS-R-5173-09-03-F)

To apply, please submit a cover letter and résumé to: Dr. Craig C. Malbon, Leading Professor Pharmacological Sciences, Health Sciences Center BST T-7, Room 162, Stony Brook University Stony Brook, NY 11794-8651

Fax (631) 444-7696

E-mail: *craig@pharm.sunysb.edu*

Equal Opportunity/Affirmative Action Employer. Women, people of color, individuals with disabilities, and veterans are encouraged to apply.

STONY BROOK

AgriLIFE RESEARCH

Improving Life Through Science and Technology

Director, Texas AgriLife Research

The Vice Chancellor for Agriculture and Life Sciences of The Texas A&M University System invites applications and nominations for the position of Director of Texas AgriLife Research (*formerly the Texas Agricultural Experiment Station*). With headquarters in College Station and scientists and facilities located throughout the state, Texas AgriLife Research is dedicated to research and technology development in food, agriculture, life sciences and natural resources. Its mission is to improve life through science and technology.

The Director serves as the chief executive officer and reports to the Vice Chancellor for Agriculture and Life Sciences of The Texas A&M University System. An earned Ph.D. in an agricultural or life sciences discipline or related field of science is required. Candidates should have 15 years of academic and/or research experience, with a minimum of 5 years of significant administrative experience, preferably in managing research. The successful candidate should have a thorough familiarity and understanding of the research mission of the land-grant university system and its relationship with the teaching, extension and service programs. The Director must possess the vision and experience necessary to lead a complex organization in developing and enhancing its research mission in service to the state, nation and the world as a premier research leader. Additional agency and search information is available at **http://agriliferesearch.tamu.edu/**.

Nominations and applications will be accepted until the position is filled. Screening of candidates will begin on **April 20, 2009**. Applications should be accompanied by a letter of application, curriculum vitae and the names of at least three (3) references. Nominations and applications are welcomed electronically via the search website (**http://agresearchdirsearch.tamu.edu**) or through the mail; information and inquiries should be directed to: **Dr. Edward G. Smith, Chair, Texas AgriLife Research Director Search Committee, 2147 TAMU, College Station, Texas 77843-2147; 979.845.7967; 979.845.0181 (fax); agresearchdirsearch@tamu.edu.**

Texas AgriLife Research is an Equal Opportunity Employer.

AICR

Cancer knows no boundaries.
Fortunately, neither do we.

AICR International Cancer Research Fellowship

Applications are invited for the Association for International Cancer Research International Cancer Research Fellowship, which may be held at a research institute anywhere in the world, commencing on or after 1st January 2010.

Candidates, who may come from any country, should have a minimum of three years and normally a maximum of eight years postdoctoral research experience when they would take up the fellowship, unless they have taken a career break. The successful candidate is expected to take up their fellowship in a new institution, chosen to complement their research programme.

Fellowships are tenable for six years and will include a significant level of research support, of around £1million. The application will include the submission of a research proposal which may be in any area of non-clinical cancer research.

The deadline for receipt of completed applications is 30th June 2009. Further information about the fellowships and an application form can be obtained from the AICR website: **http://www.aicr.org.uk/fellowships.stm**.

AICR's 30th Anniversary Conference
Today's Research – Tomorrow's Therapies
St Andrews, Scotland - 7th to 9th April 2010
www.aicrconference2010.org.uk

Association for International Cancer Research
Madras House, South Street, St Andrews, Fife KY16 9EH
Tel: +44 (0)1334 477910
Email: **debbie.wheelans@aicr.org.uk**
Charity No: SC022918

The University of Mississippi

DIRECTOR

Mississippi Mineral Resources Institute at University of Mississippi seeks scientist or engineer to lead the Institute. Must have broad interest in mineral resources onshore and offshore, be innovative scientist and skilled leader. Onshore projects include metallic, industrial, energy-related minerals and hazard assessments. Offshore efforts concentrate on completion of world's first seafloor observatory for study and monitoring of gas hydrates in Gulf of Mexico. Will lead staff of 12, oversee 20 research projects, manage a fabrication shop. Director will maintain his/her own basic and/or applied research. Non-tenured position reports to Dean of Engineering. Ph.D. from accredited university in geology, geological oceanography, geological engineering, geochemistry or relevant fields. Must have strong documented record of funding, research and management to promote Institute's leadership role and pursue growth opportunities. Should have experience in technology development and transfer and working with academic community.

Details and application at **http://www.jobs.olemiss.edu**.

The University of Mississippi is an EEO/AA/Title VI/Title IX/Section 504/ADA/ADEA Employer.

AWARDS

Harold M. Weintraub Graduate Student Awards – 2009

The Fred Hutchinson Cancer Research Center congratulates the following recipients of the 2009 Harold M. Weintraub Graduate Student Award in recognition of outstanding achievement during Graduate Studies in the Biological Sciences.

Peter Belenky
Dartmouth College
J. Muse Davis
Emory University
Nadya Dimitrova
Rockefeller University
Walter Fischler
University of California, Berkeley
Susmita Kaushik
Albert Einstein College of Medicine
Mark Kiel
University of Michigan
Wen-Hui Lien
Fred Hutchinson Cancer Research Center
Dengke Ma
Johns Hopkins School of Medicine
Marcus Noyes
University of Massachusetts Medical School
Jared Parker
Johns Hopkins University
Nitin Phadnis
University of Rochester
Kay Tye
University of California, San Francisco
Srinivas Viswanathan
Harvard Medical School

The recipients will participate in a Symposium this spring honoring **Hal Weintraub** and his commitment to innovative science. More information on this award can be found at: **http://www.fhcrc.org/science/basic/weintraub**.

Want to learn more about exciting and rewarding careers outside of academic/industrial research? Join us for a roundtable discussion that will look at the various career options open to scientists across different sectors, strategies you can use to find a nonresearch career, and the future of the scientific work force in nontraditional careers.

Join our panel of experts in a **FREE** live discussion. To participate, register at **www.sciencecareers.org/webinar**

Nontraditional Careers: Opportunities Away From the Bench

Webinar

Produced by the *Science*/AAAS Business Office.

Tuesday, April 28, 2009
12 noon Eastern;
9 am Pacific;
4 pm GMT

Science Careers
From the journal *Science* AAAS

ASSOCIATE PROFESSOR
Biological Response to Environmental Stress
McMaster University, Department of Biology

McMaster University, a research-intensive institution and leading centre for biological and biomedical research invites applications for a tenure-track position at the Associate Professor rank in the Department of Biology, effective July 1st, 2009.

We are seeking an applicant with a productive research program, who studies the response or adaptation of organisms to environmental stress at one or more levels (molecular, cellular, genetic, population or ecosystem) and with an emphasis on response to human-induced perturbations such as pollution and/or global climate change.

The Department of Biology houses the Biodiversity and Ecosystem Health Centre and is a major partner in an institutional CFI initiative to study remediation of aquatic ecosystems. Facilities of interest to applicants include the Centre For Environmental Genomics, The Centre for Functional Genomics and The Institute for Molecular Biology and Biotechnology (MOBIX).
(see **http://www.biology.mcmaster.ca/index.html**)

The successful applicant will be expected to establish and maintain an independent and externally funded research program and contribute to the education of undergraduate and graduate students. Exceptional candidates will be considered for a Tier 2 Canada Research Chair Career award (**http://www.chairs.gc.ca/**).

Applicants should submit a curriculum vitae, a statement of their research goals, a statement of their teaching interests and experience, three of their most important publications and should arrange for three letters of recommendation to be sent to: **Dr. Patricia Chow-Fraser, Professor and Chair, Department of Biology, McMaster University, 1280 Main Street West, Hamilton, Ontario L8S 4K1, Canada, biolchr@mcmaster.ca**. Electronic submission is preferred. The closing date for applications is **June 1, 2009** or until the position is filled.

All qualified candidates are encouraged to apply; however, Canadians and Permanent Residents will be given priority. McMaster University is strongly committed to employment equity within its community, and to recruiting a diverse faculty and staff. The University encourages applications from all qualified candidates, including women, members of visible minorities, Aboriginal persons, members of sexual minorities, and persons with disabilities.

Get help from the experts.

Your career is our cause.

www.sciencecareers.org

- Job Postings
- Job Alerts
- Resume/CV Database
- Career Advice
- Career Forum

Science Careers
From the journal *Science* AAAS

Abstract Submission

In anticipation of what promises to be a mass gathering and celebration of European basic, translational and clinical studies, we invite the European cancer community to submit abstracts **before the regular abstract submission deadline of 29 April 2009.**

New Late-Breaking Abstract Policy

To help ensure that the very latest findings are presented for the first time at ECCO 15 – ESMO 34, we are also pleased to report that we have revised our Late-Breaking abstract submission policy and increased the number of proffered paper slots and presidential sessions.

The Call for Late-Breaking abstracts will run from 22 July - 5 August 2009.

More

To view the Advance Programme, consult the abstract submission programme and discover the many reasons for making ECCO 15 – ESMO 34 your must attend meeting this year visit:

www.ecco-org.eu

(select 'Congresses and conferences' > 'ECCO 15 – ESMO 34').

See you in Berlin for the premier European cancer meeting – The joint ECCO 15 and 34th ESMO Multidisciplinary Congress, 20 – 24 September 2009.

ESMO European Society for Medical Oncology

ECCO European CanCer Organisation

8th INTERNATIONAL

BIO FORUM & BIO EXPO JAPAN

ASIA'S LARGEST BIO EVENT

July 1 [Wed] – 3 [Fri], 2009
Tokyo Big Sight, Japan

Organised by: Reed Exhibitions Japan Ltd.

Official Sponsors : nature Science

CONTACT US IMMEDIATELY!

Don't miss the ASIA'S LARGEST BIO EVENT!

EXHIBITION

Book your Exhibition Space Now!
Expand your Business throughout Japan/Asia!

PARTNERING EVENT

Participate in Pharma-Partnering!
Meet your Potential Partners and Grow New Seeds!

700 Exhibitors!*
250 Conferences /Seminars!*
23,000 Visitors!*

*expected

for more information ››› http://www.bio-expo.jp/english/

bioexpo

Organised by
Reed Exhibitions

INT'L BIO FORUM & BIO EXPO JAPAN Show Management Reed Exhibitions Japan Ltd.
18F Shinjuku-Nomura Bldg., 1-26-2 Nishishinjuku, Shinjuku-ku, Tokyo 163-0570, Japan
TEL: +81-3-3349-8509 FAX: +81-3-3349-4922 E-mail: bio-pr@reedexpo.co.jp

THE DIADEM CHALLENGE

$75,000 Prize

The DIADEM Challenge – short for Digital Reconstruction of Axonal and Dendritic Morphology – will bring together computational and experimental scientists to test the most promising new approaches against the latest data in a real-world environment.

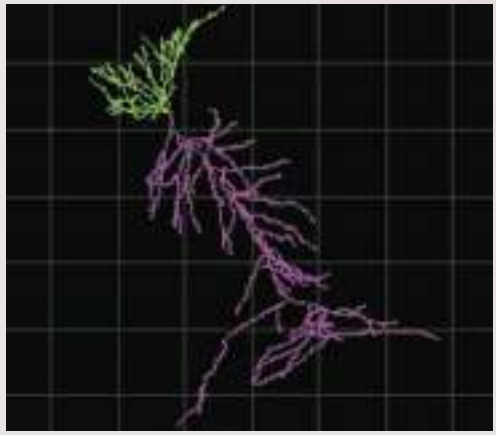

Visualization of a digital reconstruction.

The competition is open to individuals and teams from the private sector and academic laboratories.

Competitors will have a year to implement an algorithm for digital reconstruction of neuronal morphology and to test it against the manual reconstructions, the gold standard. Up to five finalists will compete in a tournament at a scientific conference at the Janelia Farm Research Campus in August 2010.

The competition is organized by the Allen Institute for Brain Science, the Howard Hughes Medical Institute (HHMI), and the Krasnow Institute for Advanced Study at George Mason University. The Allen Institute and HHMI have established the prize. The National Institutes of Health is providing support for a scientific conference that is independent of —but held in conjunction with—the tournament phase of the DIADEM Challenge.

The Timeline

Phase 1

April 9, 2009 to April 9, 2010

Contestants can download these data sets and develop software to reconstruct the neurons.

A panel of judges will then select the finalists for the second phase.

Phase 2

August 29–September 1, 2010

The finalists will meet at HHMI's Janelia Farm Research Campus for a live and real-time competition and scientific conference using previously unseen data sets.

For information on eligibility, the rules of the competition, organizers, and full details about the competition, visit www.diademchallenge.org.

NIH co-sponsorship of the conference does not represent an endorsement of the DIADEM Challenge, specific software products that may emerge from the competition, or the activities of the Allen Insitute, HHMI, or Krasnow Institute. Image from NeuroMorpho.Org (Ascoli, Nature Rev. Neurosci. 2006), cell NM1 (Brown et al., Neuroinformatics 2005).

POSITIONS OPEN

TENURE-TRACK FACULTY POSITION in Vascular Biology USC Keck School of Medicine

The USC/Norris Comprehensive Cancer Center of the Keck School of Medicine at the University of Southern California seeks applicants for a tenure-track Faculty position in vascular biology. The successful candidate will be supported by a strong startup package and housed within a new state-of-the-art research building. The USC Keck School of Medicine has strong research programs in cancer, genomics, and stem cells. Candidates with diverse backgrounds, including developmental biology, signaling pathways, translational research, and novel model systems, are encouraged to apply. Applicants should electronically submit curriculum vitae and a research plan in a single PDF file, and request three letters of reference to be sent, to**: Search Committee, c/o Isabel Lora** at **e-mail: lora_m@ccnt.usc.edu.**

USC is an Equal Opportunity/Affirmative Action Employer.

SCHOOL OF MEDICINE

University of California, Irvine offers a Neuroscience Epilepsy Research Postdoctoral Program Fellowship. The multidisciplinary postdoctoral program in epilepsy research has multiple openings for nontenured, academic-term appointments as **POSTDOCTORAL SCHOLAR.** The program supports diverse approaches to the understanding of the fundamental neurobiological processes leading to epilepsy and/or holding promise for its cure. Participating laboratories include:

Tallie Z. Baram, Ph.D., M.D.: Neuroplasticity, mechanisms of epileptogenesis, febrile seizure models, hyperpolarization activated ion channels, animal imaging.

Devin Binder, M.D.: Water transport and water channels in epilepsy, aquaporins, optical imaging.

Steven Cramer, M.D.: Functional imaging and robotics for identification and cure of excitotoxic and ischemic insults.

Christine M. Gall, Ph.D.: Neurotrophins, integrins, activity-dependent plasticity.

Alan L. Goldin, M.D., Ph.D.: Sodium channels, transgenic approaches, electrophysiology.

Gary Lynch, Ph.D.: Regulation of excitability and synaptic function and plasticity.

Charles E. Ribak, Ph.D.: Granule cell plasticity, neuroanatomy.

Mick Rugg, Ph.D.: Functional imaging of learning and memory circuits in health and disease.

Ivan Soltesz, Ph.D.: Electrophysiology, computational neurobiology, interneurons, and inhibition.

Martin Smith, Ph.D.: Novel signaling - agrin and neuronal excitability.

Oswald Steward, Ph.D.: Mechanisms of vulnerability to excitotoxicity.

John Weiss, M.D., Ph.D.: Excitotoxicity, calcium and zinc trafficking.

See **website: http://www.ucihs.uci.edu/epilepsyresearch/.**

These positions starting summer/fall 2009 are funded by an NIH training grant (T-32); eligible candidates *must be U.S. citizens or noncitizen nationals or must be lawfully admitted for permanent residence.* An M.D. or Ph.D. degree is required, and M.D.-qualified candidates are highly encouraged to apply. Salary is commensurate with experience and based on the Kirschstein-NRSA postdoctoral stipend levels for 2009. Candidates should submit resume and references to **e-mail: sara.johnson@uci.edu; Postdoctoral Search/Epilepsy, c/o Department of Anatomy and Neurobiology, University of California, Irvine, Irvine, CA 92697-1275.** Close: 60-day post.

The University of California, Irvine is an Equal Opportunity Employer committed to excellence through diversity and strongly encourages applications from all qualified applicants, including women and minorities.

POSITIONS OPEN

WISCONSIN NATIONAL PRIMATE RESEARCH CENTER DIRECTOR UW–Madison Graduate School

The University of Wisconsin–Madison is pleased to announce an exceptional employment opportunity as Director of the Wisconsin National Primate Research Center (WNPRC). The WNPRC is one of a network of eight unique national facilities for nonhuman primate research funded by the National Center for Research Resources (NCRR) of the National Institutes of Health (NIH). This center includes more than 250 WNPRC core and affiliated scientists, who conduct peer-reviewed research in primate biology with relevance to human and animal health.

The successful individual will have a doctoral degree in a biomedical sciences field, be a tenured or tenure-track faculty (or an individual who could be qualified as tenurable), and have a minimum of seven to 10 years of scientific leadership in a world-class research enterprise. The ideal candidate will have an exemplary research record and have an international reputation as a leader in his/her field.

Please see **website: http://www.ohr.wisc.edu/pvl/pv_061475.html** for the complete position description and how to apply.

Unless confidentiality is requested in writing, information regarding the applicants must be released upon request. Finalists cannot be guaranteed confidentiality. A criminal background check will be conducted prior to hiring.

UW–Madison is an Equal Opportunity/Affirmative Action Employer. We promote excellence through diversity and encourage all qualified individuals to apply.

POSTDOCTORAL FELLOWSHIPS in CARDIOVASCULAR RESEARCH and REGENERATIVE MEDICINE Feinberg Cardiovascular Research Institute Chicago, Illinois U.S.A.

Several Postdoctoral positions are available immediately at Northwestern University's Feinberg School of Medicine to study fundamental mechanisms of cardiovascular disease and regenerative medicine, with an emphasis on angiogenic growth factor pathways, progenitor/stem cell biology, epigenetics and inflammation, mechanisms and novel therapies for cardiac arrhythmias (for example atrial fibrillation), and ischemic tissue repair. M.D. and/or Ph.D. in a life science discipline and expertise in cell and molecular biology is required. Experience with relevant model systems is desirable. For details of the available positions and to apply, visit our **website: http://www.fcvri.northwestern.edu/career-opportunities/careers.**

Northwestern University is an Affirmative Action, Equal Opportunity Employer. Women and minority candidates are encouraged to apply. Hiring is contingent upon eligibility to work in the United States.

The College of Life Science at Fujian Normal University, China, invites applications for tenure-track faculty positions at the **ASSOCIATE PROFESSOR** and **PROFESSOR** levels. Individuals expert in the areas of microbiology, developmental biology, cell biology, and neurobiology are encouraged to apply. The positions offer an attractive startup package and excellent laboratory space. Candidates should have a Ph.D., suitable postdoctoral research experience, and an ability to develop innovative research programs.

For further information visit **website: http://life.fjnu.edu.cn** or contact: **Professor Yanding Zhang,** Dean of the college, at **e-mail: haitaoniu@fjnu.edu.cn.**

POSITIONS OPEN

ADIPOSE TISSUE AND LIPID BIOLOGIST

The Department of Animal and Poultry Sciences at Virginia Tech invites applications for a tenure-track **ASSISTANT PROFESSOR** position in adipose tissue biology. A Ph.D. in the life sciences is required. The candidate will be expected to develop an innovative, extramurally funded research program on aspects of adipose tissue biology and/or lipid metabolism that are relevant to growth, obesity, or the metabolic syndrome. The appointment will be 80 percent research and 20 percent teaching. Review of applications will begin May 15, 2009, and continue until the position is filled. Applicants can review the complete position description and must complete the faculty application online at **website: http://www.jobs.vt.edu (posting #080527).** A cover letter, curriculum vitae, a statement of research and teaching interests, and a list of three references with addresses, e-mail addresses, and telephone numbers must be included. Official transcripts should be mailed to: **Dr. Eric A. Wong, Department of Animal and Poultry Sciences, Virginia Tech, Blacksburg, VA 24061-0306. Telephone: 540-231-4737; e-mail: ewong@vt.edu.** *Virginia Tech is an Equal Opportunity/Affirmative Action Employer.*

CAREER OPPORTUNITY

Doctor of Optometry (O.D.) degree in 27 months for Ph.D.s in science and M.D.s. Excellent career opportunities for O.D./Ph.D.s and O.D./M.D.s in research, education, industry, and clinical practice. This unique program starts in March 2009, and features small classes and 12 months devoted to clinical care.

Contact the **Admissions Office, telephone: 800-824-5526** at the **New England College of Optometry, 424 Beacon Street, Boston, MA 02115.** Additional information at **website: http://www.neco.edu, e-mail: admissions@neco.edu.**

POSTDOCTORAL POSITION. NIH-funded position available at the University of North Carolina, Chapel Hill to investigate the regulation of translesion DNA synthesis in response to DNA damage and checkpoint signaling. For examples of related projects see *Mol. Cell Biol.* **26:**3527, 2006; *J. Biol. Chem.* **281:**30631, 2006; *Cell Cycle* **8:**125, 2009. Interested applicants with a Ph.D. and experience in biochemistry/cell biology should submit curriculum vitae, cover letter, and list of three references electronically to: **Dr. Cyrus Vaziri, e-mail: cvaziri@bu.edu.**

MARKETPLACE

INTERNATIONAL SCIENCE & ENGINEERING
VISUALIZATION CHALLENGE

CALL FOR ENTRIES

ENTRY DEADLINE: SEPTEMBER 15, 2009

SCIENCE AND ENGINEERING'S MOST POWERFUL STATEMENTS
ARE NOT MADE FROM WORDS ALONE

When the left brain collaborates with the right brain, science emerges with art to enhance communication and understanding of research results—illustrating concepts, depicting phenomena and drawing conclusions.

The National Science Foundation (NSF) and the journal *Science*, published by the American Association for the Advancement of Science, invite you to participate in the seventh annual International Science & Engineering Visualization Challenge. The competition recognizes scientists, engineers, visualization specialists and artists for producing or commissioning innovative work in visual communication.

Winners in each category will be published in the February 19, 2010 issue of *Science* and *Science* Online, and will be displayed on the NSF Web site.

Award Categories

- Photographs/Pictures
- Illustrations/Drawings
- Informational/Explanatory Graphics
- Interactive Media
- Non-Interactive Media

Complete Entry Information:
www.nsf.gov/news/scivis

R&D Systems
High Performance Antibodies.

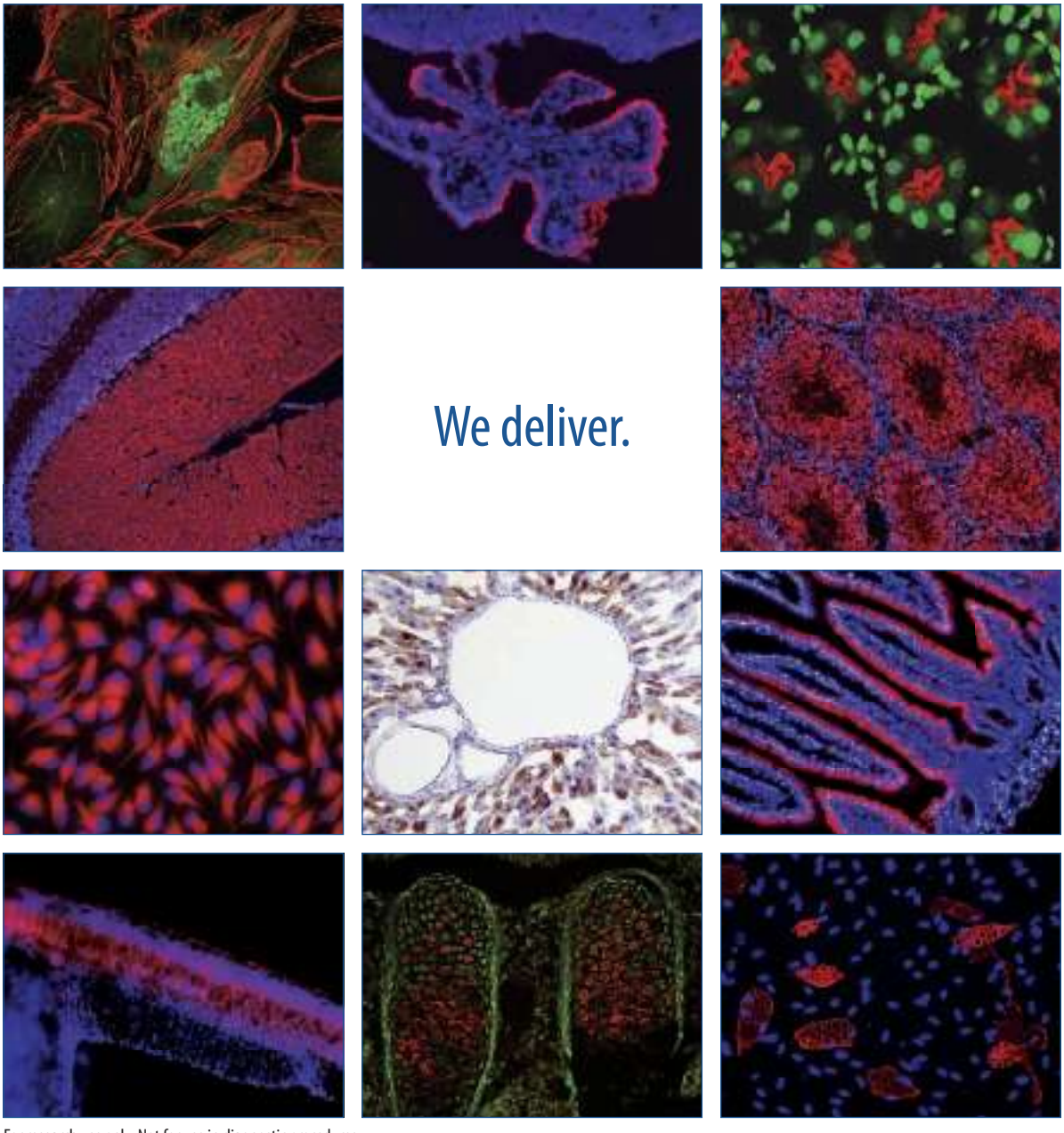

We deliver.

For research use only. Not for use in diagnostic procedures.

For details about the images above, please visit our website at www.RnDSystems.com/go/AntibodyAd

R&D Systems Tools for Cell Biology Research™

USA & Canada **R&D Systems, Inc.** Tel: (800) 343-7475 info@RnDSystems.com

Europe **R&D Systems Europe, Ltd.** Tel: +44 (0)1235 529449 info@RnDSystems.co.uk

Selection expanding weekly—visit **www.RnDSystems.com/go/request** to sign up for weekly new product updates.

R&D SYSTEMS®